SIMULATION OF ATMOSPHERIC FLOWS OVER COMPLEX TERRAIN FOR WIND POWER POTENTIAL ASSESSMENT

THÈSE N^{O} 1855 (1998)

PRÉSENTÉE AU DÉPARTEMENT DE GÉNIE CIVIL

ÉCOLE POLYTECHNIQUE FÉDÉRALE DE LAUSANNE

POUR L'OBTENTION DU GRADE DE DOCTEUR ÈS SCIENCES TECHNIQUES

PAR

Christiane MONTAVON

Dipl. Phys. ETH

originaire de Montavon (JU)

acceptée sur proposition du jury:

Prof. G. Sarlos, directeur de thèse
Dr A. Bottaro, rapporteur
Prof. D. Favrat, rapporteur
Dr J.-A. Hertig, rapporteur
Prof. D. Lalas, rapporteur
Prof. C. Schaer, rapporteur

Lausanne, EPFL
1998

A mes parents,

A Simon,

A la vie……

Abstract

When assessing the economic viability of a wind farm, the estimation of the on-site wind power potential is perhaps the most important step. The most common way of evaluating the wind power potential of an area of interest consists of making on-site measurements for a period of one year. In order to take account of the inter-annual variation of wind speed, the one year of data are normally correlated with data recorded at a reference site where long-term data (typically >10 years) are available. A correlation analysis is formulated for the concurrent data sets at the reference and prediction sites. This correlation is then used to transform the long-term wind speed at the reference site to the long-term wind speed that would have been expected at the prediction site had long-term measurements been made at this site.

An alternative approach is also used, which consists of establishing site-to-site relationships using a numerical model to simulate meteorological situations which are typical for the area of interest. These relationships are then used to transpose the known long-term wind statistics of the reference site to the prediction site. Such an approach is applied in this work to the region of Chasseral & Mt-Crosin. The wind data available for a period of 16 years at Chasseral are transposed to the Mt-Crosin site where they are then compared to the data measured at the location of the installed wind farm.

Over complex terrain, the linearised models traditionally used for wind power potential assessment fail to reproduce accurate wind fields. Therefore, to be applied to mountainous terrain such as that found in Switzerland, the approach relying on numerical simulation requires the development and validation of a numerical tool capable of simulating wind fields over complex topography. As the numerical model would have to deal with relatively steep slopes requiring a fine horizontal (50-100m) and vertical resolution (~5-10m in the lowest levels), a fluid dynamics model was used which solves the complete set of Navier-Stokes equations with k-ε turbulence closure. The standard version of the model used (CFX4) is modified in a novel way to extend its field of application so that atmospheric phenomena could be simulated which are typical of the meso-scale. The modified version solves the flow equations with the anelastic approximation (deep Boussinesq) and assuming a background rotation of the wind field (with the high altitude wind field following the geostrophic approximation).

In the first part of this work, the numerical model is validated. The results obtained in this phase show that for meteorological situations for which the wind at the ground is coupled to the high altitude wind, the numerical model is able to satisfactorily reproduce:

- the flow in the surface layer, reproducing the effects associated with the ground roughness, roughness change, or heat flux through the ground;

- the flow in the Ekman layer together with the interaction between the free flow thermal stability conditions and the boundary layer;
- the linear and non-linear effects associated with the perturbation induced by a mountain in a stably stratified flow.

In the second stage of this work, an extension of the standard Measure-Correlate-Predict method is presented to calculate the wind speed distribution at the prediction site, from transposition relationships and from the wind statistics at the reference site. The validity of the underlying assumptions is confirmed using concurrent data sets that were collected at both the reference and prediction sites. To evaluate the accuracy that can be achieved with the transposition assumptions, a back-prediction is performed using the transposition relationships obtained using the observations. Different types of transposition relationships have been investigated.

Finally, the transposition methodology is applied to calculate the wind speed conditions at Mt-Crosin from the Chasseral data, using the transposition relationships calculated by the numerical model for a range of meteorological situations typical for the area considered. The Mt-Crosin to Chasseral sector wind speed ratios calculated by the numerical model tend to slightly underestimate those observed. The mean wind speeds obtained from the transposition are underestimated by 7% to 18% at the three measuring mast locations on Mt-Crosin. The yearly energy output that can be produced by a wind turbine in these conditions is underestimated by 8% to 36%. For a further period, the actual energy production of the three installed wind turbines has been compared with the model prediction at hub height, which showed that the transposition results underestimate the actual yearly production by 22% to 24%.

From the transposition of the long-term data at Chasseral (16 years), with the relationships obtained by the numerical model, a wind power potential of between 470 MWh/year (Côte Est) and 596 MWh/year (Côte Nord) is predicted using the characteristics of a Vestas-V44 wind turbine.

From the work presented here, it appears that for well-exposed sites such as those located along the Jura Crest, the methods developed are able to give a wind power potential prediction with a similar accuracy as a one year measurement campaign performed on site.

Résumé

Lors de l'établissement de la rentabilité économique d'un parc éolien, la détermination du potentiel de vent à disposition sur le site constitue une étape primordiale. La pratique la plus courante pour évaluer le potentiel éolien d'une région particulière consiste à effectuer des mesures sur le site sur une période d'une année. Afin de diminuer l'incertitude du résultat associée à la variabilité des conditions de vent d'une année à l'autre, les données annuelles sont corrélées avec des données enregistrées sur une plus longue période (typiquement > 10 ans) à une station de référence. Les relations obtenues par corrélation sont utilisées pour transformer les données à long terme au site de référence pour retrouver les données à long terme au site de prédiction.

Une autre approche est aussi utilisée qui consiste à établir des relations entre les conditions de vents entre un site de réference et un site d'intérêt par l'intermédiaire de la simulation numérique des situations météorologiques typiques de la région en question. Ces relations sont ensuite utilisées pour transposer sur le site d'intérêt les statistiques de vent connues pour le long terme au site de référence. Une approche similaire est appliquée dans le présent travail pour la région de Chasseral & Mt-Crosin. Les 16 ans de données disponibles à Chasseral sont transposées sur le site de Mt-Crosin, où elles sont ensuite comparées avec les données mesurées à l'emplacement du parc éolien installé sur le site.

En terrain accidenté, les modèles linéarisés, utilisés traditionnellement pour l'estimation du potentiel éolien, ne reproduisent pas les champs de vent de manière satisfaisante. C'est pourquoi, pour être appliquée aux terrains complexes tels que ceux rencontrés en Suisse, l'approche se basant sur la simulation numérique nécessite le développement et la validation d'outils numériques aptes à simuler les champs de vents en terrain accidenté. Compte tenu des pentes relativement élevées et de la résolution requise (50-100m en horizontal, ~5-10m en vertical) avec lesquelles le modèle numérique devra fonctionner, notre choix s'est porté sur un modèle de dynamique des fluides complet, résolvant les équations de Navier-Stokes non-linéaires ainsi qu'un modèle de turbulence de type k-ε. Des modifications ont été apportées à la version standard du modèle retenu (CFX4) de manière à pouvoir étendre son champ d'application à la simulation de phénomènes atmosphériques caractéristiques de la méso-echelle. Ces modifications constituent un apport original de la thèse. Dans la version modifiée, les équations sont résolues avec l'approximation anélastique ('deep Boussinesq'). Une hypothèse supplémentaire admet que l'écoulement atmosphérique en altitude vérifie l'approximation géostrophique.

Dans la première partie de ce travail, l'essentiel de l'effort a été consacré à la validation du modèle numérique. Les résultats obtenus dans cette phase ont permis

de montrer que pour les situations météorologiques où le vent au sol est couplé au vent en altitude, le modèle numérique est capable de reproduire de manière satisfaisante:

- l'écoulement dans la couche de surface en reproduisant les effets associés à la rugosité, au changement de rugosité, au flux de chaleur au sol
- l'écoulement dans la couche d'Ekman ainsi que l'interaction entre les conditions de stabilité thermique de l'écoulement libre et la couche limite
- les effets linéaires et non-linéaires associés à la perturbation induite par une montagne sur un écoulement thermiquement stable.

Dans la deuxième phase du travail, une extension des méthodes de Mesure-Corrélation-Prédiction a été proposée pour calculer la distribution de vitesse au site de prédiction. La validité des hypothèses à la base de la transposition a été vérifiée à partir de données simultanées relevées au site de référence at au site de prédiction.
Afin d'évaluer la précision de la prédiction atteignable avec les hypothèses de transposition, une application de la méthode a été effectuée à l'aide de relations de transposition établies à partir des observations. Différents types de relations de transposition ont été testés.

Finalement, la méthode de tranposition a été appliquée pour recalculer les conditions de vent à Mt-Crosin à partir des données de Chasseral, en utilisant des relations de transposition calculées à l'aide du modèle numérique pour une gamme de situations météorologiques typiques de la région considérée. Les rapports de vitesse entre les sites de Mt-Crosin et Chasseral calculés par la modèle sous-estiment légèrement ceux observés en moyenne par secteur. Les vitesses moyennes obtenues suite à la transposition des données de Chasseral par les résultats du modèle numérique sont sous-estimées de 7% à 18% aux trois mats de mesure sur le site de Mt-Crosin. L'énergie annuelle qui peut être produite par une éolienne dans les mêmes conditions de vent est sous-estimée de 8% à 36%. Pour une autre période de mesure, les données de production des trois éoliennes installées ont été comparées avec les prévisions du modèle à la hauteur de la nacelle. Les résultats de la transposition sous-estiment les productions réelles annuelles de 22% à 24%.

La transposition des 16 ans de données au site de Chasseral en utilisant les résultats du modèle numérique prédit un potentiel éolien pour le site de Mt-Crosin variant entre 470 MWh/an (Côte Est) et 596 MWh/an (Côte Nord), pour la caractéristique de puissance d'une machine de type Vestas-V44.

Les travaux effectués dans le cadre de cette thèse montrent que pour des sites exposés tels ceux situés sur les Crêtes du Jura, les méthodes développées permettent d'évaluer le potentiel éolien sur un site avec une précision du même ordre de grandeur que celle qui peut être obtenue par une campagne de mesure d'une année sur le site même.

Acknowledgements

This PhD research was funded by EPFL and would not have been possible without the help and contribution from many people, to whom I wish to express my gratitude with these few lines:

- Prof. G. Sarlos, who gave me the opportunity to carry out this research and be part of his wind engineering research group. In addition to the infrastructure he provided, I also appreciate all the freedom he gave me so that I could define the research work I wanted to carry out.
- Dr. J.A. Hertig who introduced me to the topics of atmospheric numerical simulation and kindly allowed me a digression in the direction of wind energy. He followed this thesis along and provided a substantial part of the supervising. I enjoyed his enthusiasm and the fact that he is a real fountain of ideas.
- Dr. Ch. Alexandrou, for his everyday support and valuable advice. He gave me the benefit of his knowledge in the field of boundary-layer parameterisation and I had some very enjoyable exchanges with him.
- Dr. J.-M. Fallot, for his enlightening comments and remarks on the climatology of mountainous areas
- R. Perez-Suarez for starting the work on the MCP methods and for his help processing some of the data and producing some of the figures presented in this work
- Dr. G. De Cesare and Dr. F. Hermann for introducing me to the subject of visualisation with AVS
- A. Clappier, and Dr. P. Thunis for fruitful discussions about mountain waves
- MM. S. Kunz and M. Baumgartner from the METEOTEST office for kindly allowing me access to the Mt-Crosin wind measurements.
- M. Vollenweider from the FMB/Juvent company for having provided the wind turbine production data, and for being a constant source of information about the Mt-Crosin wind farm.
- The professors W. Graf, A. Bottaro, D. Favrat, D. Lalas and C. Schaer for having accepted to be part of the referee panel.
- The Swiss meteorological office for providing the access to the ANETZ database.

Also I should not forget to thank all my other colleagues, who helped at several stages and who made the everyday working atmosphere warm and friendly and not merely an entity to be modelled on a three dimensional grid.

And last but not least, I am extremely grateful to Simon for his patience and attention during these long months, for his precious help and careful reading of the manuscript … and for his kicks when I needed to be pushed ahead!

LIST OF SYMBOLS AND ABBREVIATIONS

AGL	Above ground level
ANETZ	Automatic measuring network run by the Swiss meteorological office
ASL	Above sea level
CCCT	Modified quadratic upwind advection scheme
CP	Centre point location of the Askervein Hill
CFX4	Flow solver used in this contribution
CHL	Chasseral
HT	Hill top location on Askervein Hill
HUW	Higher upwind advection scheme
ISM, SMA	Swiss meteorological office
LASEN	Laboratory of Energy systems
LES	Large eddy simulation
MCP	Measure-Correlate-Predict method
MMCP	Matrix Measure-Correlate-Predict method
MTC	Mt-Crosin
PDF	Probability density function
TKE	Turbulent kinetic energy
UTC	Universal time coordinates
WA^{s}P	Wind Atlas Analysis and Application Programme
WT1, WT2, WT3	Wind turbine no1 to no3

Roman symbols

a	1. Constant appearing in the Alexandrou formulation	[-]
	2. Mountain half-width	[m]
$a(\cdot)$	Wind speed ratio	[-]
a_1, a_2, a_3	Factors in the third order polynomial entering the expression for the u velocity component	[-]
A_0, B_0	Parameters appearing in the resistance law	[-]
A_1, B_1	Parameters appearing in the resistance law	[-]
b_1, b_2, b_3	Factors in the third order polynomial entering the expression for the v velocity component	[-]
B	Parameter appearing in the Alexandrou formulation	[-]
B'	Parameter appearing in the Coles velocity defect law	[-]
B_N	Constant in the velocity profile for flow over rough surfaces ($B_N = 8.5$)	[-]
$c = 1/a$	1. Constant appearing in the Alexandrou formulation	[-]
	2. Speed of sound	
c_i	Intercept of the site-to-site relationship	[m/s]
C	Constant in the velocity profile for flow over smooth surfaces ($C = 5$)	[-]
C_G	Geostrophic drag coefficient	[-]

$C_h, C_R, \tilde{C}_R, C_L, \tilde{C}_L, C_N$ $\tilde{C}_N, C_s, C_i, C_{sr}, C_{ir}$	Empirical constants in the Zilitinkevitch formulation	[-]
$C_1,\ C_2,\ C_3,\ C_\mu$	Turbulence model constants	[-]
C_f	Local drag coefficient	[-]
c_p, c_v	Specific heat at constant pressure, and constant volume	[J/kg K]
$E_1,\ E_m,\ E_{wf}$	Yearly energy output	[MWh/year]
$E,\ E_\theta$	Wall constant in turbulence model (default value $E = 9.793$)	[-]
$f(v), h(v)$	Wind speed distribution at the reference, and prediction site (all sectors included), respectively	[%]
f	Coriolis parameter ($f = 10^{-4}\,s^{-1}$ at 45° latitude)	[1/s]
Fr	Froude number	[-]
$f_\theta(v)$	Wind speed distribution for the sector θ	[%]
F_i	External body force	[N]
$g(\theta)$	Sector distribution	[%]
$\vec{g}$	Gravity vector	[m/s^2]
G	1. Buoyancy production term in the turbulence model	[kg/ms^3]
	2. Geostrophic wind speed	[m/s]
h	1. Boundary layer height	[m]
	2. Mountain profile	[m]
$H,\ h$	Total and static enthalpy of the fluid	[J/kg]
h_m	Maximum mountain height	[m]
h_t	Wind turbine hub height	[m]
$J_\theta,\ J_{gr}$	Potential temperature flux	[K kg/m^{2}s]
k	1. Turbulent kinetic energy	[m^2/s^2]
	2. Wave number	[1/m]
k_s	Equivalent sand roughness	[m]
K_M, K_H	Turbulent viscosity for the wind speed, and heat $K_M = \mu_{eff}/\rho$, $K_H = \mu_{eff}/(\sigma_H \rho)$	[m^2/s]
l	Scorer parameter	[1/m]
l_e	Non-dimensional dissipation length	[-]
L	Monin-Obukhov scaling length	[m]
L_x, L_y, L_z	Simulation domain dimensions in the *x*-, *y*-, and *z*-direction	[m]
m	Mole mass *m=28.9*	[g/mol]
m_i	Slope of the site-to-site relationship	[-]
M	Difference of the flow Mach number from unity	[-]
N	Brunt-Väisälä frequency ($N = \sqrt{g/\theta \cdot \partial\theta/\partial z}$)	[1/s]
p'	Pressure difference relative to hydrostatic reference state	[N/m^2]
p	Total fluid pressure	[N/m^2]
p_0	Reference total pressure at sea-level $p_0 = 1.013 \cdot 10^5$	[N/m^2]
p_h	Hydrostatic reference pressure	[N/m^2]
$P = (p_{i,j})$	Population matrix	[%]
$P(v)$	Power characteristics of a wind turbine	[kW]
P	Shear production term in the turbulence model	[kg/ms^3]
r	Correlation coefficient	[-]

R	Gas constant for air $R = 287$	[J/kg K]
R^*	Universal gas constant $R^* = 8.31$	[J/K mol]
R_x	Reynolds number at the fetch x behind the entrance (for flow over a plate)	[-]
Ro	Rossby number $Ro = G/(fz_0)$	[-]
S	1. Source/sink in a conservation equation	[kg/s m^3] *[var]
	2. Heterogeneity of the atmosphere $S = \frac{\partial}{\partial z}\ln(\frac{M}{\rho})$	[1/m]
t	time	[s]
T	Real temperature	[K]
T_M , $T_{M,\theta}$	Wall multiplier for wall treatment of velocity and temperature in turbulence model	[kg/m^2 s]
u	1. Wind velocity component along x	[m/s]
	2. Internal energy	[J/kg]
u^+	Non-dimensional wind speed	[-]
u_*	Friction velocity	[m/s]
u', v', w', θ'	Fluctuating part of the velocity components, and potential temperature	[m/s]
u_g, v_g	Geostrophic wind velocity component along the x- and y- direction	[m/s]
U_i	Mean wind speed	[m/s]
U_{in}	Inlet wind speed	[m/s]
$U_{i,geo}$	Geostrophic velocity component along i co-ordinate	[m/s]
U_∞	Wind speed in the free flow	[m/s]
v	Wind velocity component along y	[m/s]
v_{pred}	Prediction site wind speed	[m/s]
v_{ref}	Reference site wind speed	[m/s]
v_{ci} , v_{co}	Cut-in and cut-out wind speed for a wind turbine	[m/s]
w	Wind velocity component along z	[m/s]
$W = (w_{i,j})$	Population matrix, normalised according to the reference site wind direction	[%]
x_i	Space co-ordinates	[m]
z^+	Non-dimensional distance from the wall	[-]
z_0^+ , z_θ^+	Wall constant in turbulence model (default value $z_0^+ = 11.225$)	[-]
z_0	Roughness length	[m]
$z_{0,s}$, $z_{0,r}$	Roughness length for smooth, and rough terrain, respectively	[m]
$Z = (z_{i,j})$	Population matrix, normalised according to the prediction site wind direction	[%]

Greek symbols

α	1. Cross isobar angle in the Ekman spiral 2. Specific volume of a gas	[°] [m^3 mol /kg]
$\alpha_2, \beta_1, \beta_2, \gamma_1, \gamma_2$	Constants appearing in the non-dimensional surface profiles for stable/unstable surface layers	[-]
δ	Non-dimensional rotation rate	[-]
ε	Turbulent dissipation rate	[m^2/s^3]
φ	Scalar model variable (e.g. potential temperature)	[scalar]
Φ_M, Φ_H	Non-dimensional gradient functions for the wind speed and potential temperature surface layer profiles	[-]
γ	Lapse rate ($\gamma = -\partial T / \partial z$)	[K/m]
$\tilde{\gamma}$	$\tilde{\gamma} = c_P / c_v$	[-]
Γ	Scalar diffusion coefficient	[kg/ms]
η	Non-dimensional height above ground $\eta = z / h$	[-]
η_T , η_{avail} , η_{array} , η_ρ	Wind turbine efficiencies related to turbulence, availability, position in the WT array, air density	[%]
κ	Von Karman constant	[-]
λ	Fluid thermal conductivity	[W/mK]
$\lambda = N / \lvert f \rvert$	Non-dimensional stability parameter characterising the free flow	[-]
μ	Molecular viscosity	[kg/ms]
μ_T	Turbulent viscosity	[kg/ms]
$\mu = u_* / \lvert f \rvert L$	Non-dimensional stability parameter characterising the surface layer	[-]
$\mu_{eff} = \mu + \mu_T$	Effective fluid viscosity (molecular + turbulent viscosity)	[kg/ms]
ν	Kinematic viscosity	[m^2/s]
θ	1. Wind direction, 2. Potential temperature $\theta = T(p_0 / p)^{R/C_p}$	[°] [K]
θ^+	Non-dimensional potential temperature	[K]
θ_w	Wall potential temperature	[K]
θ_h	Hydrostatic reference potential temperature	[K]
θ_*	$\theta_* = -\overline{w'\theta'} / u_*$	[K]
ρ	Air density	[kg/m^3]
ρ_h	Hydrostatic density	[kg/m^3]
σ_{ij}	Stress tensor	[N/m^2]
σ_H , σ_θ , σ_k , σ_ε	Turbulent Prandtl number for heat, potential temperature, turbulent kinetic energy and dissipation rate	[-]
τ	Shear stress	[N/m^2]
τ_s	Shear stress upwind of the roughness transition	[N/m^2]
ζ	Non-dimensional height for the surface layer ($\zeta = z / L$)	[-]
Ψ_M, Ψ_H	Non-dimensional function defining the wind speed and temperature profile in the stable/unstable surface layer	[-]

Mathematical operators

$\delta_{i,j}$	Kronecker symbol
$\partial / \partial x$	Partial derivative according to x
$\Gamma(x)$	Gamma function
$\vec{\nabla}$	Gradient operator
$O()$	Order of magnitude
$\hat{()}$	Fourier transform
$\bar{()}$	1. Average operator 2. Correlation

TABLE OF CONTENTS

List of appendices

1 Introduction

When assessing the economic viability of a wind farm, the estimation of the on-site wind power potential is perhaps the most important step. The most common practice to evaluate the wind power potential of an area of interest consists of performing on-site measurements. To obtain a proper representation of the seasonal variations of the prevailing wind conditions, one year of data collection is the minimum period required. But even then, uncertainty in the evaluated potential remains and can be non-negligible, due to the inter-annual variation of the wind conditions. Cherry (1980) found from data collected at potential wind farm sites which were at exposed locations that the uncertainty in the estimates of the site-means drops quickly in the first few years, with typical values of 12% of the mean wind speed after one year reducing to 6-7% after 4 years[1]. The corresponding uncertainty for the energy density is typically 30-35% after one year going down to 17-22% after 4 years. Further increasing the length of the recording period led to a marginal reduction of the uncertainty in the estimated wind speed and energy density of the site. Salmon and Walmsley (1997) came to similar conclusions from the analysis of wind speeds for 5 pairs of stations chosen to cover various types of terrain and topography conditions. They concluded that an absolute minimum of 1 year of monitoring is needed. Increasing the monitoring period to two years significantly reduced the uncertainty of the results, while using a monitoring period between 1 and 2 years may worsen the estimates compared to only 1 year of data.

To improve the quality of the wind power estimate at the prediction site, the yearly data are often extrapolated to the long term by correlating them with data recorded over a longer period (typically ten years) at a reference site. This long-term extrapolation is based on a statistical correlation performed on the concurrent data sets recorded at both the reference and prediction sites. Using the relationships between both sites obtained from the correlation, the average wind conditions at the prediction site are reconstructed from the long-term data at the reference site (see the illustration in Figure 1.1). The accuracy that can be obtained with these so-called Measure-Correlate-Predict methods (MCP) strongly depends on the climatological conditions of the area as well as on the distance between the reference and prediction site. According to Salmon and Walmsley (1997) who looked at pairs of stations separated by 60 to 170 km, using 1 year of data leads typically to an error of the order of 4-10% in the average wind speed estimate. Taking into account data from a nearby

[1] The order of magnitudes of the values given here apply to extratropical regions and should not be considered as representative for tropical regions.

reference station to make a long-term extrapolation reduces the error by about one third.

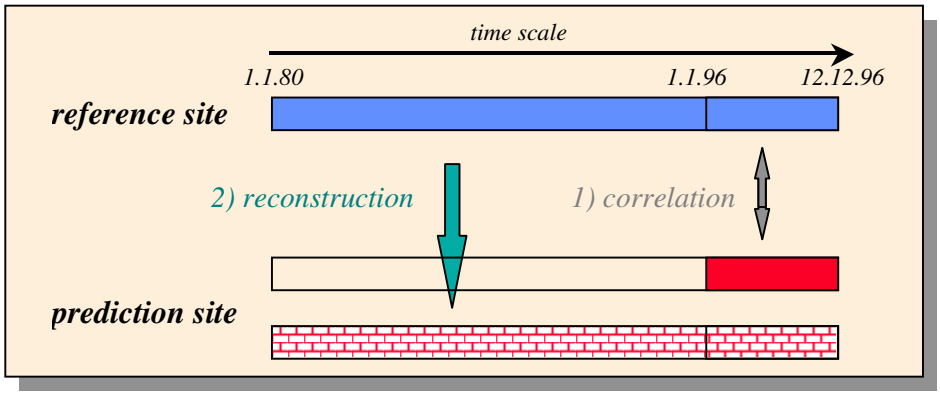

Figure 1.1. Illustration of the Measure-Correlate-Predict methods used to reduce the uncertainty in the long-term prediction inferred from short-term data collected at the prediction site. Relationships between the reference and prediction site are obtained from correlation of the concurrent datasets. These relationships are used to *reconstruct* the long-term data at the prediction site using the *actual* long-term data at the reference site.

To evaluate the wind power potential of a site from available long-term data at a nearby site, another approach has been proposed, which makes use of a numerical simulation of the wind conditions over the area of interest to establish relationships between the reference and prediction site. The main advantage of operational numerical models is the time (and possibly cost) saving relative to a complete field measurement programme. The second advantage is the ability to assess the wind speed at several locations around the main area of interest.

Another way to take advantage of numerical models is to use them in conjunction with a classification of the meteorological situations prevailing over the area of interest. The models are then used to simulate all of the situations entering the classification, and the wind statistics at a location of interest are obtained by combining the various simulated flow fields, weighed by the probability of occurrence of the meteorological situation. The same procedure is then applied at the location of the reference station, which in this case is only used to check the quality of the method. This approach has been used e.g. by Adrian et al (1996), using the model KAMM (Adrian & Fiedler, 1991) and by Mengelkamp et al (1996) who used the model GESIMA (Kapitza & Eppel, 1992 and Eppel et al, 1995). Both classified the type of situation by performing a cluster analysis on a limited number of parameters

describing the atmospheric state. From the simulations of the 120-140 different situations, they reconstructed the ground wind statistics.
The quality of this method obviously depends on the representativeness of the classification used and on the model's ability to simulate the wind fields. Similar studies have been performed in the realm of climate downscaling using regional hydrostatic models initialised from ECMWF analyses (Frey-Buness et al, 1995, and Fuentes and Heimann, 1996). These showed that 'statistical-dynamical downscaling remains an efficient alternative for diagnostic climate studies'. Fuentes and Heimann (1996) showed that some features of the wind and temperature variables close to the ground could be reproduced. They also underline that some discrepancies remain between the observations and predictions confirming the need for a classification of the meteorological situations including all the situations representative for the region. Depending on the area of interest, this implies that transient situations also need to be included in the classification.

Over relatively flat terrain, a program like WA^{S}P (see 'European Wind Atlas' by Troen and Petersen, 1989) can be used to obtain a reasonable estimate of the wind power potential for a region, from sector-wise histograms of wind speed frequencies at the reference station. This program is able to account for the effects of obstacles, roughness and topography. It has been shown however that in very complex terrain, the linearised flow models, one of which is used in the WA^{S}P package, are not able to satisfactorily reproduce the effects of the topography on the flow fields (see e.g. Meteonorm Vent, 1990, Botta et al, 1992, and Barnard, 1991). Over complex terrain, 3D full Navier-Stokes solvers with a turbulence parameterisation scheme appear to be more appropriate tools for the simulation of flow configurations showing flow separation and strongly non-linear effects (see e.g. Raithby & Stubley, 1987 or Alm & Nygaard, 1993). Some developments in the simulation of atmospheric flow fields over complex terrain have already been made at the Laboratory of Energy systems, EPFL, using the Navier-Stokes solver ASTEC (Lembessis, 1992, Hertig, 1993, Montavon, 1995).

The present work is an attempt to further develop and validate a numerical tool together with a methodology for the wind power potential evaluation over very complex topography such as that encountered in Switzerland.
The questions arising in this context are essentially of two kinds:

1. Do we have a numerical model which is able to reproduce the wind conditions over topography like that of the Swiss Jura or the Alps with sufficient accuracy to

be used for wind power potential assessment? What kind and what amount of information are required to feed the numerical model?

2. Can we reconstruct the wind statistics at a location of interest from the statistics at a reference site using simple relationships between both sites? If so, what kind of relationships can be observed? How should we define the numerical simulations to be able to reproduce them? How many different types of meteorological situations do we need to consider in order to reproduce the local climatology? How can we classify these situations?

In order to solve flow fields at a very fine resolution (down to 50 m in the horizontal with the ability to cope with steep slopes and narrow valleys, it is necessary to use a non-hydrostatic model (Wippermann, 1981). The numerical model that is chosen for the present work is CFX4 (CFX, 1997), a general purpose Navier-Stokes solver. Besides its robustness and powerful meshing facilities, it also offers large flexibility to the user, allowing the introduction of additional source terms in the equations and permitting supplementary equations to be solved.
The experience acquired with the first generation ASTEC code was transferred to the CFX4 solver within this work. Some additional implementations were included in the fluid model so that it could deal with the simulation of atmospheric flow fields covering several kilometres in the vertical. This involved the modification of the energy conservation equation, which has been formulated in terms of the potential temperature, the implementation of modified buoyancy terms in the vertical velocity equation and in the turbulence parameterisation. The option to work with variable ground roughness has been introduced and the Coriolis force has been implemented. Section 5.2 gives a summary of the standard version of the numerical model, while the modifications are presented in Section 5.3.

Before trying to answer the first question above for complex terrain conditions, we performed several validation tests to assess CFX4's ability to reproduce more simple flow configurations. These validations are presented in Appendix A to D, starting from the most simple flow configuration and increasing the complexity as one progresses through the appendices. The choice of presenting the validations in appendices was made to increase the readability of this work, and does not suggest that they be of minor significance. In fact, they represent most of the original contribution of the thesis.

The first tests deal with the model's ability to reproduce a 2D neutral boundary layer growth over a flat plate for various ground roughness conditions, as well as with

roughness change. These tests were done without including the Coriolis force and the results are shown in Appendix A.

After having shown that the model is able to successfully reproduce the effect of ground roughness over flat terrain, we proceeded with the validation of the modifications made to the $k-\varepsilon$ model and the inclusion of the Coriolis force. To that end, simulations over flat terrain were performed to see how the Ekman spiral is induced depending on the stability conditions of the free flow and stability conditions of the surface layer. The simulated boundary layer and Ekman spiral development were compared to analytical formulations, to other numerical models or to measurements depending on their respective availability. In particular, it was shown that the developments described by Zilitinkevich et al. (in press), who propose a parameterisation of the Ekman spiral depending on the roughness conditions at the ground, on the free flow stability (through the use of the Brunt-Väisälä frequency) as well as on the heat flux conditions at the ground (through the Monin-Obukhov length), are able to provide u and v profiles for the boundary layer, which are in good agreement with the numerical model results.

The next series of tests concerned the implementation of the potential temperature equation and its coupling with the vertical velocity equation. To that end, simulations were performed over a 2D theoretical mountain feature perturbing an incoming horizontal stably stratified atmospheric flow. A comparison of the simulated flow fields with analytical solutions from linear mountain wave theory was done for the quasi-neutral and for the hydrostatic case. For non-hydrostatic situations as well as for strongly non-linear flow situations such as the January 1972 Boulder foehn event, the comparison was made with other numerical models or with observations. These results are given in Appendix C.

To end the validation part for flow situations governed by the geostrophic wind, a 3D validation was performed over the Askervein Hill site (located in Scotland) which has the advantage of having a very well documented measurement campaign and against which many numerical models have been tested. The results for this 3D situation are presented in Appendix D.

A way to evaluate the wind power potential on the site is presented in Chapter 2 together with a transposition methodology to obtain the wind distribution and the underlying assumptions.

For the part of the work dealing with the application of the proposed methodology, we concentrated on the complex terrain area around the site of Chasseral and Mt-Crosin, along the Jura chain. The reason for the choice of the Mt-Crosin site is the availability of wind data that were collected during the feasibility study preceding

the recent installation of 3 wind turbines on the site. The site of Chasseral, with 15 years of data, was selected as a reference station because of its proximity to the Mt-Crosin site and mostly because it is the highest summit in the area. It therefore has the advantage of being well coupled to the high altitude wind conditions over the area. Details about the region of interest can be found in Chapter 3.

The validity of various types of relationship which are postulated to relate the wind speed at the prediction and reference site is investigated in Chapter 4 using concurrent datasets recorded at the locations of Chasseral, Mt-Crosin, Neuchâtel and La Chaux-de-Fonds. The accuracy that can be achieved for both the average wind speed and wind energy when performing a wind data transposition is evaluated by means of back predictions.

Finally, the numerical model performance in reproducing the observed relationships between the prediction and reference site is investigated. This starts with the presentation in Chapter 6 of simulation results that were performed over the Chasseral and Mt-Crosin area for two wind directions (essentially parallel and perpendicular to the Jura chain) and for various atmospheric conditions. This is followed in Chapter 7 by the derivation of site-to-site relationships calculated by the numerical model and the application of the transposition methodology to obtain the wind speed distribution at Mt-Crosin from the wind direction and wind speed distribution of Chasseral. A comparison of the predicted wind power potential for the Mt-Crosin site with the actual production data is made for the year 97.

A more detailed sensitivity study testing the effect of the atmospheric and ground conditions on the simulated transposition relationships is presented in Chapter 8. This allows us to assess the limitations associated with the proposed transposition methodology and to draw some conclusions about how to enhance the method in future developments.

The conclusions summarise the achievements realised in this work and give an overview of further developments that could be made in future work.

2 Wind power potential evaluation and transposition methodology

The wind speed distribution (also called 'probability density function' for the wind speed) at a potential wind power installation site is usually determined by performing a measurement campaign on the site itself for typically one year. To reduce the uncertainty due to the inter-annual variation of climatic conditions, some more work is usually done to take into account additional information about the local climate that would be representative in the long term.

This can be done in essentially two ways:

I. The first way consists of assuming that site-to-site relationships exist such that the wind climate at the prediction site can be obtained from transposing the wind climate of the reference site. The nature of the assumed relationships might be physical, as is postulated when using a numerical model to try to reproduce them, or purely statistical as in the application of measure-correlate-predict (MCP) methods.

II. The second way, also called 'statistical-dynamical approach' (Adrian et al, 1996, Mengelkamp et al, 1996), assumes that the local wind conditions are determined by the frequency distribution of larger scale atmospheric conditions that can be classified. This approach relies on the following assumptions:

    1. an atmospheric situation can be characterised by a limited number of parameters, like the geostrophic wind speed and direction, the vertical thermal stratification of the atmosphere, the ground heat flux, etc…
    2. the synoptic scale system is modified by the local topography and flux conditions and this effect can be reproduced by a meso-scale model (top-down approach)
    3. two situations with the same set of parameters lead to the same flow pattern at the ground
    4. both the reference and prediction sites are under the influence of the same atmospheric situation

    If these assumptions are true, then we can hope to classify the meteorological situations and attribute them a probability of occurrence. Simulating with a numerical model all the situations in the classification should allow us to reconstruct the wind distribution at the site of interest. This procedure is summarised in Figure 2.1, inspired by Mengelkamp et al (1996). In this second approach, the ground-based measurements are essentially used to

assess the quality of the procedure. These locations with well known statitistics can also be used to analyse the results in more details and help for the identification of particular effects that might not be properly accounted for when using a too simple classification. In this sense, they could give an indication of how the classification should be refined and what kind of additional parameter it could include.

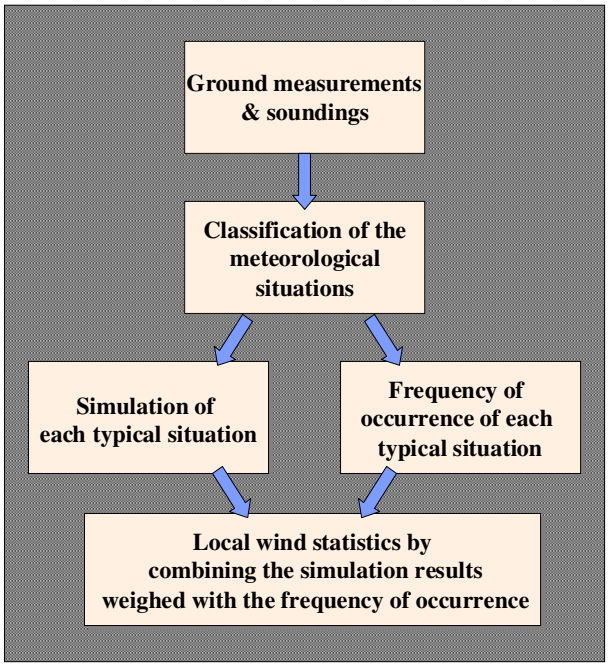

Figure 2.1. Schematic of the statistical-dynamical approach to obtain the wind climate over an area of simulation.

No attempt is made in this work to reconstruct the wind statistics at the prediction site using the 'statistical-dynamical approach' mentioned above. To do this we would require a classification of the atmospheric situations occurring over the area that would be made according to parameters appropriate for the numerical simulation. De Buman (1994) showed that the existing classifications, such as that proposed by Schüepp (1979) or that of Hess and Brezowsky (1977) adapted by Perret (1987) to the case of Switzerland, all show the same problem in this context: being proposed with the purpose of classifying daily conditions, they are not able to take into account the dynamical processes that determine the *local* wind conditions. Therefore, they cannot be used as useful classifications in the sense of the 'statistical-dynamical' approach described above. To be able to reproduce the local development of the wind conditions, it would be preferable to classify the situations in terms of homogenous events.

Kaufmann (1996) performed a cluster analysis on hourly data from 49 weather stations in an area covering some 50x50 km and located some 50 km to the north-east of our domain of interest (area around Basel). He obtained 12 clusters determining 12 flow patterns at ground from his classification. When trying to identify the obtained clusters using the classification proposed by Dütsch (1985) or that by Schüepp (1979) or the one by Hess and Brezowsky (1977), he could not find any obvious correspondence. The area for which the cluster analysis was done is quite close to the region of Chasseral and presents a similar kind of topography, since it is crossed by the Jura chain. We were therefore expecting that the classification obtained there could also be used for the Chasseral area. Using the classification for the purpose of simulation is not trivial however, since it appears, as shown by Kaufmann, that the situations belonging to a single cluster can be attributed to several high altitude wind directions (implying sometimes a rotation of 180°!). Also he did not obtain a good correlation of the vertical temperature gradient with the cluster category. These observations mean either that

- 12 clusters are not enough to describe the local climatology so that there is a good correspondence between the physical parameters categories and the cluster type,
- or that the physical parameters like geostrophic wind direction or vertical temperature gradients are not appropriate to describe the atmospheric situations (the vertical temperature gradient might be better considered in association with the geostrophic wind speed through a Froude number)
- or worse, it could also mean that assumptions 2 and 3 are far from valid for the type of topography considered.

To try a statistical-dynamical approach, it might be better to start from a cluster analysis performed on vertical profiles recorded over the area, as was done by Mengelkamp (1996). This could be done based on the analysis of the Payerne soundings presented by Furger (1990). Pursuing this classification work so that it would be applicable for the purpose of simulation would require further work, which appears to be beyond the scope of the present study.

Since the required information is not available to apply a complete statistical-dynamical approach as described above, we will try to perform something similar, starting from a very simple classification of the meteorological conditions occurring over the area, and using the Chasseral wind statistics instead of those obtained from the synoptic conditions. Fallot (1991) showed by comparing the wind roses and sector mean wind speeds, that the wind conditions at the reference site of Chasseral are representative of the wind conditions from the Payerne soundings at 700hPa

(~3000m ASL). Therefore, instead of reproducing relationships between the synoptic wind conditions and the wind conditions at the prediction site when performing the numerical simulations we will look for relationships between the reference site of Chasseral and the prediction site of Mt-Crosin. Simplifying the statistical-dynamical approach with this assumption has the drawback that it starts from a ground station, where the prevailing wind conditions are already influenced by the local conditions. However, compared to the method starting with the synoptic wind conditions for which only a few records a day are available, it has the advantage that it provides better wind statistics, with hourly data collected in a continuous mode.

When using the numerical model to obtain the wind statistics at the prediction site, a transposition methodology was applied, which is similar to an MCP method, assuming the existence of site-to-site relationships that will be obtained from the numerical simulations. It is postulated therefore that the relationships between the reference and prediction site are of a physical nature and that they can be reproduced by the numerical model.

After reviewing the traditional MCP methods in the next section, an extension of these methods is presented in Section 2.2, together with the formalism proposed to calculate the wind speed distribution at the prediction site.

2.1 Traditional methods for the prediction of the wind power potential at a site

The extension of the short-term statistics recorded at a site of interest is traditionally done using the measure-correlate-predict (MCP) method. This method is of the type I as presented above, i.e. it essentially assumes the existence of a relationship between the wind conditions prevailing at the reference and prediction site. The second assumption is that the existing relationships obtained from the short term are the same for the long term.

The nature of the site-to-site relationship used in the MCP methods is purely statistical. When performing a linear regression for one particular sector at the reference station, we mix data that were recorded for very dissimilar atmospheric conditions. No differentiation is made between records obtained during an event that showed a strong advective character over the entire troposphere or one that was definitely dominated by convective phenomena.

In the standard MCP method (see e.g. Meteonorm vent), simultaneous data sets of wind speed and direction recorded at both the reference and prediction site are grouped according to the wind direction at the reference site. A regression analysis is performed for each wind sector to produce relationships allowing us to obtain the wind speed at the prediction site, when knowing the wind speed and direction at the reference site. These relationships are then used to calculate the long-term mean wind speed at the prediction site from the long-term sector mean wind speed at the reference site.

The kind of relationships that are postulated between the wind speed at the reference site (v_{ref}) and prediction site (v_{pred}) are often simple linear relationships such that $v_{pred} = m_i \cdot v_{ref,i} + c_i$ with slopes m_i and intercepts c_i varying with the wind direction at the reference site (index i).

Starting from the normalised sector wind speed probability density function (PDF) at the reference site $f_{\theta_{ref,i}}(v_{ref})$ and knowing the sectorwise distribution $g(\theta_{ref})$, the mean wind speed at the prediction site is then:

eq. 2.1 $$\overline{v}_{pred} = \sum_{\theta_{ref,i}} g(\theta_{ref,i}) \cdot \int_0^{\infty} f_{\theta_{ref,i}}(v_{ref}) \cdot (m_i \cdot v_{ref} + c_i) \cdot dv_{ref}$$

which is in fact equivalent to:

eq. 2.2 $$\overline{v}_{pred} = \sum_{\theta_{ref,i}} g(\theta_{ref,i}) \cdot (m_i \cdot \overline{v}_{ref,i} + c_i)$$

The relationship above shows that the mean wind speed at the prediction site is easily obtained from the knowledge of the sector mean wind speed at the reference site. This kind of behaviour is only true due to the assumption of simple linear relationships between both sites. For non-linear types of relationship, the mean wind speed at the prediction site can no longer be expressed in terms of the sector mean wind speed at the reference site[2].

When applying the standard MCP method, no information is obtained concerning the sector variation of the wind speed at the prediction site. For cases where sector information would be required, Woods & Watson (1997) proposed a matrix MCP

---

[2] This can be illustrated with a relationship of the form $v_{pred} = v_{ref,i}^{a_i}$. The average wind speed at the prediction site becomes

$$\overline{v}_{pred} = \sum_{\theta_{ref,i}} g(\theta_{ref,i}) \cdot \int_0^{\infty} f_{\theta_{ref,i}}(v_{ref}) \cdot ({v_{ref}}^{a_i}) \cdot dv_{ref}$$

$$= \sum_{\theta_{ref,i}} g(\theta_{ref,i}) \overline{({v_{ref}}^{a_i})} \neq \sum_{\theta_{ref,i}} g(\theta_{ref,i}) \cdot (\overline{v}_{ref,i})^{a_i}$$

method, which allows the derivation of the wind rose at the prediction site as well as the sector mean wind speed.

Only a brief description of the matrix method will be given below. From a simultaneous set of wind speed and direction at the reference and prediction site, a population matrix $P = (p_{i,j})$ is calculated with the matrix element p_{ij} representing the frequency of occurrence of wind records with sector i at the reference site and sector j at the prediction site. This matrix gives a full description of the angular distribution during the measurement period. To eliminate the matrix bins that contain an insignificant fraction of the total number of measurements, matrix elements p_{ij} below a threshold value (typically 5%) are set to zero. From the filtered matrix, two additional matrices are formed:

- a matrix $W = (w_{i,j})$ that represents the population matrix *P* normalised such that $\sum_j w_{i,j} = 1$ for each wind direction i at the reference site. The matrix element $w_{i,j}$ represents in this case the conditional probability of having a wind blowing in the sector j at the prediction site, when it is blowing from the sector i at the reference site.
- a matrix $Z = (z_{i,j})$ that represents the population matrix *P* normalised such that $\sum_i z_{i,j} = 1$ for each wind direction j at the prediction site. The matrix element $z_{i,j}$ represents the conditional probability of having a wind blowing in the sector i at the reference site, when it is blowing from the sector j at the prediction site.

These matrices obtained from the short-term measurements are assumed to be representative of the long term as well. The long-term wind rose at the prediction site (p_j) is then obtained from the long-term wind rose at the reference site (p_i), using:

eq. 2.3 $$p_j = \sum_i w_{i,j} \cdot p_i$$

To calculate the long-term sector mean wind speed at the prediction site from the reference site, relationships are again needed, which are obtained from regression analysis. Like in the standard MCP method, it is usually postulated that the site to site relationship are linear.

Two variations of the matrix MCP methods were proposed by Woods & Watson. In the first one, which will be called '*MMCP ref*' below, the regression is performed on data sorted according to the wind direction i at the reference site. Regressions are performed for each sector i yielding the slopes and intercepts m_i and c_i. In the second method, the wind speed data are sorted according to the wind direction j at the prediction site (called '*MMCP pred*'), giving the slopes and intercepts m_j and c_j. The sector long-term mean wind speed for the direction j at the prediction site is calculated from:

eq. 2.4 $\bar{v}_{pred,j} = \sum_i z_{i,j} \cdot (m_i \bar{v}_{ref,i} + c_i)$ in the '*MMCP ref*' method

eq. 2.5 $\bar{v}_{pred,j} = m_j \cdot (\sum_i z_{i,j} \cdot \bar{v}_{ref,i}) + c_j$ in the '*MMCP pred*' method

The overall mean wind speed at the prediction site is then

eq. 2.6 $\bar{v}_{pred} = \sum_j p_j \cdot \bar{v}_{pred,j}$

with the wind rose p_j calculated above (eq. 2.3).

Which method between '*MMCP ref*' and '*MMCP pred*' gives the best results is site dependent. Woods & Watson found that in general, when the sector correlation is good there is little difference between the two, while when the correlation is poor better results are obtained with the second method.

The three MCP methods presented will be applied to transpose the Chasseral data to 5 sites in the vicinity. This will be done as a back-prediction both to evaluate the applicability of the correlation methods over the very complex topography of the Jura Chain and to estimate the accuracy of the prediction using various transposition relationships. The results from this application will be shown later on (Chapter 4), where they will be compared with results obtained from a transposition methodology introduced below, from which, the wind speed distribution at the prediction site is obtained, and not only the mean wind speed.

2.2 Transposition of the wind speed probability density function assuming the existence of site-to-site relationships

The mean wind speed is certainly a good indicator of the wind conditions prevailing on a site. However, two sites with the same mean wind speed can have very different energy densities. From the point of view of wind power assessment, it is therefore important to have some information about the wind speed probability density function. In this sense, the mean wind speed transposition methods presented in the previous section are not sufficient for the estimation of the wind power potential on a prediction site. We will therefore present an extension of these methods applied to transpose the data in order to get the wind speed distribution at the prediction site.

2.2.1 Particular case: transposition of Weibull distributions

For reference sites where the sector wind speed distributions can be represented by distributions of a Weibull type and for simple site-to-site relationships of the type

eq. 2.7 $v_{pred} = m_i \cdot v_{ref,i} + c_i$

the wind speed distribution at the prediction site can be reconstructed. This is done using the properties of the Weibull distribution under a simple variable transformation as presented in Appendix G.

Let the wind speed PDF for the sector i at the reference site be represented by the Weibull distribution

eq. 2.8 $$f_i(v_{ref}) = \frac{k_i}{A_i}\left(\frac{v_{ref}}{A_i}\right)^{k_i-1} \exp\left[-(\frac{v_{ref}}{A_i})^{k_i}\right]$$

The probability of having a wind speed between v_{ref} and $v_{ref} + dv_{ref}$ in the wind direction i is then

eq. 2.9 $$p_i \cdot f_i(v_{ref}) \cdot dv_{ref} = p_i \cdot \frac{k_i}{A_i}\left(\frac{v_{ref}}{A_i}\right)^{k_i-1} \exp\left[-(\frac{v_{ref}}{A_i})^{k_i}\right] \cdot dv_{ref}$$

where p_i stands for the probability that the wind blows from the direction i.

If the reference and prediction sites are related by eq. 2.7 we can substitute the variables and get

eq. 2.10 $$p_i \cdot f_i(v_{ref}) \cdot dv_{ref} = p_i \cdot \frac{k_i}{A_i}\left(\frac{v_{pred} - c_i}{m_i A_i}\right)^{k_i-1} \exp\left[-(\frac{v_{pred} - c_i}{m_i A_i})^{k_i}\right] \cdot \frac{dv_{pred}}{m_i}$$

Replacing $A_i m_i$ by B_i, we get

eq. 2.11 $$p_i \cdot f_i(v_{ref}) \cdot dv_{ref} = p_i \cdot \frac{k_i}{B_i}\left(\frac{v_{pred} - c_i}{B_i}\right)^{k_i-1} \exp\left[-(\frac{v_{pred} - c_i}{B_i})^{k_i}\right] \cdot dv_{pred}$$

Using a similar approach as the standard MCP method, we obtain the wind speed PDF $h(v)$ at the prediction site from summing over all the sectors, such that

eq. 2.12 $$h(v_{pred}) \cdot dv_{pred} = \sum_i p_i \cdot \frac{k_i}{B_i}\left(\frac{v_{pred} - c_i}{B_i}\right)^{k_i-1} \exp\left[-(\frac{v_{pred} - c_i}{B_i})^{k_i}\right] \cdot dv_{pred}$$

In other words, the probability density function at the prediction site is a combination of the sector Weibull distributions at the reference site, which are shifted by the intercept c_i. The A_i parameters of the original sector distributions are multiplied by the slope m_i of the linear relation, while the k_i remain unchanged.

Similarly, in the case of a transformation given by

eq. 2.13 $$v_{pred} = a_i \cdot v_{ref,i}^{\ b_i}$$

we end up with a wind speed distribution at the prediction site which is

eq. 2.14 $$h(v_{pred}) = \sum_i p_i \cdot \frac{k_i'}{B_i}\left(\frac{v_{pred}}{B_i}\right)^{k_i'-1} \exp\left[-\left(\frac{v_{pred}}{B_i}\right)^{k_i'}\right]$$

with $k_i' = k_i / b_i$ and $B_i = a \cdot A^b$ (see Appendix G).

As long as we can postulate simple relationships such as eq. 2.7 or eq. 2.13 between the reference and prediction site, the prediction site wind speed distribution can be represented by a combination of the sector Weibull distributions of the wind speed at the reference site. For other types of site-to-site relationship the transformation of the distribution is more complex and no such simple summation can be done.

2.2.2 More general case: transposition of a general distribution from two-parameter relationships

Under the assumption of existing relationships between the wind conditions prevailing at the reference site (v_{ref}, θ_{ref}) and the wind conditions at the prediction site $(v_{pred}, \theta_{pred})$ we express:

eq. 2.15 $$v_{ref} = H_1(v_{pred}, \theta_{pred})$$

eq. 2.16 $$\theta_{ref} = H_2(v_{pred}, \theta_{pred})$$

(in other words: the wind speed at the reference site depends on both the wind speed and direction at the prediction site, and so does the wind direction).

These relationships can be rewritten as:

eq. 2.17 $$(v_{ref}, \theta_{ref}) = (H_1(v_{pred}, \theta_{pred}), H_2(v_{pred}, \theta_{pred}))$$

and more generally we have for the transformation relation and its inverse operation:

eq. 2.18
$$(v_{ref}, \theta_{ref}) = H(v_{pred}, \theta_{pred}) = F^{-1}(v_{pred}, \theta_{pred})$$
and
$$(v_{pred}, \theta_{pred}) = F(v_{ref}, \theta_{ref})$$

If we have a one-to-one relationship between the wind conditions prevailing at both sites, as written in eq. 2.18, then, when wind blows at the reference site with (v_{ref}, θ_{ref}) it blows at the prediction site with the values $(v_{pred}, \theta_{pred}) = F(v_{ref}, \theta_{ref})$. This way, the probability of occurrence of both must be the same.

Let $f_{ref}(v_{ref},\theta_{ref})$ and $h_{pred}(v_{pred},\theta_{pred})$ be the probability density functions of the wind velocity and direction at both the reference and prediction sites, with the following conditions:

eq. 2.19 $$\iint f_{ref}(v_{ref},\theta_{ref})\cdot dv_{ref}\cdot d\theta_{ref}=1$$

eq. 2.20 $$\iint h_{pred}(v_{pred},\theta_{pred})\cdot dv_{pred}\cdot d\theta_{pred}=1$$

The probability of having a wind blowing with the velocity and direction between (v_{ref},θ_{ref}) and $(v_{ref}+dv_{ref},\theta_{ref}+d\theta_{ref})$ at the reference site and a wind between (v_{pred},θ_{pred}) and $(v_{pred}+dv_{pred},\theta_{pred}+d\theta_{pred})$ at the prediction site can be written as (e.g. Bury, 1986):

eq. 2.21
$$\text{Probability}(v_{ref},\theta_{ref})=f_{ref}(v_{ref},\theta_{ref})\cdot dv_{ref}\cdot d\theta_{ref}$$
$$\text{Probability}(v_{pred},\theta_{pred})=h_{pred}(v_{pred},\theta_{pred})\cdot dv_{pred}\cdot d\theta_{pred}$$

From the statement that these probabilities must be equal, we have the following equation that relates the wind probability density function of the reference site with the one of the prediction site:

eq. 2.22 $$h_{pred}(v_{pred},\theta_{pred})\cdot dv_{pred}\cdot d\theta_{pred}=f_{ref}(v_{ref},\theta_{ref})\cdot dv_{ref}\cdot d\theta_{ref}$$

With the help of the transformation between the reference and prediction site wind conditions, we can, express the second part of eq. 2.22 versus the variables (v_{pred},θ_{pred}) (Jacobian transformation):

eq. 2.23
$$h_{pred}(v_{pred},\theta_{pred})\cdot dv_{pred}\cdot d\theta_{pred}=f_{ref}(F^{-1}(v_{pred},\theta_{pred}))\cdot \underbrace{\left|F^{-1}\right|}_{\text{Jacobian of the transformation}}\cdot dv_{pred}\cdot d\theta_{pred}$$

$$=f_{ref}(H_1,H_2)\cdot\left|\frac{\partial H_1}{\partial v_{pred}}\cdot\frac{\partial H_2}{\partial \theta_{pred}}-\frac{\partial H_2}{\partial v_{pred}}\cdot\frac{\partial H_1}{\partial \theta_{pred}}\right|\cdot dv_{pred}\cdot d\theta_{pred}$$

This is equivalent to

eq. 2.24 $$h_{pred}(v_{pred},\theta_{pred})=f_{ref}(H_1,H_2)\cdot\left|\frac{\partial H_1}{\partial v_{pred}}\cdot\frac{\partial H_2}{\partial \theta_{pred}}-\frac{\partial H_2}{\partial v_{pred}}\cdot\frac{\partial H_1}{\partial \theta_{pred}}\right|$$

This last relationship is the one that defines the site-to-site data transposition, provided the functions H_1 and H_2 are known.

2.2.3 Simplified case: data transposition from one-parameter relationships

The wind data transposition can be simplified if we consider that the relationship F, between the wind conditions at the reference and prediction site, can be split in two kinds of single-parameter functions.

eq. 2.25

$$v_{pred} = V_{\theta_{ref}}(v_{ref})$$
$$\theta_{pred} = T(\theta_{ref})$$

(e.g. if we consider twelve sectors, then we have twelve relationships between the velocity values of both sites and one relationship between the wind directions).

With this assumption, we have a one-to-one relationship between the wind direction of both sites, without any angle dependence. This simplification does not allow us to take into account the fact that, due to different atmospheric stability conditions, it may be possible to encounter meteorological situations for which one wind direction at the reference station corresponds to two different wind directions at the transposition site. In other words, this latter assumption considers that the effect of a change in atmospheric stability (Froude number) on the direction transposition function is negligible.

For the establishment of the site-to-site transposition relationship in this simplified version, each sector will be treated separately, assuming that the probability densities of velocity and direction are statistically independent. Accordingly, the probability density function $f_{ref}(v_{ref}, \theta_{ref})$ will be replaced by a function $f_{\theta_{ref}}(v_{ref}) \cdot g(\theta_{ref})$ for each sector, where $g(\theta_{ref})$, the angular PDF obeys:

eq. 2.26

$$\sum_{i=1}^{36} g(\theta_{ref,i}) = 1$$

$f_{\theta_{ref}}(v_{ref})$, the probability density functions (PDF) of the wind speed at the reference site for the wind sector θ_{ref} obeys the equality

eq. 2.27

$$\int f_{\theta_{ref}}(v) \cdot dv = 1 \qquad \text{for all } \theta_{ref}$$

In this expression, the wind direction θ_{ref} is only a parameter and no longer a variable.

The PDF for the wind velocity at the reference site (all sectors included) is then:

eq. 2.28

$$f(v) = \sum_k f_{\theta_k}(v) \cdot g(\theta_k)$$

Considering the assumed relationship eq. 2.25 between the prediction and reference site velocity, we obtain the following expression for the PDF of the wind velocity at the prediction site (marginal probability, Bury, 1986):

eq. 2.29

$$h(v) = \sum_k f_{\theta_k}\left[V_{\theta_k}^{-1}(v)\right] \cdot \frac{\partial V_{\theta_k}^{-1}(v)}{\partial v} \cdot g(\theta_k)$$

The term $\frac{\partial V_{\theta_k}^{-1}(v)}{\partial v}$ in eq. 2.29 is the Jacobian corresponding to the simplified transformation.

If, for example, the transposition relationships were taken to be simple proportionality relations such as:

eq. 2.30 $$v_{pred} = a(\theta_k) \cdot v_{ref}$$

then, introducing eq. 2.30 in eq. 2.29 leads to the transposition relation:

eq. 2.31 $$h(v) = \sum_k f_{\theta_k}\left(\frac{v}{a(\theta_k)}\right) \cdot \frac{1}{a(\theta_k)} \cdot g(\theta_k)$$

The application of this simple transposition will be presented in Section 4.3 using transposition coefficients $a(\theta_k)$ that are evaluated by means of the numerical simulation performed over the Chasseral and Mt-Crosin area.

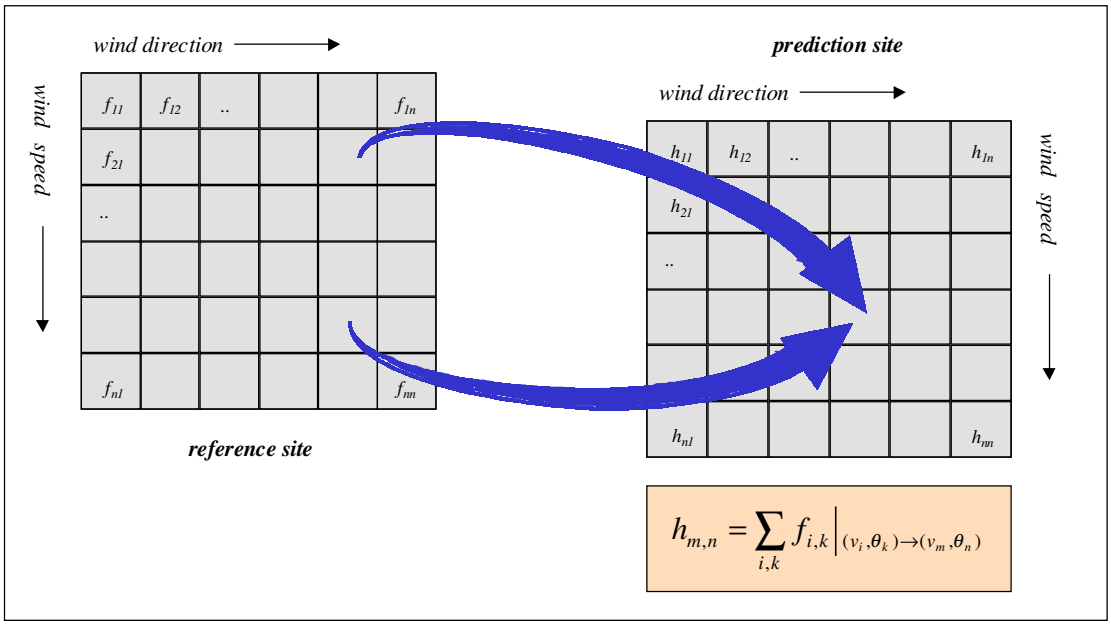

Figure 2.2. Schematic illustrating how the data transposition is performed when having a single-valued relationship instead of a one-to-one relationship between the reference and prediction site.

Note: the analytical transposition methodology presented above formally requires the existence of one-to-one relationships between the pairs (v_{ref}, θ_{ref}) and $(v_{pred}, \theta_{pred})$. For practical purposes, a wind data transposition is still possible even if we have a single-valued relationship mapping the wind conditions at the reference site to the prediction site. In the latter case, the wind speed and direction at the reference site

$(v_{ref,i}, \theta_{ref,k})$ are binned into a matrix $\tilde{F} = (f_{i,k})$. The probability of occurrence $f_{i,k}$ of each pair of $(v_{ref,i}, \theta_{ref,k})$ mapped onto the pair $(v_{pred,m}, \theta_{pred,n})$ are then added to determine the probability matrix $\tilde{H} = (h_{m,n})$ of the wind speed and direction at the prediction site (see Figure 2.2).

2.3 Wind power potential for a specific wind turbine

Once the probability density function $f(v)$ of the wind speed at a given site is known, it is possible to evaluate the amount of energy that a wind turbine can produce in one year. The machine power characteristic function $P(v)$ is thereby needed. The latter is usually established by the turbine manufacturer for working conditions corresponding to an air density of 1.22 kg/m^3 and turbulence intensity of 10%.

The yearly power output of a single machine, for a wind distribution $f(v)$, can be calculated as:

eq. 2.32
$$E_1 = 8760 \cdot \int_{v=v_{ci}}^{v=v_{co}} P(v) \cdot f(v)\, dv \qquad [kWh]$$

where

v_{ci} is the cut-in wind speed (wind speed at which the machine starts to produce electricity)

v_{co} is the cut-out wind speed (wind speed at which the machine is shut down for safety reasons)

For the wind power potential evaluation of the Mt-Crosin site, we will use the power characteristics of the Vestas-V44 600 kW machine given in Table 2.1. Three machines of this type were actually installed on the site in October 96 (see Figure 3.2 for their location on site). The power curve that has been established for an air density of 1.06 kg/m^3 should be appropriate for the average temperature conditions prevailing at the altitude of the Mt-Crosin site. For a wind speed higher than 4.5 m/s, the turbines are coupled to the grid and start to generate electricity, and they are stopped when the wind speed at hub-height exceeds 20 m/s (Figure 2.3).

Table 2.1. Power characteristic function of the Vestas V44-600kW machine at two different air density conditions (Source: Vestas-Danish Wind Systems A/S).

v	$P(v)$ at ρ =1.22 kg/m^3 [kW]	$P(v)$ at ρ =1.06 kg/m^3 [kW]
1	0	0
2	0	0
3	0	0
4	0	0
5	30.4	24.7
6	77.3	65.2
7	135	115
8	206	176
9	287	246
10	371	320
11	450	393
12	514	461
13	558	517
14	582	557
15	594	581
16	598	593
17	600	598
18	600	599
19	600	600
20	600	600
21	0	0

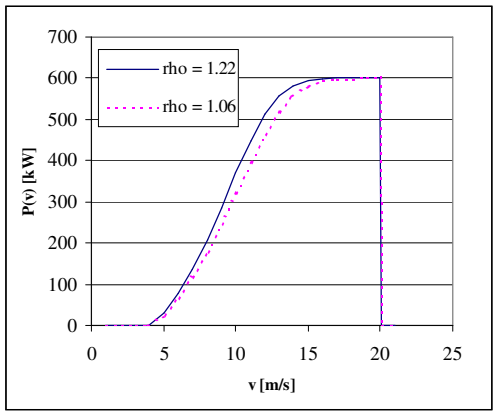

Figure 2.3. Power characteristics of the Vestas V44-600kW machine at two different air density conditions (Source: Vestas-Danish Wind Systems A/S).

2.4 Wind power potential for a wind farm.

Since operating conditions vary from site-to-site, correction factors are applied to eq. 2.32 in order to account for various losses, when evaluating the power potential of a wind farm. The above expression is modified to:

eq. 2.33 $$E_m = 8760 \cdot \eta_T \cdot \eta_\rho \cdot \eta_{avail} \cdot \eta_{array} \cdot \int_{v=v_{ci}}^{v=v_{co}} P(v) \cdot f(v) dv \qquad [kWh]$$

The correction factors η_ρ , η_T , η_{avail} , η_{array} take into consideration air density (η_ρ) and turbulence η_T effects, availability (η_{avail}) and interactions between machines (η_{array}). They are briefly discussed below.

η_ρ As the air density (due to altitude) and turbulence conditions of the prediction site do not necessarily correspond to the ones at which the power characteristics were established, correction factors must be applied to take into account such effects. If the power characteristics of the machine are

available for air density conditions valid for the site, then these are to be preferred for evaluating eq. 2.33. If no such corrected curve is available, then a simple efficiency factor $\eta_\rho = \rho_{site} / \rho_{normal}$ can be employed. However, it should be pointed out that these two procedures are not exactly equivalent. Namely, the correction factor is applied for all velocity classes and reduces the power output of all of them. This way, correcting the output with η_ρ assumes that the nominal power output of the machine is never reached. In reality, the power curve at lower air density reaches the rated power, but for velocity classes that are higher than at normal air density. Applying η_ρ for all the velocity classes underestimates the power output that the machine can produce.

η_T Turbulence acts differently on the machine power output, whether it is observed at low or high wind velocities. For the lower velocities, turbulence tends to increase the machine power output, while at higher velocities it reduces the output. However, it is not simple to estimate the effect of turbulence on the global energy output (c.f. Sheinmann & Rosen, 1992). This would require a dynamic treatment of the machine behaviour and control, which is beyond the scope of the present project. However, as turbulence intensity higher than 10% leads to a reduction of the yearly energy production and as it is expected to be in the range of typically 25% for a site in complex terrain such as Mt-Crosin, the power reduction factor η_T will be applied, in order to take into account losses due to turbulence.

η_{avail} To also consider possible machine unavailability, a further factor η_{avail} will be used in the evaluation of the yearly energy output of a single wind turbine.

η_{array} The fact that the machines are installed at the site in an array of finite dimensions also leads to losses due to machine interactions (for particular wind directions some machines lie in the wake of others). This effect can be accounted for by introducing a further η_{array}. Although η_{array} is normally expected to be a function of wind direction and position in the array, a global value of η_{array} will be included here since such calculations involve detailed micro-siting considerations.

The total output of the complete wind farm is the sum of the contributions of each single wind energy converter, which can be written as:

eq. 2.34
$$E_{wf} = 8760 \cdot \eta_T \cdot \eta_\rho \cdot \eta_{avail} \cdot \eta_{array} \cdot \sum_{k=1}^{N} \int_{v=v_{ci}}^{v=v_{co}} P(v) \cdot f_k(v)\, dv \qquad [kWh]$$

N is set to the total number of wind turbines, and the wind distribution $f_k(v)$ is that valid at the location of the *k-th* machine.

Evaluation of eq. 2.34 is carried out here for VestasV44 600kW machines. According to the constructor, and in order to keep the losses due to machine interactions under a reasonable threshold, it is recommended to leave a minimal distance of 210 m between successive turbines, along the most frequent wind direction. In the direction perpendicular to this, the minimal distance is 170 m. Noting that the most frequent winds in the area blow from the south-west and east-north-east directions, the manufacturer recommendations have been observed when installing the three wind turbines on the Mt-Crosin site (see Figure 3.2). We therefore expect that the losses due to machine interactions remain small for this particular wind farm geometry. When evaluating the power potential of the Mt-Crosin site, we will use the following values for the correction factors:

$$\eta_{array} = 1.0$$

$$\eta_T = 0.9 \qquad \text{(c.f. Sheinmann \& Rosen, 1992)}$$

$$\eta_{avail} = 0.97$$

$$\eta_\rho = 1.06/1.22 = 0.87$$

The actual values that were obtained for η_{avail} during the year 1997 for the three machines on the Mt-Crosin site are given in Table 2.2. Considering the fact that the machines were installed in autumn 1996, we expect that the availability values given in Table 2.2 represent lower estimates of the value than will be reached for the long term. Difficulties occurred at the beginning, when commissioning the machines, which reduced the availability for the year 1997 (this was particularly the case for wind turbine No.1). Hence, adopting 0.97 for η_{avail} when evaluating the power potential should be a conservative assumption for the site of Mt-Crosin.

Table 2.2. Availability[3] during the year 97 of the three wind turbines installed on the Mt-Crosin site.

	Availability [%] Period 1.97-12.97
Wind turbine 1	94.9
Wind turbine 2	97.2
Wind turbine 3	97.8

[3] The availability is defined here as the percentage of hours during which the turbine is available to operate.

3 Description of the area of application

3.1 Terrain

The site to site wind data transposition will be attempted for the region of Chasseral-Mt-Crosin using the ANETZ meteorological station of Chasseral as a reference site and the area of the Mt-Crosin wind farm as a transposition site (also called prediction site).

The area of interest is situated along the Jura mountain chain, in the north west of Switzerland. This mountain range is characterised by a succession of mountains and valleys essentially aligned on a SW-NE axis. At its southern edge the Jura range is limited by the Swiss Plateau at an altitude of 400-500m ASL and at its northern edge by the lower altitude hilly terrain of Franche-Comté. The rectangle in Figure 3.1, showing the outline of the simulation domain allows one to locate the region with respect to the complex topography which characterises the country. The reference station of Chasseral is on the top of the most elevated summit of the Jura mountain in that region and the wind conditions prevailing there are directly connected to the geostrophic wind conditions (see Ehinger et al, 1990). The most relevant characteristics of the Chasseral site are listed below according to Ehinger et al:

- Altitude: 1599 m.
- Swiss kilometric co-ordinates: 571'290 / 220'320.
- The site is the most elevated summit in a radius of 50 km.
- The topographical features in the region are aligned in the SW-NE direction (c.f. Figure 3.1).
- The soil is covered with grass and isolated groups of rocks.
- The measuring instruments are located on an intermediate level platform of a telecommunication tower.
- The wind measuring instrument is of the SIAP type (appropriate for high wind speed measurements and cold temperature conditions, which are common for the area) and it is located 60 m above ground level to the south of the telecommunication tower.

The prediction site used to test the applicability of the transposition methodology is located on Mt-Crosin (~1200 m ASL). This site is situated along the Mt-Soleil range some 6-7 km northwest from the Chasseral reference station and separated from the latter by the St-Imier valley (~750 m ASL). The choice of Mt-Crosin as a prediction site was motivated by the fact that wind data are available that were recorded during

a one year measurement campaign which was followed by the installation of three wind turbines.

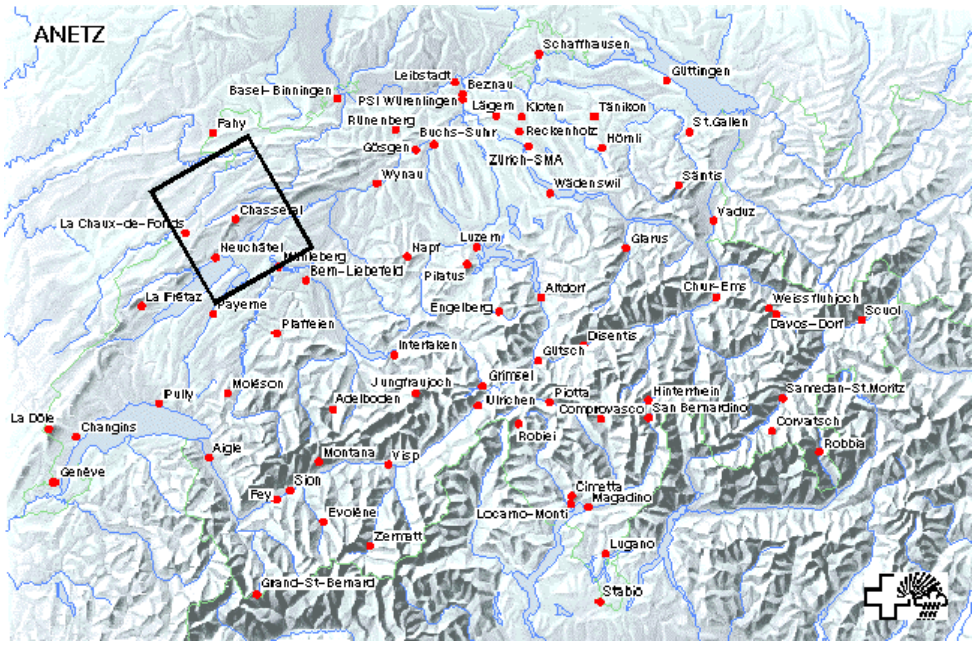

Figure 3.1. Distribution of the ANETZ meteorological stations on the Swiss topography and location of the Chasseral and Mt-Crosin area. (Source: ISM, SMA, Zurich.).

The orientation of the Mt-Crosin and Mt-Soleil range is more or less aligned in the same direction as the other topographic features of the region (i.e. SW-NE direction). Other relevant characteristics of the transposition site are summarised below:

- The hills flanks are covered with forests and the site itself is a grass pasture land on which isolated trees or groups of trees can be found.
- The site has been equipped with three measuring masts, one of them (Côte Nord) with instruments at 10 m above ground level only, and the two others (Côte Sud and Côte Est) with instruments at 10 and 30 m.
- The measuring instruments are cup anemometers, for which no calibration curve is available (Baumgartner, personal communication). Concerning the anemometers choice for the Mt-Crosin site, two aspects should be pointed out that may influence the quality of the measurements in a non-negligible way:
    1. Cup anemometers are known for their sensitivity to vertical velocity. Although this vertical component is not interesting for the energy production, it is present in flows over highly complex terrain and depends on the direction from which wind approaches the measuring point. As a consequence, the wind velocities that are registered by the

cup anemometer overestimate the actual horizontal velocity, which is the useful component from the point of view of energy production.

2. The second aspect is related to the climatic conditions that prevail for a site located at an altitude of 1200 m, as Mt-Crosin. Namely, for temperatures below 0° C, the cup anemometers can be frozen, and record no velocity values. Therefore the data recorded at Mt-Crosin need to be considered with care relative to this aspect.

A detailed map of the Mt-Crosin site together with the measuring instruments and wind turbine locations is presented in Figure 3.2. The exact locations, altitude and level above ground level of the measurement masts are summarised in Table 3.1.

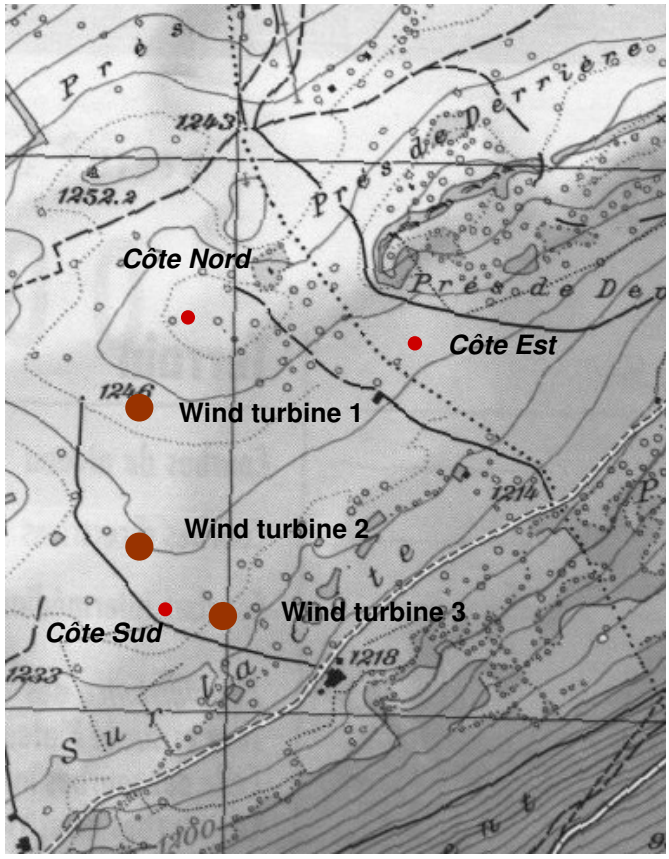

Figure 3.2. Detail topography of the Mt-Crosin site showing the position of the measuring masts and wind turbines. (Extract of the chart no. 1125 (Chasseral) reproduced by permission of the Swiss Federal Office of Topography, 20.7.1998).

Table 3.1. Location and altitude of the measurement stations at Chasseral and Mt-Crosin.

station name	co-ordinates	altitude (ASL) [m]	Height above ground of the instruments [m]
Chasseral	571'290/220'320	1599	60
Côte Nord	567'900/225'740	1256	10
Côte Sud	567'850/225'200	1238	10, 30
Côte Est	568'325/225'700	1245	10, 30

3.2 Data

3.2.1 Chasseral long term data set

The estimation of the wind power potential at Mt-Crosin will be done using a long term data set for Chasseral[4] that covers the time period starting from the 1st of January 1982 to the 31st of December 1997. Hourly averaged data will be used.
Before calculating the wind distribution at the reference site, a data correction was applied in order to take into account instrumental effects on the measured wind value. This was done according to the calibration curve of a SIAP type instrument (see Appendix J), which was determined in the wind tunnel facilities of the LASEN by Ehinger et al (1990).
No other level of data correction for Chasseral will be considered, even if this may be questionable, due to influence of the telecommunication tower on which the mast is installed. This effect is however expected to be important only for northerly wind directions, for which the instrument is in the wake of the tower. Since these directions are not the most frequent ones (Figure 3.3) and we therefore expect the wind measurements done at Chasseral to be representative of the wind conditions prevailing at the summit.
The data are sorted into velocity and direction classes. Velocity intervals of 1m/s are defined, so that the velocity class n corresponds to velocity lying in the interval $n < v < n+1$. Direction intervals of 10° are defined, so that the direction class j corresponds to direction in the interval $10j - 5 < \theta < 10j + 5$. For the period considered, the wind rose for the Chasseral location from the long-term wind measurements can be seen in Figure 3.3. Two predominant groups of wind directions occur: the first one corresponds to winds blowing from the south-western

[4] Hourly and 10 minutes averaged meteorological data from the Chasseral ANETZ station (60 m above ground) are available from February 81 on a regular basis. Source: ISM, SMA, Zurich.

to north-western directions, and the second one to winds blowing from the east (so-called 'bise').

The wind speed probability density function (PDF) at Chasseral, corrected for calibration errors, is presented in Figure 3.4). All the hours with undefined value for either the wind direction or wind speed were attributed to the zero wind speed class, explaining the peak in the PDF of Chasseral for this class. The average wind speed corresponding to the distribution of Figure 3.4 is of 7.44 m/s. The Weibull distribution (with the parameters $A = 8.36$ and $k = 1.6$) best representing this measured distribution has also been plotted. The latter was determined by a linear regression on the values of $\ln(-\ln(1 - F(v)))$ plotted versus $\ln(v)$, where $F(v)$ stands for the cumulative Weibull distribution (see Appendix G).

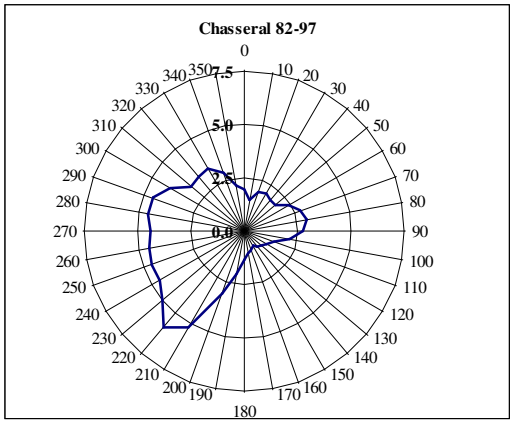

Figure 3.3. Wind rose for Chasseral, obtained from 16 years of hourly averaged wind records.

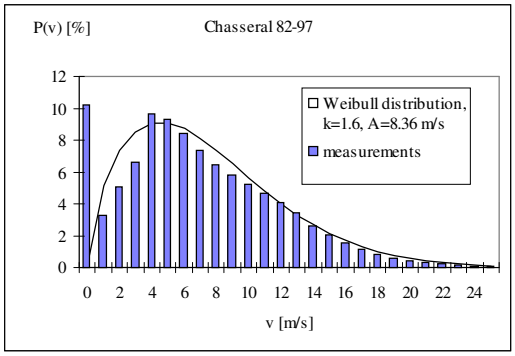

Figure 3.4. Wind speed probability density function at Chasseral from 16 years of hourly averaged wind records and best fitting Weibull distribution.

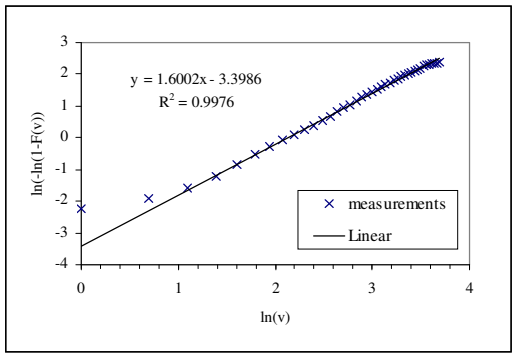

Figure 3.5. Linear regression allowing the evaluation of the *k* and *A* coefficients of the Weibull distribution best representing the Chasseral PDF.

3.2.2 Mt-Crosin data sets

Hourly averaged wind data were collected at the three locations of Côte Nord, Côte Sud and Côte Est on the Mt-Crosin (see Figure 3.2) for the wind farm feasibility study. Measurements at 10 and 30 m above ground were recorded at both Côte Sud and Côte Est, while the site of Côte Nord was only equipped with a 10m high mast. These data were kindly provided by Meteotest. Together with the simultaneous wind records at Chasseral, they have been used:

1. to determine how far the simple assumptions of the transposition methodology can be considered as appropriate
2. to give an estimate of the accuracy that can be expected from the data transposition
3. to test the model ability to reproduce the behaviour of the wind velocity at Mt-Crosin as a function of the wind velocity at Chasseral.

The raw data at the three locations were carefully checked, and questionable data corresponding to periods with non-operational or frozen instruments were eliminated. The characteristics of the remaining data sets are summarised in Table 3.2 and Table 3.3. The corresponding probability density functions and wind roses for the Mt-Crosin stations are given in Figure 3.6 to Figure 3.8, together with the simultaneous distributions for Chasseral.

Table 3.2. Parameters summarising the availability of the Mt-Crosin measuring stations.

	Period of availability	Max. possible number of data [hours]	Number of hours with records available at both Mt-Crosin and Chasseral
Côte Nord (10m)	Feb. 94- May 95	11640	6455
Côte Sud (30 m)	Feb. 94- Apr. 95	10896	6467
Côte Est (30 m)	Dec. 94- Aug. 95	6576	4669

It should be stressed that the average wind speeds and natural power density[5] at the various measuring masts were calculated with a probability density function that was normalised with the total number of defined values, without including the undefined ones in the zero wind speed bin. As a consequence, the average wind speeds obtained from the short-term data are not representative of the expected longer-term value. This can be seen from the values of Table 3.3 where the average

[5] The natural power density of a site is defined as $P_n = \frac{1}{2}\rho\int P(v)\cdot v^3 dv$, with ρ the air density and $P(v)$ the wind speed probability density function of the site.

wind speed at the station of Chasseral significantly exceeds the value of 7.44 m/s, which was obtained from the 16 years of measurements.

For the same reason, the natural power density obtained for the three measurement locations on the Mt-Crosin site are not representative of the wind power potential available on site. From the values given in Table 3.3, one could be tempted to conclude that the site of Côte Est shows the best potential. This is not true however, and again, this is only due to the fact that the period over which measurements were available simultaneously at Côte Sud and Chasseral was windier than the period with measurements at Côte Nord and Côte Est.

Table 3.3. Average wind speed and natural power density for the Mt-Crosin measuring stations. Chasseral average wind speeds for the corresponding period are also given.

	Average wind speed [m/s]	Natural power density with $\rho = 1.05 kg/m^3$ [6] [W/m^2]	Average wind speed at Chasseral for the simultaneous data [m/s]
Côte Nord (10m)	5.2	163	9.1
Côte Sud (30 m)	5.3	153	7.9
Côte Est (30 m)	5.6	229	9.5

When comparing the Chasseral wind roses shown in Figure 3.8 with those of Figure 3.6 and Figure 3.7 we can see that the sector distribution of the concurrent data set Chasseral-Côte Est is slightly different from those obtained for the periods with concurrent data at Côte Sud and Côte Nord. For the period with data at Côte Est, we can clearly see that the most frequent wind directions are the 200° to 230° wind directions, with frequencies higher than 5%. For the two other periods (of Figure 3.6 and Figure 3.7), the south-west to north-west wind sectors are more evenly distributed within the 200° and 280° sectors. For the south west to north west winds, the wind rose for Chasseral obtained for the period with simultaneous data at Côte Est appears to be more representative of the long term (Figure 3.3) than those for Côte Sud and Côte Nord. For the east to north-east wind directions the converse is observed.

[6] The value of 1.05 for the density is representative for the average temperature conditions on Mt-Crosin.

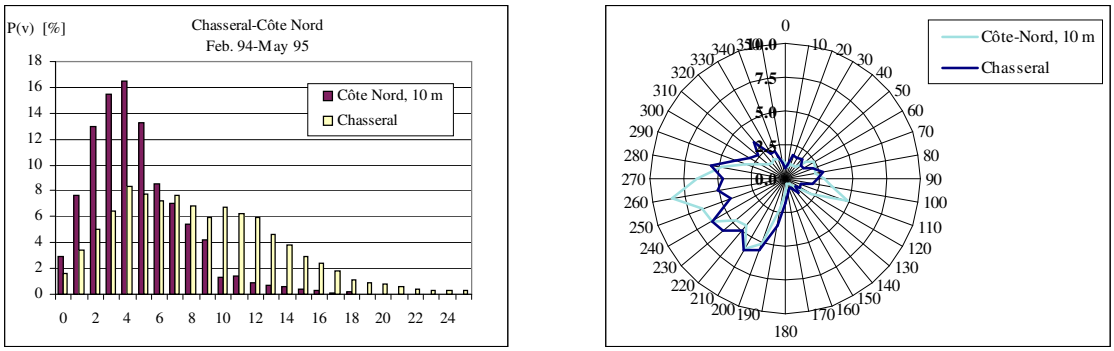

Figure 3.6. Simultaneous probability density function and wind rose at the stations of Côte Nord and Chasseral.

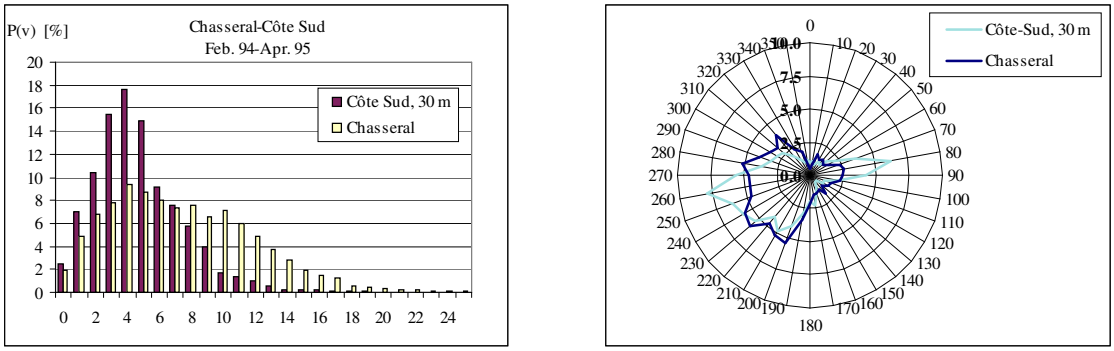

Figure 3.7. Simultaneous probability density function and wind rose at the stations of Côte Sud and Chasseral.

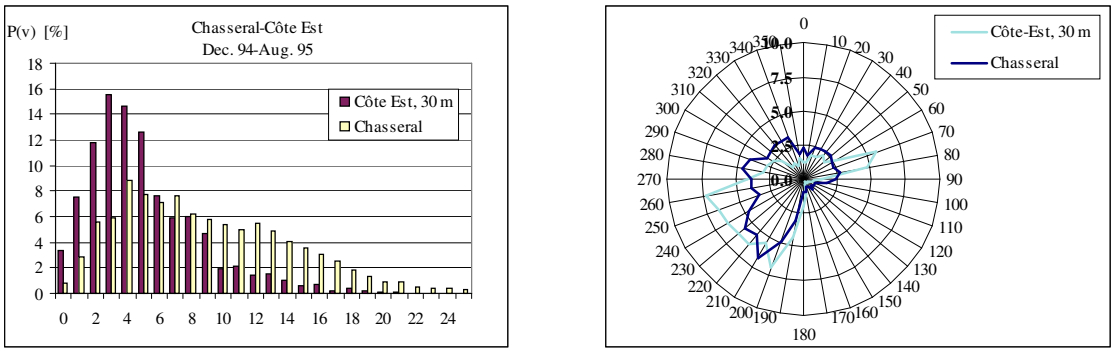

Figure 3.8. Simultaneous probability density function and wind rose at the stations of Côte Est and Chasseral.

Some channelling can also be observed from the Mt-Crosin wind roses, which is not visible in the wind roses of Chasseral. It can be observed that on Mt-Crosin, the peaks in the sector distribution are sharper than they are for Chasseral. For the winds with a northern component, there is a definite blocking effect due to the Chasseral range which tends to rotate the north-east winds at Mt-Crosin in a clockwise

direction and the north-west winds in an anticlockwise direction (Figure 3.9). Why the rotation for the east winds is stronger at Côte Nord than at the two other sites is not clear.

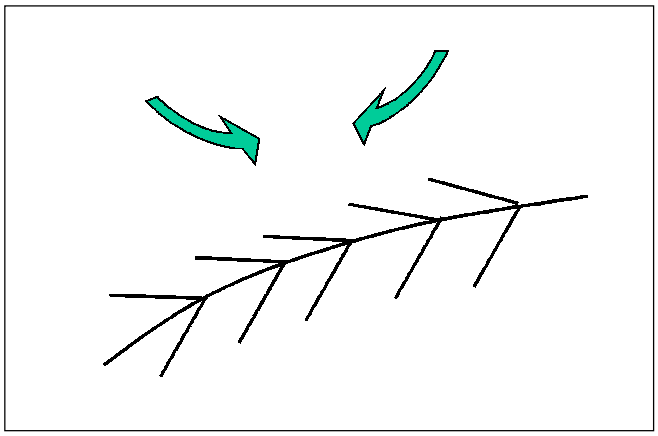

Figure 3.9. Illustration of the effect of channelling that a mountain range produces on the winds for altitudes lower than the crest. The north-east winds are rotated clockwise and become more easterly winds. Conversely, the north-west winds are rotated anticlockwise and become more westerly winds.

4 Wind data transposition from observations and assessment of the validity of the transposition assumptions

Both the usual MCP methods and the transposition of the complete wind speed distribution rely on the assumptions of existing relationships relating the wind speed at the prediction site to the wind speed at the reference site. The success and accuracy of the prediction will depend on the validity of this assumption. In MCP methods, the relationships are obtained from concurrent datasets recorded at both the prediction and reference site. Before applying any transposition, we will investigate the behaviour of the prediction site to reference site wind speed ratio, in order to see what kind of relationship between the sites can exist. This will be presented in Section 4.1.

The first step in the evaluation of the transposition method will consist of performing a so-called back-prediction. Then the relationships obtained from concurrent datasets for a given period will be used to transpose the reference site data for the same period to the prediction site. Comparing the transposition results with the data measured on the prediction site during this particular period will allow us to estimate the accuracy that can be obtained with the assumption of existing correlations. Testing various types of site-to-site relationships should also help us to determine which one best predicts both the average wind speed and wind energy density observed on the site.

The back-prediction will be applied in Section 4.2 and 4.3 for the three sites of Mt-Crosin as well as for the less exposed ANETZ stations of Neuchâtel and Chaux-de-Fonds. Being located at lower altitudes, these stations are less directly coupled to the geostrophic wind conditions. Their wind roses show the effects of significant channelling that can be associated with the presence of topographic features (the Jura chain for Neuchâtel, and the orientation of the valley for Chaux-de-Fonds). Since the matrix MCP method is meant to improve the results in the case of significant rotation of the wind vector, it will therefore be interesting to see if it outperforms the standard MCP method when predicting the sector mean wind speeds for these stations. When performing the back-predictions, we will use the longest possible data set available for all the pairs of stations considered. For the Mt-Crosin sites, data are only available for short term periods (see Chapter 3), whereas for the sites of Neuchâtel and Chaux-de-Fonds we will use 16 years of data, covering the period between January 1982 and December 1997.

4.1 Relationships between the reference and prediction sites

4.1.1 Wind speed ratios from hourly observations

Plotting the hourly wind speeds recorded at the Mt-Crosin site of Côte Nord versus the wind speed at Chasseral for various wind directions (Figure 4.1) shows a more or less linear relationship between the two sites. The linear function $v_{pred} = m \cdot v_{ref} + c$ obtained from regression has also been plotted (dark line). The proportionality relationship $v_{pred} = a \cdot v_{ref}$, with a obtained from averaging the wind speed ratios for each data pair, has been drawn as a light line. It would be difficult when comparing the plots to decide which of the two relationships best represents the observations. This would be even more difficult when looking at the similar plots showing the wind speed at Chaux-de-Fonds versus the wind speed at Chasseral (Figure 4.2). In the latter case, the correlation between the two sites is rather poor. This is not so surprising however, when knowing that the station of Chaux-de-Fonds is located in a topographical depression where thermal winds occur and can significantly affect the local climatology.

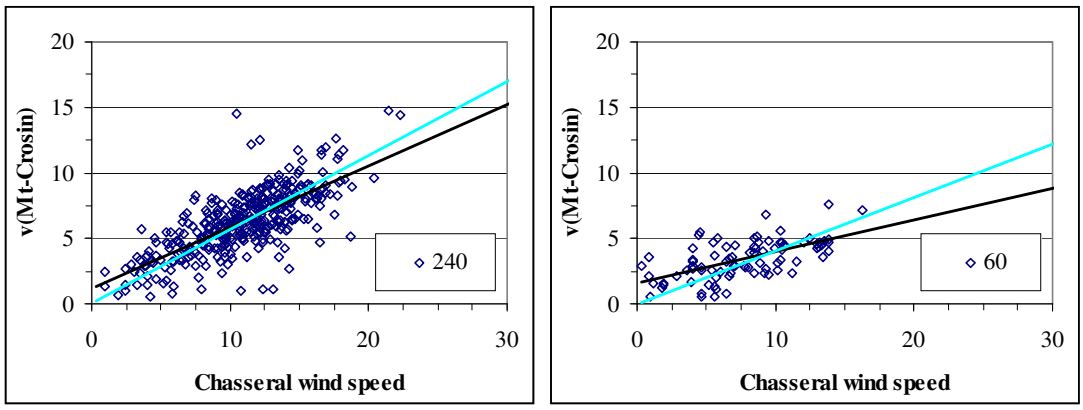

a) b)

Figure 4.1. Hourly wind speed at the Mt-Crosin site of Côte Nord vs. hourly wind speed at Chasseral for concurrent data sets (period: Feb. 1994- May 1995). All data with the wind direction at Chasseral in the interval a) 240° ±5° and b) 60°±5°.

Systematically performing the linear regression analysis on the concurrent data sets led to the parameters m and c and regression coefficients[7] r given in Table 4.1 for

[7] The regression coefficient for a set of N records x_i and y_i is defined as

$$r = \frac{N\sum x_i y_i - \sum x_i \sum y_i}{\sqrt{N\sum x_i^2 - \left(\sum x_i\right)^2}\sqrt{N\sum y_i^2 - \left(\sum y_i\right)^2}}$$

Côte Nord and Table 4.2 for Chaux-de-Fonds. This was done for data binned into sectors of 30° width, centred around the sector value (i.e. the sector 0° contains data between –15° and +15°). To reduce the error that could arise due to the known calibration difficulties that arise with SIAP type instruments, we only considered data which were above the threshold wind speed of 5 m/s at Chasseral when performing the regression. For the prediction stations, we used a threshold wind speed of 0.5 m/s (sensitivity threshold of the instrument). Since, for wind power potential estimation, we are most interested in the strong wind situations these restrictions on the low wind speed cases should help to improve the representativeness of the relationships that will be used for the transposition. The parameters with indices '*ref*' (or '*pred*') were obtained from data sorted according to the reference (or prediction) site wind direction. The same tables can be found in Appendix H for the stations of Côte Sud, Côte Est and Neuchâtel.

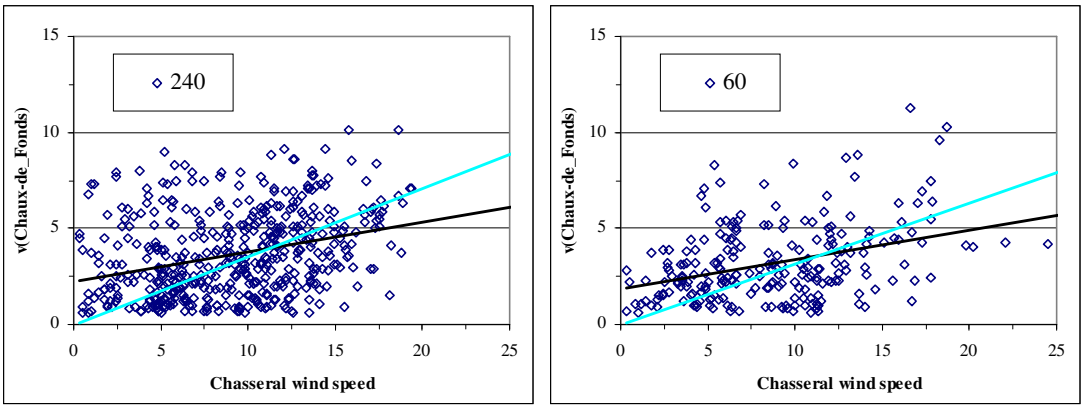

a) b)

Figure 4.2. Hourly wind speed at Chaux-de-Fonds vs. hourly wind speed at Chasseral. All data with the wind direction at Chasseral in the interval a) 240° ±5° and b) 60°±5°. For clarity purpose, only two years of concurrent data sets (years 1982-1983) have been plotted, instead of the 16 years available.

As can be seen from the values given, the correlation between the site of Côte Nord and Chasseral is acceptable for the most frequent wind directions (30°-60° and 210°-300° when binning according to the reference station wind direction) but rather poor for the others. Between the sites of Chasseral and Chaux-de-Fonds, the correlation is even poorer with only one sector with r over 0.6 when binning according to the reference direction and two when binning according to the prediction wind direction. Moreover, the highest correlations between Chasseral and Chaux-de-Fonds are obtained for the less frequent sectors, which is not very encouraging for the wind data transposition.

Table 4.1. Parameters from the linear regression relating the sites of Côte Nord and Chasseral (short term data). (see text for details).

Sector	c_{ref}	m_{ref}	r_{ref}	c_{pred}	m_{pred}	r_{pred}
0	1.49	0.47	0.17	2.26	0.20	0.30
30	1.67	0.32	0.60	3.35	0.11	0.12
60	1.11	0.31	0.64	1.79	0.33	0.66
90	2.07	0.31	0.46	1.91	0.20	0.48
120	3.41	0.10	0.10	2.46	0.33	0.53
150	2.33	0.31	0.23	2.65	0.09	0.23
180	1.94	0.54	0.75	2.76	0.30	0.38
210	2.37	0.42	0.67	1.63	0.52	0.75
240	0.83	0.50	0.69	1.01	0.48	0.69
270	-0.14	0.53	0.79	1.33	0.40	0.71
300	0.21	0.39	0.82	0.55	0.35	0.80
330	0.96	0.35	0.63	0.55	0.37	0.80

Table 4.2. Parameters from the linear regression relating the sites of Chaux-de-Fonds and Chasseral (16 years of data). (see text for details).

Sector	c_{ref}	m_{ref}	r_{ref}	c_{pred}	m_{pred}	r_{pred}
0	3.29	-0.12	-0.12	1.46	0.10	0.28
30	2.45	0.18	0.34	2.43	0.11	0.25
60	2.12	0.16	0.34	1.84	0.20	0.39
90	1.16	0.19	0.39	1.12	0.22	0.42
120	1.33	0.07	0.14	1.32	0.14	0.42
150	0.39	0.25	0.37	-0.29	0.35	0.74
180	-0.03	0.37	0.67	0.97	0.21	0.49
210	0.56	0.27	0.51	0.43	0.31	0.62
240	0.49	0.30	0.47	0.86	0.24	0.46
270	0.50	0.29	0.54	0.97	0.11	0.34
300	0.82	0.17	0.58	1.32	0.07	0.26
330	1.46	0.05	0.23	1.20	0.09	0.30

The average sector wind speed ratios relating the stations of Côte Nord and Chasseral, as well as those relating Chaux-de-Fonds and Chasseral are given in Table 4.3. These were again calculated for the data sorted according to the wind direction at Chasseral (labelled *'ref'*) and according to the direction at the prediction site (labelled *'pred'*).

The wind speed ratios, together with their standard deviation, were also calculated for data binned as a function of the Chasseral wind direction with 10° classes. The behaviour of the so-obtained wind speed ratios as a function of the wind direction is plotted in Figure 4.3.a for the three sites on Mt-Crosin and in Figure 4.4.a. for the ANETZ stations of Neuchâtel and Chaux-de-Fonds. The standard deviation of this

ratio is shown in Figure 4.3.b and Figure 4.4.b. In each sector, the values of the wind speed ratio and standard deviation were considered to be representative only where more than 30 records were available. Due to this restriction (and to the fact that we only have short term data) a gap can be seen in the plots for the northern wind directions (sectors -10° to 10°) and eastern to southern (sector about 110° to 180°) at the sites on Mt-Crosin. For the sites of Chaux-de-Fonds and Neuchâtel, with 16 years of data, all the wind directions are represented.

Table 4.3. Sector wind speed ratios between the sites of Côte Nord and Chasseral and between Chaux-de-Fonds and Chasseral.

	Côte Nord		Chaux-de-Fonds	
Sector	a_{ref}	a_{pred}	a_{ref}	a_{pred}
0	0.79	0.53	0.49	0.32
30	0.52	0.68	0.52	0.45
60	0.45	0.55	0.40	0.44
90	0.63	0.46	0.34	0.39
120	0.73	0.71	0.30	0.38
150	0.77	0.53	0.32	0.32
180	0.80	0.72	0.38	0.34
210	0.64	0.68	0.34	0.36
240	0.58	0.58	0.36	0.34
270	0.52	0.54	0.35	0.23
300	0.42	0.42	0.27	0.25
330	0.48	0.44	0.25	0.27

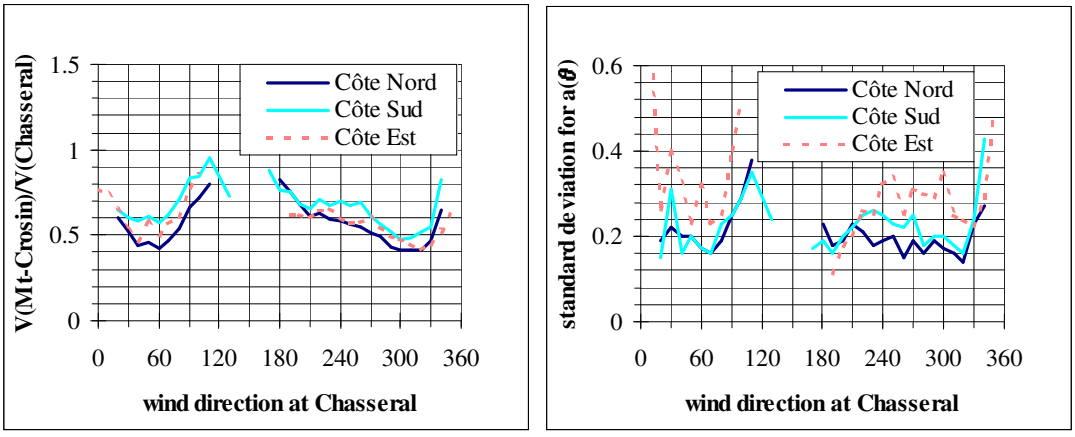

a) b)

Figure 4.3. a) Mt-Crosin to Chasseral wind speed ratio, b) Standard deviation of the wind speed ratio for the three sites of Côte Nord, Côte Sud and Côte Est versus the wind direction at Chasseral. Values obtained with the data sets described in Chapter 3, i.e. 16 months for Côte Nord, 15 months for Côte Sud, and 9 months for Côte Est.

Compared to the two other sites on Mt-Crosin, the site of Côte Nord shows in general lower wind speed ratios. The reason for this is essentially to be found in the fact that the measurements were taken at 10m above ground instead of the 30m for the sites of Côte Sud and Côte Est. Apart from this difference, the three sites on Mt-Crosin show a similar behaviour of the wind speed ratio versus the wind direction. The variation of the Mt-Crosin to Chasseral wind speed ratio with the wind direction at Chasseral does not seem to be particularly well related to the fact that the wind blows parallel or perpendicular to the main relief axis. In fact for the wind blowing from the 60° sector (more or less parallel to the mountain chain), we observe a minimum in the wind speed ratio, whereas for the wind 240° direction (also more or less parallel), we tend to observe a local maximum. The tendency of the wind speed ratio to increase for the north wind (340° to 20° sector) is probably exaggerated compared to reality, considering the shadowing effect of the telecommunication tower on the Chasseral anemometer for these wind directions. As a consequence, the wind speed ratio from the observations is suspected to be artificially increased.

The standard deviation of the wind speed ratio obtained for the Mt-Crosin sites is relatively high compared to the ratio itself, with values that represent typically some 20% to 50% of the ratio for Côte Nord and Côte Sud. The site of Côte Est shows even larger standard deviations. Whether this would correspond to a real site characteristic (e.g. larger turbulence) or reveals some instrumental problems at Côte Est is not clear. The strength of the standard deviation already indicates that the simple assumption according to which the wind speed at Mt-Crosin would be proportional to the wind speed at Chasseral, with a proportionality factor depending on the wind direction only, is a coarse approximation to the real situation.

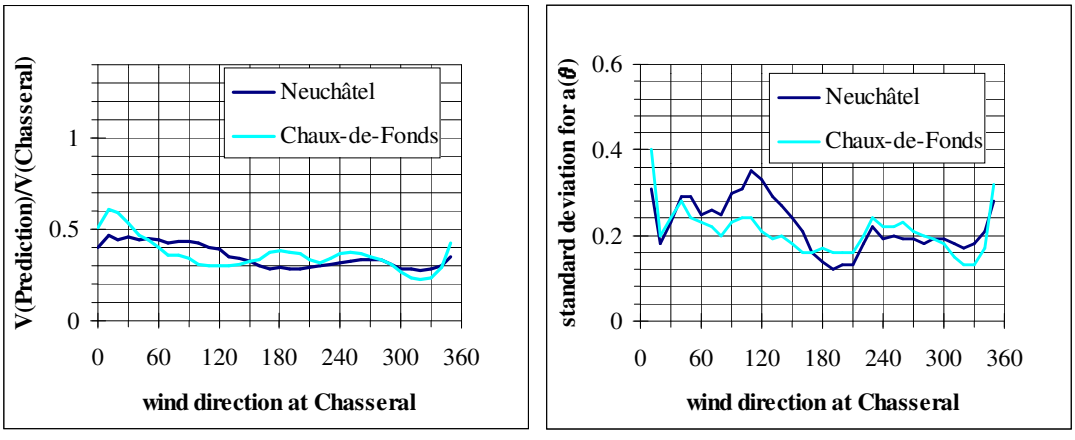

a) b)

Figure 4.4. a) Neuchâtel to Chasseral and Chaux-de-Fonds to Chasseral wind speed ratio, b) Standard deviation of the wind speed ratio versus the wind direction at Chasseral. Values obtained using 16 years of data (January 1982 to December 1997).

The Chasseral to Neuchâtel and Chasseral to Chaux-de-Fonds wind speed ratios obtained from the observations show generally lower values than the ones obtained for the Mt-Crosin site. As the two sites of Neuchâtel and Chaux-de-Fonds are at lower altitudes, they are less directly coupled to the geostrophic wind and generally exhibit lower wind speeds. The fact that the wind speed ratio at Neuchâtel shows higher values for the 'bise' situations (wind direction between 0° and 90° at Chasseral) than for the south-west to north-west situations might be due to the particular shape of the wind speed profiles typically observed in these cases. Furger (1990) found that 'bise' wind speed profiles exhibit stronger winds in the lower levels than at high altitude (jet type profiles). The standard deviation of the measured wind speed ratio for the site of Neuchâtel and Chaux-de-Fonds are even more significant than the ones of Mt-Crosin reaching values up to 35%-80% of the ratio itself.

In addition to the sector variation of the wind speed ratio, its wind speed dependency was also investigated. Figure 4.5 shows the behaviour of the Côte Nord to Chasseral wind speed ratio for the 240° and 60° wind directions. The ratio shows a decreasing tendency with increasing Chasseral wind speed with significant variations about this tendency. For Chasseral wind speeds lower than 5 m/s the wind speed ratio can vary by a factor of 10 within a wind speed class (see e.g. wind speed 4 m/s for the 240° wind direction). For higher wind speeds (v> 10 m/s), the records for the wind speed ratio within one wind speed class cluster around an average value, but still show significant variation around it.

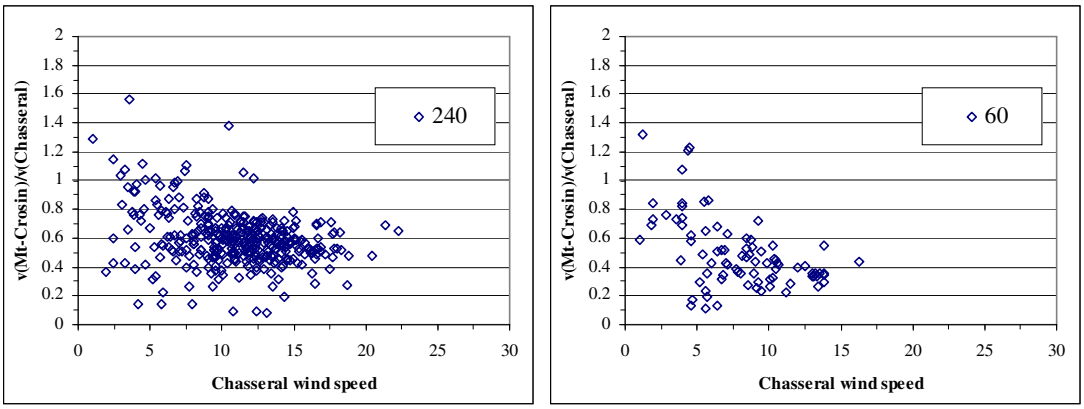

a) b)

Figure 4.5. Ratio between the Côte Nord and Chasseral wind speed for the wind direction a) 240° and b) 60°.

Averaging the wind speed ratios obtained in each Chasseral wind speed and direction classes led to the behaviour presented in Figure 4.6.a) to f) for the three sites of Mt-Crosin and in Figure 4.7.a) to d) for Chaux-de-Fonds and Neuchâtel.

From the plots versus the Chasseral wind speed, we can observe that:

- up to a wind speed of 10m/s at Chasseral the wind speed ratio decreases tendency for all the stations
- for higher wind speeds, the ratio seems to stabilise at a constant value. However, some wind directions still show a decreasing ratio (300° at Côte Sud, 330° at Côte Est and Neuchâtel) while for others (270° at Côte Nord and Neuchâtel, 180° at Chaux-de-Fonds) the ratio starts to increase again above 10m/s at Chasseral

From the Mt-Crosin plots versus the Chasseral wind direction we can see that:

- the higher ratios are clearly associated with the lowest wind speed
- the smallest wind speeds seem to be concentrated around the less frequent sectors (120° to 180°).

The plot for Neuchâtel versus the wind direction indicates that the ratio variation with the wind direction is more or less the same for all the Chasseral wind speed classes. We have in this case a maximum of the ratio occurring for the 60° wind direction, a minimum around 150°-180° followed by another maximum around 270°, and this independent of the wind speed class. This behaviour can however not be observed in the general case. In fact we can see from the Chaux-de-Fonds data versus the wind direction, that the minimum that can be observed for the lower wind speed (2 and 4 m/s) around the 150° direction corresponds more to a maximum for the wind speed classes 10 and 15 m/s. Considering the relative sparseness of data, this kind of comparison is difficult to make from the Mt-Crosin plots versus the wind direction.

From the above results (Figure 4.5), it appears that the approximation of a wind speed ratio only depending on the reference station wind direction is certainly not true when considering isolated records. However when averaging the observed ratios within the Chasseral wind speed classes, it can be seen from Figure 4.7 that for most of the sectors and for Chasseral wind speeds above ~7 m/s, the average ratio remains more or less constant when the Chasseral wind speed is changed. This feature is not so obviously apparent in the Mt-Crosin plots (Figure 4.6) probably due to the relatively sparse datasets.

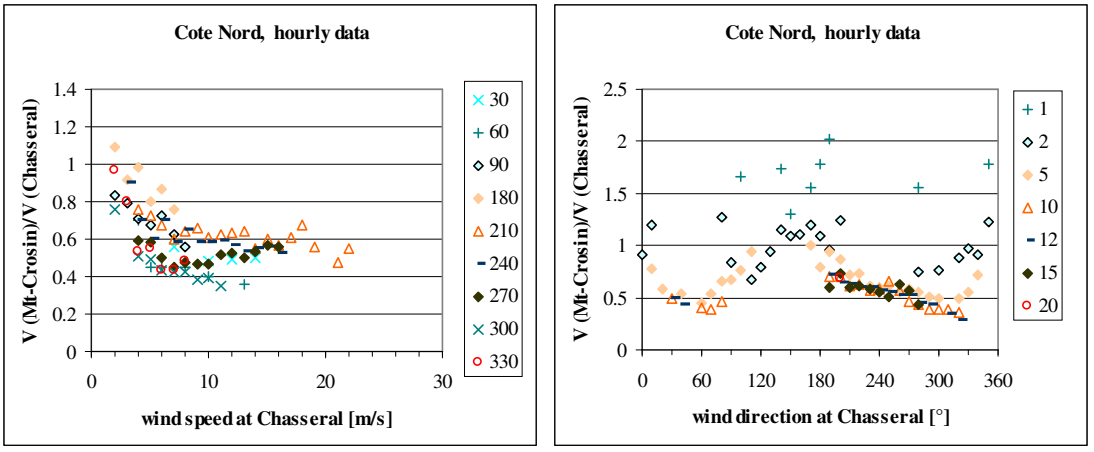

a)

b)

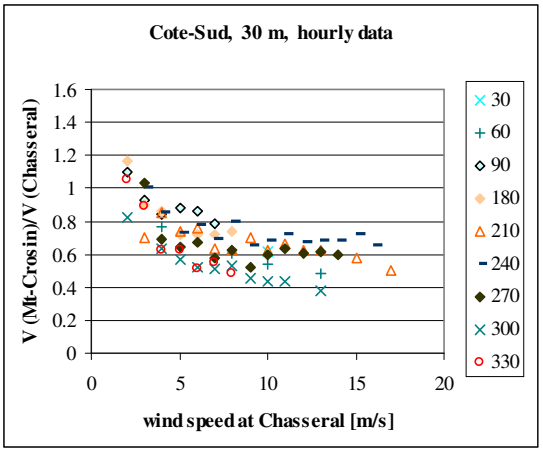

b)

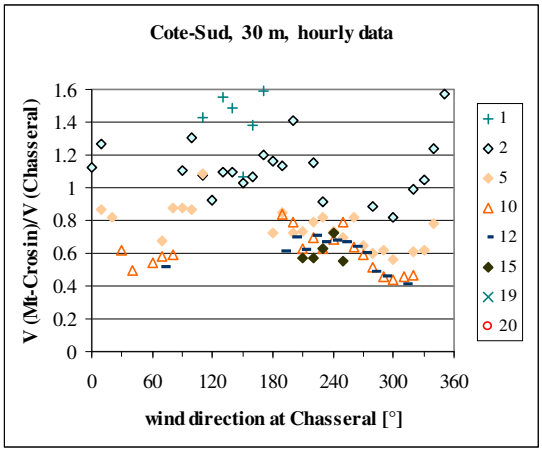

d)

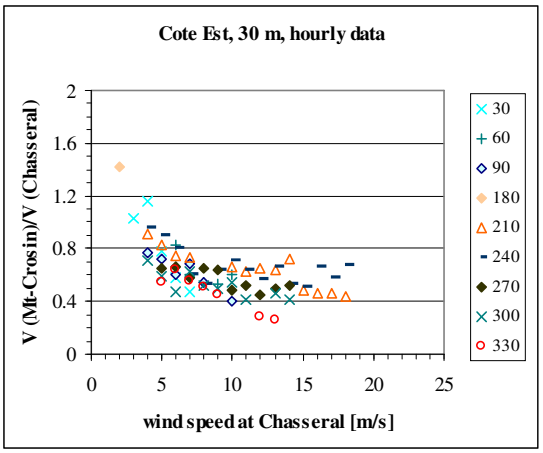

e)

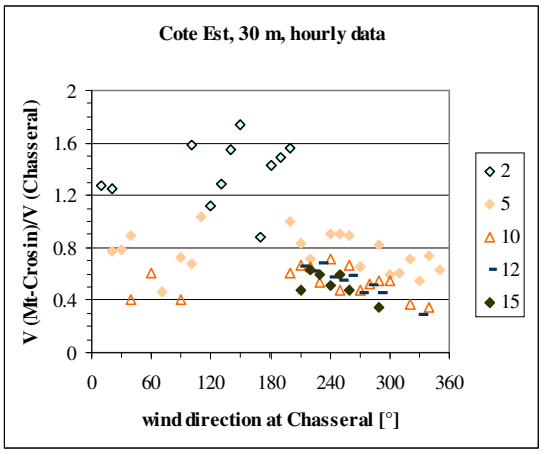

f)

Figure 4.6. Mt-Crosin to Chasseral wind speed ratio vs. Chasseral wind speed and direction for the three sites of Côte Nord (a and b), Côte Sud (c and d) and Côte Est (e and f). The labels for the symbols stand for the Chasseral wind direction in a, c, and e, and for the Chasseral wind speed in b, d, f. Values obtained with the data sets described in Chapter 3, i.e. 16 months for Côte Nord, 15 months for Côte Sud, and 9 months for Côte Est.

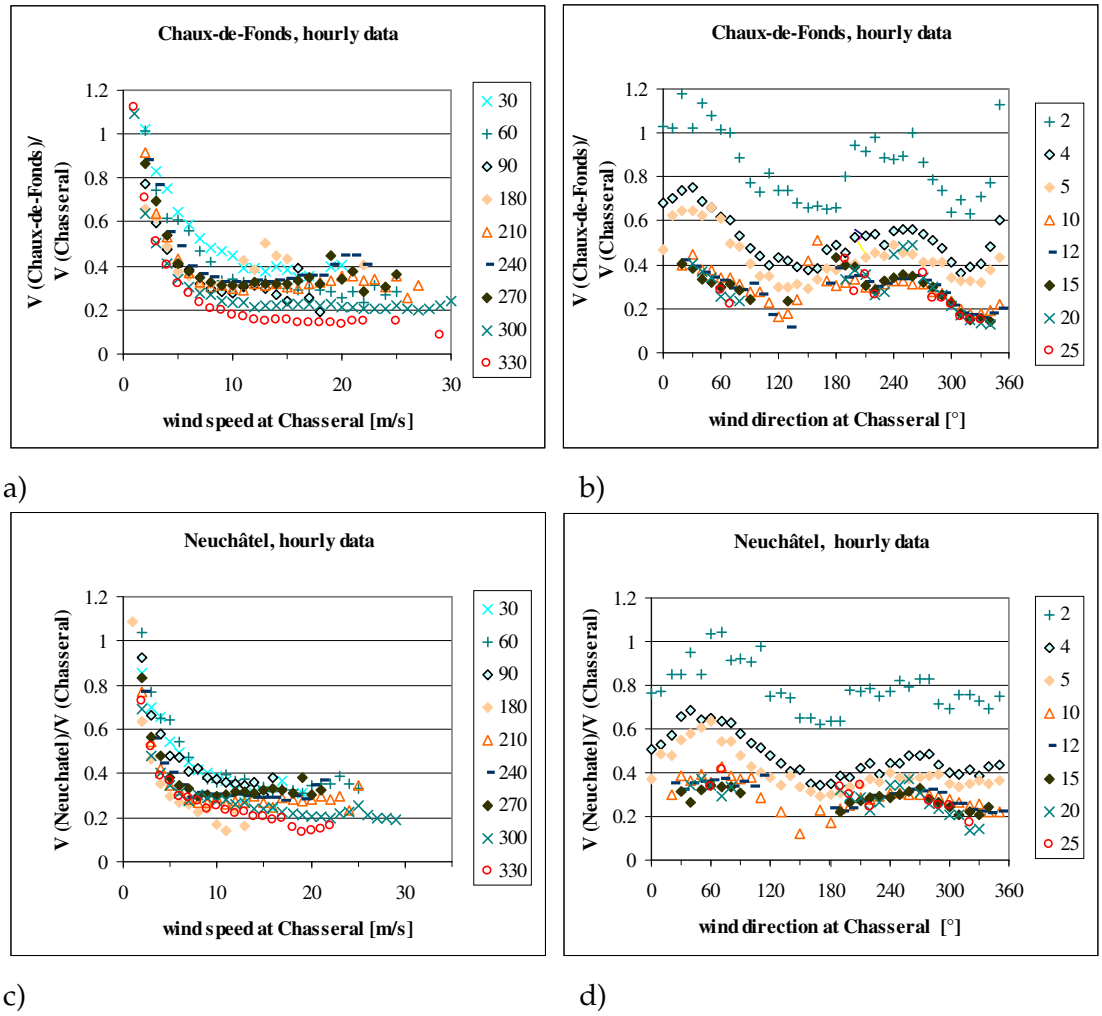

Figure 4.7. Wind speed ratio vs. Chasseral wind speed and direction for the sites of Chaux-de-Fonds (a and b), and Neuchâtel (c and d). The labels for the symbols stand for the Chasseral wind direction in a, and c, and for the Chasseral wind speed in b, and d. Values obtained with 16 years of data (January 1982 to December 1997).

Considering the behaviour observed above for the wind speed ratios $a(\theta)$ (Figure 4.6 and Figure 4.7), the evaluation of the sector mean value for $a(\theta)$ using only simultaneous records with a wind speed above the threshold of 5 m/s at Chasseral should tend to slightly underestimate its value. From the point of view of wind power assessment, this should lead to an underestimation of the available wind power potential of the site, which would bring us on the conservative side in terms of viability for a wind farm. When performing a prediction either with an MCP method or with a transposition of the entire distribution, using relationships from measurements, we will therefore use relationships established from records with a wind speed higher than 5 m/s at Chasseral.

4.1.2 Wind speed ratios during homogeneous events

Looking at events, which show a reasonable persistence like established 'bise' situations or west-south west wind situations, we can in fact observe that, for situations where the wind direction at Chasseral remains more or less constant over several hours, the ratio between the wind at Mt-Crosin and at Chasseral show significant fluctuations. This demonstrates again the level of simplification associated with the assumption of a wind speed ratio that would only vary with the wind direction at the Chasseral station. This is illustrated by Figure 4.8 for a 'bise' situation that established overnight between the 11th and 12th of June 1994.

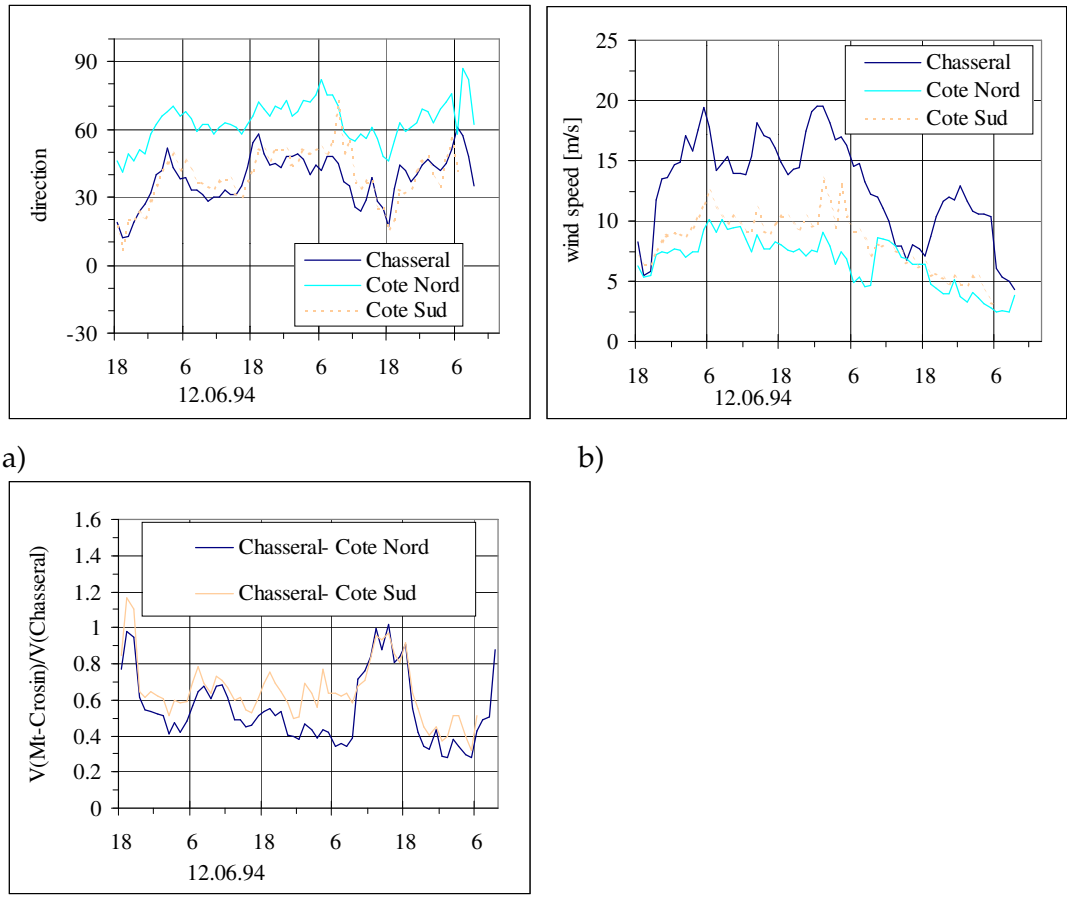

Figure 4.8. Time evolution of the measured a) wind direction, b) wind speed at the site of Chasseral, Côte Nord and Côte Sud for a persisting 'bise' situation over the period between the 11th of June (18h) and the 14th of June 1994 (9h). c) Mt-Crosin to Chasseral wind speed ratio.

For some 36 hours (from the 12th at 0h) the wind speed at Chasseral fluctuated around some 16 m/s and the wind direction remained in the sector 45°±15°. We can

observe from Figure 4.8.a that the time evolution of the wind direction at both Chasseral and Mt-Crosin are practically in phase over the whole episode, which is a good indication that both stations are under the influence of the same meteorological phenomenon. This correlation between both sites is no longer visible in the wind speed plots (Figure 4.8.b) and this results in a strong fluctuation of the Mt-Crosin to Chasseral wind speed ratio (Figure 4.8.c). The behaviour observed here indicates that though the wind direction is reasonably stationary, the wind speed ratio exhibits strong variations. This feature was observed for several events and seems to be more the rule than the exception.

4.2 Results from back-predictions using MCP Methods

Standard and matrix MCP methods have been developed to derive long-term predictions of the mean and sector mean wind speeds at the prediction site. In this section, we will apply them not for the sake of the long-term prediction but to see how far the underlying assumptions in the methods are able to reproduce the measured wind speed at the prediction site from the short-term dataset at the reference site.

For this application, we chose to show the transposition from Chasseral to the site of Côte Nord. Some results for Chaux-de-Fonds will also be shown. The population matrix $P = (p_{i,j})$ representing the number of records with the wind direction i at the reference site (row index) and j at the prediction site (column index) is given below. It shows a strong diagonal dominance.

Population matrix $P = (p_{i,j})$ for the sites of Chasseral and Côte Nord (Feb 94-May 95)

Prediction site index J →

Secteur	**0**	**30**	**60**	**90**	**120**	**150**	**180**	**210**	**240**	**270**	**300**	**330**	
0	21	**67**	52	18	8	1	2	2	1	8	3	7	**190**
30	16	39	**229**	60	5	1	0	0	1	0	3	2	**356**
60	7	8	83	**182**	46	0	3	3	0	1	1	1	**335**
90	4	2	32	**215**	206	3	4	5	1	0	1	0	**473**
120	1	8	12	41	**127**	18	6	3	1	2	1	1	**221**
150	4	6	5	15	**54**	28	52	32	3	2	2	1	**204**
180	1	3	6	12	31	16	85	**212**	34	18	6	2	**426**
210	2	1	10	8	15	10	70	**573**	333	49	10	2	**1083**
240	1	1	6	2	7	8	20	102	**580**	323	14	4	**1068**
270	7	3	2	2	4	0	9	57	147	**661**	84	10	**986**
300	13	7	1	3	4	0	1	12	26	205	**249**	95	**616**
330	139	71	3	3	5	2	0	3	7	15	71	**178**	**497**

	216	**216**	**441**	**561**	**512**	**87**	**252**	**1004**	**1134**	**1284**	**445**	**303**

Eliminating the bins with the frequency of occurrence lower then the threshold value of 5%, and normalising for the wind directions at the reference site, we end up with the matrix $W = (w_{i,j})$ that will be used to predict the wind rose at the site of Côte Nord. Repeating the operation and normalising for the wind directions at the prediction site gives the matrix $Z = (z_{i,j})$, used to evaluate the sector mean wind speed at the prediction site. Both matrices are also presented below for the case of Chasseral and Côte Nord.

Matrix Wij (*100) for the sites of Chasseral and Côte Nord (Feb 94-May 95)

Prediction site index J →

Secteur	**0**	**30**	**60**	**90**	**120**	**150**	**180**	**210**	**240**	**270**	**300**	**330**	
0	13.3	**42.4**	32.9	11.4	0.0	0.0	0.0	0.0	0.0	0.0	0.0	0.0	**100**
30	0.0	11.9	**69.8**	18.3	0.0	0.0	0.0	0.0	0.0	0.0	0.0	0.0	**100**
60	0.0	0.0	26.7	**58.5**	14.8	0.0	0.0	0.0	0.0	0.0	0.0	0.0	**100**
90	0.0	0.0	7.1	**47.5**	45.5	0.0	0.0	0.0	0.0	0.0	0.0	0.0	**100**
120	0.0	0.0	6.1	20.7	**64.1**	9.1	0.0	0.0	0.0	0.0	0.0	0.0	**100**
150	0.0	0.0	0.0	8.3	**29.8**	15.5	28.7	17.7	0.0	0.0	0.0	0.0	**100**
180	0.0	0.0	0.0	0.0	8.6	0.0	23.5	**58.6**	9.4	0.0	0.0	0.0	**100**
210	0.0	0.0	0.0	0.0	0.0	0.0	7.2	**58.7**	34.1	0.0	0.0	0.0	**100**
240	0.0	0.0	0.0	0.0	0.0	0.0	0.0	10.1	**57.7**	32.1	0.0	0.0	**100**
270	0.0	0.0	0.0	0.0	0.0	0.0	0.0	6.0	15.5	**69.7**	8.9	0.0	**100**
300	0.0	0.0	0.0	0.0	0.0	0.0	0.0	0.0	0.0	37.3	**45.4**	17.3	**100**
330	30.3	15.5	0.0	0.0	0.0	0.0	0.0	0.0	0.0	0.0	15.5	**38.8**	**100**

	43.6	**69.8**	**142.5**	**164.7**	**162.8**	**24.6**	**59.4**	**151.1**	**116.7**	**139.1**	**69.7**	**56.1**

Matrix Zij for the sites of Chasseral and Côte Nord (Feb 94-May 95)

Prediction site index J →

Secteur	**0**	**30**	**60**	**90**	**120**	**150**	**180**	**210**	**240**	**270**	**300**	**330**	
0	11.1	**37.9**	13.1	0.0	0.0	0.0	0.0	0.0	0.0	0.0	0.0	0.0	**62.1**
30	8.5	22.0	**57.8**	12.0	0.0	0.0	0.0	0.0	0.0	0.0	0.0	0.0	**100.4**
60	0.0	0.0	21.0	36.5	9.9	0.0	0.0	0.0	0.0	0.0	0.0	0.0	**67.4**
90	0.0	0.0	8.1	**43.2**	**44.4**	0.0	0.0	0.0	0.0	0.0	0.0	0.0	**95.7**
120	0.0	0.0	0.0	8.2	27.4	22.5	0.0	0.0	0.0	0.0	0.0	0.0	**58.1**
150	0.0	0.0	0.0	0.0	11.6	**35.0**	22.9	0.0	0.0	0.0	0.0	0.0	**69.5**
180	0.0	0.0	0.0	0.0	6.7	20.0	**37.4**	22.5	0.0	0.0	0.0	0.0	**86.6**
210	0.0	0.0	0.0	0.0	0.0	12.5	30.8	**60.7**	31.4	0.0	0.0	0.0	**135.5**
240	0.0	0.0	0.0	0.0	0.0	10.0	8.8	10.8	**54.7**	27.2	0.0	0.0	**111.5**
270	0.0	0.0	0.0	0.0	0.0	0.0	0.0	6.0	13.9	**55.6**	20.8	0.0	**96.3**
300	6.9	0.0	0.0	0.0	0.0	0.0	0.0	0.0	0.0	17.2	**61.6**	34.8	**120.6**
330	**73.5**	40.1	0.0	0.0	0.0	0.0	0.0	0.0	0.0	0.0	17.6	**65.2**	**196.4**

	100	**100**	**100**	**100**	**100**	**100**	**100**	**100**	**100**	**100**	**100**	**100**

The diagonal dominance is no longer so obvious when looking at the matrix $W = (w_{i,j})$ for the sites of Chasseral and Chaux-de-Fonds. In this case, we can clearly see the channelling leading to an accumulation of records for the 60° and 240° wind directions at Chaux-de-Fonds, which corresponds to the direction of the valley where the anemometer is located.

Matrix Wij (*100) for the sites of Chasseral and Chaux-de-Fonds (Jan 82-Dec 97)

Prediction site index J →

Secteur	**0**	**30**	**60**	**90**	**120**	**150**	**180**	**210**	**240**	**270**	**300**	**330**	
0	22.6	**47.1**	14.3	0.0	0.0	0.0	0.0	0.0	8.8	0.0	0.0	7.2	**100**
30	12.1	**51.3**	36.7	0.0	0.0	0.0	0.0	0.0	0.0	0.0	0.0	0.0	**100**
60	8.2	34.2	**50.3**	7.3	0.0	0.0	0.0	0.0	0.0	0.0	0.0	0.0	**100**
90	9.9	31.7	**43.8**	14.6	0.0	0.0	0.0	0.0	0.0	0.0	0.0	0.0	**100**
120	8.6	16.8	**28.0**	24.7	12.4	0.0	0.0	0.0	9.6	0.0	0.0	0.0	**100**
150	6.8	8.5	10.3	9.1	6.1	6.2	**16.3**	10.8	15.5	10.3	0.0	0.0	**100**
180	0.0	0.0	0.0	0.0	0.0	0.0	15.4	**37.3**	32.0	15.2	0.0	0.0	**100**
210	0.0	0.0	0.0	0.0	0.0	0.0	5.4	36.4	**46.4**	11.7	0.0	0.0	**100**
240	0.0	0.0	0.0	0.0	0.0	0.0	0.0	19.3	**70.8**	9.9	0.0	0.0	**100**
270	0.0	0.0	0.0	0.0	0.0	0.0	0.0	16.0	**73.4**	10.6	0.0	0.0	**100**
300	0.0	0.0	0.0	0.0	0.0	0.0	0.0	13.9	**52.2**	24.1	9.8	0.0	**100**
330	17.4	8.9	0.0	0.0	0.0	0.0	0.0	0.0	18.4	17.2	17.7	**20.3**	**100**

	85.7	**198.6**	**183.2**	**55.6**	**18.5**	**6.2**	**37.1**	**133.8**	**327.1**	**99.1**	**27.5**	**27.5**

The evaluation of the Côte Nord mean wind speed and wind rose is made using eq. 2.2 to eq. 2.6, with the linear and proportional relationships using the regression parameters given in Table 4.1 and Table 4.3.

Figure 4.9 shows the results for the wind rose predictions at both Côte Nord and Chaux-de-Fonds. For a direct comparison, the same scale is used in both figures for the frequency. The predicted wind roses correspond so well to those measured that it is barely possible to differentiate them on the plots[8]. For the site of Chaux-de-Fonds, the wind rose is very different from that of Chasseral, indicating a strong channelling of the flow along the valley direction. At Côte Nord however, as could already be guessed from the diagonal dominance in the population matrix, the wind rose does not differ much from the wind rose measured at the reference site. These comparisons show that the matrix MCP method is able to reproduce the wind rose

[8] In fact, it is expected to have a perfect matching between the measurements and the prediction, when performing a back-prediction with a threshold value of 0% when filtering the population matrix. The slight difference obtained here is a consequence of the 5% threshold value.

quite accurately in a back-prediction, also in the presence of significant topographical effects.

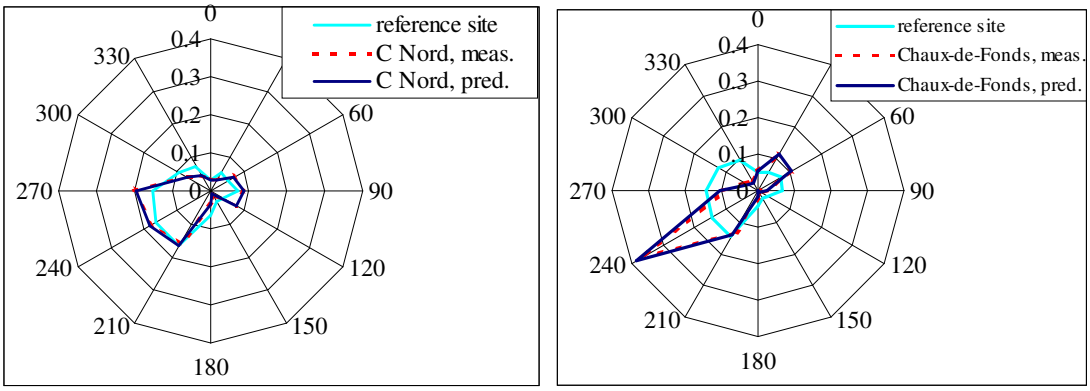

a) b)

Figure 4.9. Measured (dashed) and predicted (continuous dark line) rose at a) Côte Nord and b) Chaux-de-Fonds. The Chasseral wind rose has also been plotted (grey continuous).

The results for the sector mean wind speeds obtained from the various MCP methods are compared to the on site measurements in Figure 4.10 for the site of Côte Nord and in Figure 4.11 for the site of Chaux-de-Fonds. As far as the sector mean wind speed is concerned, both the linear and simple proportionality relationships perform well.

Concerning the choice of the MCP methods, it appears that the matrix method using relationships obtained for data binned according to the prediction site wind direction produces better predictions than the other methods.

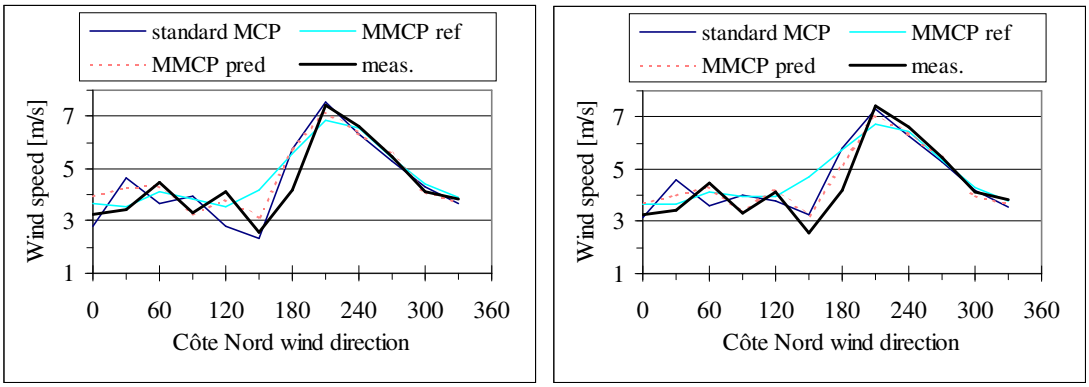

a) b)

Figure 4.10. Measured and predicted sector mean wind speed at the site of Côte Nord obtained from the various MCP methods. a) assuming proportionality relationships, b) assuming linear relationships with intercept.

For the site of Côte Nord, a summary of the measured and predicted sector mean wind speeds is given in Table 4.4, together with the relative errors of the predictions. The *MMCP pred* method performs very well for the most frequent wind directions at Mt-Crosin (60° to 120° and 210° to 270°). For the sectors where the average wind speed varies in a non-monotonic way with sector (30° to 150° sectors in Figure 4.10), the *MMCP pred* method noticeably outperforms the standard method. This is due to the fact that the standard method does not account for direction changes between the reference and prediction site. The *MMCP ref* method tends to smooth the mean sector wind speed curve and the improvement relative to the standard MCP method is not obvious.

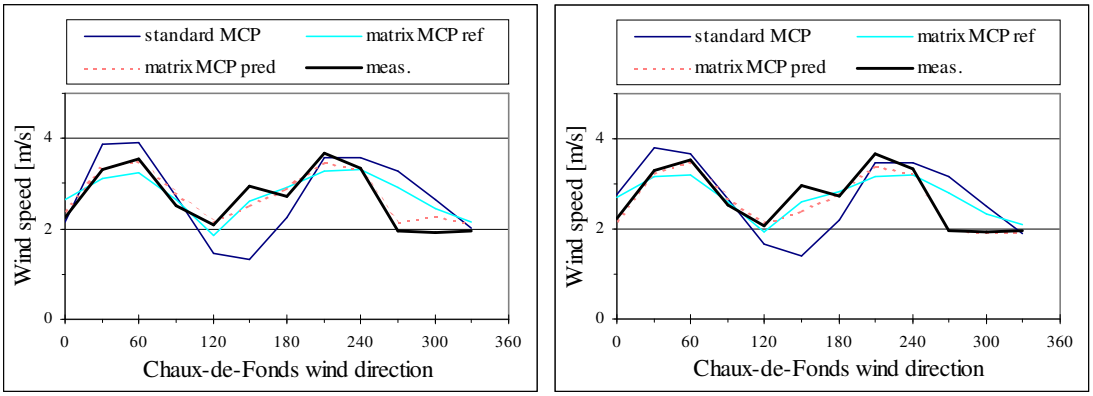

a) b)

Figure 4.11. Measured and predicted sector mean wind speed at the site of Chaux-de-Fonds obtained from the various MCP methods. a) assuming proportionality relationships, b) assuming linear relationships with intercept. (back-prediction with 16 years of data)

Table 4.4. Comparison of the measured and predicted sector mean wind speed at the site of Côte Nord, using simple proportionality relationships. (back-prediction with short term data).

Sector	Wind speed (m/s)				Relative error (%)		
	MCP-std.	MMCP-ref	MMCP-pred	Meas.	MCP-std	MMCP-ref	MMCP-pred
0	2.8	3.7	4.0	3.3	-15	12	21
30	4.7	3.5	4.3	3.45	35	3	25
60	3.7	4.2	4.3	4.45	-18	-7	-3
90	3.9	3.8	3.3	3.33	18	15	-2
120	2.8	3.5	3.9	4.11	-32	-14	-6
150	2.4	4.2	3.1	2.55	-8	64	23
180	5.7	5.6	5.8	4.21	36	32	37
210	7.5	6.9	7.2	7.42	1	-8	-3
240	6.4	6.6	6.4	6.6	-4	0	-3
270	5.3	5.4	5.6	5.45	-3	-1	2
300	4.3	4.4	4.1	4.15	4	6	-1
330	3.7	3.9	3.7	3.81	-4	2	-2

The overall predicted mean wind speeds for the five prediction sites have been calculated for the three MCP methods, also using the two types of site to site relationship. The results are summarised in Table 4.5 to Table 4.9. These show that:

- all three methods give excellent back-predictions for the overall wind speed (maximum absolute relative error: 10%)
- for the back-prediction of the overall mean wind speed, the standard MCP gives results that are as good as the matrix MCP methods.
- except for one case, the standard MCP method systematically underpredicts the mean wind speed
- the quality of the overall wind speed back-prediction obtained with both types of linear relationships is about the same. It cannot be decided from the transposition of the average wind speed, which relationship should give a better wind power prediction.

The detailed results for the other transposition sites are given in Appendix H.

Table 4.5. Overall average wind speed back-prediction for the site of Côte Nord.

Overall average wind speed: 5.2 m/s	Using relationships $v_{pred} = a(\theta) \cdot v_{ref}$		Using relationships $v_{pred} = m(\theta) \cdot v_{ref} + c(\theta)$	
	Predicted [m/s]	Relative error %	Predicted [m/s]	Relative error %
Standard MCP	5.2	-0.5	5.2	-0.3
MMCP ref	5.2	0.7	5.2	0.6
MMCP pred	5.2	1.6	5.2	0.6

Table 4.6. Overall average wind speed back-prediction for the site of Côte Sud

Overall average wind speed: 5.3 m/s	Using relationships $v_{pred} = a(\theta) \cdot v_{ref}$		Using relationships $v_{pred} = m(\theta) \cdot v_{ref} + c(\theta)$	
	Predicted [m/s]	Relative error %	Predicted [m/s]	Relative error %
Standard MCP	5.2	-1.8	5.2	-0.6
MMCP ref	5.3	0.8	5.3	0.8
MMCP pred	5.3	0.4	5.3	0.4

Table 4.7. Overall average wind speed back-prediction for the site of Côte Est

Overall average wind speed: 5.6 m/s	Using relationships $v_{pred} = a(\theta) \cdot v_{ref}$		Using relationships $v_{pred} = m(\theta) \cdot v_{ref} + c(\theta)$	
	Predicted [m/s]	Relative error %	Predicted [m/s]	Relative error %
Standard MCP	5.6	0.2	5.5	-1.4
MMCP ref	5.9	5.4	5.7	2.3
MMCP pred	6.2	10.3	5.8	4.3

Table 4.8. Overall average wind speed back-prediction for the site of Chaux-de-Fonds

Overall average wind speed: 3.1 m/s	Using relationships $v_{pred} = a(\theta) \cdot v_{ref}$		Using relationships $v_{pred} = m(\theta) \cdot v_{ref} + c(\theta)$	
	Predicted [m/s]	Relative error %	Predicted [m/s]	Relative error %
Standard MCP	3.0	-1.7	2.9	-3.9
MMCP ref	3.1	1.9	3.0	-0.6
MMCP pred	3.1	1.8	3.0	-2.0

Table 4.9. Overall average wind speed back-prediction for the site of Neuchâtel.

Overall average wind speed: 2.9 m/s	Using relationships $v_{pred} = a(\theta) \cdot v_{ref}$		Using relationships $v_{pred} = m(\theta) \cdot v_{ref} + c(\theta)$	
	Predicted [m/s]	Relative error %	Predicted [m/s]	Relative error %
Standard MCP	2.8	-2.5	2.8	-3.6
MMCP ref	3.0	2.1	2.9	0.3
MMCP pred	3.0	3.4	2.9	0.3

Note: Another reason why the stations of Neuchâtel and Chaux-de-Fonds are interesting is the fact that they are, like Chasseral, operational since 1977 and 1979 respectively. They can therefore be used to test the assumption according to which the transposition relationships determined for a short-term period are representative of the long term. This was done for the station of Neuchâtel, using transposition relationships of the kind $v_{pred} = m(\theta) \cdot v_{ref} + c(\theta)$ obtained from data of the year 1982. Transposing the 16 years of data from Chasseral to Neuchâtel with these relationships led to an error for the predicted mean wind speed of 0.3% for the standard MCP method, 5.6% for the '*MMCP ref*' method, and 5.8% for the '*MMCP pred*' method.

4.3 Results from back-predictions using the transposition of the wind distribution

To further evaluate the validity of the assumptions on which the transposition relies, we calculated the wind distributions at the 5 prediction sites of Côte Nord, Côte Sud, Côte Est, Neuchâtel and La Chaux-de-Fonds, using the method presented in Section 2.2. Again the transposition was done for both the linear and proportional relationships. These were calculated for data binned according to the Chasseral wind direction in steps of 10° (see Figure 4.3 and Figure 4.4 for the sector variation of the wind speed ratios). For the application of the transposition methodology, we linearly interpolated the wind speed ratios for the wind directions where no record was available.

The wind speed probability density function obtained from the transposition are compared to those measured in Figure 4.12 for the sites of Neuchâtel and Chaux-de-Fonds, and in Figure 4.13 for the sites on Mt-Crosin. For the assumption of proportionality relationships, the average wind speed corresponding to the calculated distributions are given in Table 4.10 together with the annual wind energy that would be produced by a Vestas-V44 wind turbine in the same wind conditions. The relative errors of the transposed average wind speed and wind energy production are also given. Table 4.11 gives the same for the assumption of linear relationships such as $v_{pred} = m(\theta) \cdot v_{ref} + c(\theta)$.

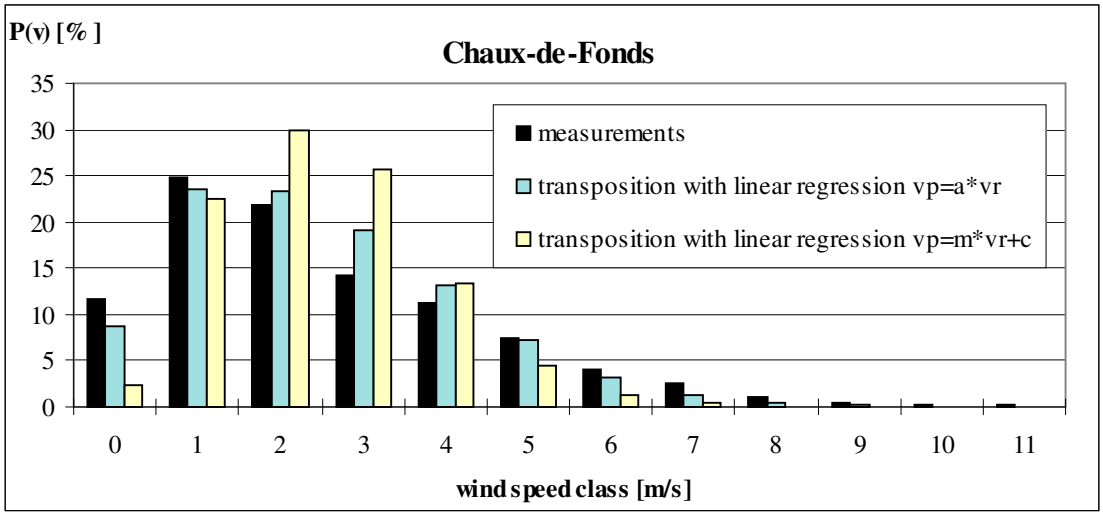

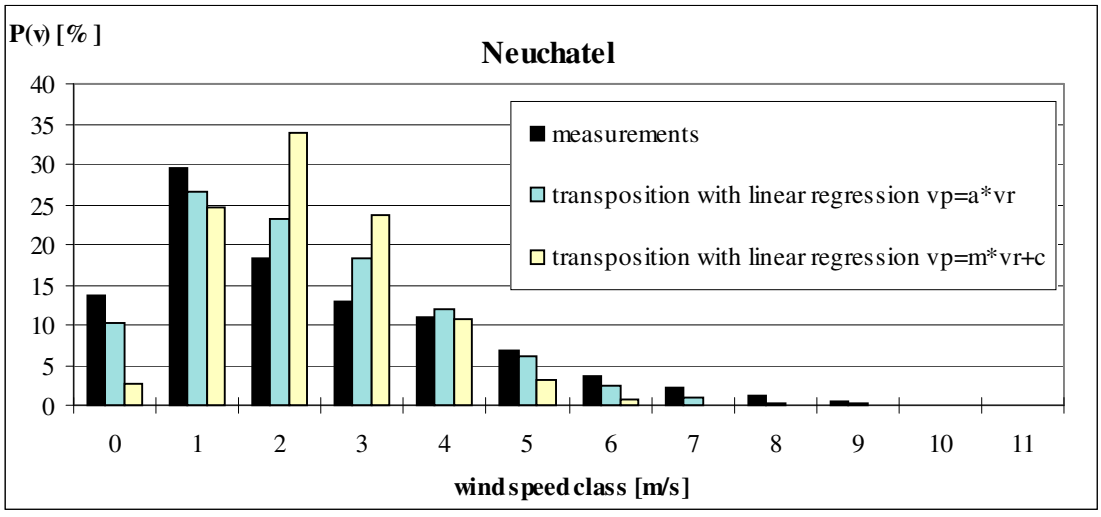

Figure 4.12. Comparison of the transposed and measured wind speed distributions at the sites of Chaux-de-Fonds and Neuchâtel.

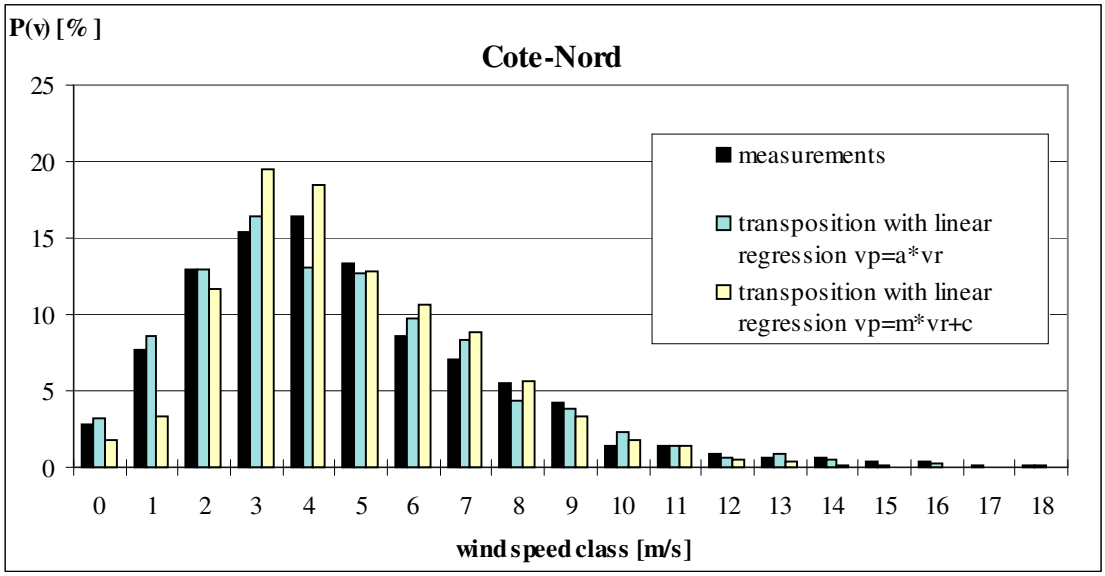

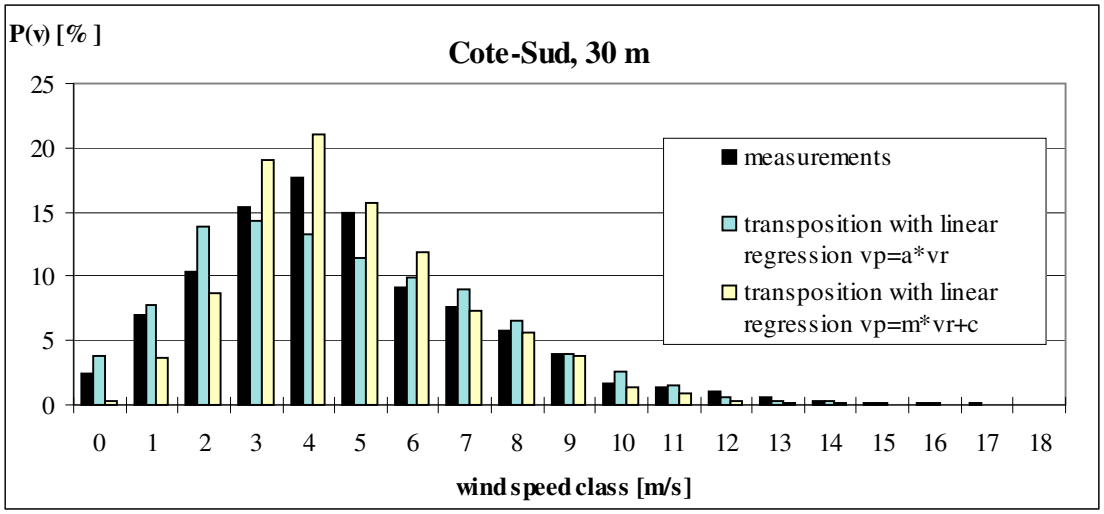

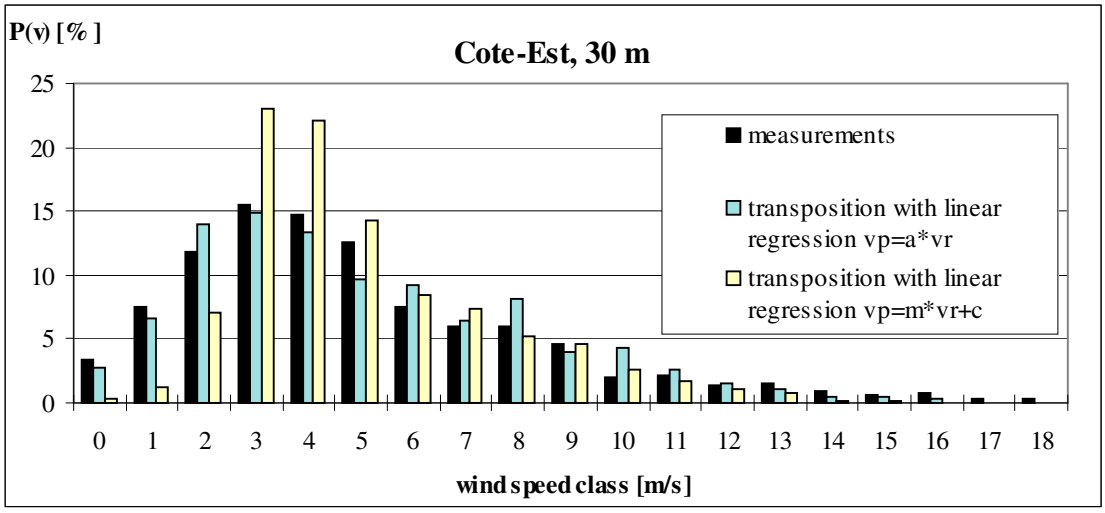

Figure 4.13. Comparison of the transposed and measured wind speed distributions at the three sites of Côte Nord, Côte Sud and Côte Est.

As was already seen in the previous section, both types of site-to-site relationship produce good predictions of the overall average wind speed (absolute relative error less then 2.6% for $v_{pred} = a(\theta) \cdot v_{ref}$ and less than 3.5% for the linear relationships $v_{pred} = m(\theta) \cdot v_{ref} + c(\theta)$).

However, as can be seen from the frequency diagrams for the 5 sites, the assumption of simple proportionality relationships produces better results for the wind speed distribution than the assumption of linear relationships. We can see that due to the shift associated with the intercept *c* imposed on the original distribution (see also Appendix G), the lower wind speed classes are systematically underpredicted when using a linear transformation. Since the slopes *m* of the linear relationships are generally smaller than the average wind speed ratio, a transposition with a linear relationship also tends to underestimate the transposed wind values for high wind speed conditions at the reference site.

To illustrate this effect, we started from a Weibull distribution with parameters *A=8.6* and *k=1.6* (quite typical values for the Chasseral wind distribution) and transformed it with the linear and proportional relationships. As an example, the transformation parameters were chosen to be *m=0.16*, *c=2.12* and *a=0.4*, which are the regression constants relating the Chasseral and Chaux-de-Fonds sites for the 60° wind direction. The transformed Weibull distributions, together with the initial one are plotted in Figure 4.14.

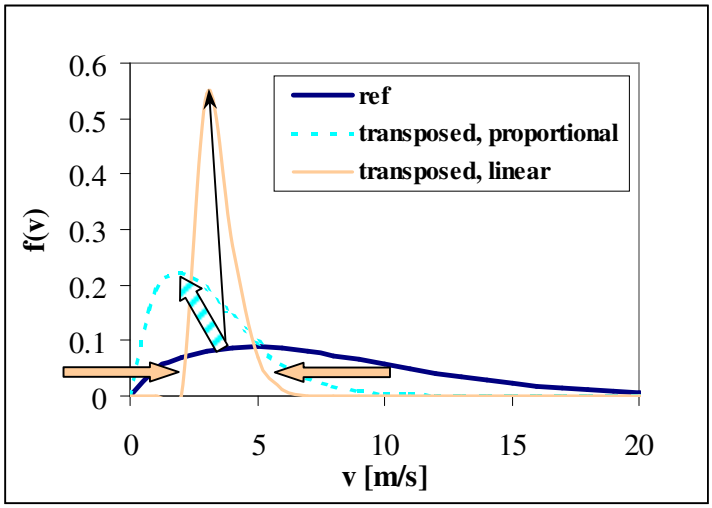

Figure 4.14. Transformation of a Weibull distribution under a linear relationship $v_{pred} = m(\theta) \cdot v_{ref} + c(\theta)$ and under a proportional relationship $v_{pred} = a(\theta) \cdot v_{ref}$. The original distribution (labelled 'ref') is given by the parameters *A=8.6* and *k=1.6*.

This clearly shows why, under a linear transformation with positive intercept, we obtain a distribution that underestimates the frequency of the lowest and highest wind speed classes. Another consequence of this observation is that if both the linear and proportional transformations produce transposed distributions that reproduce the average wind speed with good accuracy, the linear transformation will underestimate the wind power potential relative to the proportional transformation. This is what can actually be observed from the comparisons of the yearly energy production given in Table 4.10 and Table 4.11. If the error on the mean wind speed prediction is of the same order for both types of relationship, the linear one gives stronger underpredictions than the proportional relationship. This is particularly sensitive for the site of Neuchâtel and Chaux-de-Fonds, for which the introduction of an intercept strongly reduces the slope of the transformation.

Table 4.10 shows that with the relationship parameters used for the transposition, we quasi-systematically underpredict the average wind speed. This is probably a consequence of the fact that we only considered wind speed above 5 m/s at Chasseral, hence neglecting the wind speed ratios above the average that were obtained for the lower wind speed categories (see Figure 4.6 and Figure 4.7). The associated yearly energy production is overestimated by 0.3% to 10% for the Mt-Crosin sites, when using the proportionality relationships whereas it is underestimated with the linear relationships.

Table 4.10. Comparison of the measured and transposed average wind speed and yearly energy production. The transposition was done assuming the simple proportionality relationship $v_{pred} = a(\theta) \cdot v_{ref}$ with proportionality factors obtained from measurements[9].

Station name	Average wind speed [m/s]			Yearly energy production [MWh/year]		
	Measured	Transposed	Relative error	Measured	Transposed	Relative error
Côte Nord	5.2	5.2	-1%	806	806	0.3%
Côte Sud	5.3	5.2	-2%	800	817	2%
Côte Est	5.6	5.6	0.1%	983	1012	10%
Neuchâtel	2.9	2.8	-3%	220	134	-39%
Chaux-de-Fonds	3.1	3.0	-2%	241	162	-33%

[9] The relative errors given here were calculated with $\frac{\Delta v}{v} = \frac{v_{pred} - v_{meas}}{v_{meas}}$. Due to rounding of the wind speed values given in the table, there might be a difference between the values given for the relative errors and the ones that can be directly calculated from the rounded wind speed.

It is worthwhile noting that the larger relative errors on the energy production estimate occur for the low wind speed sites of Neuchâtel and Chaux-de-Fonds, for which the wind power potential is weak anyway. The significant error for these sites is also a consequence of the fact that the energy production concerns the tail of the wind speed distribution ($v \geq 5m/s$). For the case of Chaux-de-Fonds these wind speed categories only represents some 10% of the time. Estimating the relative error of the predicted natural power density of the site over the entire range of wind speed would lead to a relative error of 26% instead of the 33% given in Table 4.10.

Table 4.11. Comparison of the measured and transposed average wind speed and yearly energy production. The transposition was done assuming the linear relationship $v_{pred} = m(\theta) \cdot v_{ref} + c(\theta)$ with $m(\theta)$ and $c(\theta)$ obtained from linear regressions on the measurements.

Station name	Average wind speed [m/s]			Yearly energy production [MWh/year]		
	Measured	Transposed	Relative error	Measured	Transposed	Relative error
Côte Nord	5.2	5.2	0.1%	806	739	-8%
Côte Sud	5.3	5.3	-0.1%	800	712	-11%
Côte Est	5.6	5.5	-1%	983	830	-10%
Neuchâtel	2.9	2.8	-4%	220	61	-72%
Chaux-de-Fonds	3.1	3.0	-3%	241	89	-63%

The assumption of a linear relationship $v_{pred} = m(\theta) \cdot v_{ref} + c(\theta)$ between the reference and prediction site is in fact, in terms of the wind speed ratio, a two-parameter relationship, such that:

eq. 4.1 $$v_{pred} = a(\theta_{ref}, v_{ref}) \cdot v_{ref}$$

with the function

eq. 4.2 $$a(\theta_i, v) = m(\theta_i) + \frac{c(\theta_i)}{v}$$

Another two-parameter relationship was considered to do the data transposition, which was

eq. 4.3 $$a(\theta_i, v) = a_i \cdot v^{b_i}$$

The sector dependent parameters $a_i(\theta_i)$ and $b_i(\theta_i)$ in this relation were determined by linear regressions on the equations $\ln(v_{pred}) = \ln(a_i) + b_i \ln(v_{ref})$. The resulting values, together with the r^2 regression coefficients for the site of Chaux-de-Fonds are given in Table 4.12. The relationship above represents well the wind speed dependency of

the wind speed ratios for the north-west to east wind directions (sectors 320° to 80°). This is not so for the frequently occurring south-west winds, where neither eq. 4.2 nor eq. 4.3 is appropriate to represent the averaged wind speed ratios obtained from the measurements. This is illustrated in Figure 4.15 for the 60° and 240° wind directions, where the mean wind speed ratio from the observations is plotted (crosses), together with those obtained from eq. 4.2 and eq. 4.3.

Table 4.12. Regression parameters for the two-parameter relationship eq. 4.3 relating Chaux-de-Fonds and Chasseral. (from 16 years of data).

Sect	a_i	b_i	r^2	Sect	a_i	b_i	r^2	Sect	a_i	b_i	r^2
0	2.160	-0.966	0.972	120	1.171	-0.770	0.910	240	1.094	-0.420	0.679
10	1.899	-0.739	0.903	130	1.122	-0.787	0.785	250	0.922	-0.324	0.549
20	1.699	-0.600	0.959	140	1.137	-0.782	0.900	260	0.984	-0.339	0.478
30	1.444	-0.494	0.959	150	0.858	-0.456	0.719	270	0.978	-0.399	0.716
40	1.536	-0.552	0.944	160	0.870	-0.455	0.633	280	0.978	-0.441	0.853
50	1.395	-0.528	0.948	170	0.878	-0.397	0.675	290	0.805	-0.392	0.855
60	1.397	-0.553	0.954	180	0.841	-0.331	0.510	300	0.747	-0.420	0.859
70	1.379	-0.575	0.968	190	0.791	-0.276	0.533	310	0.813	-0.526	0.879
80	1.417	-0.631	0.981	200	0.986	-0.389	0.719	320	0.858	-0.596	0.934
90	1.096	-0.546	0.880	210	0.963	-0.397	0.722	330	1.014	-0.694	0.954
100	1.058	-0.580	0.797	220	1.164	-0.514	0.894	340	1.285	-0.789	0.984
110	1.174	-0.732	0.933	230	1.050	-0.441	0.790	350	2.008	-0.925	0.976

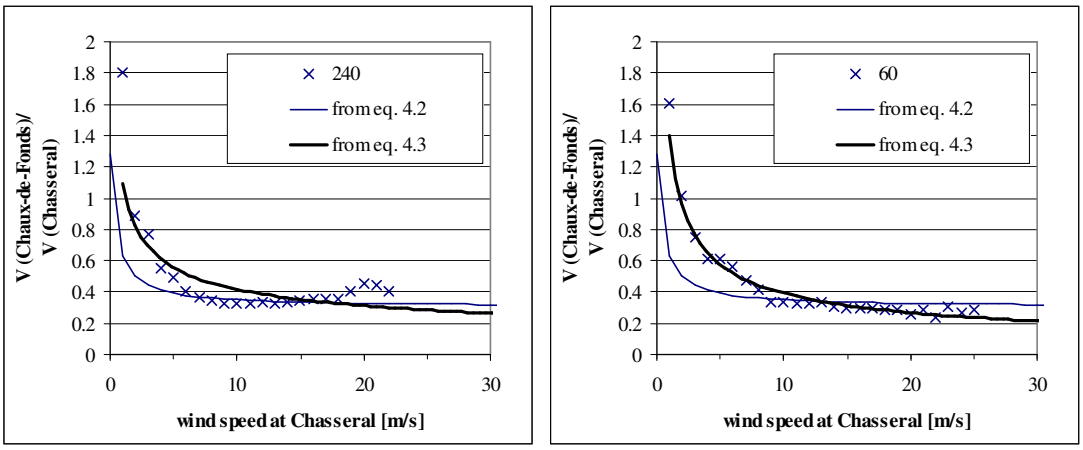

Figure 4.15. Chaux-de-Fonds to Chasseral wind speed ratio (crosses) and best fitting power function (thick line) for the a) 240° wind direction b) 60° wind direction. The function that corresponded to the linear regression $v_{pred} = m(\theta) \cdot v_{ref} + c(\theta)$ for these sectors have also been plotted (thin line).

Using eq. 4.3 to perform the wind data transposition led to the mean wind speed and yearly energy output prediction given in Table 4.13. It appears that, for both the average wind speed and energy output, the prediction made with this type of relationship is less accurate than the previous ones.

Finally we also attempted to transpose the Chasseral wind speed data using a mean wind speed ratio for each site, without considering its directional dependency. The results for the mean wind speed and yearly energy output obtained with this assumption are summarised in Table 4.14. Surprisingly enough, this simplified assumption leads to results which are only slightly less accurate than the ones produced with the sector dependent wind speed ratio (compare with Table 4.10). This is probably a consequence of the fact that, for the most frequent wind sectors, the wind speed ratio does not vary significantly from the average value.

Table 4.13. Comparison of the measured and transposed average wind speed and yearly energy production. The transposition was done assuming the relationship $v_{pred} = a \cdot v_{ref}^{\,b+1}$

Station name	Average wind speed [m/s]			Yearly energy production [MWh/year]		
	Measured	Transposed	Relative error	Measured	Transposed	Relative error
Côte Nord	5.2	5.1	-3%	806	663	-18%
Côte Sud	5.2	5.1	-3%	800	649	-19%
Côte Est	5.6	5.4	-4%	983	748	-19%
Neuchâtel	2.9	2.9	0.6%	220	60	-73%
Chaux-de-Fonds	3.0	3.2	5%	241	114	-53%

Table 4.14. Comparison of the measured and transposed average wind speed and yearly energy production. The transposition was done assuming the simple proportionality relationship $v_{pred} = a \cdot v_{ref}$ without considering direction dependency in the proportionality factors obtained from measurements.

Station name	Average wind speed [m/s]			Yearly energy production [MWh/year]		
	Measured	Transposed	Relative error	Measured	Transposed	Relative error
Côte Nord	5.2	5.1	-2%	806	820	2%
Côte Sud	5.2	5.1	-3%	800	839	5%
Côte Est	5.6	5.6	-0.2%	983	1011	10%
Neuchâtel	2.9	2.8	-3%	220	128	-42%
Chaux-de-Fonds	3.0	3.0	-3%	241	167	-31%

Though we showed that the simple proportionality assumptions are not exactly valid for isolated events, it appears that on average, this approximation leads to a reasonable estimate of the mean wind speed and energy production. It appears in fact that the introduction of additional parameters through the use of monotonically decreasing transposition function does not improve the quality of the prediction. It seems therefore that the behaviour we observed from Figure 4.6 and Figure 4.7 showing a stabilising or even increasing wind speed ratio with increasing wind speed at the reference site is significant and is better reproduced overall by a constant wind speed ratio, independent of the wind speed.

Therefore, if one wants to increase the level of complexity in the data transposition by including the wind speed variation of the transposition coefficient, it is very important that the parameterisation taking this into account allows a better representation than the average value. Considering the different behaviours observed in different sectors (see Figure 4.15), this is not easily done with a two-parameter function for the wind speed ratio. Using sector dependent quadratic functions gave results with about the same accuracy as the constant ratio assumption, but no real improvement.

Since they gave better results for the transposed wind speed distributions than the two-parameter relationships, we will use the simple proportionality relationships for the transposition using the simulation results. The results obtained in this chapter are quite encouraging as far as the transposition methodology is concerned. The next steps in the method will consist of showing that the numerical model is able to reproduce the observed values of the wind speed ratio with good accuracy. If this appears to be the case then we might hope for relative errors around 5% for the average wind speed prediction and around 10-20% for the wind energy prediction on the Mt-Crosin site.

5 Numerical model

5.1 Review of the existing models for wind power potential assessment

The numerical models used to simulate atmospheric flows over complex terrain from the point of view of wind power potential assessment can be separated into two categories: the diagnostic and prognostic models.
The diagnostic models (also called kinematic models) are not able to account for the time evolution of a given meteorological situation. This type of model only produces stationary wind fields. In addition to the stationarity assumption, these models make other simplifying assumptions to solve the flows over topography. This class of model includes, for example those that essentially solve the continuity equation ('mass-consistent models') or the linearised models (based on the developments proposed by Jackson & Hunt). These models, by resolving simplified terms of the fluid dynamics equations, have the advantage of a relatively low cost in terms of memory and CPU time. Moreover, their initialisation is relatively easy and requires few data (essentially a few wind vector values). However the application of these types of model is limited to the particular case of relatively flat topography (slopes lower than 20%) and for which thermal effects are not dominant. For steeper slopes or to reproduce the effects of flow separation downwind of summits, we need to have recourse to more complex models, which solve the entire set of fluid dynamics equations (mass, momentum and energy conservation as well as turbulence closure) or to physical modelling. For transient situations, which might be governed by thermal effects (land/sea breeze, mountain/valley breeze, heat island, etc), a prognostic model should be used.
For the various model categories mentioned above, a short description is given below. For more details concerning their use, as well as to compare their results with measurement campaigns, one can refer to the book 'Modelling of Atmospheric Flow Fields' by Lalas & Ratto (1996).

5.1.1 Mass-consistent models (diagnostic)

The mass-consistent models produce wind fields satisfying the mass conservation equation for the discrete computational mesh characterising the simulation domain.
The horizontal resolution for this type of model can vary between 50 m to some 5 km. It is possible to take into account the effects of thermal stability by introducing

an additional parameter favouring either mass continuity adjustment in the vertical (for neutral or unstable cases) or in the horizontal plane (for stable situations).

The mass-consistent models can be initialised with a wind field that is interpolated from a situation for which the geostrophic wind speed as well as wind vectors at a few ground locations are known. For some of these models, initialisation is carried out by fixing only a vertical wind profile according to an analytical expression depending on the geostrophic wind speed, ground roughness and stability conditions. Though these models are able to produce results also in steep slope situations, they will not be able to account for the effects of flow separation downwind of topographic features. The wind fields obtained this way essentially reflect the imposed initial solution and their results must be interpreted with care. Among this type of models one can quote (non-exhaustive list): NOABL (Traci et al. 1977), AIOLOS (modified version of NOABL, Tombrou & Lalas, 1990), WIND (modified version of AIOLOS, Ratto et al, 1990), CONDOR (Moussiopoulos et al, 1988).

5.1.2 Linearised Models (diagnostic)

In addition to the mass conservation equation, the linearised models solve the wind field in the computational domain, satisfying a simplified momentum conservation equation. No equation is solved for the energy conservation. This type of model is therefore not appropriate for situations in which thermal stratification of the flow plays a significant role, or for breeze type situations.
The so-called linearised models are based on the theory developed by Jackson & Hunt (1975) and assume that the flow perturbation induced by the topography is small relatively to a solution that would be described by a logarithmic wind profile close to the ground. The set of linearised equations is solved by decomposing the variables describing the perturbation, projecting them on a basis of orthogonal functions (Fourier decomposition in the x and y direction for Cartesian co-ordinates, and Bessel function decomposition for a mesh in cylindrical co-ordinates). An analytical solution in z is obtained for the different variables. The solution for the wind field in physical space is calculated by performing an inverse transformation of the Fourier and Bessel mode. Due to the linearisation, the use of such models is restricted to topographies with moderate slopes (< 20%).
For turbulence closure, a first order scheme is generally used. Examples of this type of model are MS3DJH/3R (Walmsley et al, 1986), MSFD (Beljaars et al, 1987) (Cartesian co-ordinates) as well as BZ (cylindrical co-ordinates, Troen & De Baas,

1986). The BZ model is the orographic model used to take into account the effect of topography in the WA^{S}P programme that was used for the development of the European Wind Atlas (Troen & Petersen, 1989).

5.1.3 Non-linear models (prognostic)

As was mentioned earlier, when the terrain is extremely complex (steep slopes, succession of hills or mountain chains) and when the effects associated with thermal stratification (mountain waves, flow blocking) or with the diurnal cycle can no longer be neglected, we need to have recourse to prognostic models, which include a better parameterisation of the underlying physics.

Among the non-linear models, some result directly from developments realised in the field of meso-scale meteorology. In this category, we find for example the model KAMM (Adrian & Fiedler, 1991), GESIMA (Kapitza & Eppel, 1992 and Eppel et al, 1995), MEMO (Moussiopoulos, 1996) or TVM (Thunis, 1995). Some others stem from general Navier-stokes solvers, originally conceived to calculate 'industrial' types of flow, which have been adapted for atmospheric flows. Examples of these are e.g. TASCFLOW (Raithby et al, 1987) or PHOENICS (Alm & Nygaard, 1993). For turbulence parameterisation, these models use either a first order closure scheme (mixing length) (KAMM, GESIMA, MEMO and TVM) or a k-ε closure scheme (TASCFLOW, PHOENICS).
Compared to the diagnostic models, the non-linear prognostic models are more sensitive to input data and require more data for both the model initialisation and boundary conditions. They are also more expensive in terms of computer resources.

If we wish to comment on the abilities of the different types of models, we can refer to the literature review in Appendix D where the models have been tested on the relatively gentle topography of Askervein Hill. Comparing their results with the observations allows one to draw the following conclusions:

- The diagnostic models (linearised or mass-consistent) give good results upwind and at the top of the mountain. On the downwind side however, where flow separation occurs, they clearly overestimate the wind speed.
- Only the non-linear models are able to accurately reproduce both the flow deceleration upwind and downwind of the mountain as well as its acceleration at the summit.

The good performance of the simplified models, for the particular case of Askervein Hill, is due on the one hand to the relatively flat mountain profile and on the other

hand to the fact that the measuring conditions correspond to strong wind situations where the thermal stability conditions can be considered as neutral.
For more complex terrain conditions (succession of mountains, non-negligible stability effects), in which many wind farms are installed, these simple models are no longer appropriate tools to reproduce the wind fields. The full Navier-Stokes solvers appear to be more promising from the point of view of wind power assessment. With this in mind, the code that is used in this work is the CFX4 flow solver (CFX, 1997), which is such a general purpose Navier-Stokes solver. The standard version together with the additional implementations that were made are described in the following sections.

5.2 Standard CFX4

5.2.1 Numerical model equations

The default equations solved by CFX4 are formulated in the flux form. These are the standard averaged equations used in fluid mechanics:

Continuity equation:

eq. 5.1 $$\frac{\partial \rho}{\partial t} + \frac{\partial (\rho U_i)}{\partial x_i} = 0$$

Momentum conservation equation:

eq. 5.2 $$\frac{\partial (\rho\ U_i)}{\partial t} + \frac{\partial (\rho\ U_i U_j)}{\partial x_j} = F_i + \frac{\partial \sigma_{ij}}{\partial x_j}$$

with

eq. 5.3 $$\sigma_{ij} = -p'\delta_{ij} + \mu_{eff}\left(\frac{\partial U_i}{\partial x_j} + \frac{\partial U_j}{\partial x_i}\right)$$

F_i stands for the body force vector acting on the fluid parcel (e.g. Coriolis or buoyancy force)
$\mu_{eff} = \mu + \mu_T$ is the effective fluid viscosity which, with the adoption of an eddy-viscosity model, is the sum of the molecular viscosity and turbulent viscosity
$p' = p + \frac{2}{3}\rho\ k + \frac{2}{3}\mu_{eff}\ \frac{\partial U_i}{\partial x_i} - \rho\ \vec{g}\cdot\vec{x}$ is the total fluid pressure p plus contributions associated with the turbulent kinetic energy k and flow divergence are added. When the gravity vector is considered in the simulation, the hydrostatic contribution is removed.

Energy conservation equation:

eq. 5.4 $$\frac{\partial(\rho\ H)}{\partial t}+\frac{\partial}{\partial x_j}(\rho\ U_j H-(\lambda+\frac{\mu_T}{\sigma_H}c_P)\frac{\partial T}{\partial x_j})=\frac{\partial p}{\partial t}$$

with

λ the fluid thermal conductivity

T the real temperature

$H=h+\frac{1}{2}(U^2+V^2+W^2)$ the total enthalpy (h being the static enthalpy)

c_P the specific heat at constant pressure

σ_H the turbulent Prandtl number for heat

The energy conservation equation is closed using a constitutive equation relating the static enthalpy h to pressure and real temperature.

In addition to the equations listed above, the model allows the solution of transport-diffusion equations for additional scalars φ:

eq. 5.5 $$\frac{\partial(\rho\varphi)}{\partial t}+\frac{\partial}{\partial x_i}(\rho\varphi U_i-\Gamma\frac{\partial\varphi}{\partial x_i})=S$$

where Γ is the scalar diffusion coefficient

S source/sink terms specified by the user

Various turbulence closures are available within the standard version of CFX4. Among them we only present the $k-\varepsilon$ model (Launder & Spalding, 1972), with two conservation equations for the turbulent kinetic energy k and turbulent dissipation rate ε:

eq. 5.6 $$\frac{\partial(\rho\ k)}{\partial t}+\frac{\partial(\rho\ kU_i)}{\partial x_i}=\frac{\partial}{\partial x_i}[(\mu+\frac{\mu_T}{\sigma_k})\frac{\partial k}{\partial x_i}]+P+G-\rho\varepsilon$$

eq. 5.7 $$\frac{\partial(\rho\varepsilon)}{\partial t}+\frac{\partial(\rho\varepsilon\ U_i)}{\partial x_i}=\frac{\partial}{\partial x_i}[(\mu+\frac{\mu_T}{\sigma_\varepsilon})\frac{\partial\varepsilon}{\partial x_i}]+C_1\frac{\varepsilon}{k}(P+C_3\max(G,0))-C_2\rho\frac{\varepsilon^2}{k}$$

with the shear production term:

eq. 5.8 $$P=\mu_{eff}\frac{\partial U_i}{\partial x_j}(\frac{\partial U_i}{\partial x_j}+\frac{\partial U_j}{\partial x_i})-\frac{2}{3}\frac{\partial U_j}{\partial x_j}(\rho k+\mu_{eff}\frac{\partial U_l}{\partial x_l})$$

the buoyancy production term:

eq. 5.9 $$G=-\frac{\mu_{eff}}{\rho\sigma_H}\vec{g}\vec{\nabla}\rho$$

and the turbulent viscosity:

eq. 5.10 $$\mu_T = C_\mu \rho \frac{k^2}{\varepsilon}$$

The default values for the turbulence model constants are $C_1 = 1.44$, $C_2 = 1.92$, $C_3 = 0$, $C_\mu = 0.09$, and $\sigma_\varepsilon = 0.7179$, $\sigma_k = 1$, $\sigma_H = 0.9$.

The complete set of equations is solved on a non-staggered grid by means of a finite volume approach, all the variables being defined at the centre of the control volumes. Pressure and velocity are coupled through the iterative SIMPLE algorithm (Van Doormal & Raithby, 1984). To avoid chequerboard oscillations between pressure and velocity, the normal velocity components at the control volume faces are interpolated by means of the Rhie & Chow algorithm (Rhie & Chow, 1983). More details on the numerical model characteristics and flow solver options can be found in the CFX-4.2 user guide (CFX, 1997).

5.2.2 Wall treatment for the velocity and potential temperature specifying the ground boundary condition.

The ground of the computational domain is treated as a rigid wall. A problem with the $k-\varepsilon$ model is that it does not reproduce accurately the turbulence close to the wall when the mesh is too coarse. To avoid the need for an extremely fine resolution at ground, a special treatment is therefore applied, using wall functions to specify the behaviour of the flow variables close to the ground. The wall function concept assumes that, for a control volume adjacent to the ground, the velocity vector is tangential to the ground surface. Hence, the advection term through the ground surface disappears for all variables.
Two further assumptions are made for the behaviour of the velocity profile and for the turbulent energy dissipation rate ε close to the ground:

Assumption 1: the boundary layer is fully developed and the velocity profile is determined by:

eq. 5.11 $$u^+ = z^+ \qquad \text{for} \quad z^+ < z_0^+ \quad \text{(viscous sub-layer)}$$

eq. 5.12 $$u^+ = \frac{1}{\kappa}\ln(Ez^+) \qquad \text{for} \quad z^+ > z_0^+ \quad \text{(logarithmic region)}$$

where z^+ and u^+ are dimensionless distance and velocity defined as:

eq. 5.13 $$z^+ = \frac{z \cdot u_*}{\nu}$$

eq. 5.14 $$u^+ = \frac{u}{u_*}$$

with

eq. 5.15 $u_* = \sqrt{\frac{\tau}{\rho}}$ the friction velocity,

ν the kinematic viscosity and

τ the wall shear stress.

The continuity of the velocity profile at z_0^+ requires that E and z_0^+ satisfy:

eq. 5.16 $$z_0^+ = \frac{1}{\kappa}\ln(Ez_0^+)$$

The default model values for E and z_0^+ are $E = 9.793$ and $z_0^+ = 11.225$.

Assumption 2: the production term balances the dissipation term in the equation for k close to the wall.

In other words, assuming equilibrium close to the wall, we obtain the following equation for ε:

eq. 5.17 $$\rho\varepsilon = \mu\left(\frac{\partial u}{\partial z}\right)^2$$

Together with the relationships $|\tau| = \mu\frac{\partial u}{\partial z}$ and $\mu = \rho \cdot C_\mu \frac{k^2}{\varepsilon}$ and using the fact that

eq. 5.18 $$\frac{\partial u}{\partial z} = \frac{\partial u^+}{\partial z^+}\cdot\frac{u_*^2}{\nu} = \frac{1}{\kappa z^+}\cdot\frac{u_*^2}{\nu}$$

we get

eq. 5.19 $$\tau = \rho \cdot C_\mu^{1/2} k$$

which means for ε:

eq. 5.20 $$\varepsilon = C_\mu^{3/4}\cdot k^{3/2}\cdot\frac{1}{\kappa z}$$

The turbulent kinetic equation for k is solved for the control volumes adjacent to the ground, with the above parameterisation for ε and with a treatment of the production terms using variables interior to the flow, as well as the boundary conditions for the velocity and temperature.
The wall shear stress τ is then obtained from the values of k and used to formulate the ground boundary condition for the velocity.

The velocity close to the ground can be separated into parts parallel and perpendicular to the ground surface (bold symbols stand for vectors)

eq. 5.21 $$\mathbf{U} = \mathbf{U}_{par} + \mathbf{U}_{perp} = (\mathbf{U} - (\mathbf{U}\cdot\mathbf{n})\mathbf{n}) + (\mathbf{U}\cdot\mathbf{n})\mathbf{n}$$

With the wall function approximation, the perpendicular component disappears, while the parallel component is proportional to the wall shear stress $\boldsymbol{\tau}$. For a non-moving ground face, we have:

eq. 5.22 $$\begin{aligned}\mathbf{U}_{par} &= -\frac{\boldsymbol{\tau}}{T_M} \\ \mathbf{U}_{perp} &= 0\end{aligned}$$

with T_M given by:

eq. 5.23 $$T_M = \begin{cases} \dfrac{\mu}{z} & \text{for } z^+ < z_0^+ \\ \dfrac{\rho^{1/2}\cdot|\boldsymbol{\tau}|^{1/2}\cdot\kappa}{\ln(Ez^+)} & \text{for } z^+ > z_0^+ \end{cases}$$

For a control volume adjacent to the ground (cf. Figure 5.1), the flux of momentum I_{U^i} for the *i-th* component of the velocity through the ground surface A_b is

eq. 5.24 $$I_{U^i}\Big|_{A_b} = \int_{A_b} d\mathbf{A}\cdot(\rho\mathbf{U}U^i - \mu\nabla U^i) = -\int_{A_b} d\mathbf{A}\cdot\mu\nabla U^i = -|A_b|\cdot\tau^i$$

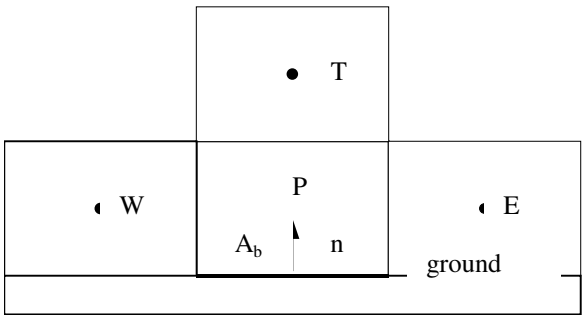

Figure 5.1. Schematic representation of a control volume adjacent to the ground.

The advection term in the above equation disappears with the assumption that the velocity component perpendicular to the ground face vanishes. Using eq. 5.22, this becomes

eq. 5.25 $$I_{U^i}\Big|_{A_b} = |A_b|\cdot T_M\cdot U^i_{par} = |A_b|\cdot T_M\cdot(U^i_P - (\mathbf{U}\cdot\mathbf{n})n^i)$$

with U^i_P the velocity at the centre of the control volume (point *P*).

5.2.3 Ground roughness and ground heat flux parameterisation

In the case of rough ground, the same treatment as above is applied for the ground boundary condition of velocity with a modified wall multiplier T_M to take into account the ground roughness length z_0 . The wall multiplier for a rough wall is modified to:

eq. 5.26
$$T_{M,v} = \begin{cases} \dfrac{\mu}{z} & \text{for } z^+ < z_0^+ \\ \dfrac{\rho^{1/2} \cdot |\tau|^{1/2} \cdot \kappa}{\ln(\dfrac{z}{z_0})} & \text{for } z^+ > z_0^+ \end{cases}$$

For the additional scalars, and hence for the potential temperature θ, a similar treatment is applied, using

eq. 5.27
$$\theta^+ = \frac{(\rho|\tau|)^{1/2}}{J_\theta}(\theta_w - \theta)$$

with J_θ the potential temperature flux through the wall

eq. 5.28
$$J_\theta = \rho u_* \theta_* = \frac{\mu}{\sigma_\theta}\frac{\partial \theta}{\partial z}$$

and θ_w the wall potential temperature.

From eq. 5.15 and eq. 5.28, eq. 5.27 can be rewritten as

eq. 5.29
$$\theta^+ = \frac{(\theta_w - \theta)}{\theta_*} = \begin{cases} \mathrm{Pr}_\theta \, z^+ & \text{for} \quad z^+ < z_\theta^+ \\ \dfrac{\sigma_\theta}{\kappa}\ln(E_\theta z^+) & \text{for} \quad z^+ > z_\theta^+ \end{cases}$$

where $\mathrm{Pr}_\theta = \mu/\Gamma_\theta$.

To simulate the logarithmic behaviour of the temperature profile in the element closest to the ground, the wall multiplier for the potential temperature is set to:

eq. 5.30
$$T_{M,\theta} = \begin{cases} \dfrac{\Gamma_\theta}{z} & \text{for } z^+ < z_\theta^+ \\ \dfrac{\rho^{1/2} \cdot |\tau|^{1/2} \cdot \kappa}{\sigma_\theta \ln(\dfrac{z}{z_\theta})} & \text{for } z^+ > z_\theta^+ \end{cases}$$

5.3 Additional implementations and assumptions to simulate atmospheric flow fields

The standard version of the code works with the energy conservation equation and buoyancy term in the vertical velocity equation formulated in terms of the real temperature *T*. Also, the pressure term appearing in the momentum conservation equation is defined as a deviation from a hydrostatic reference state for which the pressure linearly decreases with altitude. This makes it inappropriate for simulating stratified atmospheric flows with a vertical extent of several kilometres.

To better represent the fact that static stability in the atmosphere is defined relatively to an adiabatic reference state, we implemented an energy conservation equation in terms of the potential temperature θ[10]. This variable has the advantage of being conserved along the flow trajectories when only adiabatic processes are involved (see Appendix E). Also, the buoyancy term can easily be described as a function of the potential temperature when defining a reference state for the atmosphere, which corresponds to a hydrostatic equilibrium. To implement the potential temperature equation, we used the option given by the model allowing us to solve an additional transport-diffusion equation for a new scalar variable.

For the purpose of solving atmospheric flow fields, the numerical model equations are solved with the deep Boussinesq approximation, neglecting the effect of temperature variations on density, except in the buoyancy term, which is introduced in the vertical velocity equation. In all the other terms, the density is kept constant with time to a reference hydrostatic reference profile $\rho_h(z)$.

The Coriolis force is added in the momentum conservation equations for u and v components to reproduce the effect of the Earth's rotation on the boundary layer wind speed profiles. We thereby assume that the high altitude wind vector $U_{i,geo}$ follows the geostrophic approximation, linking the large scale horizontal pressure gradient to the geostrophic wind in such a way that $\frac{\partial p}{\partial x} = \rho f U_{2,geo}$ and $\frac{\partial p}{\partial y} = -\rho f U_{1,geo}$.

Consideration of the order of magnitude of the various terms in the vertical momentum equation shows that the contribution of the Coriolis force for w can be neglected.

The continuity and **modified momentum conservation** equations read:

- Continuity equation in the anelastic approximation:

eq. 5.31 $$\frac{\partial(\rho_h U_i)}{\partial x_i} = 0$$

[10] Up to now no moist process have been considered with CFX4. Therefore, we will only use the dry potential temperature along this work.

- Momentum conservation equation:

eq. 5.32
$$\frac{\partial(\rho_h U_i)}{\partial t}+\frac{\partial(\rho_h U_i U_j)}{\partial x_j}=-\frac{\partial p'}{\partial x_j}\delta_{ij}+\frac{\partial}{\partial x_j}\left[\mu_{eff}\left(\frac{\partial U_i}{\partial x_j}+\frac{\partial U_j}{\partial x_i}\right)\right] + (\rho_h-\rho)g\cdot\delta_{i3}+\rho_h\left[f(U_2-U_{2,geo})\delta_{i1}-f(U_1-U_{1,geo})\delta_{i2}\right]$$

where $f=2\Omega\sin(\varphi)$ is the so called Coriolis parameter (Ω stands for the angular velocity of rotation of Earth and φ for the latitude of the location).

5.3.1 Potential temperature equation, and definition of a hydrostatic reference state

Instead of solving the energy equation for the enthalpy (eq. 5.4), we solve the **energy conservation for the potential temperature** θ [11], which is more appropriate for atmospheric situations than the real temperature T. The equation for the potential temperature reads (see Appendix E):

eq. 5.33
$$\frac{\partial(\rho\theta)}{\partial t}+\frac{\partial(\rho\theta\cdot u_i)}{\partial x_i}=\frac{\partial}{\partial x_i}\left[\frac{\mu_T}{\sigma_\theta}\frac{\partial}{\partial x_i}\theta\right]+sources$$

This is an advection-diffusion equation for the variable θ similar to the scalar equations that the standard version of CFX4 can solve (eq. 5.5). The sources in eq. 5.33 represent the radiative or latent heat flux that can appear for non-adiabatic processes (evaporation, condensation).

A **reference hydrostatic state** (denoted by the subscript *'h'*) is defined, which corresponds to an atmosphere in hydrostatic equilibrium. Starting from a real temperature profile $T(z)$, the hydrostatic pressure profile $p_h(z)$ is obtained by numerically integrating $dp_h=-\rho_h(z)\cdot g dz$, assuming the ideal gas law $\rho_h=p_h/RT(z)$ is true for each altitude *z*. The hydrostatic potential temperature profile is calculated from $\theta_h(z)=T(p_0/p_h(z))^{R/c_p}$.

Assuming that the departure of the atmospheric state from the hydrostatic reference state is small and that the Mach number of the flow is low, an approximate form for the buoyancy term $(\rho_h-\rho)g$ is derived (see Appendix F):

$$(\rho_h-\rho)=\frac{\rho_h}{\theta_h}(\theta-\theta_h)$$

This expression is used in order to couple the modified momentum and energy conservation equations (eq. 5.32 and eq. 5.33).

---

[11] The potential temperature is defined as $\theta=T(p_0/p)^{R/c_p}$, where T is the real temperature, p_0 is the reference pressure at sea-level, p the total pressure, R the gas constant for dry air and c_p the specific heat of air at constant pressure.

5.3.2 Introduction of a buoyancy source term in the k-ε model depending on the potential temperature

To take into account the fact that the atmospheric static stability influences the production and destruction of the turbulence, a buoyancy term (eq. 5.9) is included in the $k-\varepsilon$ model. In the standard version, the density gradient used to compute G is written in terms of the real temperature T with the assumption that the Boussinesq approximation is valid. Since we are solving the energy conservation equation formulated in terms of the potential temperature we need to redefine the buoyant source term G as a function of the vertical potential temperature gradient.

This was re-introduced in the turbulence model, following the formulation proposed by Duynkerke (1988). After the modification, the equations for k and ε read:

eq. 5.34
$$\frac{\partial(\rho\ k)}{\partial t}+\frac{\partial(\rho\ kU_i)}{\partial x_i}=\frac{\partial}{\partial x_i}[(\mu+\frac{\mu_T}{\sigma_k})\frac{\partial k}{\partial x_i}]+P+G-\rho\varepsilon$$

eq. 5.35
$$\frac{\partial(\rho\varepsilon)}{\partial t}+\frac{\partial(\rho\varepsilon\ U_i)}{\partial x_i}=\frac{\partial}{\partial x_i}[(\mu+\frac{\mu_T}{\sigma_\varepsilon})\frac{\partial\varepsilon}{\partial x_i}]+C_1\frac{\varepsilon}{k}\left[P+\max(G,0)+\max(0,D)\right]-C_2\rho\frac{\varepsilon^2}{k}$$

with the turbulent viscosity

eq. 5.36
$$\mu_T=C_\mu\rho\frac{k^2}{\varepsilon}$$

the shear production term:

eq. 5.37
$$P=\mu_{eff}\frac{\partial U_i}{\partial x_j}(\frac{\partial U_i}{\partial x_j}+\frac{\partial U_j}{\partial x_i})-\frac{2}{3}\frac{\partial U_j}{\partial x_j}(\rho k+\mu_{eff}\frac{\partial U_l}{\partial x_l})$$

the buoyancy production term formulated in terms of the potential temperature

eq. 5.38
$$G=-\frac{\mu_{eff}}{\rho\sigma_H}\vec{g}\vec{\nabla}\rho=-\frac{\mu_{eff}}{\sigma_H}\frac{g}{\theta_h}\frac{\partial\theta}{\partial z}$$

and an additional turbulent diffusion term

eq. 5.39
$$D=\frac{\partial}{\partial x_i}\left[\mu_T\frac{\partial\varepsilon}{\partial x_i}\right]$$

The differences relative to the default $k-\varepsilon$ model are:

- The introduction of a buoyancy term depending on the potential temperature, which acts as a sink for turbulent kinetic energy when the atmosphere is stably stratified ($\partial\theta/\partial z>0$), and which is only active in the equation for ε when positive (i.e., when the atmosphere is unstable)

- The introduction of an additional turbulent diffusion term as a source in the ε equation, which in a similar way to the buoyancy term is only active when positive (c.f. Duynkerke, 1988).
- The model constants which differ from the default values. Duynkerke proposes the following values for the atmosphere: $C_1 = 1.46$, $C_2 = 1.83$, $C_\mu = 0.033$, and $\sigma_\varepsilon = 2.38$, $\sigma_k = 1$, $\sigma_H = 0.9$ [12]. The constant C_μ is determined from the assumption that in the neutral surface layer $C_\mu = (u_*^2 / k)^2$ and using measurements performed by Panofsky & Dutton (1984) for u_* and k close to the ground. C_2 is derived from experimental results of grid turbulence decay, while C_1 was obtained from experimental results in shear dominated turbulent flows.

[12] The constants C_1 and C_2 are linked to the critical Richardson number through the relationship $C_1 = C_2(1 - Ri_c)$ (c.f. Duynkerke, 1988). The choice of $C_1 = 1.46$, $C_2 = 1.83$ corresponds to a critical Richardson number $Ri_c = 0.2$.

6 Simulations over the Chasseral & Mt-Crosin sites

6.1 Simulation domain

The wind fields over the Chasseral and Mt-Crosin region are calculated by the model over a simulation domain which covers an area of 45 km along the x direction and 51.56 km along the y-direction. As can be seen from Figure 3.1, the three ANETZ stations of Chasseral, Neuchâtel and La Chaux-de-Fonds are included in the simulation domain. The site of Payerne, belonging to the international network of aerological stations and from which a balloon sounding to measure the wind, temperature and humidity profile is launched twice a day, lies just outside. The domain has a vertical extent of 10 km. Its orientation has been chosen so that both Chasseral and Mt-Crosin lie in the constant x-plane in the middle of the simulation domain. As a consequence the domain x-axis is rotated by 32° with respect to the East-West direction. The centre point of the domain (569'595 and 223'030 in Swiss co-ordinates) lies exactly halfway between Chasseral and Mt-Crosin. To increase the horizontal resolution in the immediate surroundings of Chasseral and Mt-Crosin, the domain is made of 15 blocks (numbered B1, to B15) with varying number of cells and varying cell distributions as presented in Figure 6.1. The block dimensions, number of cells and type of cell distribution applied for each block are summarised in Table 6.1. The finest horizontal resolution is of 50 x 50 m around Chasseral and Mt-Crosin, while the coarsest resolution is of about 4.5 x 4.5 km for the cells close to the boundaries.

The ground of the simulation domain has been projected on the surface topography for the area. The surface file was built using data with a horizontal resolution of 25m for the central part of the domain (blocks B5, B8 and B11) and 250m for the external part. The topographic data were obtained from the Swiss federal office for topography. Figure 6.2 shows a three-dimensional view of the simulation domain, with the locations of both the Chasseral and Mt-Crosin sites. The topography, which is actually seen by the model, is presented in Figure 6.3 for the whole simulation domain. Note that the altitude difference between the Swiss Plateau and the Chasseral summit is of some 1200m. Also, the St-Imier valley, between the Chasseral and Mt-Crosin sites is some 700m lower than the Chasseral summit.

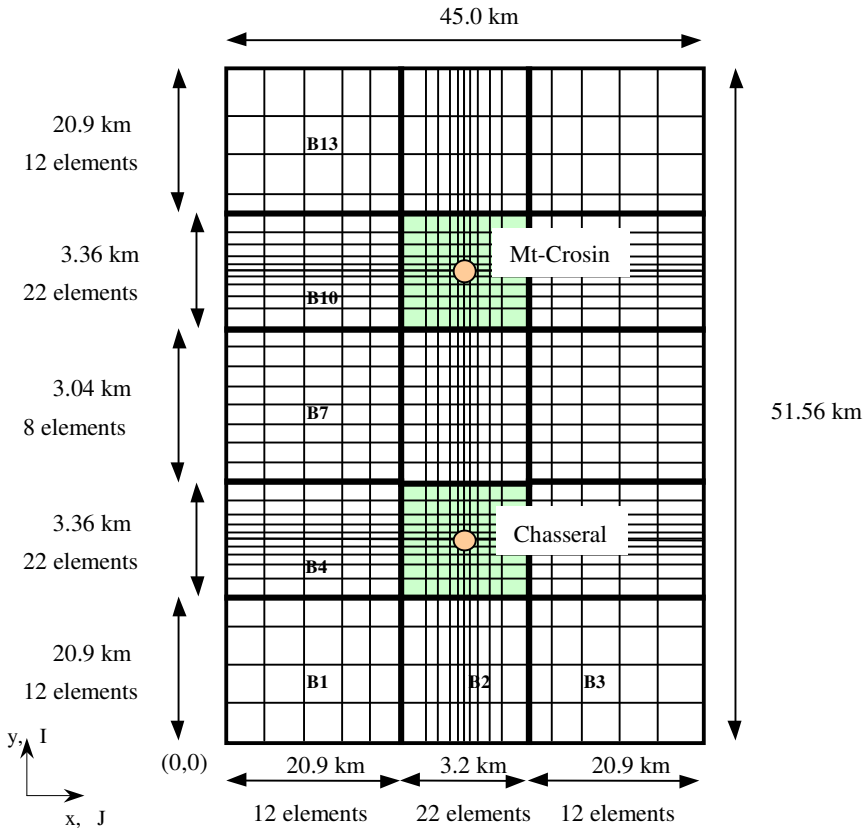

Figure 6.1. Schematic view (not to scale) of the simulation domain, showing the type of cells distributions in the horizontal plane. The actual numbers of elements and subdomains dimensions are given in the drawing.

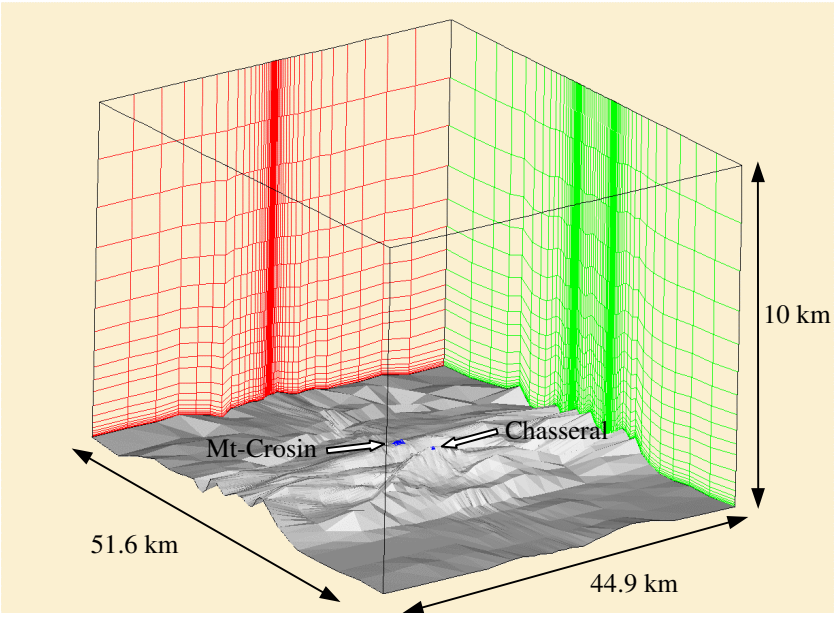

Figure 6.2. Three-dimensional view of the simulation domain and topography, with location of the Chasseral and Mt-Crosin sites.

Table 6.1. Parameters describing the horizontal cell distribution in the 15 blocks forming the simulation domain.

Block name	**x-direction**					
	L_x [km]	Number of cells	Cell distribution	Geom. progr. factor	Δx min [m]	Δx max [m]
B1, B3, B13, B15	20.9	12	Geom. progr.	1.250	586	4488
B2, B14	3.2	22	Symm. geom. progr.	1.199	50	307
B4, B6, B10, B12	20.9	12	Geom. progr.	1.250	586	4488
B5, B11	3.2	22	Symm. geom. progr.	1.199	50	307
B7, B9	20.9	12	Geom. progr.	1.250	586	4488
B8	3.2	22	Symm. geom. progr.	1.199	50	307

Block name	**y-direction**					
	L_y [km]	Number of cells	Cell distribution	Geom. progr. factor	Δy min [m]	Δy max [m]
B1, B3, B13, B15	20.9	12	Geom. progr.	1.250	586	4488
B2, B14	20.9	12	Geom. progr.	1.250	586	4488
B4, B6, B10, B12	3.36	22	Symm. geom. progr.	1.208	50	331
B5, B11	3.36	22	Symm. geom. progr.	1.208	50	331
B7, B9	3.04	10	Regular	1.000	304	304
B8	3.04	10	Regular	1.000	304	304

In the vertical, 20 elements are distributed in two different layers (see Figure 6.4). Between 2000 and 10000 m, 10 elements are distributed according to a geometric progression given by a factor $f_2 = 1.2$. For the lowest part of the domain, between the ground and 2000 m, 10 other elements are distributed in a terrain-following mesh, which also follow a geometric progression. The factor of the geometric progression for this layer varies between 1.4 and 1.5 depending on the altitude difference between the level at 2000 m and the ground. The resulting height above ground for the cell centres of the levels 1 to 6 are given in Table 6.2 for the Chasseral and the Mt-Crosin locations. Level 4, at 61 m above ground for Chasseral will be taken as the representative level for the Chasseral station. For the stations of Côte Sud and Côte Est, where measurements at 30 m above ground were recorded, the third level will be taken as representative of the measurement point. For the station of Côte Nord, data were available at 10 m above ground only. For the latter the second model level will be considered as representative, bearing in mind that this choice might result in a slight overestimation of the predicted wind speed, since the model cell centre lies at 14 m above ground level.

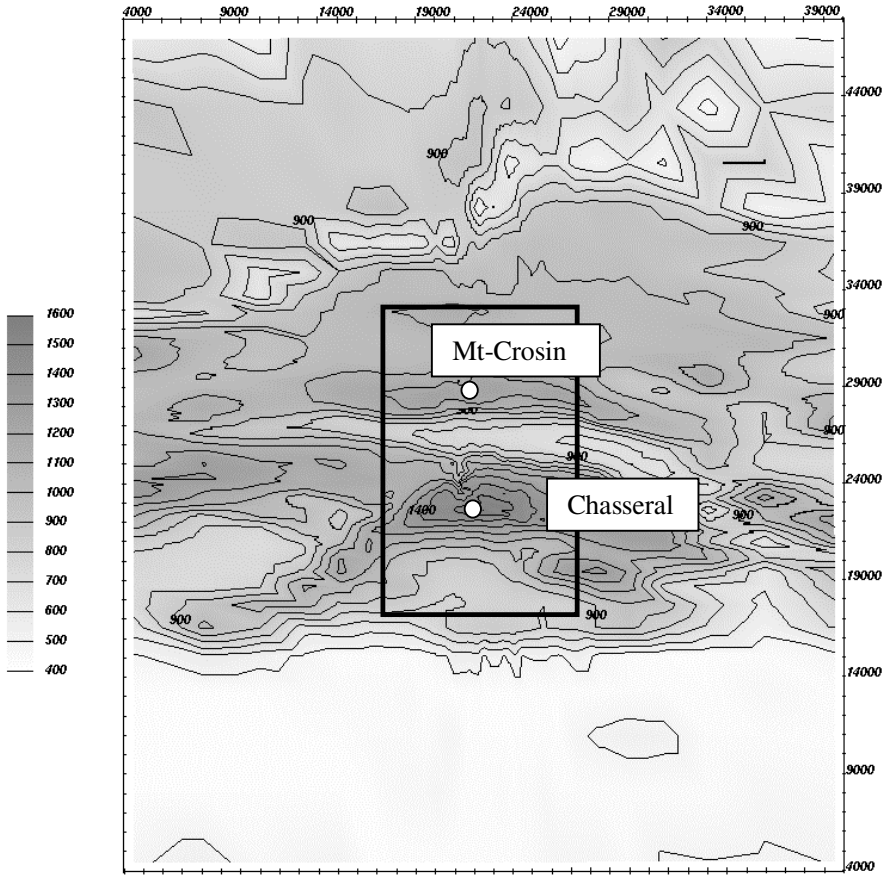

Figure 6.3. Topography of the Chasseral Mt-Crosin area as seen by the model. The rectangle outlines the limit of the domain for which we will restrict ourselves when presenting results in a horizontal plane.

Table 6.2. Height above ground for the 6 lowest grid levels of the simulation domain.

Chasseral		Mt-Crosin	
Level	Height (m)	Level	Height (m)
1	5	1	4
2	17	2	14
3	35	3	29
4	61	4	52
5	97	5	89
6	150	6	144

A summary of the horizontal Swiss and model co-ordinates for the various locations around the Mt-Crosin and Chasseral area is presented in Table 6.3. Information

about the closest model grid node co-ordinates has also been included, where I and J stand for the cell numbering in the y- respectively x direction[13].

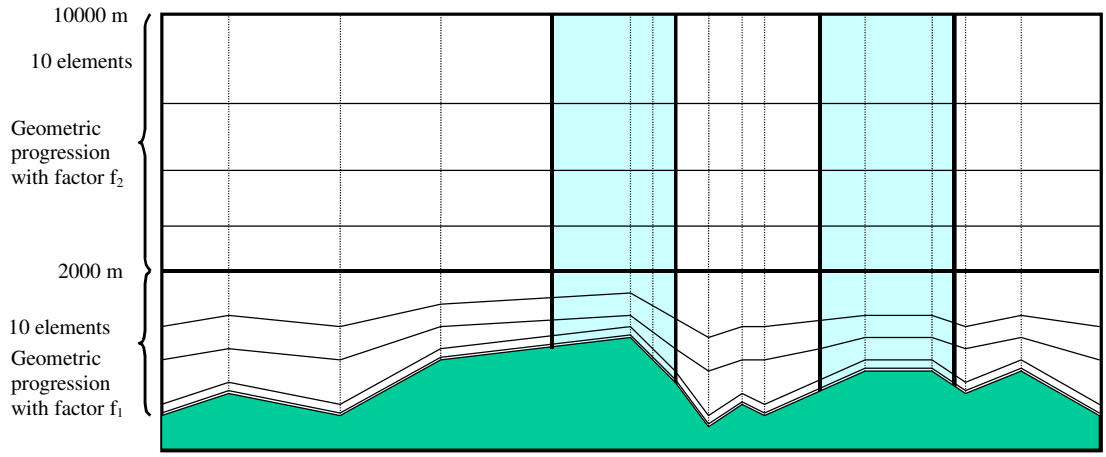

Figure 6.4. Schematic view of the simulation domain, showing the type of cell distributions in the vertical plane. The upper layer, between 2000 and 10000m consists of 10 elements following a geometric progression with a factor 1.2, whereas the lower layer, below 2000 m, is made of 10 elements, whose sizes also follow a geometric progression with factors varying between 1.4 and 1.5.

Table 6.3. Location of the various sites in terms of model co-ordinates. I and J given for the model grid nodes stand for the cell numbering along the y- and x-directions respectively. The model co-ordinates are relative to the domain origin, which lies at the point (564'190, 189'242) in Swiss co-ordinates.

	Swiss co-ordinates [m]		Model co-ordinates [m]		Closest grid node			
			x	y	I	J	X [m]	Y [m]
Chasseral	571'290	220'320	22'500	22'584	23	24	22'504	22'546
Côte Nord	567'900	225'740	22'500	28'976	54	24	22'525	28'985
Côte Sud	567'850	225'200	22'171	28'545	48	19	22'179	28'509
Côte Est	568'325	225'700	22'839	28'717	50	28	22'819	28'729
Wind turbine 1	567'846	225'667	22'416	28'943	53	22	22'420	28'934
Wind turbine 2	567'846	225'308	22'225	28'639	49	19	22'179	28'628
Wind turbine 3	568'000	225'154	22'274	28'427	47	20	22'274	28'367

In the first step, all the simulations performed in the present work were done assuming a constant ground roughness of 0.03m for the whole domain. At a later stage, an attempt was made to take into account a more realistic roughness length

[13] For optimal program vectorisation, the I direction was set in the direction with the bigger number of elements, i.e. in the y-direction.

distribution over the area. A roughness length map was inferred from the soil occupation map published by the Swiss Federal Office for Topography (scale of the map 1:300000). We thereby used four roughness classes to characterise the type of terrain, the first roughness class being attributed to lake surfaces, the second one for crops, the third for forests and the fourth for towns. Table 6.4 shows the roughness values that were used in the simulation for each roughness class. These values are in agreement with those proposed by Wieringa (1986) apart from the forested area for which the value of 1 postulated here is slightly higher than the value of 0.75 given by Wieringa. Though the difference between these two values does not appear to be very significant, we will see later on that it affects the simulated site-to-site relationships in a significant way. The horizontal distribution of the roughness classes (shading) that we used for the simulations is shown in Figure 6.5, together with the underlying topography. It should also be added at this point that the available roughness map has a rather coarse resolution (2 km in the horizontal). Due to this, most of the Mt-Soleil range (and hence the site of Mt-Crosin itself) is considered as forested area, which will tend to overestimate the roughness length of the area. This also will have to be taken into account when analysing the results.

Table 6.4. Roughness classes and corresponding roughness lengths for the various types of soil occupation. (Wieringa, 1986).

Roughness class	Roughness length [m]	Type of terrain
1	0.0002	Lake
2	0.05	Crops
3	1.0	Forest
4	1.6	Town

6.2 Numerical schemes

Regarding the numerical aspects of the simulations, it could be shown from the work presented in Appendix C that to properly reproduce the expected mountain wave phenomena the use of an advection scheme of at least second order was required. For the example of application over the Chasseral and Mt-Crosin area, we used a second order upwind advection scheme for the velocity components and a modified quadratic upwind scheme for the potential temperature (CCCT, 3rd order).

The equations were solved using an adaptive time stepping method (implicit backward differencing), for which the time step during the simulation is changed depending on the convergence ease/difficulty encountered by the solver. The time

steps used in this context vary between 1.5 s and 12 s, with most of the simulation done with a time step of 12 s. This upper value for the time step seems to be the maximum that can be used with the model resolution used for the Chasseral and Mt-Crosin area. Further increasing the time step led to diverging solutions in the case of low wind speeds and high stability conditions (i.e. for Froude numbers lower than unity). The variable time stepping procedure chosen was the following:

- The initial time step was 6 s,
- The time step length is doubled, when 5 consecutive time steps are converged,
- If the solution is not converged after the maximum number of iterations allowed within a time step, then the solution is recalculated from the solution at the previous time step, using a time step length which is divided by two,
- If the solver fails to converge when using the minimum time step length, the calculation is stopped.

A wall boundary condition is used for the ground with the variables at the ground being determined with the wall treatment given in Section 5.2.2. The top boundary is allocated a pressure boundary condition. Inlet boundary conditions are used for the lateral domain faces with incoming flow, while pressure boundaries are used in case of outflow (see Appendix L for the definition of the various types of boundary conditions). Table 6.5 summarises the numerical parameters retained for the simulations performed over the Chasseral and Mt-Crosin area.

Table 6.5 Simulation conditions used for the Chasseral & Mt-Crosin area.

Turbulence model	k-ε	
Turbulence model constants	Duynkerke values	
Advection scheme	Higher upwind CCCT	Wind speed Potential temperature
Boundary condition type (see Appendix L for definition)	Inlet Pressure Wall (no slip) Pressure	Inflow boundaries Outflow boundaries Ground Top
Under relaxation factors	0.5 0.5	Wind speed Potential temperature
Time step	Variable ($1.5 < \Delta t < 12s$)	
Maximum number of iterations per time step	15	
Density profile	Hydrostatic (deep Boussinesq)	

6.3 Simulation results

In the following wind fields simulated over the Chasseral and Mt-Crosin area will be presented to illustrate the significance of the combined topography and atmospheric stratification effects on the very complex terrain. Results will be shown for two different wind directions: the first set with a high altitude wind blowing from the sector 240°, which is essentially aligned with the mountain chain (and with the model x-axis), and the second set with a high altitude wind direction 330°, perpendicular to the Jura mountain range (i.e. parallel to the model y-axis).

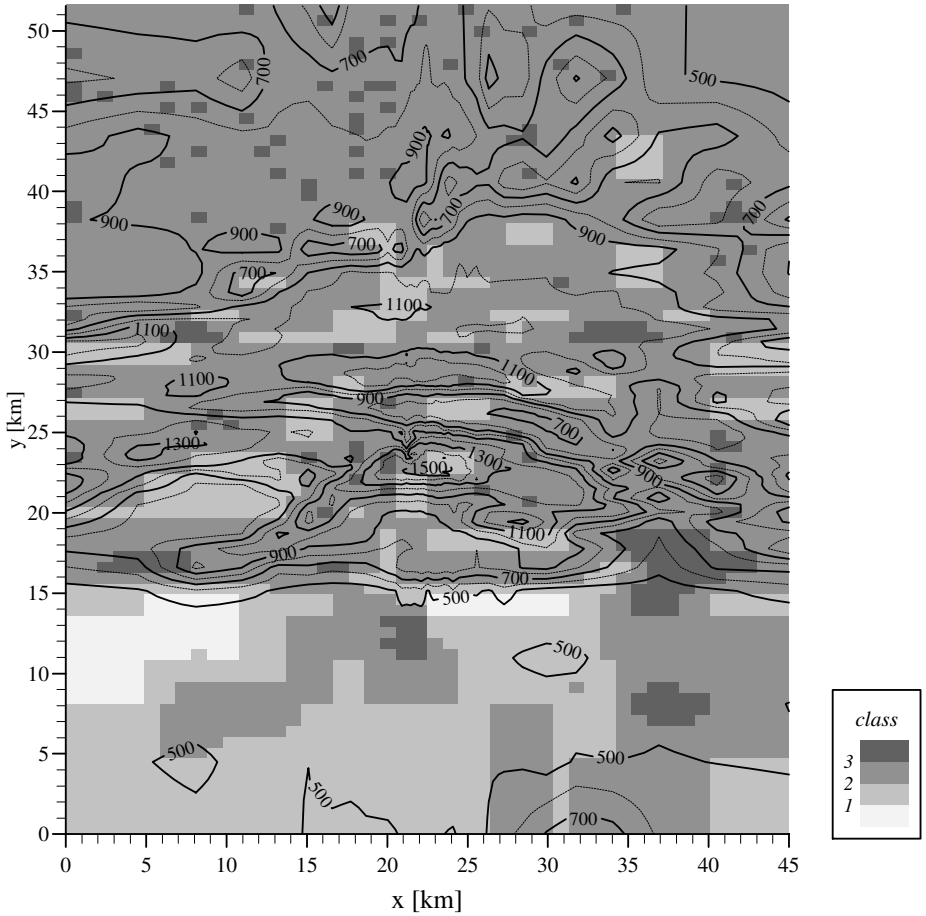

Figure 6.5. Horizontal roughness distribution (shading) over the simulation domain inferred from the soil occupation map for the area (source: Swiss Federal Office for Topography). The roughness values corresponding to the 4 roughness classes can be found in Table 6.4. Light grey zones stand for lower roughness lengths, dark grey ones for higher roughness lengths. The underlying topography is also given by the isolines, in steps of 100 m.

The simulations presented below have been initialised with velocity profiles following the Zilitinkevich formulation (see Appendix B). The use of this formulation also means that we will have a rotation of the wind vector with altitude corresponding to the Ekman spiral. Hence, for a high altitude wind parallel to the main mountain chain direction, we will have a wind field close to the ground turned anticlockwise, implying the existence of a flow component perpendicular to the mountain chain in the boundary layer. The equations are solved in the deep Boussinesq approximation. The boundary conditions at the model inflow boundaries are kept constant with time at the same values as the initial solution.

6.3.1 The 240° geostrophic wind direction

For the high altitude 240° wind direction, the effect of the atmospheric stability and heat flux conditions at the ground were investigated. As will be shown with the results presented below, the atmospheric stratification plays a major role in the wind field development over the complex topography such as that around Chasseral. This will be illustrated with 3 simulation results that were obtained for situations with zero heat flux through the ground with various thermal stratification and high altitude wind speed conditions (see Table 6.6). For all the three simulations, we assumed the atmosphere to be stratified with a constant vertical temperature gradient. The ground roughness was set to 0.03m for the whole simulation domain.
A fourth simulation will be presented for the 240° geostrophic wind direction showing the effect of ground cooling on the wind field development and the formation of down slope winds in the domain (katabatic winds[14]).

For the neutrally stratified case (simulation NN), the wind field at the first level of nodes (4-5 m above ground) over the central part of the domain is presented in Figure 6.6. The shading corresponds to the horizontal wind speed. The limits between two wind speed classes are given by black isolines, with an isoline step of 1 m/s. To help locate the sites of interest, the topography was indicated by white isolines, in steps of 200m. The length of the wind vector is proportional to the wind speed and the wind vector density gives an idea of the model resolution, with higher densities for both the Chasseral and Mt-Crosin areas. The wind field presented in Figure 6.6 corresponds to the model solution after an integration time of 1h 35' (600 time steps). The required CPU time was ~17h on a DEC ALPHA EV56 processor (375 Mhz, 640 Mw).

[14] We will use the term of 'katabatic wind' as a synonym of downslope winds as defined in Atkinson (1989).

Table 6.6. Parameters defining the wind speed profiles, temperature profiles and ground boundary conditions for the simulations done with a geostrophic wind from the 240° direction.

Simulation name	G [m/s]	$\partial T / \partial z$ [K/km]	Ground temperature condition	Roughness [m]	Froude[15]
NN	10	-9.7	Zero heat flux	0.03	4.6
NS1	10	-6.5	Zero heat flux	0.03	0.8
NS2	5.0	-6.5	Zero heat flux	0.03	0.4
SS1	4.7	-9.5, for z < 2000m -7.0, for z > 2000m		0.03	~0.4

The resulting wind field for the neutrally stratified atmosphere does not show major channelling effects. The wind vectors close to the ground show more or less the same direction as the initial solution (rotated anticlockwise with respect to the high altitude wind due to the initial Ekman spiral). The influence of the topography can be seen with the induced flow acceleration or slowdown. The wind speed is increased when passing the highest elevations and reaches its maximum value around the Chasseral location, with a value of some 7 m/s. On the Mt-Crosin site, the wind speed is about 5 m/s. The minimum wind speed (< 2 m/s) can be observed in the 'Combe Grède', a steep and very narrow valley, immediately downwind of Chasseral and aligned perpendicularly with the main mountain features in the area.

When looking at a vertical cross-section through a constant y plane and going through the Chasseral location (Figure 6.7), the horizontal wind speed does not show any significant influence due to the topography. From the vertical velocity plot (Figure 6.8), we can see that in the case of neutral stratification, the perturbation of the flow field induced by the topography is essentially confined to the lowest 2000m above ground, with positive vertical velocities upwind of the highest elevation and negative vertical velocities downwind.

The time evolution of the solution has been monitored for the model nodes closest to the locations of Côte Nord (10 m AGL), Côte Sud (30 m AGL) and Côte Est (30 m AGL) at Mt-Crosin as well as for the Chasseral site (60 m AGL). The horizontal wind speed and wind direction for these locations have been plotted versus time in Figure

[15] The Froude number is obtained using $Fr = G \Big/ H\sqrt{\frac{g}{\theta_0}\frac{\partial\theta}{\partial z}}$, with H the height difference between the Chasseral summit and Swiss Plateau altitude ($H \cong 1200m$).

6.9.a and b. The ratio of the wind speed at Mt-Crosin to the wind speed at Chasseral is shown in Figure 6.9.c for the pairs Chasseral-Côte Nord, Chasseral-Côte Sud, and Chasseral-Côte Est.

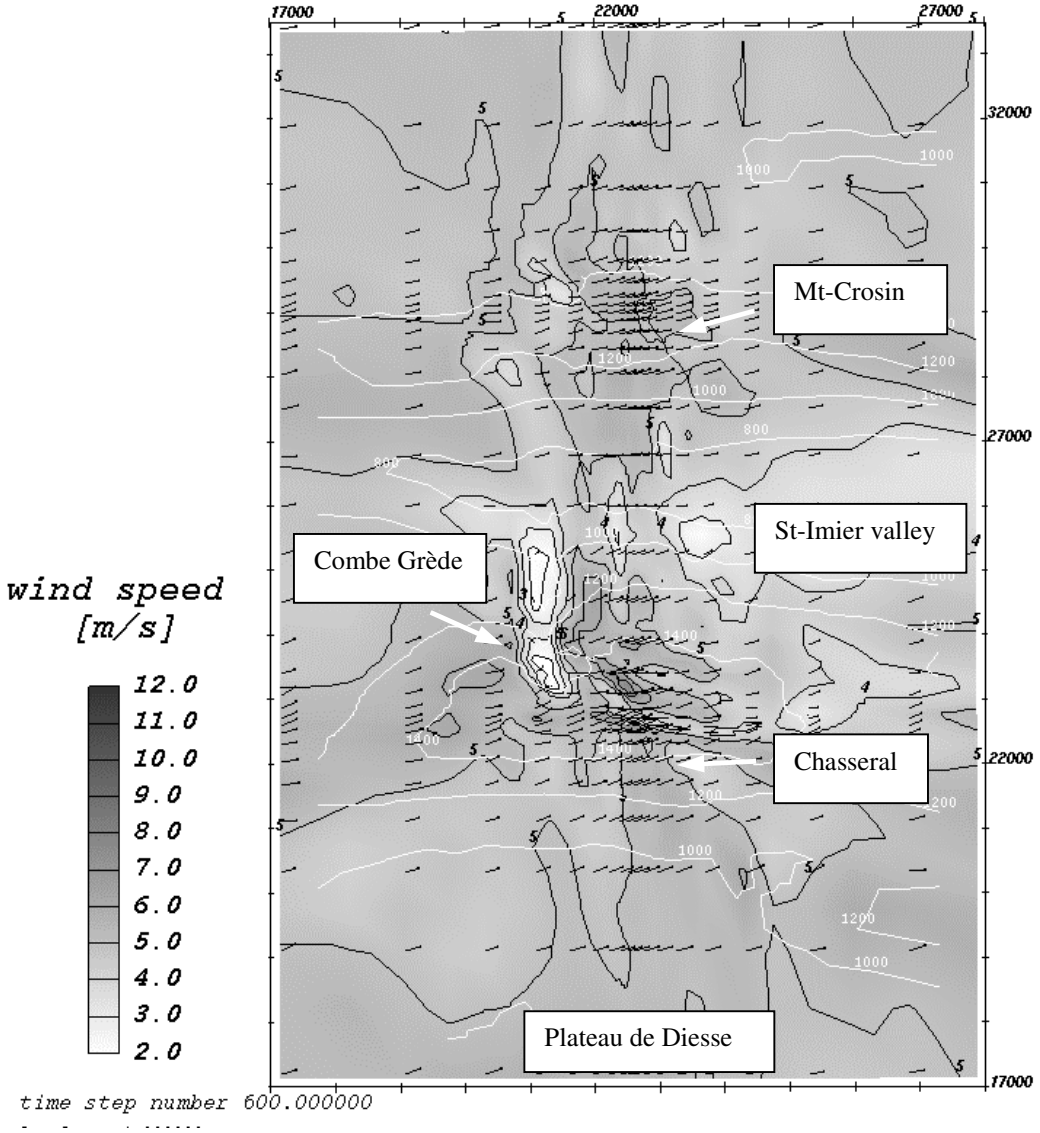

Figure 6.6. Wind field calculated by the model for a geostrophic wind of 10 m/s, blowing from the 240° direction. The initial atmosphere was neutrally stratified (-9.7 K/km for the real temperature gradient). The results shown here correspond to the first level of grid cells (4-5 m above ground) for the central part of the simulation domain. For clarity only one vector in two has been drawn. The black isolines give the horizontal wind speed values in steps of 1 m/s, while the white isolines represent the topography in steps of 200 m.

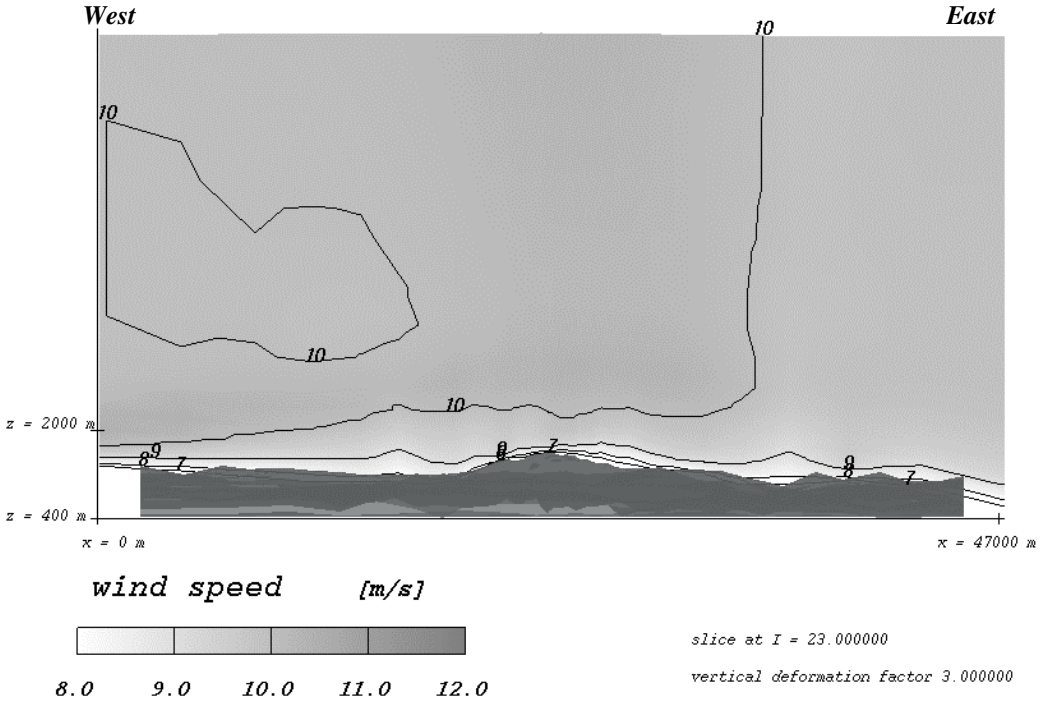

Figure 6.7. Vertical cross-section showing the horizontal wind speed distribution along a constant y-plane through Chasseral. The situation has been initialised with a neutral temperature profile and with a geostrophic wind speed of 10 m/s blowing from the 240° sector. Shading and isolines give the wind speed in steps of 1 m/s. The z levels are given in m above sea-level, and the ground is represented in dark grey.

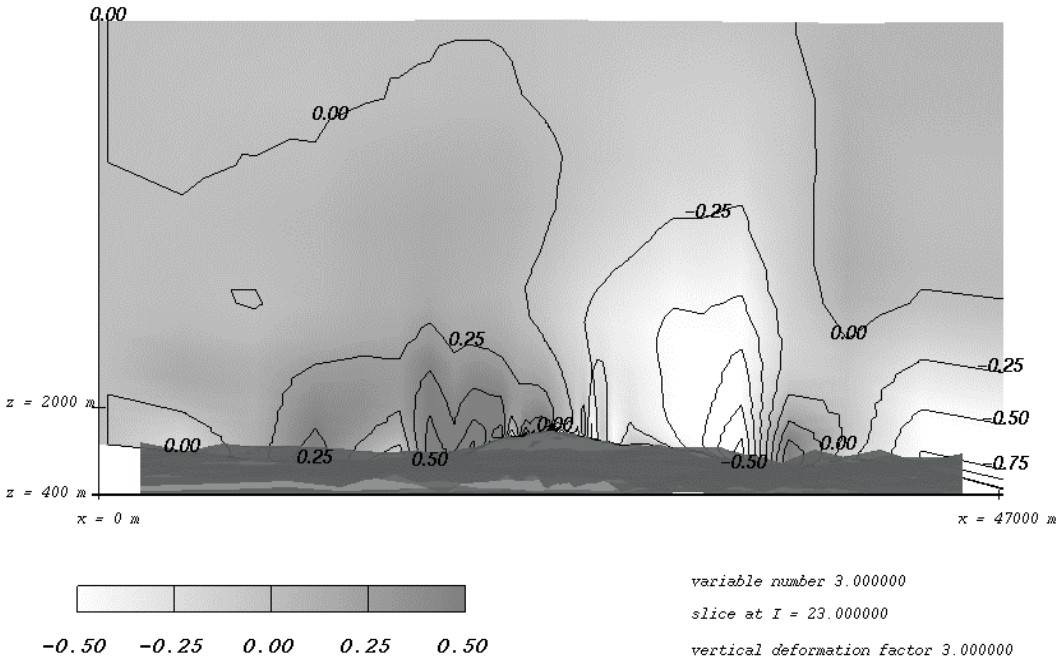

Figure 6.8. Same as Figure 6.7 for the vertical velocity component. Steps between isolines: 0.25 m/s.

As can be seen from the time evolution, the solution reaches a converged state after about 1 h, which is slightly less than the required time for the inlet boundary condition to be propagated across the whole domain (size of the domain: 50 km, high altitude wind speed: 10 m/s).

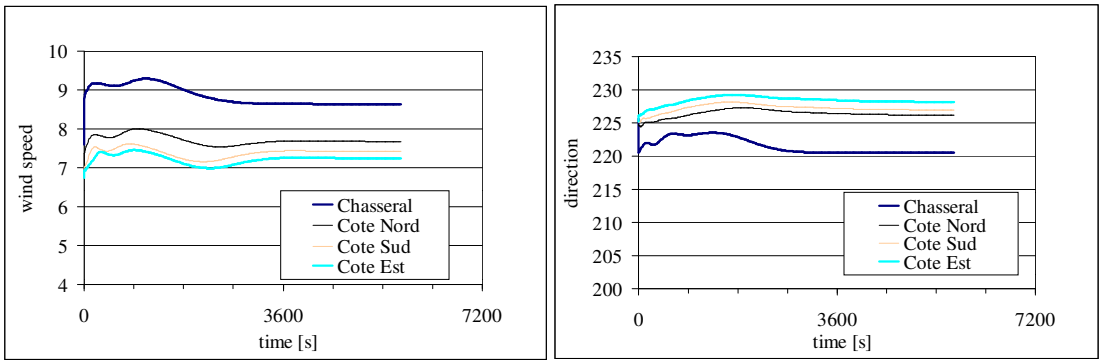

a) b)

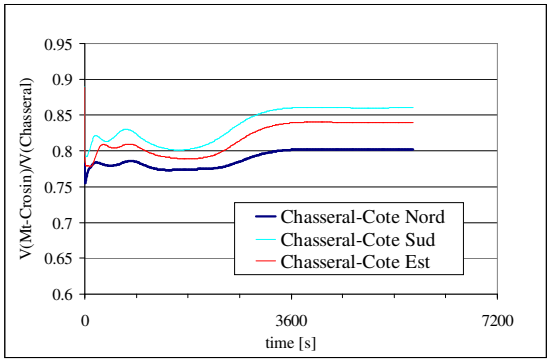

c)

Figure 6.9. Time evolution of the wind speed (a) and direction (b) for the model nodes closest to the locations of Côte Nord, Côte Sud, Côte Est and Chasseral, for a neutrally stratified atmosphere. c) Ratio of the Mt-Crosin to Chasseral horizontal wind speed.

A similar situation as the one presented above was performed, introducing a more realistic thermal stratification for the area (simulation NS1). The initial hydrostatic equilibrium was computed using a real temperature gradient of –6.5 K/km throughout the entire troposphere, and the high altitude wind speed was set to 10 m/s. The results after 4 h for this simulation are presented in Figure 6.10 to Figure 6.12.

Contrary to what was obtained for the neutrally stratified case, the channelling effects are very significant in the presence of a stable stratification. Major wind vector deflection can be seen upwind of the Chasseral mount as well as on the upslope towards Mt-Crosin in the St-Imier Valley. Significant blocking also occurs as can be

seen with the strong wind speed reduction over the 'Plateau de Diesse' upwind of Chasseral, resulting in wind speeds lower than 1 m/s. Flow speed up takes place when passing the highest elevations again. The wind speed at Chasseral reaches a value of 8 m/s, which is higher than for the neutrally stratified situation. It should also be stressed that the maximum wind speed (~10 m/s) at this level occurs further north, on the eastern flank of the 'Combe Grède' (co-ordinates 22000; 25000).

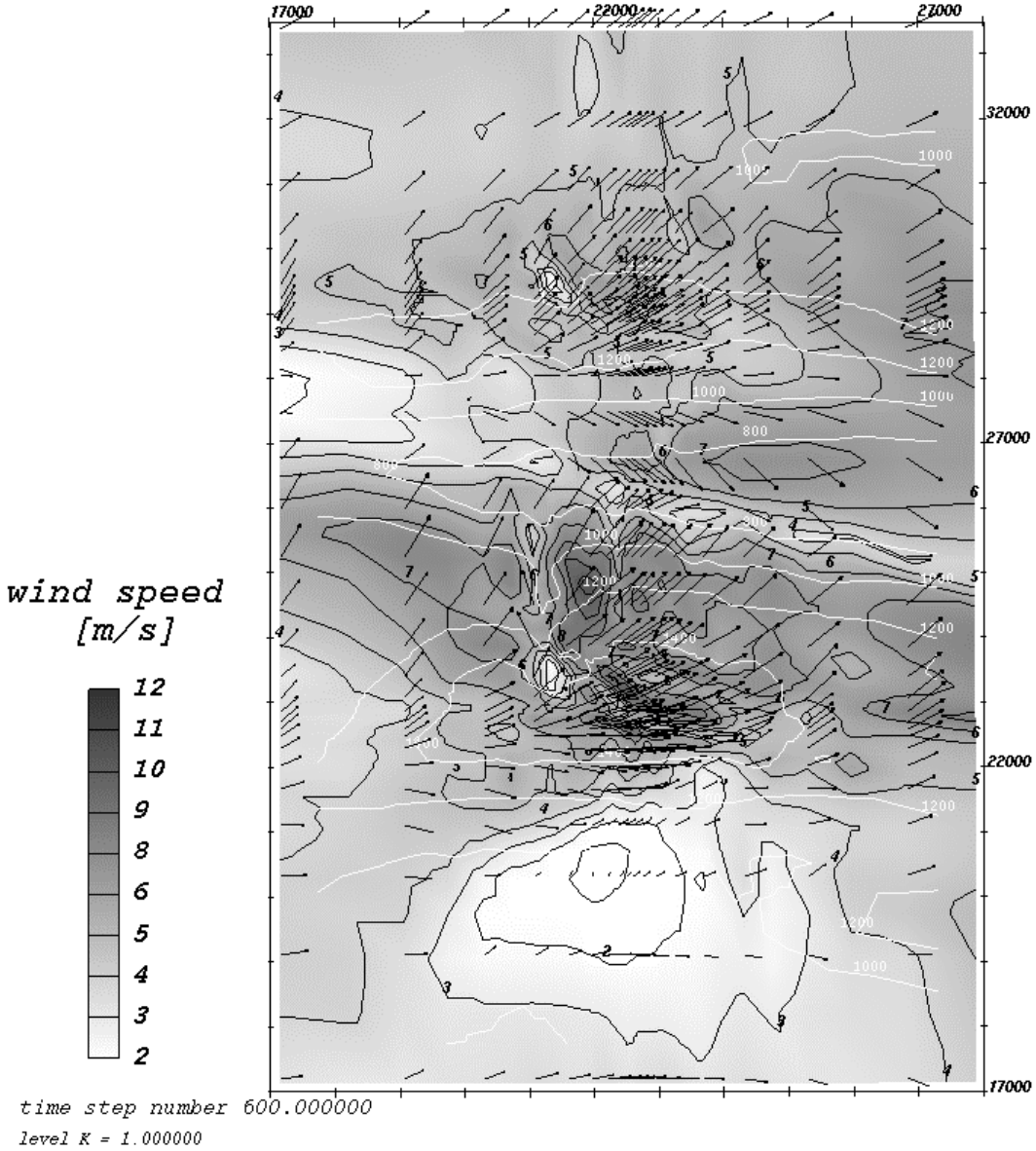

Figure 6.10. Same as Figure 6.6 for an initial stable thermal stratification given by a real temperature gradient of –6.5 K/km.

From the vertical cross-sections of both wind speed (Figure 6.11) and vertical velocity (Figure 6.12), we can see that the flow perturbation for the stably stratified case is no longer confined to the lowest levels as it was the case for the neutrally stratified

situation. Moreover, the induced flow acceleration is stronger in the presence of a stratified atmosphere (compare Figure 6.7 and Figure 6.11).

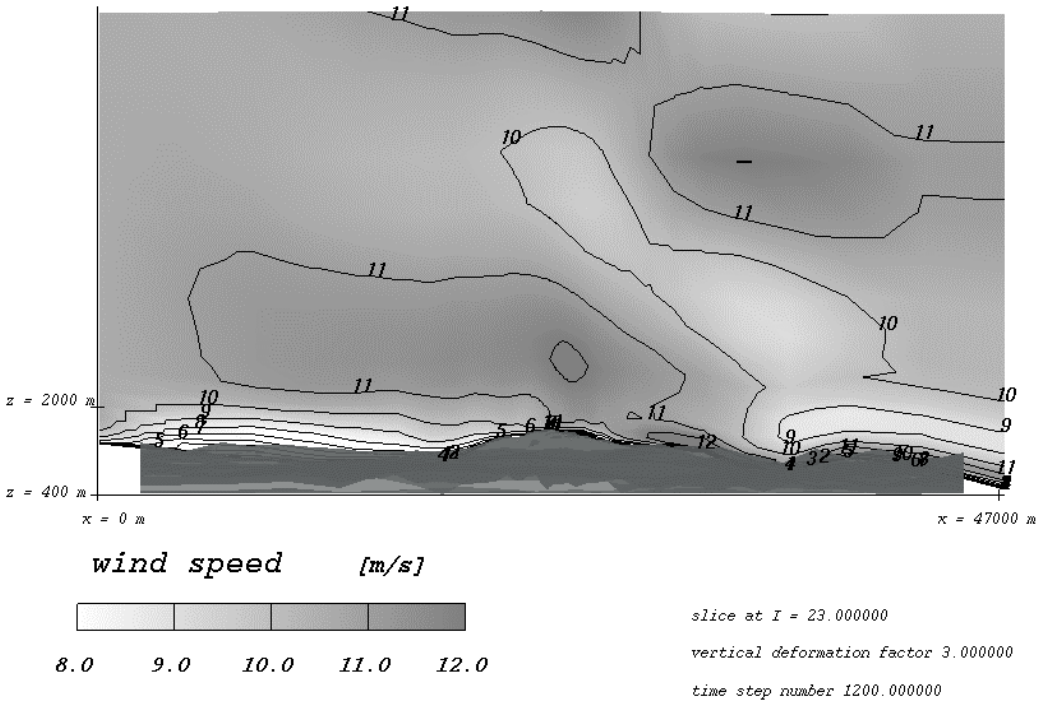

Figure 6.11. Same as Figure 6.7 for an initial stable thermal stratification given by a real temperature gradient of –6.5 K/km. Steps between isolines: 1 m/s.

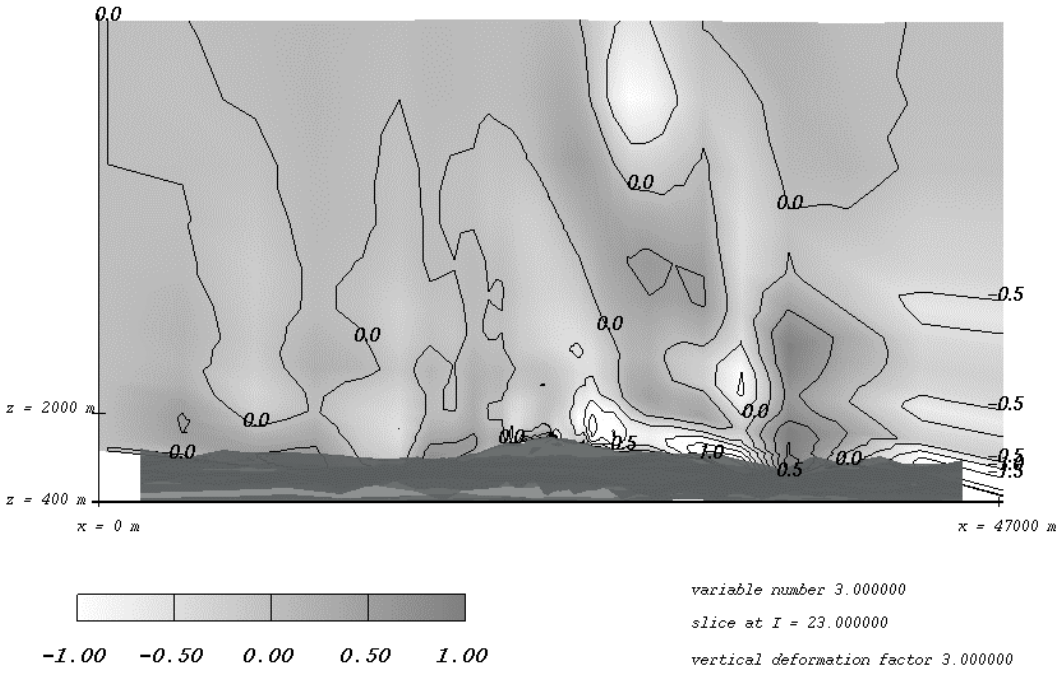

Figure 6.12. Same as Figure 6.8 for an initial stable thermal stratification given by a real temperature gradient of –6.5 K/km. Steps between isolines: 0.5 m/s.

Vertical profiles were extracted at various locations along a constant x plane going through Chasseral and Mt-Crosin. These locations were chosen on the Swiss Plateau, the Plateau de Diesse, at Chasseral, on the southern flank of the St-Imier valley as well as on the Mt-Crosin site (see Figure 6.23 for the definition of the exact locations). The horizontal wind speed profiles obtained with a stable stratification (continuous lines) are compared to the ones from a neutrally stratified atmosphere (dashed lines) in Figure 6.13 for three of the above listed locations. The comparison clearly shows that the introduction of a more realistic stable stratification drastically modifies the simulated wind profiles. For the neutral case, the wind speed profile obtained on the Swiss Plateau, over a rather flat topography, exhibit wind speeds that are only slightly lower than those obtained over the elevated sites of Chasseral and Mt-Crosin. For the stably stratified atmosphere, the results are completely different: the profiles at both Chasseral and Mt-Crosin exhibit a strong speed-up whereas the one on the Swiss Plateau, upwind of the Jura Chain, shows a significant reduction in the lowest 1000m above ground, which is due to the blocking of the flow caused by the mountain range.

For the stable case, the simulated potential temperature profiles are shown in Figure 6.14 for the five locations mentioned previously. The sites are located at different altitudes, and since the profiles are plotted as a function of the height above ground, they appear to be horizontally shifted in the graph, the highest sites showing the highest potential temperature. Consequently, at the zero heat flux boundary condition set at the ground, a neutral layer develops in the lowest levels ($z < 200$-300m above ground) for the upwind locations on the Swiss Plateau and 'Plateau de Diesse'. An interesting effect can also be seen when comparing the potential temperature profiles taken at the locations labelled St-Imier and Diesse. These profiles are taken above ground stations located at the same altitude. Therefore, these were the same when initialising the model. As can be seen from Figure 6.14, the potential temperature profile obtained on the southern flank of the St-Imier valley shows a temperature increase below 1000m relative to that obtained on the 'Plateau de Diesse'. This can be identified as a foehn effect[16], with a warming of the air mass on the downwind side of the Chasseral chain (see also Figure 6.23 for a definition of the profiles locations). The maximum temperature difference between two levels

[16] Some authors use the term 'foehn' for a warm downdraft behind a mountain range only in association with precipitation formation on the upwind side. In the case presented above, we do not have any precipitation. We thereby extend the notion of 'foehn' to include situations for which no latent heat release is involved.

with the same altitude over the Plateau de Diesse and St-Imier is of 2.9 K. The maximum difference is reached at 400m above ground.

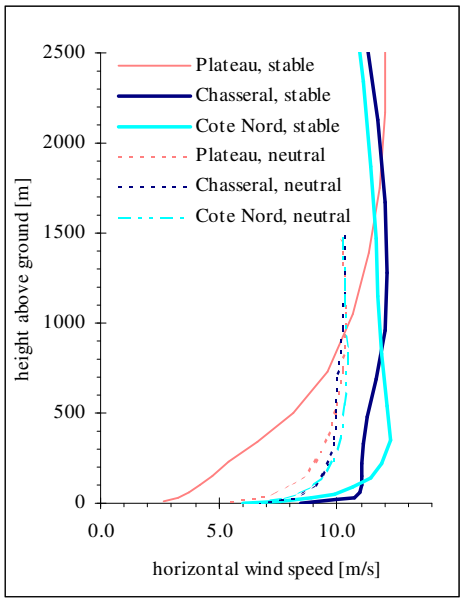

Figure 6.13. Vertical profiles of horizontal wind speed for a stably (continuous lines) and neutrally (dashed lines) stratified atmosphere at locations on the Swiss Plateau, at Chasseral and Mt-Crosin.

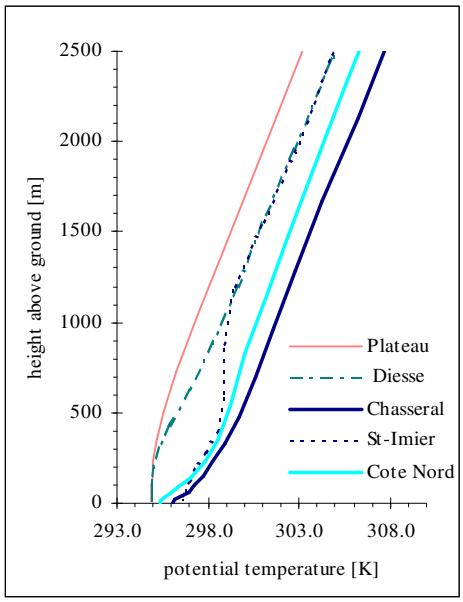

Figure 6.14. Vertical profiles of potential temperature for a stably stratified atmosphere at locations on the Swiss Plateau, Plateau de Diesse, at Chasseral, on the flank of the St-Imier valley and at Mt-Crosin.

For the stably stratified case, the time evolution of the wind speed and direction at the nodes closest to the Chasseral and Mt-Crosin measurement masts is presented in Figure 6.15.a and b, whereas the Mt-Crosin to Chasseral wind speed ratio is shown in Figure 6.15.c. After some strong oscillation during the first hour, the solution tends towards a converged state. After more than 2 hours, a slight oscillation is still visible in the wind speed values, with a period of some 5500s. The oscillation is also visible in the wind speed ratio, since the wind speed variations at Chasseral and Mt-Crosin are out of phase. From the wind direction plot, we can see that, even after 6 h of simulation, the convergence for this stably stratified situation has not exactly been achieved. For the stable stratification, the wind direction at Chasseral tends to more or less the same direction as for the neutrally stratified atmosphere (around 220°). This is not true however for the Mt-Crosin sites. For the neutrally stratified case, the wind at Mt-Crosin was rotated clockwise, relatively to the Chasseral direction, whereas for the stably stratified atmosphere we have the opposite.

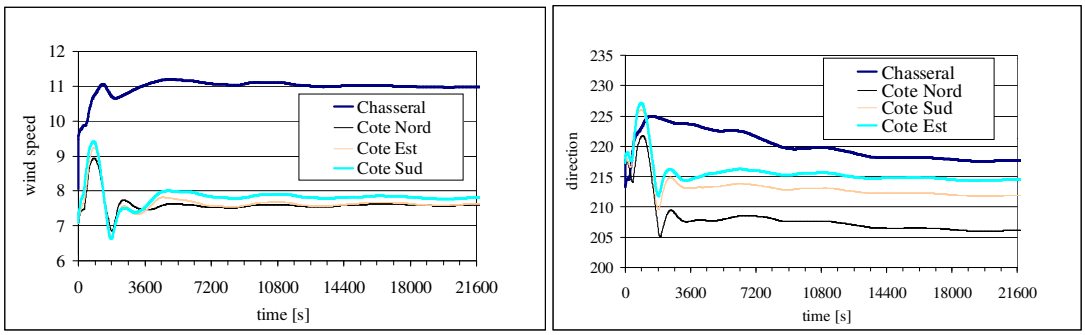

a) b)

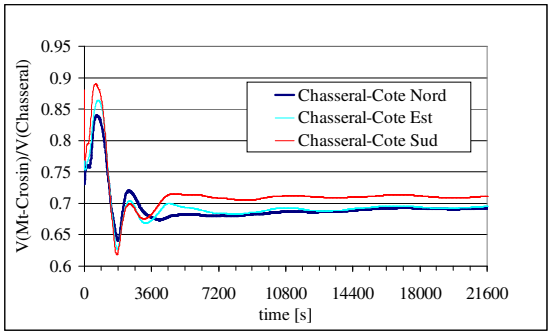

c)

Figure 6.15. Time evolution of the wind speed (a) and direction (b) for the model nodes closest to the locations of Côte Nord, Côte Sud, Côte Est and Chasseral, for a stably stratified atmosphere. c) Ratio of the Mt-Crosin to Chasseral horizontal wind speed.

Comparing the values obtained for the Mt-Crosin to Chasseral wind speed ratios (between 0.69 and 0.71 for the stably stratified case, and between 0.8 and 0.86 for the neutrally stratified case), we can already conclude that the thermal stratification of the atmosphere will play a major role when determining the site to site relationships to be used in the wind data transposition.

Further reducing the Froude number of the simulation, we performed an additional simulation with the same stratification conditions as above (vertical real temperature gradient of –6.5 K/km), with a high altitude wind speed of 5 m/s. The horizontal wind speed distribution (not shown) shows similar characteristics as the one in Figure 6.10, with even more pronounced blocking effects on the 'Plateau de Diesse' upwind of Chasseral and channelling effects in the St-Imier valley. The wind speed regime obtained with this atmospheric condition is favourable for the formation of mountain waves, as can be observed from the vertical cross-sections of the horizontal wind speed (Figure 6.16) and vertical velocity component (Figure 6.17) (solution after 4 h). The perturbation induced by the topography affects the entire troposphere.

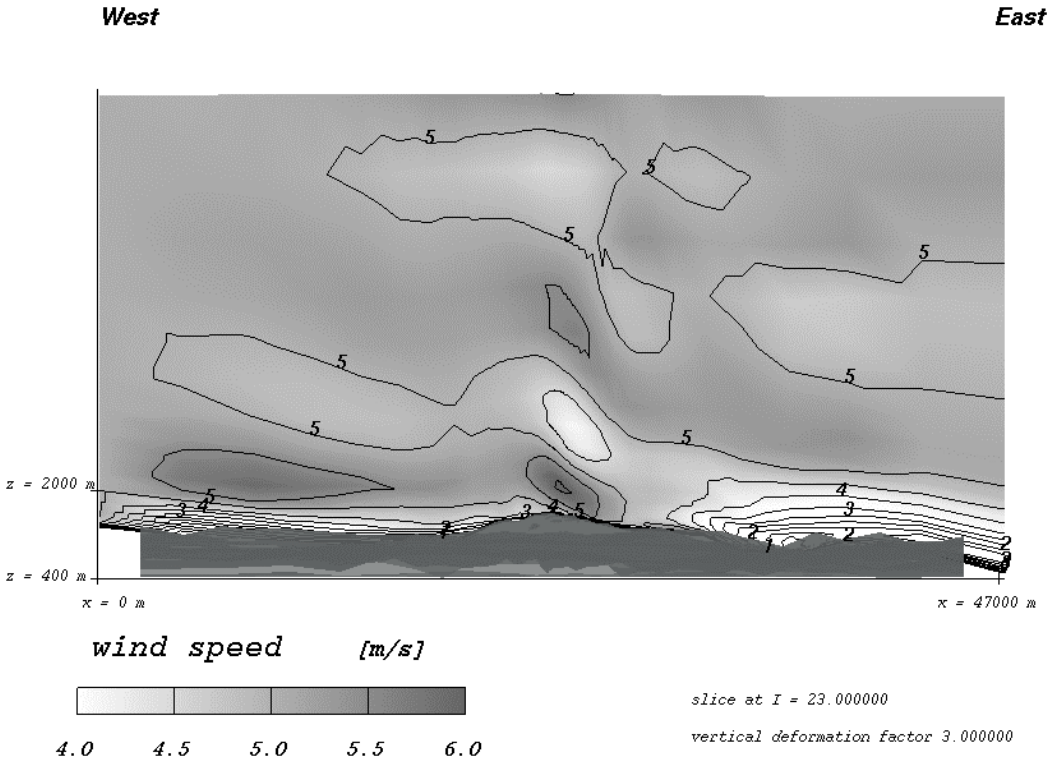

Figure 6.16. Vertical cross-section of the horizontal wind speed for a geostrophic wind of 5 m/s from the 240° sector. The initial atmospheric stability was given by a real temperature gradient of –6.5 K/km. Steps between isolines: 0.5 m/s. Simulation time: 4h.

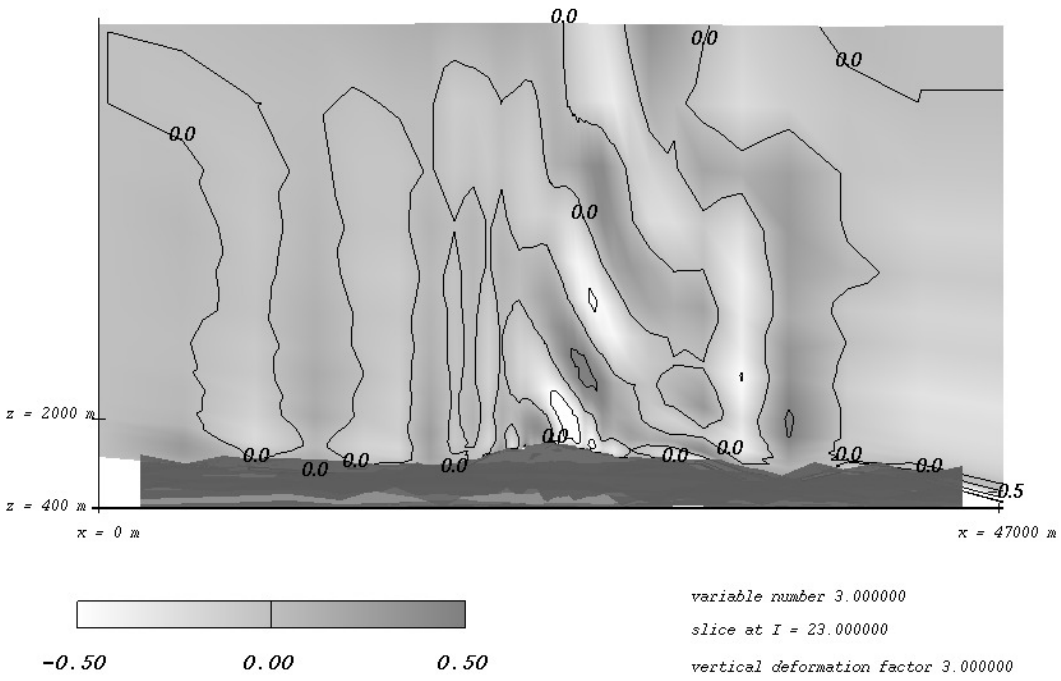

Figure 6.17. Vertical cross section of the vertical wind velocity for a geostrophic wind speed of 5 m/s from the 240° sector. The initial atmospheric stability was given by a real temperature gradient of –6.5 K/km. Steps between isolines: 0.5 m/s

As before the wind speed profiles in Figure 6.18 show a significant wind speed reduction for the profile obtained over the Swiss Plateau and a strong speed up over the highest Mt-Crosin and Chasseral elevations. A major difference with the previous simulation, however, concerns the fact that with 5 m/s for the high altitude wind, we get a higher wind speed at Mt-Crosin than at Chasseral for the levels below 300 m. This observation again shows the significance of the atmospheric stability (defined in terms of the Froude number) for the establishment of relationships between the wind at Mt-Crosin and the wind at Chasseral. For the potential temperature profiles (Figure 6.19), we obtain similar results compared to what was observed with the higher geostrophic wind speed. The essential difference with the reduced high altitude wind speed is that the neutral boundary layer developing upwind of the Jura chain is smaller. Also, the layer in which the simulated potential temperature departs from the original profile is smaller, when the high altitude wind speed is reduced.

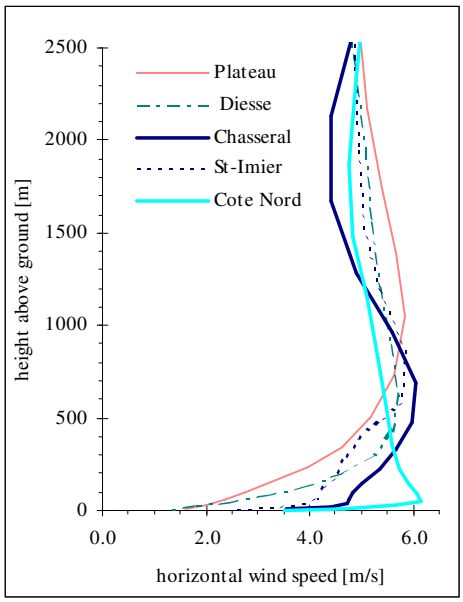

Figure 6.18. Vertical profiles of horizontal wind speed for a stably stratified atmosphere with a high altitude wind speed of 5 m/s.

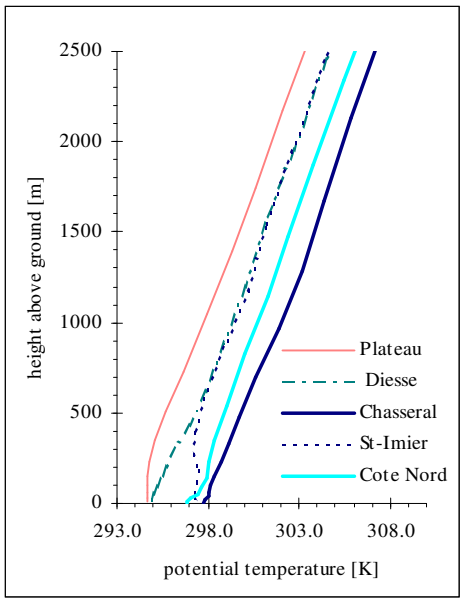

Figure 6.19. Vertical profiles of potential temperature for a stably stratified atmosphere with a high altitude wind speed of 5 m/s

As can be seen from Figure 6.20 it appears that the convergence of the solution is even more difficult for the 5 m/s geostrophic wind speed than it was for the 10 m/s case. After 1 ½ hour of simulation the wind direction at the three measuring stations

of Mt-Crosin are more or less stable. This is however not exactly the case at Chasseral, where it is not even obvious that the direction has been stabilised after 6 hours of simulation. After the initial oscillations that can be observed during the first hour of simulation, the wind speed at both Chasseral and Mt-Crosin keeps changing, rising to the value of 5m/s at Mt-Crosin and then oscillating around this value. At Chasseral, after having been reduced to some 4.5 m/s, the wind speed increases again to values slightly higher than 5 m/s. These simultaneous wind speed changes, which are partly in antiphase, drastically affect the Mt-Crosin to Chasseral wind speed ratio. The latter goes from some 0.65 after 1 h of simulation to some 1.1 one hour later, and further reduces to about 0.95.

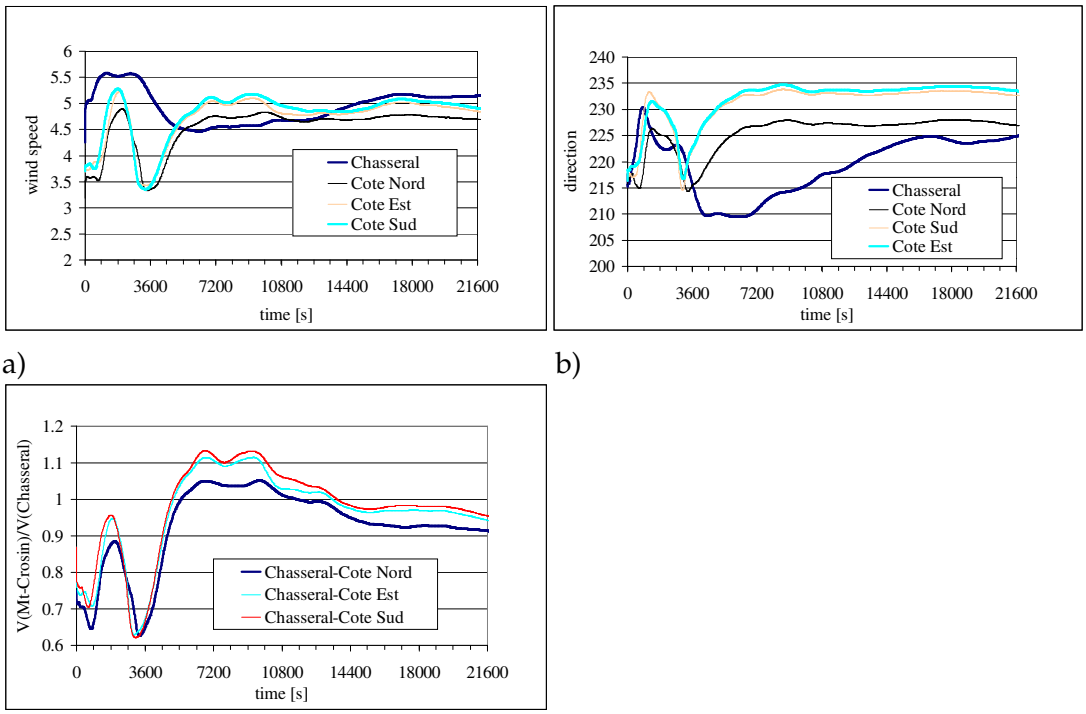

a) b)

c)

Figure 6.20. Time evolution of the wind speed (a) and direction (b) for the model nodes closest to the locations of Côte Nord, Côte Sud, Côte Est and Chasseral, for a stably stratified atmosphere with a high altitude wind speed of 5 m/s. (c) Ratio of the Mt-Crosin to Chasseral horizontal wind speed.

To make sure that the simulated variation was not merely due to some spurious numerical effects which could have been related to convergence criteria, that might have been too loose, we run exactly the same situation imposing stricter convergence, thereby increasing the number of iterations within the time steps. The time evolution of the stricter solution (not shown) appeared to be the same as the one presented in Figure 6.20. Therefore, we expect the time evolution presented below to

correspond to physical transient effects and not just to numerical convergence problems. In the relatively weakly stratified case (simulation NS1 with the non-dimensional mountain height $Fr^{-1} = NH / G \approx 1$), the transient effects might be related to the formation of mountain waves, whereas in the more strongly stratified situation NS2 ($Fr^{-1} = NH / G \approx 2.5$) they could be explained by atmospheric vortex shedding associated with flow splitting as shown by Schär and Durran (1997).
The effect of reducing the high altitude wind speed, when keeping the atmosphere stable, tends to increase the Mt-Crosin to Chasseral wind speed ratio. We can in fact observe from Figure 6.20.c that after 1 ½ hours of simulation, the wind speed ratio stays above 0.9, which is significantly higher than the value of 0.7 obtained with the 10 m/s geostrophic wind speed case. Apart from showing again the strong sensitivity of the relative wind speeds at Chasseral and Mt-Crosin to the simulation conditions, the present situation also points out the difficulty inherent to the non-stationarity of the obtained solutions in situations with Froude numbers much lower than unity (either strong stability or weak winds).

The three simulations presented above for the 240° geostrophic wind direction were calculated assuming a zero heat flux through the ground. To test the effect of a ground cooling on the wind field development, a simulation was done starting with initial conditions representative of a late afternoon summer situation, with a weak southwest wind at high altitude. We therefore set a wind profile according to the Zilitinkevich parameterisation, with a geostrophic wind speed of 4.7 m/s. The thermal stratification was quasi-neutral below 2000m ($\partial T / \partial z = -9.5 K / km$) and stable aloft ($\partial T / \partial z = -7 K / km$). A ground cooling was imposed on the model with a potential temperature decrease of *–2 K/h* during the first hour and *–1 K/h* later on.
As a first remark, we can note that due to the change in the stratification conditions (neutral stratification below 2000m and slight reduction of the stability aloft) the mountain waves that appeared in the previous simulation are no longer as strong (compare Figure 6.22 to Figure 6.16). Whether the introduction of ground cooling also had an effect on the mountain wave reduction is not clear.
Figure 6.21 shows the wind field obtained after 4 h of simulation at the first level of grid nodes. We can clearly see the development of katabatic winds with slopes oriented towards the north-west exhibiting positive v velocity components (along the y direction) and slopes oriented towards the south-east showing negative ones. The time evolution of the induced breeze is illustrated by means of vertical cross-sections showing the wind vectors in a plane perpendicular to the mountain range after 2h, 4h and 6h and 20′ (Figure 6.23 to Figure 6.25). Vertical profiles of the v velocity component (Figure 6.27, Figure 6.29 and Figure 6.31) and potential temperature

(Figure 6.28, Figure 6.30 and Figure 6.32) are also plotted for the 5 locations presented in Figure 6.23.

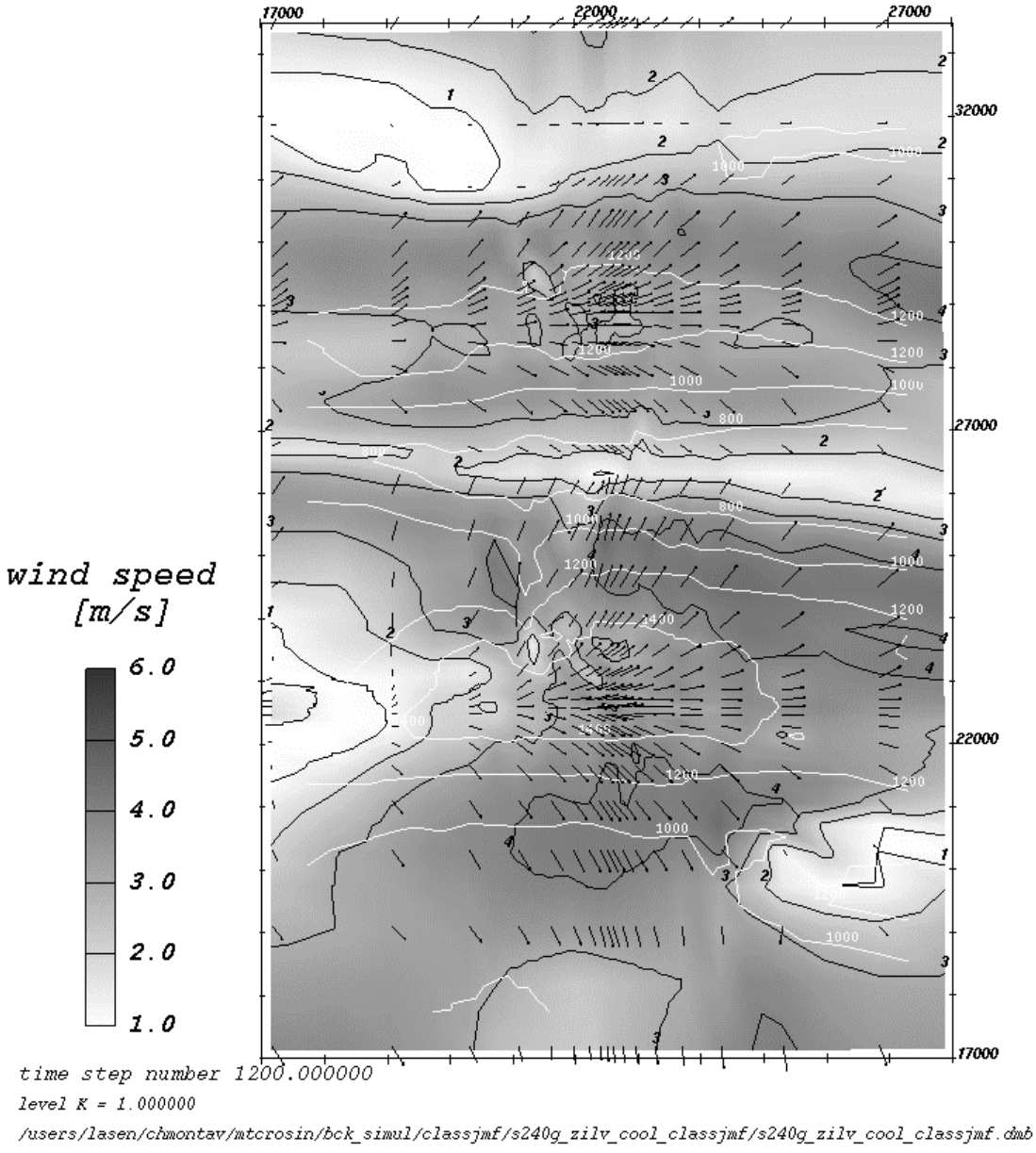

Figure 6.21. Wind field calculated by the model for a geostrophic wind of 4.7 m/s, blowing from the 240° direction for a situation with ground cooling (see text for details about the simulation conditions). The results shown here correspond to the first level of grid cells (4-5 m above ground) after 4 h of simulation.

After two hours of simulation, the breeze has formed and reaches the foot of the Jura chain. However, it still has not reached the location where the profiles over the Swiss Plateau have been extracted. In fact, the v velocity profile obtained at this location still shows positive v velocities, under the influence of the inlet boundary condition which is set at the southern face of the domain. Two hours later, the downslope wind

progressed over the Swiss Plateau and is about to reach the southern end of the domain (see Figure 6.24). Since we applied Dirichlet type boundary conditions on the velocity components and potential temperature at the southern face of the domain without varying them with time, we do not expect that the solution behaves like it would for a real situation after the breeze has reached the domain boundaries. In fact, in a real situation, we would have cold air advection from the south, that would be brought by a breeze induced by the Alps and Pre-Alp chain. Such a situation usually ends up with the formation of a pool of cold air over the Swiss Plateau, with an inversion height around 1200m above sea level (Fallot, personal communication). To properly simulate this phenomenon, we would need either to extend the simulation domain to include the Alps and their effects or to trigger the inlet boundary conditions to reproduce the effect of the Alps. Both of these workarounds appear to be beyond the scope of the present work and will not be attempted at this stage.

Nevertheless letting the model continue with this conflict between the boundary conditions and the breeze, we obtained a solution after 6 hours and 20 minutes (Figure 6.25), still showing the presence of the downslope winds over the Jura chain, but with the winds reducing on the Swiss Plateau. Beyond this time, the model had some convergence difficulties and the calculation was stopped.

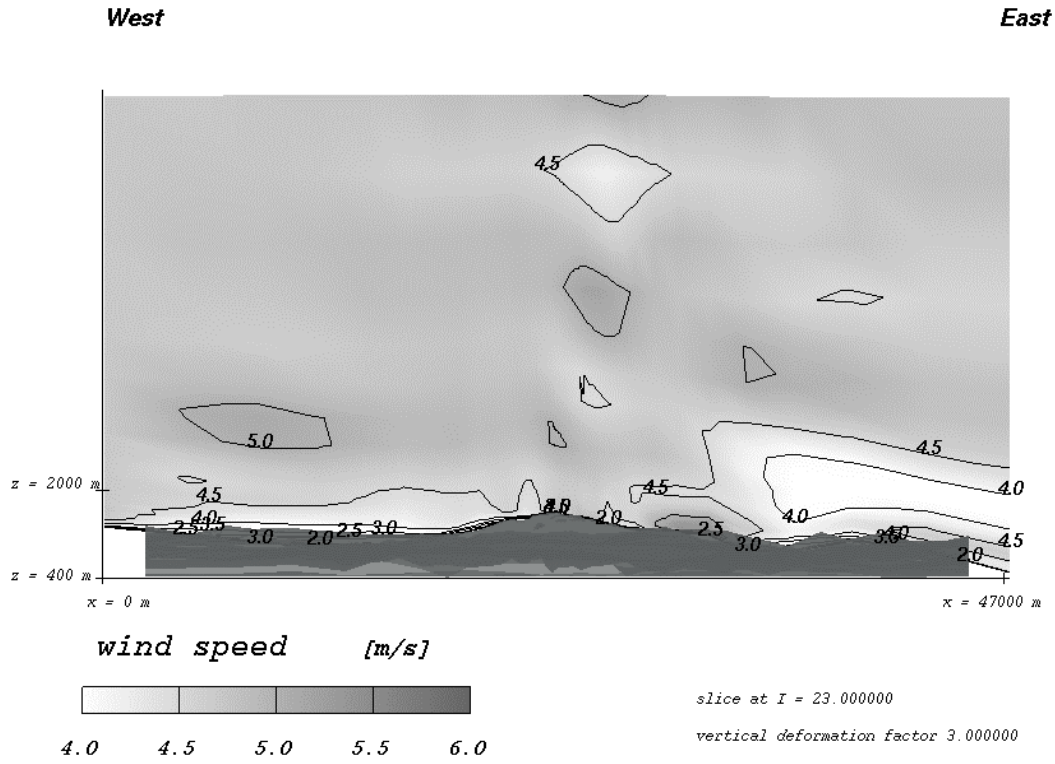

Figure 6.22. Vertical cross-section along a constant y-plane through Chasseral showing the horizontal wind speed after 4 hours of simulation for the simulation with ground cooling.

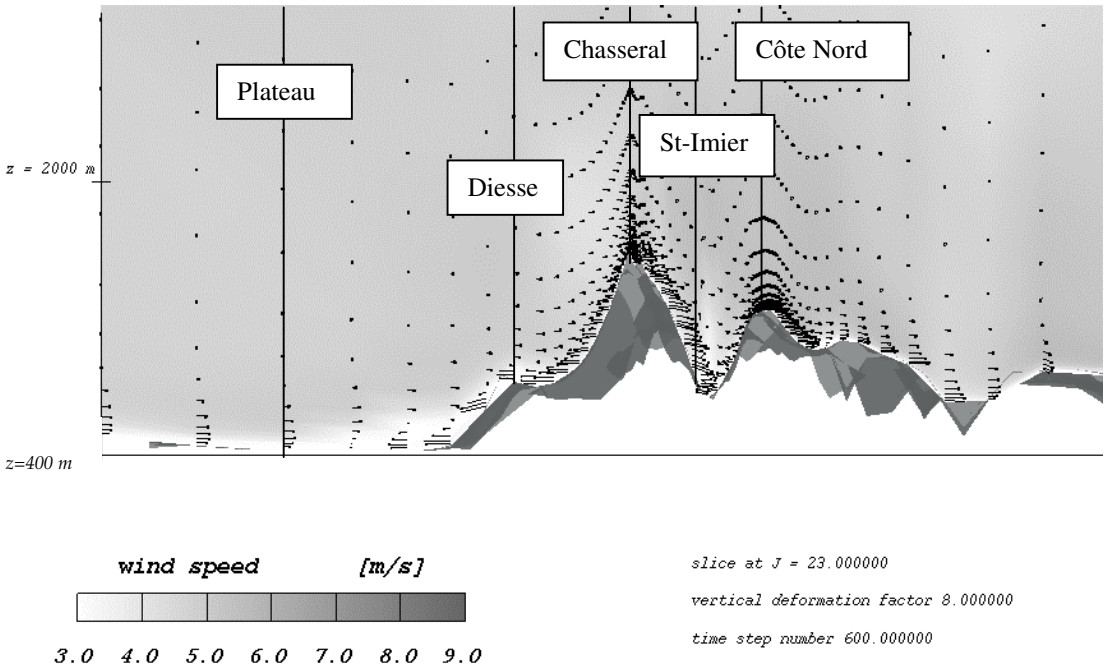

Figure 6.23. Vertical cross-section along a constant x-plane through Chasseral and Mt-Crosin, showing the development of katabatic winds after 2 hours of simulation. The vertical lines define the 5 locations at which vertical profiles were extracted.

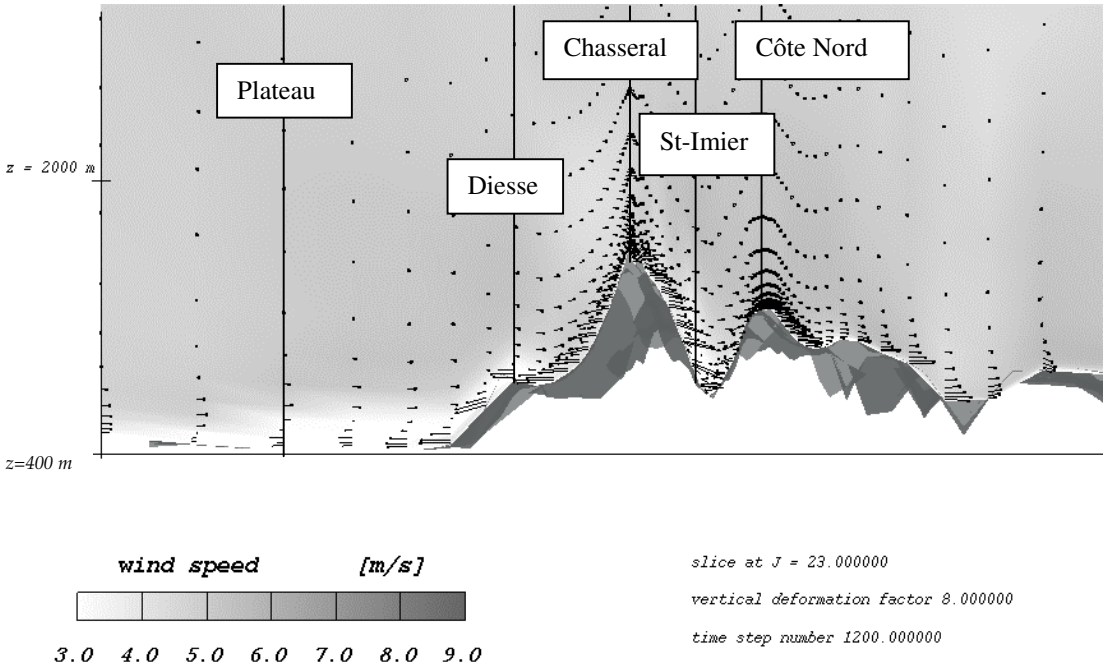

Figure 6.24. Same as Figure 6.23 after 4 hours of simulation.

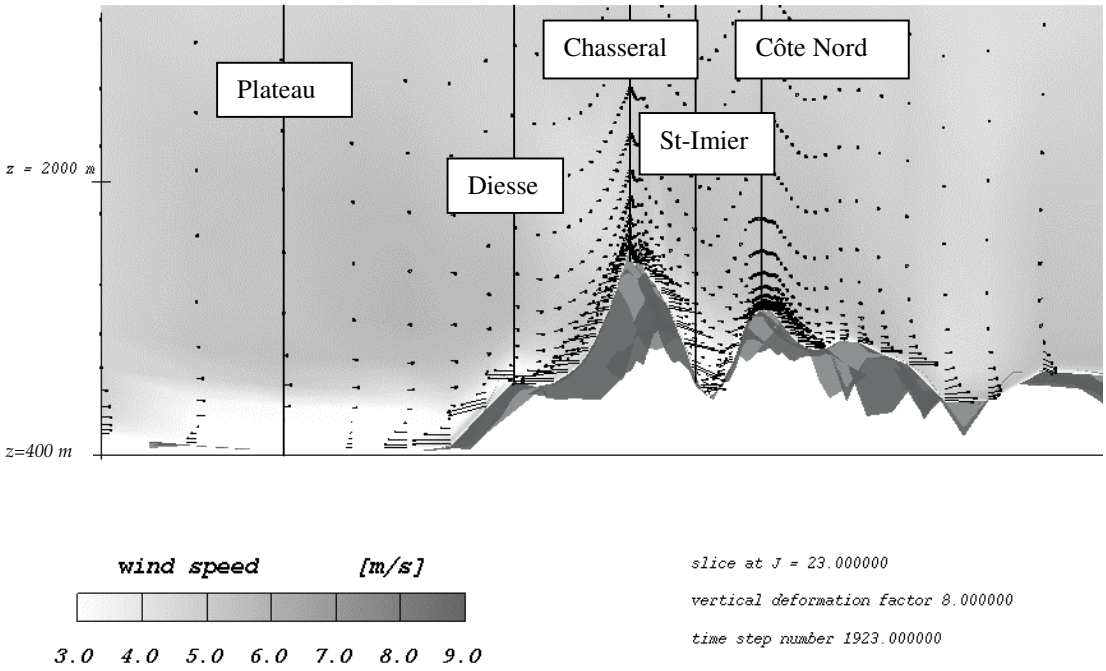

Figure 6.25. Same as Figure 6.23 after 6 hours and 20 minutes of simulation.

The simulated breeze layer depth and intensity were compared to an improved version of the Prandtl model (1942) which was proposed by Hertig (1983, 1986). The latter is a model that allows us to compute the wind speed and potential temperature profiles for katabatic winds developing over a slope of known characteristics as a function of the temperature perturbation (Figure 6.26). Prandtl (1942), assuming that the breeze develops on an infinite slope and parallel to it proposes the following expressions for the katabatic winds:

eq. 6.1 $$\theta(n) = \theta_0 \exp(-\frac{n}{l})\cos(\frac{n}{l})$$

eq. 6.2 $$u(n) = \Delta\theta_0 \sqrt{\frac{g \cdot \alpha \cdot K_T}{B \cdot K_M}} \exp(-\frac{n}{l})\sin(\frac{n}{l})$$

with

eq. 6.3 $$l = \sqrt[4]{\frac{4 \cdot K_T \cdot K_M}{g \cdot \alpha \cdot \sin^2(\varphi)}}$$

where n = distance normal to the slope

θ = potential temperature

θ_0 = ground potential temperature before cooling

$\Delta\theta_0$ = amplitude of the temperature perturbation (ground cooling)

g = gravity acceleration (9.81 m/s^2)

α = thermal expansion coefficient (1/273 K^{-1})

B = vertical potential temperature gradient

φ = slope angle

K_M, K_T = mechanical, resp. thermal diffusivities

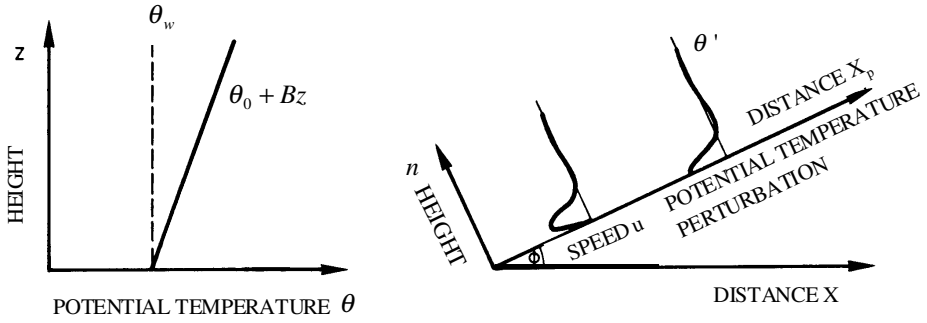

Figure 6.26. Vertical profiles of the horizontal velocity u and potential temperature perturbation θ' for a downslope wind. (source: Hertig).

The breeze layer thickness is defined as the first level at which the wind speed vanishes, i.e. at $n_t = \pi \cdot l$. The maximum wind speed is reached at the height $n_{\max} = \frac{\pi l}{4}$. Experiments show however that the breeze intensity and thickness also depend on the slope length. This was taken into account by Hertig who modified the Prandtl formulation to include the slope length. The modification yields:

eq. 6.4 $$\theta(z) - \theta_0 = \Delta\theta_0 \exp(-\frac{z}{l_T}) \cos(\frac{z}{l_T})$$

eq. 6.5 $$u(z) = A \cdot \Delta\theta_0 \sqrt{\frac{g \cdot \sin(\varphi)\alpha \cdot K_T}{\Delta\theta_x \cdot K_M}} \exp(-\frac{z}{l_v}) \sin(\frac{z}{l_v})$$

with

eq. 6.6 $$\Delta\theta_x = \frac{\Delta\theta_0}{x} + B$$

eq. 6.7 $$l_T = 1.89 \cdot \sqrt[4]{\frac{4 \cdot K_T \cdot K_M}{g \cdot \alpha \cdot \Delta\theta_x \sin(\varphi)}}$$

eq. 6.8 $$l_v = 1.38 \cdot \sqrt[4]{\frac{4 \cdot K_T \cdot K_M}{g \cdot \alpha \cdot \Delta\theta_x \sin(\varphi)}}$$

The breeze layer thickness is therefore $h_t = \pi \cdot l_v$ and the height at which the maximum wind speed occurs is $h_{\max} = \frac{\pi l_v}{4}$. The constant A appearing in eq. 6.5 for the wind speed profile is a constant that needs to be calibrated. From wind tunnel simulations and with relatively laminar flow, Hertig obtains a value of 1.71 for A.

Fallot (1992) compared this formulation with breeze observations recorded in the Haute-Gruyère and found that this model gave reliable results for the katabatic winds, taking a value of 1 for *A*.

The maximum breeze intensity and layer thickness after 4 hours have been evaluated with the above expressions, using *A=1*, for the two locations called Diesse and St-Imier. The mechanical and thermal diffusivities were approximated to 0.8 and 0.9, which correspond to representative values simulated by the model in the area. The thermal expansion coefficient was set to 1/273 K^{-1}. For the vertical potential temperature gradient we took the initial gradient that was used below 2000 m (i.e. $B = 3 \cdot 10^{-4}$ K/m). The values of the other parameters together with the results are given in Table 6.7. A comparison of the numerical and analytical model values shows a fairly good agreement between the predicted breeze layer thickness. For the breeze intensity, it appears that the numerical model gives wind speeds that agree quite well with the analytical method, underestimating them by some 13-17%. Due to the steeper slope on the St-Imier side compared to the Plateau de Diesse side, the breeze developing on the St-Imier side is expected to be thinner and faster than the one on the Plateau de Diesse. This tendency is reproduced by the numerical model.

The simple analytical model above assumes that there is no wind apart from the katabatic wind developing on the slope. In the simulation, this assumption was not exactly fulfilled, since, in addition to the main flow component along the x-axis, we had in fact a *v* velocity component in the boundary layer, which is associated with the Ekman spiral. Considering this departure from the analytical model assumptions, and taking into account the fact that the topography of the area is more complex than assumed by the simple slope model used to derive the analytical expressions, it appears that the katabatic winds simulated by the numerical model show reasonable characteristics.

Table 6.7. Breeze layer thickness and intensity obtained from the analytical and numerical models for the locations of Diesse and St-Imier (simulation time: 4 hours). The parameters needed for their evaluation are also given.

	Diesse		St-Imier	
	Analytical	Numerical	Analytical	Numerical
$\sin(\varphi)$	0.177		0.229	
x [m]	4400		3500	
$\Delta\theta_0$ [K]	5		5	
$h_t = \pi \cdot l_v$ [m]	103	118	92	65
u_{max} [m/s]	3.6	3.0	3.7	3.2

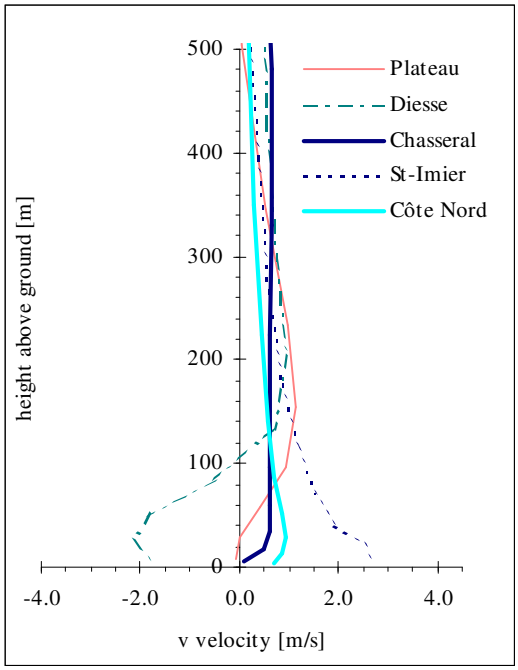

Figure 6.27. Vertical profiles of v velocity component after 2 hours of simulation for the situation with ground cooling.

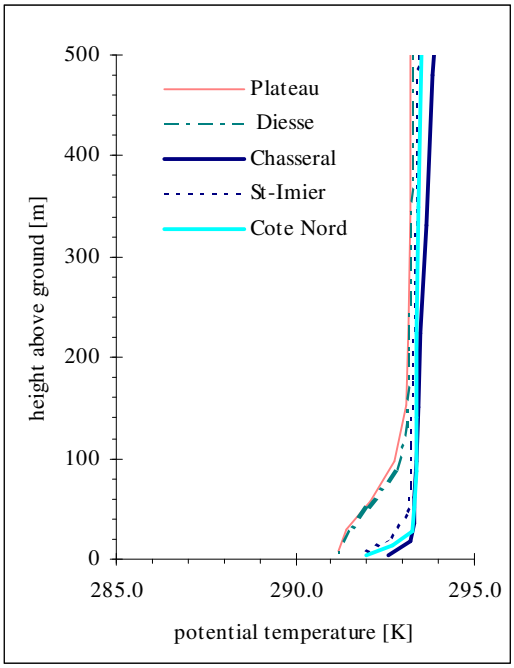

Figure 6.28. Vertical profiles of potential temperature after 2 hours of simulation for the situation with ground cooling.

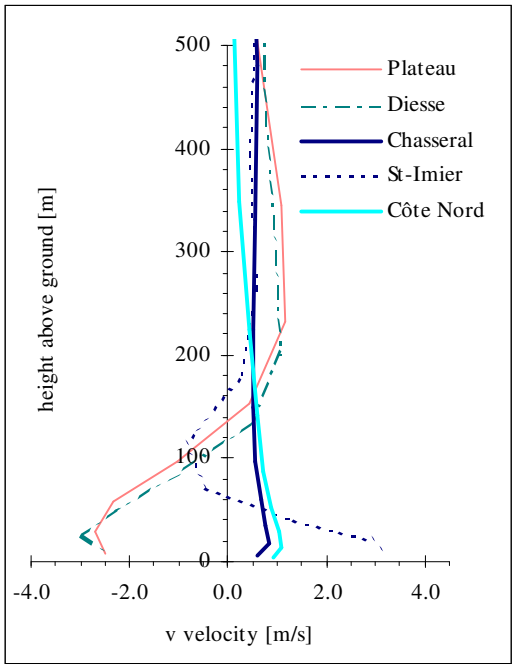

Figure 6.29. Vertical profiles of v velocity component after 4 hours of simulation for the situation with ground cooling.

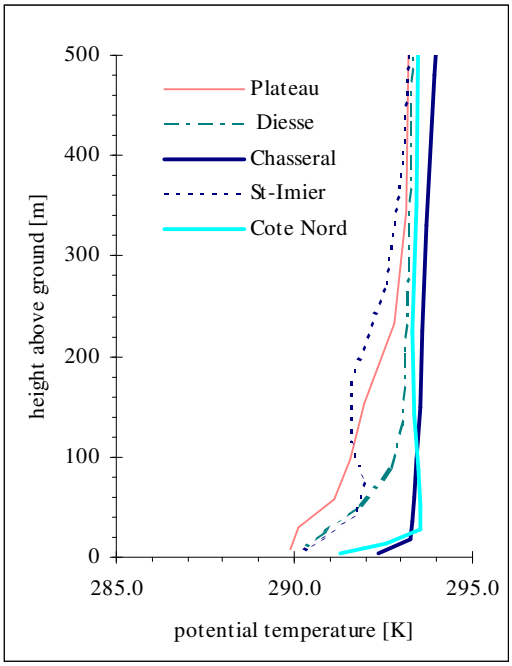

Figure 6.30. Vertical profiles of potential temperature after 4 hours of simulation for the situation with ground cooling.

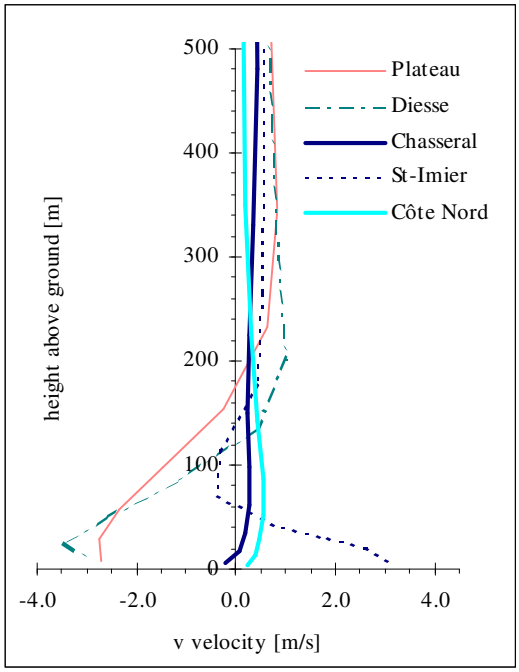

Figure 6.31. Vertical profiles of v velocity component after 6 hours and 20 minutes of simulation for the situation with ground cooling.

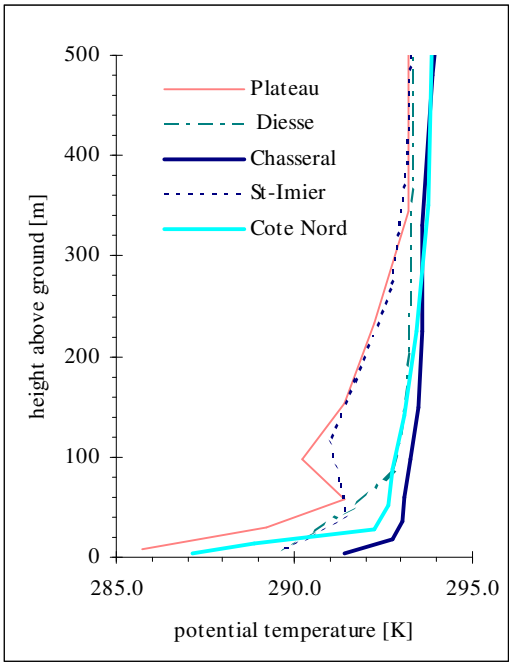

Figure 6.32. Vertical profiles of potential temperature after 6 hours and 20 minutes of simulation for the situation with ground cooling

The time evolution of the wind speed, wind direction and Mt-Crosin to Chasseral wind speed ratio for the katabatic wind simulation are presented in Figure 6.33. Apart from the sudden wiggle observed at Chasseral after 4 hours, the simulated wind speed tends to converge fairly rapidly. After 2 hours of simulation, the Mt-Crosin to Chasseral wind speed ratio is relatively stable at a value around 0.98 for the site of Côte Nord and around 1.05 for both Côte Sud and Côte Est. Comparing the simulation NS2 (Figure 6.20) to the present one, which was similar, apart from the ground cooling and the initial neutral stratification below 2000m, we can see that the wind speed ratio tends to converge to a higher value for the simulation with ground cooling. However, it is difficult to conclude whether this is really an effect of the ground cooling, or an effect of the neutral stratification of the lowest layer. To sort out this question, some more sensitivity tests have been done, which are presented in Section 8.2.

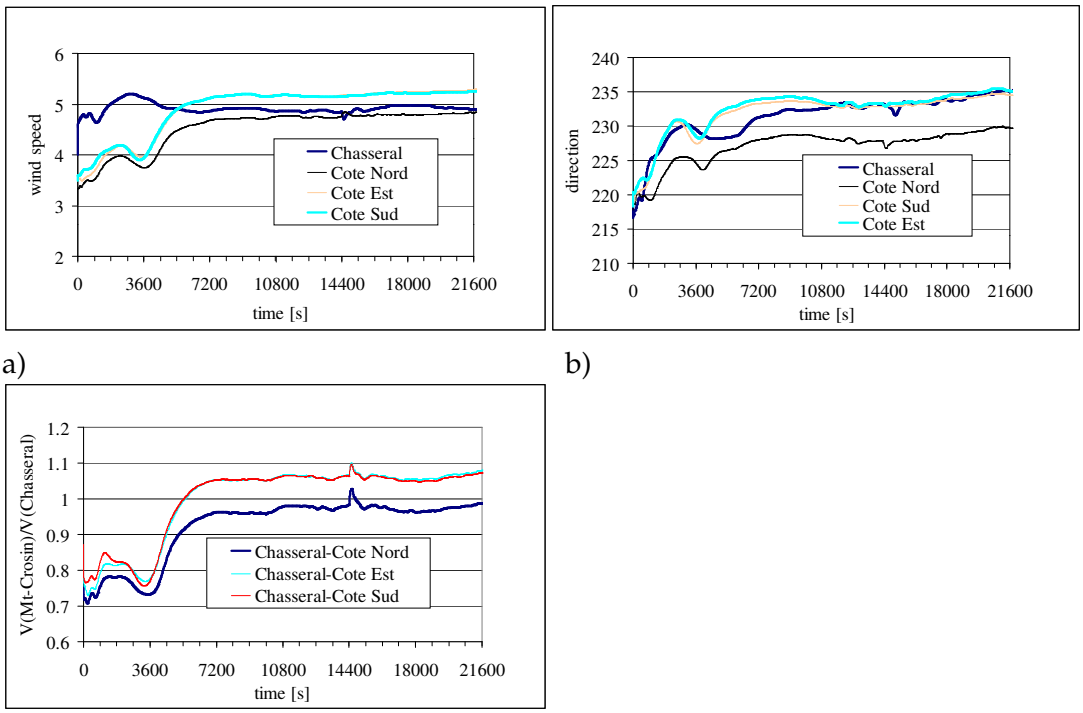

Figure 6.33. Time evolution of the wind speed (a) and direction (b) for the model nodes closest to the locations of Côte Nord, Côte Sud, Côte Est and Chasseral, for the simulation with ground cooling (simulation SS1). (c) Ratio of the Mt-Crosin to Chasseral horizontal wind speed.

6.3.2 The 330° geostrophic wind direction

For the 240° wind direction, some noticeable differences could be observed in the flow field development between the neutrally and stably stratified atmosphere. Though the flow direction was essentially aligned with the main mountain axis, we could see some mountain waves forming when the flow stability was increased. For flow situations with the 330° wind direction, perpendicular to the main mountain axis, the difference in the flow behaviour is much more pronounced.

Two runs were performed which show this, the first one with a high altitude wind speed of 10 m/s, neutrally stratified, and the second one with a high altitude wind speed of 5 m/s and a thermal stratification given by $\partial T / \partial z = -6.5$ K/km. A detailed vertical cross-section along a constant x-plane through Chasseral and Mt-Crosin is shown for both the neutrally and stably stratified cases in Figure 6.34 and Figure 6.35. The wind vectors are plotted together with the horizontal wind speed. The wind enters the domain from the right (corresponding to North-Northwest). The most striking difference between the two results is the appearance of the wind field calculated downwind of Chasseral. In the neutrally stratified case, we end up with

almost no wind in the wake of Chasseral, whereas for the stably stratified situation, the opposite behaviour is obtained. In the latter case wind speed of more than 10 m/s can be observed immediately downwind of Chasseral. Note that this is more than twice the geostrophic wind speed that was set to 5 m/s for the initial field.

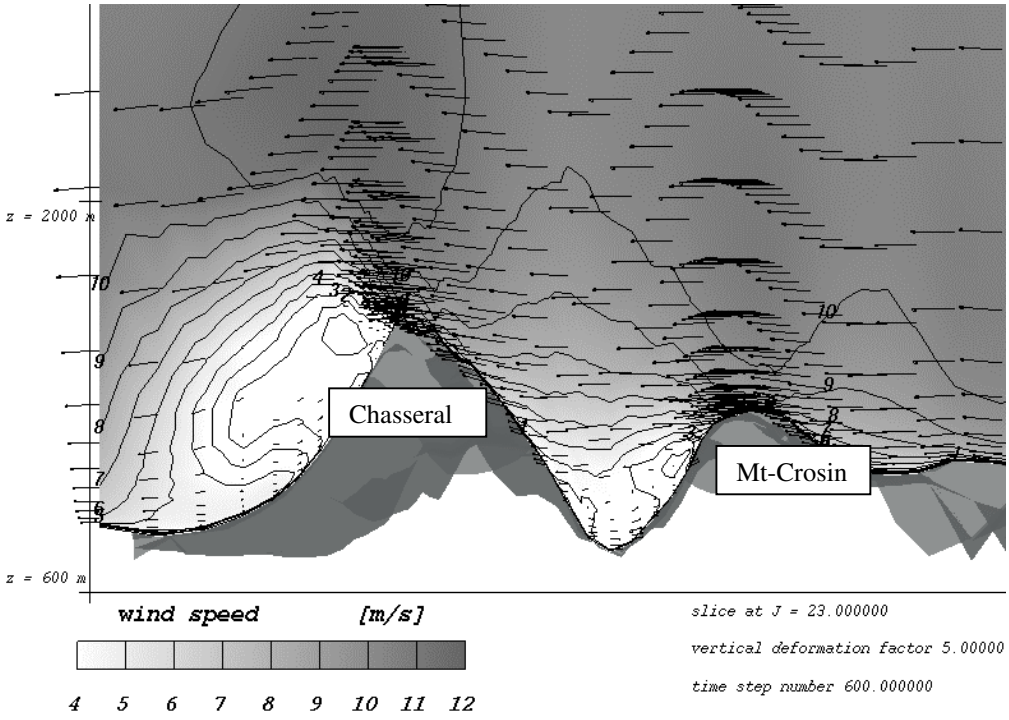

Figure 6.34. Detailed vertical cross-section along a constant x-plane through Chasseral and Mt-Crosin, showing the horizontal wind speed (shading and isolines) as well as the wind vectors. The situation was initialised with a geostrophic wind speed of 10 m/s from the 330° sector, with a neutral atmospheric stratification (real temperature gradient of –9.7 K/km). Steps between isolines: 1 m/s.

The very strong flow acceleration is due to resonance phenomena associated with mountain wave generation (similarly to what was measured in the Boulder foehn event presented in Appendix C). This mountain wave production can best be seen in the vertical cross-sections showing the vertical velocity (Figure 6.36) and the potential temperature (Figure 6.37). With vertical velocities of more than 2 m/s, we are in the presence of strong wave generation and the perturbation induced by the topography propagates throughout the entire troposphere. We can also observe from the potential temperature plot the strong downdraft downwind of Chasseral associated with the downward displacement of the 300 K potential temperature isoline.

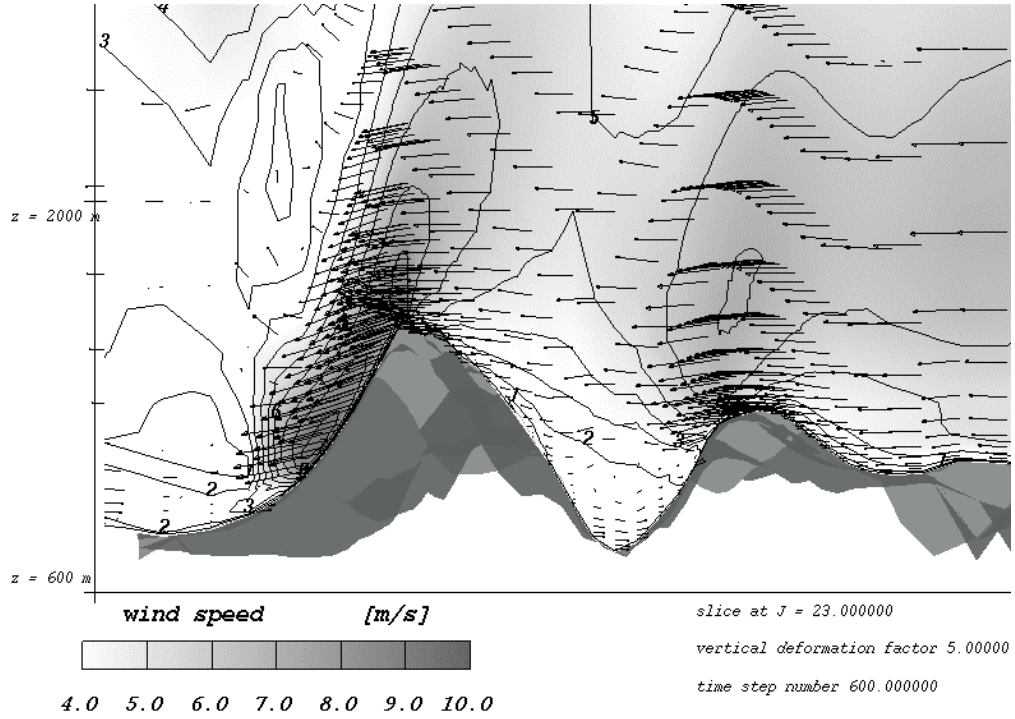

Figure 6.35. Same as Figure 6.34 for the stably stratified atmosphere ($\partial T / \partial z = -6.5$ K/km), with a high altitude wind speed of 5 m/s. Steps between wind speed isolines: 1 m/s.

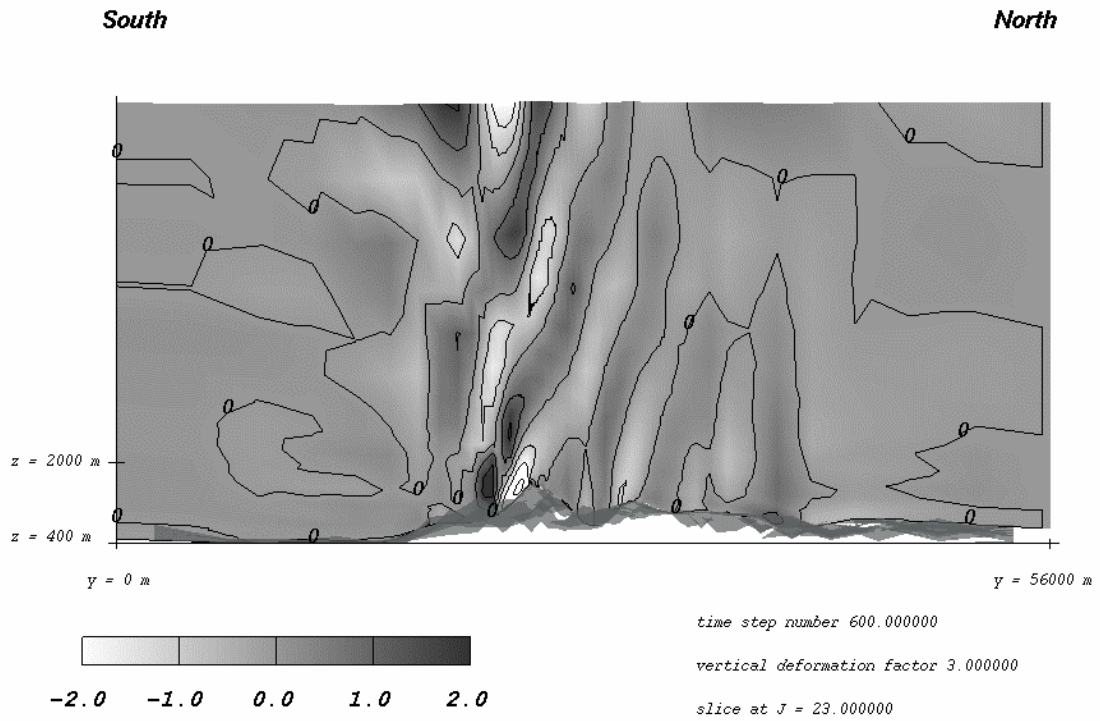

Figure 6.36. Vertical cross-section along a constant x-plane through Chasseral and Mt-Crosin (whole domain extent), showing the vertical velocity component (shading and isolines). The situation was initialised with a high altitude wind speed of 5 m/s and a stably stratified atmosphere ($\partial T / \partial z = -6.5$ K/km). Isolines steps: 1 m/s.

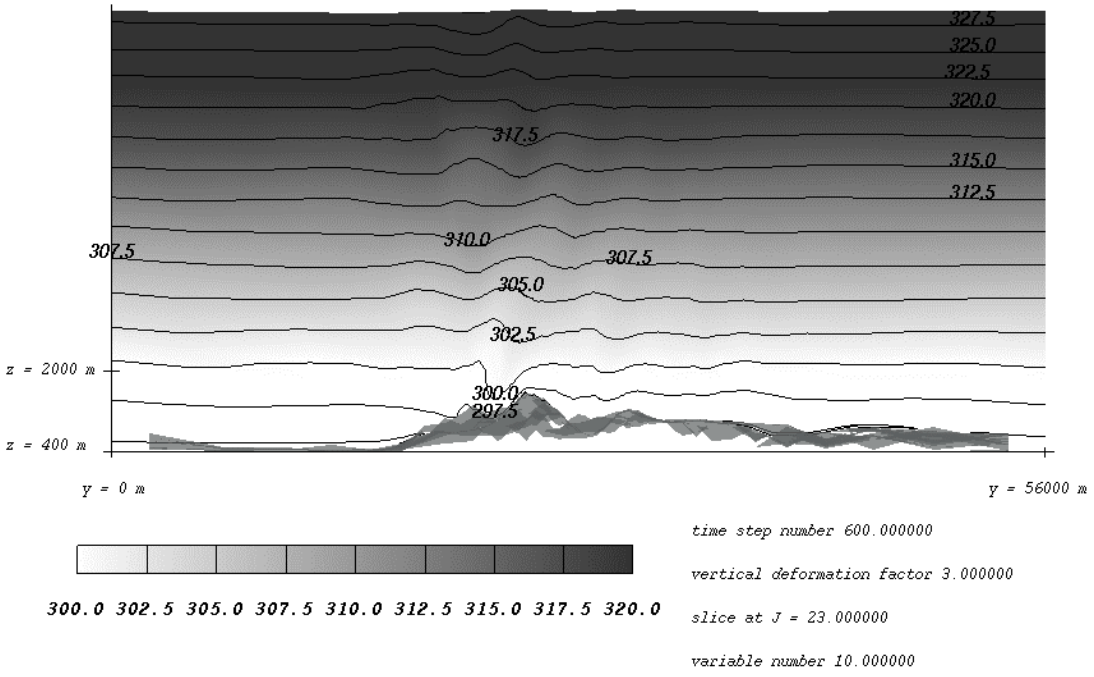

Figure 6.37. Same as Figure 6.36 for the potential temperature. Steps between isolines: 2.5 K.

In the St-Imier valley, a cavity type flow is obtained for both the neutrally and stably stratified cases, with a major wind speed reduction in the valley. As can be seen from Figure 6.38 for the stably stratified case, the model generates some return flows close to the ground on the slope downwind of Mt-Crosin and on the Plateau de Diesse. Figure 6.38 also clearly shows that with a very stable atmosphere, the maximum wind speed does not appear on the highest elevations but downwind of the mountain crest. The maximum wind speed of more than 8 m/s obtained in this case at 4 m above ground level is significantly higher than the geostrophic wind speed.

With the simulations presented in this chapter, we could see that the flow pattern and wind speed distribution at the ground changes significantly when changing the stability conditions. Since on average for Swiss latitudes the free flow stratification of the atmosphere is stable (-6.5 K/km for the US standard atmosphere, 1966) and far from neutral, it is important to have a numerical model that is able to take these effects into account when simulating atmospheric flows over complex terrain. After having shown qualitatively[17] the model's ability to reproduce interesting phenomena such as flow channelling, mountain waves, foehn effects, rotor formation or downslope winds, we will proceed in the following chapters with some more

[17] Some of these effects were validated in a quantitative way in the appendices (C and D essentially).

simulations and sensitivity tests to quantify the effects that changes in the atmospheric conditions will have on the site-to-site relationships needed for the application of the transposition methodology.

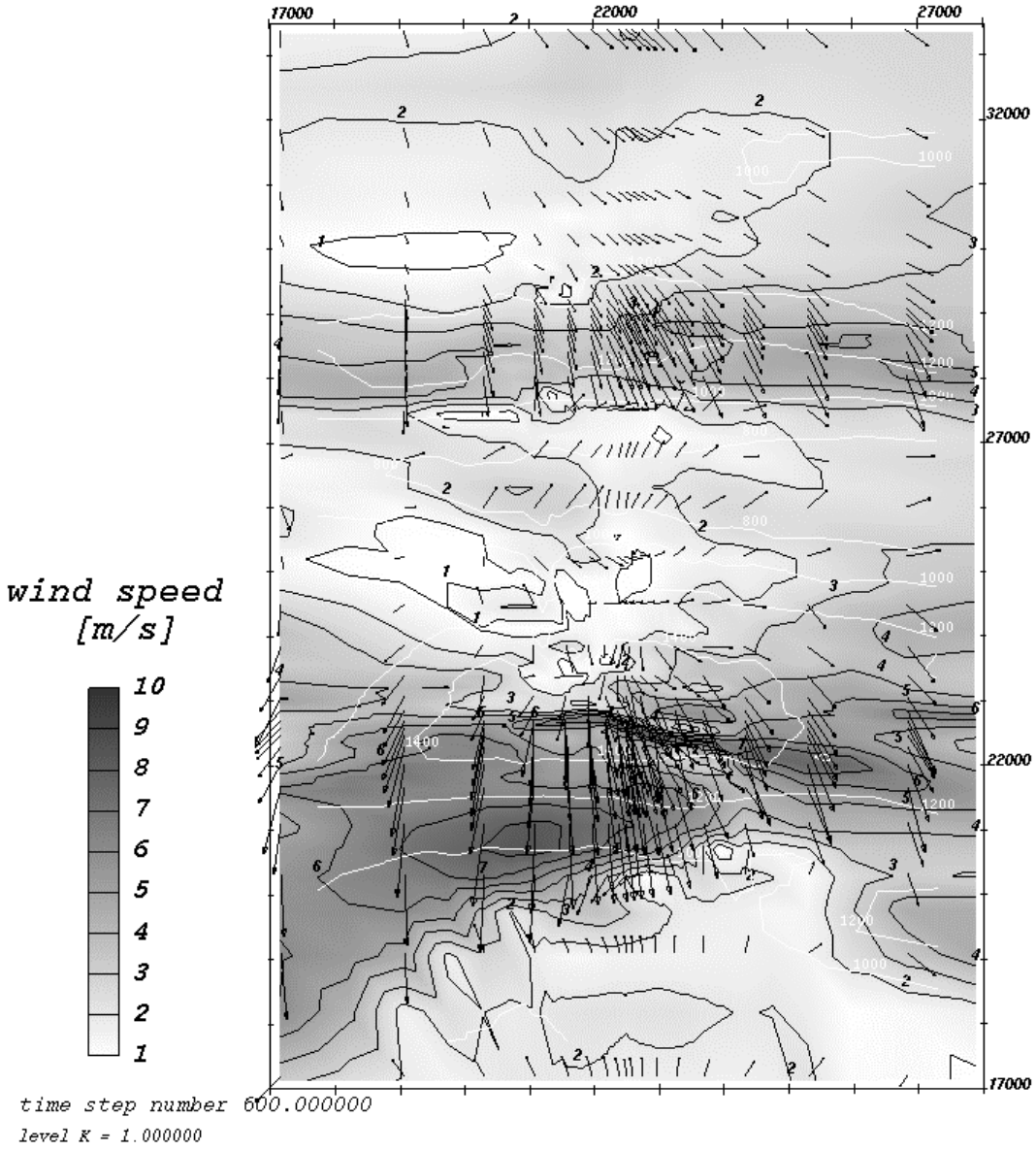

Figure 6.38. Same as Figure 6.6 for a geostrophic wind of 5 m/s blowing from the 330° sector. The initial atmospheric stratification is given by a real temperature gradient of –6.5 K/km. Steps between wind speed isolines: 1 m/s.

7 Wind data transposition using the numerical simulation results

The numerical model has been successfully validated for various flow conditions (see Appendix A to D) essentially over flat and hilly terrain. We also showed in Section 4.3 that the transposition methodology performed with proportionality relationships obtained from the analysis of wind data was able to give a good prediction of the wind speed distribution at the site of Mt-Crosin. The object of the present chapter is to perform a similar transposition with sector wind speed ratios obtained from numerical simulations. For this task, we will restrict ourselves to the prediction sites of Mt-Crosin and not consider the sites of Chaux-de-Fonds and Neuchâtel. The reason for this choice is the proximity of the latter locations to the model boundaries, and the coarse horizontal resolution (~1-4km) of the simulation domain around these sites. For this reason, the wind speed calculated at the closest mesh points to the Chaux-de-Fonds and Neuchâtel locations cannot be representative of the very local wind conditions.

To see how the numerical model performs on the very complex terrain conditions encountered in the area of Chasseral and Mt-Crosin, we will compare some of the model results with observations for a real event (Section 7.1) and for 'average wind conditions' (Section 7.2). The wind speed ratios obtained by the numerical simulation will then be used to calculate the Mt-Crosin wind distributions from the Chasseral data. These will be compared with those measured in Section 7.3. Since monthly energy production and turbine availability data for the year 97 were provided by Juvent S.A, a transposition was also done at hub height for this period, from which the wind power potential of the site was inferred and compared to the measured values (Section 7.4)[18]. Finally a wind power potential map for the whole Mt-Crosin area was elaborated from the long term data recorded at Chasseral.

7.1 Simulation of a real event

We simulated the persistent 'bise' event of the 12th of June 1994, using the temperature and wind profiles (Figure 7.1) from the Payerne soundings for this date

[18] Unfortunately, no wind speed data for the same period are available on the Mt-Crosin site. Consequently, we will not be able to simultaneously compare the transposed wind speed distributions and the energy production.

(0h UTC) as initial conditions. For the boundary conditions to be given at the domain inlet, we kept the temperature profile constant with time while the wind speed profiles were linearly interpolated with time from the sounding of the 12th and 13th of June 1994 (0h UTC). For the ground roughness we used a variable distribution as given in Figure 6.5.

The simulation was performed for 6 hours, keeping the ground heat flux zero during the run. Considering the fact that we set a uniform solution as initial guess and since we apply the sounding profiles uniformly at both the inlet north and east face of the simulation domain, we do not expect the model to be able to reproduce the time evolution with good accuracy. Moreover, for this particular wind direction, it should be kept in mind that the Payerne sounding is more representative of the conditions prevailing at the model outlet than at the inlet boundary. The profile might actually be influenced by the presence of the Jura topography.

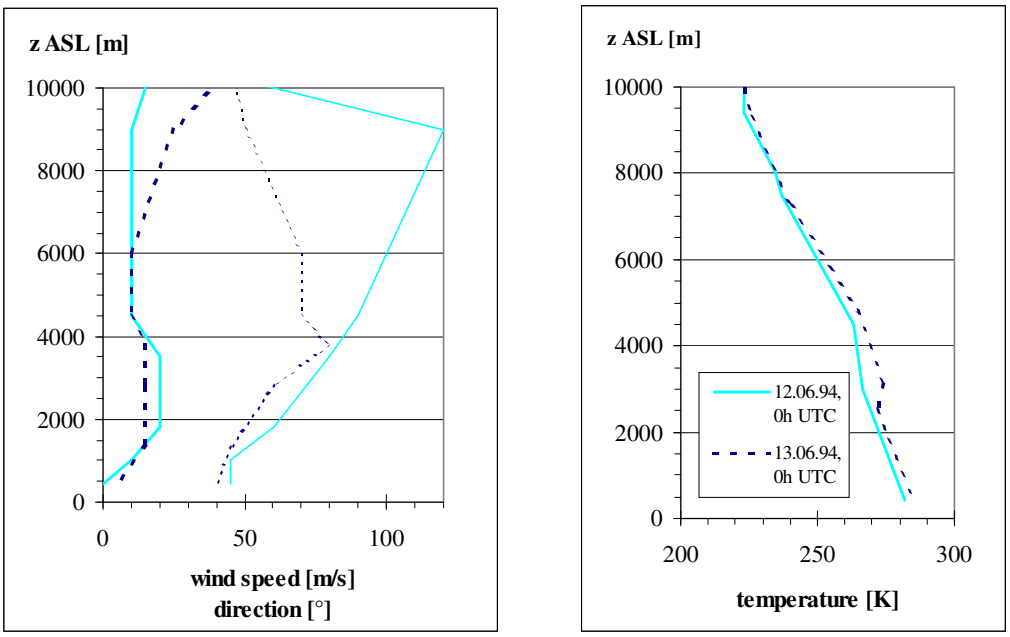

a) b)

Figure 7.1. Initial and boundary conditions used to simulate the real situation of the 12th of June 1994. a) Wind speed (thick lines), wind direction (thin lines) and b) real temperature profiles from the Payerne soundings of the 12th (continuous line) and 13th of June 1994, 0h UTC (dashed line).

Despite these rough approximations in the model initialisation, we can still observe from Figure 7.2 that the model predictions are in qualitative agreement with the observations. The Chasseral wind speed is well reproduced, while the wind speeds at Côte Nord and Côte Sud are underpredicted by ~27% and 21% respectively,

implying an underprediction of the wind speed ratio. As expected from the observations, the simulation produces a higher wind speed at the site of Côte Sud than at the site of Côte Nord. Although the *absolute* wind direction is not so well reproduced, the *difference* between the Chasseral and Côte Nord wind direction corresponds well to that observed.

As will be seen later on (Section 8.3), the fact that we reproduce the Chasseral wind speed pretty well but underpredict the wind speed at Mt-Crosin might be due to slightly excessive roughness values for the forested areas.

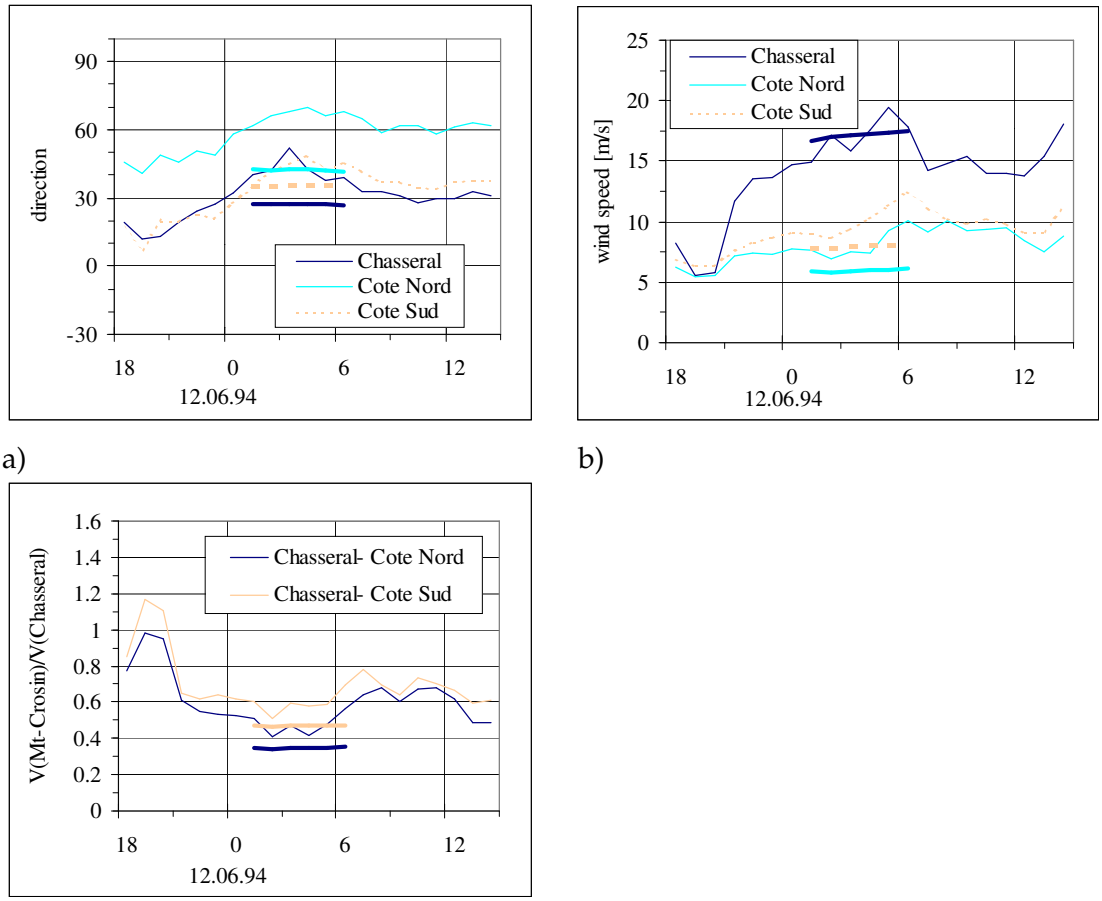

Figure 7.2. Comparison of the observations (thin lines) and simulation results (thick lines) for the persistent 'bise' situation of the 12th of June 1994. a) Wind direction, b) wind speed and c) Mt-Crosin to Chasseral wind speed ratio.

7.2 Transposition relationships obtained from numerical simulations for 'average wind conditions'

The sector wind speed ratios needed for the one-parameter wind data transposition will be calculated from a set of simulations performed for stably stratified atmospheric conditions, also using the variable roughness distribution of Figure 6.5. The simulation conditions were defined following a simple classification of the situations that was proposed by Fallot & Hertig (1991). From one year of wind data at Chasseral and on the Ajoie Plateau, he sorted the situations into two groups (see Appendix K). The first one is characterised by situations that are essentially advective (57.4% of the cases), showing persistent winds on the Ajoie Plateau, and the second one is thermally dominated (42% of the cases), with variable (breeze) winds in Ajoie. The advective situations correspond to the stronger wind conditions. From the point of view of wind power potential they represent therefore the most interesting cases. As a first approximation, the variable wind situations will be discarded and we will assume that only the advective situations are important for the transposition we are interested in.

To define the set of simulations to be performed, Fallot (personal communication) proposed a simplified classification, using only two types of temperature profiles. The first type of temperature profile with a constant gradient of –7.0 K/km should be representative of the south-west to north advective situations while the second type, showing a more stable stratification below 1400m should be representative for the 'bise' situations (north to east advective situations). Following this suggestion, we finally simulated the set of stably stratified situations presented in Table 7.1, concentrating on the most frequently occurring wind directions. The wind speed profiles for these simulations were initialised with the Zilitinkevich formulation (Appendix B) setting the model parameters so as to reproduce as close as possible the advectively dominated situations of Table K.1.

The wind speed ratios obtained from this simple classification for the sites of Côte Nord and Côte Sud are shown in Figure 8.7 (circles), where they can be compared to the mean observed values (continuous line). The standard deviation of the observed wind speed ratio around its mean value has also been plotted (dashed line).
We can see that except for the 190° and 240° wind directions at Côte Nord and the 30°, 190° and 240° wind directions at Côte Sud, the simulated ratios compare quite well with those observed. For the north and south winds we do not have sufficient data to validate the results. Generally, when the simulated wind speed ratio departs

significantly from the mean measured value, it underestimates the observed value. Again, this might indicate that we used too large roughness lengths for the area (see Section 8.3).

Table 7.1. Set of parameters defining the stable situations representative of the average advectively dominated situations. Shaded cells correspond to model input parameters.

geostrophic wind direction [°]	Vertical temperature gradient [K/km]	Friction velocity [m/s]	Resulting Chasseral wind speed [m/s]	Resulting Chasseral wind direction [°]
30	-4.5 for z<1400m ASL -7.0 above	0.12	4.5	15.5
60	-4.5 for z<1400m ASL -7.0 above	0.23	7.8	38
70	-4.5 for z<1400m ASL -7.0 above	0.3	8.5	57
80	-4.5 for z<1400m ASL -7.0 above	0.3	8.6	75
120	-4.5 for z<1400m ASL -7.0 above	0.2	7.2	129
210	-7.0 for all z	0.53	14.8	185
240	-7.0 for all z	0.53	13.6	220
250	-7.0 for all z	0.42	11.1	241
260	-7.0 for all z	0.4	10.7	263
270	-7.0 for all z	0.4	10.9	282
300	-7.0 for all z	0.3	11.5	314
330	-7.0 for all z	0.3	12.5	329
360	-4.5 for z<1400m ASL -7.0 above	0.1	4.5	361

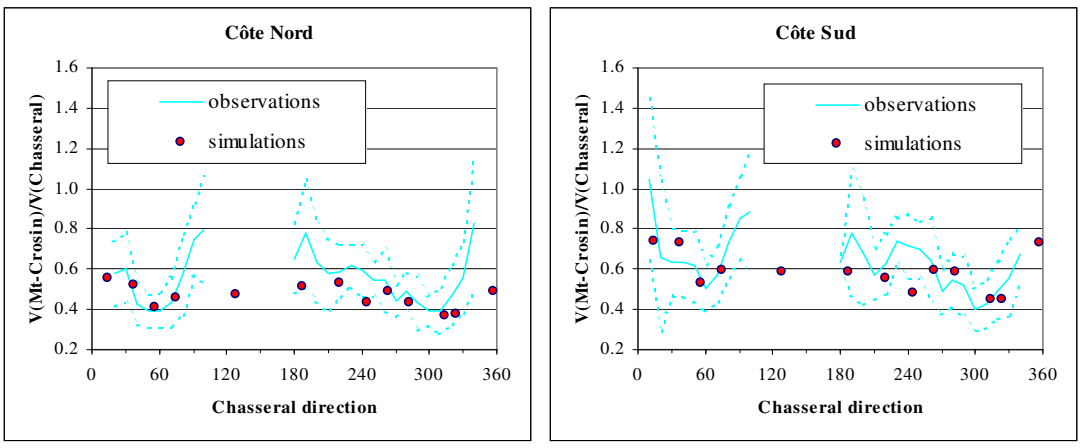

Figure 7.3. Wind speed ratios at Côte Nord and Côte Sud obtained from the simulation of the set of stable situations (circles) as defined by the Fallot classification. The simulations were run with a variable ground roughness as in Figure 6.5. The mean observed values (continuous line) are also given together with the standard deviation around the average (dashed lines).

For the set of simulations presented above, we also compared the simulated direction change between the Chasseral and Mt-Crosin as a function of the Chasseral wind direction with that observed. Figure 7.4 shows that apart from the north-east wind directions (20°to 40°), the general variation of the direction change with the Chasseral wind direction is fairly well reproduced, though there seems to be a shift of some 15° between the observed and simulated values.

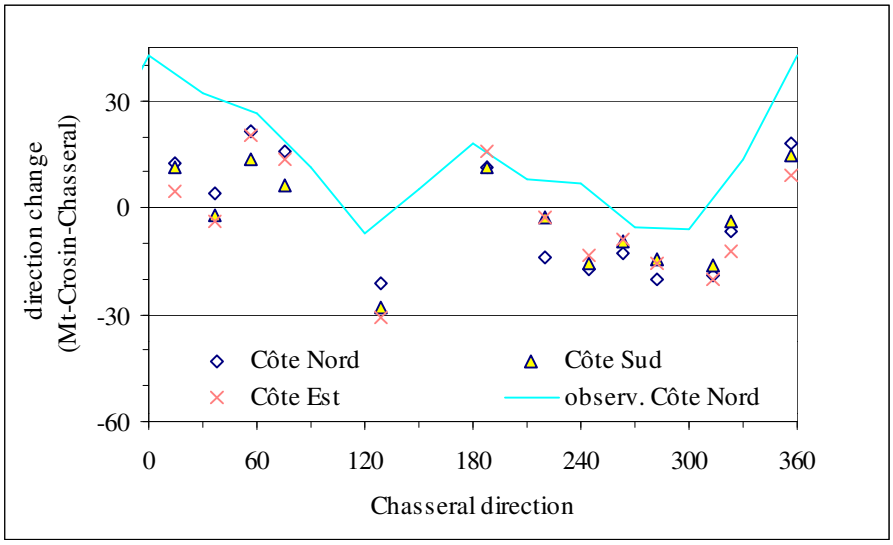

Figure 7.4. Simulated (symbols) and mean observed (line) direction change between the Chasseral and Mt-Crosin sites.

7.3 Wind data transposition and comparison with the observed distributions

The wind speed ratios obtained from the numerical simulations of the stable situations representing the advective situations of the Fallot classification (Figure 7.3) were linearly interpolated as a function of the Chasseral wind direction, in steps of 10°. These were then used to transpose the Chasseral wind data to the Mt-Crosin sites producing the wind speed distributions shown in Figure 7.5 to Figure 7.7. The transposed distributions compare quite well with those observed, though we tend in this case to underpredict the wind speed. This could already be expected from the comparison of the simulated and observed wind speed ratios (Figure 7.3). Using the Mt-Crosin transposed distributions, we end up with a prediction of the mean wind speed and yearly energy output on the Mt-Crosin site that are underestimated by 7% to 18% and 8% to 36%, respectively (Table 7.2).

The results for the wind data transposition obtained from the simulations with variable roughness with the simplified Fallot classification are remarkably good. The accuracy of the prediction is typically of the same order of what can be achieved when performing one year of measurements on the prediction site itself.

Table 7.2. Mean wind speed and yearly energy output obtained with proportionality factors obtained from the numerical simulations, considering the set of stably stratified situations defined in Table 7.1. Simulations performed with a variable ground roughness.

Station name	Average wind speed [m/s]			Yearly energy production [MWh/year]		
	Measured	Transposed	Relative error	Measured	Transposed	Relative error
Côte Nord	5.2	4.3	-18%	806	517	-36%
Côte Sud	5.3	4.4	-16%	800	536	-33%
Côte Est	5.6	5.2	-7%	983	851	-8%

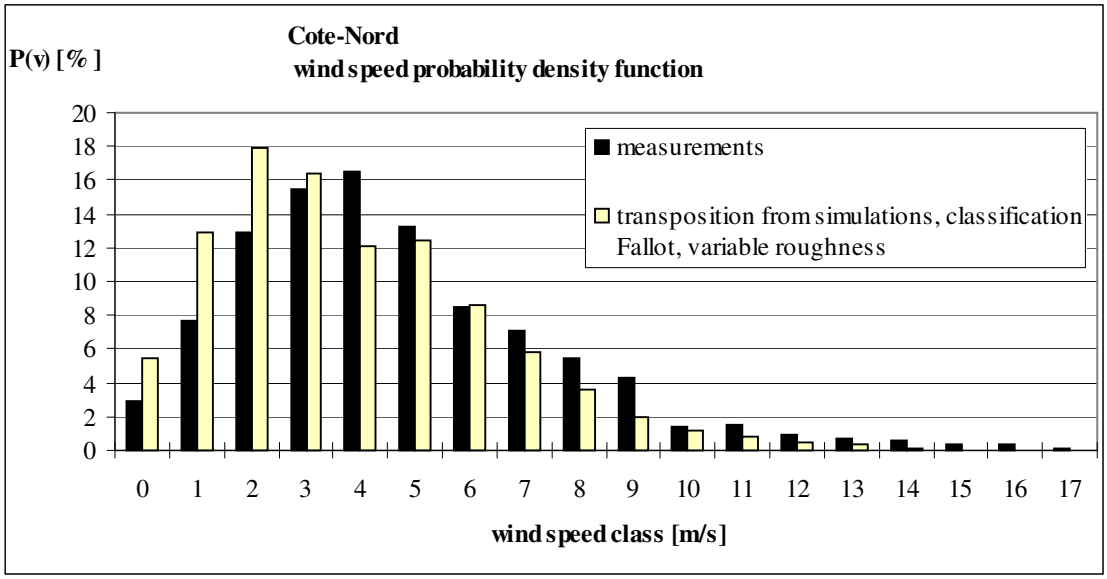

Figure 7.5. Comparison of the observed (black) and transposed (light grey) wind speed distributions at Côte Nord, obtained from the set of simulation presented in Table 7.1. The simulations were run with a variable roughness length as in Figure 6.5.

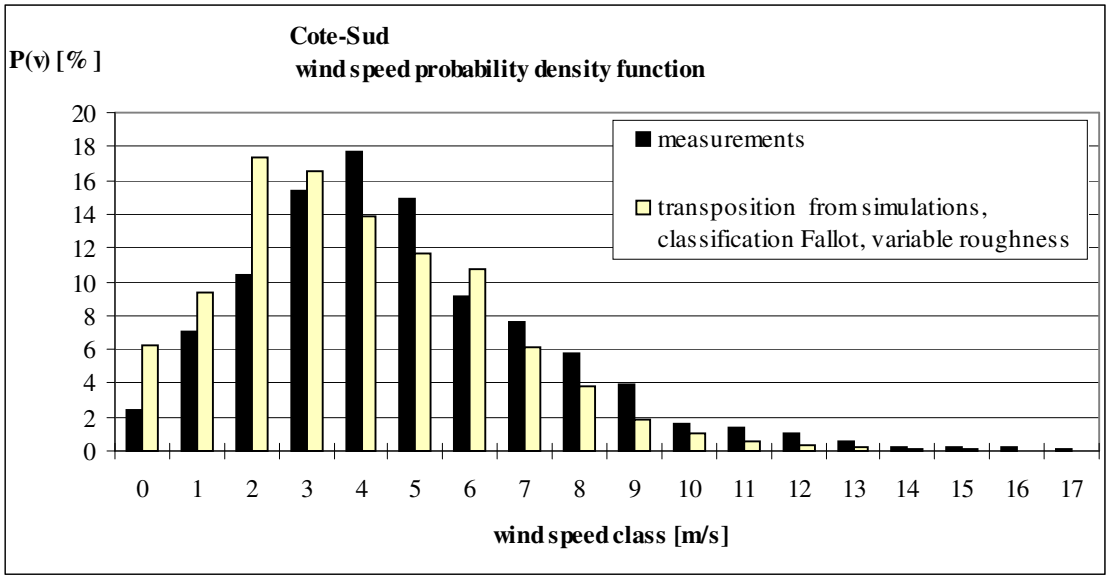

Figure 7.6. Same as Figure 7.5 for the site of Côte Sud.

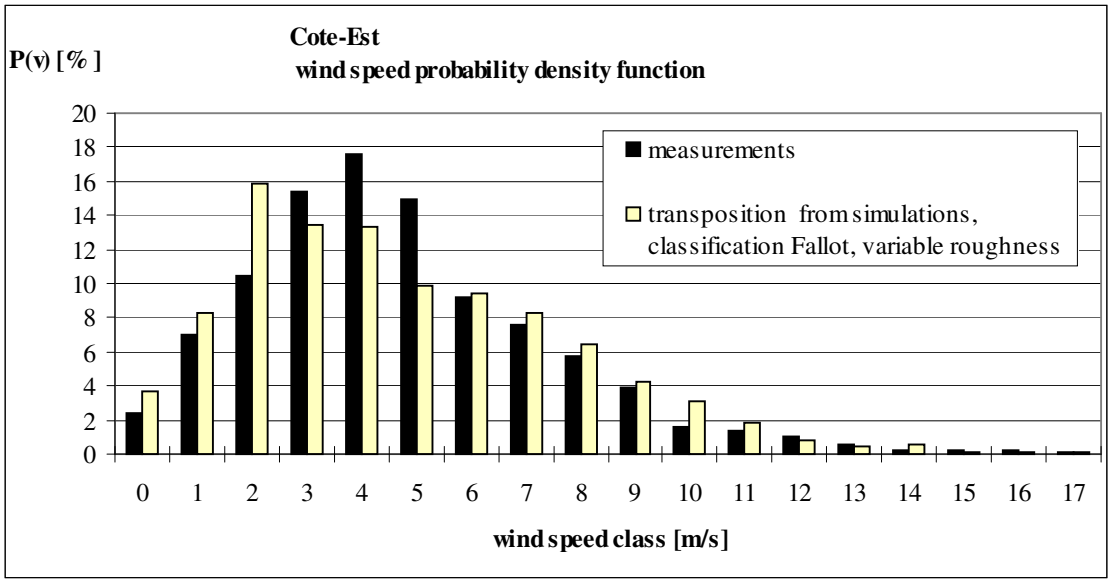

Figure 7.7. Same as Figure 7.5 for the site of Côte Est.

The fact that we obtain a better predictions for the site of Côte Est than for the sites of Côte Sud and Côte Nord is certainly related to the fact that the transpositions are done for different periods with different wind roses at Chasseral (see Section 3.2.2). Comparing the Chasseral wind roses for the various concurrent datasets, we could observe that the 240° to 270° wind directions occur more often in the wind rose concurrent with data at Côte Sud and Côte Nord, than in that concurrent with Côte Est. Since for these wind directions (particularly for the 240°) we clearly underpredict

the wind speed ratio, we tend to underestimate the wind speed at the transposition site in these cases. We also observed that the Chasseral wind rose concurrent with data at Côte Est seems to be more representative of the long term for the south-west to north-west wind directions. We can therefore hope that the relative error for a long-term transposition might be of the same order of magnitude as that obtained for Côte Sud than for the other sites.

7.4 Transposition at the hub height level for the year 97 and comparison with the actual production data

The wind speed ratios shown in Figure 7.3 were calculated for the measurement heights at Mt-Crosin. To transpose the Chasseral wind data to the wind turbine hub height (45m) we used the wind speed ratios calculated for the third level of cells (29m above ground at Mt-Crosin) and the vertical gradient of the wind speed between the third and fourth level of cells (29m and 52m). The modified wind speed ratio is obtained from:

eq. 7.1 $$a'(\theta) = a(\theta) + \frac{\partial u}{\partial z} \cdot \frac{(h_t - 30)}{v_{CHL}}$$

which results from the fact that one can write the wind speed at the wind turbine hub height h_t as

eq. 7.2 $$v_{MTC}(h_t) = v_{MTC}(30m) + \frac{\partial u}{\partial z} \cdot (h_t - 30)$$

and from the proportionality assumption between the Mt-Crosin and Chasseral wind speed implying that $v_{MTC}(30m) = a(\theta) \cdot v_{CHL}$ and $v_{MTC}(h_t) = a'(\theta) \cdot v_{CHL}$.
The vertical gradient of the wind speed at Mt-Crosin, which was obtained from the simulations, is presented in Figure 7.8, while the corrected wind speed ratio for the height of 45m at Mt-Crosin is plotted in Figure 7.9.

Using a simple power law[19] to calculate the wind speed at hub height from the level of 30 m with an exponent value of $\alpha = 0.25$ would imply a factor of 1.11 between the 30m and 45m wind speeds. The value of this factor, when calculated from the numerical simulation results, varies from sector to sector between 1.1 and 1.22 for the

[19] The power law $v(z_1)/v(z_2) = (z_1/z_2)^{\alpha}$ is often used to obtain the wind speed at the level z_1 from the known wind speed at the level z_2, with an exponent α depending on the turbulence conditions on the terrain (see e.g. Davenport, 1963). Typically for areas surrounded by woods, one would expect a value of about 0.25 for α.

site of Côte Nord (mean value 1.16), between 1.11 and 1.31 for Côte Sud (mean value 1.19) and between 1.13 and 1.27 for Côte Est (mean value 1.19). In other words, calculating the wind speed values at 45 m with the numerical model results leads therefore to higher wind speeds at hub heights than the use of the simple power law.

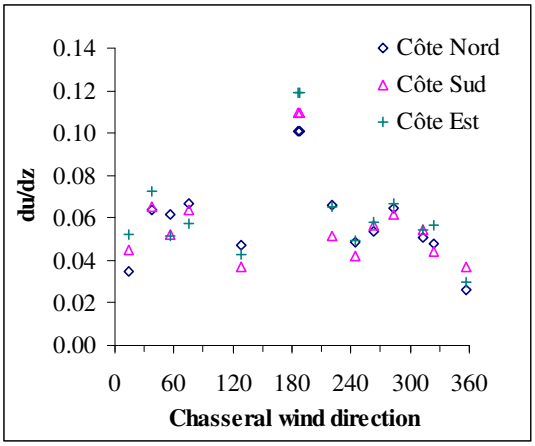

Figure 7.8. Wind shear at the three sites of Côte Nord, Côte Sud and Côte Est calculated by the model between the third and fourth levels of cells (29 and 52m above ground level).

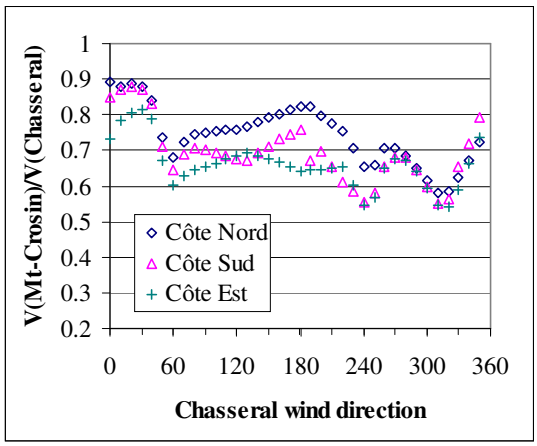

Figure 7.9. Mt-Crosin to Chasseral wind speed ratios to transpose the data at 45 m above ground at Mt-Crosin.

Using the corrected wind speed ratios calculated for the model grid nodes closest to the actual wind turbine locations, we transposed the Chasseral monthly wind speed data for the year 97 at hub height. The monthly power output for these three locations was then inferred using the power characteristics of the Vestas-V44 machine and the monthly-predicted wind speed distributions. For each generator, we took into account the monthly availability to reduce the estimated power output accordingly. For the efficiency factor associated with losses due to higher turbulence, we used a value of 0.9. The resulting energy output predictions are plotted in Figure 7.10 to Figure 7.12 together with the actual production data. Table 7.3 to Table 7.5 gives the detailed figures. For the complete year, the predictions are compared to the production data in Table 7.6.

As could be expected from the results of the wind data transposition to the measuring heights (Table 7.2) that were performed with the same set of simulations, we tend to systematically underpredict the actual values. Month by month the prediction errors can be quite significant (up to –57%), and this is related to the fact

that one month is a too short period to be represented by average situations. Over the year, however, the prediction errors reduce between –22% and –24%.

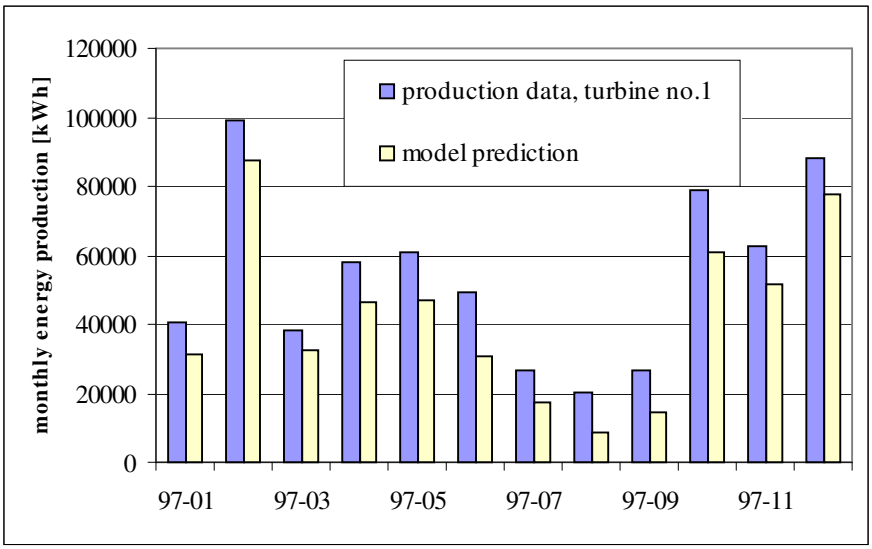

Figure 7.10. Comparison of the predicted (light grey) and measured (dark grey) monthly production data for the wind turbine no.1 for the year 1997.

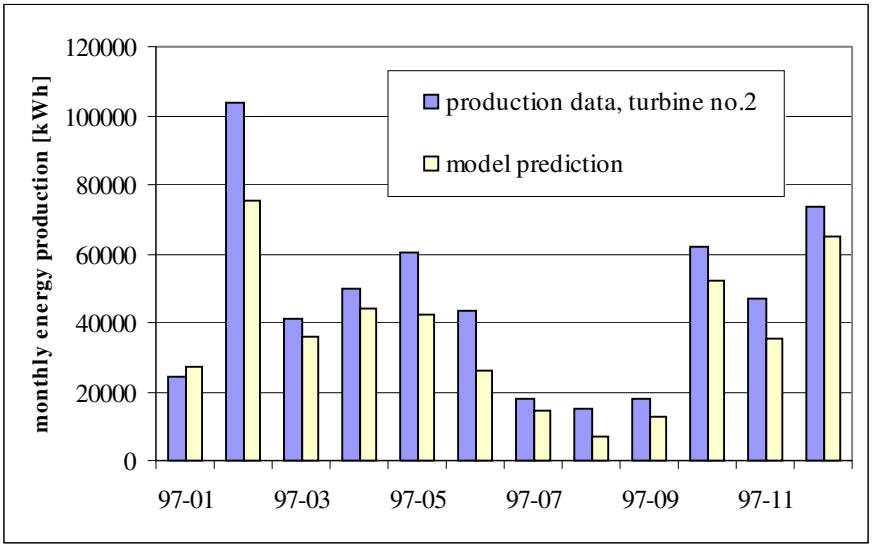

Figure 7.11. Comparison of the predicted (light grey) and measured (dark grey) monthly production data for the wind turbine no.2 for the year 1997.

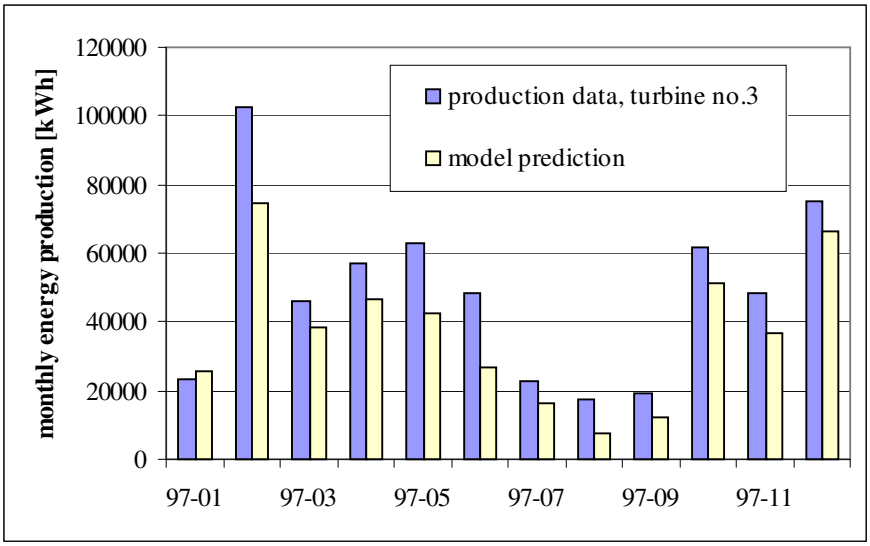

Figure 7.12. Comparison of the predicted (light grey) and measured (dark grey) monthly production data for the wind turbine no.3 for the year 1997.

The maximum relative error occurs for all the three stations during the less windy month (August). The month of July, also showing a relatively low energy output is not as badly predicted. An explanation of these different behaviours can be found when plotting the sector distribution of the wind speeds higher than 12 m/s (Figure 7.13) for these two months. It appears that the 220° to 270° wind directions are much more frequent in August than in July, and we could see from Figure 8.7 that the simulated wind speed ratios for these directions clearly underestimate the observed values.

Table 7.3. Monthly production data for the wind turbine no.1 and comparison with the monthly energy output prediction.

month	N hours	N hours with data at Chasseral	Availability [%]	Energy production [kWh]	Energy prediction WT1 [kWh]	$\Delta E / E$ [%]
97-01	744	676	99.9	40449	31297	-23%
97-02	672	634	90.8	99267	87655	-12%
97-03	744	700	81.6	38518	32305	-16%
97-04	720	674	93.3	58167	46225	-21%
97-05	744	684	90.7	60824	47096	-23%
97-06	720	675	86.7	49447	30673	-38%
97-07	744	677	99.9	26746	17437	-35%
97-08	744	649	99.9	20212	8600	-57%
97-09	720	609	100.0	26844	14673	-45%
97-10	744	665	99.6	78686	60650	-23%
97-11	720	643	99.9	62662	51333	-18%
97-12	744	734	96.9	88023	77446	-12%

Table 7.4. Monthly production data for the wind turbine no.2 and comparison with the monthly energy output prediction.

month	N hours	N hours with data at Chasseral	Availability [%]	Energy production [kWh]	Energy prediction WT2 [kWh]	$\Delta E / E$ [%]
97-01	744	676	99.3	24411	27069	11%
97-02	672	634	96.3	103635	75150	-27%
97-03	744	700	97.2	41449	35749	-14%
97-04	720	674	93.1	49890	43771	-12%
97-05	744	684	99.7	60420	42241	-30%
97-06	720	675	99.7	43521	26357	-39%
97-07	744	677	93.7	17867	14747	-17%
97-08	744	649	95.6	15333	6887	-55%
97-09	720	609	97.5	18031	12815	-29%
97-10	744	665	98.3	62231	51901	-17%
97-11	720	643	97.1	46815	35233	-25%
97-12	744	734	98.8	73913	64794	-12%

Table 7.5. Monthly production data for the wind turbine no.3 and comparison with the monthly energy output prediction.

month	N hours	N hours with data at Chasseral	Availability [%]	Energy production [kWh]	Energy prediction WT3 [kWh]	$\Delta E / E$ [%]
97-01	744	676	93.8	23512	25619	9%
97-02	672	634	94.3	102490	74589	-27%
97-03	744	700	98.8	46106	38548	-16%
97-04	720	674	99.0	56986	46625	-18%
97-05	744	684	99.1	62923	42412	-33%
97-06	720	675	99.6	48062	26914	-44%
97-07	744	677	100.0	22513	16537	-27%
97-08	744	649	99.9	17593	7718	-56%
97-09	720	609	93.2	19081	12365	-35%
97-10	744	665	97.3	61929	51026	-18%
97-11	720	643	99.9	48472	36500	-25%
97-12	744	734	98.5	74950	66640	-11%

Table 7.6. Measured and predicted energy output for the year 1997 for the three turbines on the Mt-Crosin site.

	Energy production year 97 [MWh]	Energy prediction by the model [MWh]	$\Delta E / E$ [%]
WT1	650	505	-22
WT2	558	437	-22
WT3	585	445	-24

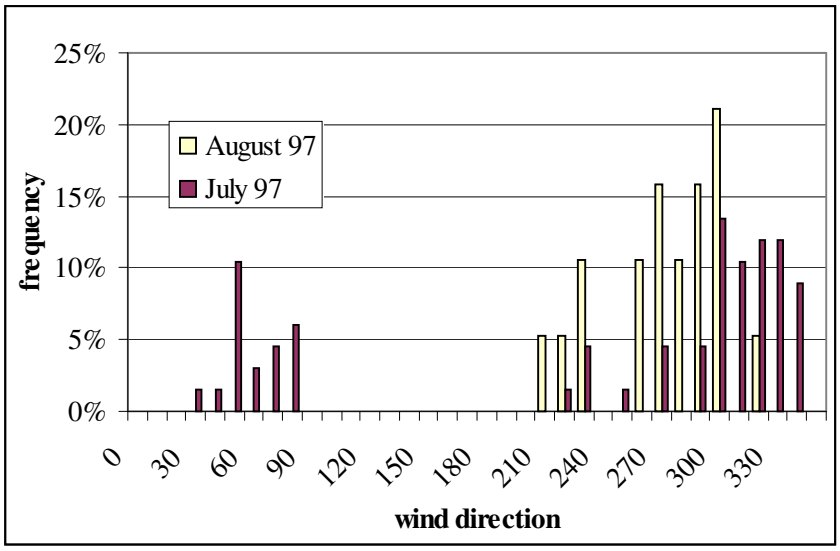

Figure 7.13. Sector frequency distribution of the Chasseral wind speeds higher than 12 m/s for the months of July and August 1997.

From the above results obtained with the variable roughness distribution it appears that the transposition methodology based on the numerical simulation results is already a powerful tool to estimate the wind power potential of sites located on high altitude sites along the Jura chain. Also, the fact that the relative prediction error is fairly constant over the various wind turbine locations shows that the transposition has been able to distinguish between the most and less favourable sites. In this light, the wind data transposition appears to be useful also in the perspective of wind turbine micrositing.
For the sites considered, the accuracy of the predicted wind power potential is of the same order of magnitude as that which can be achieved when performing one year of measurements on site.

7.5 Long-term prediction and wind power potential map for the Mt-Crosin area

After having validated the numerical model, tested the validity of the assumptions and controlled the applicability of the wind data transposition for short period data sets, we finally come to the application for which all the developments presented in this contribution were designed for. We will perform a wind data transposition to predict the long-term wind speed distribution at the Mt-Crosin site, starting from the long-term wind statistics at Chasseral.

Applying the transposition methodology on the 16 years of data collected at Chasseral and using the wind speed ratios obtained from the numerical simulation (Figure 7.9), we calculated wind speed distributions at 45m above ground over the whole simulation domain as shown in Figure 7.14 for the site of Côte Nord.

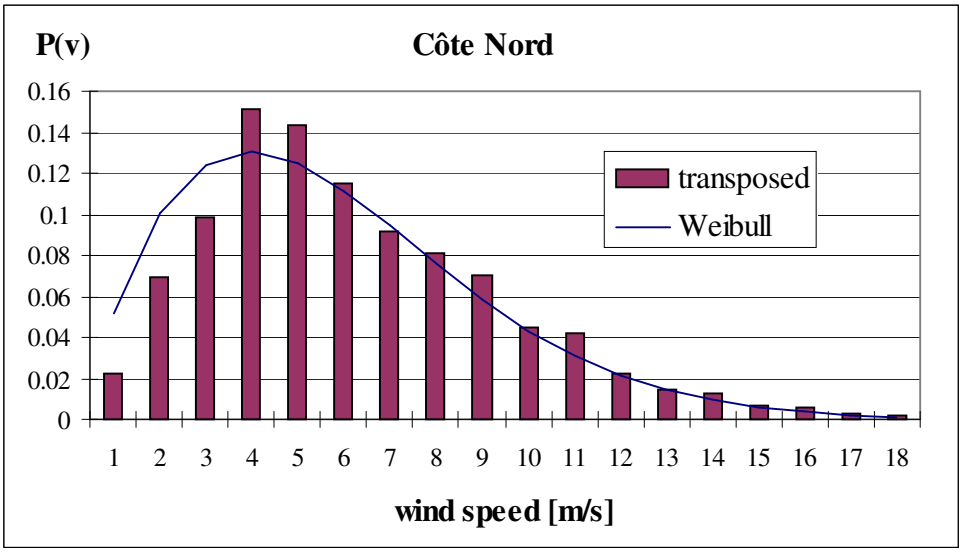

Figure 7.14. Long term transposed wind distribution for the site of Côte Nord at 45 m above ground level. The best fitting Weibull distribution is also plotted.

The predicted long-term mean wind speeds at 45m above ground for the three measurement locations are summarised in Table 7.7. The *A* and *k* parameters of the Weibull distributions best representing the transposed wind distributions are also given. The shape parameter *k* of the transposed Weibull distribution is more or less constant over Mt-Crosin (less than 2% variation between the sites), whereas the *A* parameter varies by some 10%. Among the three sites, Côte Nord with 5.7 m/s at 45 m above ground exhibits the highest wind speed and shows the most favourable wind power potential. The site of Côte Est would be the least productive site with 5.2 m/s.

The corresponding yearly energy output for a Vestas-V44 wind turbine has been calculated, assuming a 3% loss due to machine unavailability and 10% loss due to increased turbulence conditions. The resulting spatial distribution of the so-obtained yearly energy output is shown in Figure 7.15 for the Mt-Crosin area. From this map the most favourable location on this site appears to be located around the co-ordinates (22.5 km, 29.3 km) with a potential of 645 MWh/year (11% higher than the evaluated potential at the location of the wind trubine No.1). Such a map can be used to decide where to locate the wind generators, keeping in mind that local obstacles

such as isolated groups of trees have not been considered when performing the evaluation.

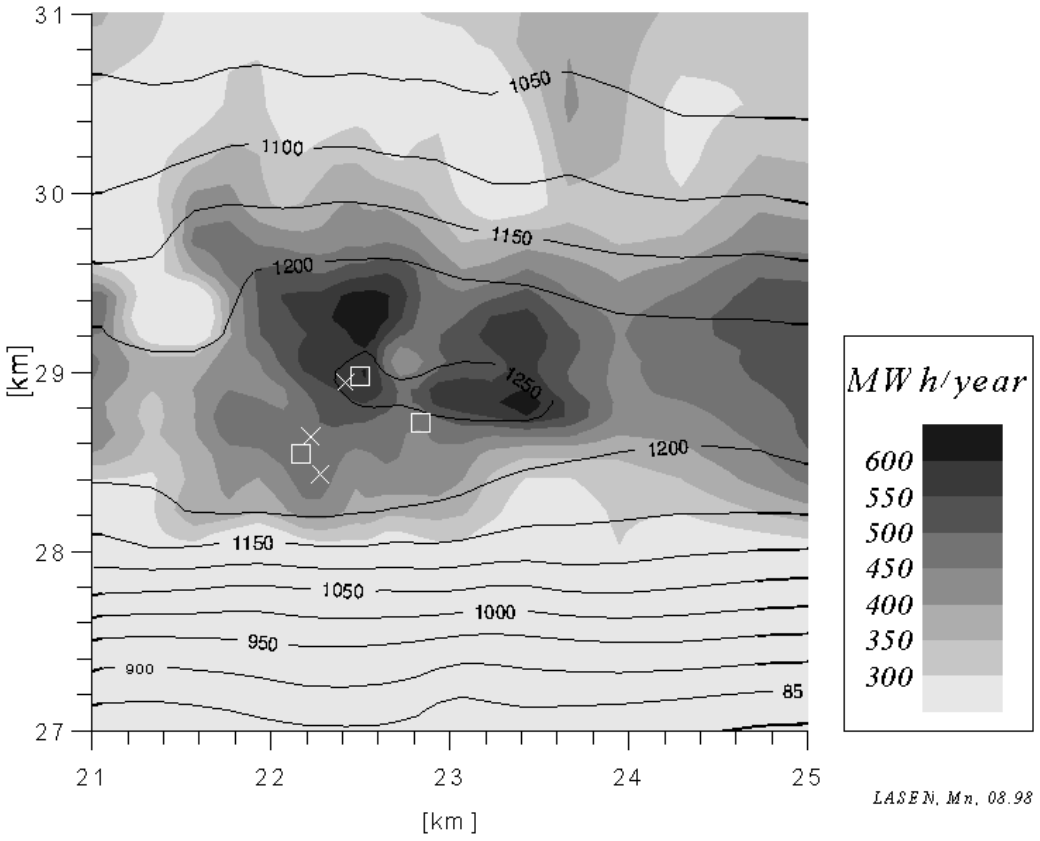

Figure 7.15. Long-term estimated wind power potential map for the Mt-Crosin site (shaded) calculated from the 16 years of data recorded at the Chasseral reference station. The topography is given with the black isolines. Crosses show the locations of the installed wind turbines, while squares represent the measurement masts. The x and y coordinates refer to the origin of the simulation domain presented in Figure 6.3.

Between the location of Côte Est and Côte Nord, we have a factor 1.33 between the predicted yearly energy output for a distance between the sites which is only 430m. This difference in the power potential of the two locations is impressive. If we assume that the relative errors we had for the short term prediction at measurement height (Table 7.2) are representative of the long-term errors, then this factor of 1.33 is even a conservative value of the real factor, since the underprediction was stronger for the site of Côte Nord than for Côte Sud.

Considering that the transposition using the numerically simulated wind speed ratios tends to underpredict the actual wind distribution, the long-term predicted

mean wind speed and yearly energy output given in Table 7.7 are expected to be conservative predictions for the actual Mt-Crosin conditions.

Table 7.7. Predicted long-term average wind speed and parameters of the Weibull distribution at 45 m above ground level for the three sites of Côte Nord, Côte Sud and Côte Est. The yearly energy output for a Vestas–V44 power characteristics is also given.

	Average wind speed [m/s]	Weibull parameters		Predicted energy output[20] [MWh/year]
		A [m/s]	k	
Côte Nord	5.7	5.9	1.68	596
Côte Sud	5.3	5.5	1.67	493
Côte Est	5.2	5.3	1.65	470
WT1	5.4	5.4	1.70	580
WT2	5.1	5.1	1.75	483
WT3	5.2	5.2	1.76	493

[20] Evaluation using efficiencies of $\eta_T = 0.9$, $\eta_{array} = 1.0$, $\eta_{avail} = 0.97$.

8 Sensitivity tests and limits of the method

As could already be concluded from the results showing the time evolution of the wind speed ratios presented in Section 6.2, these exhibit a strong sensitivity to the atmospheric conditions. In the present chapter we will further investigate the effect of a change in the atmospheric conditions on the resulting wind speed ratios, testing their sensitivity to changes of:

- geostrophic wind speed,
- thermal stratification,
- ground cooling,
- roughness.

Wind data transpositions will also be attempted with simulation results calculated for various conditions that are not necessarily appropriate to represent the local climatology of the Chasseral area. This will be done in order to assess the error on the transposition results that can be induced by a poor knowledge of the local terrain or wind conditions to be used as initial or boundary conditions.

8.1 Stability conditions and geostrophic wind speed

For the 240° and 330° wind directions, some simulations were performed, for various vertical temperature gradients and various geostrophic wind speed values. The wind speed ratios obtained from these are plotted for the site of Côte Sud and for the 240° geostrophic wind direction versus the resulting Chasseral wind speed in Figure 8.1.a and versus the Froude number of the simulation in Figure 8.1.b. The same results for the 330° geostrophic wind direction are shown in Figure 8.2. The various symbols used in the figures refer to the vertical real temperature gradient of the simulation. As can be observed from Figure 8.1.a and Figure 8.2.a, the wind speed ratio for the same wind speed at Chasseral can vary significantly when the stratification is changed, and the variation is not a monotonic function of the vertical temperature gradient . This can be seen e.g. for the 240° geostrophic wind direction, where, for a wind speed of 12 m/s at Chasseral, the more stable case (-6.5 K/km) and the less stable case (-9.0 K/km) give higher wind speed ratios than the intermediate stability defined by –8.0 K/km. Even more surprising, two situations with the same stratification conditions and same Chasseral wind speed can result in wind speed ratios that can differ by a factor as large as 1.6. See e.g. the 330° geostrophic wind direction (Figure 8.2.a) showing wind speed ratios of 0.4 and 0.65 that are obtained

for a vertical real temperature gradient of –7.0 K/km for a Chasseral wind speed around 14 m/s. These two different wind speed ratios correspond in fact to two different values of the geostrophic wind speed.

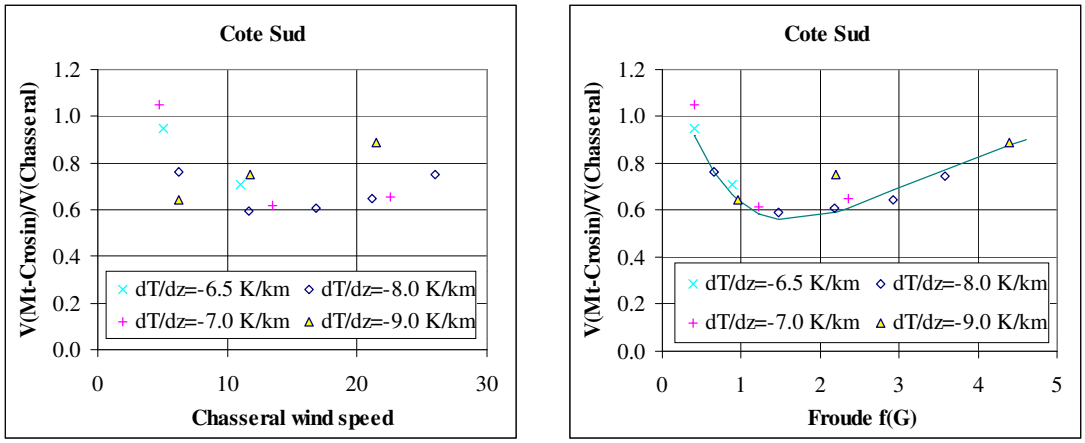

a) b)

Figure 8.1. Wind speed ratio for the 240° geostrophic wind direction for various stability vertical temperature gradients and geostrophic wind speeds. a) Ratios vs. resulting Chasseral wind speed. b) Ratios vs. simulation Froude number. The simulations were performed with a constant ground roughness of 0.03m.

When plotted versus the Froude number of the simulation (defined as a function of the geostrophic wind speed) (Figure 8.1.b and Figure 8.2.b), the calculated wind speed ratios appear to align along a trend function. For the 240° geostrophic wind direction, apart from one simulation, which shows a significant departure from the curve, the points align quite well on an analytical expression of the form

eq. 8.1 $$ratio = a\exp(-b \cdot Fr) + c - d\exp(-e \cdot Fr)$$

with Fr the Froude number of the simulation and the constants *a=3.2*, *b=0.9*, *c=1.15*, *d=3.0*, *e=0.5*.

For the 330° wind direction, it is not so obvious that the points show a behaviour depending on the Froude number of the simulation. When still trying to reproduce, for the 330° wind direction, the behaviour of the wind speed ratio in terms of the Froude number with eq. 8.1, we obtain the set of constants *a=5.0*, *b=3.6*, *c=0.65*, *d=4.1*, *e=2.6*. For the latter case, it should however also be mentioned that since the main flow component is perpendicular to the Jura range, the amplitude of the mountain waves is more significant than for the 240° direction. For this reason it is more difficult to reach a stationary state. For some situations, such a stationary state does not necessary exist. Moreover, due to vertical gradients in the wind speed, it is not easy to define a single value for the geostrophic wind speed to be used to calculate

the Froude number. Both these reasons imply a larger uncertainty in both the values of the wind speed ratio and the Froude number, which might explain the larger dispersion observed in Figure 8.2.b.

The sites of Côte Nord and Côte Est show the same type of behaviour as shown here for Côte Sud.

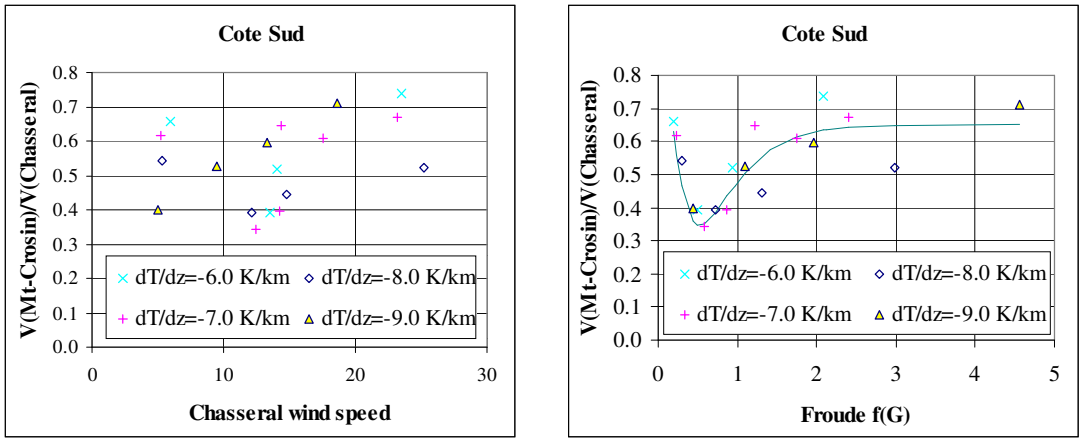

a) b)

Figure 8.2. Same as Figure 8.1 for the 330° geostrophic wind direction and from simulations performed with a variable ground roughness.

Another interesting feature shown by the simulations is the variation of the simulated Chasseral wind direction as a function of the Froude number (Figure 8.3).

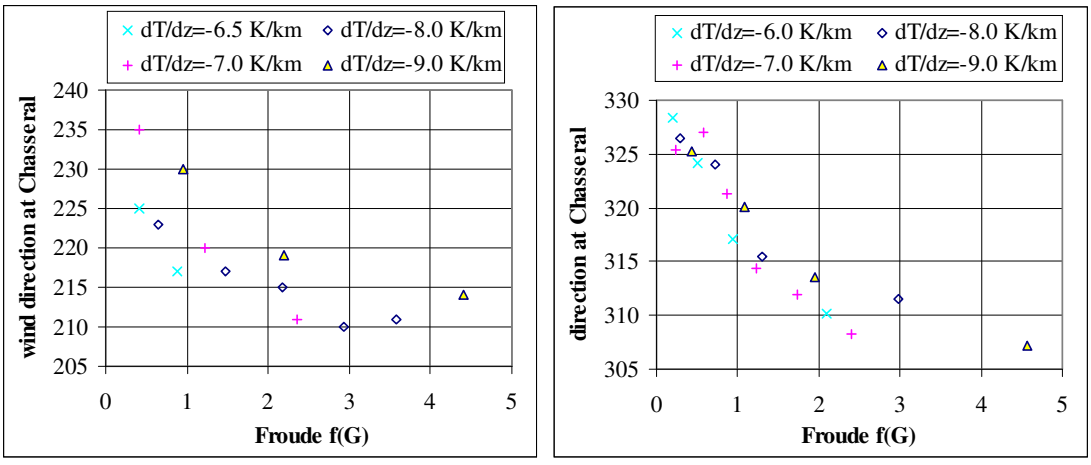

a) b)

Figure 8.3. Resulting Chasseral wind direction vs. Froude number of the simulation for the a) 240° geostrophic wind direction and b) 330° wind direction.

It appears that for all the simulations, the Chasseral wind direction shows an anticlockwise rotation relative to the geostrophic wind speed. From similarity theories over flat terrain (see Appendix B), we would expect for a given thermal stratification that the absolute value of the cross isobar angle (difference between the geostrophic and ground wind direction) would increase when the geostrophic wind speed (or Froude number) is reduced (see Figure 8.4)

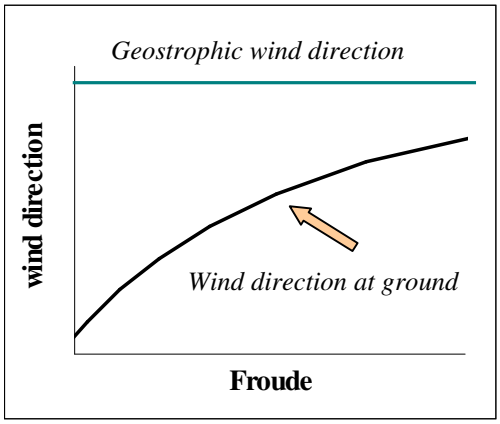

Figure 8.4. Expected behaviour of the wind direction at ground relative to the geostrophic wind direction for various stability conditions (northern hemisphere, flat terrain).

This is not the case in Figure 8.3, since we can see that the simulations with the lowest Froude numbers show wind directions at Chasseral that are close to the 330° geostrophic wind direction, whereas the largest Froude numbers show a larger departure of the Chasseral wind direction from the geostrophic wind direction. It appears in fact that the Ekman spiral that is set as an initial condition is not conserved during the run. The influence of topography is strong enough to impose a rotation of the wind vector at Chasseral so that the tendency that is present in the initial solution is reversed. As would be expected from theory (see, e.g. Stull, 1988, or Banta et al, 1990), this rotational effect due to the topography is stronger for low Froude numbers than for high ones.

If we assume that the behaviour shown by the model results is representative of the real atmosphere, then it is not so surprising that, when plotted versus the Chasseral wind speed, the observed wind speed ratios show the significant scatter visible in Figure 4.5. If one wants to classify the situations and attribute them a value for the wind speed ratio, it seems from Figure 8.1 and Figure 8.2, that the combined geostrophic wind speed and thermal stratification of the free flow are better considered through the use of the Froude number for the simulation. This gives a

strong indication that this non-dimensional number should be taken into account when classifying the meteorological situations over an area of interest.

Noting the trend shown above in terms of the Froude number, we tried to identify the same behaviour in the observed wind speed ratios. From temperature data recorded at the ground based stations of Chasseral (1599m ASL), Chaux-de-Fonds (1018m ASL), Neuchâtel (485m ASL) and Jungfraujoch (3580m ASL, some 100 km to the south-east of Chasseral) we calculated vertical real temperature gradients for each concurrent record. Using this gradient and the Chasseral wind speed for each concurrent record, we derived a Froude number from

eq. 8.2
$$Fr = \frac{v_{Chl}}{H\sqrt{\frac{g}{T_0}\left(\frac{\partial T}{\partial z} - 9.8\cdot 10^{-3}\right)}} \text{ using } H = 1200m$$

The observed wind speed ratios were then binned according to the Chasseral wind direction and Froude number. Figure 8.5.a and b shows a comparison of the observed and simulated wind speed ratios versus the Froude number calculated as a function of the Chasseral wind speed. For the simulated values, we used the vertical temperature gradient of the simulations to compute the Froude number, whereas for the observed data we used temperature records from Chasseral and Jungfraujoch. It should also be stressed before making the comparison between the observations and simulations, that concerning the wind direction it is difficult to have equivalent sets of data. First, we do not have hourly measurements of the geostrophic wind direction, and secondly, from the model point of view, we can only set the high altitude wind direction, without knowing a priori what the resulting Chasseral wind direction will be. Looking at the resulting Chasseral wind direction for the 240° and 330° geostrophic wind direction (Figure 8.3), we decided to compare the simulated ratios for the observed Chasseral wind direction 220° and 320° respectively.

As can be seen from Figure 8.5 plotting the ratios versus the Froude number did not help reduce the scatter of the wind speed ratios and align them along a trendline. The values obtained from the numerical simulations were also plotted (triangles). The model values for the 240° wind direction tend to overpredict those measured. For the 330° wind direction the model values tend to give a lower envelope to the observations with Froude numbers below unity. For higher Froude numbers, the

scatter of the simulated results appears to be well representative of that observed[21]. The overprediction for the 240° geostrophic wind directions is related to the fact that these simulations were done with a roughness length of 0.03m over the whole domain, which is certainly too low for the actual terrain conditions. The 330° predictions were simulated with a variable roughness as shown in Figure 6.5, which shows larger roughness values that should be more representative of the site.

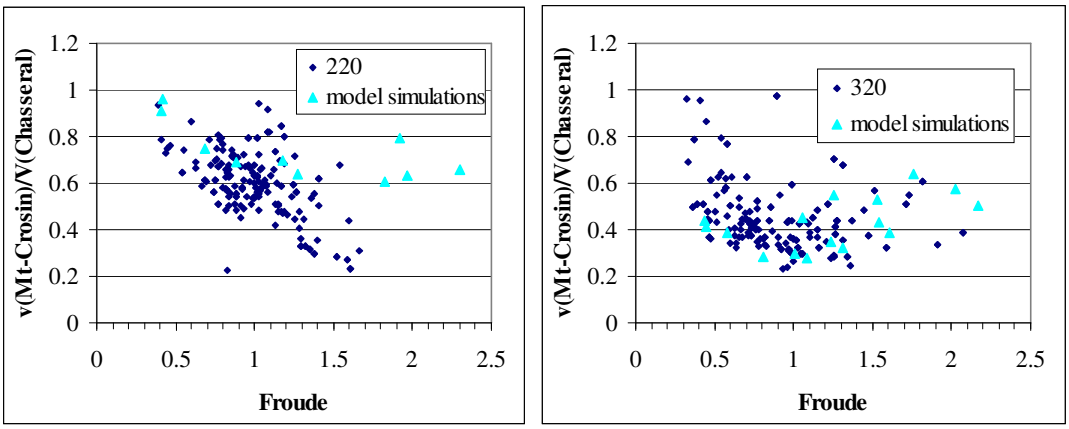

a) b)

Figure 8.5. Côte Nord to Chasseral observed (diamonds) and simulated (triangles) wind speed ratio versus a Froude number calculated according to eq. 8.2 with the Chasseral wind speed and using the temperature gradient between Chasseral and Jungfraujoch. a) 220° and b) 320° Chasseral wind direction for the observations.

Concerning the fact that the behaviour in terms of the Froude number is not so apparent from the observed data, it might be worth pointing out that:

- The Froude number for the observed data was calculated with the Chasseral wind speed. It is also influenced by the atmospheric stability conditions, and does not vary linearly with the geostrophic wind speed. Hence, the Froude number calculated with the Chasseral wind speed does not contain the same information as the Froude number obtained from the geostrophic wind speed.
- The vertical temperature gradient to obtain the Froude number for the observations is calculated from ground based stations and might therefore not be representative of the free flow stability conditions. Trying to use different pairs of ground stations (Chasseral and Neuchâtel or Chasseral and Chaux-de-Fonds) did

[21] When plotted against a Froude number calculated with the Chasseral wind speed instead of the geostrophic wind speed, the trend for the wind speed ratio is no longer so good, which explains the larger scatter of the simulated ones presented in Figure 8.5.b compared to Figure 8.2.b.

not improve the behaviour of the observed wind speed ratios as a function of the Froude number.

In the light of the above remarks, it is possible that the associated error in the calculation of the Froude number is responsible for a significant part of the large scatter of the observed wind speed ratio. It would therefore be interesting to repeat the analysis with data obtained from vertical profiles of wind speed and temperature recorded over the area, to see whether the behaviour of the simulated wind speed ratio as a function of the Froude number can be observed in natural atmospheric flows.

Another possible explanation for the large scatter in Figure 8.5 is related to the fact that the type of vertical profiles we used for both the wind speed and temperature do not cover the wide range of profiles that can actually be observed in nature. The type of wind speed profile we used to obtain Figure 8.1 and Figure 8.2 assumes that we have barotropic conditions, which is certainly not appropriate to represent all the situations. In addition to significant wind speed shear, the actual observed vertical profiles also show wind direction shear (see e.g. Furger, 1990). Inversions in the temperature profiles are also common and are responsible for a reduced coupling between the various layers. Further physical phenomena such as the ground heating or cooling or the latent heat release can also significantly affect the local flow conditions.

The main conclusion that can be drawn regarding the combined effect of the vertical stratification and geostrophic wind speed is that the wind speed ratio is extremely sensitive to their variation. Depending on how we define our simulation conditions for e.g. the 330° wind direction we can end up with a Mt-Crosin to Chasseral wind speed ratio varying between 0.35 and 0.72! In terms of the wind data transposition, using one value instead of the other means a factor 2 between the predicted wind speeds. This shows clearly that if we want to reproduce the observed sector average wind speed ratio we need to define our simulation conditions in such a way that they represent the 'average situation' for this particular direction. This observation clearly highlights the fact that the numerical model, even if it were perfect, cannot be used for a wind power potential estimation without a classification of the meteorological situations occurring over the area of interest.

8.2 Ground heat flux

The effect of a ground heat flux on the simulated wind speed ratio was tested through the application of a ground cooling. We imposed a cooling rate of –2.0 K/h on the ground potential temperature during the first hour, following by a cooling rate of –1.0 K/h for the next 6 hours.

Compared to the same situations performed with zero heat flux through the ground, the wind speed ratio obtained with the ground cooling was increased in some situations and reduced in others. For the 240° wind direction, this behaviour appeared to be consistent with the behaviour shown in Figure 8.1. More precisely, when starting with atmospheric conditions corresponding to a Froude number in the region where the wind speed ratio increases with the Froude number (Zone II in Figure 8.6), imposing a ground cooling leads to a reduction of the wind speed ratio. This is consistent with the fact that the ground cooling tends to stabilise the atmospheric conditions, and hence reduces the Froude number of the simulation. Conversely, when starting with atmospheric conditions corresponding to a Froude number in Zone I, imposing a ground cooling also leads a reduction of the Froude number and hence to an increase in the simulated wind speed ratio.
Typical values of the change in the wind speed ratio due the ground cooling are given in Table 8.1 for the 240° wind direction.

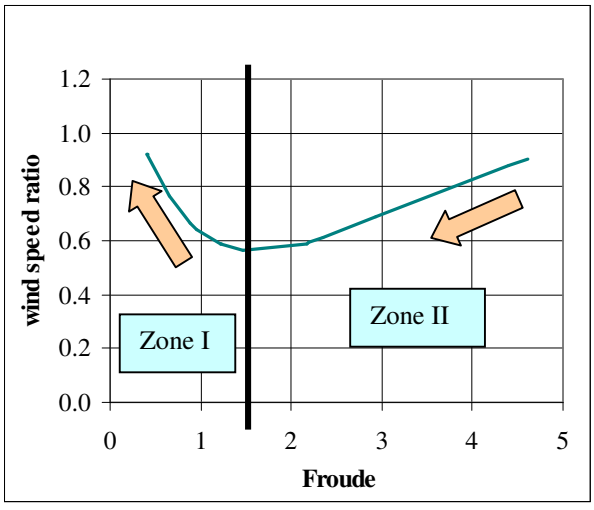

Figure 8.6. Typical behaviour of the wind speed ratio as a function of the Froude number of the simulation. When imposing a ground cooling, we tend to reduce the initial Froude number of the simulation (moving to the left). Therefore, for an initial solution in Zone I, the imposition of a ground cooling implies an increase in the wind speed ratio. In Zone II we have the opposite tendency.

Table 8.1. Order of magnitude of the effect of ground cooling on the wind speed ratios for two simulations with different initial Froude numbers done for the 240° geostrophic wind direction.

Initial Froude number	Côte Nord	Côte Sud	Côte Est	Côte Nord	Côte Sud	Côte Est
	Δ*ratio / neutral ratio* After 2 hours			Δ*ratio / neutral ratio* After 6 hours		
3.6	-4%	-5%	-5%	-9%	-13%	-12%
1.22	+2%	+9%	+8%	+5%	+22%	+18%

In an attempt to include the thermally dominated situations in the transposition methodology the behaviour observed here could be incorporated as a modification of the wind speed ratio depending on the sign of the ground heat flux.

8.3 Ground roughness

Another parameter in the simulations, which appears to play a major role in the resulting wind speed ratios is the ground roughness. To test its influence, the set of stable situations summarised in Table 7.1 was repeated using a constant ground roughness of 0.03m. Compared to the variable roughness map used previously, the use of 0.03m significantly reduces the mean roughness over the domain. This value is certainly too low compared to the actual terrain conditions and it will only be used to appreciate the effect of the roughness on the calculated wind speed ratios.

For both the sites of Côte Nord and Côte Sud, we plotted the wind speed ratios obtained with the reduced roughness in Figure 8.7 (diamonds). For comparison, the values previously obtained with the variable ground roughness were also given (circles). A consequence of the roughness reduction is an overall increase in the wind speed ratios.

Compared to the results obtained with the variable ground roughness, the increase of the calculated wind speed ratio can be explained by the following:

- the Chasseral wind speed has not been changed much with the introduction of lower roughness lengths. This is due to the fact that the Chasseral anemometer location is on an exposed ridge at 60m above ground. The wind speed at this level is therefore not affected so much by the surface layer. In fact, though the roughness length at Chasseral has been decreased (0.05m instead of 0.03m), the Chasseral wind speed is not systematically increased.
- at Mt-Crosin, the wind speed at 10m and 30m above ground is significantly increased. This is due to the fact that the measurement locations on the Mt-Crosin

lie on a gentle slope, in the surface layer. There is therefore a longer fetch over which the wind profiles are affected by the local roughness. With a reduced roughness, and a same geostrophic wind condition we therefore obtain an increased wind speed at 10m or 30m above ground.

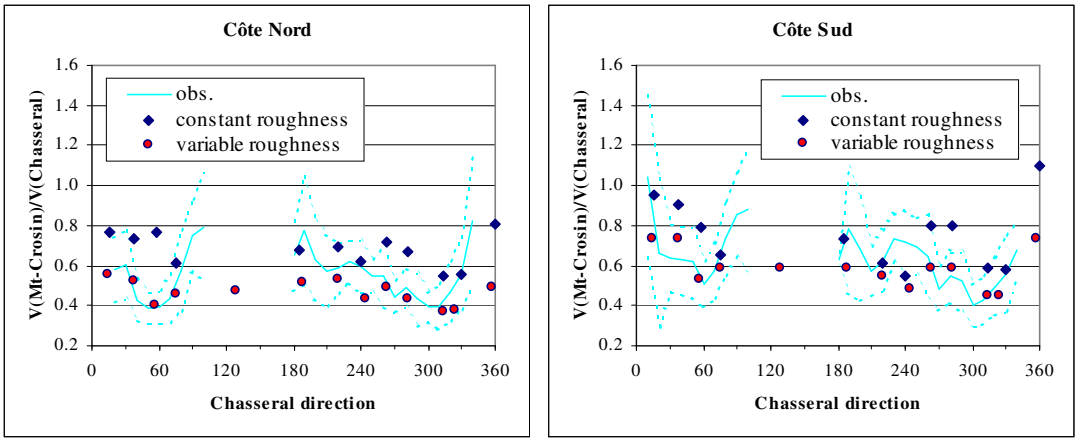

Figure 8.7. Wind speed ratios at Côte Nord and Côte Sud obtained from the set of stable situations (diamonds) defined in Table 7.1. Diamonds: simulations with constant $z_0 = 0.03m$, circles: variable ground roughness as in Figure 6.5. The mean observed values (continuous line) are also given together with the standard deviation about the average (dashed lines).

The strong sensitivity of the results to the estimated ground roughness demonstrates that this parameter must be considered with extreme care when attempting to perform a wind data transposition from numerical simulations. The quality and precision of the roughness data is a key factor determining the accuracy of the investigated site-to-site relationships. In the case we presented here, we can say that the roughness distribution we used is certainly too coarse (horizontal resolution: 2 km). As a consequence, most of the Mt-Crosin surroundings are set to a forested area, which does not correspond to the real terrain. Moreover, the roughness length of 1m that we used for the forested area might also be a bit exaggerated.

For the 270° geostrophic wind direction (Chasseral wind direction ~280°), two additional simulations were performed to test the influence of different roughness values. For the first test, the variable roughness map was used with a local reduction of the roughness length to 0.05m over an area covering some 600 x 600 m on the Mt-Crosin site. Similarly to what was seen for the case of Askervein Hill (Appendix D), the local modification of the roughness length did not significantly affect the resulting wind speed ratios. For the second test, we used a variable roughness map

as in Figure 6.5, taking a value of 0.8m[22] instead of 1m for the roughness length of the forested areas. Reducing the roughness length this way implied an increase of the simulated wind speed ratio by 3% at Côte Sud and Côte Est and by 5% at Côte Nord. This different sensitivity of the various stations is due to the fact that the measuring instruments at Côte Nord are located at 10m AGL, whereas they are at 30m AGL for the two other sites.
As observed from the two additional simulations that were described above, the tendency to underestimate the sector proportionality factors might be explained by slightly to high roughness values more than by a too coarse resolution of the roughness map. However, since the latter behaviour might not necessarily be observed for all the wind directions, it would still be interesting to see how the results would be changed when using a roughness map that has the same resolution as the numerical model.

8.4 Neutral static stability

Finally, we will present some results showing the consequences of neglecting the static stability of the atmosphere on the simulated wind speed ratios.
A set of 12 simulations was thereby performed for a geostrophic wind speed of 10 m/s, with a vertical temperature gradient of –9.7 K/km (quasi-neutral), by varying the geostrophic wind direction by steps of 30°. These simulations were done assuming a constant ground roughness of 0.03m. As the conditions chosen (quasi-neutral stratification and geostrophic wind speed that is constant with the wind direction) are not at all representative of the climatology of the area, it is not expected that they will lead to wind speed ratios that agree with the observations. These runs are only done to evaluate the order of magnitude of the errors when using the code as a black box, without any valuable input about the type of situations that occur over the area of interest.

For both the sites of Côte Nord and Côte Sud, the resulting wind speed ratio is plotted in Figure 8.8 (triangles) versus the resulting Chasseral wind direction and compared to the average ratios obtained from the observations. For comparison, we also plotted the wind speed ratios obtained previously with the set of stable situations representative of the local climatology (diamonds).

[22] The value of 0.8m corresponds more to the value recommended in the European Wind Atlas.

With the use of a neutrally stratified atmosphere, and constant geostrophic wind speeds, the wind speed ratios are increased for most of the wind directions. The increase can be very significant for some of the sectors (about 40% at Côte Sud for the resulting Chasseral wind direction 220° and 300° to 330°) and negligible for others (wind direction ~40° at Chasseral). The change in the simulation conditions can also lead to a slight reduction in the wind speed ratio (sector 20° or 190°).
For the most frequent wind directions at Chasseral (30° to 90° and 210° to 330°), the wind speed ratios lie even above the range of variation that would be given by the standard deviation. Also, the agreement of the sector variation of the simulated and measured wind speed ratio is not good.

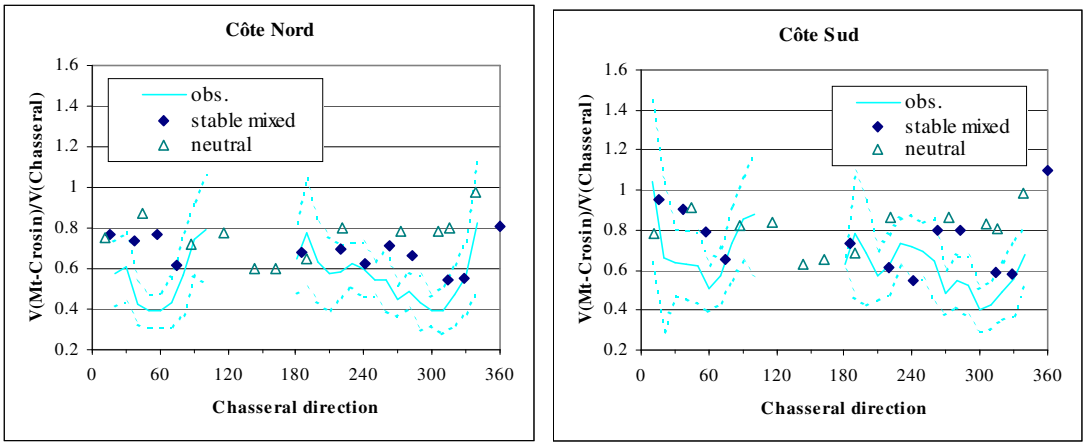

Figure 8.8. Wind speed ratios obtained from neutral (triangles) and the set of stable situations (diamonds) as defined by the Fallot classification (see Table 7.1). The mean observed values (continuous line) are also given together with the standard deviation about the average (dashed lines).

8.5 Effects on the transposed wind speed distribution

The transposed wind distributions obtained from the set of simulations performed with a constant roughness length of 0.03m are shown in Figure 8.9 for the measurement locations of Côte Nord. Both results obtained from the stable situations representing the advective situations entering the Fallot classification (dark grey) and from the neutral simulations (light grey) are plotted. For comparison, the observed wind speed distributions (black) has also been included in the diagram.
The comparison clearly shows that the transposition done this way produces too high wind speeds. From Table 8.2 we can see that the neutral simulations that were done with a roughness length of 0.03m lead to an overestimation of 25% to 41% for

the mean wind speed. The corresponding estimated yearly energy output is overestimated by 81% to 100%. With the introduction of stable conditions, the overestimation is reduced but the relative errors on the predicted mean wind speed (4%-19%) and yearly energy output (19%-55%) are still large (see Table 8.3).
The transposed distributions on the sites of Côte Sud and Côte Est presented a similar behaviour as the site of Côte Nord.

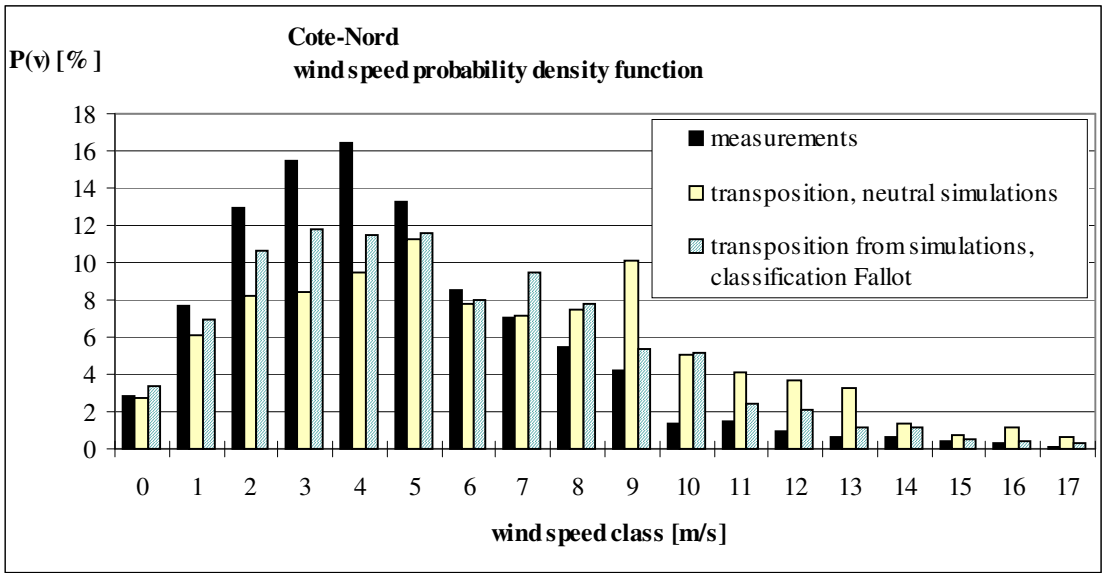

Figure 8.9. Comparison of the observed (black) and transposed wind speed distributions at Côte Nord, obtained from numerical simulations with a neutral stratification (light grey), and from the set of simulation presented in Table 7.1 (hatched). The simulations were run with a roughness length of 0.03m.

Table 8.2. Mean wind speed and yearly energy output obtained with proportionality factors from the numerical simulations, only considering a neutrally stratified atmosphere.

Station name	Average wind speed [m/s]			Yearly energy production [MWh/year]		
	Measured	Transposed	Relative error	Measured	Transposed	Relative error
Côte Nord	5.2	7.0	35%	806	1618	101%
Côte Sud	5.3	6.6	25%	800	1450	81%
Côte Est	5.6	7.9	41%	983	1907	94%

Table 8.3. Mean wind speed and yearly energy output obtained with proportionality factors obtained from the numerical simulations, considering the set of stably stratified situations defined in Table 7.1.

Station name	Average wind speed [m/s]			Yearly energy production [MWh/year]		
	Measured	Transposed	Relative error	Measured	Transposed	Relative error
Côte Nord	5.2	6.0	16%	806	1197	49%
Côte Sud	5.3	5.5	4%	800	948	19%
Côte Est	5.6	6.6	19%	983	1424	55%

If one wanted to take advantage of the tendencies observed from the sensitivity tests performed in this chapter when performing the wind data transposition, then we could no longer use the simple methodology starting from the reference station wind statistics. We would require in this case a classification of the meteorological situations that would include parameters such as the geostrophic wind direction θ_g, geostrophic wind speed G, the Froude number of the simulation Fr (from the free flow stability conditions and geostrophic wind speed) as well as the ground heat flux J_{gr}. In this case, each point $(\theta_g, G, Fr, J_{gr})$ would be attributed a frequency of occurrence $f(\theta_g, G, Fr, J_{gr})$.

Trendlines such as those shown in Figure 8.1 or Figure 8.2 could be determined for the ratio between the prediction site and geostrophic wind speeds by performing a dozen simulations for each of the 12 geostrophic sectors[23]. Each point in the classification could be mapped to the prediction site in a similar way as presented in Figure 2.2 to obtain the wind speed distribution at the prediction site from

eq. 8.3 $$h(v_{pred}) = \sum_{i,j,k,l} f(\theta_i, G_j, Fr_k, J_l)\Big|_{a(\theta_i, Fr_k, J_l)\cdot G_j = v_{pred}}$$

The wind speed ratio $a(\theta_g, Fr, J_{gr})$ would be a function of the geostrophic wind direction θ_g and Froude number Fr, with a correction taking into account the effect of the ground heat flux J_{gr}. This would be one way to refine the transposition methodology in order to take into account a larger range of atmospheric situations and have a better representation of the local climatology.

Such a refinement would be quite expensive in terms of measurements (vertical profiles and geostrophic wind speed are not necessarily available and if so certainly not as hourly data), classification work and CPU time to perform the additional

[23] The ratio between the Mt-Crosin and the geostrophic wind speeds also appears to be a function of the Froude number. So does the ratio between the Chasseral and geostrophic wind speeds.

simulations. This refinement would bring a valuable piece of information that would be useful to perform a data transposition in the bottom of valleys where thermal effects play a significant role. However, for sites potentially interesting for wind power application (more exposed, located on a ridge), the increase in complexity in the transposition methodology does not ensure that the transposition results will be significantly improved (see also Section 4.3).

Considering the amount of additional work that this refinement would require it is considered to be beyond the scope of the present work.

9 Conclusions and further work

The present work concerned the development and testing of a numerical tool, together with a transposition methodology for wind power assessment over complex topography.

To this end, several modifications were made to the CFX4 flow solver, to make it suitable for solving atmospheric flows. Since for the meteorological scales considered in this work (meso-γ to meso-β scale following the classification by Orlanski, 1975) this kind of implicit full Navier-Stokes solver is not commonly used, it was felt that a model validation was required. The validation was therefore done firstly to check that the implementations made to CFX4 were done properly and secondly to give confidence in the model's ability to reproduce atmospheric flows.

Comparing the model results with empirical formulations or with observations showed that over flat terrain, the effect of ground roughness or a roughness change on the boundary layer development was properly accounted for. For purely 2D neutral boundary layers (i.e. for boundary layers where the effect of the Earth's rotation is not significant), it was found that for smooth ground conditions the simulated wind speed profiles are in good agreement with the Coles velocity defect profile. It also appeared for both smooth and rough conditions, that the simulated wind profiles could be represented very accurately by an analytical formulation proposed by Alexandrou.
In the case where we assume that the incoming flow entering the domain is fully developed and its turbulence characteristics are in equilibrium with the ground roughness conditions representative of the area, it would be very useful to have a parameterisation of the wind speed, k and ε profiles to be used as inlet boundary conditions. This can avoid the need to extend the simulation domain upwind of the area of interest and therefore reduce the cost of the simulation (reduced domain size and CPU time). From this point of view the Alexandrou formulation is a very useful tool since it provides wind speed, as well as the k and ε profiles which describe a turbulent boundary layer in equilibrium. This could be demonstrated from simulations performed over the real terrain of Askervein Hill.

The introduction of a buoyancy term formulated in terms of the potential temperature in the $k-\varepsilon$ model allowed the effect of the free flow stability on the development of the entire boundary layer to be taken into account. The model results

presented in Appendix B, where the Ekman layer development over flat terrain was reproduced, were in relatively good agreement with results from other models and from laboratory data. It was also shown that for a range of roughness up to 0.1m, for free flow stratification given by $\partial T / \partial z$ between –6.5 and –9.8 K/km and for various geostrophic wind speeds, the Zilitinkevich parameterisation, with a modified set of constants, is suitable for representing the resulting u and v profiles simulated by the model. For cases where a heat flux through the ground was applied, the model and the Zilitinkevich parameterisation agree only for situations with moderate ground cooling ($\partial T / \partial t < -0.5K / h$). From the work presented in Appendix B.4, it appears that the Zilitinkevich formulation is very useful in providing the numerical models with an initial solution and a boundary condition for the u and v profiles in the case where it becomes important to properly represent the Ekman spiral and when relatively few data are available.

From simulations performed over a 2D theoretical mountain profile, for a stably stratified atmosphere, it could also be shown that the model is able to reproduce flow features like mountain waves for both linear and strongly non-linear situations. Therefore, the model appears be able to simulate phenomena that would be more representative of the meso-β scale and take into account their effect on the flow development close to the ground.

For flow situations which exhibit a good coupling between the ground and high altitude, i.e. situations where the boundary layer development is governed by the free flow wind speed, it could be shown from the validation tests reviewed above that the model is able to satisfactorily reproduce both the flow development close to the ground and at higher levels.

For flow situations with significant thermal effects close to the ground, reasonable solutions for the downslope winds developing along the Jura chain were obtained. The breeze intensity and breeze layer thickness simulated by the numerical model agree fairly well with the analytical expressions given by Hertig. Some comparisons with the numerical model TVM (Thunis, 1995) were also performed for the simulation of a land-sea breeze system with the evolution of a convective cell associated with the diurnal cycle. These agree quite well with the results presented by Thunis, but are not shown in the present contribution, for the reason that it is felt that some more validation work would be required for the simulation of thermally dominated situations.

Another question which remains unanswered concerning the numerical model is the choice of appropriate turbulence constants to simulate atmospheric flows. So that the simulations are able to reproduce the non-dimensional turbulent kinetic energy close to the ground measured by Hinze, or Panofsky & Dutton, the set of constants proposed by Duynkerke would be more suitable than the standard values. The wind speed profiles measured by Bradley behind a smooth-to-rough transition were also slightly better reproduced by the model when using the set of constants proposed by Duynkerke. However from the 3D simulations over Askervein Hill, the superiority of Duynkerke constants relative to the standard constants could not be fully demonstrated. We showed from this validation case that both the standard and Duynkerke's turbulence model constants lead to horizontal wind speed distributions that are in good agreement with the observations. When the standard constants are used, good results are obtained with a roughness length of 0.03m, whereas for Duynkerke's constants, it was required to assume a roughness reduction over the hill to reproduce the horizontal wind speed distribution. When the normalised turbulent kinetic energy profile over the hill top is accurately reproduced with the standard model constants, the vertical profile of the speed-up ratio is not well reproduced for the lowest 5 m AGL. On the other hand, the profile of the speed up ratio is very well reproduced when using the constants given by Duynkerke, but then we obtain an overestimation in the turbulent kinetic energy profile.

Concerning the site to site wind data transposition, we proposed an extension of the standard MCP method applied to reproduce the wind probability density function at the prediction site from the wind direction and wind speed distribution at the reference site.

A back-prediction was performed, using various types of site-to-site relationships obtained from concurrent data sets, to obtain the wind speed distributions at the elevated prediction sites of Mt-Crosin as well as at the less exposed sites of Chaux-de-Fonds and Neuchâtel. From this we found that:

- With both the linear relationship $v_{pred} = m(\theta) \cdot v_{ref} + c(\theta)$ and the simple proportionality relationship $v_{pred} = a(\theta) \cdot v_{ref}$ between the reference and prediction sites, we were able to obtain a good prediction of the mean wind speed. The relative error between the predicted and measured mean wind speed was less than 5% for the five sites considered.
- When evaluating the yearly energy output that could be obtained from a Vestas-V44 wind turbine using the predicted wind speed distribution, we found

that the proportionality relationships gave better results than the linear relationships with a non-zero intercept.

As derived from the observations, the assumption of a constant wind speed ratio for a given reference site wind direction is far from valid when considering hourly concurrent records. It appears however that using average sector wind speed ratios to perform the transposition leads to a good prediction of the transposed wind speed distribution. Generally, the use of two-parameter instead of one-parameter relationships worsened the transposition results. Simply increasing the complexity of the transposition relationships by adding one more parameter to represent the behaviour of the observations does not ensure that the transposition will be improved.

Though slightly underestimated, the observed sector wind speed ratios were fairly well reproduced by the numerical model, when using a roughness distribution more or less representative of the area and performing simulations with atmospheric conditions that closely correspond to the average observed situations.

Transposing the short-term Chasseral wind data to the Mt-Crosin site using the wind speed ratios calculated by the numerical model, the Mt-Crosin wind speed distributions were calculated at the three measurement locations and were compared to those observed. This showed that the energy output which would be produced by a Vestas-V44 in these conditions is underpredicted by 8% to 36% and the mean wind speed by 7% to 18%. When predicting the wind speed distribution at the wind turbine hub heights and comparing with the actual production data for the year 1997, the yearly energy output was underestimated by 22% to 24% for the three machines. When comparing the production data month by month, the relative errors of the prediction were more significant, showing the strong sensitivity of the results to the fact that from one month to another, the meteorological situation occurring are distributed differently. When the wind directions for which the simulated wind speed ratios depart from the observations occurred more frequently than on average during a given month, a larger error in the monthly prediction is obtained.

The results obtained for the transposition made with the relationships established by the numerical model show that this model is a valuable tool for the wind power potential assessment over complex terrain. In fact, the accuracy obtained for the prediction is typically of the same order of magnitude as that which can be achieved with one year of measurements on site.

From the numerical simulations performed with various geostrophic wind speeds and free flow stratification conditions, it could be observed that, for a given geostrophic wind direction, the wind speed ratio is a function of the Froude number of the simulation and is extremely sensitive to a variation in this parameter. When imposing a ground cooling, the simulated wind speed ratios were modified in a way that is coherent with the behaviour in terms of a Froude number.
In addition to the sensitivity to the atmospheric stability conditions, the simulated wind speed ratios are also very sensitive to the ground roughness conditions.

Assuming that the strong sensitivities observed for the calculated wind speed ratios are correct, it was concluded that a good numerical tool to simulate the wind fields over the area of interest is not sufficient to perform an accurate wind data transposition. In addition to the model, it is necessary to have some more information about the typical meteorological situations occurring, in the form of a classification. Fortunately, it is possible to obtain good results for the wind data transposition, when using a very simple set of situations representative of the average meteorological conditions observed in a dozen wind directions. This was verified at least for the well-exposed site of Mt-Crosin, but might not necessarily be true for lower altitude sites, which often lie below thermal inversion levels. For these cases, instead of using the simple transposition methodology used in this work, it might be better to apply one that would be more like a 'statistical-dynamical' approach mentioned earlier.
With this in mind and from the point of view of further work, it is suggested, using the Payerne soundings and ground data from several stations, that the various climatic situations are sorted in two groups: one for the advectively and one for the thermally dominated situation. From the tendencies observed for the simulated wind speed ratios it might be a good idea to classify the meteorological situations as a function of the geostrophic wind speed and direction, and Froude number of the free flow. It would then be informative to see whether all the days belonging to a given cluster would correspond to a similar flow pattern at the ground. This could be done e.g. for the area around Basel, using the REKLIP data set and by applying a classification similar to that carried out by Kaufmann. The essential difference with the approach used by Kaufmann would be the consideration of a top-down approach, starting from the physical parameters *including* the Froude number of the simulations, which appears to be an essential parameter from the numerical model results.
If this approach is successful, than one could try to repeat the work also considering the thermally dominated situations.

The reason for doing such a classification starting from the geostrophic conditions is that it is expected to be representative of a larger area than just the Chasseral and Mt-Crosin immediate surroundings. It could then be used make wind data transpositions over most of the Jura chain.

From the numerical model point of view, so that one could deal with a larger range of meteorological situations, it would be worth including moist processes, as well as a soil model. To reproduce real events, it would be necessary to couple the numerical model with a larger scale model that could provide the time dependent boundary conditions. It should however be borne in mind, that due to the high computing time required to perform a simulation, it will not be possible in the immediate future to use such a model for the purpose of weather forecasting.

Concerning the good agreement that was observed when comparing the numerical model results with the Zilitinkevich parameterisation for the Ekman spiral development over flat terrain, it would be interesting to further investigate this type of boundary layer development by comparing the results with observations. This is to be the subject of further work using data collected over the Greenland ice sheet during well developed katabatic flows with rather low synoptic forcing.

And finally, to further evaluate the origin of errors in the wind data transposition, it would be useful to continue with the wind measurement campaign on the Mt-Crosin site. Considering the complex terrain of the area, the machine characteristics that were used to calculate the predicted energy production might not be appropriate for the actual Mt-Crosin site conditions, given that turbine performance can be influenced by local turbulence. Also the profiles that were calculated on site by the numerical model were not validated. Since the wind speed vertical gradients obtained by the model were used to transpose the wind data to the turbine hub height, it would be useful to investigate the variation of the wind speed over the turbine rotor more thoroughly.

10 Bibliography

Adrian, G., Dotzek, N., Frank H., 1996, 'Influence of thermally induced wind systems on the wind climate of the Baltic sea analysed by numerical simulations', *Proceedings of the European Union Wind Energy Conference*, Goeteborg, pp 608-610.

Adrian, G., Fiedler, F., 1991, 'Simulation of unstationary wind and temperature fields over complex terrain and comparison with observations', *Beitr. Phys. Atmosph.* 64, pp 27-48.

Alexandrou, C., 1996, 'Dissipation length and the mean velocity profile of a two dimensional turbulent boundary layer', *Rapport LASEN*, Ecole Polytechnique Fédérale de Lausanne, Switzerland.

Alm, L.K., Nygaard, T.A., 1993, 'Flow Over Complex Terrain Estimated By A General Purpose Navier-Stokes Solver', in *Proceedings of the European Community Wind Energy Conference*, Lübeck-Travemünde, Germany.

Andrén, A., Moeng, C.-H., 1993, 'Single-Point Closures In A Neutrally Stratified Boundary Layer', *Jour. Atmos. Sci.*, 50, pp 3366-3379.

Atkinson, B.W., 1989, 'Mesoscale atmospheric circulations', Academic Press, London, 495 pp.

Banta, R.M., et al, 1990, 'Atmospheric processes over complex terrain', W. *Blumen Eds, AMS, Meteorol. Monogr.*, vol23, 45, 323pp.

Barnard, J.C., 1991, 'An evaluation of three models designed for siting wind turbines in areas of complex terrain', *Solar Energy*, 46, No.5, pp 283-294.

Beljaars, A.C.M., Walmsley, J. L., and Taylor, P.A., 1987, 'A Mixed Spectral, Finite-Difference Model For Neutrally Stratified Boundary-Layer Flow Over Roughness Changes And Topography', *Boundary-Layer Meteorol.*, 38, pp 273-303.

Botta, G., Castagna, R., Borghetti, M., Mantegna, D., 1992, 'Wind analysis on complex terrain- The case of Acqua Spruzza', *J. Wind Eng. and Ind. Aero.*, 39, n°1-3, pp 357-366.

Bradley, E. F., 1968, 'A micrometeorological study of velocity profiles and surface drag in the region modified by a change in surface roughness', *Quart. J. Roy. Meteorol. Soc.*, 94, pp 361-379.

Britter, R.E., Hunt, J.C.R., and Richards, K.J., 1981, 'Air Flow Over A Two Dimensional Hill: Studies Of Velocity Speed-Up, Roughness Effects And Turbulence', *Quart. J. R. Meteorol. Soc.,* 107, pp 91-110.

Bury, K.V., 1986, 'Statistical Models in Applied Science', *Robert E. Krieger Publishing Company*, Malabar, Florida.

Businger, J.A., Wyngaard, J.C., Jzumi, Y., Bradley, E.F., 1971, 'Flux-Profile Relationships In The Atmospheric Surface Layer', *Jour. Atmos. Sci*., 28, pp 181-189.

Caldwell, D.R., Van Atta, C.W., Helland, K.N., 1972, 'A Laboratory Study Of The Turbulent Ekman Layer', *Geophys. Fluid Dyn*., 3, pp 125-160.

CFX, 1997, 'CFX-4.2 Flow solver', *CFX International, AEAT*, 8.19 Harwell, Oxfordshire OX11 0RA, UK.

Cherry, N.J., 1980, 'Wind energy resource survey methodology' in *J. Wind Eng. and Ind. Aero.,* Vol. 5, n°3-4.

Clarke, R.H., 1970, 'Observational Studies in the atmospheric boundary layer', *Quart. Jour. Roy. Meteor. Soc*., 96, 91.

Coles, D., 1956, 'The law of the wake in the turbulent boundary layer', *J. Fluid Mech*. 1, 191.

Colson, DeVer, 1954, 'Meteorological problems in forecasting mountain waves'. *Bull. Amer. Met. Soc*. 35, pp 363-371.

Cousteix, J., 1989, 'Turbulence et couche limite', *CEPADUES Editions*, Toulouse. 627 pp.

Davenport, A.G., 1963, 'The relationship of wind structure to wind loading', Proceedings of the 1st Conference on 'Wind effects on buildings and structures'.

Deardorff, J.W., 1972, 'Numerical investigation of neutral and unstable boundary layers', *Jour. Atmos. Sci*., 29, pp 91-115.

Deaves, D. M., Harris, R.I., 1978, ' A Mathematical Model of the Structure of Strong Winds', in *Construction Industry Research and Information Association, Rep. 76*.

De Buman-Ruffieux, A.-M., 1994, 'Régimes de vent et qualité de l'air en Valais', *Thèse No. 1071*, Institut de géographie, Université de Fribourg (CH).

Durran, D.R., Klemp, J.B., 1983, 'A compressible model for the simulation of moist mountain waves', *Mon. Wea. Rev*., 111, pp 2341-2361.

Durran, D.R., 1990, 'Mountains waves and downslope winds', in Atmospheric Processes over complex terrain, W. *Blumen Eds, AMS, Meteorol. Monogr*., vol23, 45, pp 59-81.

Dütsch, H.U., 1985, 'Large-scale domination of a regional circulation during winter-time anticyclonic conditions', *Meteor. Rundsch*., 38, pp 65-75.

Duynkerke, P.G., 1988, 'Application of the E-ε Turbulence Closure Model To The Neutral And Stable Atmospheric Boundary Layer', *Jour. Atmos. Sci*, 45, pp 865-880.

Dyer, A.J., 1974, 'A review of flux-profile relationships', *Bound. Layer Meteor*., 7, pp 363-372.

Ehinger, J., Hertig, J.A., Alexandrou, C., Berney, M., Christinat, M.O., 1990, 'Analyse de l'influence de la topographie sur les conditions d'exposition des bâtiments', 'Klimadatentransfer-Transfert de données météorologiques', *Rapport FN*, subside no 20-5189.86, EPF Lausanne, LASEN.

Eliassen, A., Palm, E., 1960, 'On the transfer of energy in stationary mountain waves', *Geophys. Publ*., 22, pp 1-23.

Eppel, D.P., Kapitza, H., Claussen, M., Jacob, D., Koch, W., Levkov, L., Mengelkamp, H.-T., Werrmann, N., 1995, 'The Non-Hydrostatic Mesoscale Model GESIMA. Part II: Parameterizations and Applications', *Beitr. Phys. Atmos*.,vol.68, no.1, pp. 15-41.

Fallot, J.-M-, Hertig, J.-A., 1991, 'Prévision d'immissions atmosphériques pour les sections 1 à 3 (Queue du Loup à Porrentruy-Est) de la route nationale N16 (Transjurane)', *Projet No. 900.102, ZACE Service SA-DIVISION IMPACT*, 1025 St-Sulpice, Switzerland.

Fallot, J.-M., 1992, 'Etude de la ventilation d'une grande vallée préalpine: la vallée de la Sarine en Gruyère', Thèse no. 995, Institut de Géographie, Univ. de Fribourg. Switzerland.

Favre, A., Kovasznay, L.S.G., Dumas, R., Gaviglio, J., Coantic, M., 1976, 'La turbulence en mécanique des fluides', *CNRS, Gauthier-Villars*, Bordas, Paris, 411 pp.

Frey-Buness, F., Heimann D. and Sausen R., 1995, 'A statistical-dynamical downscaling procedure of global climate simulations'. *Theor. Appl. Climatol.*, 50, pp. 117 131.

Fuentes, U. and Heimann D., 1996, 'Verification of statistical-dynamical downscaling in the Alpine region'. *Climate Research*, 7, pp. 151-168.

Furger, M., 1990, 'Die Radiosondierung von Payerne', *Lenticularis Verlag*, 8152 Opfikon (CH), 191 pp.

Garrat, J.R., 1992, 'The Atmospheric Boundary Layer', *Cambridge Atmosph. and Space Science Series*, Cambridge Univ. Press. 316 pp.

Glekas, J., Prospathopoulos, J., Voutsinas, S., 1996, 'Efficient Estimation Of Wind Potential For Sites In Complex Terrain: Assessment Of The Applicability Of A Navier-Stokes Code', *NTUA, Dept. Mech. Engineer., Fluid Section*.

Harris, V.G., Graham, J.A.M., Corrsin, S., 1977, 'Further experiments in nearly homogeneous turbulent shear flows', *J. Fluid Mech.*, vol.81, part 4.

Hertig, J.-A., Liska, P., 1983, 'Simulation of regional atmospheric flows on small scale topographical models', *J. Wind. Eng. Industr. Aerodyn.*, 15, pp 77-89.

Hertig, J.-A., Wooldridge, G., Beniston, M., Liska, P., 1986, 'Modélisation expérimentale des échanges de masse d'air entre la Broye, le bassin lémanique et la vallée du Rhône', Rapport interne IENER-EPFL, N532.101, Lausanne.

Hertig, J.-A., 1993, 'Modélisation du vent a travers les Alpes. Méthode des volumes finis', *Communication au Fachkolloquium 93/1*, ISM, Zurich.

Hess, G.D., Hicks, B.B., Yamada, T, 1981, 'The impact of Wangara experiment', *Bound. Layer Meteor.*, 20, pp 135-174.

Hess, P., Brezowsky, H., 1977, 'Kataklog des Grosswetterlagen Europas', *Ber. des Deutschen Wetterdienstes*, 113, DWD, Offenbach a. M.

Hinze, J.O., 1975, 'Turbulence', *Mc-Graw Hill*, 790 pp.

Holmboe, J., Klieforth, H., 1957, 'Investigations of mountain lee waves and the airflow over the Sierra Nevada', *Final Report*, Contract No AF 19(604)-728. 290pp.

Jackson, P.S., Hunt, J.C.R., 1975, 'Turbulent Windflow Over A Low Hill', *Quart. J. R. Meteorol. Soc.*, 101, pp 929-955.

Jensen, N.O., Petersen, E.L., Troen, I., 1984, 'Extrapolation Of Mean Wind Statistics With Special Regard To Wind Energy Applications', in *Rep. WCP-86*, WMO, Geneva, 85 pp.

Kapitza, H., Eppel, D.P., 1992, 'The Non-Hydrostatic Mesoscale Model GESIMA. Part I: Dynamical Equations and Tests', *Beitr. Phys. Atmos.*,vol.65, no2, pp. 129-146.

Kaufmann, P., 1996, 'Bodennahe regionale Windfelder über komplexer Topographie', *Diss. ETH Nr.11565*, ETH Zürich, 147 pp.

Klemp, J.B., Lilly, D.K., 1978, 'Numerical simulation of hydrostatic mountain waves', *J. Atmos. Sci.*, 35, pp 78-107.

Lalas, D.P., Ratto, C.F., 1996, 'Modelling Of Atmospheric Flow Fields', *World Scientific Publishing Co*, Singapore, 751 pp.

Landberg, L., 1994, 'Short term prediction of local wind conditions', *Risoe National Laboratory*, Roskilde, Denmark.

Launder, B.E., Spalding, D.B., 1972, 'Mathematical models of turbulence', *Acad. Press*.

Lembessis, V., 1992, 'Influence of the use of the residual heat from an incineration plant on the atmospheric pollution and energy consumption', *Msc Thesis*, LASEN, EPFL, 1015 Lausanne.

Lettau, H., 1950, 'A re-examination of the 'Leipzig wind profile' considering some relations between wind and turbulence in the frictional layer', *Tellus*, 2, pp 125-129.

Long, R.R., 1953, 'Some aspects of the flow of stratified fluids. I: A theoretical investigation', *Tellus*, 5, pp 42-58.

Mason, P.J., Thomson, D.J., 1987, 'Large-Eddy Simulations Of The Neutral-Static-Stability Planetary Boundary Layer', *Quart. Jour. Met. Soc.*, 113, pp 413-443.

Mengelkamp, H.T., Kapitza, H., Pflueger, U., 1996, 'Regional and local wind climatologies over heterogeneous terrain', *Proceedings of the European Union Wind Energy Conference*, Goeteborg, pp 506-509.

Meteonorm Vent', *Office fédéral de l'énergie*, Edition 1990, 187 pp.

Mickle, R. E., Cook, N.J., Hoff, A.M., Jensen, N.O., Salmon, J. R., Taylor, P.A., Tetzlaff, G., Teunissen, H. W., 1988, 'The Askervein Hill Project: Vertical Profiles Of Wind And Turbulence', *Boundary Layer Meteorol.*, 43, pp 143-169.

Miles, J.W., Huppert, H.E., 1969, 'Lee waves in stratified flow. Part 4. Perturbation approximations', *J. Fluid Mech.*, 35, pp 497-525.

Montavon, C., 1995, 'Wind power potential evaluation over complex terrain by means of a numerical model: application to one site in the Swiss Jura mountains', *Msc Thesis*, LASEN, EPFL, 1015 Lausanne.

Montavon, C., 1998, 'Askervein Hill site: a sensitivity study using the numerical model CFX4 testing the effect of the flow parameters on the resulting flow field', *Rapp. Interne no.548.104*, LASEN, EPFL, 1015 Lausanne.

Moussiopoulos, N., Flassak, Th., Knittel, G., 1988, 'A refined diagnostic wind model', Environ. Software 3, pp 85-94.

Moussiopoulos, N., 1996, 'Mesoscale Models and Their Use', in Modelling of Atmospheric Flow Fields, Eds Lalas, Ratto, World Scientific Publishing Co Pte Ltd, Singapore.

Nicholls, S., 1985, 'Aircraft observations of the Ekman layer during the Joint air-sea interaction experiment', *Quart. Jour. Roy. Meteor. Soc.*, 111, pp 391-426.

Nicholls, S., 1982, 'An Observational Study Of The Mid-Latitude Marine Atmospheric Boundary Layer'. *PhD thesis, University of Southampton*. [Available from Dept of Oceanography, Southampton SO9 5NH Hampshire, England.]

Nieuwstadt, F.T.M., 1981, 'The Steady State Height And Resistance Laws Of The Nocturnal Boundary Layers: Theory Compared With Cabauw Observations', *Bound. Layer Meteor.*, 20, pp 3-17.

Nieuwstadt, F.T.M., 1985, 'A Model For The Stationary, Stable Boundary Layer', in *J.C.R. Hunt (ed.), Turbulence and Diffusion in Stable Environment*, Claredon Press, Oxford, pp 149-179.

Orlanski, I., 1975, 'A rational subdivision of scales for atmospheric processes', *Bull. Amer. Meteor. Soc.*, 56, pp 529-530.

Panofsky, H.A., Dutton, A.J., 1984, 'Atmospheric turbulence', *Wiley & Sons*, 397 pp.

Peltier, W.R., Clark, T.L., 1979, 'The evolution and stability of finite-amplitude mountain waves. Part II: Surface wave drag and severe downslope windstorms', *J. Atmos. Sci.*, 36, pp 1498-1529.

Perret, R., 1987, 'Une classification des situations météorologiques à l'usage de la prévision', *Publications de l'ISM*, cahier no. 46.

Prandtl, L., 1942, 'Führer durch die Strömungslehre', Braunschweig, F. Vieweg & Sohn.

Queney, P., 1948, 'The problem of airflow over mountains: A summary of theoretical studies', *Bull. Amer. Meteor. Soc.*, 29, pp 16-26.

Queney, P., Corby, G.A.:, Gerbier, N., Koschmieder, H., Zierep, J., 1960, Technical Note N° 34 : 'The Airflow over mountains', *WMO- N° 98*. TP.43, Geneva, Switzerland, 135 pp.

Raithby, G. D., Stubley, G. D., Taylor, P. A., 1987, 'The Askervein Hill Project: A Finite Control Volume Prediction Of Three-Dimensional Flows Over The Hill', *Boundary Layer Meteorol.*, 39, pp 247-267.

Ratto, C.F., Festa, R., Nicora, O., Mosiello, R., Ricci, A., Lalas, D.P., Frumento, O.A., 1990, 'Wind Filed Numerical Simulation: a new user friendly code', in W. Palz, editor, Resource Assessment. European Community Wind Energy Conference, H.S. Stephens & Assoc., Madrid.

Rebuffet, P., 1969, 'Aérodynamique expérimentale', *Tome I, Dunod*, Paris.

Rhie, C.M., Chow, W.L., 1983, 'Numerical study of the turbulent flow past an airfoil with trailing edge separation', *AIAA J1*, 21, pp 1527-1532.

Salmon, J. R., Bowen, A. J., Hoff, A.M., Johnson, R., Mickle R. E., Taylor, P.A., Tetzlaff, G., Walmsley, J. L., 1988, 'The Askervein Hill Project: Mean Wind Variations At Fixed Heights Above Ground', *Boundary Layer Meteorol.*, 43, pp 247-271.

Salmon, J.R., Walmsley J.L., 1997,'Testing a correlation model for wind speed and direction estimates', *Proceedings 2nd European and African wind energy conference*, Genova, Italy.

Schär, C. and Durran D. R., 1997, 'Vortex formation and vortex shedding in continously stratified flows past isolated topography'. *J. Atmos. Sci.*, 54, pp. 534-554.

Schlichting, H., 1968, 'Boundary-Layer Theory', *Mc-Graw Hill*, London.

Schüepp, M., 1979,'Witterungsklimatologie', *Beiheft zu den Annalen der Schweizerischen Meteorologischen Anstalt* (Jahrgang 1978), SMA, Zürich.

Scorer, R.S., 1949, 'Theory of waves in the lee of mountains' *Quart. J. Roy. Meteorol. Soc.*, 75, pp 41-56.

Sheinmann, Y. & Rosen, A., 1992, 'A dynamical model of the influence of turbulence on the power output of a wind turbine', in *J. Wind Eng. and Ind. Aero.*, 39, pp 329-341.

Shir, C.C., 1972, 'A numerical computation of air flow over a sudden change of surface roughness', *Jour. Atmos. Sci.*, 29, pp 304-310.

Smith, R.B., 1979, 'The influence of mountains on the atmosphere', *Adv. Geophys.*, 21, pp 87-230.

Stull, R.B., 1988, 'An introduction to boundary layer theory', *Kluwer academic Publishers*, 668 pp.

Taylor, P.A., Teunissen, H. W., 1987, 'The Askervein Hill Project: Overview And Background Data', *Boundary Layer Meteorol.*, 39, pp 15-39.

Tennekes, H., 1982, 'Similarity relations, scaling laws and spectral dynamics', in *Atmospheric Turbulence and Air Pollution Modelling*, eds F.T.M. Nieuwstadt and H. Van Dop, pp 37-68, Reidel, Dordrecht.

Teunissen, H. W., Schokr, M. E., Bowen, A. J., Wood, C. J., Green, D. W. R., 1987, 'The Askervein Hill Project: Wind Tunnel Simulations At Three Length Scales', *Boundary Layer Meteorol.*, 40, pp 1-29.

Thunis, P., 1995, 'Formulation and Evaluation of a Nonhydrostatic Vorticity-mode Mesoscale Model', Joint Research Centre, European Commission, Environm. Inst., Report EUR 16141 EN, 151 pp.

Tombrou, M., Lalas, D.P., 1990, 'A telescoping procedure for local wind energy: potential assessment', in W. Palz, editor, Resource Assessment. European Community Wind Energy Conference, H.S. Stephens & Assoc., Madrid.

Traci, R.M., Phillips, G.T., Patnaik, P.C., Freeman, B.E., 1977, 'Development of a wind energy site selection methodology', Technical Report, RLO/2440-11, NTIS U.S. Dept. of Energy.

Tripoli, G. J., Cotton, W.R., 1982, 'The Colorado State University three dimensional cloud/mesoscale model. Part 1 : General theoretical framework and sensitivity experiments', J. Rech. Atmos.,16, no3, pp 185-219.

Troen, I., De Baas, A., 1986, 'A spectral diagnostic model for wind flow simulation in complex terrain', Proc. European Wind Energy Assoc. Cont. and Exhibition, Rome, Italy, pp 243-249.

Troen I., Petersen E.L., 1989, 'European Wind Atlas,' *Risø National Laboratory*, Roskilde, Denmark, 656 pp.

US Standard Atmosphere Supplements, 1966, US Government Printing Office, Wash. DC.

Van Doormal, J.P., Raithby, G.D., 1984, 'Enhancement of the SIMPLE method for predicting incompressible fluid flows', *Numer. Heat Transfer*, 7, pp 147-163.

Van Dyke, M., 1975, 'Perturbation Methods in Fluid Mechanics (annotated edition)', *The Parabolic Press*, Stanford, CA, 271 pp.

Walmsley, J. L., Salmon, J.R., 1984, 'A Boundary-Layer Model For Wind Flow Over Hills: Comparison Of Model Results With Askervein '83 Data', in *Proceedings European Wind Energy Conference*, Hamburg, October 1984.

Walmsley, J.L., Taylor, P.A., Keith, T., 1986, 'A Simple Model of Neutrally Stratified Boundary-Layer Flow Over Complex Terrain With Surface Roughness Modulations (MS3DJH/3R)', Bound. Layer Meteorol., 52, 259-281.

Walmsley, J. L., Taylor, P. A., 1995, 'Boundary-Layer Flow over Topography: Impacts of the Askervein Study', *Boundary Layer Meteorol.*, 78, pp 291-320.

Wieringa, J., 1986, 'Roughness dependent geographical interpolation of surface wind speed averages', *Quart. J. Roy. Meteorol. Soc.*, 112, pp 867-889.

Wilcox, D.C., 1995, 'Perturbation Methods In The Computer Age', *DCW Industries*, 5354 Palm Drive, La Canada, California, 224 pp.

Wippermann, F., 1973, 'The planetary boundary layer' *Deutscher Wetterdienst*, Offenbach.

Wippermann, F., 1981, 'The applicability of several approximations in meso-scale modelling- A linear approach', *Contrib. to Atmosph. Phys*., 54, 2, pp 298-308.

Wood, D.H., 1982, 'Internal boundary layer growth following a step change in surface roughness elements of varying geometry', *Bound. Layer Meteorol*., 22, pp 241-244.

Woods, J.C., Watson, S.J., 1997, 'A new matrix method of predicting long-term wind roses with MCP', *J. Wind. Eng. Industr. Aerodyn*., 66, pp 85-94.

Wyngaard J.C., Coté O.R., Rao, K.S., 1974, 'Modelling the atmospheric boundary layer', *Advances in Geophys*., 18a, pp 193-211.

Yamada, T., 1975, 'On the similarity functions A, B and C of the Planetary Boundary Layer', *Jour. Atmos. Sci*., 33, pp 781-793.

Zeman, O., Jensen, N.O., 1987, 'Modification of turbulence characteristics in flow over hills', *Quart. J. Roy. Meteorol. Soc*., 113, pp 55-80.

Zilitinkevich, S.S., Laikhtman, D.L., Monin, A.S., 1967, 'Dynamics of Atmospheric Boundary Layer', *Izv. Akad. Nauk SSSr, Fisika Atmosfery I Okeana*, 3, pp 287-333.

Zilitinkevich S.S., 1989, 'Velocity Profiles, The Resistance Law And The Dissipation Rate Of Mean Flow Kinetic Energy In A Neutrally And Stably Stratified Planetary Boundary Layer', *Bound. Layer Meteorol*., 46, pp 367-387.

Zilitinkevich S.S., Mironov, D.V., 1996, 'A Multi-Limit Formulation For The Equilibrium Depth Of A Stably Stratified Boundary Layer', *Bound. Layer Meteorol*., 81, pp 325-351.

Zilitinkevich S.S., Johansson P.-E., Mironov D.V., Baklanov A., in press, 'An Analytical Similarity Theory Model For Wind Profile And Resistance Law In Stably Stratified Planetary Boundary Layers', *J. Wind. Eng. Industr. Aerodyn*.

Appendix A

A Boundary layer growth over a 2D flat plate for neutral atmospheric conditions (without including the Coriolis force)

In the following Sections A.1 to A.3, simulation results are shown for the development of a two-dimensional neutral boundary layer over flat terrain. The idea behind the various tests performed in this part was to check the implementation of the ground roughness using the wall treatment presented in Section 5.1.2 for both smooth and rough terrain conditions.

Local drag coefficients and boundary layer height obtained with an incoming uniform velocity profile have been compared to experimental results available from the literature (Rebuffet, 1969, and Wood, 1982).

The wind speed profiles obtained with the model for both smooth and rough ground surfaces have been compared to two analytical formulations:

- One given by Coles (1956) valid for profiles developing over a smooth surface
- One proposed by Alexandrou (1996) (see Appendix I), which has the advantage of being able to reproduce profiles developing over both smooth and rough surfaces.

And finally, simulation results with a non-uniform roughness distribution were compared to Bradley's measurements for smooth-to-rough and rough-to-smooth transitions (Bradley, 1968).

A.1 Smooth plate with incoming uniform wind profile

The growth of a neutral turbulent boundary layer over a flat plate simulated by the numerical model has been compared to theoretical and experimental results. For this purpose, 2D simulations were performed with a computational domain similar to the one presented in Figure A.1. The horizontal length of the domain L_x was of 1000 m, separated into 100 elements of increasing size which follows a geometric progression with a factor of 1/0.95. The vertical length L_y was 200 m and was divided into 20 elements, with element's size also varying according to a geometric progression. The latter progression is given by a factor 1.44.

As boundary conditions at the domain entrance, we fixed a uniform wind speed profile with $U(z) = U_\infty = 5\,\text{m/s}$. For the turbulence variables we assumed a low turbulence level, setting k and ε to 10^{-4}, the default model values.

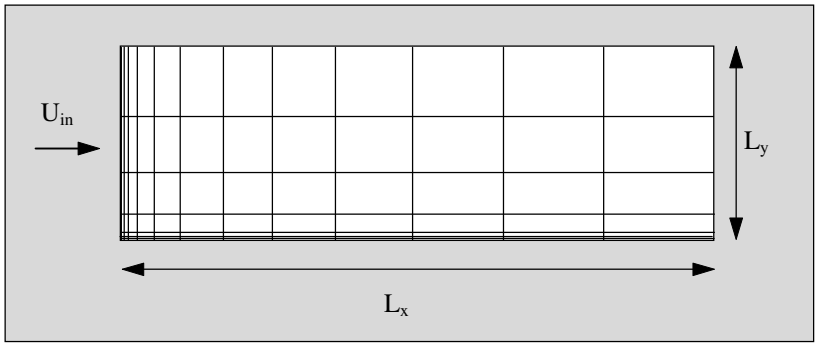

Figure A.1. 2D computational domain used to simulate the boundary layer growth.

A.1.2 Local drag coefficient

For a turbulent boundary layer developing over a flat plate without horizontal pressure gradients, von Karman gives the following semi-empirical expression for the evolution of the local drag coefficient C_f as a function of R_x the Reynolds number along the main flow direction:

eq. A.1 $C_f = 0.059 \cdot R_x^{-0.2}$ (for $R_x < 5 \cdot 10^6$)

with the definitions

eq. A.2 $C_f = \tau / (\frac{1}{2} \rho U_\infty^2)$ and

eq. A.3 $R_x = U_\infty x / \nu$

This behaviour for C_f has been empirically verified for Reynolds number up to $5 \cdot 10^6$ (Rebuffet, 1969).

From other theoretical calculations von Karman derived an implicit formulation for C_f which reads:

eq. A.4 $$\frac{1}{\sqrt{C_f}} = 1.7 + 4.15 \cdot \log_{10}(R_x C_f)$$

Instead of the implicit expression for C_f, Michel proposed an explicit relationship of the form

eq. A.5 $C_f = 0.0368 \cdot R_x^{-1/6}$

which also compares well to experimental results (c.f. Rebuffet (1969), p. 102).

For a uniform incoming wind profile given by $U(z) = U_\infty = 5$ m/s, the local drag coefficient at ground obtained by the numerical simulation has been plotted versus R_x and compared to the explicit relationships given by von Karman and Michel (Figure A.2).

As can be seen from Figure A.2, the model results compare very well with both formulations for Reynolds numbers between $5 \cdot 10^5$ and $5 \cdot 10^6$. For higher Reynolds numbers, above which the von Karman formulation (eq. A.1) is no longer verified, the model results conform well to the formulation given by Michel (eq. A.5). The underestimation of the local drag coefficient for Reynolds numbers smaller than $5 \cdot 10^5$ is not a problem as such. As explained in Schlichting (1968), the expressions given above for the local drag coefficient are valid with the assumption that the flow is turbulent at the entrance of the simulation domain already. With the default values for the turbulent variables set at the model inlet, the incoming flow is laminar and changes downstream to a turbulent flow. The distance at which the transition occurs depends on the turbulence intensity of the incoming flow.

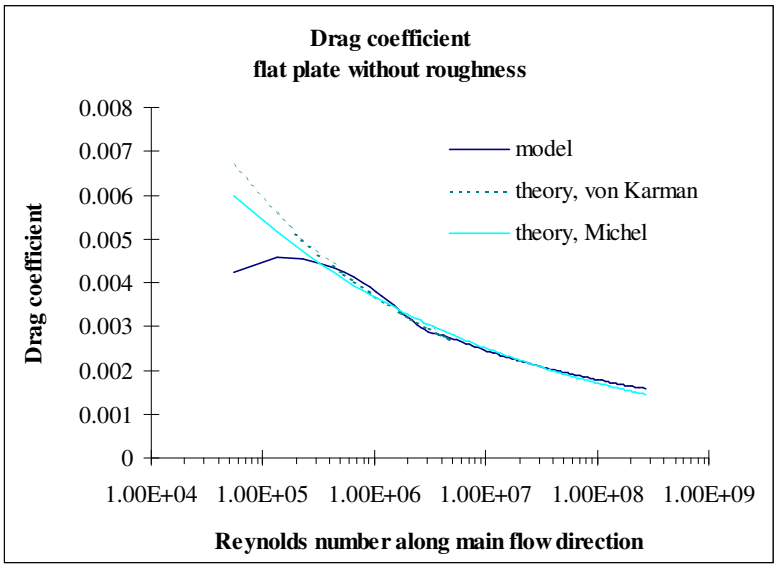

Figure A.2. Comparison of the local drag coefficient obtained from the simulation with empirical formulations.

A comparison of the model simulated drag coefficient with the implicit relationship (eq. A.4) proposed by von Karman was also done. For that purpose, the behaviour of both $\sqrt{C_f}$ and $(1.7+4.15 \cdot \log_{10}(R_x C_f))^{-1}$ were plotted in Figure A.3.

For values of R_x larger than $5 \cdot 10^6$ both curves compare very well, hence verifying the implicit relationship eq. A.4. For $5 \cdot 10^5 < R_x < 5 \cdot 10^6$ there is still a reasonable agreement between both curves, but the agreement starts really to break down for values of R_x lower than $5 \cdot 10^5$, for the same reason as mentioned above.

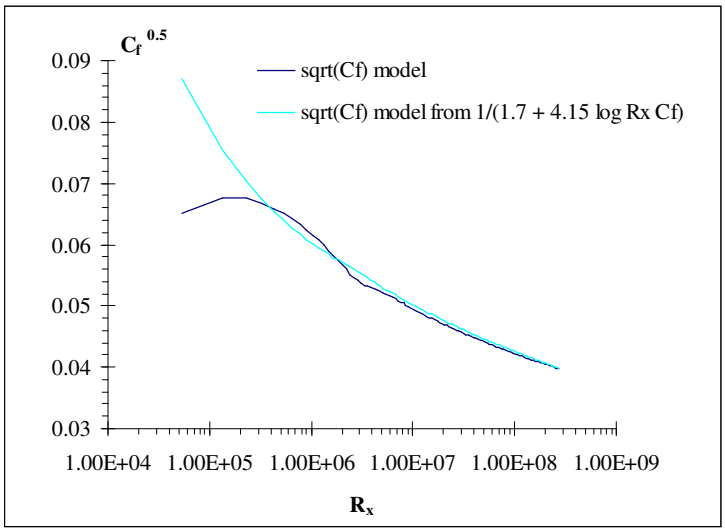

Figure A.3. Comparison of the right and left-hand side terms appearing in the implicit equation (eq. A.4) for $\sqrt{C_f}$ obtained by the model[M3].

A.1.2 Velocity profiles

The velocity profiles resulting from the simulation of a neutral flow over a smooth plate without pressure gradients have been compared to the analytical formulations presented by Coles (1956) and by Alexandrou (1996). Both formulations were proven to reproduce experimental results. The Coles formulation is reproduced below, while Alexandrou's formulation is given in Appendix I.

A.1.2.1 Coles formulation

When representing the boundary layer wind speed profile by an analytical expression, the distinction is usually made between the **internal region** of the boundary layer, where the profile verifies the so-called law of the wall, and the **external region**, where the profile is given by a velocity defect law.

For the **internal region**, the theoretical non-dimensional velocity profile in the logarithmic region follows the relationship

eq. A.6 $$u^+ = \frac{1}{\kappa} \ln y^+ + C$$

with the non-dimensional wind speed $u^+ = \frac{u}{u_*}$ and the non-dimensional distance from the wall $y^+ = \frac{y \cdot u_*}{\nu}$.

Formulated in terms of the wall variables, the above relationship becomes (Cousteix, 1989):

eq. A.7 $$u = U_\infty \cdot \sqrt{\frac{C_f}{2}}\left(\frac{1}{\kappa}\ln\left[\frac{yU_\infty}{\nu}\cdot\sqrt{\frac{C_f}{2}}\right]+C\right)$$

with $C = 5$, $\kappa = 0.4$ (von Karman constant) and U_∞ the free stream velocity.

In the **external region**, the velocity profile is expressed in the form of a velocity defect law, such as:

eq. A.8 $$\frac{U_\infty - u}{u_*} = \phi(\eta) \qquad \eta = \frac{y}{h}$$

where *h* stands for the boundary layer height.

Assuming the existence of the logarithmic region, Coles (1956) proposed a velocity defect profile of the form

eq. A.9 $$\phi(\eta) = -\frac{1}{\kappa}\ln(\eta) + \frac{B'}{\kappa}(2 - \varpi(\eta))$$

From a systematic comparison with experimental results, Coles retains the following formulation for ϖ :

eq. A.10 $$\varpi = 1 - \cos(\pi\eta)$$

The parameter B' is not a universal constant. It is related to the local drag coefficient C_f and the boundary layer height h. Considering that for the limit $\eta \to 0$, the defect law must correspond to the logarithmic law, the following relationship between B', C_f and h can be derived:

eq. A.11 $$\frac{U_\infty}{u_*} = \left(\frac{C_f}{2}\right)^{-1/2} = \frac{1}{\kappa}\ln\left(\frac{u_* h}{\nu}\right) + C + \frac{2B'}{\kappa}$$

Assuming that eq. A.11 is verified, then the velocity defect law (eq. A.8) is only a function of the boundary layer height h and friction velocity u_* (or drag coefficient C_f).

The simulated velocity profiles were fitted to the velocity defect law (eq. A.8). Since we used the drag coefficient C_f calculated by the model, the only parameter remaining to be fitted is the boundary layer thickness h. Repeating the fit for several distances downwind of the entrance of the computational domain gave the boundary layer heights shown in Table A.1. The values of B' inferred from eq. A.11 were also reported. These increase with the downstream distance *x*, reaching a value of 0.5 for the largest *x*'s.

Figure A.4 shows two velocity profiles obtained from the numerical simulation (isolated symbols) at the arbitrary distnaces *x=205 m* and *x=926 m*. The logarithmic profile (eq. A.6) as well as the best fit for the velocity defect law have also been plotted for

comparison. The agreement between the simulation results and the theoretical formulation given by Coles is very good.

Table A.1. Boundary layer thickness h and B' values resulting from fitting profiles at varying distances with the velocity defect law.

Downstream distance [m]	*boundary layer thickness [m]*	*B'*
12	0.225	0.414
102	1.39	0.459
205	2.53	0.495
498	5.73	0.502
793	8.71	0.498
926	9.84	0.502

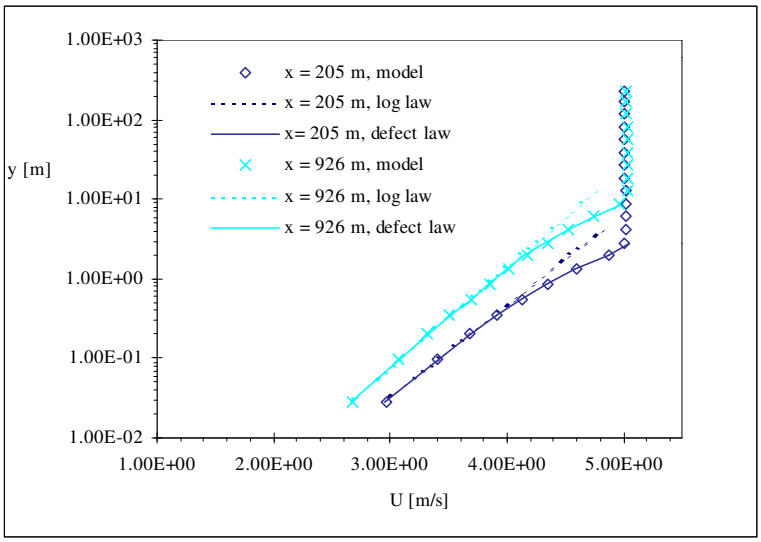

Figure A.4. U velocity profiles for a boundary layer developing over a smooth surface. Model calculated profiles are compared to the logarithmic and velocity defect law.

In addition to the comparison with the Coles profiles, we also compared the simulated profiles for the smooth case with the formulation proposed by Alexandrou (Appendix I). In the latter, the parameters to be varied during the fit are the boundary layer thickness h and the constant c[1]. For the friction velocity u_*, we used the value calculated by the numerical model. The parameters values resulting from the fitting procedure at the fetch *x=205 m* and *x=926 m* are presented in Table A.2, together with the values of *a, c* and *B* obtained by Alexandrou when fitting Klebanoff's measurements on a flat smooth plate. Comparing both sets of values shows that we obtain a constant *c*, which exceeds by 10% the one given by Alexandrou. This difference is probably due to the fact that when

[1] See Appendix I for the definition of the three constants *a, c* and *B* appearing in the Alexandrou formulation.

fitting Klebanoff's data, Alexandrou had the friction velocity as an additional parameter to be fitted, whereas in our case, it is given by the numerical model result. Considering that a change of 1% in the friction velocity implies a change of 3% in the value of the constant c obtained from the fit, the difference of 10% between both values can easily be explained by a difference in the friction velocity.

One can note that the boundary layer height obtained with Alexandrou's formulation are higher than the one resulting from the fit using the Coles velocity defect law (see Table A.1 and Table A.2). The approximation in eq.I.6 proposed for B is verified to within 5%.

A comparison of the simulated and analytical wind speed profile is given in Figure A.5, which shows that the analytical formulation given by Alexandrou is also very appropriate to represent the model results.

Table A.2. Parameters resulting from fitting the model calculated profiles with Alexandrou's formulation at the downstream distances *x=205 m* and *x=926 m.*

	x=205 m	*x=926 m*	*Alexandrou's results fitting Klebanoff's measurements for a smooth plate*
c (varied during fit)	0.183	0.183	0.166
$a = 1/c$	5.453	5.453	6.022
h (varied during fit)	3.193 m	12.446 m	
B (calculated from eq.I.2)	9.873	11.15	7.326
B (expected from eq.I.6)	9.549	10.82	
u_* (from the model)	0.155	0.142	

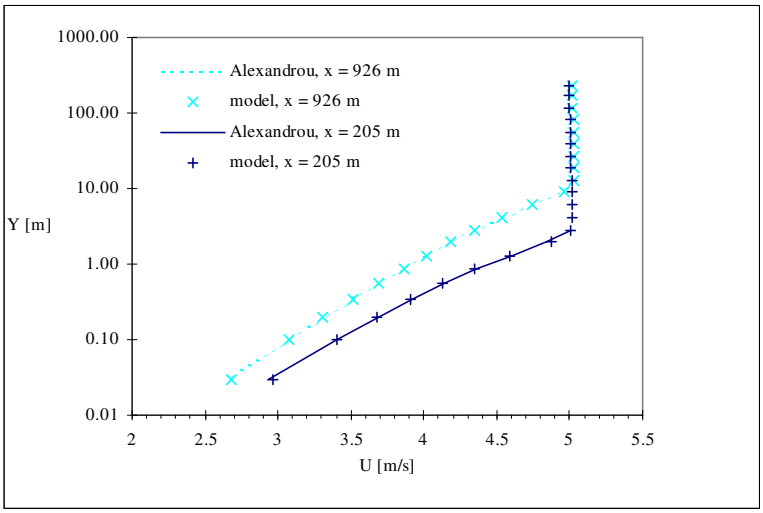

Figure A.5. u velocity profiles for a boundary layer developing over a smooth surface. Model calculated profiles are compared to Alexandrou's formulation for the downstream distances *x=205 m* and *x=926 m*.

A.1.3 Boundary layer height

For a zero pressure gradient boundary layer development over smooth terrain, von Karman established the following relationship for the boundary layer height h, which is defined as the height at which $u(h) = U_\infty$:

eq. A.12 $$h = 0.38 \cdot x \cdot \sqrt{C_f}$$

Figure A.6 presents the boundary layer height versus the horizontal Reynolds number. The continuous line is for the von Karman relationship. The values for h resulting from fitting the velocity defect law is represented by triangles, while crosses are used for the boundary layer height obtained from fitting Alexandrou's formulation. Again, the agreement between the model values and the von Karman formulation is very good. It is even better when the boundary layer height is established by fitting the simulated profiles with Alexandrou's formulation.

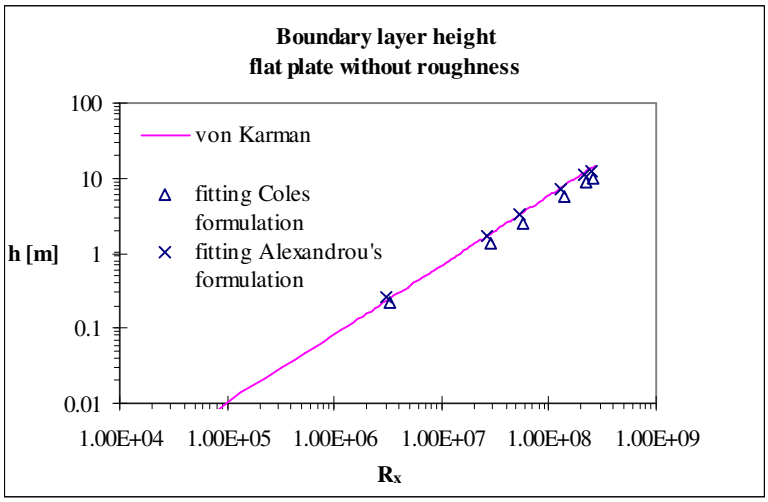

Figure A.6. Comparison of the boundary layer heights obtained by fitting the velocity defect law and Alexandrou's formulation with the von Karman relationship.

A.2 Rough plate with incoming uniform wind profile

Similar simulations with uniform incoming velocity profiles have been performed for a rough surface. The ground roughness was introduced by modifying the wall multiplier T_M according to the treatment presented in Section 5.1.2 setting a fixed value for the roughness length z_0.

A.2.2 Drag coefficient

Extending the experimental results obtained by Nikuradse for flows in rough pipes to the case of a rough plate, Schlichting (1968) gave the following interpolation formula for the local drag coefficient in terms of the equivalent sand roughness k_s:

eq. A.13 $$C_f = \left(c_{n1} + c_{n2} \cdot \log \frac{x}{k_s} \right)^{-2.5} \quad \text{with } c_{n1} = 2.87 \text{ and } c_{n2} = 1.58$$

The above expression is valid for $10^2 < x / k_s < 10^6$.

The equivalent sand roughness is inferred using the fact that, in the logarithmic region, the relationship given by Nikuradse

eq. A.14 $$\frac{u}{u_*} = \frac{1}{\kappa} \ln \frac{y}{k_s} + B_N$$

must represent the same profile as given by

eq. A.15 $$\frac{u}{u_*} = \frac{1}{\kappa} \ln \frac{y}{z_0}$$

This requires that k_s and z_0 obey

eq. A.16 $$k_s = z_0 \exp(\kappa B_N)$$

The constant B_N assumes different values, depending on the range of roughness. For the completely rough regime ($\frac{k_s u_*}{\nu} > 70$), Nikuradse's experiments show that $B_N = 8.5$.

The drag coefficient resulting from three simulations with the roughness lengths $z_0 = 0.02m$, $z_0 = 0.002m$ and $z_0 = 0.00002m$ is shown in a log-log representation versus the Reynolds number R_x in Figure A.7 (continuous lines). For comparison, the values of C_f obtained from the interpolation formula eq. A.13 are also presented (dashed lines). For the lower value of the ground roughness ($z_0 = 2 \cdot 10^{-5} m$), the simulated drag coefficient could be reproduced by eq. A.13 without any modifications, whereas for the rougher simulations, the constant c_{n1} needed to be changed to $c_{n1} = 3.3$ so that the simulations and analytical expressions agree. Considering that eq. A.13 was obtained using experimental results that were performed with low roughness conditions, and since the model reproduced the behaviour of the drag coefficient for low roughness values, we do not consider this different behaviour between the model results and analytical expression to be a problem. It would however be interesting to do a comparison with data obtained for higher roughness conditions.

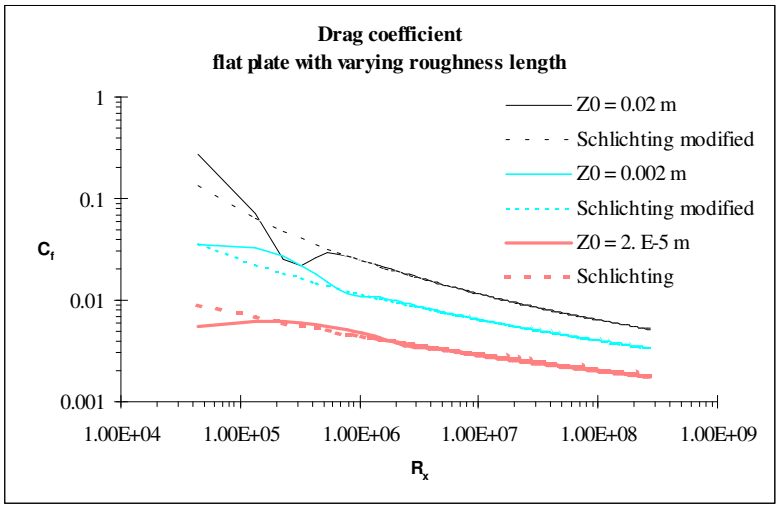

Figure A.7. Local drag coefficient for simulations performed at varying roughness lengths, compared to the interpolation formula eq. A.13 given by Schlichting (1968).

A.2.3 Velocity profiles

Concerning the velocity profiles, the same fitting operation as for the smooth case was repeated, using the formulation given by Alexandrou. For a roughness length of 0.02 m, an example of a simulated profile at the downstream distance $x=926\ m$ is presented in Figure A.8, together with the best fitting profile. For comparison, the logarithmic profile for the corresponding roughness length and friction velocity is also plotted. The agreement between the simulated and logarithmic profiles in the logarithmic region shows that the ground roughness is correctly taken into account.

The parameters resulting from fitting the profile at the fetch $x=926\ m$, for varying roughness lengths, are given in Table A.3. One can observe that the value of c (and hence a as well) varies only slowly from one simulation to the other. Whether these constants should effectively be constant for any boundary layer with zero pressure gradient or not is not yet clear. At this point one should mention that the small variation observed in c might be due to the fact that we do not exactly have a zero pressure gradient in the simulations. In fact, we can observe a slight increase in the free stream velocity due to uniform velocity profile at the entrance of the simulation domain and the momentum decrease in the boundary layer. For each of the simulations, the value of

eq. A.17
$$\beta = -\frac{h}{u_*}\frac{\partial U_\infty}{\partial x}$$

has been reported. Though not exactly 0, the values of β remain small, so that we can consider that the zero pressure gradient assumption is valid.

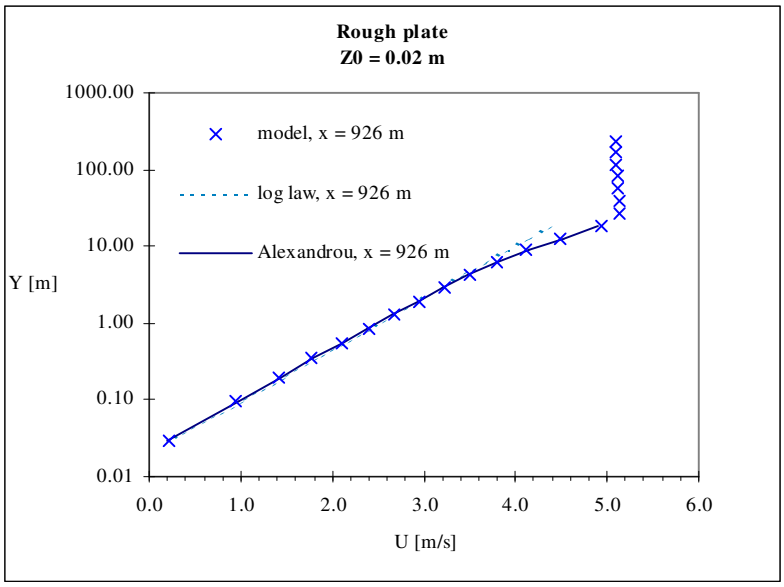

Figure A.8. U velocity profile for a boundary layer developing over a rough surface with $z_0 = 0.02m$. Model calculated profile at $R_x = 2.6 \cdot 10^8$ is compared to the log law and Alexandrou's formulation.

The change in the surface roughness strongly affects the boundary layer height h and the parameter B. Using eq.I.5 the roughness length resulting from the best fit has also been recalculated. As can be seen from the values given in Table A.3, the best-fit profiles exhibit a roughness length which slightly overestimates the roughness length introduced for the ground parameterisation. The overestimate decreases with increasing ground roughness, with an overestimate of about 25 % for a z_0 of 2. 10^{-5} m down to 5% for a z_0 of 0.02 m.

Table A.3. Parameters resulting from fitting the model calculated profiles with Alexandrou's formulation at *x=926 m* for varying roughness lengths.

	z_0=0.00002 m x=926m	z_0=0.002 m x=926 m	z_0=0.02 m x=926 m
c (varied during fit)	0.182	0.184	0.184
$a = 1/c$	5.49	5.44	5.44
h [m] (varied during fit)	13.34	21.24	28.63
B (calculated from eq.I.2)	10.58	6.55	4.62
z_0 (expected from eq.I.5	2.53 10^{-5}	0.0023	0.0212
u_* (from the model)	0.148	0.210	0.263
$\beta = -h/u_* \cdot \partial U_\infty / \partial x$	-3.61 10^{-3}	-8.09 10^{-3}	-1.41 10^{-2}

A.2.4 Boundary layer height

Some studies have attempted to include the effect of the roughness length (or roughness change) in the boundary layer development. Shir (1972) starting from the proportionality relationship $h \propto x^{0.8}$ which is applicable for the smooth case (see Schlichting, chap 21) proposed the following expression in the case of a roughness change:

eq. A.18 $$h = f_1(z_{01}/z_{02})x^{0.8+f_2(z_{01}/z_{02})}$$

Similarly and to be consistent with the observation we made in Figure A.6 that the boundary layer height obtained with CFX4 for the smooth case behaves more like $h \propto x^{0.92}$ (see eq. A.12 and eq. A.5), we tried a formulation of the type

eq. A.19 $$h(z_0) = f_1(z_0)x^{0.92+f_2(z_0)}$$

with the functions $f_1(z_0) = c_1 \cdot z_0^{0.2}$ and $f_2(z_0) = -\frac{1}{c_2}\ln(\frac{z_0}{z_{0s}})$. In the former, z_{0s} represents the default model smooth ground condition, whereas z_0 would be the one specified for a rough ground. The boundary layer heights obtained by the model for the three different roughness lengths are plotted versus R_x in Figure A.9. The isolated points are the values obtained by fitting the simulated profiles with Alexandrou's formulation, while the dashed lines represent the behaviour given by eq. A.19 with values of $c_1 = 0.27$, $c_2 = 85$ and $z_{0s} = 1 \cdot 10^{-6}$. In addition to being able to reproduce the model results in a satisfactory way, eq. A.19 also agrees fairly well with the relationship $h \propto z_0^{0.2}x^{0.8}$ suggested by Wood (1982).

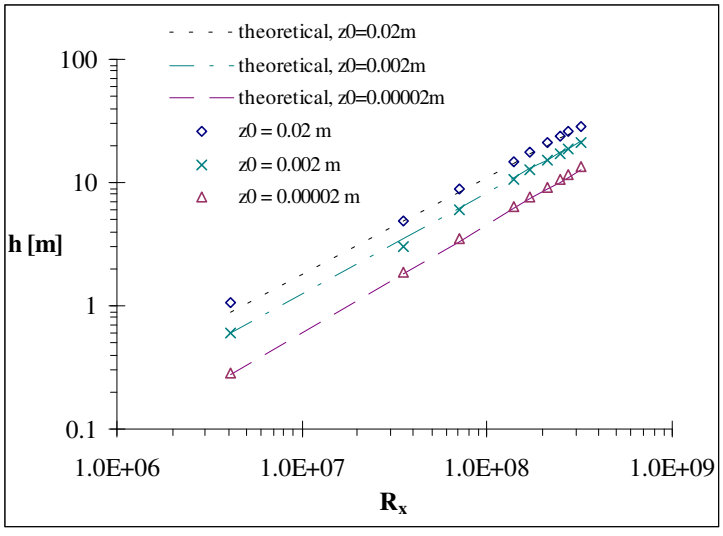

Figure A.9. Boundary layer height versus Reynolds number in the flow direction for three different roughness lengths. Point values are obtained from fitting the model-simulated profiles with Alexandrou's formulation. Continuous lines represent the behaviour expected from eq. A.19.

A.3 Roughness change- comparison with Bradley's experiments

From the results presented above, it appears that the ground treatment is appropriate to simulate the behaviour of a neutral boundary layer over smooth or rough terrain. The next step was to check the model behaviour in the presence of a roughness change. The following experiment was designed to compare the model results with the measurements reported by Bradley (1968), who performed a series of experiments on a little-used air field located in New South Wales. He measured a variation of the surface shear stress as well as velocity profiles downwind of a smooth to rough (resp. rough to smooth) transition. The surface shear stress was measured using drag plates. Bradley reports roughness lengths of 0.0025 m for the rough surface (spikes) and 0.00002 m for the smooth one (tarmac).

The computational domain we used to simulate the roughness transition has the same dimensions as the one used for the constant ground roughness (L_x=*1000 m*, L_y=*200 m*). The only difference with the previous domain is that we used a symmetric geometric progression for the element size in the horizontal direction, with a factor of 1.138. The roughness transition was applied exactly at the middle of the domain (*x=500 m*).

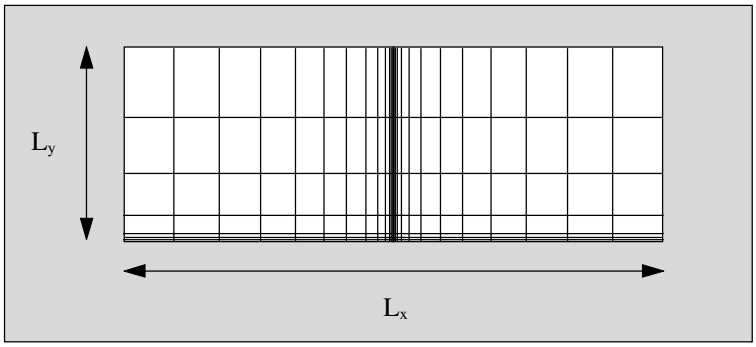

Figure A.10. 2D computational domain to simulate roughness change**.**

The wind speed profile at the entrance of the domain was set to follow the formulation presented by Alexandrou (1996), with a value of $c = 0.183$ and B was chosen so that the profiles of u, k and ε were in equilibrium with the roughness length specified in the first half of the domain.

Bradley presented results for the spatial variation of the shearing stress in the form of normalised shearing stress versus the horizontal distance (fetch) downwind of the roughness transition. He used the upwind value of the shearing stress (τ_s) to normalise his measurements. Figure A.11 presents the model predicted spatial variation of the normalised shearing stress (continuous line) compared to Bradley's measurements

(circles), for the case of a smooth to rough transition. Two simulations were done with $z_{0,r}=2.5\cdot10^{-3}$ m, the first one with $z_{0,s}=2.\cdot10^{-5}$ m and the second one with an even smaller value in the smooth part with $z_{0,s}=2.\cdot10^{-6}$ m. The same results for a rough to smooth transition are shown in Figure A.12.

Most of the spatial variation of the shearing stress occurs within 2-5 m downwind of the transition. For the smooth to rough transition, the model predicts an overshoot just after the roughness change for the ratio τ/τ_s. The overshoot is followed by a rapid decrease of τ/τ_s. A slight oscillation is visible around 1 m behind the transition with a local minimum appearing. Although Bradley suggests that such a minimum also appears in the measurements in the region of 2-3 m, the scatter in the observed values is too large to comment on the significance of this feature.

The slower recovery that could be seen in the case of a rough to smooth compared to a smooth to rough transition is also reproduced by the model.

Generally, for the smooth to rough transition, the results obtained with a roughness of $2.\cdot10^{-5}$ m for the tarmac surface slightly underpredict the observations, while with a value of $2.\cdot10^{-6}$ m the model slightly overpredicts them. For the rough to smooth case, the best agreement between the observations and simulation is obtained with $z_{0,s}=2.\cdot10^{-5}$ m.

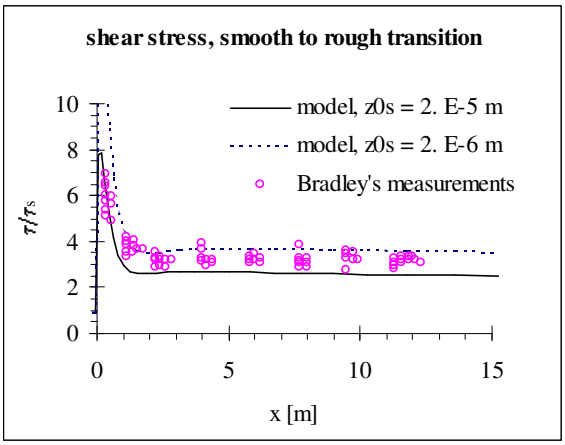

Figure A.11. Normalised shearing stress versus horizontal distance downwind of a smooth to rough transition. Continuous line: model results, circles: Bradley's measurements. ($z_{0,s}$ according to legend and $z_{0,r}=2.5\cdot10^{-3}$).

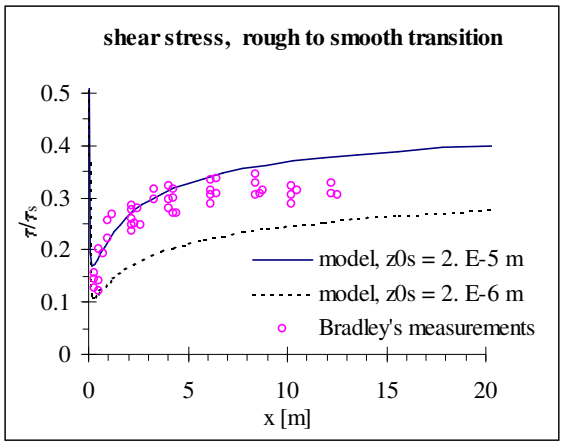

Figure A.12. Normalised shearing stress versus horizontal distance downwind of a rough to smooth transition. Continuous line: model results, circles: Bradley's measurements. ($z_{0,s}$ according to legend and $z_{0,r}=2.5\cdot10^{-3}$).

The development of the velocity profiles downwind of the roughness transition is presented in Figure A.13, for the case of a smooth to rough transition with $z_{0,s} = 2.\cdot 10^{-6}$ m and $z_{0,r} = 2.5\cdot 10^{-3}$ m. The profiles are normalised with the values at *z=209 cm*. Bradley's measurements are represented with isolated symbols, with the distance from the roughness transition indicated in the legend. Dashed lines stand for model results at the closest grid cells to the fetches where profiles were measured by Bradley. The logarithmic profiles obtained with a roughness length of $2.\cdot 10^{-6}$ m (continuous dark line) and $2.5\cdot 10^{-3}$ m (continuous light line) were also plotted. The comparison between the observations and model results shows a good agreement. Also, the height of the developing inner layer corresponds fairly well with Bradley's observations.

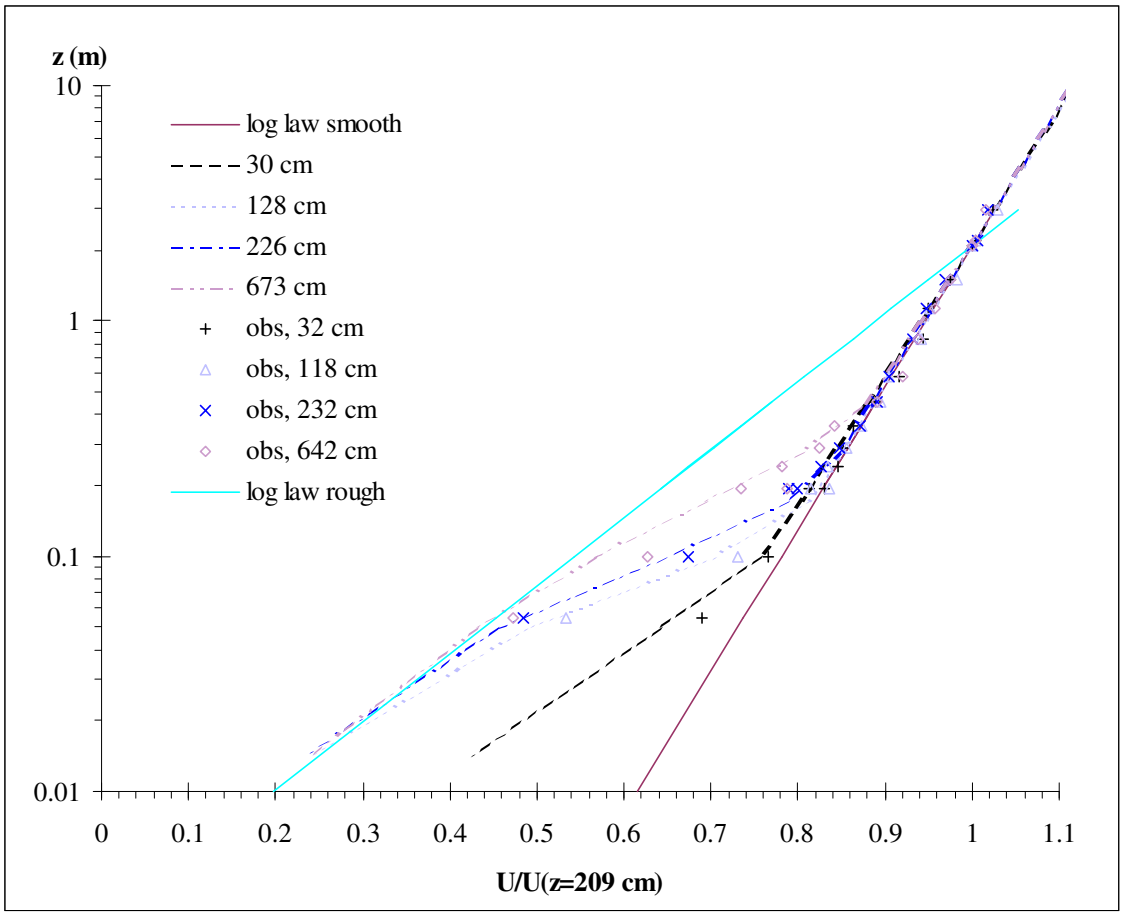

Figure A.13. Development of the velocity profiles downwind of a smooth to rough transition. Profiles are normalised with the wind speed at z=209 cm. Continuous lines: log law corresponding to the unperturbed profiles over smooth (dark) and rough terrain (light). Dashed lines: model results. Isolated symbols: Bradley's observations .

Note: This simulation presented above with $z_{0,s} = 2.\cdot 10^{-6}$ m gave better results than the one performed with $z_{0,s} = 2.\cdot 10^{-5}$ m. In the latter case, the profiles closest to the roughness transition could not be satisfactorily reproduced (c.f. Figure A.15).

The simulation results presented in Figure A.11 to Figure A.13 were obtained with the turbulence model constants that were suggested by Duynkerke (1988) for the $k-\varepsilon$ model, i.e. using C_μ= *0.034*, C_1=*1.46*, C_2=*1.83* and σ_ε=*2.38.* Using the default values decreased the ratio τ/τ_s within the first metre downwind of the roughness change, whereas it increased it for further distances downstream (Figure A.14). The maximum difference is reached at a fetch of 2.2 m downwind of the transition with an increase of 26% for τ/τ_s. Further downstream, this difference is reduced to 3-4% after 500m. The slight oscillation with the local minimum that appeared at about 1 m behind the roughness transition is more obvious when using the default model constants.

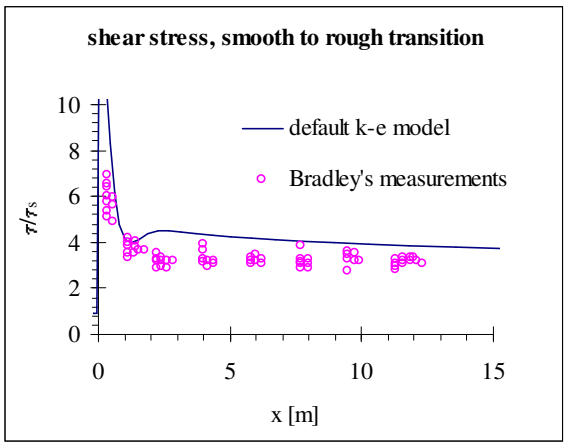

Figure A.14. Same as Figure A.11 using the default turbulence model constants assuming a roughness length of $2.\cdot 10^{-6}$ m for the tarmac and $2.5\cdot 10^{-3}$ m for the spikes.

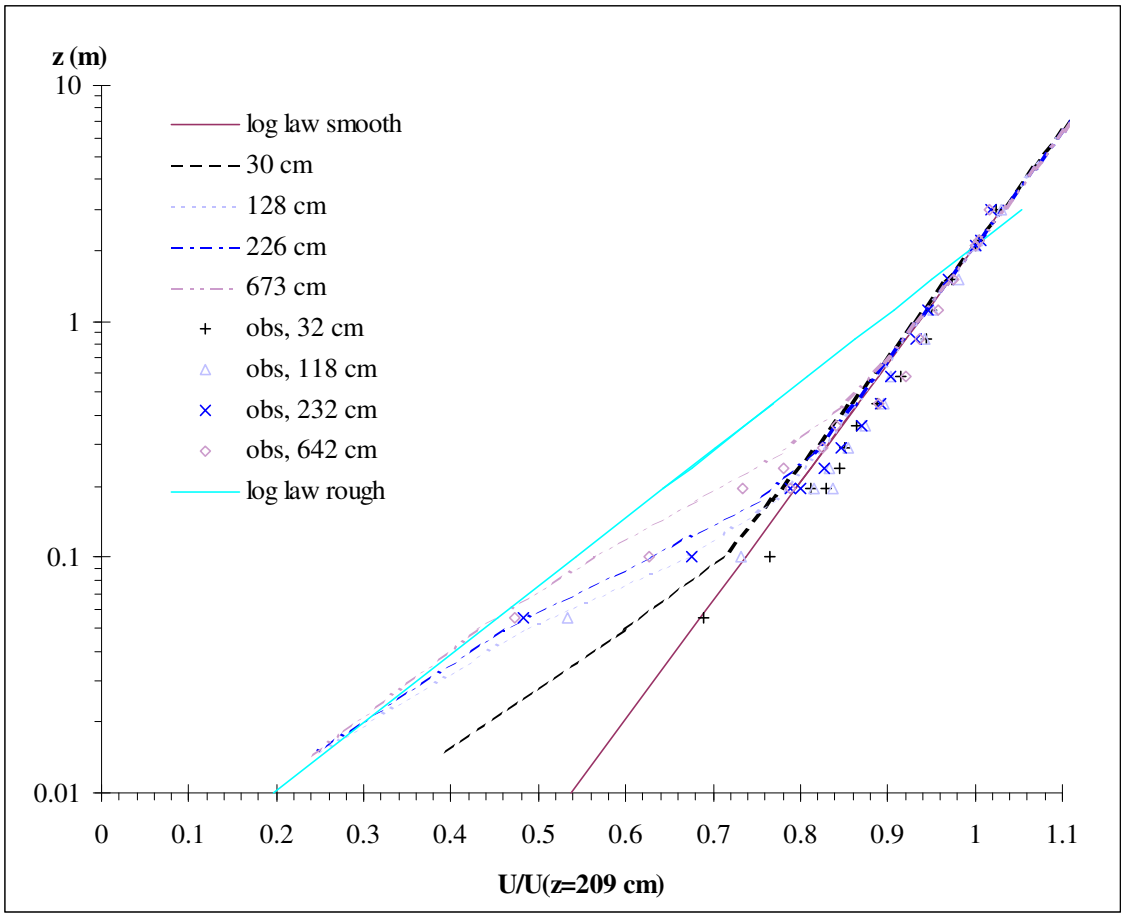

Figure A.15. Same as Figure A.13 for $z_{0,s} = 2.\cdot 10^{-5}$ and $z_{0,r} = 2.5\cdot 10^{-3}$.

Appendix B

B Boundary layer growth and Ekman spiral development over flat terrain

As presented in Section 5.2.2. some additional source terms were introduced in the $k-\varepsilon$ model to take into account the effect of the vertical stratification on the production/destruction of turbulent kinetic energy and dissipation rate. The Coriolis force was also added in the momentum equations for the u and v velocity components. (No effect of the Coriolis force was considered in the turbulence model).

To check that both implementations were done successfully, simulations of the boundary layer and Ekman spiral development were done over flat terrain, assuming horizontally uniform conditions (i.e., horizontal gradients $\partial/\partial x$ and $\partial/\partial y$ identically vanishing).

B.1 Test case definition

The simulation domain was a column with the dimensions 1x 1 x 9 km, consisting of 2x2x25 elements. Along the vertical, 25 elements were distributed according to a geometric progression (factor 1.35), the element closest to the ground having a height of 1.7 m, and the one closest to the top a height of 2335 m. To ensure that no horizontal gradients can be established, periodic boundary conditions were set for all the four lateral sides of the flow domain. The geostrophic wind speed G is assumed to be aligned with the x-axis. At the top boundary, the velocity components are set to $u = G$, $v = 0$ and $w = 0$.

The model is initialised with a uniform wind profile, also with $u = G$, $v = 0$ and $w = 0$. The initial turbulent kinetic energy is set to 1 and the initial dissipation rate to 0.3.

Various initial real temperature profiles were used, essentially to test the effect of the static stability in the free flow on the profile development.

The ground treatment presented in Section 5.2.2 is used for the velocity to specify the friction due to the ground roughness. The same treatment is applied for the potential temperature. When simulating neutral situations, the potential temperature flux through the ground was set to zero, whereas for stable/unstable situations, the potential temperature at ground was reduced/increased assuming a constant cooling/heating rate.

Section B.2 presents the development of the surface profiles for both wind speed and temperature for the neutral, stable and unstable cases. For all the three situations, comparisons with the Businger profiles are given.

The effect of the static stability in the free flow on the development of the entire boundary layer profiles was investigated for situations with zero heat flux through the ground. These results are presented in Section B.3 .

Considering that, starting with a uniform wind speed profile, several physical hours are required for the boundary layer to develop, it would be difficult with the present computational resources to perform similar simulations over real terrain, with a domain containing some 60000 to 100000 cells. On the other hand, the type of profiles set at the inlet boundaries can significantly affect the development of the flow solution inside the domain (see Appendix D). Consequently, we found that it would be most interesting to obtain analytical expressions for the profiles to be set as initial guesses and boundary conditions depending on the ground roughness, static stability of the free flow, and surface buoyancy flux. Such a parameterisation would be particularly useful when only sparse measurements are available to determine the situation to be simulated. An attempt to produce analytical expressions for the average u and v profiles exactly follows the formulation proposed by Zilitinkevich et al (in press) and is presented in Section B.4.

B.2 Surface profiles development

B.2.1 Monin-Obukhov similarity theory

In their similarity theory, Monin-Obukhov assume that any dimensionless characteristics of the turbulence in the buoyancy dominated surface layer can be expressed in terms of $u_*, z, g/\theta$ and $\overline{w'\theta'}$ (see e.g. Garratt, 1992). The effect of stratification in the description of turbulent transport and mean profiles can be represented through the non-dimensional height $\zeta = z/L$, where the Monin-Obukhov scaling length L is defined by:

eq. B.1
$$L = -\frac{u_*^3}{\kappa \frac{g}{\theta} \overline{w'\theta'}}$$

For the case where we take the x-axis along the mean surface wind direction, we get $v = 0$ in the surface layer. The non-dimensional gradient form of the u component profile can be written as:

eq. B.2 $$\frac{\kappa z}{u_*}\frac{\partial u}{\partial z} = \Phi_M(\zeta)$$

Note that for the neutral case limit ($|L| \to \infty$), we have $\Phi_M \to 1$, so that a logarithmic form of the wind speed profile is obtained, with

eq. B.3 $$u(z) = \frac{u_*}{\kappa}\ln(\frac{z}{z_0})$$

Similarly we have for the potential temperature:

eq. B.4 $$\frac{\kappa z}{\theta_*}\frac{\partial \theta}{\partial z} = \Phi_H(\zeta)$$

From the above expressions and using the flux gradient relationships

eq. B.5 $$\tau_x = -\rho\overline{u'w'} = -\rho u_*^2 = \rho \cdot K_M \frac{\partial u}{\partial z}$$

eq. B.6 $$\rho \cdot c_p \overline{w'\theta'} = \rho \cdot c_p u_* \theta_* = -\rho \cdot c_p K_H \frac{\partial \theta}{\partial z}$$

we get for the turbulent Prandtl number P_t:

eq. B.7 $$P_t = \frac{K_M}{K_H} = \frac{\Phi_H}{\Phi_M} = f(\zeta)$$

The analytical forms of the Φ functions have been extensively studied in the past using surface observations of wind speed and potential temperature profiles. These observations suggest the following expressions for Φ_M and Φ_H, for moderate ranges of ζ (c.f. Businger et al, 1971):

- for $-5 < \zeta < 0$ (unstable cases):

eq. B.8 $$\Phi_M(\zeta) = (1-\gamma_1\zeta)^{-1/4}$$

eq. B.9 $$\Phi_H(\zeta) = \alpha_2(1-\gamma_2\zeta)^{-1/2}$$

- for $0 < \zeta < 1$ (stable cases):

eq. B.10 $$\Phi_M(\zeta) = 1 + \beta_1\zeta$$

eq. B.11 $$\Phi_H(\zeta) = \alpha_2 + \beta_2\zeta$$

Evaluating the constants from observations, Businger et al (1971) give the following set:

eq. B.12 $\kappa = 0.35$, $\alpha_2 = 0.74$, $\beta_1 = 15$, $\beta_2 = 9$, $\gamma_1 = 4.7$ and $\gamma_2 = 4.7$

while Dyer (1974) proposes:

eq. B.13 $\kappa = 0.41$, $\alpha_2 = 1$, $\beta_1 = 16$, $\beta_2 = 16$, $\gamma_1 = 5$ and $\gamma_2 = 5$

Integration of the gradient forms of the wind and temperature profiles gives (see Garratt (1992) for an exact derivation):

eq. B.14 $$\frac{\kappa u}{u_*} = \ln(\frac{z}{z_0}) - \Psi_M(\zeta)$$

eq. B.15 $$\frac{\kappa(\theta - \theta_0)}{\alpha_2 \theta_*} = \ln(\frac{z}{z_T}) - \Psi_H(\zeta)$$

where z_T is such that $\theta = \theta_0$ at $z = z_T$, which needs not necessarily be z_0.
For stable situations ($\zeta > 0$), we have

eq. B.16 $$\Psi_M(\zeta) = \Psi_H(\zeta) = -\beta_1 \zeta$$

Whereas for unstable cases ($\zeta < 0$)

eq. B.17 $$\Psi_M(\zeta) = 2\ln(\frac{1+x}{2}) + \ln(\frac{1+x^2}{2}) - 2\tan^{-1} x + \frac{\pi}{2} \quad \text{with } x = (1-\gamma_1\zeta)^{1/4}$$

eq. B.18 $$\Psi_H(\zeta) = 2\ln(\frac{1+y}{2}) \text{ with } y = (1-\gamma_2\zeta)^{1/2}$$

B.2.2 Simulated surface profiles

B.2.2.1 Neutral case

Simulation results for the wind speed and potential temperature profiles after 24 hours (1 h 10′ CPU time on a DEC ALPHA EV56 processor, 375 Mhz) are presented in Figure B.1 and Figure B.2 for a neutral situation, i.e. a situation for which the heat flux at ground was set to 0. With a vertical gradient of –9.8 K/km for the real temperature profile, the initial state for that case corresponds to a neutral stratification of the external flow.

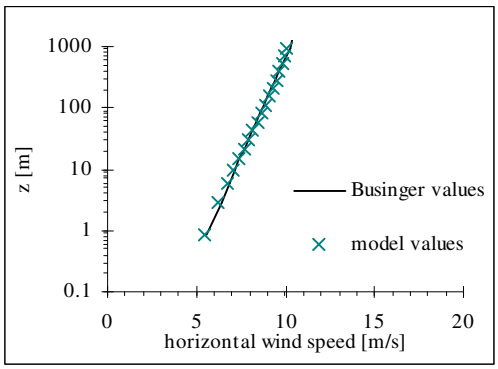

Figure B.1. Wind speed profile for a situation with zero potential temperature flux through the ground.

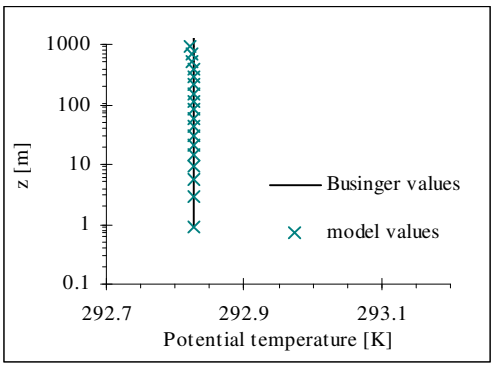

Figure B.2. Potential temperature profile for the same conditions as in Figure B.1.

The ground roughness was set to $z_0 = 0.0002\,\mathrm{m}$, the Coriolis parameter to $f = 10^{-4}\,\mathrm{s}^{-1}$ and the geostrophic wind speed to $G = 10\,\mathrm{m/s}$. The model gives a friction velocity of $u_* = 0.272\,\mathrm{m/s}$.

In addition to the model results (crosses), the Businger profiles (continuous line) for the corresponding u_*, z_0 and θ_* were plotted in Figure B.1 and Figure B.2. The comparison shows that the model results are in good agreement with the theoretical formulation.

B.2.2.2 Stable case

Similarly we simulated stable situations, specifying a ground cooling with cooling rates of –0.2 K/hour, -0.5 K/hour, and –1.0 K/hour. Figure B.3 and Figure B.4 present the wind speed and potential temperature profiles after 10 hours of simulation for a situation with $z_0 = 0.01\,\mathrm{m}$, $f = 10^{-4}\,\mathrm{s}^{-1}$, $G = 10\,\mathrm{m/s}$ and $\partial\theta/\partial t = -0.5\,\mathrm{K/hour}$ at ground. The initial vertical temperature gradient was $\partial T/\partial z = -8.0\ \mathrm{K/km}$. The friction velocity calculated by the model is $u_* = 0.266\,\mathrm{m/s}$.

For comparison, the Businger profiles for a value of $\theta_* = 0.075$ and u_*, z_0 corresponding to the model results were also plotted. The potential temperature flux at ground for this particular case is $-\rho u_* \theta_* = -0.024$ corresponding to a Monin-Obukhov length of $L = 67\,\mathrm{m}$. In the surface layer ($z < 20\,\mathrm{m}$), the correspondence between the analytical profiles and model results is fairly good.

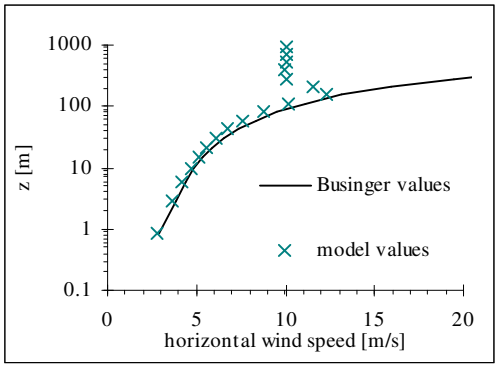

Figure B.3. Wind speed profile for a stable situation where the stability of the atmosphere is induced by a ground cooling of –0.5 K/hour. (See text for other parameters).

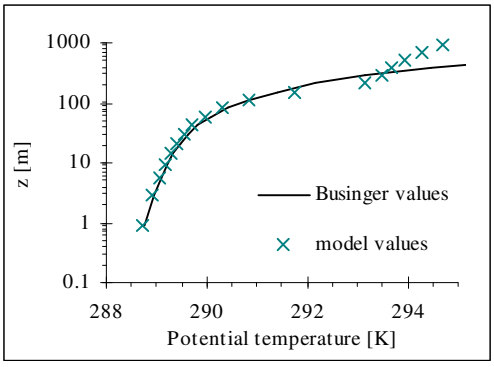

Figure B.4. Potential temperature profile for the same situation presented in Figure B.3.

B.2.2.3 Unstable case

An unstable situation was also simulated, setting a ground heating of +0.2 K/hour. The other parameters were $z_0 = 0.01\,\mathrm{m}$, $f = 10^{-4}\,\mathrm{s}^{-1}$ and $G = 10\,\mathrm{m/s}$. The free flow stratification is given by a vertical real temperature gradient of $\partial T/\partial z = -8.0$ K/km. For the friction velocity the model gives $u_* = 0.381$ m/s. The model results are compared to the Businger formulation in Figure B.5 and Figure B.6.

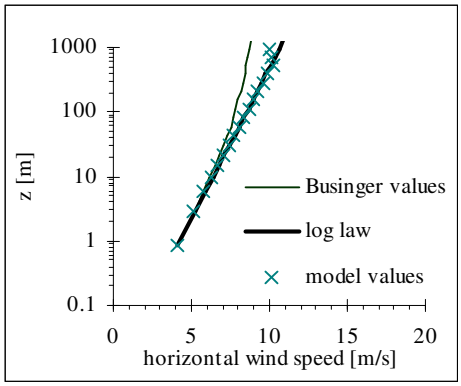

Figure B.5. Wind speed profile for an unstable situation, where a ground heating of +0.2 K/hour drives the instability. The overall atmospheric stability is maintained by a stable stratification of the free flow. (See text for other parameters).

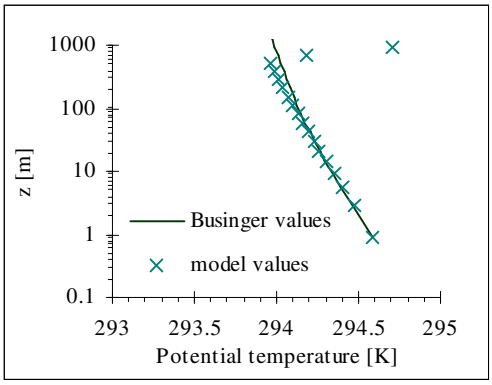

Figure B.6. Potential temperature profile for the same situation as Figure B.5.

Although the potential temperature profile is in good agreement with the analytical formulation within the surface layer ($z < 70m$), this is not the case for the simulated wind speed profile. The latter is better represented by a logarithmic profile (eq. B.3) over the whole extent of the boundary layer ($z < 700m$).

B.3 Atmospheric boundary layer development for neutral situations testing the effect of static stability

By definition, neutral situations correspond to conditions with zero heat flux through the ground. In these conditions, due to the turbulent mixing in the boundary layer, a neutral layer (characterised by a zero potential temperature lapse rate) forms close to the ground in an initially stable atmosphere. The depth of the

boundary layer developing can be strongly influenced by the static stability of the free flow (see e.g. Duynkerke (1988), or Zilitinkevich et al. (1998)). For real atmospheric conditions, purely neutral situations, with zero heat flux through the ground and with neutral static stability of the free flow are very rare occurrences (if ever observed).

For situations without heat flux through the ground, it is common practice to relate the boundary layer height h to the friction velocity u_* and the Coriolis parameter f, using the Rossby-Montgomery relationship $h = C_h\, u_*/f$. The range of values found in the literature for the 'constant' C_h is quite big, since for neutral conditions they can vary between ~0.16 and ~1 depending on how they are determined. Mason & Thomson (1987), using a LES model, found a boundary layer height of about $0.6\,u_*/f$ from the simulation of a neutral case. Wyngaard et al (1974) simulated a neutral atmospheric boundary layer using a second order closure model and found a boundary layer height of $0.7\,u_*/f$. As quoted in Duynkerke (1988), Deardorff (1972) obtained a boundary layer height between $0.45\,u_*/f$ and u_*/f, also using a LES model.

Nicholls (1985) from observations of a well-mixed Ekman layer over sea concludes that for near-neutral and barotropic conditions the boundary layer height was limited to $0.2\,u_*/f$. Observational data from the 'Leipzig wind profile' (Lettau, 1950) also indicates a boundary layer height between $0.16\,u_*/f$ and $0.2\,u_*/f$.

To summarise, it appears that model results give values of the boundary layer height around $0.6\,u_*/f$ for the neutral atmospheric boundary layer, whereas observations give $0.2\,u_*/f$.

As already concluded by Duynkerke (1988), it is probable that the discrepancy between the observations and simulations is due to the very strong sensitivity of the boundary layer development to the static stability of the free flow. It appears indeed that some stability effect could be very important in the case of the Leipzig wind profile, since Lettau reported that from the sounding of Lindenberg (in the 'same air mass') a rather uniform lapse rate of –6.5 K/km could be observed. As mentioned in Duynkerke (1988), some stability effects can also be seen in the potential temperature profiles measured by Nicholls, who reported that a neutral profile was observed up to the height of $0.2\,u_*/f$, above which a stable region existed with potential temperature gradients of 1-3 K/km.

In the following sections, the behaviour of CFX4 regarding this issue will be presented. First some comparisons between results obtained with and without the modification of the $k-\varepsilon$ closure scheme will be shown. The validity of the modification will be demonstrated by comparing the simulated profiles with observations and with results presented by other authors.

B.3.1 Comparison of results obtained with the modified turbulence model and with the standard version

Figure B.7 to Figure B.11 show the comparison of the model calculated profiles obtained with the modified version of the turbulence model (continuous line) and with the standard version of the code (dashed line). The variables were plotted in a non-dimensional form versus the non-dimensional height zf/u_*.

These results were obtained with a zero heat flux through the ground, a real temperature lapse rate of -9.7 K/km, a roughness length of 0.0002m and a Coriolis parameter $f = 10^{-4}$ s^{-1}. We chose these parameter values following Duynkerke (1988), in order to be able to compare our results with the ones he presented. The model calculated friction velocity is $u_* = 0.273$ m/s.

Figure B.7 presents the non-dimensional turbulent kinetic energy profile, while Figure B.8 shows the non-dimensional turbulent diffusion profile. It can already be observed from these two graphs that the modification of the $k-\varepsilon$ model has very important effects on the way the boundary layer develops. From the k/u_*^2 profile, we can infer a boundary layer height of about $0.35u_*/f$ with the modified version, whereas with the standard version, we would have $h > 1.5u_*/f$. The behaviour of the turbulent diffusion is also very different. Without the modification, we get a turbulent diffusion constantly increasing up to a height of $\sim u_*/f$ reaching a maximum value of 0.083 and then slowly decreasing. With the modifications, the calculated turbulent diffusion profile reaches a maximum of 0.025 at the height of $0.14u_*/f$ to decrease rapidly to zero at the height of $\sim 0.35u_*/f$. For the diffusion profile in neutral conditions, Wippermann (1973) (quoted in Lalas & Ratto, 1996) proposed the following behaviour :

eq. B.19
$$\frac{\mu_t f}{u_*^2} = \frac{\rho \kappa f}{u_*} z \exp(-7.6(z/h)^{0.764})$$

This behaviour is also plotted in Figure B.8 (continuous thin line), which shows that the modified version of the turbulence model gives more realistic results than the standard one. The significant difference between the maximum values obtained with CFX4 and the diffusion profile given by Wippermann is probably due to the use of a different vertical stratification. The latter parameter strongly influences the development of the boundary layer as will be shown below.

Figure B.9 shows the effect of the modification on the non-dimensional stress tensors $-\overline{u'w'}/u_*^2$ and $\overline{v'w'}/u_*^2$. Non-dimensional velocity defect profiles for the u and v velocity components are given in Figure B.10 and Figure B.11, where u_g and v_g stand for the geostrophic wind components. From these profiles again, the same

conclusion can be drawn, i.e. without the modification, the model overestimates the boundary layer height.

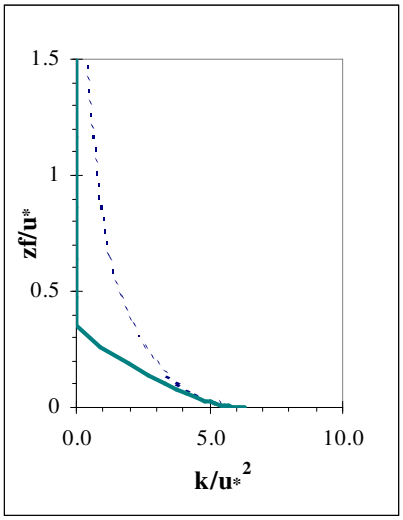

Figure B.7. Non-dimensional turbulent kinetic energy profiles for a neutral situation. Continuous line: modified $k-\varepsilon$ model, dashed line: standard version of CFX4.

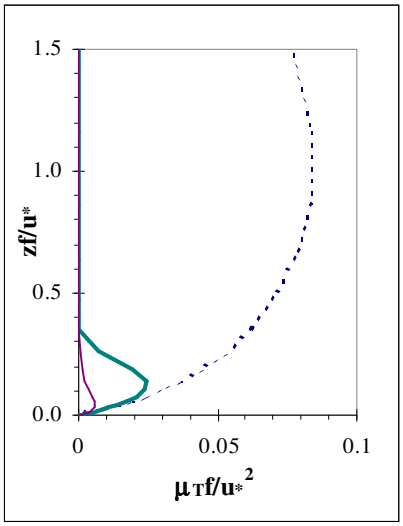

Figure B.8. Non-dimensional turbulent diffusion profiles. Continuous thick line: modified $k-\varepsilon$ model, dashed line: standard version of CFX4, continuous thin line: Wippermann formulation.

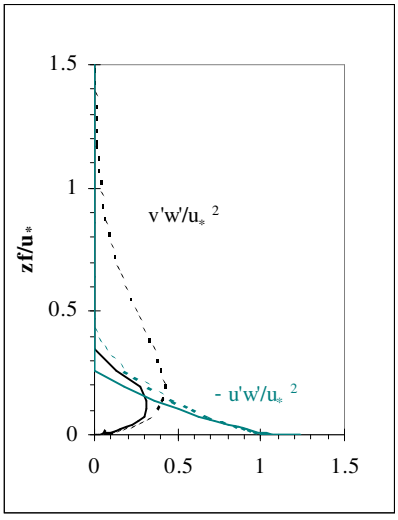

Figure B.9. Non-dimensional stress tensors $-\overline{u'w'}/u_*^2$ and $\overline{v'w'}/u_*^2$ profiles. Continuous line: modified $k-\varepsilon$ model, dashed line: standard version of CFX4.

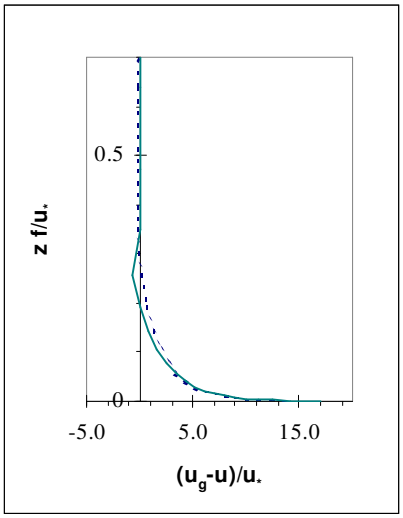

Figure B.10. Non-dimensional velocity defect profile for the u velocity component. Continuous line: modified $k-\varepsilon$ model, dashed line: standard version of CFX4.

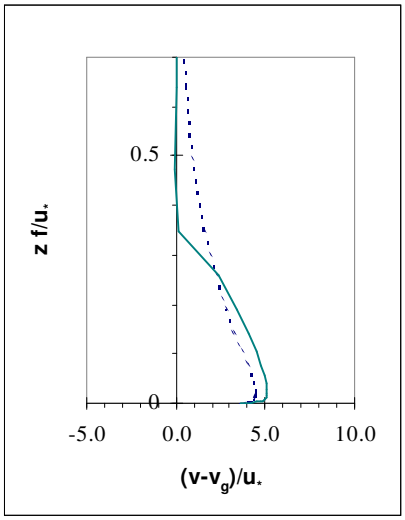

Figure B.11. Non-dimensional velocity defect profile for the v velocity component. Continuous line: $k-\varepsilon$ model, dashed line: standard version of CFX4.

B.3.2 Comparison with other models and observations

The two neutral simulations presented in the previous section, which only differed by their real temperature lapse rate are compared in Figure B.12 to Figure B.16 to results from a neutral simulation by Duynkerke and to laboratory data obtained by Hinze (1975) .

The most striking feature that can be seen from all of these figures is the extreme sensitivity of the boundary layer height to the tiny change in the stratification of the free flow. Slightly increasing the stability of the external flow by changing the lapse rate from –9.8 K/km to –9.7 K/km reduced the boundary layer height from $0.86u_*/f$ to $0.35u_*/f$. The effect of changing this parameter will be investigated in more details in next section. Otherwise, the profiles obtained with CFX4 present a behaviour that is qualitatively very similar to the one obtained by Duynkerke (1988) and Hinze (1975).

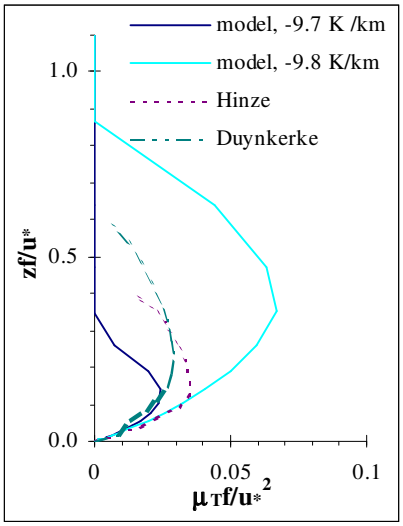

Figure B.12. Non-dimensional turbulent diffusion profiles. Light continuous line: CFX4 with a lapse rate of –9.8 K/km, dark continuous line: CFX4 with a lapse rate of –9.7 K/km, long-dashed line: Duynkerke (1988), short-dashed line: Hinze (1975).

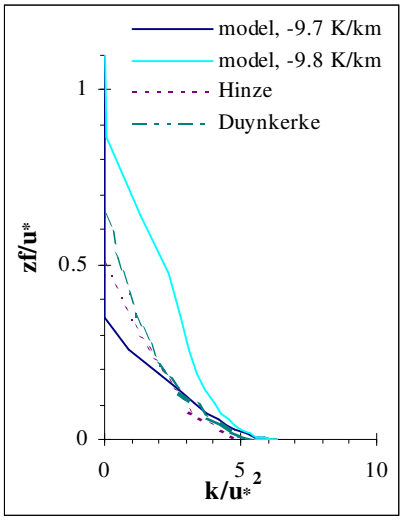

Figure B.13. Non-dimensional turbulent kinetic energy profiles. Light continuous line: CFX4 with a lapse rate of –9.8 K/km, dark continuous line: CFX4 with a lapse rate of –9.7 K/km, long-dashed line: Duynkerke (1988), short-dashed line: Hinze (1975).

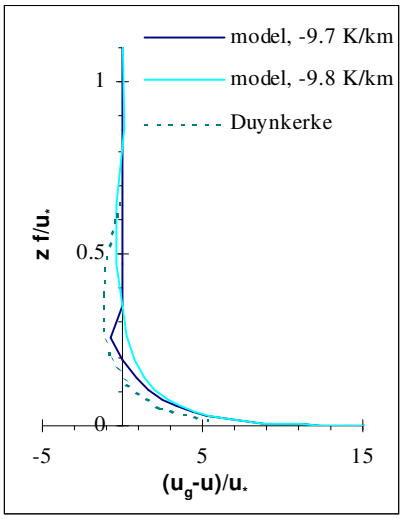

Figure B.14. Velocity defect profile for *u*. Light continuous line: CFX4 with a lapse rate of –9.8 K/km, dark continuous line: CFX4 with a lapse rate of –9.7 K/km, dashed line: Duynkerke (1988).

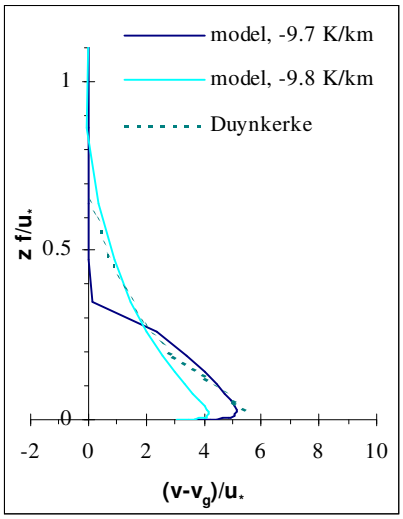

Figure B.15. Velocity defect profile *v*. Light continuous line: CFX4 with a lapse rate of –9.8 K/km, dark continuous line: CFX4 with a lapse rate of –9.7 K/km, dashed line: Duynkerke (1988).

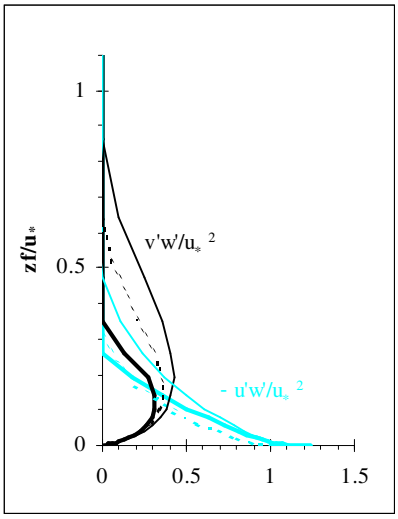

Figure B.16. Non-dimensional stress tensors $-\overline{u'w'}/u_*^2$ (light) and $\overline{v'w'}/u_*^2$ (dark) profiles. Continuous lines: CFX4 with a lapse rate of –9.7 K/km (thick), and with a lapse rate of –9.8 K/km (thin), dashed lines: Duynkerke (1988).

B.3.3 Effect of the stratification of the free flow

To further investigate the significant effect of the free flow stability on the development of the boundary layer, some more simulations were done with real temperature lapse rates of –9.0 K/km, -8.0 K/km and –6.5 K/km. All of these were performed with the ground heat flux set to zero, with a roughness length of 0.0002m and the Coriolis parameter $f = 10^{-4}$ s^{-1}. As can be seen from Figure B.17, the cross isobar angle[1] of the Ekman spiral increases with increasing stability of the free flow. The potential temperature profiles (**Figure B.18**) shows the creation of a neutral layer over the ground up to a height that strongly depends on the initial potential temperature gradient. Above the neutral layer, a transition layer exist with a slightly stronger stability than the initial one, and finally above this layer one finds the free flow region with the same stability conditions as initially set. As already mentioned, the increase of stability in the free flow tends to significantly decrease the boundary layer height. Determining the latter from the non-dimensional kinetic energy profiles

[1] The cross isobar angle is defined as the angle between the geostrophic wind vector and the ground wind vector.

would lead to the values given in Table B.1 for the 'constant' C_h in the Rossby – Montgomery relationship.

Table B.1. Values of the normalised boundary layer height for neutral situations with various free flow stratification conditions.

Ground	Initial real temperature gradient	C_h
No heat flux	-9.8 K/km	0.86
No heat flux	-9.7 K/km	0.35
No heat flux	-9.0 K/km	0.20
No heat flux	-8.0 K/km	0.16
No heat flux	-6.5 K/km	0.14

The range of values for C_h obtained when varying the stability of the free flow covers the range that can be found in the literature. As was already shown by Duynkerke the external stability might explain why Nicholls and Lettau found a boundary layer height of about $0.2u_*/f$. This tends to be confirmed for the Leipzig wind profile (Lettau, 1950) by Figure B.19 and Figure B.20, in which the observations are better reproduced by the simulation with a lapse rate of –6.5 K/km. For the Nicholls observations, Figure B.20 to Figure B.22 would suggest that the observations are best reproduced by a situation with a lapse rate between –8.0 and –9.0 K/km. In the velocity defect profile for the u component (Figure B.20), the simulations results show some negative values, whereas Nicholls measurements do not. As already pointed out by Duynkerke, this might reveal a problem with the measurements since we expect from the Ekman equations for the boundary layer (see later on, eq. B.21) that the integral $\int_0^h (u-u_g)dz$ vanishes[2]. The simulated kinetic energy profile (Figure B.23) tends to underestimate the turbulent kinetic energy measured by Nicholls in a similar way to what was obtained by Duynkerke.

[2] The integral $\int_0^h (u-u_g)dz$ does not exactly vanish for the presented model results. This is certainly related to the lack of resolution in the vertical for the upper part of the boundary layer height.

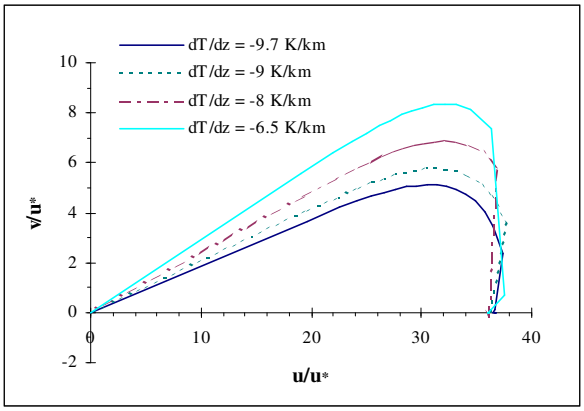

Figure B.17. Dimensionless Ekman spiral after 24 h of simulation for various free flow stability conditions.

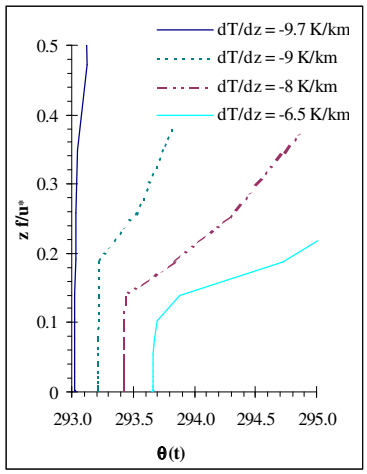

Figure B.18. Potential temperature profiles after 24 h of simulation for various free flow stability conditions. See Figure B.17 for the definition of the stability conditions.

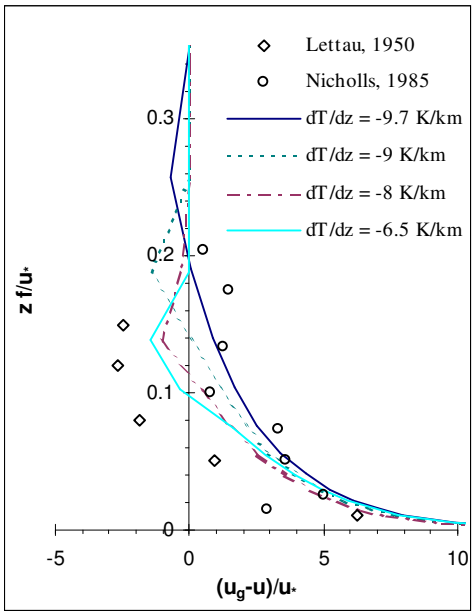

Figure B.19. Non-dimensional velocity defect profile for u after 24 h of simulation for various free flow stability conditions and observations from Lettau, 1950 (diamonds), and from Nicholls, 1982 (circles).

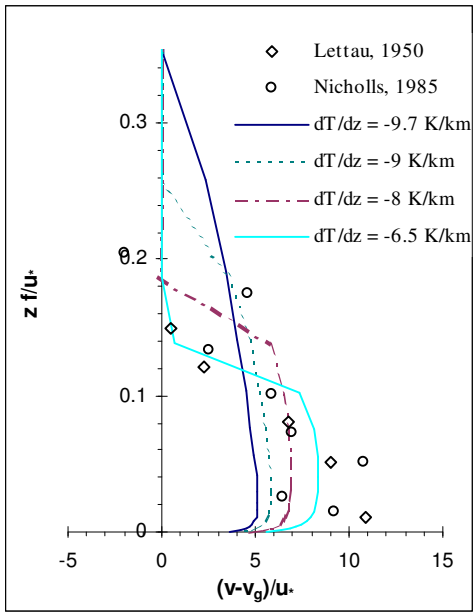

Figure B.20. Non-dimensional velocity defect profile for v after 24 h of simulation for various free flow stability conditions and observations from Lettau, 1950 (diamonds), and from Nicholls, 1982 (circles).

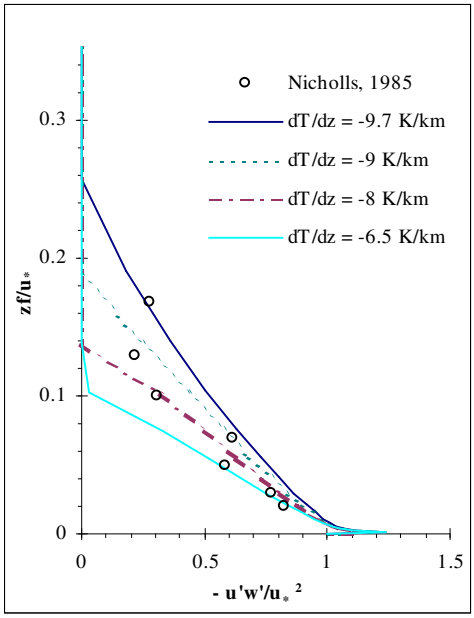

Figure B.21. Non-dimensional $-\overline{u'w'}/u_*^2$ stress profiles after 24 h of simulation for various free flow stability conditions and observations from Nicholls (circles).

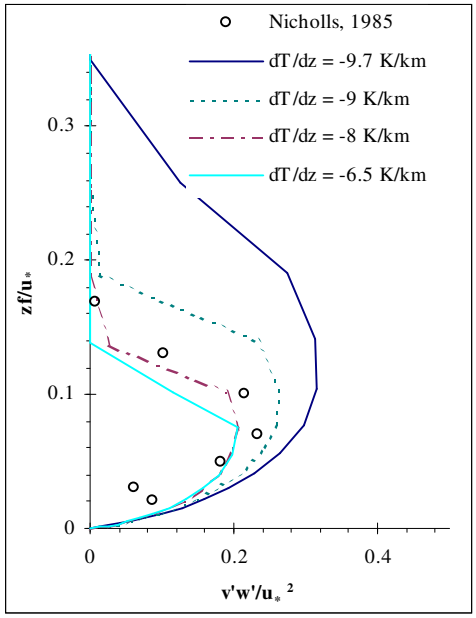

Figure B.22. Non-dimensional $\overline{v'w'}/u_*^2$ stress profiles after 24 h of simulation for various free flow stability conditions and observations from Nicholls (circles).

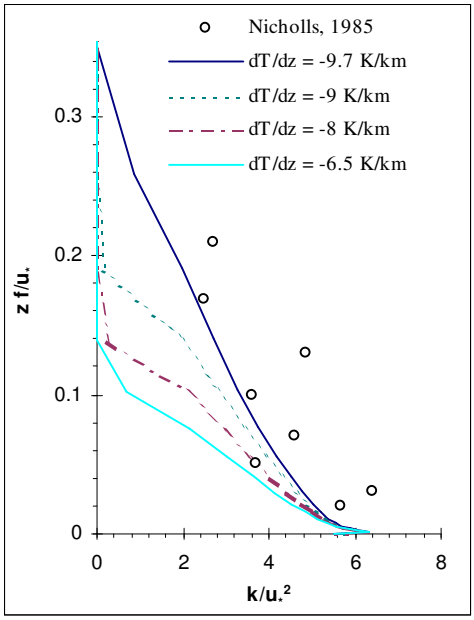

Figure B.23. Non-dimensional kinetic energy profiles after 24 h of simulation for various free flow stability conditions and observations from Nicholls (circles).

In conclusion, we can say that the implementation of additional source terms taking into account the effect of stability in the production/destruction of turbulence

significantly improves the solutions. With these modifications, CFX4 is able to reproduce the results and behaviour that were presented by Duynkerke (1988) and other authors.

B.4 Parameterisation of the wind profiles taking into account ground roughness, free flow static stability and ground heat flux

From the results presented in Section B.2 and Section B.3, it would be very useful to obtain a parameterisation of the wind profiles and boundary layer height depending on the roughness and heat flux conditions at the ground and also including the effect of the stratification of the free flow.

In an attempt to do so, we will follow the similarity theory proposed by Zilitinkevich et al (in press), and test how far the model results for various types of situations can be reproduced by the Zilitinkevich formulation. The latter was chosen because it also takes into account the effect of the external free flow stability in addition to the ground roughness and surface layer stability, which makes it unique.

B.4.1 Similarity theory model for wind profile and drag law in the planetary boundary layer

B.4.1.1 Rossby-number similarity for neutral flows

For steady state situations, which are neutral, horizontally homogeneous, and barotropic (no vertical gradient of the geostrophic wind speed) expressions for the wind profiles in the inner and outer layer of the atmospheric boundary layer can be inferred from similarity considerations. In the inner layer (constant flux layer), the scaling length is given by the ground roughness z_0, whereas in the outer layer, the scaling length is a combination of the geostrophic wind speed G and the Coriolis parameter f and is given by $G/|f|$. The relation

eq. B.20 $$u_* = G \cdot F(G/|f|z_0)$$

is in the form of a drag law, expressing the friction velocity at ground u_* in terms of the geostrophic wind speed G and the *surface Rossby number* of the flow $Ro = G/fz_0$. The quantity $C_G = (u_*/G)^2$ is called *geostrophic drag coefficient*.

For the above mentioned approximations, the momentum equations in the atmospheric boundary layer can be simplified to

eq. B.21 $$0 = -f(u - u_g) - \partial(\overline{v'w'})/\partial z$$

eq. B.22 $0 = f(v - v_g) - \partial(\overline{u'w'})/\partial z$

In a non-dimensional form, the equations can be rewritten as

eq. B.23 $(u - u_g)/u_* = -\partial(\overline{v'w'}/u_*^2)/\partial(zf/u_*)$

eq. B.24 $(v - v_g)/u_* = \partial(\overline{u'w'}/u_*^2)/\partial(zf/u_*)$

The above non-dimensional form is only valid in the *outer layer*, since u_*/f is not an appropriate scaling length close to the ground. With this scaling, the velocity defect profiles become independent of the surface Rossby parameter and can be expressed as

eq. B.25 $(u - u_g)/u_* = F_x(zf/u_*)$

eq. B.26 $(v - v_g)/u_* = F_y(zf/u_*)$

This way of writing the velocity defect law is the *Rossby similarity theory* of the neutral and barotropic boundary layer. It suggests that the boundary layer height is proportional to u_*/f, hence the relationship $h = C_h u_*/f$ known as the *Rossby-Montgomery formula* for the boundary layer height.

In the surface layer, the non-dimensional form is changed using the roughness length z_0 as the scaling length, so that eq. B.23 and eq. B.24 become:

eq. B.27 $(fz_0/u_*)(u - u_g)/u_* = -\partial(\overline{v'w'}/u_*^2)/\partial(z/z_0)$

eq. B.28 $-(fz_0/u_*)(v - v_g)/u_* = -\partial(\overline{u'w'}/u_*^2)/\partial(z/z_0)$

The left-hand side of eq. B.27 and eq. B.28 can be at most $|f|z_0 G/u_*^2$ or equivalently $Ro^{-1}(G/u_*)^2$. In the limit of high Rossby numbers, the left-hand sides vanish, and the momentum fluxes in the surface layer are then constant (Tennekes, 1982). The wind speed in the surface layer has a constant direction and does not feel the effect of the Coriolis force. For a co-ordinate system with the x-axis along the surface wind, the wind profiles are such that

eq. B.29 $u/u_* = f_x(z/z_0)$

eq. B.30 $v/u_* = 0$

Now, eq. B.25 and eq. B.26 are not valid in the limit $zf/u_* \to 0$, whereas eq. B.29 and eq. B.30 can not be used for $z/z_0 \to \infty$. Asymptotic matching (van Dyke, (1975) Wilcox, (1995)) is used to make the solutions overlap in the so-called *matching layer*. The procedure leads to the relationship

eq. B.31 $(z/u_*)\,\partial u/\partial z = \text{constant} = 1/\kappa$

In the surface layer, to be consistent with eq. B.29 integration of eq. B.31 leads to

eq. B.32 $$\kappa u / u_* = \ln(z / z_0)$$

while in the outer layer, to be consistent with eq. B.25 we obtain

eq. B.33 $$\kappa(u - u_g) / u_* = \ln(z|f| / u_*) + A_0$$

For the v component, asymptotic matching gives $v = 0$ with

eq. B.34 $$\kappa v_g / u_* = \text{constant} = -B_0 \ \text{sgn}\ f$$

Since in the overlap layer both eq. B.32 and eq. B.33 must be verified, we get a relationship for the geostrophic wind speed

eq. B.35 $$\kappa u_g / u_* = \ln(u_* / |f| z_0) - A_0$$

This equation, together with eq. B.34 (so called drag law or resistance law), allow the derivation of an implicit expression for the geostrophic drag coefficient

eq. B.36
$$\begin{aligned} C_G = (u_* / G)^2 &= \kappa^2 / \left[\left\{ \ln(u_* / |f| z_0) - A_0 \right\}^2 + B_0^2 \right] \\ &= \kappa^2 / \left[\left\{ \ln(Ro \cdot C_G^{1/2}) - A_0 \right\}^2 + B_0^2 \right] \end{aligned}$$

For the cross isobar angle (angle between the surface and geostrophic wind) we obtain:

eq. B.37 $$\sin\alpha = -\frac{B_0}{\kappa} \cdot \text{sgn}\ f \cdot C_G^{1/2}$$

Hence for the neutral barotropic and steady-state atmospheric boundary layer, eq. B.36 allows the determination of the friction velocity in terms of the parameters G, f and z_0. The values taken by the constants A_0 and B_0 are still a matter of debate. Table B.2 gives a non-exhaustive review of typical values found in the literature for A_0 and B_0 in neutral situations.

The Rossby similarity theory can be extended for non-neutral situations, in which case the A_0 and B_0 constants appearing in the drag law are no-longer constants but become functions of the stability parameters μ and λ defined as

eq. B.38 $$\mu = u_* / |f| L$$

eq. B.39 $$\lambda = N / |f|$$

where L is the Monin-Obukhov length and $N = \sqrt{\frac{g}{\theta}\frac{\partial\theta}{\partial z}}$ the Brunt-Väisälä frequency.

For non-neutral situations, typical values for A_0 and B_0 are given in Table B.3. Many different empirical formulations have been proposed for the A_0 and B_0 as a function of the surface stability parameter μ, showing a very big scatter. We will not go in more details about these, but rather refer to the reviews given by Zilitinkevich (1989) or Landberg (1994) about the existing formulations.

Table B.2. Values of the constants A_0 and B_0 obtained from various sources for a neutral atmospheric boundary layer.

Authors	**Origin of the data**	A_0	B_0
Favre et al (1976)	Not specified	2.0	4.0
Mason & Thomson (1987)	LES simulation	1.2	2.3
Andren & Moeng (1993)	LES data	0.8	2.0
Caldwell et al. (1972)	laboratory experiments	2.0-3.0	1.3-3.6
Zilitinkevich et al (1967)	atmos. observations	1.5	5.3
Yamada (1976)	atmos. observations	1.855	3.020
Nieuwstadt (1981)	atmos. observations	1.9	2.3
Hess et al (1981)	atmos. observations	1.1±0.5	4.3±0.7
Troen & Petersen (1989)	atmos. observations	1.8	4.5

Table B.3. Values of the constants A_0 and B_0 for non-neutral situations.

	Origin of the data	A_0	B_0
Clarke (1970)	Very unstable, atmos. Observations $\mu = -100$	5.0	2.0
Clarke (1970)	Very stable, atmos. Observations $\mu = 100$	-20	21

From the bottom to the top of the boundary layer, the wind vectors (obeying eq. B.25 and eq. B.26) rotate with height following a spiral (so called 'Ekman spiral') as schematically illustrated in hodograph form in Figure B.24 (thick curve). The height z increases when moving towards the right along the spiral. In the inner layer ($z < z_c$), the wind direction is constant with height, whereas in the Ekman layer ($z_c < z < h$) the wind vector turns to adjust to the geostrophic wind vector *G*. Two co-ordinates systems have been defined, the first one (*x*-*y* system) with the *x*-axis along the geostrophic wind vector and the second one (*x*′-*y*′ system) with the *x*-axis along the surface stress vector (also corresponding to the wind direction at ground). The cross-isobar angle is also shown which is defined as the angle between the surface and geostrophic wind vectors.

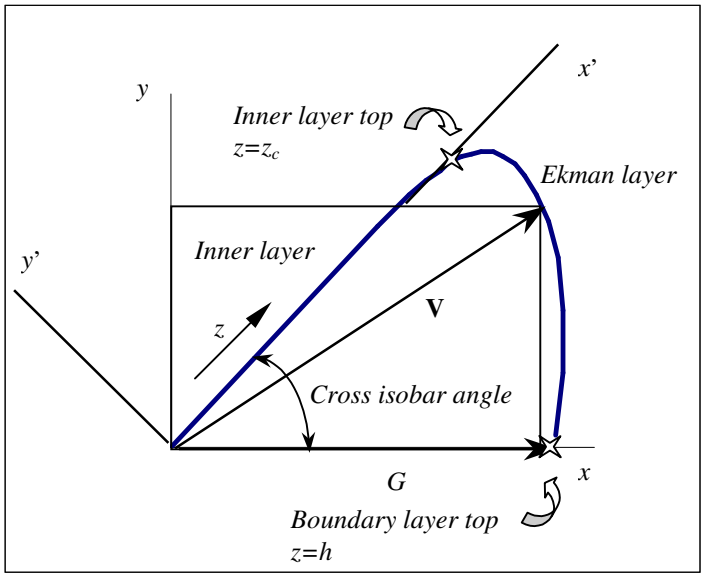

Figure B.24. Hodograph of the wind vectors **V** in the boundary layer forming the Ekman spiral.

B.4.1.2 Zilitinkevich parameterisation for the wind profiles

In their approach to obtain a formulation for the u and v profiles for the neutral, steady state and barotropic boundary layer, Zilitinkevich et al (in press), based on symmetry and self-consistency requirements, proposed analytical expressions for u and v yielding

eq. B.40 $$u(z) = \frac{u_*}{\kappa}\left[\ln(\frac{z}{z_0}) + a_1\eta + a_2\eta^2 + a_3\eta^3\right] \qquad \text{with} \qquad \eta = \frac{z}{h}$$

eq. B.41 $$v(z) = -\frac{fh}{\kappa^2}\left[-\eta\ln(\eta) + b_1\eta + b_2\eta^2 + b_3\eta^3\right]$$

With this formulation, the x-axis is along the wind direction at ground.
From the condition that the wind velocity equals the geostrophic wind velocity at the top of the boundary layer ($z = h$), we obtain

eq. B.42 $$\kappa u_g / u_* = \ln(h / z_0) - A_1$$

eq. B.43 $$\kappa v_g / u_* = -B_1$$

with

eq. B.44 $$A_1 = -(a_1 + a_2 + a_3) \qquad B_1 = \delta(b_1 + b_2 + b_3)$$

where

eq. B.45 $\delta \equiv fh / \kappa u_*$

is a non-dimensional rotation rate.

The a_i and b_i coefficients, and therefore A_1 and B_1 are specified in terms of the flow governing parameters, which are the boundary layer height *h*, the Coriolis parameter *f*, the friction velocity u_*, the Monin-Obukhov length *L* characterising the heat flux conditions through the ground and the Brunt-Väisälä frequency *N* accounting for the thermal stratification of the free flow.

For a steady state situation, Zilitinkevich et al (in press), using dimensional analysis arguments, expressed the a_i and b_i coefficients in terms of the dimensionless parameters δ, μ and λ (eq. B.45, eq. B.38 and eq. B.39). Taking into account further considerations relative to the boundary conditions which must apply at both ground and boundary layer top for the velocity profiles and momentum fluxes, Zilitinkevich et al (in press) obtained the following relationships for the a_i and b_i coefficients:

eq. B.46 $a_1 = -3 + \Pi \qquad a_2 = -\frac{3}{2}\Pi \qquad a_3 = \frac{2}{3} + \frac{2}{3}\Pi$

eq. B.47 $b_1 = \frac{4}{\delta^2} + \tilde{\Pi} \qquad b_2 = -\frac{3}{2}\tilde{\Pi} \qquad b_1 = \frac{1}{3} - \frac{4}{3\delta^2} + \frac{2}{3}\tilde{\Pi}$

where Π and $\tilde{\Pi}$ are defined such that:

eq. B.48 $\Pi \equiv C_R \delta^2 + C_L h / L + C_N N h / u_*$

eq. B.49 $\tilde{\Pi} \equiv \tilde{C}_R \delta^2 + \tilde{C}_L h / L + \tilde{C}_N N h / u_*$

C_R, $\tilde{C}_R$, C_L, $\tilde{C}_L$, C_N and $\tilde{C}_N$ are dimensionless constants that need to be determined empirically.

To close the model, so that the *u* and *v* profiles are fully determined by the analytical formulation given above, we still need an analytical expression for the boundary layer height *h*. This is provided by Zilitinkevich and Mironov (1996), who proposed a multi-limit diagnostic method ending up with a relationship of the form

eq. B.50 $h = \frac{1}{2} C_h^2 \frac{u_*}{|f|} \left(\sqrt{\Pi_0^2 + 4/C_h^2} - \Pi_0 \right)$

where

eq. B.51 $\Pi_0 \equiv \frac{\mu}{C_s} + \frac{\lambda}{C_i} + \frac{\sqrt{\mu}}{C_{sr}} + \frac{\sqrt{|\lambda|}}{C_{ir}}$

C_h, C_s, C_i, C_{sr}, C_{ir} are additional constants, which need to be estimated empirically.

It can be noted that in the limit of a purely neutral case ($N = 0$ and $L \to \infty$, implying that $\lambda = 0$ and $\mu = 0$), the above equation for the boundary layer height h tends towards the Rossby-Montgomery relationship

eq. B.52 $$h = C_h \frac{u_*}{f}$$

From eq. B.45 ,eq. B.46 and eq. B.47, A_1 and B_1 can be rewritten as

eq. B.53 $$A_1 = \frac{7}{3} - \frac{1}{6}\Pi$$

eq. B.54 $$B_1 = \frac{1}{6}\delta(2 + \frac{16}{\delta^2} + \tilde{\Pi})$$

Comparing eq. B.34 and eq. B.35 with eq. B.42 and eq. B.43, and furthermore using the Zilitinkevich relationship (eq. B.50) for the boundary layer height allows us to derive relationships for the A_0 and B_0 'constants' appearing in the drag law:

eq. B.55
$$\begin{aligned} A_0 &= A_1 - \ln\left[\frac{1}{2}C_n^2\left(\sqrt{\Pi_0^2 + 4/C_n^2} - \Pi_0\right)\right] \\ &= \frac{7}{6} - \frac{1}{6}\Pi - \ln\left[\frac{1}{2}C_n^2\left(\sqrt{\Pi_0^2 + 4/C_n^2} - \Pi_0\right)\right] \end{aligned}$$

eq. B.56 $$B_0 = B_1 = \frac{1}{6}\delta(2 + \frac{16}{\delta^2} + \tilde{\Pi})$$

Relying on LES data by Mason and Thomson (1987), Zilitinkevich et al (in press) adopt for the truly neutral case $A_0 = 1.2$ and $B_0 = 2.3$. From these values and using $C_h = 0.5$, they obtain tentative estimates of $C_R \approx 7$ and $\tilde{C}_R \approx 0$. For the other model constants they suggest:

$C_L \approx 4.5$, $C_N \approx 0.1 - 0.4$, $\tilde{C}_L \approx -7$, $\tilde{C}_N = -1.5$

$C_s \approx 10$, $C_i \approx 20$, $C_{sr} \approx 1$, $C_{ir} \approx 1.7$

B.4.2 Model results and drag law

CFX4 was used to simulate boundary layer profiles for various types of conditions, with and without ground heat flux, with various free flow stratification conditions, and for various roughness lengths and geostrophic wind speeds. In addition to test the agreement between the numerical simulations and the Zilitinkevich formulation, the idea behind this was also to check whether the model followed the Rossby-similarity theory for the neutral situations.

A summary of the parameters characterising the various simulations that were performed is given in Table B.4 for neutral cases and in Table B.5 for the stable cases.

Results for the cross isobar angle and geostrophic drag coefficient $C_G^{1/2}$ versus the Rossby number of the flow are presented in Figure B.25 and Figure B.26. Triangles, diamonds and crosses are obtained with simulations with zero heat flux through the ground (neutral situations), whereas circles correspond to stable situations with a constant ground cooling applied. For the triangles and diamonds, the model was initialised with a quasi-neutral stratification (-9.7 K/km), while crosses were obtained for a stable external stratification (-8.0 K/km). All the simulations were performed with a Coriolis parameter $f = 10^{-4}$ s^{-1} except for the diamonds, which were calculated for various values of f (see Table B.4). In addition to the model results, a line was plotted which represents the behaviour that would be expected for $\sin(\alpha)$ and $C_G^{1/2}$ from the drag law (eq. B.36 and eq. B.37) with $A_0 = 1.5$ and $B_0 = 2.8$. As it appears from the figures, these values of A_0 and B_0 represent fairly well the model results for the neutral situations with quasi-neutral stratification. These values are higher than the ones obtained by LES simulations, and generally lower than the ones estimated from atmospheric observations (c.f. Table B.2).

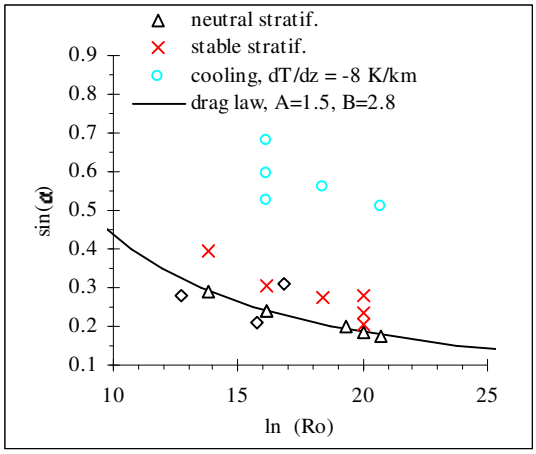

Figure B.25. Sine of the cross isobar angle vs. natural logarithm of the Rossby number. See text for details.

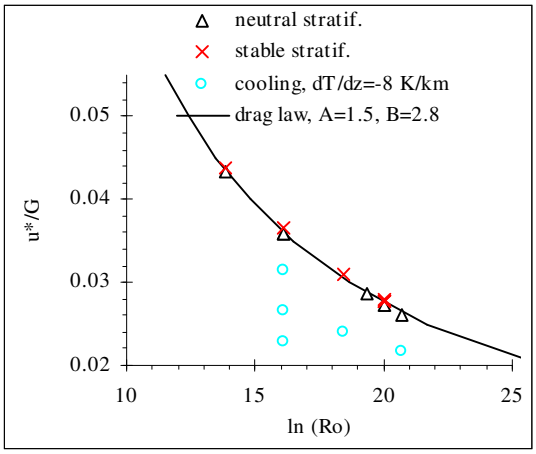

Figure B.26. Geostrophic drag coefficient vs. natural logarithm of the Rossby number. See text for details.

It can be observed from Figure B.26 that a change in the free-flow stratification does not significantly affect the behaviour of $C_G^{1/2}$, whereas from Figure B.25 it influences the cross isobar angle. This points out the sensitivity of B_0 to a change in the external stratification. A decrease in the value of f has a similar effect as an increase in the free flow stability (both imply an increase in the non-dimensional parameter λ).

Imposing a ground cooling affects more significantly the behaviour of both cross isobar angle and geostrophic drag coefficient. With a stable surface layer developing

over ground, the drag coefficient is reduced and the opening of the Ekman spiral becomes more important.

Table B.4. Parameters characterising the simulated neutral situations. Shaded cells correspond to model input.

Simul. name	f [s^{-1}]	z_0 [m]	G [m/s]	Ground heat flux	$\frac{\partial T}{\partial z}$ [K/km]	u_* [m/s]	α [°]	μ [10^{-3}]	λ	δ
S0	$1.\cdot10^{-4}$	$2.\cdot10^{-4}$	10	0	-9.7	0.273	10.6	5.02	18.1	1.023
S1	$1.45\cdot10^{-4}$	0.1	5	0	-9.7	0.245	16.3	1.69	12.5	1.127
Z1	$1.\cdot10^{-4}$	0.01	10	0	-9.7	0.359	13.7	3.59	18.1	1.024
Z2	$1.\cdot10^{-4}$	0.1	10	0	-9.7	0.434	17.0	4.34	18.1	1.024
F1	$5.\cdot10^{-5}$	0.01	10	0	-9.7	0.358	17.9	7.16	36.2	0.815
F2	$1.4\cdot10^{-4}$	0.01	10	0	-9.7	0.375	12.1	2.68	12.9	1.116
G1	$1.\cdot10^{-4}$	$2.\cdot10^{-4}$	5	0	-9.7	0.143	11.7	1.43	18.1	1.027
G2	$1.\cdot10^{-4}$	$2.\cdot10^{-4}$	20	0	-9.7	0.522	10.2	5.22	18.1	1.023
NIS1	$1.\cdot10^{-4}$	$2.\cdot10^{-4}$	10	0	-9.0	0.276	11.9	2.76	51.1	0.710
NIS2	$1.\cdot10^{-4}$	$2.\cdot10^{-4}$	10	0	-8.0	0.279	13.6	2.79	76.7	0.587
NIS3	$1.\cdot10^{-4}$	$2.\cdot10^{-4}$	10	0	-6.5	0.278	16.3	2.78	103.9	0.500
NIS2Z2	$1.\cdot10^{-4}$	0.001	10	0	-8.0	0.310	16.1	3.10	76.7	0.586
NIS2Z3	$1.\cdot10^{-4}$	0.01	10	0	-8.0	0.366	17.7	3.66	76.7	0.586
NIS2Z4	$1.\cdot10^{-4}$	0.1	10	0	-8.0	0.438	23.4	4.38	76.7	0.586

Table B.5. Parameters characterising the simulated stable situations. Shaded cells correspond to model input.

Simul. name	f [s^{-1}]	z_0 [m]	G [m/s]	Ground cooling [K/h]	$\frac{\partial T}{\partial z}$ [K/km]	u_* [m/s]	α [°]	μ [10^{-3}]	λ	δ
ST1	$1.\cdot10^{-4}$	0.01	10	-1.0	-8.0	0.227	42.7	68.8	76.7	0.167
ST2	$1.\cdot10^{-4}$	0.01	10	-0.5	-8.0	0.266	36.7	39.5	76.7	0.230
ST3	$1.\cdot10^{-4}$	0.01	10	-0.2	-8.0	0.314	31.7	19.9	76.7	0.312
ST2ISZ2	$1.\cdot10^{-4}$	$1.\cdot10^{-4}$	10	-0.5	-8.0	0.216	30.6	49.5	76.7	0.203
ST2ISZ3	$1.\cdot10^{-4}$	0.001	10	-0.5	-8.0	0.240	34.0	46.5	76.7	0.210

Summarising the effect of the parameter changes over the boundary layer development, a list of the values of A_0 and B_0 best fitting the model results can be found in Table B.6. It is interesting to stress that for the simulation performed with zero heat flux though the ground and with an external free flow stability of –6.5 K/km (value corresponding to the assumed 'standard atmosphere' lapse rate), we obtain a value of 2 for A_0 and 4.2 for B_0, which come closer to the values resulting from atmospheric observations.

Table B.6. Summary of the A_0 and B_0 values best fitting the CFX4 results.

Simulation name	A_0	B_0	Simulation name	A_0	B_0
S0 *	1.35	2.80	NIS3 *	2.00	4.20
S1	1.55	2.40	NIS2Z2 *	1.95	3.75
Z1 *	1.45	2.75	NIS2Z3 *	1.90	3.50
Z2 *	1.45	2.80	NIS2Z4 *	1.90	3.80
F1	2.35	3.60			
F2	1.57	2.32			
G1 *	1.45	2.95	ST1 *	-1.25	12.5
G2 *	1.30	2.80	ST2 *	-0.5	9.5
			ST3 *	1.3	7.0
NIS1 *	1.70	3.10	ST2ISZ2 *	0.2	9.85
NIS2 *	1.80	3.55	ST2ISZ3 *	0.2	9.75

B.4.3 Calibration of the Zilitinkevich model constants to fit CFX4 results

Trying to minimise the difference between the Zilitinkevich parameterisation and the model results for all the simulations marked with a * in Table B.6 (16 simulations), we obtained the values of the constants presented in Table B.7. Assuming that the constants appearing in the parameterisation are universal constants, the fitting procedure was done simultaneously over the 16 simulations. The differences were minimised using a least square approach, applied for the u and v velocity components as well as for the wind speed.

Regarding the reliability of this result, we should stress that the values obtained this way are very sensitive to a change in the set of profiles used for the fits. Adding or removing one profile from the set significantly affects the resulting model constants. This was particularly true for C_R, $\tilde{C}_R$, $\tilde{C}_L$, C_i and C_{ir}, but also for C_h which varied typically between 0.45 and 0.8. From this observation, it is therefore not surprising that some of the resulting constants show values, which are very different from those obtained by Zilitinkevich et al (in press). Since they estimated their own values by fitting measurements and simulation results, we can therefore expect that the values they gave contain as much uncertainty as those obtained here. Some more comparisons would be required of profiles obtained from both sets of constants and from observations for which the free flow stability conditions would be measured. It might also be well inspired to perform some simulations over a larger range of μ and λ values to reduce the uncertainty in the fitted model constants.

Table B.7. Comparison of Zilitinkevich constants with the ones obtained fitting CFX4 simulation results.

	Zilitinkevich constants	CFX4 constants
C_N	0.1-0.4	0.45
C_L	4.5	6.63
C_R	7	5.48
$\tilde{C}_N$	-1.5	-0.74
$\tilde{C}_L$	-7	-9.68
$\tilde{C}_R$	0	5.24
C_h	0.5	0.73
C_s	10	9.31
C_i	20	78.3
C_{sr}	1	2.63
C_{ir}	1.7	3.36

To test the internal coherence of the results obtained with the fitting procedure, we compared the A_0 and B_0 values obtained directly from the simulations (Table B.6) with those calculated with the Zilitinkevich formulation (eq. B.55 and eq. B.56) using the constants resulting from the fitting procedure. The comparison is presented in Figure B.27 and Figure B.28. Symbols in the figures are exactly the same as for Figure B.25. For a perfect match between theory and model results, the symbols should lie along the solid line. Though this is not exactly the case, the correspondence is still good.

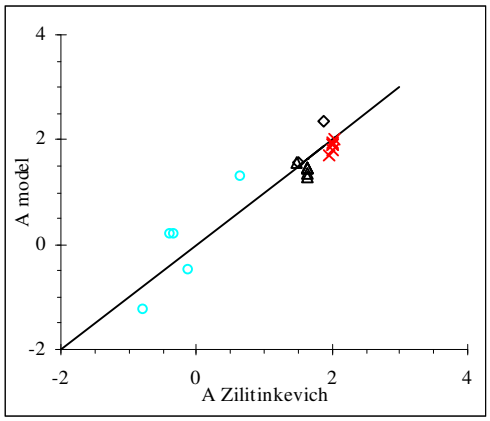

Figure B.27. A_0 best fitting the model results vs. A_0 from eq. B.55 using the constant values from Table B.7 (2nd column). Symbols are the same as for Figure B.25.

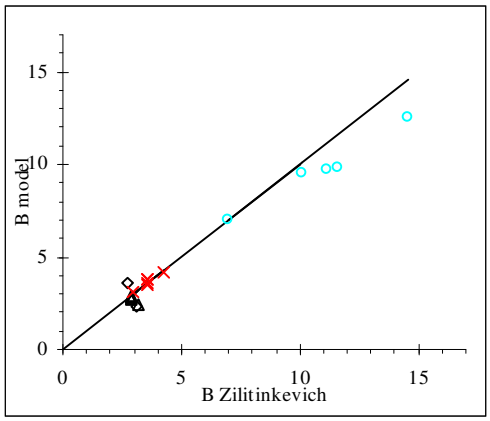

Figure B.28. B_0 best fitting the model results vs. B_0 from eq. B.56 using the constant values from Table B.7 (2nd column). Symbols are the same as for Figure B.25.

Regarding the simulated wind speed profiles, a comparison of the model results with the Zilitinkevich formulation[3] is presented in Figure B.29 and Figure B.30 for a case with zero heat flux through the ground for two different roughness lengths (simulations S0 and Z1, as described in Table B.4). These two situations were simulated with a lapse rate of –9.7 K/km. From Figure B.29 and Figure B.30 we obtain a good agreement between the analytical formulation and the model results.

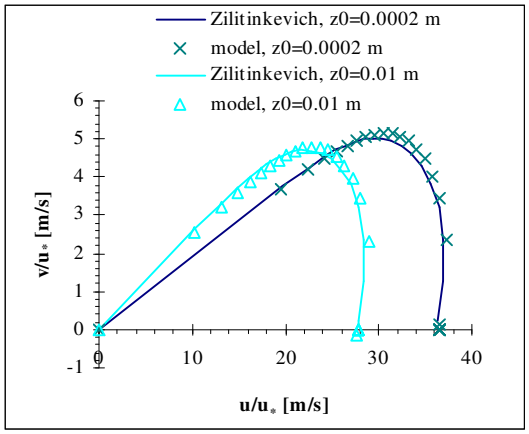

Figure B.29. Non-dimensional Ekman spiral for two neutral cases with neutral static stability and varying roughness length (simulations S0 and Z1). Comparison of model results and Zilitinkevich formulation.

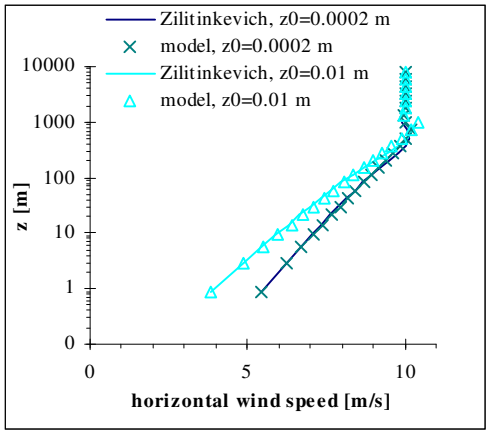

Figure B.30. Wind speed profiles for two neutral cases with neutral static stability and varying roughness length (simulations S0 and Z1). Comparison of model results and Zilitinkevich formulation.

To further compare the analytical and simulated profiles, the absolute and relative errors for the u and v velocity component as well as for the wind speed as a function of the non-dimensional height $\eta = z/h$ were calculated (Table B.8). With maximum relative errors of 2% resp. 1.7%, these demonstrate again the very good agreement for the u velocity component and for the wind speed From the error values, it appears that the v velocity component is reasonably well reproduced by the Zilitinkevich formulation up to a non-dimensional height of 0.25. Above, the

[3] We applied a rotation on the u and v component to align them so that the geostrophic wind is along the x-axis as fixed in the numerical model.

analytical formulation underpredicts the simulated v component. The reason for this more significant difference for v is related to the fact that we do not have a very fine resolution in the upper part of the boundary layer. Since in this region, the v component varies rapidly with η, the errors due to a too coarse resolution have a significant impact on the quality of the solution. Moreover, since v becomes small at the top of the boundary layer, a small absolute error becomes significant in relative terms. Nevertheless, as can be seen from the diagrams, we can state that the Zilitinkevich parameterisation can suitably be used as initial and boundary conditions for a neutral situation, with neutral stratification conditions of the free flow.

Table B.8. Relative and absolute difference between the Zilitinkevich formulation and numerical model result (simulation S0) for the u and v velocity component and wind speed.

$\eta = z / h$	u		v		*Wind speed*	
	$\Delta u / u$	$\lvert\Delta u\rvert$	$\Delta v / v$	$\lvert\Delta v\rvert$	$\frac{\Delta(u^2+v^2)}{(u^2+v^2)}$	$\lvert\Delta(u^2+v^2)\rvert$
0.815	0.9%	0.32	40.3%	0.09	0.9%	0.09
0.603	1.1%	0.42	84.7%	1.08	1.3%	0.13
0.445	1.1%	0.41	46.3%	1.09	0.9%	0.09
0.329	2.0%	0.71	25.6%	0.82	1.7%	0.17
0.242	1.8%	0.65	16.1%	0.62	1.6%	0.16
0.178	1.4%	0.49	9.8%	0.42	1.2%	0.12
0.131	0.8%	0.28	7.1%	0.33	0.7%	0.06
0.096	0.4%	0.11	4.8%	0.23	0.2%	0.02
0.070	0.2%	0.06	3.6%	0.18	0.3%	0.02
0.051	0.5%	0.15	2.3%	0.12	0.6%	0.05
0.037	0.7%	0.22	1.3%	0.07	0.8%	0.06
0.026	0.9%	0.27	1.1%	0.06	0.9%	0.07
0.018	0.9%	0.24	0.2%	0.01	0.9%	0.07
0.012	0.8%	0.22	0.1%	0.01	0.8%	0.06
0.008	0.6%	0.16	0.5%	0.02	0.6%	0.04
0.005	0.4%	0.08	1.4%	0.06	0.3%	0.02
0.002	0.1%	0.03	1.4%	0.06	0.2%	0.01
0.001	0.3%	0.06	2.5%	0.10	0.4%	0.02
Max	**2.0%**	**0.71**	**84.7%**	**1.09**	**1.7%**	**0.17**
Min	**0.1%**	**0.03**	**0.1%**	**0.01**	**0.2%**	**0.01**
Average	**0.8%**	**0.27**	**13.8%**	**0.30**	**0.8%**	**0.07**

A similar comparison is presented in Figure B.31 and Figure B.32 for a situation with zero heat flux through the ground and with a free flow stratification given by a lapse rate of –8.0 K/km (simulation NIS2Z2). For this case as well, it appears from the plots that the Zilitinkevich formulation is appropriate to parameterise the calculated velocity profiles. From the errors on the profiles given in Table B.9 the same conclusions can be drawn for the initially stable case as for the neutrally stratified

situation. Though the maximum errors in this case are slightly higher than for the previous case, the u velocity component and the wind speed profiles are very well reproduced by the parameterisation. The v velocity component shows the same difficulties in the stable case as in the neutrally stratified case.

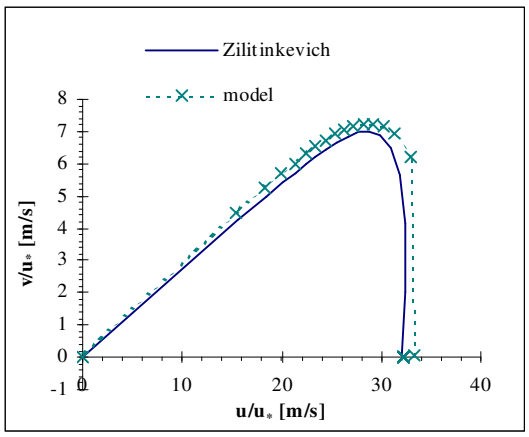

Figure B.31. Non-dimensional Ekman spiral for a neutral case with external stability (simulation NIS2Z2). Comparison of model results and Zilitinkevich formulation.

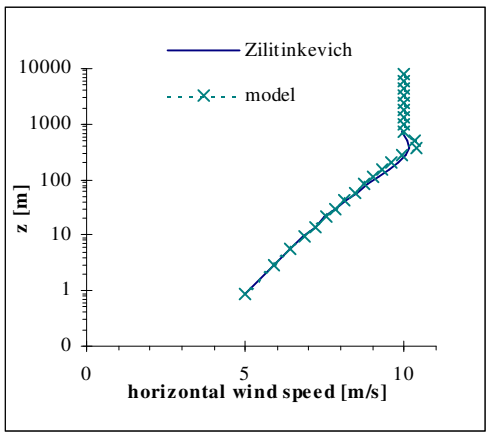

Figure B.32. Wind speed profiles for a neutral case with external stability (simulation NIS2Z2). Comparison of model results and Zilitinkevich formulation.

Comparisons between the simulated profiles and Zilitinkevich formulation for two stable situations (simulations ST1 and ST3) are given in Figure B.33 and Figure B.34. The flow stability is imposed by setting a constant ground cooling. For the situation with a moderate cooling of –0.2 K/h, the Zilitinkevich formulation reproduces the simulated profiles fairly well. For the more stable situation, where the ground cooling is set to –1 K/h, the agreement between the model results and the analytical formulation is no longer so good. With the constants obtained by the fitting procedure, the Zilitinkevich formulation overestimates the wind speed in the surface layer and underestimates it close to the top of the boundary layer.

For the situation with the stronger ground cooling (–1 K/h) the relative and absolute differences between the numerical results and the analytical formulation for the u, v and wind speed profiles have been calculated (Table B.10). Compared to the neutral cases, the maximum relative difference on both the u and wind speed profiles have been significantly increased, with values of 28.5% and 26.3%. For the v velocity component, the difference between the analytical formulation and the numerical

results shows the same disagreement in the upper part of the boundary layer as for the neutral situations. Even for the lower levels, the agreement breaks down with relative differences around 16%.

To possibly improve the representativity of the Zilitinkevich parameterisation for the stable cases, it might be worth trying to perform some more simulations, with a wider range of λ and μ values. Another thing that might have to be considered would be an increase in the model resolution in the upper part of the boundary layer. This would allows us to better take into account the layer showing a rapid decrease of the v velocity component when fitting the profiles and determining the model constants.

Table B.9. Relative and absolute difference between the Zilitinkevich formulation and numerical model result (simulation NIS2Z2) for the u and v velocity component and wind speed.

$\eta = z / h$	u		v		*Wind speed*	
	$\Delta u / u$	$\lvert\Delta u\rvert$	$\Delta v / v$	$\lvert\Delta v\rvert$	$\frac{\Delta(u^2+v^2)}{(u^2+v^2)}$	$\lvert\Delta(u^2+v^2)\rvert$
0.928	0.8%	0.24	96.1%	0.05	0.8%	0.08
0.686	2.5%	0.80	96.1%	1.92	2.3%	0.23
0.506	1.4%	0.47	50.4%	2.09	2.4%	0.24
0.373	1.9%	0.61	23.1%	1.30	1.0%	0.11
0.275	2.7%	0.85	10.4%	0.67	2.2%	0.21
0.202	2.5%	0.76	4.9%	0.34	2.1%	0.20
0.148	2.0%	0.57	2.7%	0.19	1.7%	0.16
0.108	1.4%	0.40	2.4%	0.17	1.2%	0.11
0.078	0.9%	0.23	3.0%	0.20	0.6%	0.05
0.056	0.4%	0.11	3.8%	0.25	0.2%	0.01
0.040	0.2%	0.05	4.1%	0.26	0.1%	0.01
0.028	0.0%	0.00	4.7%	0.29	0.3%	0.02
0.019	0.1%	0.03	5.2%	0.31	0.5%	0.03
0.012	0.0%	0.00	5.0%	0.29	0.3%	0.02
0.007	0.4%	0.08	5.2%	0.28	0.0%	0.00
0.004	0.9%	0.16	4.9%	0.24	0.5%	0.03
0.001	1.1%	0.17	5.2%	0.22	0.6%	0.03
Max	**2.7%**	**0.85**	**96.1%**	**2.09**	**2.4%**	**0.24**
Min	**0.0%**	**0.00**	**2.4%**	**0.05**	**0.0%**	**0.00**
Average	**1.1%**	**0.33**	**19.2%**	**0.53**	**1.0%**	**0.09**

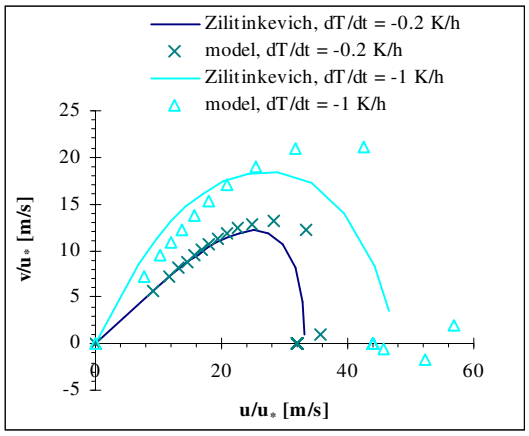

Figure B.33 Non-dimensional Ekman spiral for two stable cases with varying ground cooling (simulations ST1 and ST3). Comparison of model results and Zilitinkevich formulation.

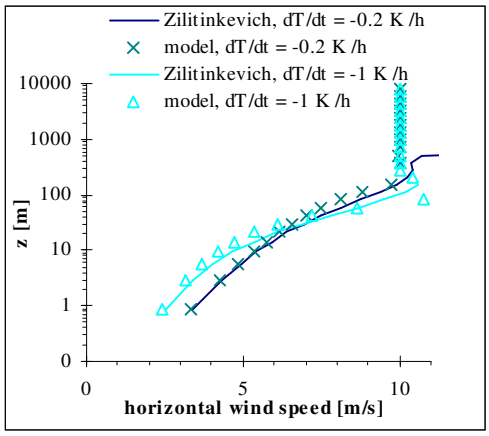

Figure B.34 Wind speed profiles for two stable cases with varying ground cooling (simulations ST1 and ST3). Comparison of model results and Zilitinkevich formulation.

Table B.10. Relative and absolute difference between the Zilitinkevich formulation and numerical model result (simulation ST1) for the u and v velocity component and wind speed.

$\eta = z / h$	u		v		*Wind speed*	
	$\Delta u / u$	$\lvert\Delta u\rvert$	$\Delta v / v$	$\lvert\Delta v\rvert$	$\frac{\Delta(u^2+v^2)}{(u^2+v^2)}$	$\lvert\Delta(u^2+v^2)\rvert$
0.964	12.4%	5.77	150.4%	5.25	12.1%	1.29
0.706	28.5%	12.59	77.3%	6.46	26.3%	2.69
0.515	7.6%	3.00	51.9%	7.22	13.3%	1.27
0.373	7.1%	2.42	21.0%	3.62	0.7%	0.06
0.268	12.6%	3.66	3.0%	0.55	7.9%	0.61
0.191	14.0%	3.40	7.2%	1.32	11.5%	0.79
0.133	12.4%	2.54	12.4%	2.16	12.4%	0.76
0.091	8.9%	1.52	15.0%	2.41	11.7%	0.62
0.059	4.1%	0.59	16.2%	2.37	10.1%	0.47
0.036	1.5%	0.18	16.3%	2.14	7.8%	0.31
0.018	6.9%	0.67	16.4%	1.85	5.9%	0.20
0.005	12.8%	0.89	16.2%	1.39	3.7%	0.09
Max	**28.5%**	**12.59**	**150.4%**	**7.22**	**26.3%**	**2.69**
Min	**1.5%**	**0.18**	**3.0%**	**0.55**	**0.7%**	**0.06**
Average	**10.7%**	**3.10**	**33.6%**	**3.06**	**10.3%**	**0.76**

From the results presented here, it was felt that for the sake of producing wind profiles to be used as initial and boundary conditions in the case where no

observations are available, the Zilitinkevich parameterisation would already be useful as such. It would however be very interesting to see whether it compares well with atmospheric measurements when using the set of parameters obtained from the fitting procedure (Table B.7).

Another piece of useful information that can be derived from the Zilitinkevich parameterisation is the boundary layer height behaviour as a function of the stability parameters λ and μ. Using eq. B.50, with the values of the constants obtained from fitting the 16 simulation profiles, the normalised boundary layer height $h/(u_* / f)$ has been plotted in Figure B.35. The maximum value for the normalised boundary layer height appears at the origin ($\mu = \lambda = 0$) and is equal to $C_h = 0.72$.

We can see from Figure B.35 that for small values of λ (weak stability of the free flow), the normalised boundary layer height $h/(u_* / f)$ varies very strongly with a change of λ. Changing the stratification of the external flow from purely neutral ($\lambda = 0$) to a situation with a vertical gradient of –9.7 K/km for the external flow already leads to a value of λ of order 20. This already implies a reduction of $h/(u_* / f)$ from 0.72 to about 0.42. Again, the behaviour presented in Figure B.35 is consistent with the fact that numerical models, which are able to deal with purely neutral situation, predict a value of $h/(u_* / f)$ around 0.7, whereas observations, for which pure neutrality can barely be observed, gives much lower values of $h/(u_* / f)$ around 0.2.

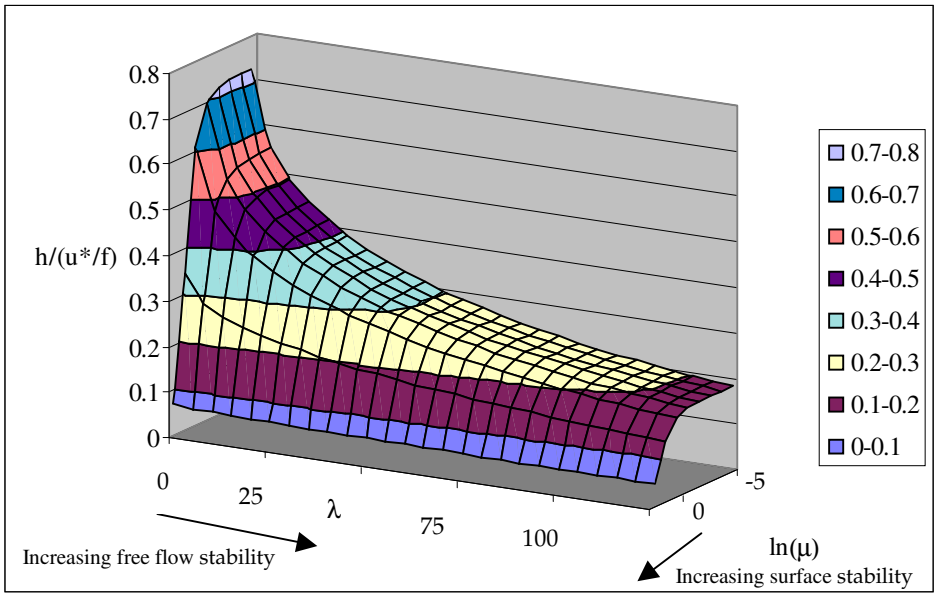

Figure B.35. Normalised boundary layer height behaviour vs. λ and μ (λ increasing from 0 to 125 and $\log_{10}(\mu)$ increasing from –5 to 2 .).

The boundary layer height also decrease when μ increases. A noticeable effect of the surface stratification is only observed for values of μ above 1 ($u_* / L \approx \mathrm{O}(10^{-4})$). This behaviour however needs to be considered with care, since the simulations used for the fitting procedure presented essentially values of L in the range 30-200, as well as some situations with very large values of L (around 10^5 and 10^6), but nothing in-between.

Appendix C

C Validation of the implementation of the potential temperature equation

Instead of using the standard enthalpy equation to satisfy the first principle of thermodynamics, we implemented an equation for the potential temperature and introduced a buoyancy source term in the vertical velocity equation, which is written as a function of the potential temperature.
The aim of the present appendix is to demonstrate, from test situations for which analytical solutions are available, as well as from comparisons with observations, that the implementation was done properly and that a full Navier-Stokes solver is able to satisfactorily reproduce flow features typical for the mesoscale.

A short introduction to linear mountain wave theory and its application over two-dimensional mountain features will be presented in the next section. Analytical solutions for the flow perturbation generated by a theoretical mountain profile will be derived for the two particular situations of hydrostatic mountain waves and quasi-neutral flow. These will provide two test cases for the validation of the numerical model.
Solutions from CFX4 for intermediate conditions leading to the formation of non-hydrostatic lee-waves will also be presented and compared to results from the non-hydrostatic version of TVM (Thunis, 1995) as well as to results from RAMS (Tripoli and Cotton, 1982). And finally simulation results will be shown reproducing the strongly non-linear extreme foehn event that was recorded over Boulder (Colorado) in January 1972. CFX4 results are compared to observations and with numerical results presented by Peltier and Clark (1979) and by Thunis (1995).

C.1 Introduction to linear mountain wave theory

The presence of a mountain barrier can significantly affect the behaviour of the atmospheric flow field in its proximity. As an example, one can quote the formation of thermal winds, which can be generated by differential heating/cooling of air masses located at mountain summits or at the bottom of valleys. For the case of a well-established atmospheric flow, under the influence of a synoptic scale situation, a mountain chain can modify the general direction of the flow. In addition to the important amplifications imposed to the horizontal velocity component, it can be noted that the presence of relief can induce very impressive vertical wind speeds. Colson (1954) mentions a pilot's experience who reported having observed vertical

velocities reaching values up to 40 m/s. For stable free flow stratification conditions, hydrostatic mountain waves can form throughout the entire troposphere. Waves propagating horizontally in the lee of the mountain ('trapped lee waves') can also be observed. For an excellent review of various observations made to characterise atmospheric flows over mountainous terrain one can refer to the publication of Queney et al (1960).

The theoretical aspects presented below are inspired by Holmboe and Klieforth (1957) and deal with the various flow regimes that an air mass can undergo when crossing a mountain barrier. From the point of view of the numerical model validation, we will restrict ourselves to the particular case of a theoretical bell-shaped mountain ('witch of Agnesi' mountain shape), for which, in a linearised approximation, analytical solutions can be found that describe the perturbed flow.

The mountain profile considered (Figure C.1) is given by the expression

eq. C.1 $$h(x) = \frac{h_m \cdot a^2}{x^2 + a^2}$$

with: h_m the maximum mountain height

a the mountain half-width (distance at which the mountain height is half the maximum height)

The reference atmospheric state (without any perturbation induced by the orography) corresponds to a horizontal flow in the x direction, with an identically vanishing vertical wind speed. In this reference state the atmosphere is assumed to be in hydrostatic equilibrium.

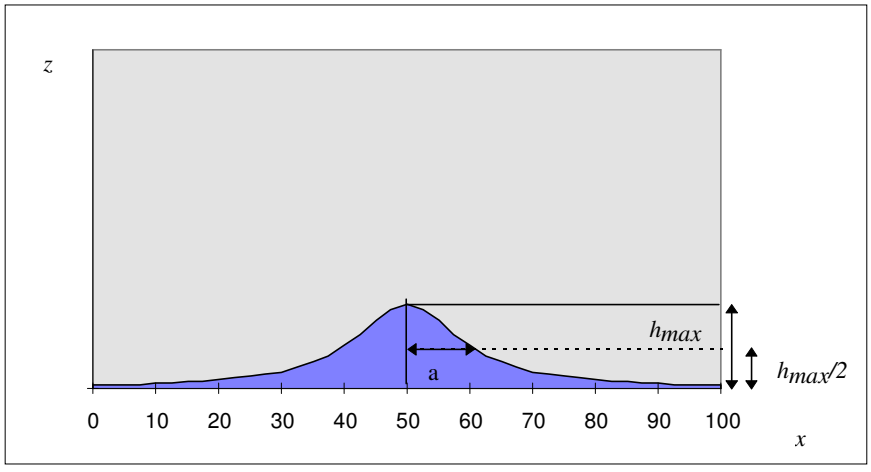

Figure C.1. Theoretical bell-shaped mountain profile.

In a three-dimensional situation, the presence of the mountain forces the flow to go up or round the mountain. For the two-dimensional case however, the only remaining option for the air parcel is to go over the obstacle. The type of flow regime that can be observed in an atmosphere perturbed by a mountain feature will depend on the flow stability conditions. In the following, we will try to summarise this for the particular case of a dry atmosphere (i.e. more precisely for conditions in which no evaporation/condensation processes can affect the energy balance of the atmosphere).

The equation for the vertical displacement ξ of an air parcel around its equilibrium level is

eq. C.2 $$\frac{d^2\xi(t)}{dt^2} + g\frac{\gamma^* - \gamma}{T}\xi(t) = 0$$

where

ξ = vertical displacement of the air parcel (m)

t = time (sec)

g = acceleration due to gravity (m/s^2)

T = real temperature (K)

γ^* = vertical real temperature gradient (lapse rate) of a dry adiabatic atmosphere (K/m) (defining the neutral stratification)

$\gamma = -\partial T/\partial z =$ vertical real temperature gradient (lapse rate) for the actual atmospheric (K/m)

For the particular case of an atmosphere with neutral stratification ($\gamma = \gamma^*$), an air parcel moved out of its equilibrium position will also be in equilibrium with the atmospheric conditions at the level at which it will have been displaced. Therefore it will not experience any buoyancy force.

For a stably stratified atmosphere however, the density of the moved air parcel will be changed relatively to the density of the ambient air mass. The density difference will be such that the buoyancy force acting on the air parcel will force it back to its original level. In such a stable situation ($\gamma < \gamma^*$), an air parcel in a horizontally moving air mass will oscillate around its equilibrium level. The frequency of the oscillation will be determined by the Brunt-Väisälä frequency $N = \sqrt{\frac{g}{\theta}\frac{\partial\theta}{\partial z}}$. If this frequency also coincides with frequencies of other atmospheric processes, (e.g. with the Fourier modes of the terrain perturbation), resonance can occur which can lead to important modifications of the flow pattern. Lee waves can be generated which

horizontally propagate over some 50 kilometres, or vertically throughout the entire troposphere.

To quantitatively develop a theory of mountain waves in a stably stratified atmosphere, the following assumptions are made:

1. The flow perturbation induced by the topography is weak, so that the flow equations can be linearised.
2. The effects of condensation, heat conduction and radiation can be neglected. The same is assumed to be valid for the friction term in the Navier-Stokes equations.
3. The scales under consideration (meso-scale) allow us to neglect the effect of the Earth rotation.

C.1.1 Variables of state for the atmosphere

The atmosphere can be described by the following variables:

$\bar{u}(z)+u(x,z)$	horizontal velocity component
$w(x,z)$	vertical velocity component
$\bar{p}(z)+p(x,z)$	pressure
$\bar{\rho}(z)+\rho(x,z)$	density
$\bar{T}(z)+T(x,z)$	real temperature

Variables with overbars describe the unperturbed atmospheric state, whereas the others represent the difference between the perturbed and unperturbed atmosphere.

C.1.2 Equations and linearisation

With the above mentioned assumptions 1-3, the equations describing a two-dimensional stationary ($\partial/\partial t = 0$) flow become:

continuity

eq. C.3 $$(\bar{u}+u)\frac{\partial\rho}{\partial x}+w\frac{\partial(\bar{\rho}+\rho)}{\partial z}+(\bar{\rho}+\rho)\left(\frac{\partial u}{\partial x}+\frac{\partial w}{\partial z}\right)=0$$

momentum conservation

eq. C.4 $$(\bar{u}+u)\cdot\frac{\partial u}{\partial x}+w\cdot\frac{\partial(\bar{u}+u)}{\partial z}=-\frac{1}{(\bar{\rho}+\rho)}\frac{\partial p}{\partial x}$$

eq. C.5 $$(\bar{u}+u)\cdot\frac{\partial w}{\partial x}+w\cdot\frac{\partial w}{\partial z}=-\frac{1}{(\bar{\rho}+\rho)}\frac{\partial(\bar{p}+p)}{\partial z}-g$$

energy conservation

eq. C.6 $$(\overline{u}+u)\cdot\frac{\partial p}{\partial x}+w\cdot\frac{\partial(\overline{p}+p)}{\partial z}=(\overline{c}+c)^2\left[(\overline{u}+u)\cdot\frac{\partial \rho}{\partial x}+w\cdot\frac{\partial(\overline{\rho}+\rho)}{\partial z}\right]$$

ideal gas law

eq. C.7 $$\frac{\overline{p}+p}{\overline{\rho}+\rho}=R(\overline{T}+T)$$

where

eq. C.8 $R=c_p-c_v$ gas constant

eq. C.9 $c^2=\tilde{\gamma}RT$ square of the speed of sound

eq. C.10 $\tilde{\gamma}=c_p/c_v$

After linearisation and with some manipulations, a second order differential equation for the vertical velocity can be derived, which reads:

eq. C.11 $$\overline{M}\frac{\partial^2 w}{\partial x^2}+\frac{\partial^2 w}{\partial z^2}-\overline{S}\frac{\partial w}{\partial z}+(\frac{\overline{\beta}g}{\overline{u}^2}+\frac{\overline{S}}{\overline{u}}\frac{\partial \overline{u}}{\partial z}-\frac{1}{\overline{u}}\frac{\partial^2 \overline{u}}{\partial z^2})w=0$$

with

eq. C.12 $$\overline{S}=\frac{\partial}{\partial z}\ln(\frac{\overline{M}}{\overline{\rho}})$$

eq. C.13 $$\overline{\beta}=\frac{\partial}{\partial z}\ln(\overline{M}\overline{\theta})$$

where

eq. C.14 $\overline{M}=1-\frac{\overline{u}^2}{\overline{c}^2}$ stands for the difference of the flow Mach number from unity

eq. C.15 $\theta=T(\frac{p_0}{p})^{R/c_p}$ represents the potential temperature

eq. C.16 $p_0=1.013\cdot10^5$ Pa is the sea-level reference pressure

With the substitution,

eq. C.17 $$w=\sqrt{\frac{\overline{M}}{\overline{M}_0}\frac{\overline{\rho}_0}{\overline{\rho}}}\cdot w_1(x,z)$$

a simplified equation can be written for w_1 which yields:

eq. C.18 $$\overline{M}\cdot\frac{\partial^2 w_1}{\partial x^2}+\frac{\partial^2 w_1}{\partial z^2}+l^2(z)\cdot w_1=0$$

with

eq. C.19 $$l^2(z) = \frac{g\overline{\beta}}{\overline{u}^2} + \frac{\overline{S}}{\overline{u}}\frac{\partial \overline{u}}{\partial z} - \frac{1}{4}\overline{S}^2 + \frac{1}{2}\frac{\partial \overline{S}}{\partial z} - \frac{1}{\overline{u}}\frac{\partial^2 \overline{u}}{\partial z^2}$$

βg being the square of the Brunt-Väisälä number and

S being the heterogeneity of the atmosphere

The parameter l is commonly known as the Scorer parameter.

(Note: variables with a subscript '0' stand for values at sea level)

C.1.3 Method of resolution

The differential equation for the vertical wind speed is to be solved in the half plane $z>0$, subject to the boundary conditions:

1. At **ground**, the flow vectors are tangential to the mountain profile. For a mountain shape given by $h(x)$ the requirement of tangency implies:

eq. C.20 $$\frac{dh}{dx} = \frac{w(x,h(x))}{\overline{u}(h(x)) + u(x,h(x))}$$

With the additional assumption that the mountain is small, the ground boundary condition can be approximated by

eq. C.21 $$\frac{dh}{dx} = \frac{w(x,0)}{\overline{u}(h(x))}$$

For a case where the wind shear is weak, and considering that at ground $w = w_1$, the boundary condition becomes:

eq. C.22 $$\frac{dh}{dx} = \frac{w(x,0)}{\overline{u}(0)} = \frac{w_1(x,0)}{\overline{u}(0)}$$

2. At the **top** of the simulation domain, we have a condition of vanishing kinetic energy term $\frac{1}{2}\overline{\rho}\cdot w^2$ in the vertical.

Hence, we have:

eq. C.23 $$\lim_{x^2+z^2\to\infty} \frac{1}{2}\overline{\rho}\cdot w^2 = \lim_{x^2+z^2\to\infty} \frac{1}{2}\frac{\overline{\rho}_0 \overline{M}}{\overline{M}_0} {w_1}^2 = 0$$

For $\overline{M}$ varying slowly with height, this is equivalent to the condition

eq. C.24 $$\lim_{x^2+z^2\to\infty} w_1 = 0$$

The equation for w_1 is solved using a Fourier decomposition with

eq. C.25 $$w_{1,k}(x,z) = \hat{w}_{1,k}(z)\cdot \sin(kx)$$

Introducing $w_{1,k}$ in the differential equation for w_1, we obtain for each mode $\hat{w}_{1,k}(z)$ the differential equation

eq. C.26 $$\hat{w}_{1,k}'' + (l^2(z) - \overline{M} \cdot k^2)\hat{w}_{1,k} = 0$$

The Fourier decomposition is also applied to the mountain profile *h(x)*, giving

eq. C.27 $$h_k(x) = \hat{h}(k) \cdot \cos(kx)$$

The boundary conditions for $\hat{w}_{1,k}(z)$ are then:

eq. C.28 $$\hat{w}_{1,k}(0) = -\overline{u}(0) \cdot k \cdot \hat{h}(k)$$

and

eq. C.29 $$\lim_{z \to \infty} \hat{w}_{1,k}(z) = 0$$

For a function $W(k,z)$ satisfying the differential equation eq. C.26, the following expression is then a solution for the vertical velocity equation with the wave number *k*:

eq. C.30 $$w(k,x,z) = -\sqrt{\frac{\overline{M} \cdot \overline{\rho}_0}{\overline{M}_0 \cdot \overline{\rho}}} \cdot \overline{u}(0) \cdot k \cdot \hat{h}(k) \cdot \frac{W(k,z)}{W(k,0)} \cdot \sin(kx)$$

The vertical velocity w being a superposition of the modes $w(k,x,z)$, the solution to the problem will essentially depend on the behaviour of the functions $W(k,z)$. If for any value of *k*, the function $W(k,z)$ never becomes 0, then the Fourier integral for the vertical velocity component w will be defined.
In the case where the denominator vanishes for one or several values of *k*, the Fourier integral can not be evaluated directly. A solution for w can be obtained applying the Cauchy theorem, in which case, the main contribution to the integral will depend on the behaviour of the function in the vicinity of the singularity.

C.1.4 Solution for the particular case of a uniform flow over a 'Witch of Agnesi' mountain profile

In the following, we will only treat the particular case of uniform flow over a bell-shaped mountain, with the mountain profile given by eq. C.1. The Fourier decomposition of the mountain profile gives the components

eq. C.31 $$h_k(x) = \hat{h}(k) \cdot \cos(kx)$$

with

eq. C.32 $$\hat{h}(k) = h_m a \cdot e^{-ka}$$

The atmospheric conditions used are given by the following wind and temperature profiles:
The wind profile is chosen such that $\bar{u}(z) = u_0 = 10m/s$ over the whole vertical extent, whereas the thermal stratification is given by:

eq. C.33 $$\bar{T}(z) = T_0 - \gamma \cdot z$$

with γ= 6.5 K/km constant over the whole troposphere. T_0 is the real temperature at ground.

With the additional assumption that the flow Mach number is low over the whole atmosphere ($\bar{M} \cong 1$), an analysis of the order of magnitude of the various terms appearing in the Scorer parameter shows that the latter simplifies to

eq. C.34
$$\begin{aligned} l^2(z) &= \frac{g}{\bar{u}^2}\frac{1}{\theta}\frac{d\theta}{dz} - \frac{1}{4}\bar{S}^2 \\ &= \frac{g}{\bar{u}^2}\frac{\gamma^* - \gamma}{\bar{T}} - \frac{1}{4}\bar{S}^2 \\ &\cong \frac{g}{\bar{u}^2}\frac{\gamma^* - \gamma}{\bar{T}} \end{aligned}$$

The last approximation, neglecting the density variation with height with regard to the effect of thermal stratification, is only valid in the case of a stably stratified atmosphere ($\gamma \neq \gamma^*$).

Assuming that the Scorer parameter is independent of the altitude z, the equation to solve for $\hat{w}_{1,k}(z)$ becomes:

eq. C.35 $$\hat{w}_{1,k}'' + (l^2 - k^2)\hat{w}_{1,k} = 0$$

The general solution of eq. C.35 is

eq. C.36 $$\hat{w}_{1,k}(z) = A \cdot e^{-\sqrt{k^2 - l^2}z} + B \cdot e^{+\sqrt{k^2 - l^2}z}$$

Using the ground boundary condition allows a first equation to be derived for the constants *A* and *B*:

eq. C.37 $$A + B = u(0) \cdot ik \cdot h_m \cdot a \cdot e^{-ka}$$

The solution for the vertical velocity component reads (Fourier integral over the single modes):

eq. C.38 $$w_1(x,z) = \mathrm{Re}\int \hat{w}_{1,k}(z) \cdot e^{ikx} \cdot dk = \mathrm{Re}\int A \cdot e^{i(kx + \sqrt{l^2 - k^2}z)} + B \cdot e^{i(kx - \sqrt{l^2 - k^2}z)} dk$$

To apply the boundary condition for the case $z \to \infty$, we need to distinguish two types of modes:

- $k^2 > l^2$, in which case the solution for the vertical velocity component can be written as $w_1(x,z) = \mathrm{Re}\int A \cdot e^{-\sqrt{k^2-l^2}z} \cdot e^{ikx} + B \cdot e^{\sqrt{k^2-l^2}z} \cdot e^{ikx} dk$. So that the latter remains bounded for $z \to \infty$, the constant *B* needs to be zero.
- $l^2 > k^2$. For these values of *k*, the amplitude of the modes remains bounded for any value of *z*. The condition requiring that the modes must be of finite amplitude is no longer sufficient to impose a condition on *A* and *B*. Durran (1990) applies for these circumstances a 'radiation' condition, according to which the energy flux transported by the waves at a sufficiently high altitude can only be transported away from the obstacle. This condition also requires according to Eliassen and Palm (1960) that the constant *B* is zero.

Taking the boundary conditions into account, the solution becomes:

eq. C.39
$$w_1(x,z) = \overline{u}(0) \cdot \mathrm{Re}\left[\int_0^l ik \cdot \hat{h}(k) \cdot e^{i\sqrt{l^2-k^2}z} \cdot e^{ikx} dk + \int_l^\infty ik \cdot \hat{h}(k) \cdot e^{-\sqrt{k^2-l^2}z} \cdot e^{ikx} dk\right]$$

For the 'witch of Agnesi' mountain profile, ones obtains:

eq. C.40
$$\begin{aligned} w_1(x,z) &= \overline{u}(0) \cdot h_m a \cdot \mathrm{Re}\left[\int_0^l ik \cdot e^{-ka} \cdot e^{i\sqrt{l^2-k^2}z} \cdot e^{ikx} dk + \int_l^\infty ik \cdot e^{-ka} \cdot e^{-\sqrt{k^2-l^2}z} \cdot e^{ikx} dk\right] \\ &= \overline{u}(0) \cdot h_m a \cdot \mathrm{Re}\left\{\frac{\partial}{\partial x}\left[\int_0^l e^{-ka} \cdot e^{i\sqrt{l^2-k^2}z} \cdot e^{ikx} dk + \int_l^\infty e^{-ka} \cdot e^{-\sqrt{k^2-l^2}z} \cdot e^{ikx} dk\right]\right\} \end{aligned}$$

Queney studied in details the various types of solutions for the above problem. The behaviour of the resulting flow field and the type of waves that can develop essentially depend on the non-dimensional numbers al (characteristic width of the mountain multiplied by the Scorer parameter) and $h_m l$ (maximum mountain height multiplied by the Scorer parameter). A good review of the expected type of flows depending on the atmospheric conditions is given by Thunis (1995).

From this point onwards, we will restrict ourselves to the presentation of solutions for the two limiting cases where the characteristic mountain width is much larger than the natural vertical wavelength of the flow l^{-1} ($al >> 1$) as well as for the opposite situation ($al << 1$)). As long as the mountain maximum height is not too important ($h_m l << 1$), linear theory as presented above can be applied. Non-linear effects become significant for values of $h_m l$ of the order of 1 (Miles & Huppert, 1969).

C.1.4.1 Quasi-neutral flow situation

In the case where $al << 1$ (narrow mountain, weak atmospheric stability, strong winds) we have a quasi-neutral flow blowing over the obstacle. In this case, the analytical solution is obtained setting $l = 0$. The vertical velocity w_1 is then calculated from:

eq. C.41
$$w_1(x,z) \cong \overline{u}(0) \cdot h_m a \cdot \mathrm{Re}\left\{ \frac{\partial}{\partial x} \left[\int_0^\infty e^{-ka} \cdot e^{-kz} \cdot e^{ikx} dk \right] \right\}$$

After integration, the solution for w_1 becomes:

eq. C.42
$$\begin{aligned} w_1(x,z) &= \overline{u}(0) \cdot h_m a \cdot \frac{\partial}{\partial x} \left(\frac{a+z}{(a+z)^2 + x^2} \right) \\ &= \overline{u}(0) \cdot h_m a \cdot \frac{-2x(a+z)}{\left[(a+z)^2 + x^2 \right]^2} \end{aligned}$$

Remark:

For a real atmosphere in quasi-neutral conditions, the heterogeneity term $S = \partial \ln \rho / \partial z$ appearing in the Scorer parameter can no longer be neglected relative to the thermal stratification contribution. When the relative variation of the heterogeneity with the altitude is non-negligible, the assumption in the derivation of an analytical solution that the Scorer parameter remains constant with height is therefore not true for the case of a deep Boussinesq approximation. As a consequence, the analytical solution for the quasi neutral situation (eq. C.42) only makes sense with the additional assumption that the density is constant with height ('shallow Boussinesq approximation', $-S = \partial \ln \rho / \partial z = 0$).

C.1.4.2 Hydrostatic mountain waves

In the opposite approximation $al >> 1$ (wide mountain, strong atmospheric stability, relatively weak winds) hydrostatic mountain waves are generated. For this situation, the solution for the vertical velocity component is obtained from eq. C.40, neglecting the value of *k* relative to the one of *l* in the root of the exponential. We therefore get:

eq. C.43
$$\begin{aligned} w_1(x,z) &\cong \overline{u}(0) \cdot h_m a \cdot \mathrm{Re}\left\{ \frac{\partial}{\partial x} \left[\int_0^l e^{-ka} \cdot e^{ilz} \cdot e^{ikx} dk \right] \right\} \\ &\cong \overline{u}(0) \cdot h_m a \cdot \mathrm{Re}\left\{ \frac{\partial}{\partial x} \left[\int_0^\infty e^{-ka} \cdot e^{ilz} \cdot e^{ikx} dk \right] \right\} \end{aligned}$$

The analytical solution for w, valid for a uniform stratified flow field over a bell-shaped mountain, is obtained by integrating eq. C.43 and reads:

eq. C.44

$$w(x,z) = \sqrt{\frac{\overline{\rho}_0}{\rho}} \cdot \overline{u}(0) \cdot h_m a \cdot \frac{\partial}{\partial x}\left(\frac{a\cos lz - x\sin lz}{a^2 + x^2}\right)$$
$$= \sqrt{\frac{\overline{\rho}_0}{\rho}} \cdot \overline{u}(0) \cdot h_m a \cdot \frac{\left(x^2 - a^2\right)\sin lz - 2xa\cos lz}{\left(a^2 + x^2\right)^2}$$

C.2 Simulations

All the simulation results presented in this appendix have been computed for a two-dimensional domain. The type of treatment applied to the variables at the various domain boundaries is summarised in Table C.1 for the horizontal and vertical wind speed, potential temperature, pressure, turbulent kinetic energy and dissipation rate. The ground is treated as a wall, assuming free slip conditions when comparisons are made with analytical solutions and with no-slip conditions when comparing with the observations of the Boulder foehn event. Dirichlet boundary conditions are applied at the entrance as well as at the top of the simulation domain . For the domain outlet, von Neumann conditions are applied, assuming the flow to be fully developed at the model exit.

For the cases with a stably stratified atmosphere, where the model is used in a laminar flow mode, some additional viscosity is introduced in a damping layer ($10000m < z < 25000m$), to prevent any wave reflection at the top boundary.

Table C.1. Type of boundary condition used at various boundaries, and treatment applied to the flow variables.

Variable	Ground	Entrance	Outlet	Top
	wall	inlet	mass flow boundary	inlet
Velocity	Free slip / No Slip	Dirichlet	Neumann	Dirichlet
Temperature	Dirichlet	Dirichlet	Neumann	Dirichlet
Pressure		Neumann	Neumann	Neumann
Turbulent kinetic energy	Log. Wall treatment	Dirichlet	Neumann	Dirichlet
TKE dissipation	Log. Wall treatment	Dirichlet	Neumann	Dirichlet

C.2.1 Neutral case, shallow Boussinesq approximation

The following test consists of simulating a neutral flow above a mountain with maximum height $h_m = 500\,\mathrm{m}$ and half-width $a = 10\,\mathrm{km}$. The model is initialised with a constant horizontal wind speed profile of 10 m/s and a vertical wind speed of 0 m/s over the whole domain. The simulation is done without any buoyancy force implemented (corresponding to a zero vertical gradient of potential temperature $\partial\theta/\partial z = 0$).

The boundary condition at the entrance of the computational domain (x= -50 km in the plots) is kept constant with time. The simulation is done with a density constant with height (shallow Boussinesq approximation), to fulfil the requirement of a constant Scorer parameter over the whole vertical extent.

For such simulation conditions, the Scorer parameter is therefore zero and simulation results will be compared to the analytical solution obtained in the approximation $al << 1$ (eq. C.42).

The horizontal and vertical dimensions of the domain are $L_x = 100\,km$ and $L_z = 28\,km$. The domain is divided into 65 elements in the horizontal and 41 in the vertical. Simulation conditions are summarised in Table C.2.

Table C.2 Simulation conditions used for the case of a neutral flow over the theoretical bell-shaped mountain.

Turbulence model	None (laminar flow mode)	
Damping layer	None	
Advection scheme	Hybrid: upwind-centred differences	Wind speed
Boundary condition type (see Appendix L for definition)	Inlet Mass flow boundary Wall (free slip) Inlet	Entrance Exit Ground Top
Under relaxation factors	0.3	Wind speed
Time step	30 s	
Density profile	Constant (shallow Boussinesq)	
Ground temperature	288 K	
Thermal stratification	neutral	$\partial\theta/\partial z = 0$
Wind speed	10 m/s	
Mountain maximum height	500 m	
Mountain half-width	10 km	

Figure C.2 presents the simulation results for the vertical wind speed (continuous line), which can be compared to the analytical solution (dashed line). For reader's ease, results are only plotted up to an altitude of 15 km. Points in the figure represent the centre of the control volumes forming the mesh. The mountain profile is shown in black. Wind speed labels are given in m/s.

The simulated flow enters the domain from the left. The solution for the vertical wind speed is symmetrical with regard to the mountain summit. It gives some positive vertical wind speeds on the upwind side and some negative ones downwind. The comparison between the model predicted vertical velocity component (continuous line) and the analytical solution (dashed line) shows that the model reproduces very well both the spatial distribution and the amplitude of the phenomenon.

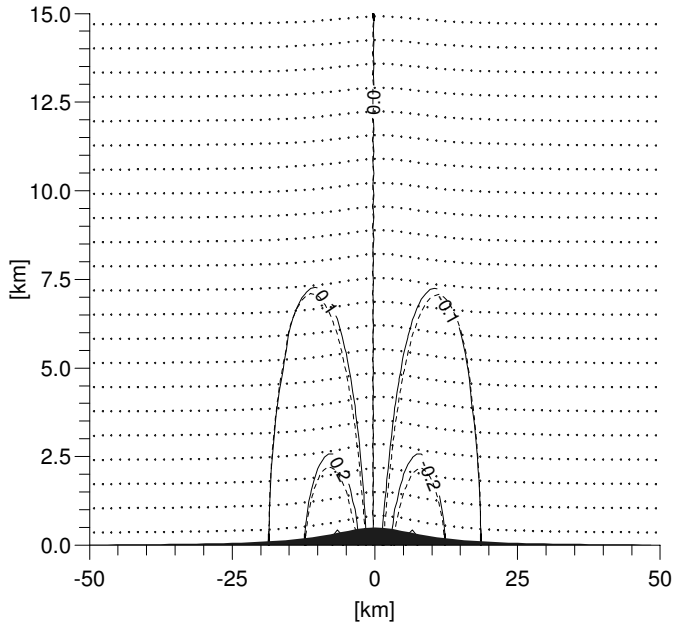

Figure C.2. Vertical wind speed from the numerical simulation of the neutral case with the shallow Boussinesq approximation. (See text for more details).

C.2.2 Hydrostatic mountain waves

The situations considered in the present section allow us to validate the formulation of the energy conservation equation in terms of the potential temperature implemented in the numerical model.

With that aim in mind, the generation of hydrostatic mountain waves will be attempted for a stably stratified flow situation over a mountain of 500 m high and with a half-width of 10 km. Hydrostatic mountain waves are produced in situations

where the buoyancy term in the equation for the vertical velocity component is sufficiently strong to balance the term of the vertical pressure gradient. This type of situation, which is well reproduced by a hydrostatic model, is a good test to determine how far a full Navier-Stokes solver is able to reproduce this limiting case with good accuracy.

C.2.2.1 Shallow Boussinesq approximation

The simulation conditions used for the flow are given by:

- Shallow Boussinesq approximation with a reference density of $\rho = 1.22$ kg/m^3.
- Constant vertical potential temperature gradient $\partial\theta/\partial z = +3.3K/km$ over the whole vertical extent.
- Horizontal wind speed of 10 m/s, constant over the whole vertical extent.

For the conditions mentioned, the Scorer parameter l is:

eq. C.45 $$l = \frac{1}{10}\sqrt{\frac{9.81}{290}3.3\cdot 10^{-3}} = 1.05\cdot 10^{-3} \text{ m}^{-1}$$

We therefore have $al = 10$. In such a situation, linear mountain wave theory predicts the formation of internal gravity waves, propagating vertically throughout the entire troposphere. The corresponding vertical velocity obeys eq. C.44 with a periodicity given by the wavelength $\lambda = 2\pi/l = 6.0\,km$. The maximum amplitude of the vertical velocity is $w_{1,\max} = Uh_m/a = 0.5\,m/s$. Since in this situation, the density has been kept constant with height, the amplitude of the waves is also constant. Table C.3 gives a summary of the simulation conditions for the hydrostatic mountain waves with the shallow Boussinesq approximation, while Figure C.3 shows the expected analytical solutions for the u and v velocity components for the corresponding situation.

Figure C.4 shows the simulation results after 100 time steps of 30 s each. The mountain waves are progressively coming from downstream and form above the mountain. After 300 time steps the waves are reaching the top of the simulation domain (Figure C.5). The simulated vertical wavelength is about 5.7 km and is in fairly good agreement with the theoretical value (λ~6 km).
The amplitude of the simulated wave of vertical velocity is 0.5 m/s, which fully agrees with the theoretical prediction.

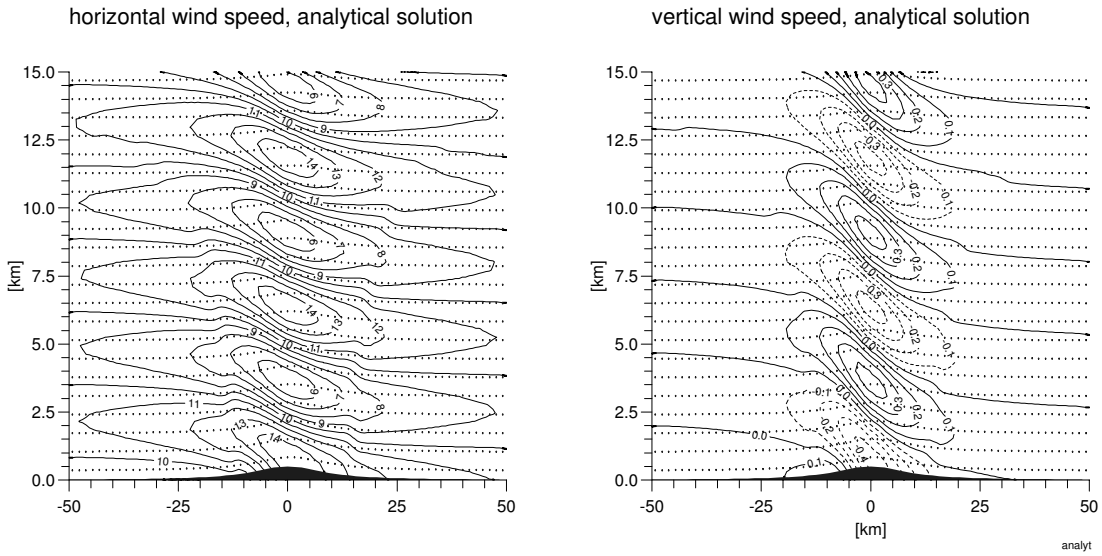

Figure C.3. Analytical solution for the expected u (left) and v (right) velocity components for the shallow Boussinesq hydrostatic case.

Table C.3. Simulation conditions used for the case of a stratified flow, inducing some hydrostatic waves above the theoretical bell-shaped mountain.

Turbulence model	None (laminar flow mode)	
Damping layer	Linearly increasing viscosity from $1.8 \cdot 10^{-5}\, kg/ms$ to $10^{3}\, kg/ms$ for $10km < z < 25km$	
Advection scheme	Higher upwind (2nd order) CCCT (3rd order, modified quadratic upwind)	Wind speed Temperature
Boundary condition type (see Appendix L for definition)	Inlet Mass flow boundary Wall (free slip) Pressure	Entrance Exit Ground Top
Under relaxation factors	0.3 0.7	Wind speed Potential temperature
Time step	30 s	
Density profile	Constant (shallow Boussinesq)	
Ground temperature	288 K	
Thermal stratification	stable	$\partial\theta/\partial z = 3.3 \cdot 10^{-3}$
Wind speed	10 m/s	
Mountain maximum height	500 m	
Mountain half-width	10000 m	

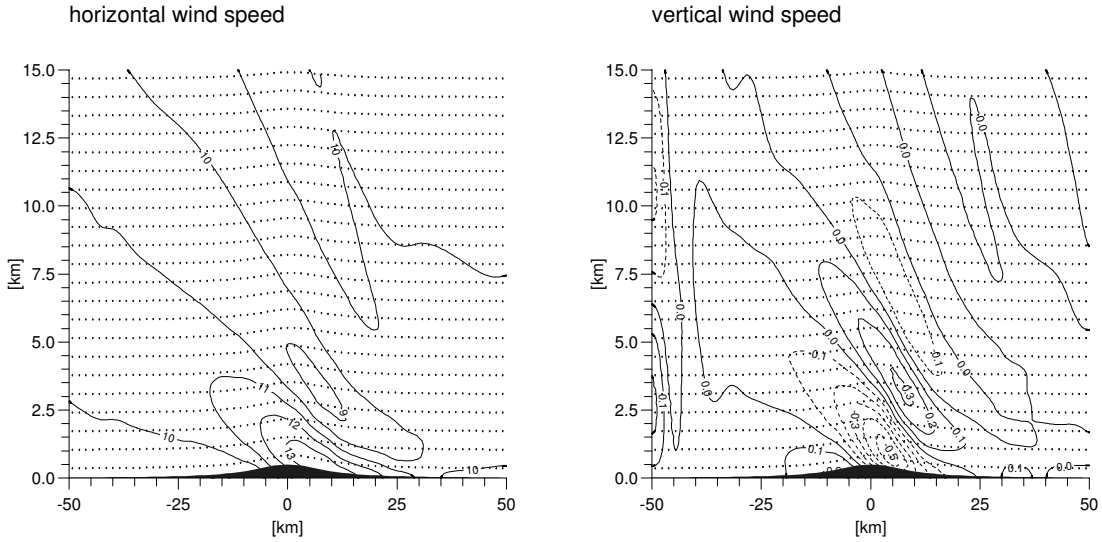

Figure C.4. Simulation results after 100 time steps for the stably stratified case generating hydrostatic waves with the shallow Boussinesq approximation. The stratification conditions are given by a potential temperature gradient of 3.3 K/km and a constant wind speed of 10 m/s blowing into the domain.

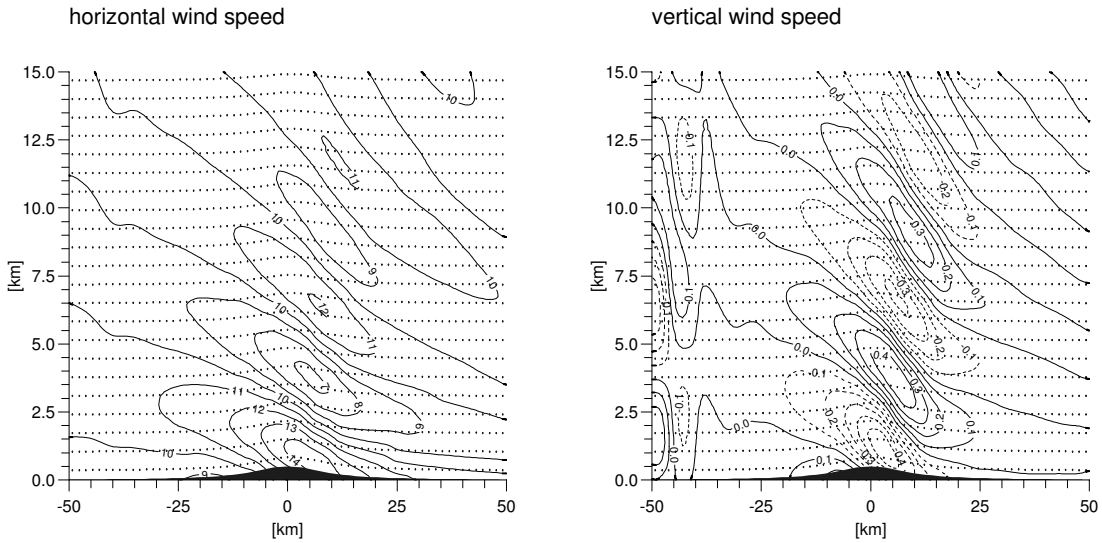

Figure C.5. Same Figure C.4 as after 300 time steps.

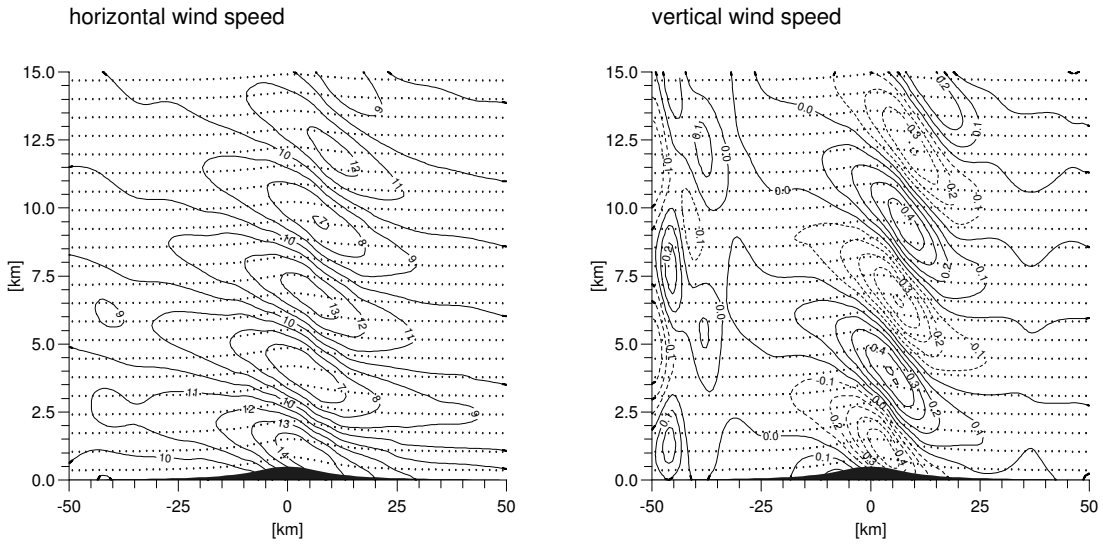

Figure C.6. Same as Figure C.4 after 1000 time steps.

It can be seen that there are some perturbations to the solution for the vertical velocity at the domain entrance. This is due to some wave reflection occurring at the inlet boundary where the boundary condition does not exactly correspond to the condition used for the theoretical development. However, as can be seen from Figure C.6, even after 1000 time steps of simulation, this perturbation remains close to the entrance and does not adversely affect the solution. This difficulty can be alleviated, using a mass flow boundary condition at the entrance to the domain, where the flux through the whole entrance is specified to correspond to a mass flux associated with a constant velocity profile of 10 m/s. A simulation result after 500 time steps for this case is presented in Figure C.7. The problem however, when imposing a mass flow boundary condition, is that after a reasonably long simulation time (some 1000 time steps), the mass flow at the entrance surface is no longer homogeneously distributed and we tend to observe a flow acceleration in the lower part of the troposphere and a deceleration in the upper part. As a consequence, the flow regime changes and we drift towards a situation which is non-hydrostatic (*al* is reduced in the lower part of the atmosphere due to the increase in the velocity) with trapped lee waves propagating horizontally forming downwind of the mountain. (see Figure C.8).

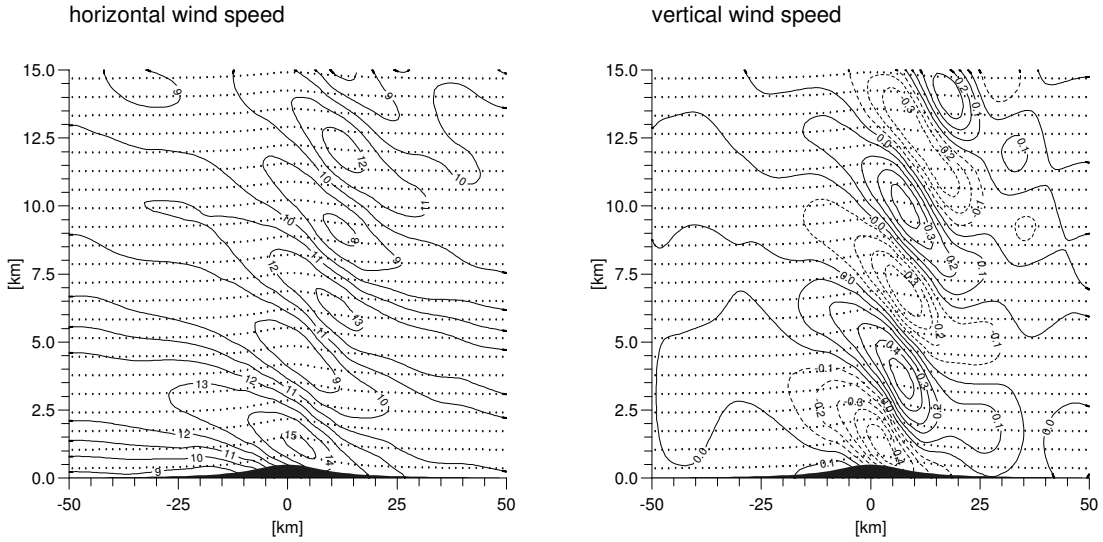

Figure C.7. Simulation results after 500 time steps for the same conditions as presented in Figure C.4, with the difference that the entrance boundary condition is a mass flow boundary condition.

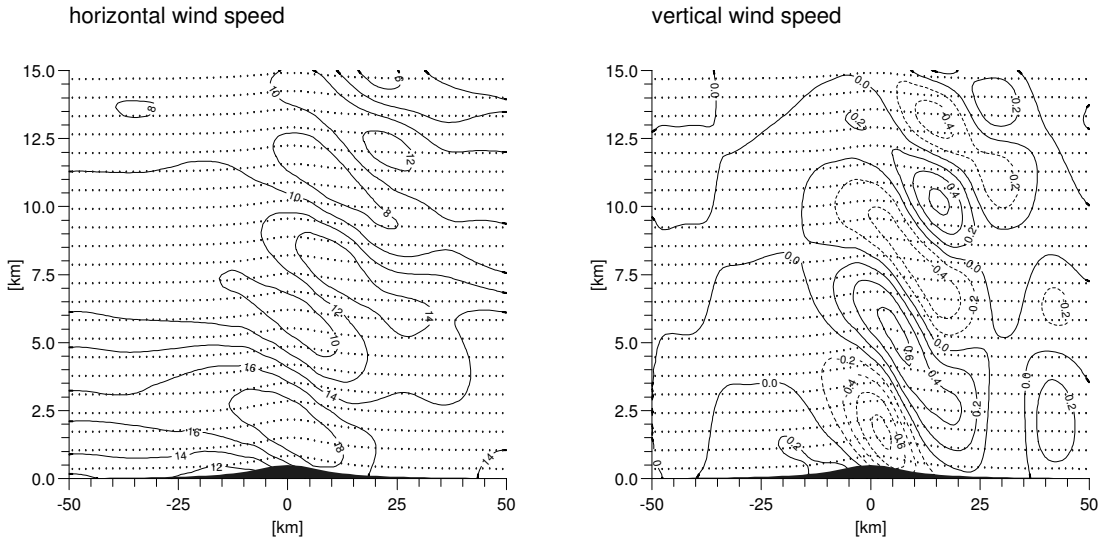

Figure C.8. Same as Figure C.7 after 1000 time steps.

It should be added at that point that the simulation results presented above needed the introduction of a viscous damping layer in the upper part of the simulation domain, where the viscosity was linearly increased from its normal value (1.8e-5) at 10000m to 1000 m^2/s at 25000m. Without the damping layer, some spurious wave reflection occurred at the top of the domain, which after 1000 time steps significantly altered the simulation result (see Figure C.9 showing the vertical velocity distribution after 1000 time steps without any damping layer).

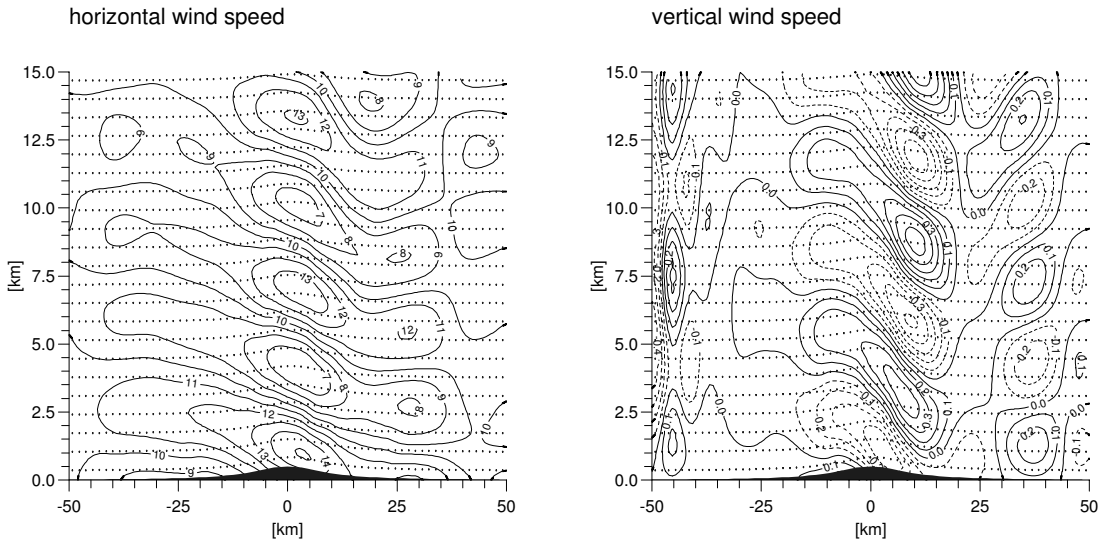

Figure C.9. Horizontal and vertical velocity distribution after 1000 time steps without the viscous damping layer. (Other simulation conditions as in Figure C.6).

Another important remark, which needs to be made, is that we need to use a 2nd order advection scheme to be able to reproduce the wave pattern of Figure C.3. If we only use the default hybrid upwind and central differencing scheme, we get a distribution of vertical velocity which produces the same wavelength as the theoretical one, but the amplitude of the waves is not properly reproduced. With the default scheme, we were only able to get waves with an amplitude decreasing with altitude (see Figure C.10).

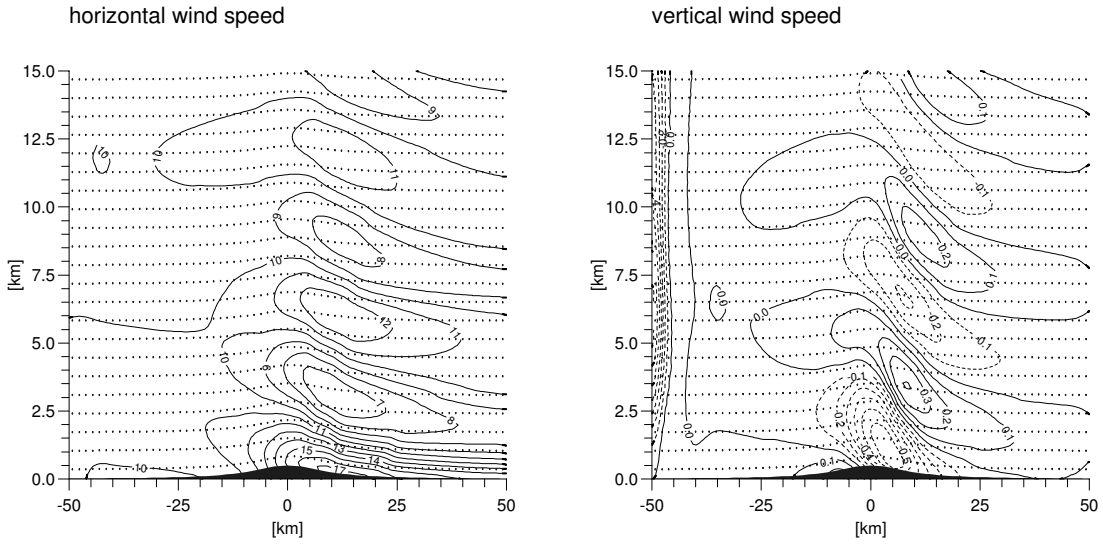

Figure C.10. Vertical velocity distribution after 1000 time steps using the default hybrid upwind and central differencing advection scheme.

To test the model reaction to changes in the atmospheric stability, some additional simulations were performed for various stratification conditions (not presented here). After this sensitivity study, the same conclusions as above remain valid, which are:

- The vertical wavelength associated with the initial stability conditions is well reproduced by the model.
- The amplitude of the waves are quite well reproduced. The code only tends to underestimate the wave amplitude at high altitudes. This however is certainly a consequence of the artificially increased viscosity, which was introduced to reduce the spurious wave reflection occurring at the top boundary condition.

C.2.2.2 Deep Boussinesq approximation

Another simulation was performed, with a density profile corresponding to an atmosphere in hydrostatic equilibrium with the potential temperature profile specified (deep Boussinesq approximation). Apart from this modification, the simulation conditions are exactly the same as the ones presented in the previous section.

From the analytical solution (eq. C.44) we expect similar behaviour as before, with the difference that the amplitude of the waves should increase with height, instead of being constant.

The simulated vertical velocity component (time step 300) for this case is compared to the analytical solution in Figure C.11. Here again, except in the viscous damping layer, the correspondence between the model solution and the theoretical prediction is fairly good.

C.2.3 Non-hydrostatic mountain waves

Between the two extreme approximations of neutral conditions ($al \ll 1$) and stable conditions leading to the production of hydrostatic mountain waves ($al \gg 1$), one can find intermediate situations for which the buoyancy term in the vertical velocity equation is important, but not to such an extent that it balances the vertical pressure gradient term. For cases with $al \approx 1$, no analytical solution can be derived. Using asymptotic methods however, a solution can be obtained for regions far away from the mountain (Queney (1948) and Smith (1979)). Figure C.12 shows an example of such asymptotic behaviour for a situation with hydrostatic waves propagating vertically and non-hydrostatic waves propagating horizontally downwind of the

topography. Scorer (1949) mentions that with a Scorer parameter varying abruptly with height, as can be the case in the presence of an inversion such as at the tropopause level, the hydrostatic waves generated by the mountains can be partially reflected downwards at the discontinuity. Interference between downward and upward propagating waves can lead to the resonant production of so called 'trapped lee-waves' propagating horizontally downwind of the mountain crest (Figure C.13). The nature of these waves is non-hydrostatic, and they are distinguished by the fact the lines of constant phase in the streamline displacement are vertical. Since the streamlines can be associated with the potential temperature isolines (for an adiabatic atmosphere), the above is equivalent to saying that the crests of the potential temperature isolines are aligned vertically in the zone with trapped-lee waves.

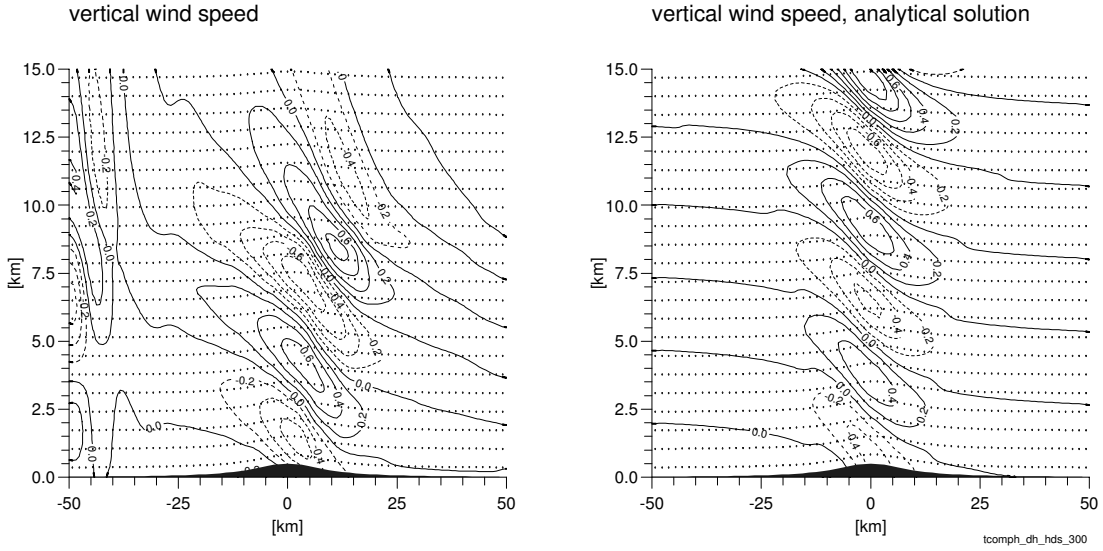

Figure C.11. Comparison of the simulated vertical velocity component (left) with the theoretical distribution (right) for a stratified situation with a potential temperature gradient of 3.3 K/km and a constant wind of 10 m/s blowing into the domain. The simulation was performed with a hydrostatic density profile (deep Boussinesq approximation).

C.2.3.1 Shallow Boussinesq approximation

To simulate a case with $al = 1$, the model is initialised with the following atmospheric conditions:

- A wind speed of 20 m/s constant over the whole vertical extent.

- A real temperature gradient of -6.5 K/km ($\partial\theta/\partial z$ = +3.3 K/km) below 11000m, and a constant real temperature above ($\partial\theta/\partial z$ = +9.0 K/km). The Scorer parameter in the troposphere is $5 \cdot 10^{-4}$ m^{-1}.
- Shallow Boussinesq approximation with a reference density of $\rho = 1.22$ kg/m^3.

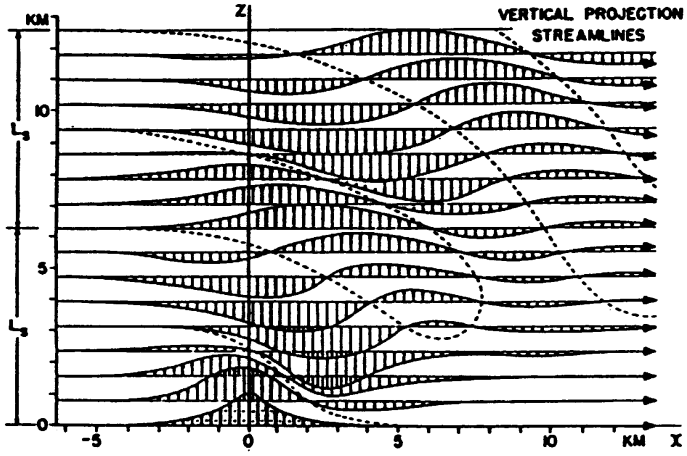

Figure C.12. Asymptotic solution (after Queney, 1948) for the streamline displacement in a flow generating non-hydrostatic waves behind a theoretical mountain, for a Scorer parameter **independent** of the altitude z.

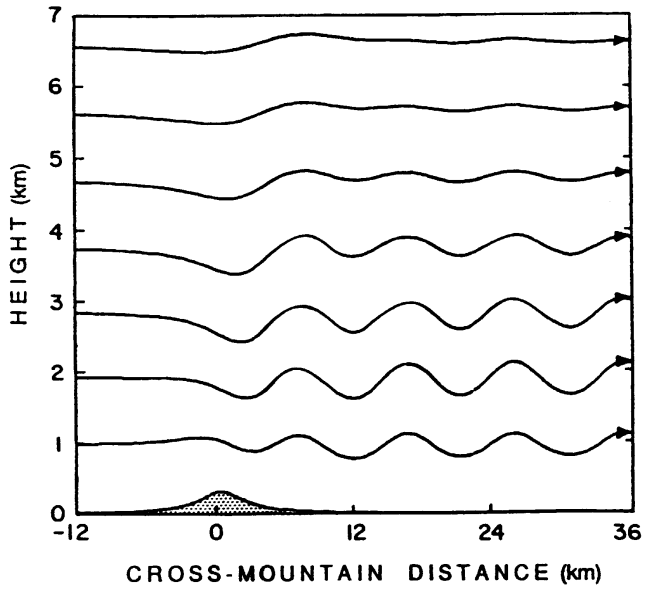

Figure C.13. Asymptotic solution for the streamline displacement in a flow generating trapped lee-waves behind a theoretical mountain, for a Scorer parameter **varying** with the altitude z.

The simulations are performed on a bell-shaped mountain with a half-width of 2 km and a maximum height of 1000 m. The simulation domain for this case has a

horizontal dimension of $L_x = 120\,km$ (65 elements) and a vertical dimension of $L_z = 28\,km$ (25 elements). Table C.5 gives a summary of the simulation conditions.

Results after 100 time steps (3000s) are presented in Figure C.14 for a) the potential temperature, b) the difference between the total and hydrostatic pressure, c) the vertical wind speed component and d) the horizontal wind speed component. Hydrostatic waves, formed above the mountain are inclined towards the downwind side of the mountain. After 300 (Figure C.15) and 500 time steps (Figure C.16), waves appear for altitudes between 2 and 7 km which propagate downwind. These waves are trapped lee waves formed through constructive interference of waves reflected downwards at the discontinuity at the tropopause. They are visible in both the plots of the potential temperature and vertical velocity component.

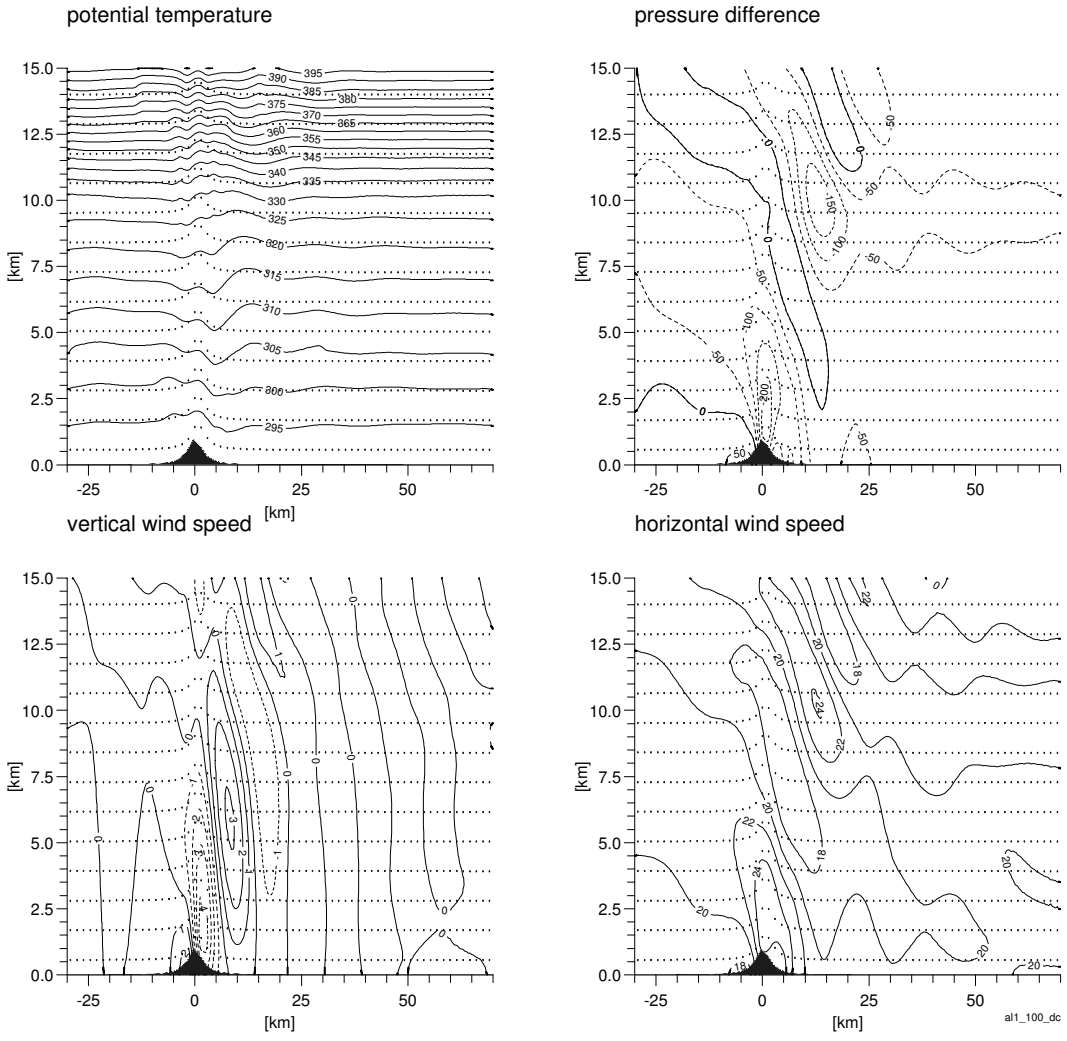

Figure C.14. Simulation results after 100 time steps for the situation with stably stratified flow generating non-hydrostatic mountain waves. The incoming wind speed was set to 20 m/s, the potential temperature was 3.3 K/km for the whole troposphere and 9.8 K/km above. a) potential temperature, b) pressure, c) vertical wind speed, d) horizontal wind speed.

Since no analytical solution is available for the validation of this particular case, we will only be able to compare our model results with simulations results presented by other authors. Thunis (1995) simulated the same flow configuration with the non-hydrostatic version of TVM. Figure C.17 presents the time evolution he obtained for the vertical velocity component over a bell-shaped mountain defined by a half-width of 2 km and a maximum height of 1000m. Results produced with RAMS with the same simulation conditions are presented in Figure C.18. A comparison between the three models is summarised in Table C.4. It appears that all the three models agree fairly well for the prediction of the horizontal wavelength of the trapped lee waves, with a wavelength between 11 and 13 km. Concerning the amplitude and location of the first lobe of positive vertical velocity on the lee side, the prediction of CFX4 lies in the range of predictions of the two other models.

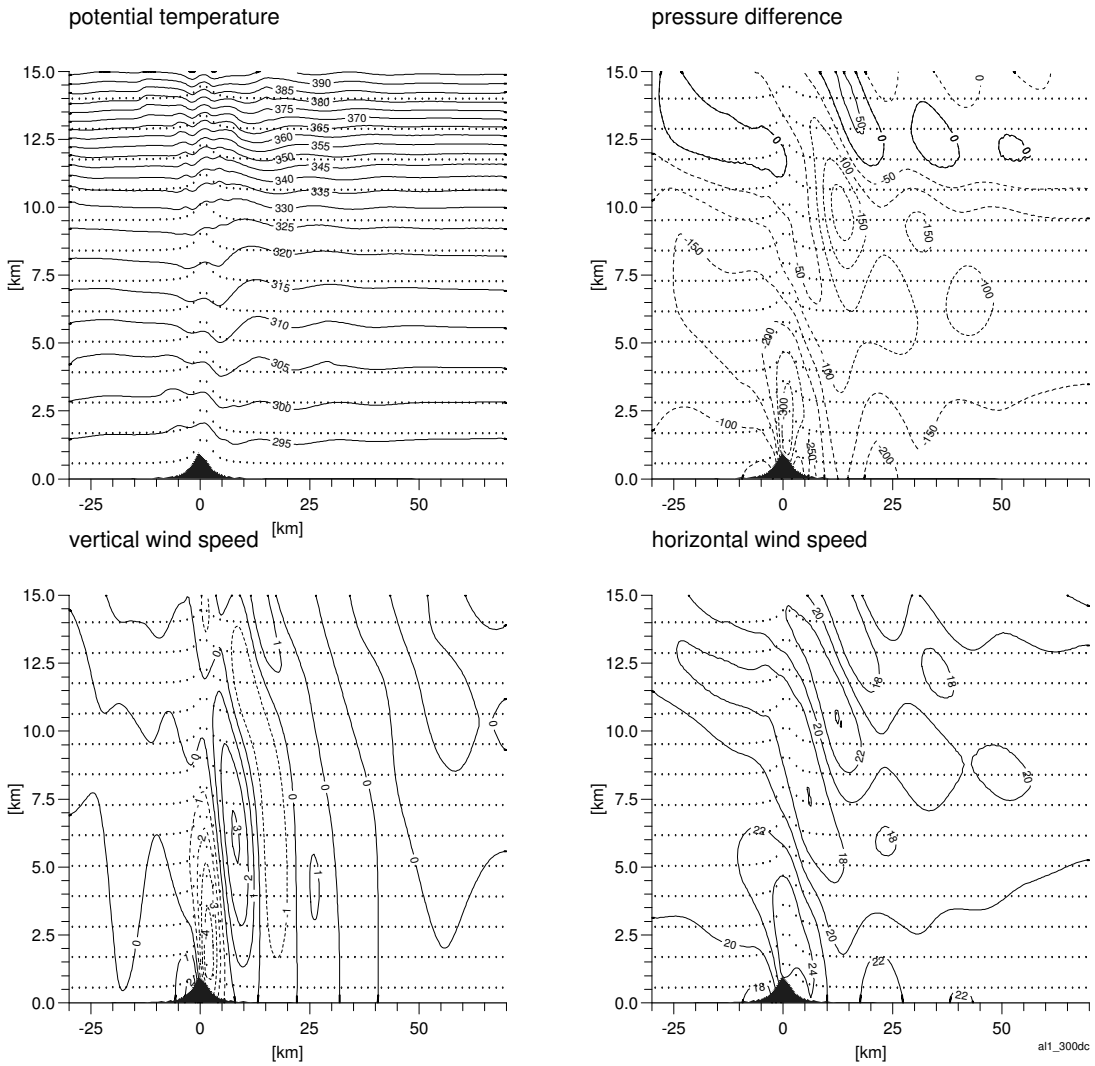

Figure C.15. Same as Figure C.14 after 300 time steps.

Table C.4. Comparison of flow features obtained with CFX4, TVM and RAMS for the simulation of non-hydrostatic waves calculated with the shallow Boussinesq approximation ($\rho = 1.22$ kg/m^3) and the same set of parameters as in Figure C.14.

	Amplitude and location of the first lobe of positive vertical velocity in the lee side		Horizontal lee wavelength
CFX4	3.16 m/s	x = 7.6 km, z = 6.2 km	10-12 km
TVM	~ 3.25 m/s	x ≅ 7.0 km, z ≅ 8.0 km	~ 11 km
RAMS	~ 2.75 m/s	x ≅ 7-8 km, z ≅ 8.0 km	~ 13 km

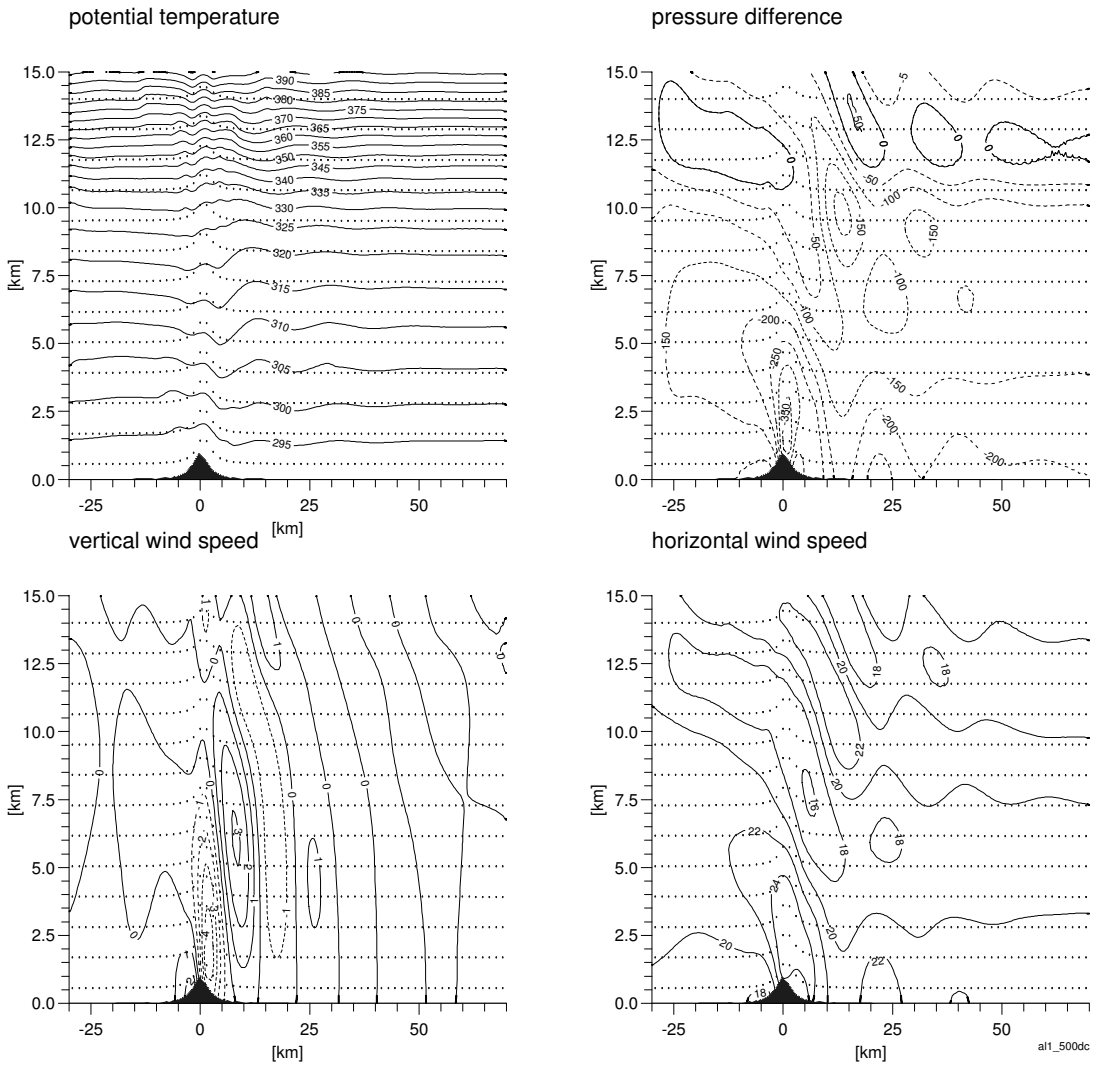

Figure C.16. Same as Figure C.14 after 500 time steps.

Table C.5. Simulation conditions used for the case of a stably stratified flow generating non-hydrostatic mountain waves in the lee of a theoretical bell-shaped mountain**.**

Turbulence model	None (laminar flow mode)	
Damping layer	Linearly increasing viscosity from $1.8 \cdot 10^{-5}\, kg/ms$ to $10^{3}\, kg/ms$ for $10km < z < 25km$	
Advection scheme	Higher upwind (2nd order) Higher upwind (2nd order)	Wind speed Temperature
Boundary condition type (see Appendix L for definition)	Inlet Mass flow boundary Wall (free slip) Inlet	Entrance Exit Ground Top
Under relaxation factors	0.3 0.7	Wind speed Potential temperature
Time step	30 s	
Density profile	Constant (Shallow Boussinesq)	
Ground temperature	288 K	
Thermal stratification	Stable	$\partial\theta/\partial z = 3.3 \cdot 10^{-3}$ (for z<11000 m) $\partial\theta/\partial z = 9.8 \cdot 10^{-3}$ (for z>11000 m)
Wind speed	20 m/s	
Mountain maximum height	1000 m	
Mountain half-width	2 km	

In all the simulations presented above, we used a 2nd order upwind advection scheme (HUW) for the wind velocity and potential temperature. A simulation with exactly the same parameters as the simulation presented in Figure C.14 was performed using the default mixed upwind and central differences advection scheme (1st order). As can be seen from Figure C.19 the latter did not reproduce the formation of waves downwind of the mountain. With the first order advection scheme, results after 300 time steps only show the formation of hydrostatic waves.

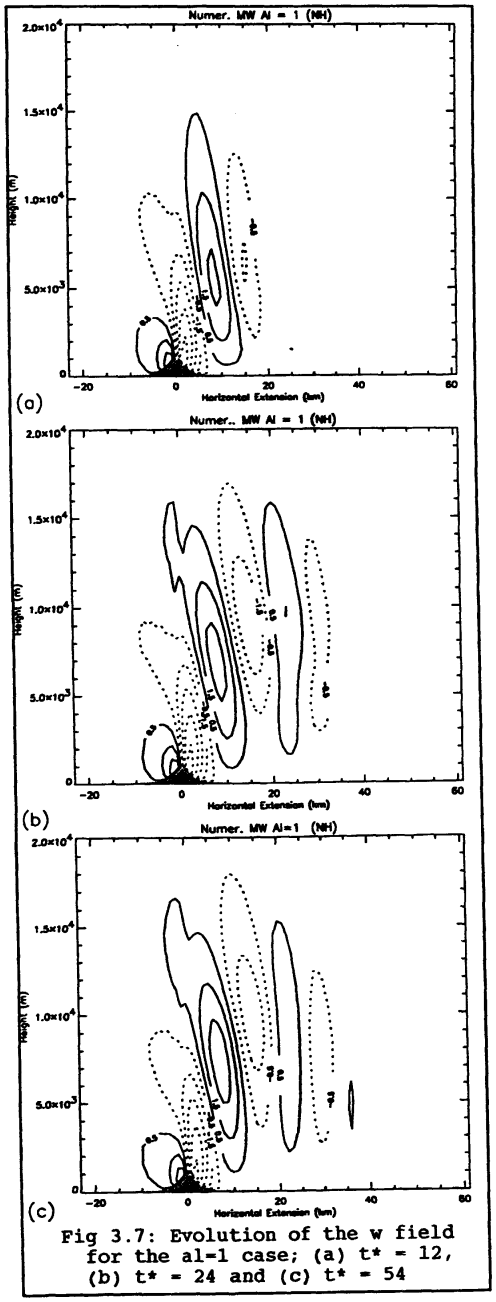

Fig 3.7: Evolution of the w field for the al=1 case; (a) t* = 12, (b) t* = 24 and (c) t* = 54

Figure C.17. Time evolution of the vertical wind speed component obtained with the non-hydrostatic version of TVM (Thunis, 1995), for the same simulation conditions used here to reproduce the formation of non-hydrostatic waves

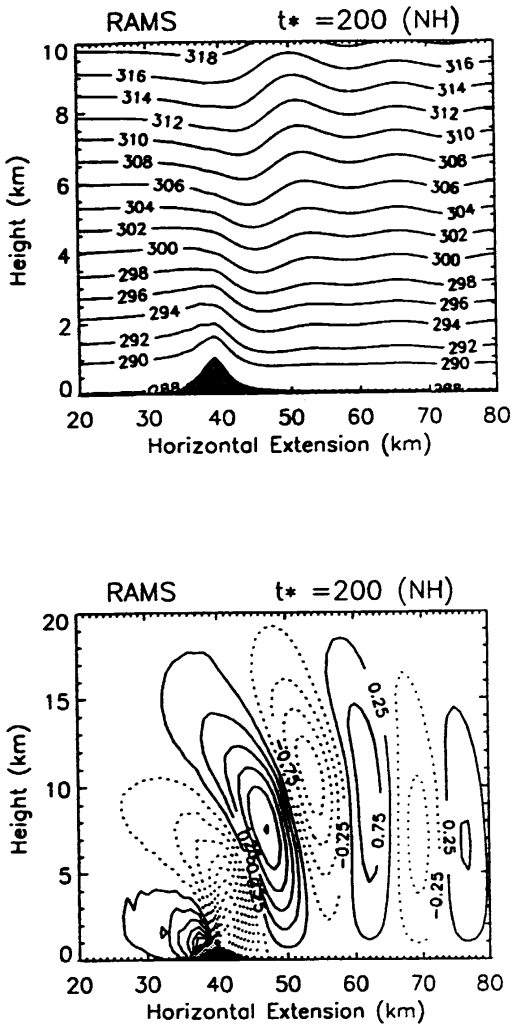

Figure C.18. Potential temperature and vertical wind speed obtained with an incompressible and non-hydrostatic version of RAMS, for the same simulation conditions used here to reproduce the formation of non-hydrostatic waves.

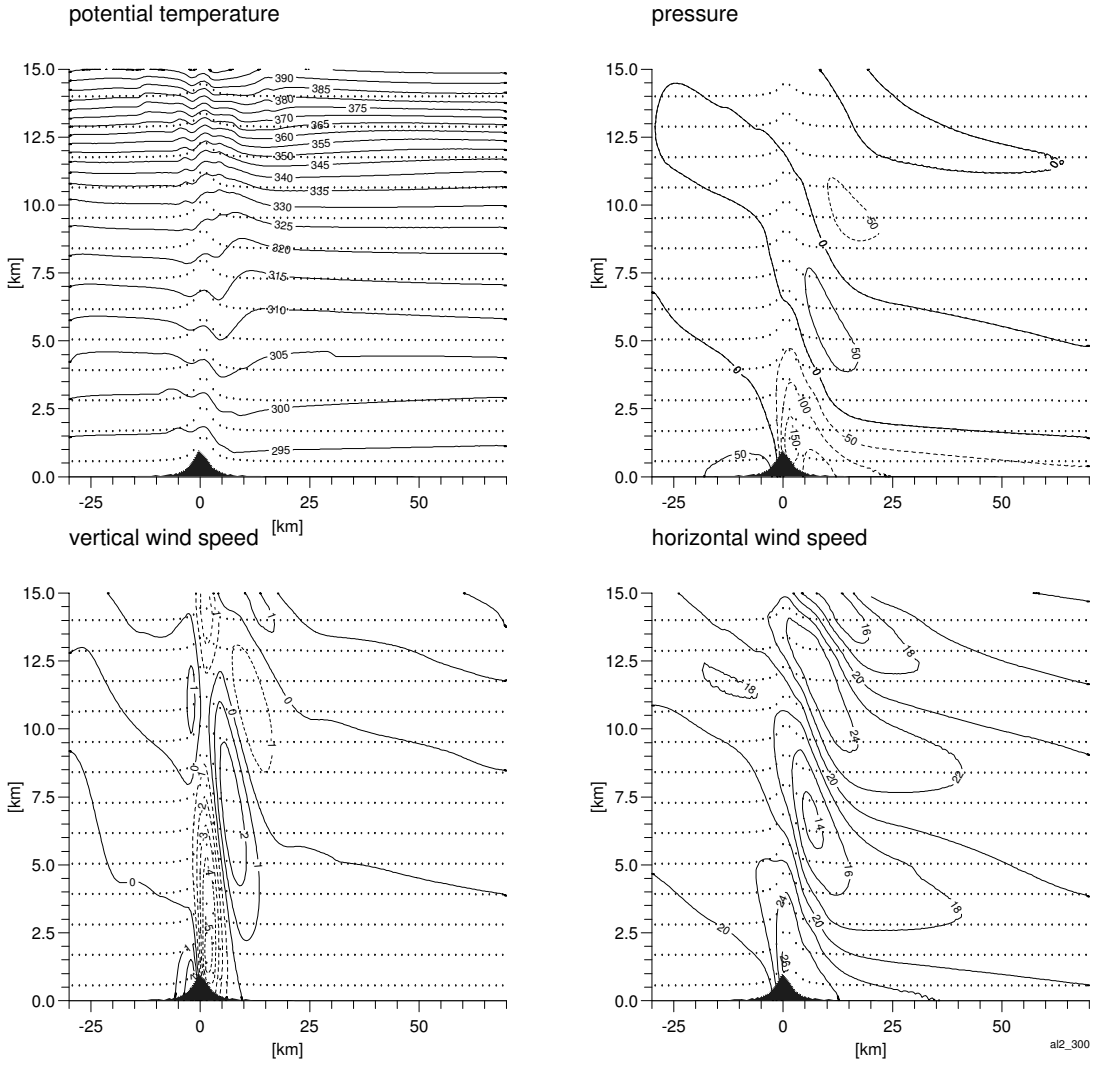

Figure C.19. Same as Figure C.14 after 300 time steps, for a simulation done with the default mixed upwind and central differences advection scheme.

C.2.3.2 Deep Boussinesq approximation

To test the sensitivity of the results to the approximation of a constant density, a simulation was performed with exactly the same set of parameters as the one of the previous section. The difference was that we imposed a density changing with height (deep Boussinesq), according to a profile in hydrostatic equilibrium with the temperature profile specified. The results for this case are presented in Figure C.20 (time step 300) and Figure C.21 (time step 500). The change of the density profile (with the associated reduction of inertia in the higher elevations) significantly affects the amplitude of the waves building on the lee side. The maximum vertical positive velocity (located some 10 km downwind at an altitude of approximately 7.5km) now

exceeds the value of 5 m/s, instead of the 3.2 m/s obtained with the shallow Boussinesq approximation.

The reduction in the density at higher levels also implies an increased production of waves in the upper part of the domain, above the discontinuity of the tropopause (at 11 km).

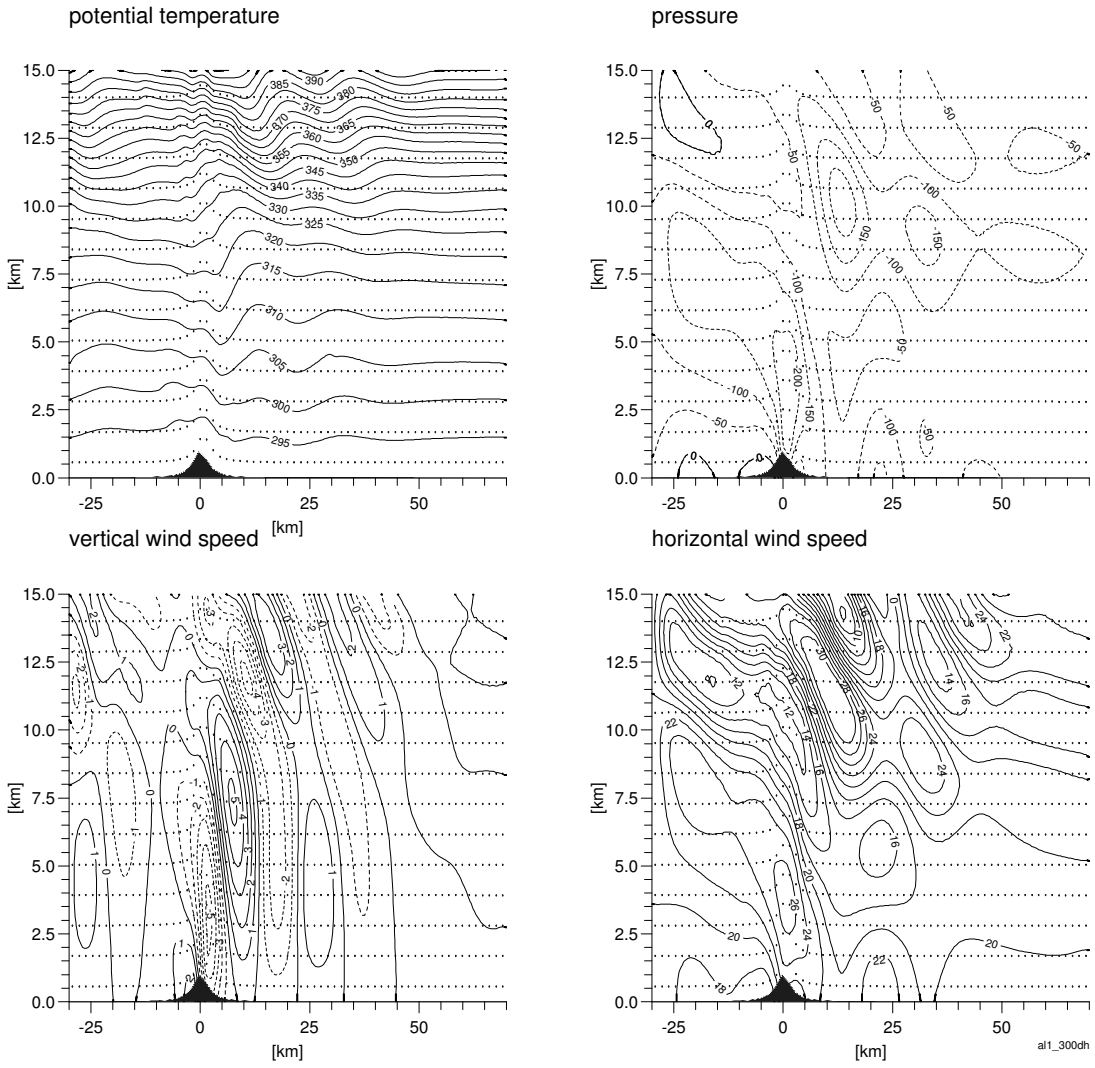

Figure C.20. Same as Figure C.14 after 300 time steps, for a simulation with a hydrostatic density profile (deep Boussinesq).

C.2.4 Strongly non-linear situations (January 1972 Boulder foehn event)

The simulations presented earlier in Sectors C.2.1 to C.2.3 were performed for flow situations that were homogeneous over the whole tropospheric extent with $h_m l < 0.85$. According to Long (1953), the value of 0.85 corresponds to the limit for a homogeneous atmosphere above which non-linear effects start to dominate. For a

multi-layer atmosphere, non-linearity can already be significant for values of $h_m l$ as low as 0.3. In the present section, the model will be run to simulate a non-linear flow situation to test its ability to reproduce this category of flow situations. The test case chosen for this purpose is the well-documented severe foehn event that was recorded at Boulder (Colorado) in January 1972. This event was used by several authors (Klemp & Lilly 1978, Peltier & Clark 1979, Durrran & Klemp 1983) who compared their model results with the observations of the day.

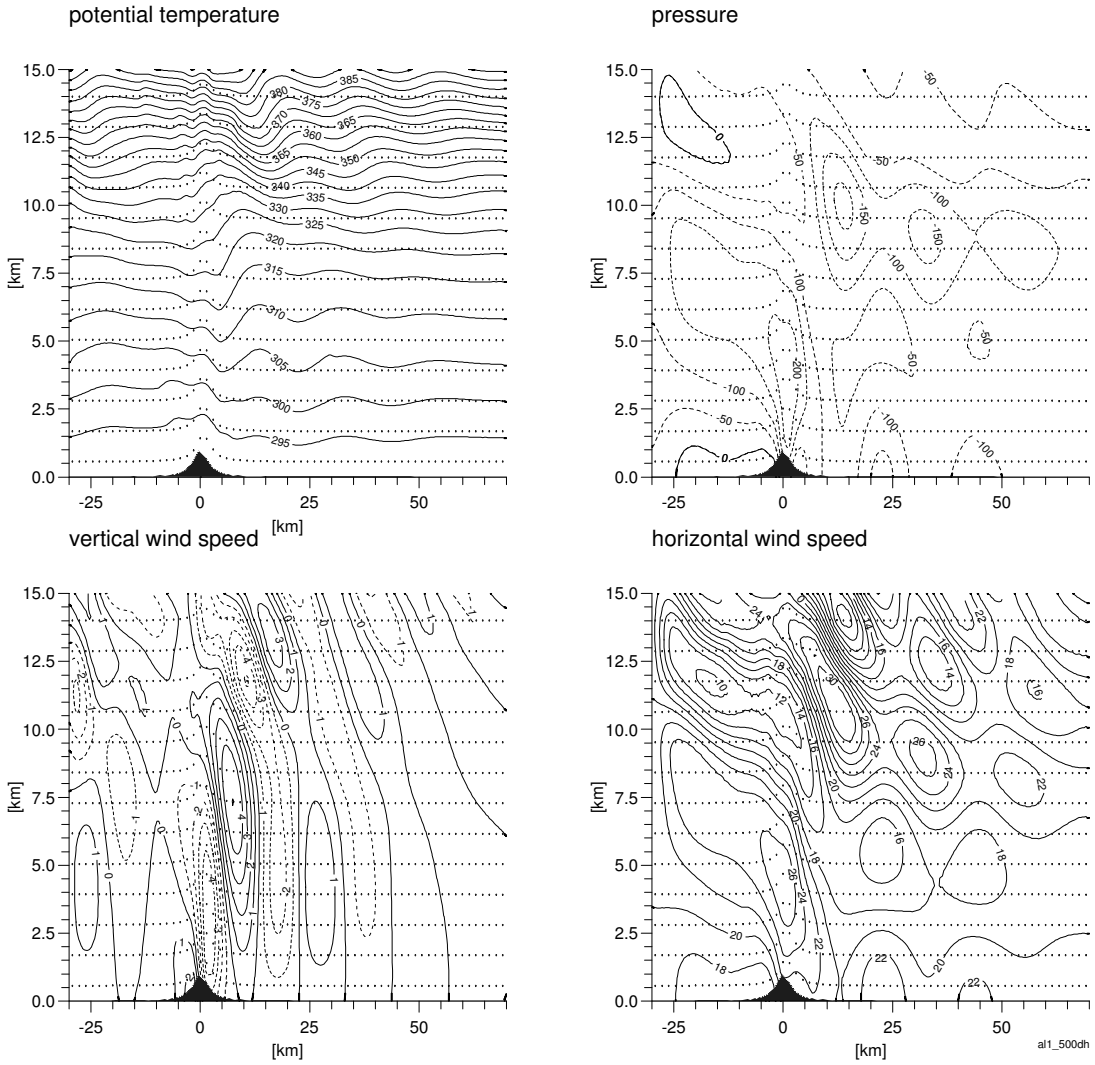

Figure C.21. Same as Figure C.14 after 500 time steps, for a simulation with a hydrostatic density profile (deep Boussinesq).

Vertical slices of the potential temperature and horizontal wind velocity obtained from observation by plane in the region of Boulder are presented in Figure C.22 and Figure C.23 (source Klemp & Lilly 1978). Isolines of observed potential temperature show the presence of waves building downstream of the mountain crest (wind blows

from the west) as well as a very strong descent of air originating from the higher troposphere. Wind speeds exceeding 60 m/s were recorded at Boulder on the eastern flank of the Rocky Mountains.

For the numerical simulation, the mountain profile for the region is idealised and represented by a bell-shaped mountain with a maximum height of 2000m, and a half-width of 10 km. The simulation domain has a dimension of $L_x = 120\,km$ (60 elements) in the horizontal and $L_z = 25\,km$ (25 elements) in the vertical.

Wind and temperature profiles used by Peltier & Clark (1979) are taken to initialise the numerical model. These profiles (see Figure C.24 and Figure C.25) were derived from meteorological soundings measured at the station of Grand Junction located some 300 km upwind of Boulder. Compared to the actual measurements, Peltier & Clark slightly modified the wind profile, reducing the wind speed above 13000m to 20 m/s instead of the observed 30 m/s. Without the modification, the numerical model used by Peltier & Clark was not able to reproduce the extreme wind speeds of 60 m/s, whereas it did with the reduction in the high altitude wind speed. A summary of the simulation conditions is presented in Table C.6.

Table C.6. Simulation conditions used to simulate the January 1972 Boulder foehn event.

Turbulence model	$k-\varepsilon$ (modified)	
Damping layer	none	
Advection scheme	Higher upwind (2nd order) CCCT (3rd order, modified quadratic upwind)	Wind speed Temperature
Boundary condition type (see Appendix L for definition)	Inlet Mass flow boundary Wall (no slip, $z_0 = 0.01m$) Inlet	Entrance Exit Ground Top
Under relaxation factors	0.3 0.7	Wind speed Potential temperature
Time step	30 s	
Density profile	Hydrostatic (Deep Boussinesq)	
Thermal stratification	Stable	See Figure C.25
Wind speed		See Figure C.24
Mountain maximum height	2000 m	
Mountain half-width	10000 m	

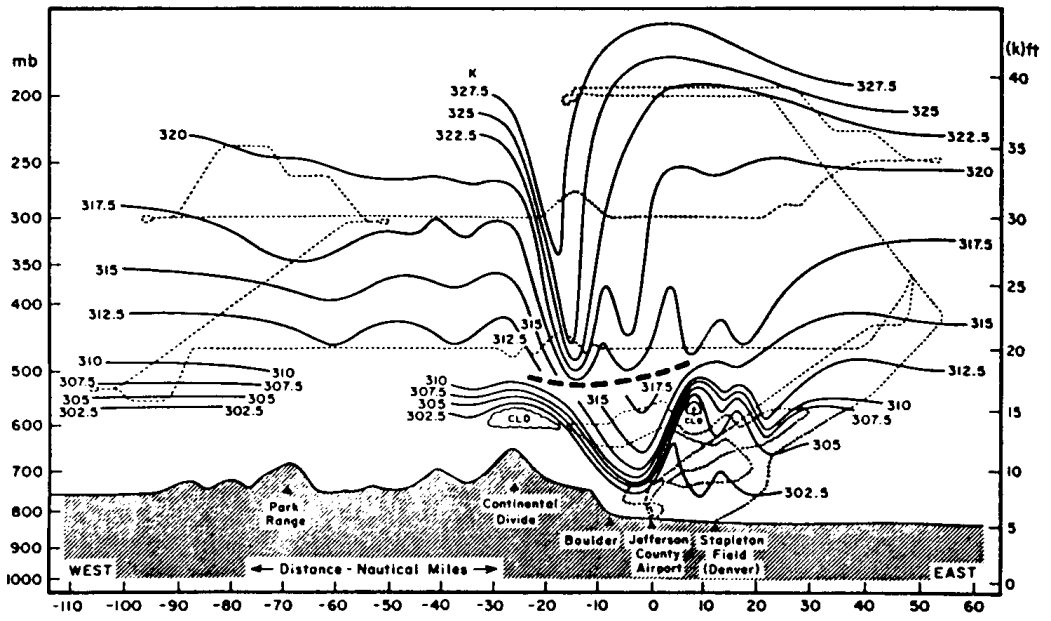

Figure C.22. Vertical slice of potential temperature observed by plane in the region of Boulder for the severe foehn event of January 1972. (Klemp & Lilly, 1978).

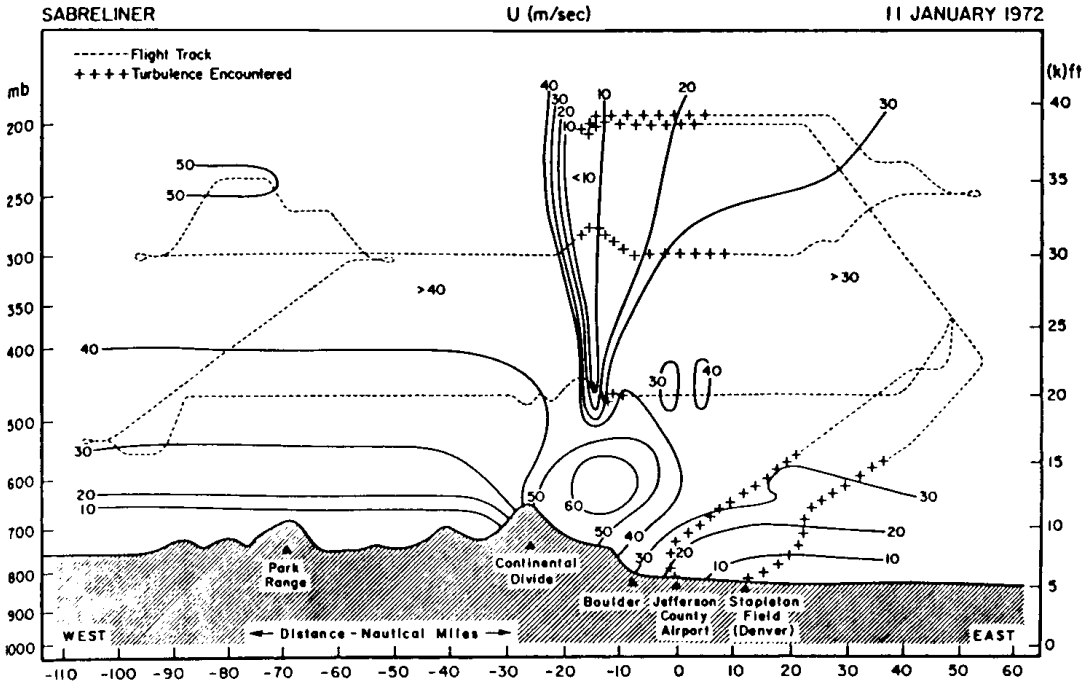

Figure C.23. Same as Figure C.22 for the horizontal wind speed component.

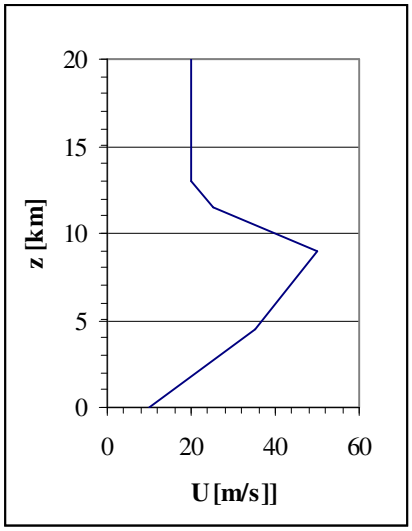

Figure C.24. Wind speed profile used as initial and entrance boundary conditions to reproduce the Boulder foehn event (from Peltier et Clark, 1979).

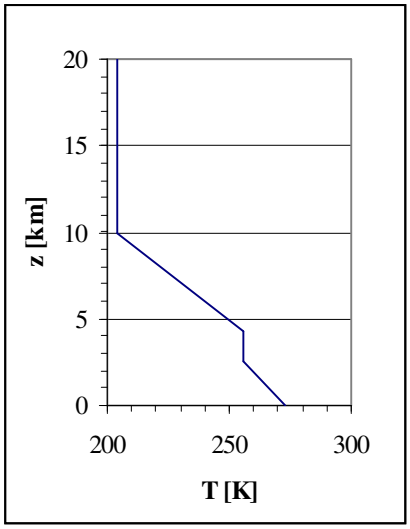

Figure C.25 Real temperature profile used as initial and entrance boundary conditions to reproduce the Boulder foehn event (from Peltier et Clark, 1979)

Time evolution of the simulation results for the potential temperature, pressure, vertical and horizontal wind speed is presented for the time steps 100 (Figure C.26), 160 (Figure C.27), 200 (Figure C.28) and 240 (Figure C.29). An significant displacement (more than 4 km downwards) of the potential temperature isolines can already be observed after 100 time steps together with an overturning of the flow above the mountain at altitudes between 7.5 and 11km. In this region, some wave-breaking occurs, inducing some back flows (negative horizontal wind velocity). Downhill of the summit, the horizontal wind speed reaches a maximum value of the order of 35 m/s, whereas at higher altitudes (around z=5000m) the flow is accelerated up to wind speeds of the order of 65 m/s. Waves start to form downstream.

After 160 time steps (4800 s), these waves are clearly distinguishable. The descent of potential temperature isolines is more pronounced and displacements of the order of 5.5 km can be observed. The region where the potential temperature isolines are tightly packed, immediately downhill of the summit, coincides with the zone of maximum acceleration of the flow. In this region, horizontal wind speeds greater than 65 m/s can be seen. The highest wind speeds close to the ground are obtained some 10 km downwind of the mountain's highest elevation. At time step 240 (Figure C.29), the maximum wind speed close to the ground reaches a value of some 57 m/s which is only slightly lower than the maximum of 60 m/s that was recorded at Boulder.

Even if the wind speed and potential temperature distributions presented in Figure C.22 and Figure C.23 are obtained from measurements which were not exactly simultaneous, and which consequently must be interpreted with care, it can be stated that the numerical model results reproduce fairly well the strongly non-linear process involved.

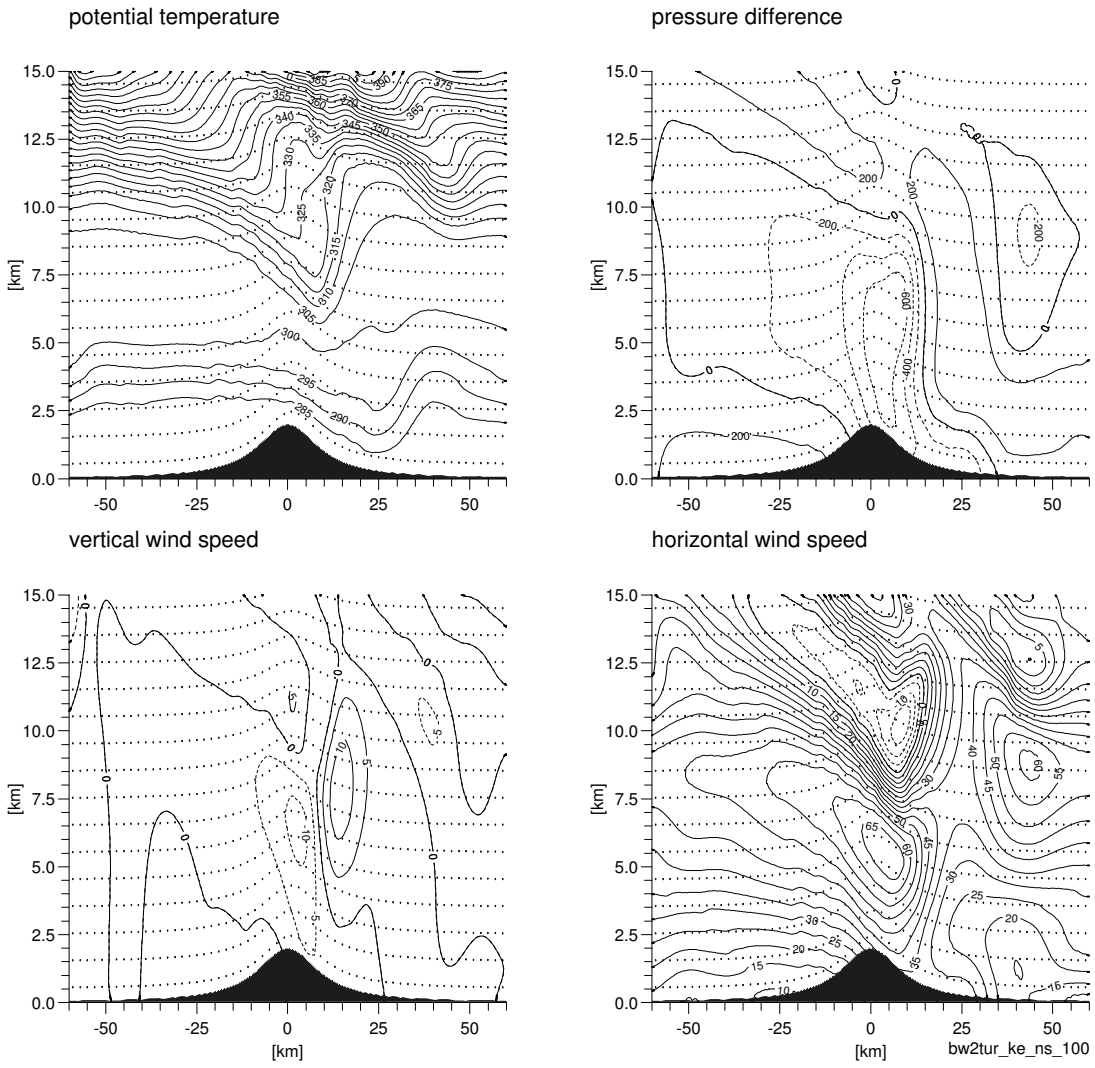

Figure C.26. Simulation results after 100 time steps (3000 s), for the severe foehn at Boulder a) potential temperature, b) pressure, c) vertical wind speed, d) horizontal wind speed.

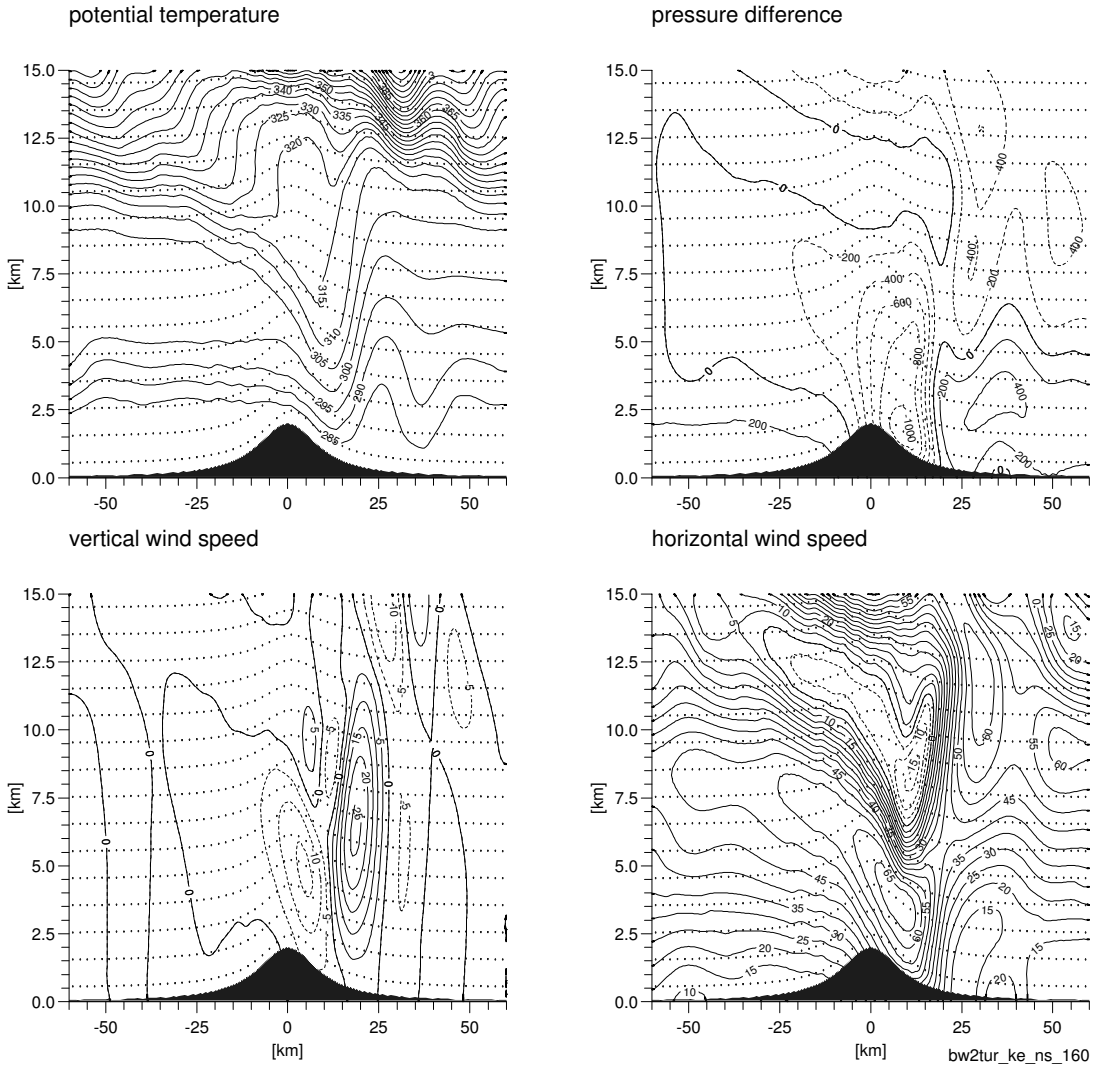

Figure C.27. Same as Figure C.26 after 160 time steps (4800 s)**.**

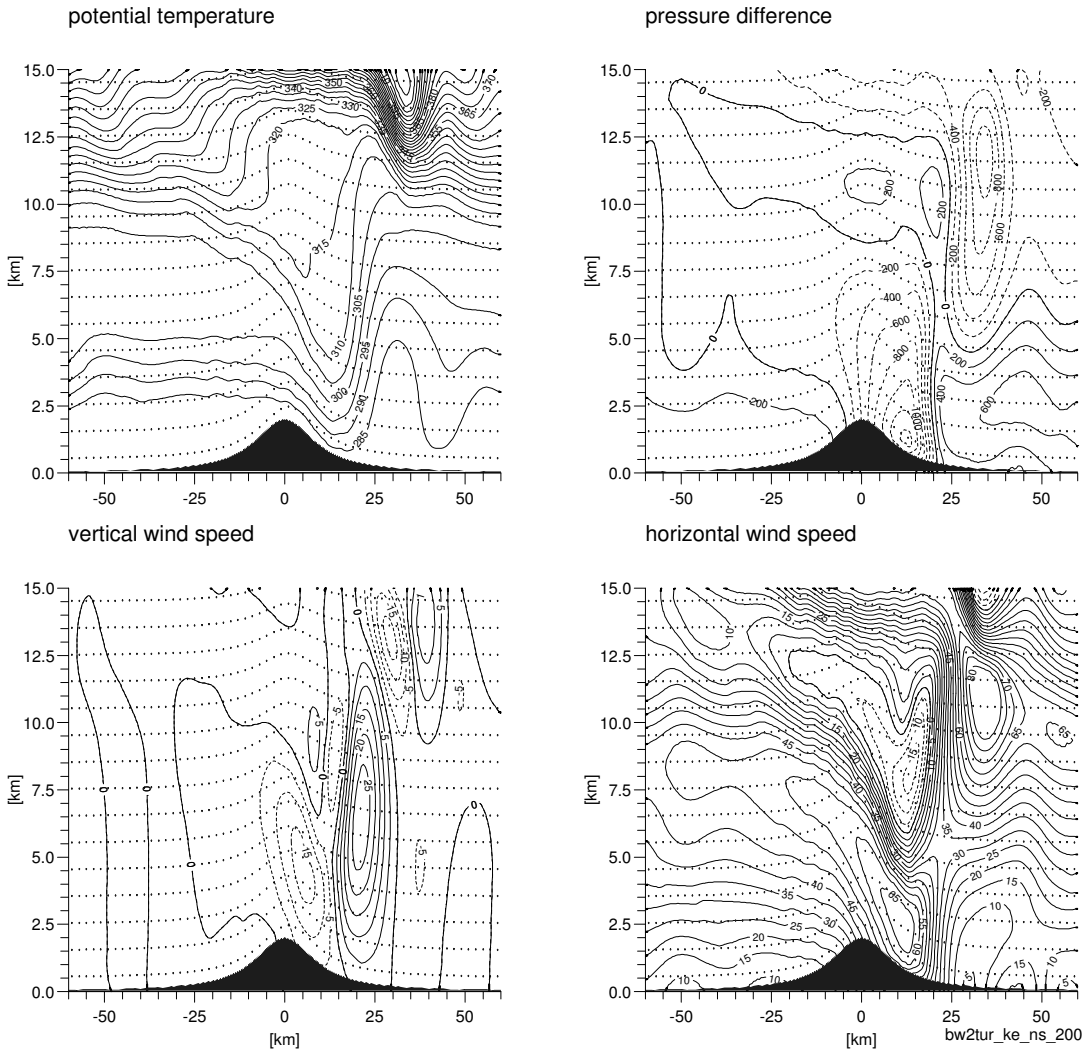

Figure C.28. Same as Figure C.26 after 200 time steps (6000 s).

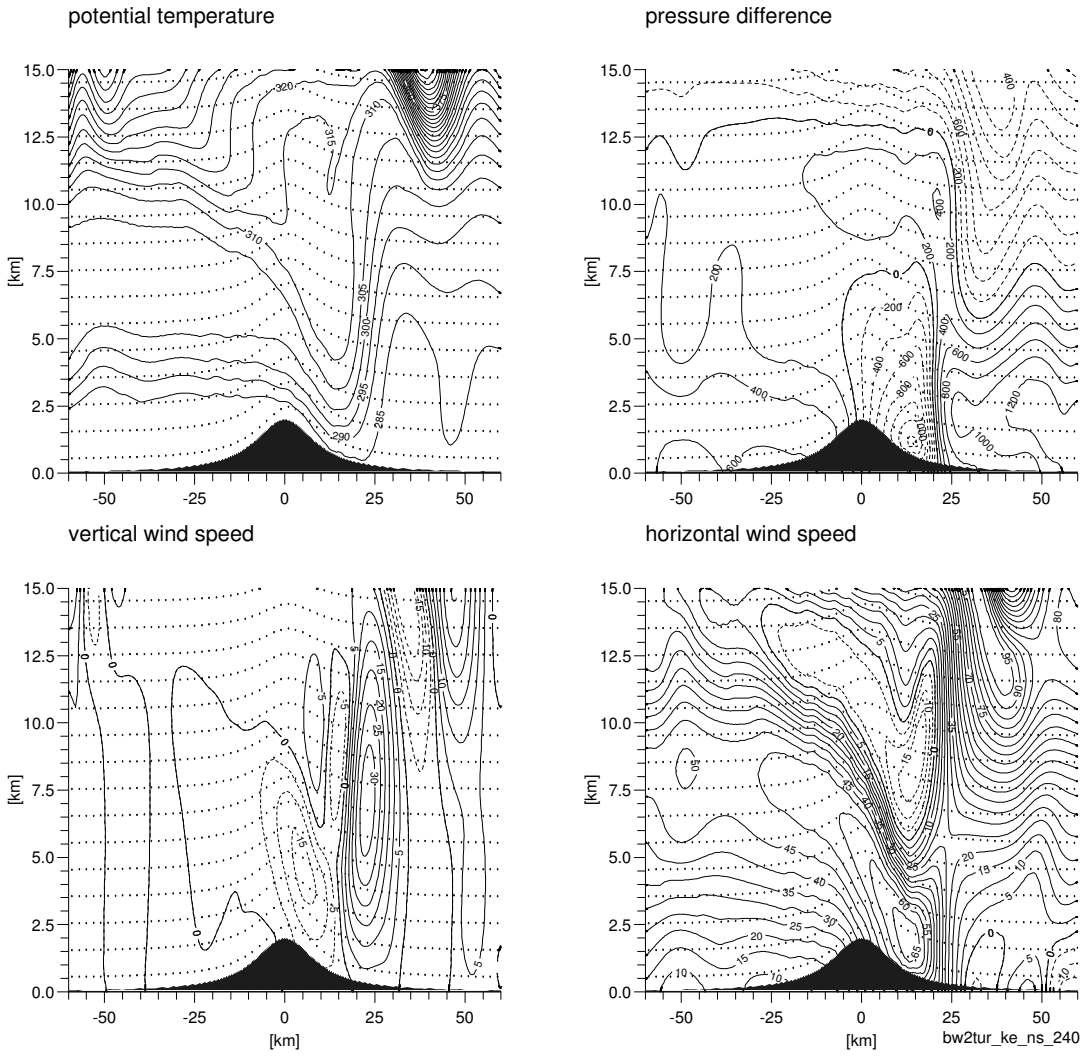

Figure C.29. Same as Figure C.26 after 240 time steps (7200 s).

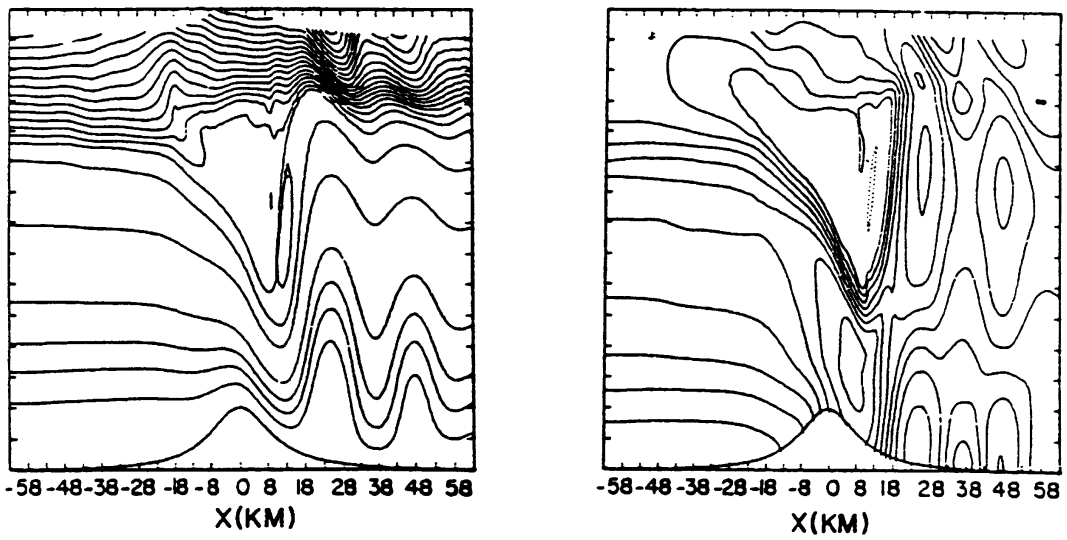

Figure C.30. Simulation results for the potential temperature and horizontal wind speed obtained by Peltier and Clark. Steps between the isolines: 10 m/s for the wind speed, 5° K for the potential temperature.

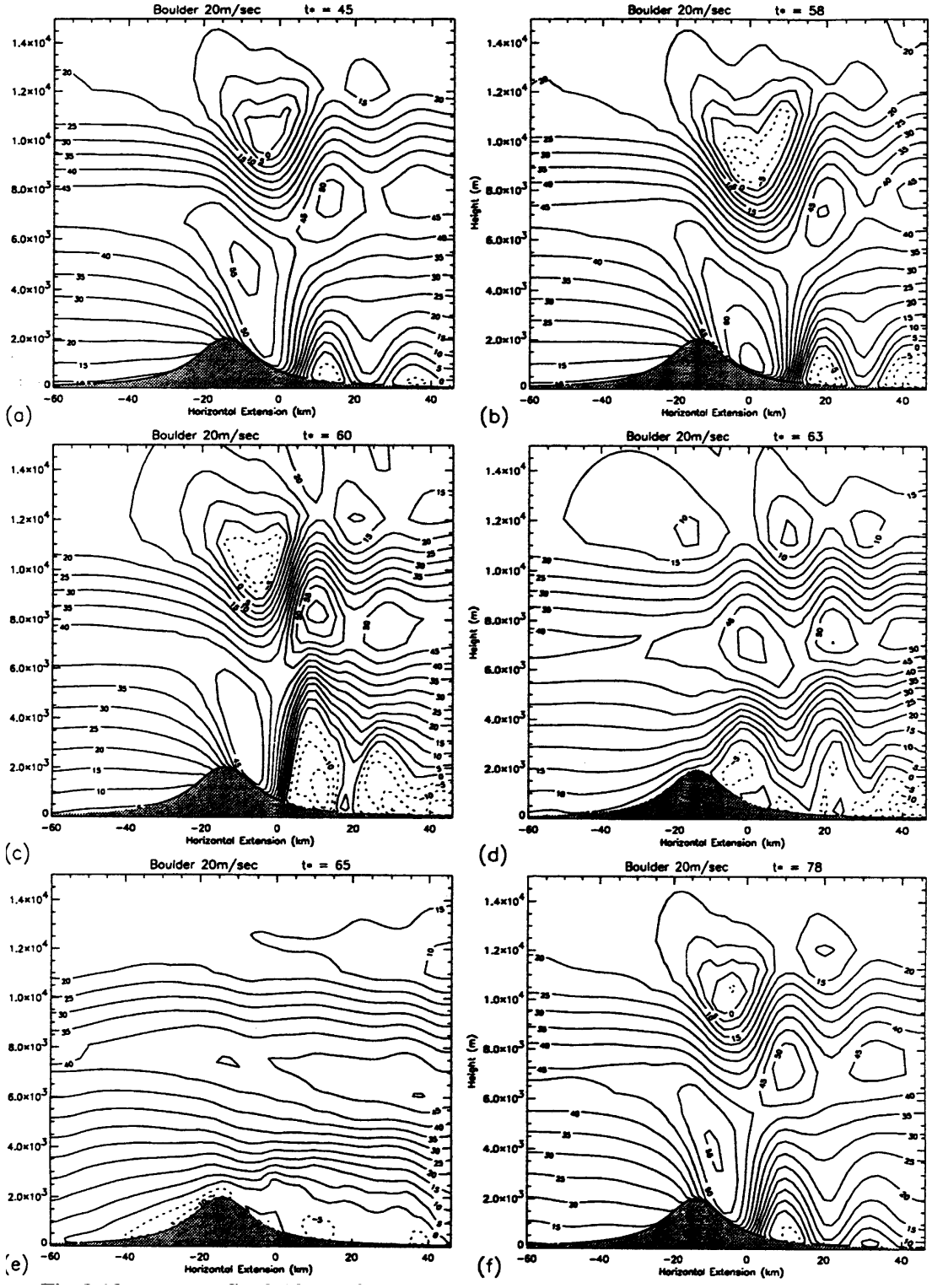

Figure C.31. Time evolution for the horizontal wind speed calculated with the non-hydrostatic version of TVM (Thunis, 1995).

A comparison of the model solution at time step 200 with the results presented by Peltier and Clark (Figure C.30) show that both results look very similar, qualitatively as well as quantitatively.

From time step 240, one can also see some zones with negative horizontal wind speeds close to the ground, corresponding to regions where rotors form in the wake of the mountain.

Thunis (1995) presented the time evolution of solutions obtained with TVM for the same simulation conditions. His results for the horizontal wind speed are reproduced in Figure C.31. Contrarily to what can be observed with CFX4, TVM generates some return flows close to the ground before generating some at high altitude. Apart from the fact that TVM produces bigger rotors in the wake of the mountain than CFX4, both models give comparable results.

Remark: Concerning the advection scheme used for the velocity components and potential temperature, it can be pointed out that, similarly to what was noticed in the previous sections, a simulation using the default 'mixed upwind and central difference scheme' was not able to reproduce the formation of waves in the lee of the mountain. A second order advection scheme seems to be a pre-requisite to satisfactorily reproduce oscillations associated with buoyancy effects in the atmosphere.
Results obtained with the first order advection scheme are presented in Figure C.32 to Figure C.35 for the time steps 100 (t=3000 s), 160 (t=4800 s), 200(t=6000 s) and 240 (t=7200 s). The maximum wind speed close to the ground also reaches a value around 56 m/s (time step 240). However, the overall amplitude of the phenomenon is reduced with the more diffusive 1^{st} order scheme. The displacement of the potential temperature isolines, the vertical wind speeds and the maximum horizontal wind speeds are reduced. The rotors in the wake of the mountain are no longer reproduced with the default advection scheme.

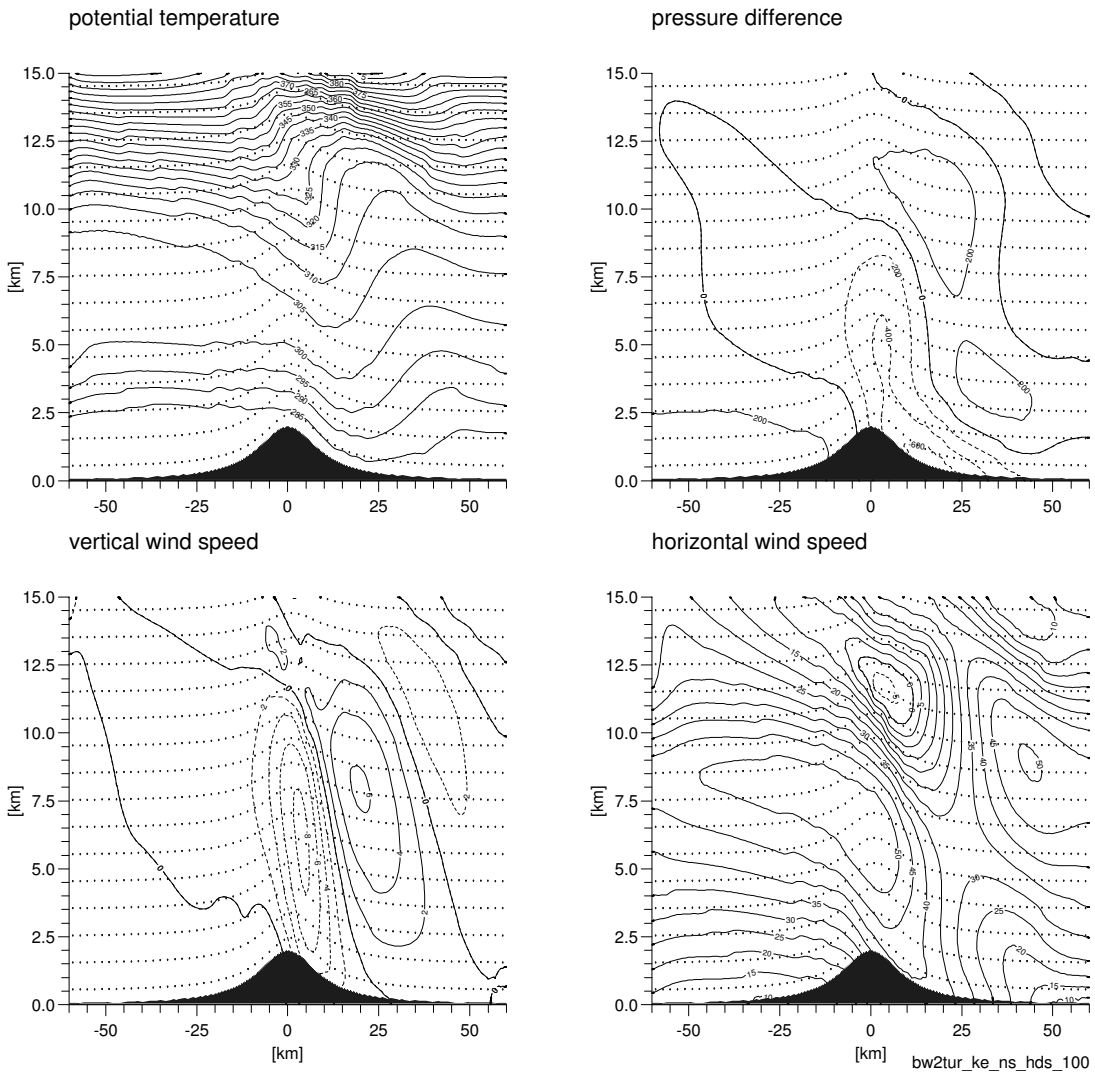

Figure C.32. Same results as Figure C.26 (time step number 100) for a mixed upwind and central difference advection scheme.

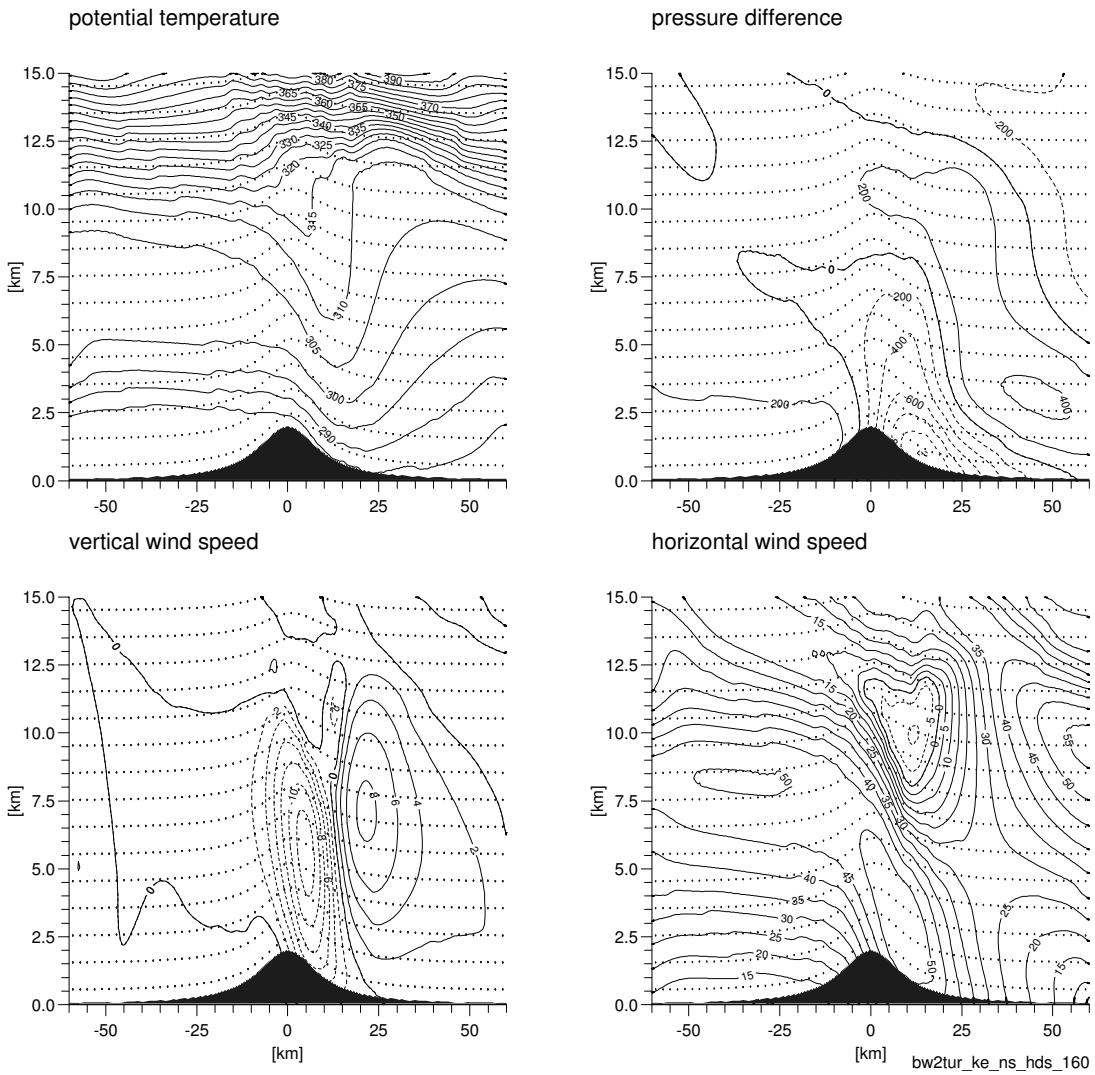

Figure C.33. Same results as Figure C.27 (time step number 160) for a mixed upwind and central difference advection scheme.

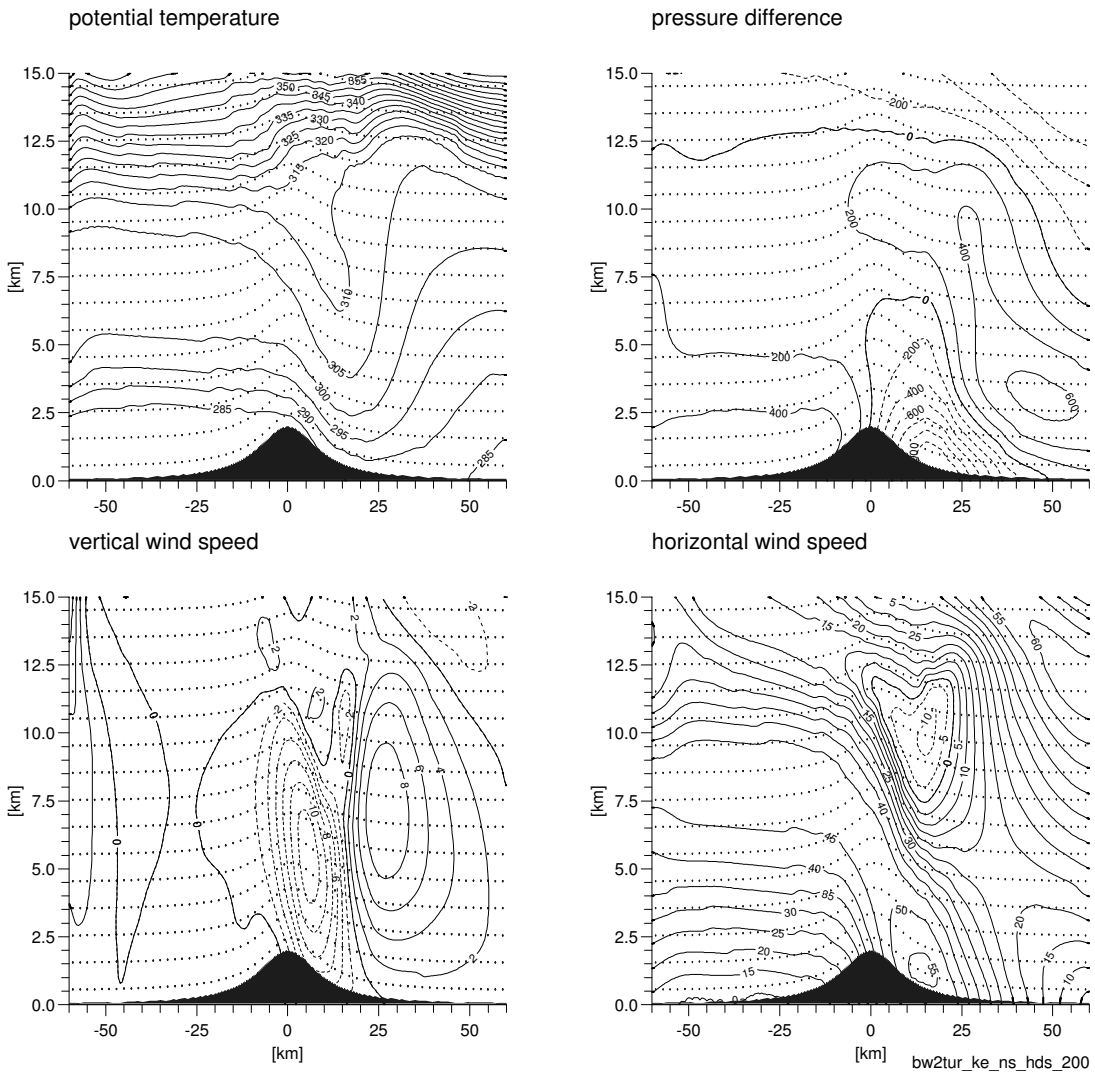

Figure C.34.. Same results as Figure C.28 (time step number 200) for a mixed upwind and central difference advection scheme.

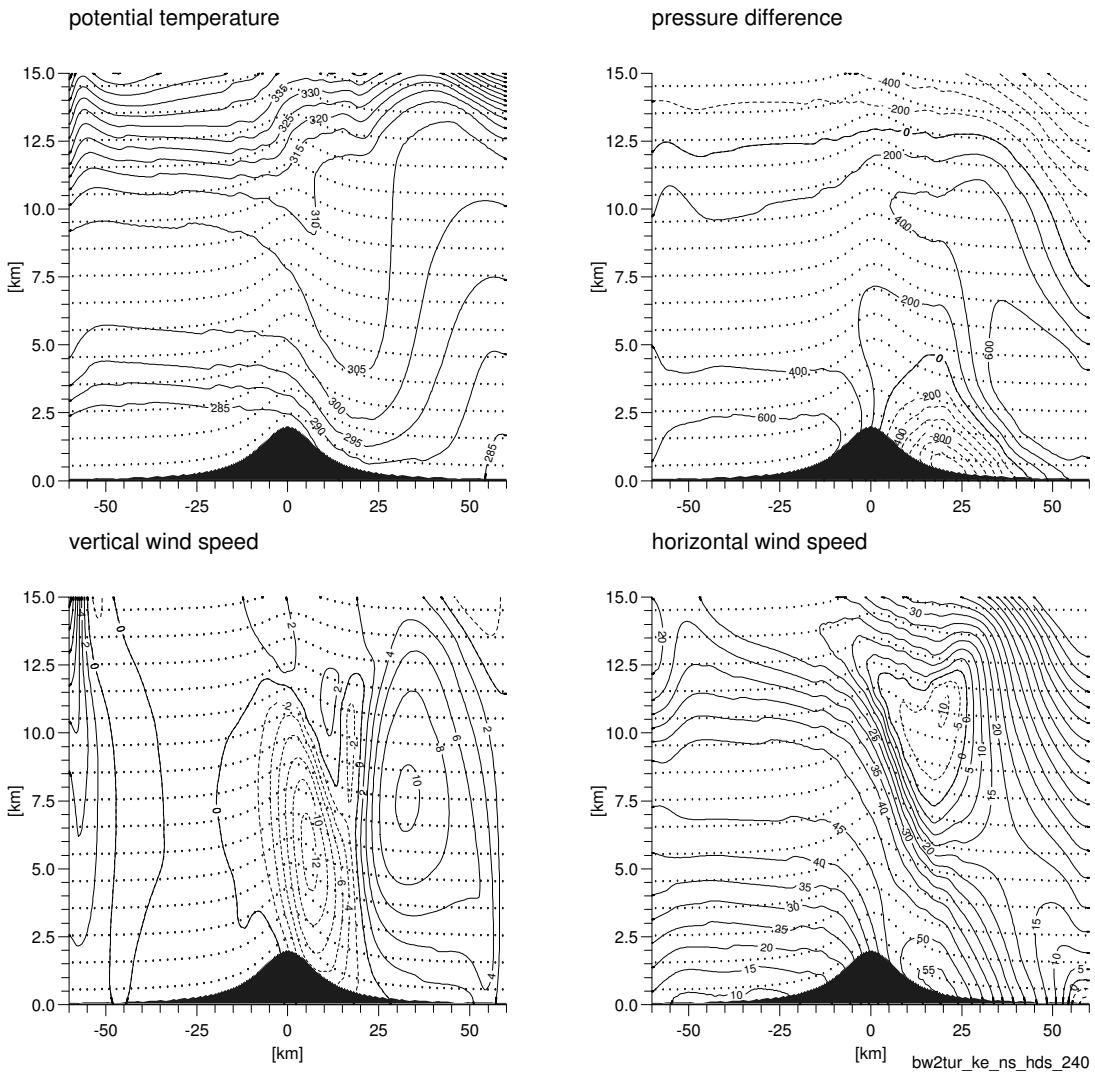

Figure C.35. Same results as Figure C.29 (time step number 240) for a mixed upwind and central difference advection scheme.

Appendix D

D Three dimensional wind field over real terrain (Askervein Hill)

As a last validation test case for situations dominated by the geostrophic wind, we chose to simulate the flow conditions around the real terrain of the Askervein Hill site. This choice was essentially motivated by the fact that a large amount of literature exists, which documents not only the measurement campaign, but also some physical and numerical modelling of the flow behaviour around this rather gentle topographic feature. A short review of the existing literature about Askervein Hill is presented in Section D.1. A description of the site and simulation conditions used in this work will be given in Section D.2 and Section D.3, while the simulation results will be compared to the observations later on.

D.1 Short literature review

The Askervein Hill area has been the subject of an extensive **observation campaign** over the years 1982-1983. An overview of the Askervein Hill project is given by Taylor and Teunissen (1987). An analysis of the mean wind variation at a fixed height above ground, along three measurement lines, has been performed by Salmon et al (1988) for various incident wind directions. Mickle et al (1988) studied vertical profiles of wind and turbulence at the hill top as well as at a reference station located upwind of the hill for winds blowing from the wind direction 210°.

In addition to the field experiment, **wind tunnel simulations** at three different length scales were performed by three different research groups and are documented in Teunissen et al (1987). The authors of these simulations concluded that the wind tunnel tests reproduced very well the changes in mean flow speed-up. They used various roughness conditions for the model surfaces and recognised that the changes in surface roughness only affected the flow on the lee side of the hill, as far as the mean wind speed is considered. The use of an excessively smooth surface tended to result in an overestimation of the flow speeds in the hill wake. The rough-surfaced model, on the other hand, was able to reproduce the spatial variation of the flow speed up along the measurement lines. Concerning turbulence variables, Teunissen et al. (1987) conclude that the changes in the longitudinal-component turbulence level σ_u is qualitatively well modelled and sometimes even quantitatively. They also point out that, when switching from a smooth to a rough surface, the significant change of the turbulence level in the approaching flow did not significantly affect the

behaviour of the longitudinal-component turbulence level. The effect of a roughness change was more important for the spatial variation of the mean flow variables.

The Askervein Hill experiment has also been used by many authors to test their **numerical model** ability to reproduce wind fields over real topography. For linearised models, detailed comparisons between observed and simulated normalised horizontal wind speed have been presented by Beljaars et al (1987) (model MSFD with k-ε closure) and Walmsley & Salmon (1984) (model MS3DJH/3). A general conclusion from the use of the linearised models to predict the spatial distribution of wind speed is that the results are in good agreement with the observations for the upwind side and near the summit of the hill (see e.g. Salmon et al, 1988). However, in the lee of the mountain, where flow separation possibly occurs, linear models tend to overpredict the mean wind speed (Beljaars et al, 1987).

Various 3D fully non-linear models have also been used to simulate wind fields over Askervein Hill. Raithby et al (1987), Glekas et al (1996) and Alm & Nygaard (1993) tested 3D full Navier-Stokes code, solving the equations by means of a finite-volume approach and using a k-ε two equations model for turbulence closure. All of them used the assumption of neutrally stratified flow and neglected buoyancy effects in the vertical velocity equation.

Alm & Nygaard (1993) presented results for the spatial variation of the mean wind along the three measurement lines and showed that they are in good agreement with the observations, also in the lee of the hill.

Glekas et al (1996) compared simulated and observed spatial distribution of the mean velocity along the A and AA measurement lines only (see Figure D.1 for definition). They obtained results which they qualify as 'satisfactory', even if the maximum overspeed value over the hill was not well-predicted. Testing various domain size and various grid resolution, they showed that the spatial distribution of the mean wind speed is strongly dependent on the boundary condition and model resolution. To decrease the sensitivity of the results to the boundary values, they suggest using a nesting procedure to isolate the boundaries from the region of interest.

Raithby et al (1987) proposed a more extensive numerical study, comparing not only the mean wind speed at constant height above ground, but also considering vertical profiles of variables like direction changes, turbulent kinetic energy, and stress tensors. From simulations done for the 210° and 180° wind directions, they also came to the conclusion that the predicted mean flow variables, flow speed-up and angle are in good agreement with the observations. Compared to a linearised model, the simulation results are more accurate in the lee of the hill. When analysing vertical

profiles of turbulent kinetic energy and turbulent stresses, they found large discrepancies between simulated and observed values. From this, they suggest that the k-ε turbulence model might be inadequate to properly reproduce such flows.

In a more recent paper, reviewing the various studies that were done using the Askervein Hill experiment results, Walmsley and Taylor (1995) give a summary of the unresolved questions related to this particular case study. These questions mainly concern the following topics:

A roughness length of 0.03 m has been suggested to be representative for the whole region around Askervein Hill. Several authors however contest the use of a constant roughness length for the whole domain. From vertical profile measurements (Mickle et al (1988)) or from numerical simulations assuming varying roughness length (Zeman & Jensen (1987)), they suspect that the hill top surrounding surface might be smoother than the surroundings of the reference measuring station. To reduce the discrepancy between observed and simulated mean wind speed profiles in the lowest 1-4 m, Zeman and Jensen would need to decrease the roughness length to about 0.001 m. Walmsley and Taylor (1995) on the other hand do not believe this significant roughness change to be realistic and expect that other effects might explain the difference between observed and simulated profiles in the lowest levels. In their view, a satisfactory explanation for the near-surface wind speed profiles over the hilltop is still lacking.

Various formulations to determine the inner-layer depth have been compared to values derived from the observed vertical profiles as well as from the simulated profiles. Which formulation, among the ones proposed by Jackson and Hunt (1975), Jensen et al (1984) or Britter et al (1981), is more appropriate is still a matter of debate.

The role of flow distortion in the lee of the hill, due to the presence of other terrain features, is not yet completely understood. Walmsley and Taylor (1995) suggest that further numerical tests with an extended topography would bring valuable information to help answer this question.

D.2 Site description

D.2.1 Topographical and roughness data

Askervein Hill is located on the West Coast of South Uist, an island of the Outer Hebrides off the west coast of mainland Scotland. The hill is quite isolated and close to elliptical in shape with a major axis of about 2 km and a minor axis of about 1 km. The major axis is aligned in a NW-SE direction. The hilltop is at an altitude of 126 m while the surroundings are at about 10 m above sea level.

As described by Taylor and Teunissen (1987) 'the ground cover around the hill is mainly heather, grass, low scrub and some flat rocks'. They consider that the surface roughness on the hill and in the surrounding terrain can be taken as uniform. From the analysis of wind profile measurements at a site called the reference site (RS), located some 2.8 km upwind of the hill for south-westerly flows, Taylor and Teunissen proposed a roughness length of 0.03 m that would be representative for the site.
The topographical data for the Askervein Hill area were kindly provided by J. Walmsley, who also supplied a roughness length map.

For convenience at the results analysis stage, the data were transformed to place the so-called mountain central point (CP) in the middle of the computational domain and the x and y co-ordinates were rotated clockwise by an angle of 47.3° to align the mountain major axis along the y direction. To get the altitudes at the co-ordinates corresponding to the grid resolution, a bilinear interpolation was performed using the rotated data. The site topography so obtained (isolines) is presented in Figure D.1.
The simulations that will be presented below were done assuming a constant roughness length of 0.03 m over the whole simulation domain. Some additional runs were also done with a spatially varying roughness length and are presented elsewhere (Montavon, 1998). For these simulations, the spatial distribution of the two roughness classes used is also given in Figure D.1, where the dark shaded areas correspond to a roughness length of 0.0001 m and the light shaded area to a roughness length of 0.03m.

D.2.2 Definitions

The measurement campaign of the Askervein Hill field experiment is extensively documented in the literature referenced in Section D.1. It is not our purpose to describe it again, but since many terms used as reference terms in the original literature will be used in this work, it seems convenient, for the reader's ease to give some more information about it.
The following abbreviations will be used to describe particular locations on the site:

Abbrev.	*location*	
HT	Hill top	(intersection between the A and B lines)
CP	Centre Point	(intersection between the AA and B lines)
RS	Reference site	

Mean wind speed measurements were collected at 10 m above ground along three lines of masts:

- one along the hill major axis (referred to as line B), going through both HT and CP
- two lines perpendicular to the major axis, one through HT (line A) and one through CP (line AA).

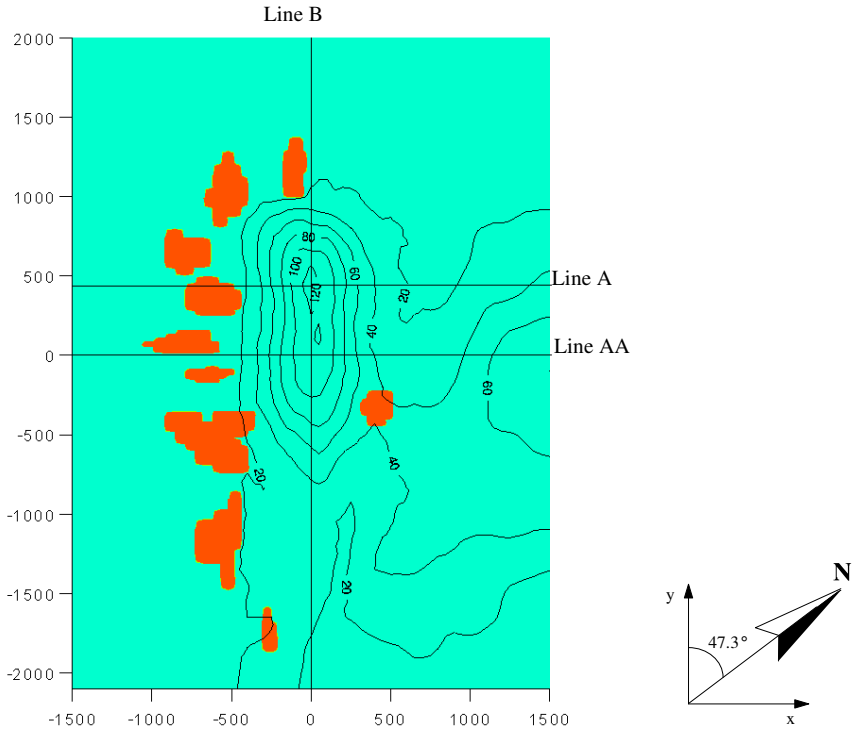

Figure D.1. Topography (isolines) and roughness length distribution (shading) for the Askervein Hill area. Light grey corresponds to a roughness length of 0.03m, while dark grey is for a roughness length of 0.0001m. (Source: adapted from data provided by J. Walmsley).

D.3 Simulation conditions

D.3.1 Computational domain

The domain used for the simulations over Askervein Hill consisted of 60 x 82 x 15 elements. The dimensions of the domain were 3 km in the x direction, 4.1 km in the y direction (corresponding to the hill major axis) and 3 km in the vertical. The element size was varied according to a symmetric geometric progression in the horizontal given by a stretching factor of 1/0.95. In the vertical, the element size followed a normal geometric progression with a stretching factor of 1.53, the smallest element being close to the ground. A summary of the parameters used for the grid construction is presented in Table D.1.

The ground and the top boundaries were deformed to correspond to the topography presented in Figure D.1. The top deformation has been done to ensure that all the control volumes in a given layer are at the same height above ground. The choice of the stretching factor in the vertical was conditioned by the fact that we wanted to have the centre point of the third level of cells lying at 10 m above ground, the height at which the mean wind speed measurements were recorded. This choice avoided the need for an additional interpolation at the results analysis stage. The corresponding computational domain is presented in Figure D.2.

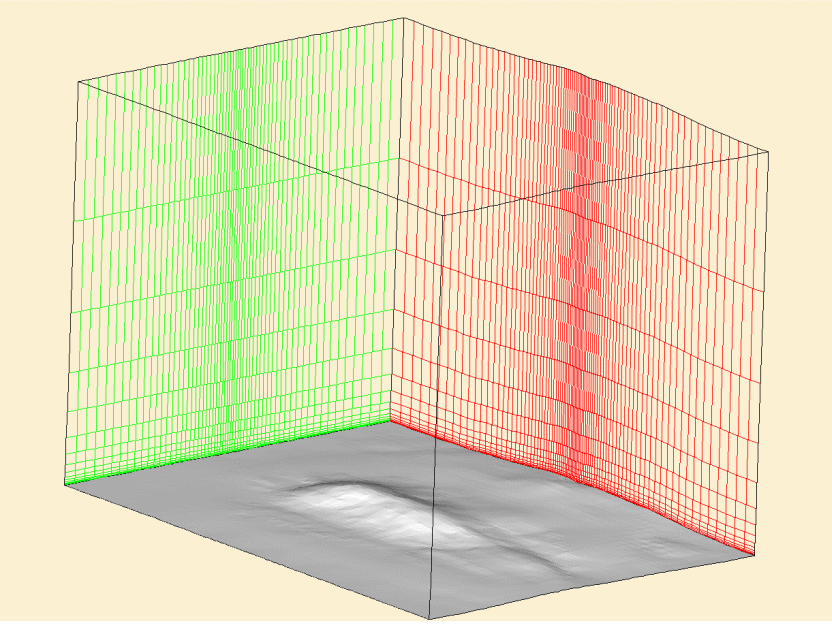

Figure D.2. Domain used for the simulation of atmospheric flows above Askervein Hill.

Table D.1. Parameters defining the grid used for the simulation of the wind fields over Askervein Hill.

direction	dimension [m]	number of elements	elements distribution	element's size [m]	
				largest	smallest
x	3000	60	symmetric geometric progression, r=1/0.95	95.5	21.5
y	4100	82	symmetric geometric progression, r=1/0.95	116.8	15.0
z	3000	15	geometric progression, r=1.53	1041	2.7

D.3.2 Boundary conditions

The ground level of the computational domain was allocated a 'wall' boundary condition, with the variables at the ground being determined by means of wall functions as explained in Section 5.2.2. This wall treatment basically assumes that the velocity profiles follow a logarithmic law close to the ground, with a velocity vector tangential to the surface. The second assumption is that the rate of dissipation balances the rate of production of turbulent kinetic energy.

For the vertical boundaries $x = 0$ or $x = x_{max}$, and $y = 0$ or y_{max}, the type of boundary condition used for the simulation depends on the mean flow direction. Figure D.3 shows a schematic representation of the computational domain seen from above. **Inlet** boundary conditions are set for the two boundaries at which the flow enters the domain, while **pressure boundaries** are set at the two faces with outgoing flow. (See Appendix L for the definitions of the various boundary condition types). The top of the domain is also set to be a pressure boundary.

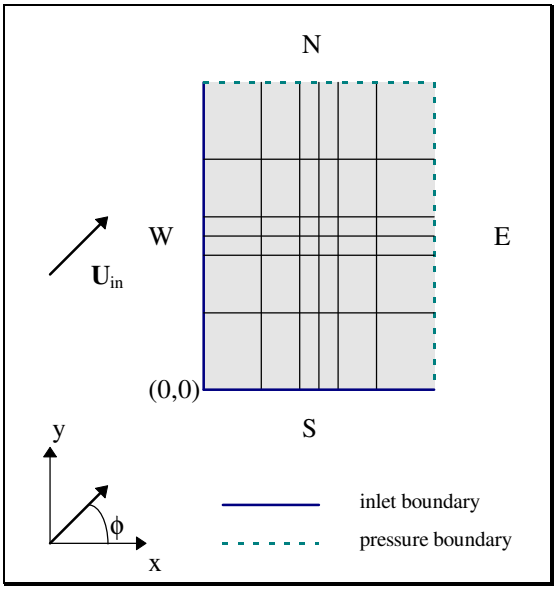

Figure D.3. Schematic of the computational domain seen from above. Definition of the boundary condition type for the vertical boundaries, depending on the main flow direction. Borders with entering flow are attributed 'inlet' boundary condition type (continuous line), while borders with outgoing flow are set to be pressure boundaries (dashed line).

All the pressure boundaries are set a value of 0 for the pressure p', assuming thereby that the total pressure corresponds to the hydrostatic reference state. The conditions used for the velocity components, turbulent kinetic energy and dissipation rate at the inlet boundaries are identical to the initial solution described below.

D.3.3 Initial solution

As input to solve the flow field equations, the model requires an initial solution. The vertical profiles used to initialise the flow variables are also used for the 'inlet' boundary conditions, and the latter are kept constant with time during the simulation.

For the strong wind conditions prevailing for the cases to be simulated, as well as from the fact that the stability conditions can essentially be considered as neutral (see Salmon et al, 1988), we expect boundary layer heights of the order of 1500m to develop over the area. Since for the lowest 10% of the boundary layer (typically 150m in these cases), the wind direction is constant with height, and considering that the mountain height is less than 120m, we do not expect the Ekman spiral and the Coriolis force to significantly affect the solution over the Askervein Hill terrain. The simulations presented below are obtained without including the effect of the Coriolis force, either in the model equations, or in the profiles used as entrance boundary conditions.

The model was initialised following a formulation proposed by Alexandrou (1996) (see Appendix I), who derived an alternative formulation to express the mean velocity profile of a two dimensional turbulent boundary layer flow. Instead of using the boundary layer height h and the roughness length z_0 as scaling height for the profiles, he used a dissipation length l_ε together with the boundary layer height h.

For the Alexandrou model constants we used c=0.183 and B was set according to eq. I.5 to correspond to a roughness length of 0.03 m with the boundary layer height h calculated from the relationship

eq. D.1 $$h = \frac{u_*}{6 \cdot f}$$

which corresponds to typical values obtained from observations (cf Appendix B, Section B.3).

Figure D.4 shows a typical velocity profile from Alexandrou's formulation, which was used as initial and boundary condition for the simulation. These profiles were obtained with the set of constants summarised in Table D.2. The values of the friction velocity and ground roughness were chosen to correspond to the values best representing the measured profile at RS for the run MF03-D (wind direction: 210°, cf.

Raithby et al., 1987). The corresponding dissipation rate and normalised turbulent kinetic energy[1] profiles are given in Figure D.5 and Figure D.6 respectively. Two turbulent kinetic energy profiles are presented for two different values of C_μ ($C_\mu = 0.09$ is the standard value for the k-ε model, and $C_\mu = 0.034$ is the value proposed by Duynkerke, 1988).

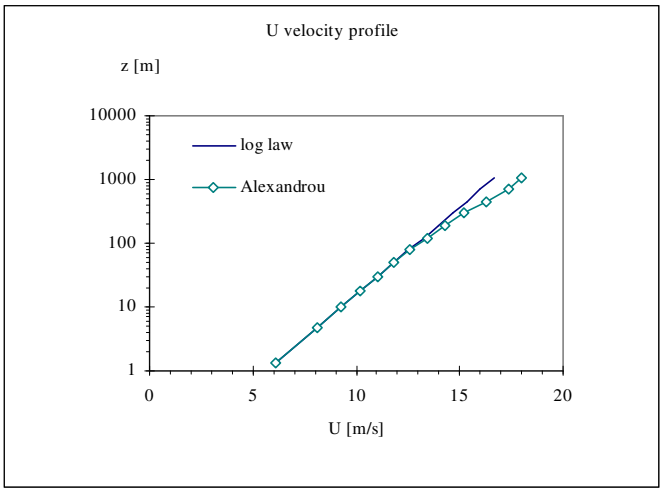

Figure D.4. Typical wind speed profile from the Alexandrou formulation used as initial and boundary conditions for simulations over Askervein hill.

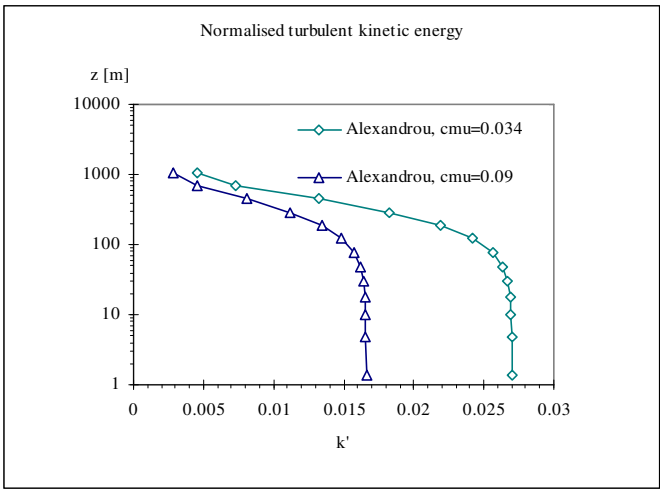

Figure D.5. Typical normalised kinetic energy profile from the Alexandrou formulation used as initial and boundary conditions for simulations over Askervein hill. The two different profiles are obtained for different values of C_μ.

[1] The normalised turbulent kinetic energy k' is defined such that $k' = k / u^2(z = 10m)$.

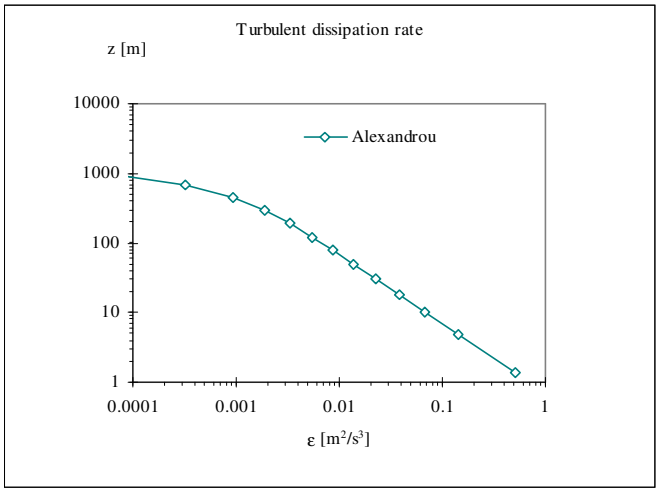

Figure D.6. Typical dissipation rate profile from the Alexandrou formulation used as initial and boundary conditions for simulations over Askervein hill.

Table D.2. Constants determining the profiles presented in Figure D.4, Figure D.5 and Figure D.6.

	Alexandrou formulation
u_* [m/s]	0.654
$h = u_*/6f$ [m]	1090
c [-]	0.183
B [-]	7.91

D.3.4 Simulation results for the 210°, 180°, 235° and 270° wind directions

Simulations were performed for various flow directions and the behaviour of the mean wind speed at 10 m above ground level along the three A, AA and B lines was compared with the measurements.

The first simulation was done for a wind blowing from the 210° sector (corresponding to ϕ= 12.7° in our model). The initial and 'inlet' profiles were set according to the Alexandrou formulation with the parameter values given in Table D.2. A constant ground roughness of 0.03 m was used. The atmosphere was set to be stable with a vertical real temperature gradient of -6.7 K/km over the whole vertical extent of the simulation domain (3000m). The density of the atmosphere is set to be constant in time and corresponds to the hydrostatic equilibrium state determined by the temperature profile. All the runs presented here, except one, have been

performed using the standard values for the turbulence model constants, i.e. using C_μ= *0.09*, C_1=*1.44*, C_2=*1.92* and σ_ε=*1.217.*

D.3.4.1 Horizontal mean wind speed variation

In Figure D.7 the normalised mean horizontal wind speed[2] at 10 m above ground level obtained from the simulation (lines) are compared to the measurements (isolated symbols) which were recorded during the simultaneous runs MF03-D and TU03-B (210° wind direction) as described in Taylor and Teunissen (1987). The measured values were actually read from the paper by Salmon et al (1988). Mean wind speeds are presented along the A line (Figure D.7a), AA line (Figure D.7b) and B line (Figure D.7c). Model results are extracted for several lines close to and parallel to the measurement lines. The only reason for extracting several parallel profiles to compare with one measurement line was to make sure that we would not have a high sensitivity of the results to an error in representation of the measurement masts locations. As will be seen later on, no drastic change in the solution behaviour can be seen when comparing e.g. the J44, J45 or J46 lines. Table D.3 gives the definition and exact location of the labels used later on.

Table D.3. Definition of the line labels in terms of co-ordinates

AA line		A line		B line	
label	distance from meas. line [m]	label	distance from meas. line [m]	label	distance from meas. line [m]
J44	-10.9	J60	0.2	I29	-32.9
J45	6.2	J61	39.0	I30	-10.8
J46	24.2	J62	79.8	I31	10.8

The vertical angle of the velocity vector relative to the horizontal is plotted in Figure D.7d and compared to the measurements for both the A and AA line. A positive value indicates an ascending flow. Figure D.7e presents the change of direction of the horizontal wind velocity relative to the wind direction used at the boundary. A positive change indicates a clockwise rotation of the wind vector.

[2] The normalised horizontal wind speed is defined as $\tilde{v}_h = \sqrt{u_{10m}^2 + v_{10m}^2} \,/\, \sqrt{u_{ref,10m}^2 + v_{ref,10m}^2}$. Since the exact location of the reference station was not included in the simulation domain, we chose a reference point located in the domain 900 m upwind of the hill, along the A line.

As can be seen from Figure D.7a and b, the velocity decrease upwind of the hill, the increase over the summit and the velocity reduction in the lee of the hill are fairly well reproduced by the numerical model. The agreement between measurements and simulations along the AA line is excellent. Along the A line, the agreement is not exactly as good with the overspeed over the hill top being underpredicted by about 0.2/1.9 (10 %) and the wind speed in the lee of the hill overpredicted by 0.13/0.33 (about 40 %). From Figure D.7c, it can also be noticed that the model generally tends to slightly underpredict the overspeed along the mountain major axis. The overprediction in the normalised wind speed at locations between 1500 and 2000 m south-east of the hilltop is probably due to the fact that the interpolated topography does not exactly represent the real topography.

Concerning the wind direction, Figure D.7d shows that the angle of the velocity vector relative to the horizontal (so-called upwash angle) is well reproduced. For the horizontal change of direction with respect to the incoming wind direction, the behaviour along the A and AA lines is qualitatively reproduced. Upwind of the hill, the observations tend to show an anticlockwise rotation of about 10°-15° between the wind at CP (AA line) and the wind at HT (A line). Such a rotation is also predicted by the model, with a smaller amplitude however than the observed one (some 5°). The increased anticlockwise rotation in the lee of the hill observed along the A line is captured by the simulation, with an amplitude that is underpredicted by about 10 degrees compared to the observations.

The horizontal wind speed distribution over the whole simulation domain is presented in Figure D.8. Grey shading represents the wind speed values. The white isolines separate wind speed classes of 1 m/s. The Askervein Hill topography is indicated by means of the black isolines. Altitude difference between two consecutive topography isolines is 20 m. To give an idea of direction changes, the wind vectors were also plotted. The flow features that can be observed on this figure are very similar to the ones that were presented by Raithby et al (1987). The most striking feature is the strong overspeed region along the main hill axis. A stagnation region with a slight wind speed reduction in the upstream region can be seen. The most significant reduction is observed in the lee of the hill, with wind speed values as low as 3.3 m/s (to be compared with a value of 9.3 m/s at the entrance and a maximum value of 16.3 m/s close to the hill top). The strong wind speed reduction in the lee of the mountain is accompanied by an anticlockwise rotation of the velocity vectors, which is even more pronounced when looking at lower levels (not shown).

After some 1000 m behind the hill crest, the flow seems to have recovered to its original wind speed. And it appears that secondary hills present in the domain also affect the flow.

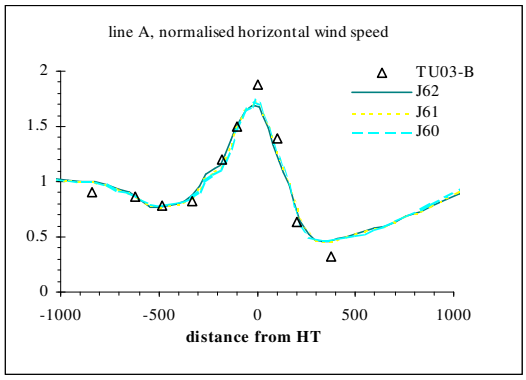

a)

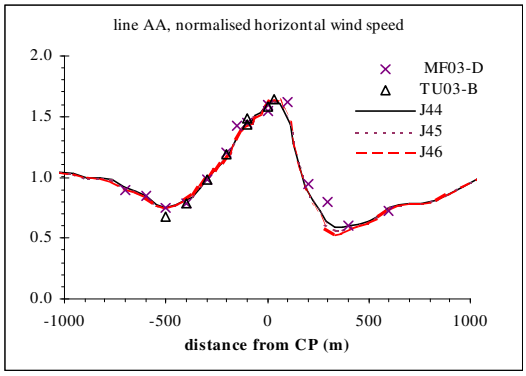

b)

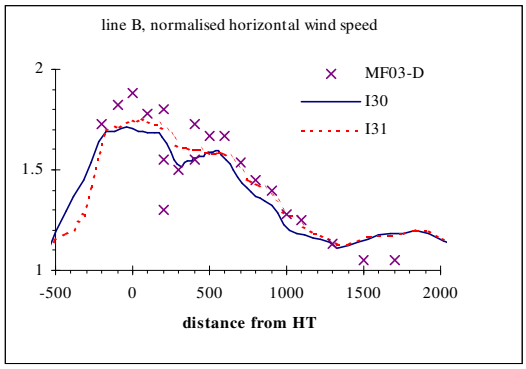

c)

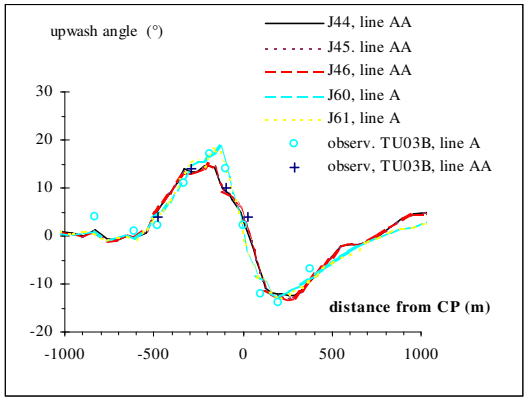

d)

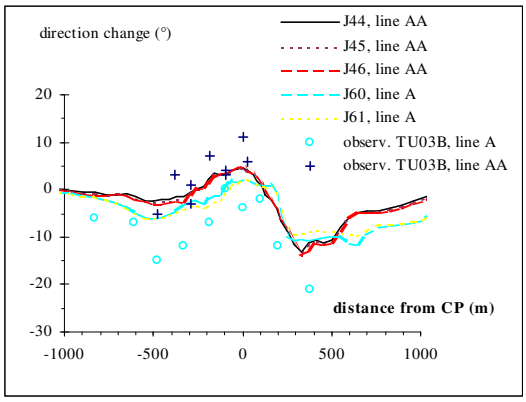

e)

Figure D.7. Normalised wind speed along the measurement lines A, AA and B (figures a-c), vertical angle (figure d) and wind direction change (figure e) at 10 m above ground level for a simulation with incoming 210° wind direction. Model results are drawn with lines, while the isolated symbols correspond to the observations.

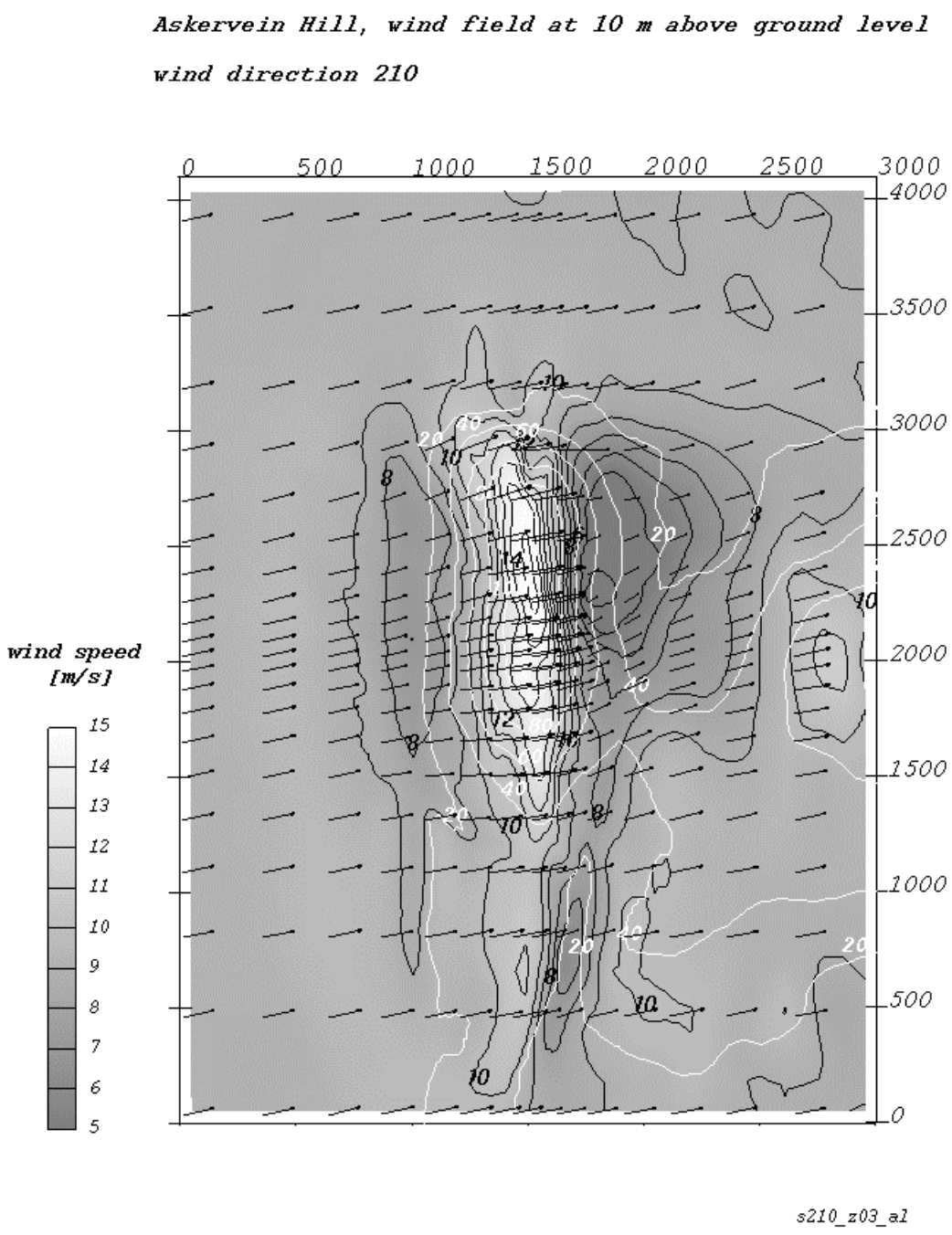

Figure D.8. Wind field at 10 m above ground level over the Askervein topography for an incoming wind blowing with the 210° direction. Grey shading gives the horizontal wind speed scale. Wind speed classes of 1 m/s are separated by black isolines. For clarity purpose, only one vector in four has been plotted. The topography is represented by means of white isolines.

Simulations were also performed for the 180°, 235° and 270° wind directions. Except for the incoming 235° wind direction, for which the friction velocity u_* has been set to 0.42 m/s, the simulation conditions for these simulations were exactly the same as for the 210° wind direction. As far as measurements were available, the mean wind and direction variation at 10 m above ground have been compared to the observations. For that purpose, results from the runs MF01-D and TU01-B (direction: 180°), the run MF2.29b (direction: 235°) and the run MF04-C (direction: 270°) were used (Salmon et al, 1988).

The comparisons presented in Figure D.7 to Figure D.11 show that the model is able to satisfactorily reproduce the horizontal variation of the mean flow properties at 10 m above ground level.

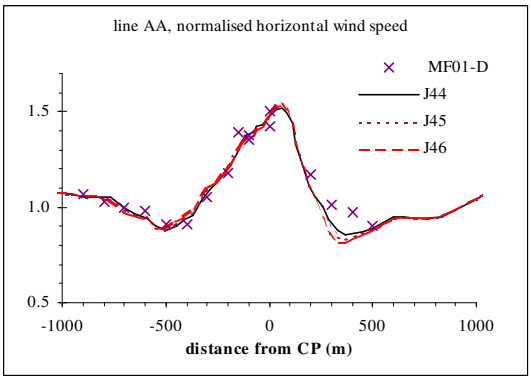

a)

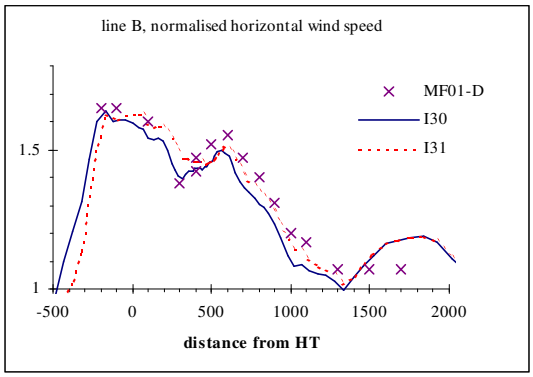

b)

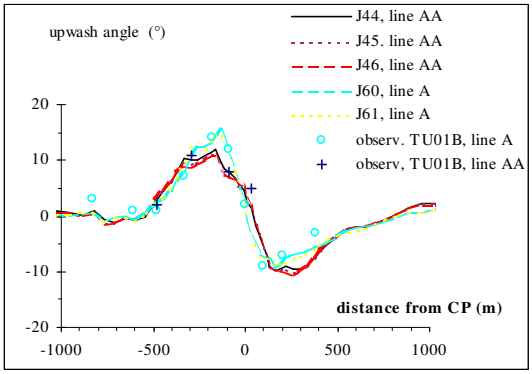

c)

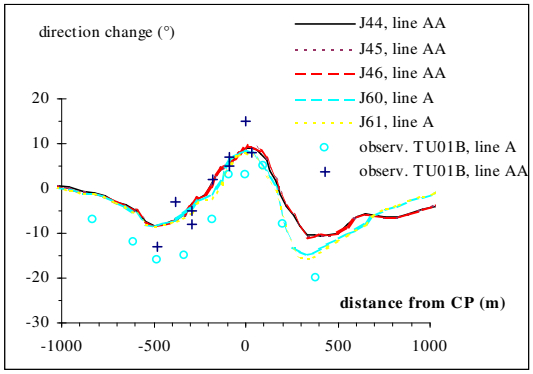

d)

Figure D.9. Same as Figure D.7 for the wind direction 180°. (Source: Salmon et al., 1988).

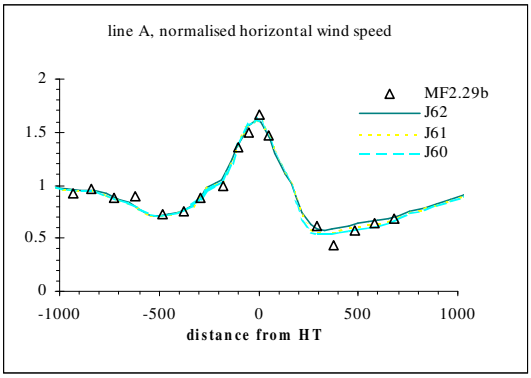

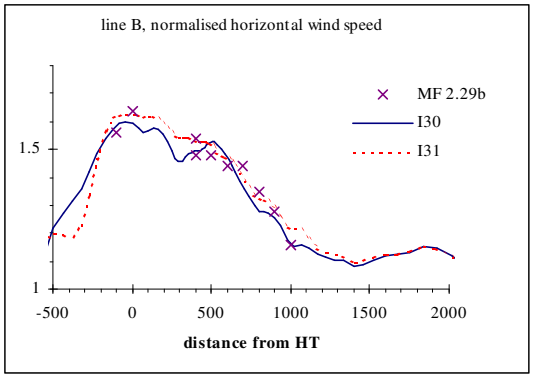

a) b)

Figure D.10. Normalised wind speed along the A and B line for the 235° wind direction. Model results are drawn with lines, while the isolated symbols correspond to the observations. (Source: Salmon et al., 1988).

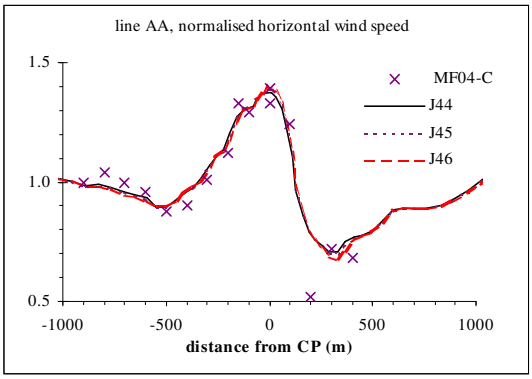

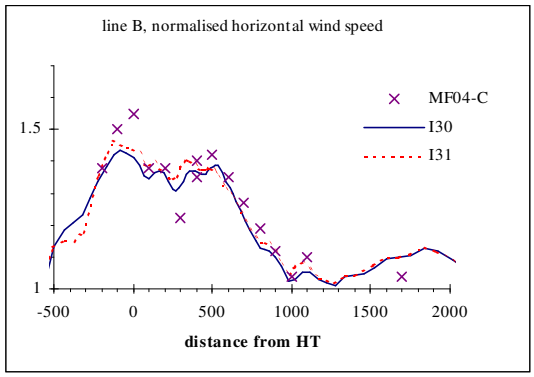

a) b)

Figure D.11. Normalised wind speed along the AA and B line for the 270° wind direction. Model results are drawn with lines, while the isolated symbols correspond to the observations. (Source: Salmon et al., 1988).

D.3.4.2 Vertical profiles

Figure D.12 shows, for the lowest 100 m above ground, the behaviour of the horizontal wind speed (Figure D.12a), normalised turbulent kinetic energy k' (Figure D.12b) and the fractional speed up ratio[3] ΔS (Figure D.12c) at hill top for the 210°

[3] The fractional speedup ratio ΔS (also called 'overspeed ratio') is defined according to $\Delta S(\tilde{z}) = \frac{v_h(\tilde{z}) - v_{h,ref}(\tilde{z})}{v_{h,ref}(\tilde{z})}$ and the normalised turbulent kinetic energy k' by $k' = k / v_{ref}^2(10m)$.

wind direction. To appreciate the effect that the choice of the reference location can have on the results, the horizontal wind speed at the entrance and at the reference point have also been plotted in Figure D.12a. It can be seen from the present simulation that the wind speed profile at the reference location has not been changed much compared to the inlet profile. This observation tends to support that, for the chosen boundary conditions, the incoming flow is in equilibrium.

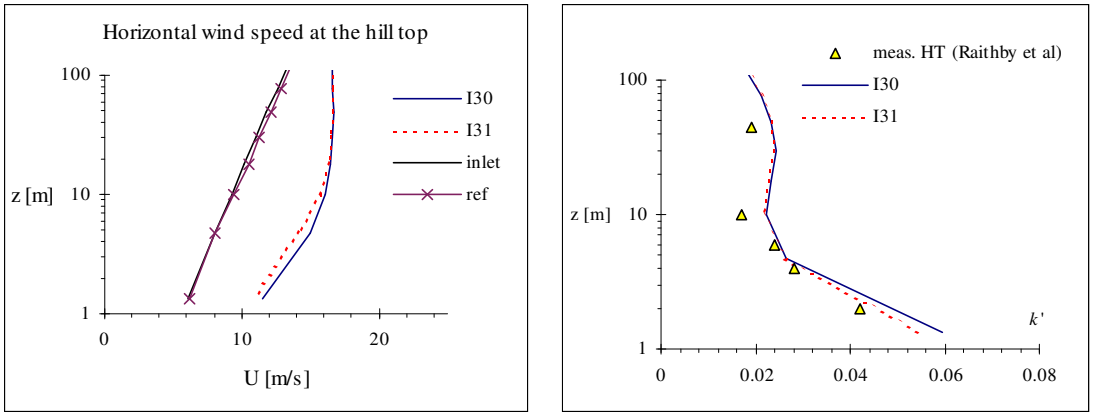

a) b)

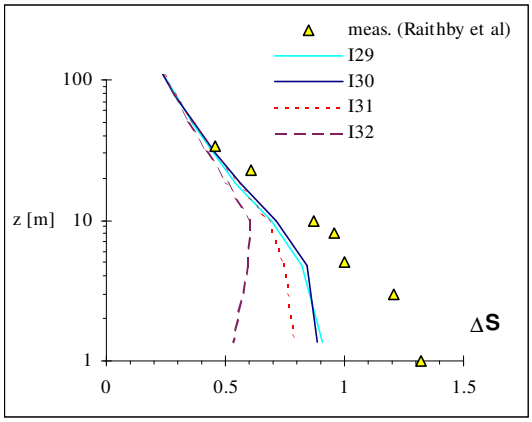

c)

Figure D.12. Vertical profiles of horizontal wind speed (a), normalised turbulent kinetic energy *k'* (b) and fractional speed up ratio ΔS over the hill top. The wind speed profiles at the domain entrance as well as the reference profile have also been plotted in (a). Isolated triangles stand for measurements at the hill top (source: Raithby et al, 1987) and lines are for profiles obtained from the numerical simulation at various locations (I= 29, 30, 31 and 32) along the J= 61 line (see Table D.3 for the definition of the exact locations in metres).

From Figure D.12b, it appears that the behaviour of the simulated *k'* profile is in good agreement with the observations, with the simulated values slightly overpredicting the measurements. For the heights above ground which are of interest for wind energy applications (between 20 and 100 m), the speed up ratio is quite well

reproduced. For lower levels however, the values obtained for ΔS clearly underpredict the measurements.

D.4 Sensitivity study

To obtain a better understanding of the effects of the various flow parameters and model constants on the resulting flow pattern, a sensitivity study was performed for the 210° wind direction. The latter considered the effects of

- the **vertical resolution** and **total vertical extent** of the computational domain
- the **atmospheric stability** by varying the vertical temperature gradient.
- the **friction velocity** used to determine the profiles at the inlet boundary conditions
- the **ground roughness** by using various constant ground roughnesses, by introducing a roughness length in the domain which differs from the one used at the entrance and finally by spatially varying the roughness length,
- the **turbulence profiles at the entrance** by changing the type of profiles used for the k and ε parameterisation.

And finally, simulations were also performed with **various turbulence models**. This last step included the use of an algebraic stress model, of a differential stress model as well as the k-ε turbulence model with modified constants.

The results of the sensitivity study are extensively presented elsewhere (Montavon, 1998), and we will only review here the conclusions which could be drawn:

- As far as wind power potential evaluation is concerned, the obtained results show that the vertical resolution adopted seems to be sufficient and the flow acceleration above the hill was well reproduced for levels located at more than 10 m above ground. An increase in the vertical resolution did not bring any significant improvement of the results.
- With the relatively small vertical dimension of the hill, static stability effects can be considered as negligible for the case of relatively strong winds.
- Keeping all the other parameters constant and changing the friction velocity u_* only affected the absolute values of the flow variables, but not the normalised values. At this point, it should be stressed that the friction velocity can be considered as a scaling variable for the case of Askervein Hill because of the fact that the topography is not very high and that static stability effects are negligible.
- From simulations done with an homogeneous roughness length (same roughness length over the whole domain and for the profiles set at the entrance), it can be observed that:

1. the maximum overspeed along the hill major axis is reduced when the roughness length is decreased,
2. the wind speed reduction in the lee of the hill becomes less important when the roughness length is decreased,
3. the change of roughness length does not significantly affect the upwash angle (angle of the wind vector relative to the horizontal),
4. upwind of the hill, the direction change in the horizontal plane is not modified by a change in the roughness length. However, it can be seen that the amplitude of the anticlockwise rotation between the hill top and the lee region decreases with decreasing roughness length,
5. a decrease in the roughness length tends to decrease the values of the speed up ratio ΔS in the lowest levels
6. the normalised turbulent kinetic energy profile is significantly reduced when the roughness length is decreased.

- From simulations done with homogenous ground roughness but with inlet profiles corresponding to a different roughness value, conclusion 5 above is no longer true. In the case where the roughness length in the simulation domain is reduced compared to the one characterising the inlet profiles, the speed up ratio is increased in the lowest levels (lower than 10 m above ground), without being significantly altered in the higher levels.
- It appeared that the consideration of local roughness changes (like the distribution presented in Figure D.1) had no significant impact on the wind speed distribution. For a roughness change to show an effect, it needs to take place over distances larger than a few hundred meters upwind of the location considered. However, it was also shown that a roughness change located a few kilometres upwind of the hill would affect the flow development on the terrain.
- The model results appear to be very sensitive to the type of profiles set for k and ε as inlet boundary conditions. For situations where the k and ε profiles are not in equilibrium with the flow conditions, the model results were as if there were a roughness change. Situations using e.g. constant values for k and ε at the entrance present simulation results similar to the case of a smooth to rough transition, causing an excessive reduction of the wind speed in the hill wake. The strong sensitivity to the boundary conditions requires that the latter are fixed carefully. Otherwise, misleading conclusions could easily be drawn regarding the values of other model parameters like the roughness length or the turbulence model constants. This observation can actually be considered as one of the strongest limitations of the model since in most of the cases, which are to be simulated, we

only have a very poor knowledge of the turbulence conditions to be used at the model entrance.

- If reliable information is not available regarding the values to be specified for the stress tensor at the entrance to the simulation domain, the use of more sophisticated turbulence models does not bring better results than the simpler k-ε model.

Taking advantage of the many observations obtained from the sensitivity study, we tried to improve the simulation results, with particular attention to the speed up ratio in the lowest 10 m. At this stage, remembering that the wind speed profile, the turbulence characteristics of the approaching flow, together with the equilibrium or non-equilibrium that they describe, appear to be very significant for the evolution of the flow field in the simulation domain, we tried to set them so that they gave a better agreement with the observations available at the reference station. Keeping in mind that, for a wind blowing from the 210° direction, there is a flat uniform fetch of about 3-4 km between the coastal line and Askervein Hill, and looking at the vertical profiles of wind speed measured at the reference station for the run MF03-D (see Figure D.13a) it seems quite possible that the flow approaching the Askervein Hill area is still affected by the roughness change associated with the sea-land transition. To see how the 'history of the flow' can change the results on the domain, we made an additional simulation with entrance profiles obtained from a two-dimensional run simulating the development of a boundary layer over flat terrain behind a roughness change for a neutral free flow stratification. The 2D case assumed that the profiles of the wind speed, turbulent kinetic energy and dissipation at the entrance represent atmospheric conditions in equilibrium with a roughness value of 0.0001m, which would describe smooth conditions typical for the sea. The formulation used for this purpose was again the formulation given by Alexandrou. The profiles at the entrance to the 2D domain have the characteristics given in Table D.4. For this simulation again, the turbulence model constants were set to the standard ones, with $C_\mu = 0.09$, $C_1 = 1.44$, $C_2 = 1.92$ and $\sigma_\varepsilon = 1.217$. The ground roughness of both the 2D and 3D simulation domain was set to 0.03m

Profiles of wind speed, turbulent kinetic energy and turbulent dissipation rate were extracted from the 2D simulation at a fetch of 4 km behind the roughness change (see Figure D.13a to c). They were then utilised as initial and boundary conditions for the 3D Askervein Hill domain.

Table D.4. Parameters characterising the inlet profiles used as inlet boundary condition for the 2D simulation with roughness change.

ground roughness	0.01m
friction velocity	0.42 m/s
boundary layer height	700 m
free stream velocity	19 m/s
c (constant in Alexandrou formulation)	0.1

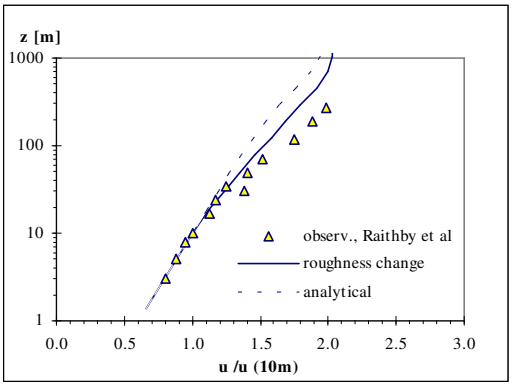

a)

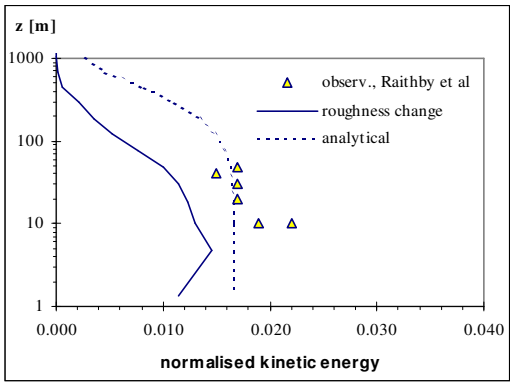

b)

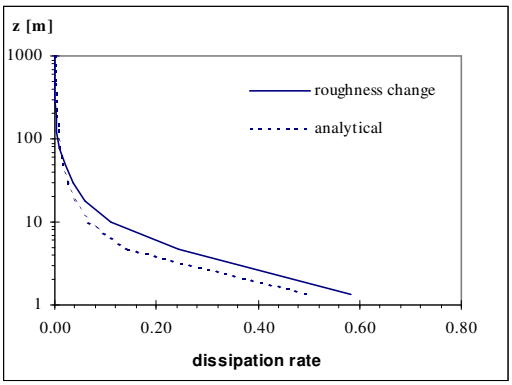

c)

Figure D.13. Normalised wind speed (a), normalised turbulent kinetic energy and dissipation rate profiles resulting from the 2D simulation after a fetch of 4 km behind a roughness change (continuous line) for the **standard turbulence model constants**. The profiles are compared to the analytical profiles used for the simulation for the 210° wind direction presented in D.3.4 and to values observed at the reference site (isolated triangles) (source Raithby et al, 1987).

Compared to the analytical formulation that was used previously, the wind speed profile after the roughness change exhibits, for heights above 30 m, a behaviour which is more similar to the one that was observed at the reference station, with a higher wind speed for levels above 30 m (see Figure D.13). The normalised turbulent kinetic energy profile however seems to slightly underpredict the measured values.

This effect might be due to the fact that we used the standard model constant for $C\mu$, which might be slightly too high for atmospheric flows. No observations for the dissipation rate were available, so that it can not be stated whether the profile used for ε is appropriate or not.

The results of the 3D simulation are presented in Figure D.14 and Figure D.15.

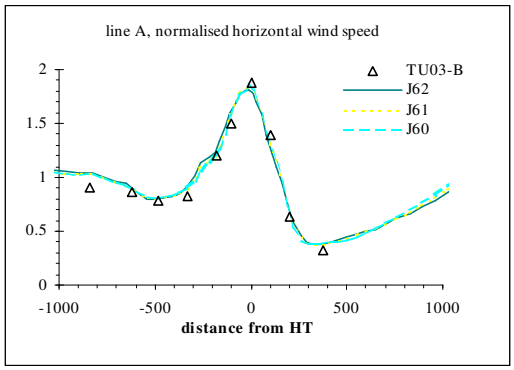

a)

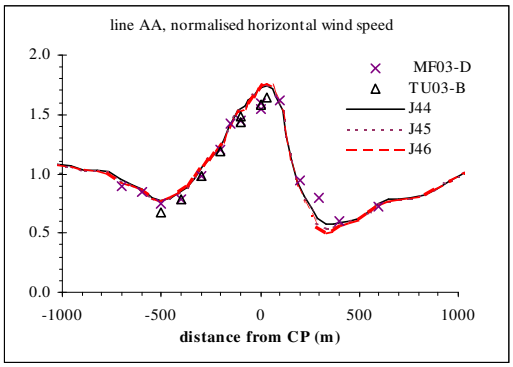

b)

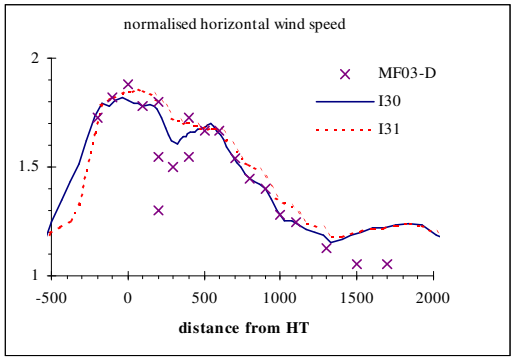

c)

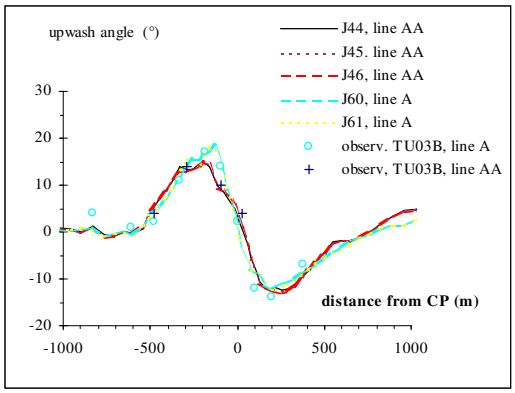

d)

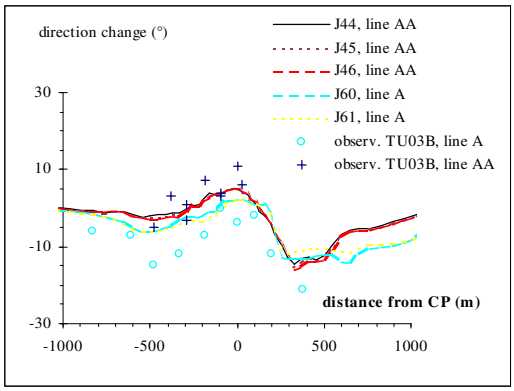

e)

Figure D.14. Same as Figure D.7 for a simulation using the profiles presented in Figure D.13 as boundary conditions.

From Figure D.14a and b, it can be seen that both the maximum overspeed and maximum wind speed reduction along the A and AA lines are well reproduced by

the simulation. Figure D.14c shows a noticeable improvement of the maximum overspeed prediction along the hill major axis. The simulated vertical profile of normalised turbulent kinetic energy over the hill top compares very well with the observations, while the overspeed ratio prediction has also been improved, with the profile agreeing with the measurements down to a height of 5 m above ground. This improvement of the vertical profile of ΔS is definitely related to the fact that the velocity profile at the entrance of the simulation domain gives higher velocities for levels above 30m. Among the various simulations that were performed using the standard turbulence model constants, the one shown here best reproduces the observations.

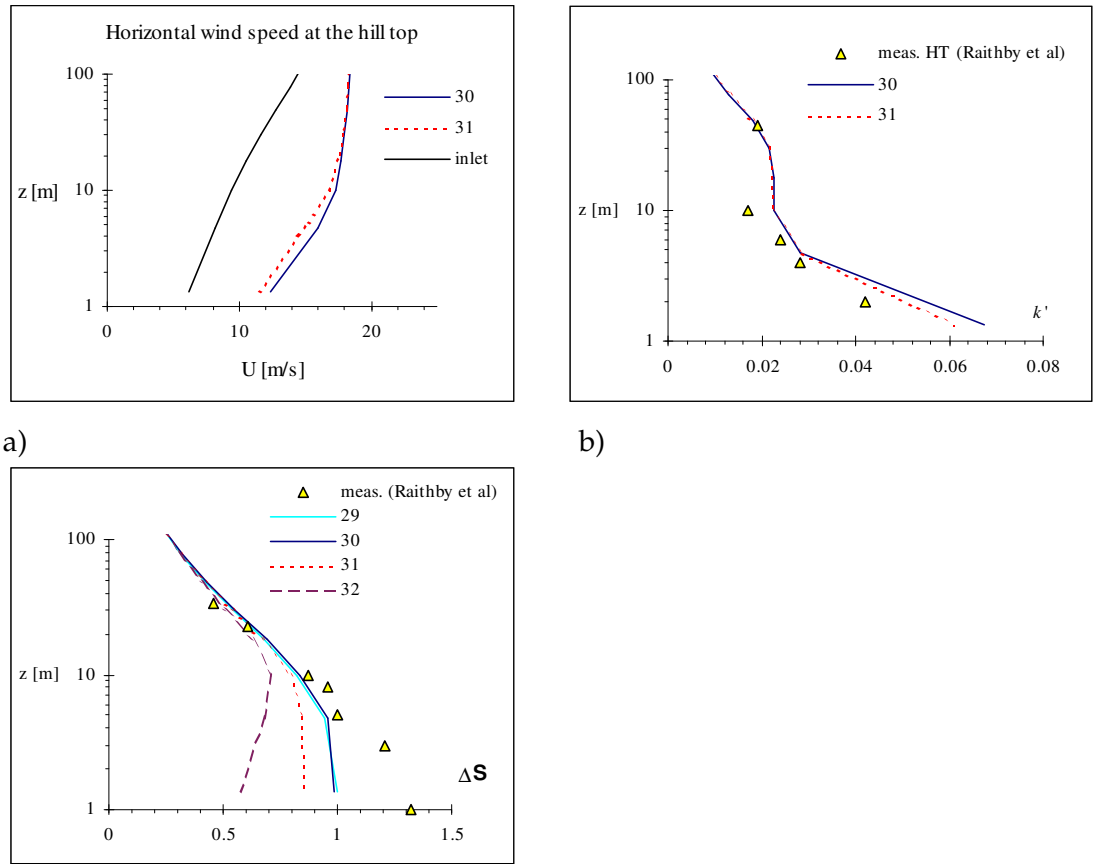

Figure D.15. Same as Figure D.12 for a simulation using the profiles presented in Figure D.13 as boundary conditions.

Apart from the prediction of the speed up ratio in the lowest 5 m above ground, the results presented above are good, even though the kinetic energy profile specified at the entrance of the domain underestimates the values that were measured at the reference site. Despite the good agreement obtained between the observations and

measurements, there are still some questions, which remain unanswered regarding the choices to be made to simulate atmospheric flows. One of these questions concerns the values to be used for the turbulence model constants. Instead of the standard values (C_μ= *0.09*, C_1=*1.44*, C_2=*1.92* and σ_ε=*1.217*), Duynkerke (1988) suggested the modified set C_μ= *0.034*, C_1=*1.46*, C_2=*1.83* and σ_ε=*2.38*, which should be more appropriate for atmospheric flows. To illustrate the influence of such a choice, the simulation presented above was repeated with the set of constants proposed by Duynkerke. The profiles 4 km downwind of the roughness change, obtained from the 2D simulation for this case are presented in Figure D.16. Changing the model constants (more particularly reducing the value of C_μ) tends to increase the normalised turbulent kinetic energy profile close to the ground. A comparison with the observations at the reference site shows that, for that particular case, the prediction of the kinetic turbulent energy profile is improved.

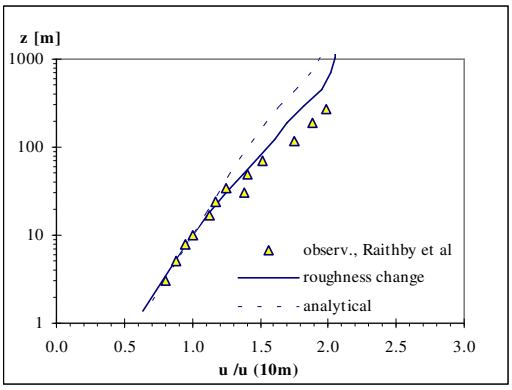

a)

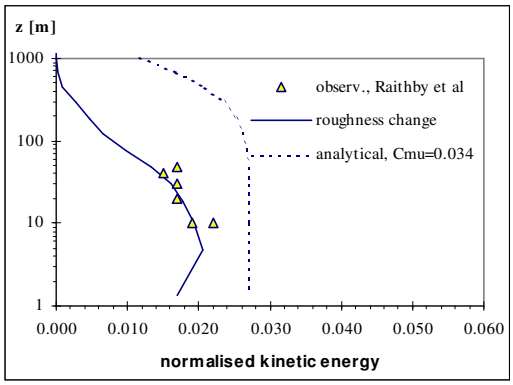

b)

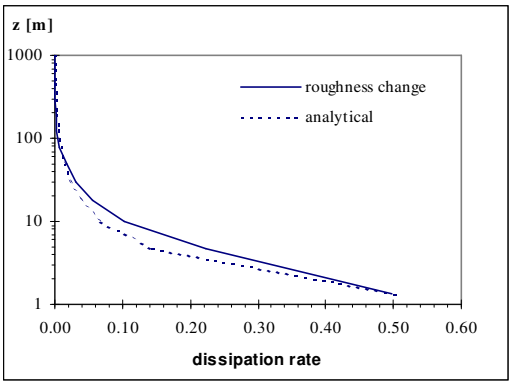

c)

Figure D.16. Normalised wind speed (a), normalised turbulent kinetic energy and dissipation rate profiles resulting from the 2D simulation after a fetch of 4 km behind a roughness change (continuous line) for the **turbulence model constants proposed by Duynkerke**. The profiles are compared to the analytical profiles used for the simulation for the 210° wind direction presented in D.3.4 and to values observed at the reference site (isolated triangles) (source Raithby et al, 1987).

The 3D simulation results using the profiles calculated after a fetch of 4 km as entrance boundary conditions are given in Figure D.17 and Figure D.18 for the Duynkerke turbulence model constants. Here also, compared to the case using the standard model constants, we can notice an increase in the normalised kinetic turbulent kinetic energy close to the ground (c.f. Figure D.17b). As a consequence, we observe a much stronger reduction of the normalised wind speed in the wake of the hill, especially visible along the A line (Figure D.18a). A further implication of this significant wind speed reduction behind the mountain is a significant modification of the upwash angle and direction change of the flow along the A line. With the reduction of C_μ, the simulated flow behaves as if the ground roughness (and hence the turbulence intensity close to the ground) would be excessive.

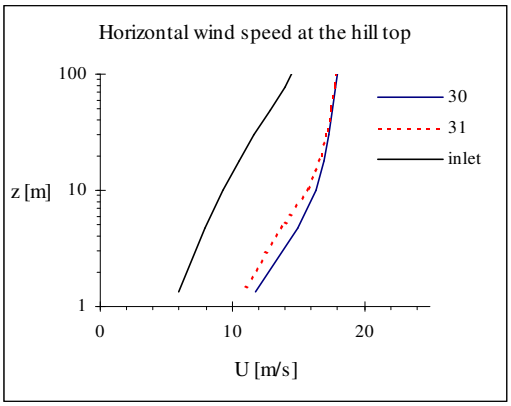

a)

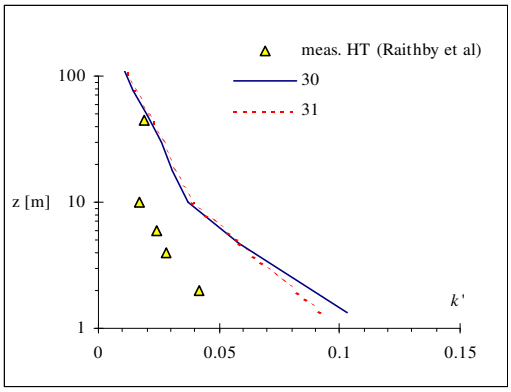

b)

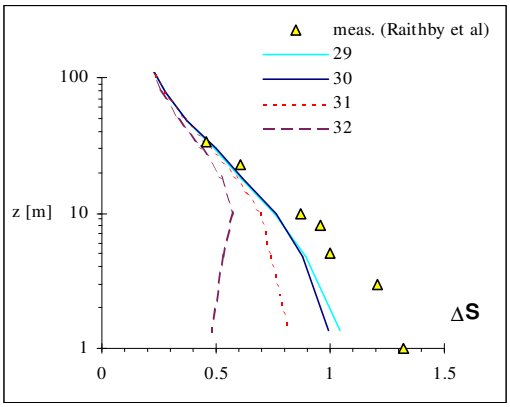

c)

Figure D.17. Same as Figure D.15 using the profiles presented in Figure D.16 as inlet boundary conditions, and with the turbulence model constants proposed by Duynkerke.

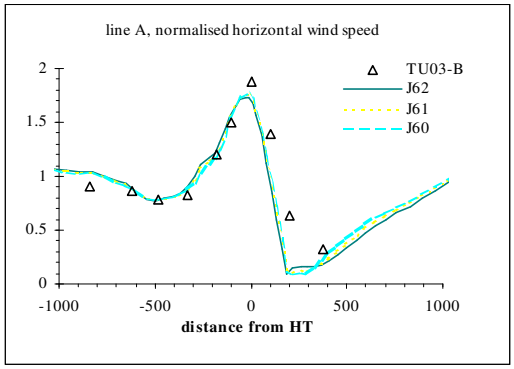

a)

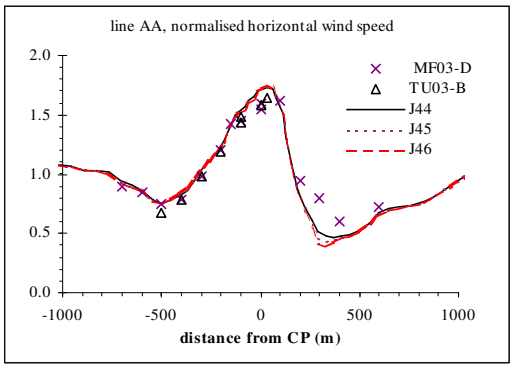

b)

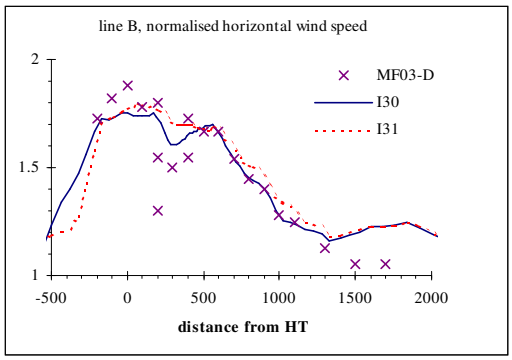

c)

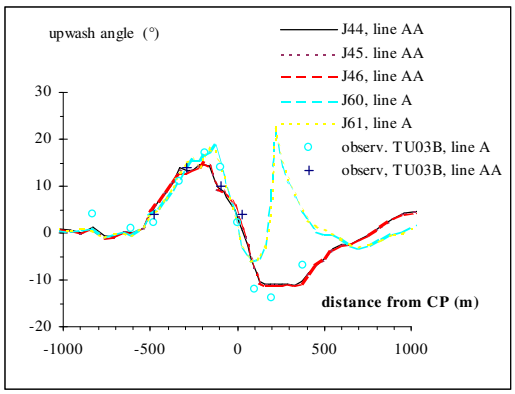

d)

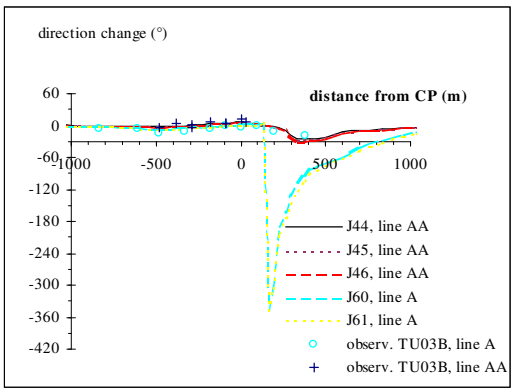

e)

Figure D.18. Same as Figure D.14 using the profiles presented in Figure D.16 as inlet boundary conditions, and with the turbulence model constants proposed by Duynkerke.

Using the turbulence constants proposed by Duynkerke, it appears that the quality of the simulation results could only be restored when simultaneously assuming that the roughness length above the hill was reduced. Such a simulation was performed, taking the profiles of Figure D.16 as inlet boundary conditions, and reducing the roughness length over the 3D simulation domain to 0.005m instead of the 0.03m used previously. The horizontal and vertical profiles for this simulation are shown in Figure D.19 and Figure D.20. With the roughness reduction over the Askervein Hill domain, the excessive wind speed reduction in the wake is no longer observed.

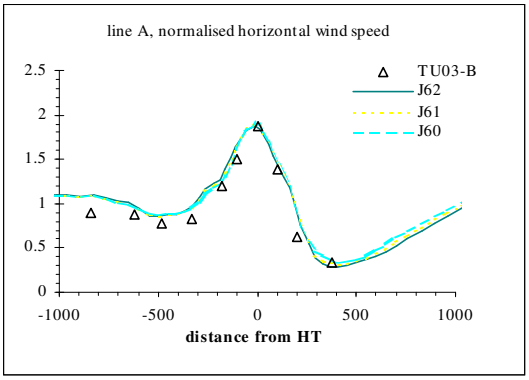

a)

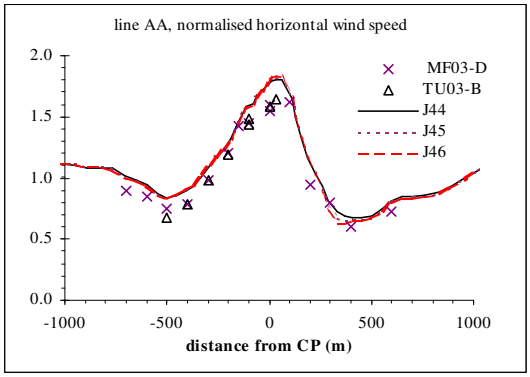

b)

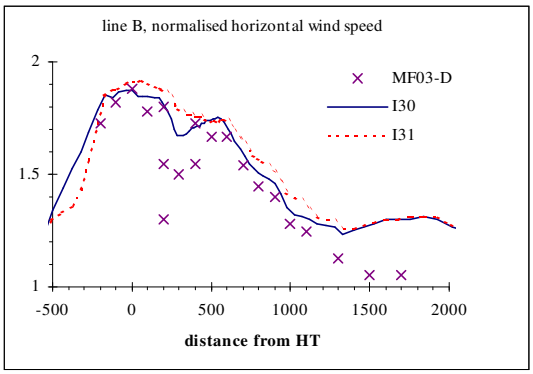

c)

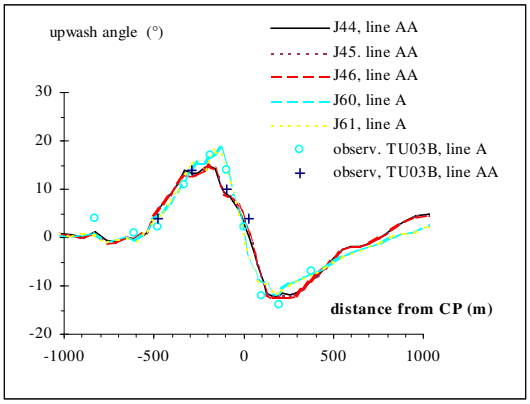

d)

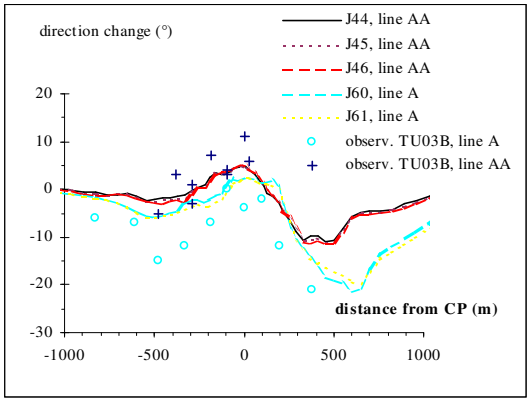

e)

Figure D.19. Same as Figure D.18 but using a roughness length of 0.005m over the 3D domain, instead of the 0.03m previously used.

The associated significant changes in the upwash angle and direction change also disappeared. The most spectacular improvement is observed for the vertical profile of the speedup ratio, which is now well reproduced also for the lowest levels (Figure D.20c). With the decrease in the ground roughness, the normalised kinetic energy profile over the hilltop has been reduced but still overestimates the measured values (Figure D.20b). From the roughness reduction we also obtain a slight overestimation of the normalised wind speed upwind of the hill along the A and AA line. This might

be an indication that the roughness reduction to be applied should not be applied to the entire simulation domain, but rather the hill itself as was already pointed out by Mickle et al (1988) or Zeman & Jensen (1987).

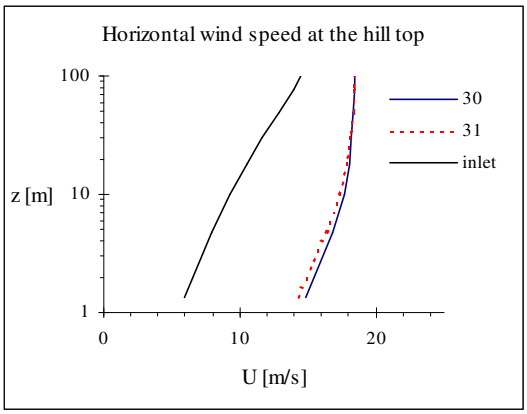

a)

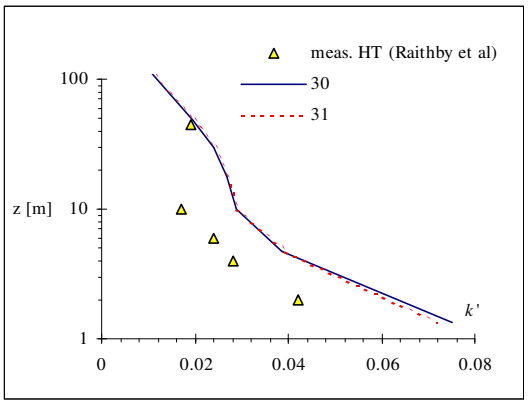

b)

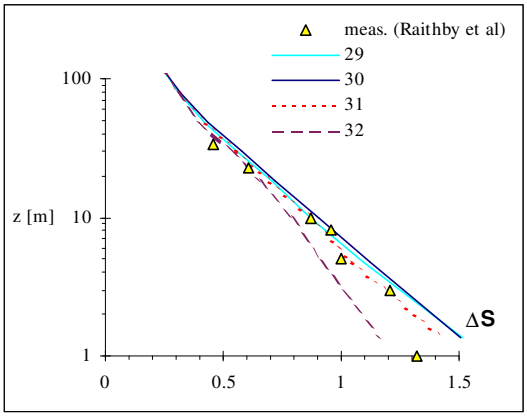

c)

Figure D.20. Same as Figure D.17 but using a roughness length of 0.005m over the 3D domain, instead of the 0.03m previously used.

To close this appendix about the validation of the model to simulate 3D wind fields over real topography, we can say that the model was able to satisfactorily reproduce the observed flow behaviour.

Using the standard values for the turbulence model constants, we obtained a very good agreement between the observations and model predictions for the horizontal profiles of average wind speed, upwash angle and vertical profile of normalised turbulent kinetic energy above the hill top. Good agreement was also achieved for the horizontal profiles of direction change. The vertical profile of the speed up ratio could only be well reproduced for levels higher than 5 m above ground over the hill top. The best simulation results with the standard turbulence model constants was obtained with entrance profiles calculated 4km downwind of a roughness change

representing the sea-land transition. The roughness length associated with the sea was set to 0.0001m while the one over land was 0.03m.

Changing the turbulence model constants to the values suggested by Duynkerke, which seems more appropriate for atmospheric flows (see, e.g., Duynkerke, 1988, Raithby et al, 1987), slightly changes the conclusions of this study. With the modified model constants we are also able to satisfactorily reproduce the observed flow field over Askervein Hill, but with the requirement that the roughness length over the hill itself is reduced, confirming similar conclusions which were drawn by Mickle et al (1988) or Zeman & Jensen (1987). Instead of the 0.03m suggested by Taylor & Teunissen (1987) as an homogeneous value for the roughness length to be used over the site, we found that a value of 0.03 m is certainly representative of the area close to the reference mast, while a value of 0.005m would be more appropriate for the hill itself. The prediction of the speed up ratio was considerably improved for the lowest levels (< 5m) when using the modified turbulence model constants, but at the same time with this modification the model tends to systematically overpredict the turbulence intensity over the hill.

From the results presented above, we can not give a definitive conclusion regarding the choice of constants to be used in the *k-ε* model to simulate atmospheric flows. From observations recorded during the 1983 Askervein Hill experiment, Raithby et al (1987) report values of k/u_*^2 between 4.2 and 5.4. Using the relationship $k/u_*^2 = 1/\sqrt{C_\mu}$, which is valid close to the ground, we get a range of variation of C_μ between 0.034 and 0.057. With CFX4, we could get very good results with both standard and Duynkerke's value for C_μ by changing other parameters for which some uncertainty remains. These model constants could certainly be tuned to even refine the results obtained so far. However, considering the sensitivity of the model results to the inlet and ground boundary conditions, we would need to reduce the uncertainty in these parameters before attempting such a tuning. It would definitely be interesting to increase the confidence level in the constants to be used in the turbulence model. However, at this stage, we feel that, from the point of view of a numerical simulation of a flow field over more complex topographies (succession of various hills), the limiting factor will be more related to the relatively poor knowledge of the profiles to be specified for the turbulence variables at the model inlet.

Appendix E

E Formulation of the energy conservation equation in terms of the potential temperature θ.

First law of thermodynamics:

eq. E-1 $$du = c_v dT = dh - pd\alpha$$

(Note: u stands for the internal energy of the fluid and α for the specific volume[1])

Ideal gas law:

eq. E-2 $$p\alpha = RT$$

eq. E-3 $$R = \frac{R^*}{m},$$

R^* being the universal constant for gases and m the mole mass for the corresponding gas

From eq. E-2 one derives:

eq. E-4 $$pd\alpha + \alpha dp = RdT$$

and therefore:

eq. E-5 $$\frac{dp}{p} = \frac{R}{p\alpha}dT - \frac{d\alpha}{\alpha}$$

With the definition of potential temperature θ,

eq. E-6 $$\theta = T(\frac{p_0}{p})^{R/c_p}$$

one shows that:

eq. E-7
$$\begin{aligned}\frac{d\theta}{\theta} &= \frac{dT}{T} - \frac{R}{c_p}\frac{dp}{p} \\ &= \frac{dT}{T} - \frac{R}{c_p}(\frac{R}{p\alpha}dT - \frac{d\alpha}{\alpha})\end{aligned}$$

Applying the first law of thermodynamics, we obtain:

eq. E-8 $$\frac{d\theta}{\theta} = \frac{dT}{T} - \frac{R}{c_p}(\frac{R}{p\alpha}dT - \frac{dh - c_v dT}{p\alpha})$$

Using the relationships:

---

[1] The specific volume is defined as $\alpha = V/m$, V being the volume and m the mole mass.

eq. E-9 $$c_p = c_v + R$$

and eq. E-2, eq. E-8 becomes:

eq. E-10
$$\frac{d\theta}{\theta} = \frac{dT}{T}(1 - \frac{R}{c_p}) - \frac{R}{c_p}(\frac{c_v dT}{RT} + \frac{dh}{p\alpha})$$
$$= \frac{R}{c_p}\frac{dh}{p\alpha}$$

The energy conservation equation formulated in terms of the potential temperature is therefore:

eq. E-11
$$\frac{d\theta}{dt} = \frac{R}{c_p}\frac{\theta}{p\alpha}\frac{dh}{dt}$$
$$= \frac{1}{c_p}\frac{\theta}{T}\frac{dh}{dt}$$

where the right-hand side of the equation represents the non-adiabatic heat exchanges.

From the identity

eq. E-12
$$\frac{\partial}{\partial t}(\rho\theta) + \vec{\nabla}(\vec{v}\rho\theta) = \rho\underbrace{\left[\frac{\partial}{\partial t}\theta + \vec{v}\vec{\nabla}(\theta)\right]}_{\frac{d\theta}{dt}} + \theta\underbrace{\left[\frac{\partial}{\partial t}\rho + \vec{\nabla}(\vec{v}\rho)\right]}_{=0,\text{continuity}}$$

the energy conservation equation for the potential temperature can be written in flux form as:

eq. E-13
$$\frac{\partial}{\partial t}(\rho\theta) + \vec{\nabla}(\vec{v}\rho\theta) = \rho\frac{d\theta}{dt} = \rho\frac{1}{c_p}\frac{\theta}{T}\frac{dh}{dt}$$

For purely adiabatic processes, the energy conservation equation is therefore a simple advection-diffusion equation for the potential temperature, with a vanishing diffusion term. Hence for processes without radiative heat flux or latent heat release ($dh/dt = 0$), the potential temperature is conserved along the flow trajectories, which makes it a very convenient variable to simulate atmospheric processes.

Note: In general, a diffusion term is reintroduced in eq. E-13 to account for turbulent mixing.

Appendix F

F Hydrostatic equilibrium and derivation of the buoyancy term.

For an atmosphere in hydrostatic equilibrium, with a vertical real temperature profile given by $T_h(z)$, the vertical profile of hydrostatic pressure $p_h(z)$ is obtained by integration of the relationship:

eq. F-1
$$\begin{aligned} dp_h &= -\rho_h \cdot g \cdot dz \\ &= -\frac{p_h}{RT_h(z)} g \cdot dz \end{aligned}$$

For an isothermal atmosphere, integration yields:

eq. F-2
$$p_h(z) = p_h(0)\exp(-\frac{g}{RT_h} z)$$

For a more realistic situation, where the real temperature varies with the altitude, integration is done in a discrete way, assuming that for each level z_i the real temperature is constant, having the value $T(z_i)$.

The hydrostatic density profile is then calculated from the ideal gas law:

eq. F-3
$$\rho_h(z) = \frac{p_h(z)}{R \cdot T_h(z)}$$

Similarly, the hydrostatic potential temperature profile is inferred from:

eq. F-4
$$\theta_h(z) = T_h(z)\left(\frac{p\ (0)}{p_h(z)}\right)^{\frac{R}{c_p}}$$

For the derivation of the buoyancy term appearing in the vertical velocity equation as a function of the potential temperature, we first assume that the departure of the atmospheric conditions from the hydrostatic equilibrium is small. For this assumption, we can write:

$$\rho = \rho_h + \rho' \qquad \theta = \theta_h + \theta'$$

eq. F-5
$$p = p_h + p' \qquad T = T_h + T'$$

with $\rho' << \rho_h$, $\theta' << \theta_h$, $T' << T_h$, and $p' << p_h$

From the perfect gas law and the definition of the potential temperature we obtain:

eq. F-6
$$\frac{dp}{p} = \frac{d\rho}{\rho} + \frac{dT}{T}$$

eq. F-7
$$\frac{d\theta}{\theta} = \frac{dT}{T} - \frac{R}{c_p}\frac{dp}{p}$$

which leads to:

eq. F-8 $$\frac{d\rho}{\rho} = -\frac{d\theta}{\theta} + \left(1 - \frac{R}{c_p}\right) \cdot \frac{dp}{p}$$

If the Mach number of the flow is much smaller than unity, the second term in eq. F-8 can be neglected, and we end up with the approximation:

eq. F-9 $$\frac{d\rho}{\rho} = -\frac{d\theta}{\theta}$$

or equivalently:

eq. 10 $$(\rho_h - \rho) = \frac{\rho_h}{\theta_h}(\theta - \theta_h)$$

which is the expression that will be used to couple the energy conservation equation with the momentum conservation equation for the vertical velocity component.

Appendix G

G Weibull distributions

G.1 Properties

The Weibull distribution is defined as

eq. G.1 $$f(v) = \frac{k}{A}\left(\frac{v}{A}\right)^{k-1} \exp\left[-(\frac{v}{A})^k\right]$$

The mean wind speed for a wind speed distribution following eq. G.1 is

eq. G.2 $$\overline{v} = \int_0^\infty f(v)\cdot v \cdot dv = \int_0^\infty k\left(\frac{v}{A}\right)^k \exp\left[-(\frac{v}{A})^k\right]\cdot dv$$

With the substitution $y = (\frac{v}{A})^k$ and $dv = \frac{A}{k}\, y^{(1/k-1)} dy$ this simplifies to

eq. G.3 $$\overline{v} = \int_0^\infty k \cdot y \cdot \exp[-y]\cdot \frac{A}{k}\, y^{(1/k-1)} dy$$

eq. G.4 $$\overline{v} = A\int_0^\infty y^{1/k} \cdot \exp[-y]\cdot dy = A\cdot\Gamma(1+\frac{1}{k})$$

In a similar way we obtain for the higher order momentum of the variable v

eq. G.5 $$\overline{v^m} = A^m \cdot \Gamma(1+\frac{m}{k})$$

G.2 Cumulative distribution

The cumulative Weibull distribution is given by $F(v) = \int_0^v f(v')\cdot dv' = 1-\exp(-(\frac{u}{A})^k)$ and it obeys the equation $\ln(-\ln(1-F(v))) = k\cdot\ln(v) - k\cdot\ln(A)$. Plotting $\ln(-\ln(1-F(v)))$ versus $\ln(v)$ allows one to easily determine the *A* and *k* parameters of the distribution.

G.3 Behaviour of the Weibull distribution under a variable transformation

The probability of having a wind speed between v_1 and $v_1 + dv_1$ is

eq. G.6 $$f_1(v_1)\cdot dv_1 = \frac{k}{A}\left(\frac{v_1}{A}\right)^{k-1} \exp\left[-(\frac{v_1}{A})^k\right]\cdot dv_1$$

Under a linear variable transformation such as

eq. G.7 $$v_2 = m \cdot v_1 + c$$

eq. G.6 becomes

eq. G.8 $$f_1(v_1) \cdot dv_1 = \frac{k}{A}\left(\frac{v_2 - c}{mA}\right)^{k-1} \exp\left[-\left(\frac{v_2 - c}{mA}\right)^{k}\right] \cdot \frac{dv_2}{m} = f_2(v_2) \cdot dv_2$$

The distribution in terms of the variable v_2 is therefore

eq. G.9 $$f_2(v_2) = \frac{k}{B}\left(\frac{v_2 - c}{B}\right)^{k-1} \exp\left[-(\frac{v_2 - c}{B})^{k}\right]$$

which is a shifted Weibull distribution with the same shape parameter k and a modified wind speed parameter $B = mA$.

Under a transformation of the type

eq. G.10 $$v_2 = a \cdot v_1^{\,b}$$

the Weibull distribution is transformed into

eq. G.11 $$f_2(v_2) = \frac{k}{A}\left(\left[\frac{v_2}{a}\right]^{1/b}\frac{1}{A}\right)^{k-1}\left[\frac{v_2}{a}\right]^{1/b}\frac{1}{bv_2}\exp\left[-\left(\left[\frac{v_2}{a}\right]^{1/b}\frac{1}{A}\right)^{k}\right]$$

which after some manipulation simplifies to

eq. G.12 $$f_2(v_2) = \frac{k'}{A'}\left(\frac{v_2}{A'}\right)^{k'-1} \exp\left[-(\frac{v_2}{A'})^{k'}\right]$$

with $k' = k/b$ and $A' = a \cdot A^b$. In other words the wind speed transformation according to eq. G.10 transforms the Weibull distribution with parameters A and k into another Weibull distribution with the parameters $k' = k/b$ and $A' = a \cdot A^b$.

Appendix H

H Results from the application of the MCP methods

H.1 Chasseral Côte-Nord

H.1.1 Matrices

Population matrix $P = (p_{i,j})$ ***for the sites of Chasseral and Côte Nord***

Prediction site index J →

Sector	0	30	60	90	120	150	180	210	240	270	300	330	
0	21	67	52	18	8	1	2	2	1	8	3	7	**190**
30	16	39	229	60	5	1	0	0	1	0	3	2	**356**
60	7	8	83	182	46	0	3	3	0	1	1	1	**335**
90	4	2	32	215	206	3	4	5	1	0	1	0	**473**
120	1	8	12	41	127	18	6	3	1	2	1	1	**221**
150	4	6	5	15	54	28	52	32	3	2	2	1	**204**
180	1	3	6	12	31	16	85	212	34	18	6	2	**426**
210	2	1	10	8	15	10	70	573	333	49	10	2	**1083**
240	1	1	6	2	7	8	20	102	580	323	14	4	**1068**
270	7	3	2	2	4	0	9	57	147	661	84	10	**986**
300	13	7	1	3	4	0	1	12	26	205	249	95	**616**
330	139	71	3	3	5	2	0	3	7	15	71	178	**497**

	216	**216**	**441**	**561**	**512**	**87**	**252**	**1004**	**1134**	**1284**	**445**	**303**

Matrix Wij (*100) for the sites of Chasseral and Côte Nord

Prediction site index J →

Sector	0	30	60	90	120	150	180	210	240	270	300	330	
0	13.3	42.4	32.9	11.4	0.0	0.0	0.0	0.0	0.0	0.0	0.0	0.0	**100**
30	0.0	11.9	69.8	18.3	0.0	0.0	0.0	0.0	0.0	0.0	0.0	0.0	**100**
60	0.0	0.0	26.7	58.5	14.8	0.0	0.0	0.0	0.0	0.0	0.0	0.0	**100**
90	0.0	0.0	7.1	47.5	45.5	0.0	0.0	0.0	0.0	0.0	0.0	0.0	**100**
120	0.0	0.0	6.1	20.7	64.1	9.1	0.0	0.0	0.0	0.0	0.0	0.0	**100**
150	0.0	0.0	0.0	8.3	29.8	15.5	28.7	17.7	0.0	0.0	0.0	0.0	**100**
180	0.0	0.0	0.0	0.0	8.6	0.0	23.5	58.6	9.4	0.0	0.0	0.0	**100**
210	0.0	0.0	0.0	0.0	0.0	0.0	7.2	58.7	34.1	0.0	0.0	0.0	**100**
240	0.0	0.0	0.0	0.0	0.0	0.0	0.0	10.1	57.7	32.1	0.0	0.0	**100**
270	0.0	0.0	0.0	0.0	0.0	0.0	0.0	6.0	15.5	69.7	8.9	0.0	**100**
300	0.0	0.0	0.0	0.0	0.0	0.0	0.0	0.0	0.0	37.3	45.4	17.3	**100**
330	30.3	15.5	0.0	0.0	0.0	0.0	0.0	0.0	0.0	0.0	15.5	38.8	**100**

	43.6	**69.8**	**142.5**	**164.7**	**162.8**	**24.6**	**59.4**	**151.1**	**116.7**	**139.1**	**69.7**	**56.1**

Matrix Zij for the sites of Chasseral and Côte Nord

Prediction site index J →

Sector	0	30	60	90	120	150	180	210	240	270	300	330	
0	11.1	37.9	13.1	0.0	0.0	0.0	0.0	0.0	0.0	0.0	0.0	0.0	**62.1**
30	8.5	22.0	57.8	12.0	0.0	0.0	0.0	0.0	0.0	0.0	0.0	0.0	**100.4**
60	0.0	0.0	21.0	36.5	9.9	0.0	0.0	0.0	0.0	0.0	0.0	0.0	**67.4**
90	0.0	0.0	8.1	43.2	44.4	0.0	0.0	0.0	0.0	0.0	0.0	0.0	**95.7**
120	0.0	0.0	0.0	8.2	27.4	22.5	0.0	0.0	0.0	0.0	0.0	0.0	**58.1**
150	0.0	0.0	0.0	0.0	11.6	35.0	22.9	0.0	0.0	0.0	0.0	0.0	**69.5**
180	0.0	0.0	0.0	0.0	6.7	20.0	37.4	22.5	0.0	0.0	0.0	0.0	**86.6**
210	0.0	0.0	0.0	0.0	0.0	12.5	30.8	60.7	31.4	0.0	0.0	0.0	**135.5**
240	0.0	0.0	0.0	0.0	0.0	10.0	8.8	10.8	54.7	27.2	0.0	0.0	**111.5**
270	0.0	0.0	0.0	0.0	0.0	0.0	0.0	6.0	13.9	55.6	20.8	0.0	**96.3**
300	6.9	0.0	0.0	0.0	0.0	0.0	0.0	0.0	0.0	17.2	61.6	34.8	**120.6**
330	73.5	40.1	0.0	0.0	0.0	0.0	0.0	0.0	0.0	0.0	17.6	65.2	**196.4**
	100	**100**	**100**	**100**	**100**	**100**	**100**	**100**	**100**	**100**	**100**	**100**	

H.1.2 Transposition from proportionality relationships $v_{pred} = a \cdot v_{ref}$

Table H.1. Mean sector wind speed ratios for the Mt-Crosin sites obtained from data binned according to the Chasseral (m_{ref}) and Mt-Crosin (m_{pred}) site wind direction. Threshold wind speed at Chasseral: 5m/s, at Mt-Crosin: 0.5 m/s.

	Côte Nord		Côte Sud		Côte Est	
Sector	m_{ref}	m_{pred}	m_{ref}	m_{pred}	m_{ref}	m_{pred}
0	0.79	0.53	0.86	0.66	0.71	0.35
30	0.52	0.68	0.61	0.63	0.55	0.43
60	0.45	0.55	0.60	0.72	0.55	0.54
90	0.63	0.46	0.79	0.77	0.72	0.63
120	0.73	0.71	0.85	0.62	0.98	0.31
150	0.77	0.53	0.75	0.51	0.92	0.35
180	0.80	0.72	0.77	0.66	0.63	0.69
210	0.64	0.68	0.68	0.65	0.62	0.70
240	0.58	0.58	0.69	0.68	0.62	0.66
270	0.52	0.54	0.62	0.64	0.57	0.55
300	0.42	0.42	0.50	0.50	0.48	0.48
330	0.48	0.44	0.58	0.59	0.46	0.33

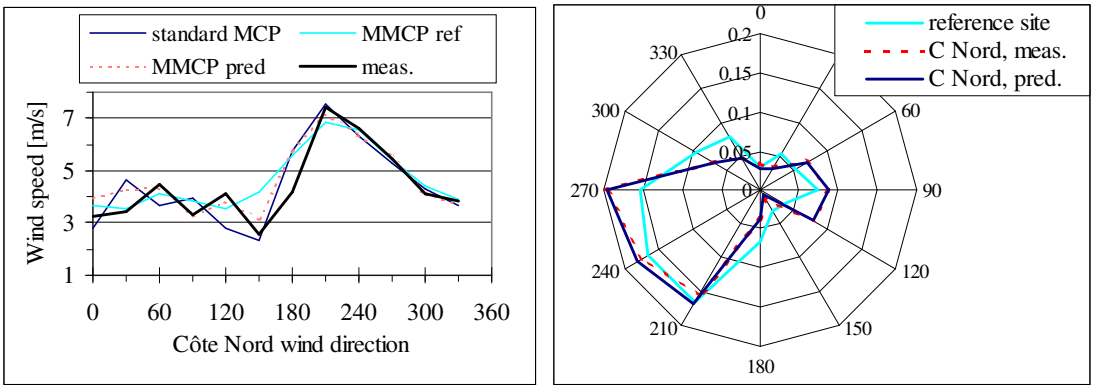

Figure H.1. Comparison of the measurements and MCP prediction using proportionality relationships for a) the sector mean wind speed and b) the wind rose.

Table H.2. Comparison of the measured and predicted sector mean wind speed at the site of Côte Nord, using simple proportionality relationships.

Sector	Wind speed (m/s)				Relative error (%)		
	MCP-std.	MMCP-ref	MMCP-pred	Meas.	MCP-std	MMCP-ref	MMCP-pred
0	2.8	3.7	4.0	3.3	-15	12	21
30	4.7	3.5	4.3	3.5	35	3	25
60	3.7	4.2	4.3	4.5	-18	-7	-3
90	3.9	3.8	3.3	3.3	18	15	-2
120	2.8	3.5	3.9	4.1	-32	-14	-6
150	2.4	4.2	3.1	2.6	-8	64	23
180	5.7	5.6	5.8	4.2	36	32	37
210	7.5	6.9	7.2	7.4	1	-8	-3
240	6.4	6.6	6.4	6.6	-4	0	-3
270	5.3	5.4	5.6	5.5	-3	-1	2
300	4.3	4.4	4.1	4.2	4	6	-1
330	3.7	3.9	3.7	3.8	-4	2	-2

H.1.3 Transposition from relationships of the type $v_{pred} = m \cdot v_{ref} + c$

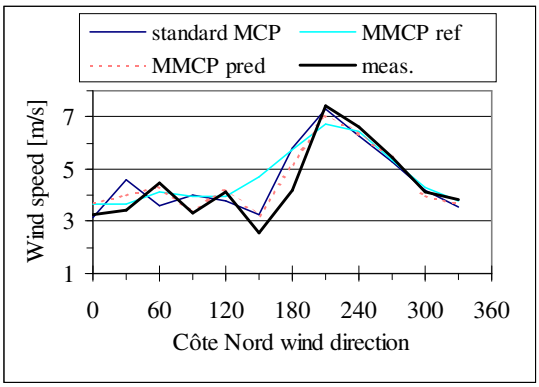

Figure H.2. Comparison of the measurements and MCP prediction using linear relationships for the sector mean wind speed.

Table H.3. Parameters from the linear regression relating the sites of Côte Nord and Chasseral.

Sector	c_{ref}	m_{ref}	r_{ref}	c_{pred}	m_{pred}	r_{pred}
0	1.49	0.47	0.17	2.26	0.20	0.30
30	1.67	0.32	0.60	3.35	0.11	0.12
60	1.11	0.31	0.64	1.79	0.33	0.66
90	2.07	0.31	0.46	1.91	0.20	0.48
120	3.41	0.10	0.10	2.46	0.33	0.53
150	2.33	0.31	0.23	2.65	0.09	0.23
180	1.94	0.54	0.75	2.76	0.30	0.38
210	2.37	0.42	0.67	1.63	0.52	0.75
240	0.83	0.50	0.69	1.01	0.48	0.69
270	-0.14	0.53	0.79	1.33	0.40	0.71
300	0.21	0.39	0.82	0.55	0.35	0.80
330	0.96	0.35	0.63	0.55	0.37	0.80

Table H.4. Comparison of the measured and predicted sector mean wind speed at the site of Côte Nord, using linear relationships**.**

Sector	Wind speed (m/s)				Relative error (%)		
	MCP-std.	MMCP-ref	MMCP-pred	Meas.	MCP-std	MMCP-ref	MMCP-pred
0	3.2	3.7	3.7	3.3	-3.7	11.4	14.2
30	4.6	3.6	4.0	3.5	32.8	5.4	16.5
60	3.6	4.1	4.4	4.5	-19.0	-6.8	-1.7
90	4.0	3.9	3.4	3.3	21.0	17.8	0.6
120	3.8	4.0	4.2	4.1	-7.7	-3.8	3.0
150	3.3	4.7	3.2	2.6	28.2	84.4	24.6
180	5.8	5.7	5.2	4.2	38.2	36.2	23.1
210	7.3	6.7	7.1	7.4	-1.6	-9.2	-4.4
240	6.3	6.5	6.4	6.6	-4.8	-2.1	-3.4
270	5.3	5.4	5.4	5.5	-3.5	-1.7	-0.1
300	4.2	4.3	4.0	4.2	1.4	4.0	-4.0
330	3.6	3.8	3.7	3.8	-6.3	-0.5	-3.6

H.2 Chasseral Côte-Sud

H.2.1 Matrices

Population matrix $P = (p_{i,j})$ ***for the sites of Chasseral and Côte Sud***

Prediction site index J →

Sector	0	30	60	90	120	150	180	210	240	270	300	330	
0	42	25	30	7	5	3	6	3	1	1	3	14	**140**
30	18	105	100	38	8	4	13	2	0	0	1	3	**292**
60	8	22	129	143	16	2	8	8	0	0	0	3	**339**
90	4	12	98	303	25	9	12	6	0	0	2	4	**475**
120	6	10	28	137	57	21	7	2	2	0	9	4	**283**
150	8	3	20	58	36	55	64	27	9	6	3	3	**292**
180	1	5	12	38	16	39	138	145	33	29	4	3	**463**
210	3	3	20	37	11	18	124	423	278	56	8	4	**985**
240	2	7	3	17	6	19	38	157	546	234	16	7	**1052**
270	2	3	2	8	5	8	23	49	222	525	70	15	**932**
300	15	6	4	7	3	10	15	14	25	246	297	49	**691**
330	102	15	28	12	3	8	11	3	5	16	145	175	**523**

	211	**216**	**474**	**805**	**191**	**196**	**459**	**839**	**1121**	**1113**	**558**	**284**	**6467**

Matrix Wij (*100) for the sites of Chasseral and Côte Sud

Prediction site index J →

Sector	0	30	60	90	120	150	180	210	240	270	300	330	
0	35.6	21.2	25.4	5.9	0.0	0.0	0.0	0.0	0.0	0.0	0.0	11.9	**100**
30	6.9	40.2	38.3	14.6	0.0	0.0	0.0	0.0	0.0	0.0	0.0	0.0	**100**
60	0.0	7.5	43.9	48.6	0.0	0.0	0.0	0.0	0.0	0.0	0.0	0.0	**100**
90	0.0	0.0	23.0	71.1	5.9	0.0	0.0	0.0	0.0	0.0	0.0	0.0	**100**
120	0.0	0.0	11.5	56.4	23.5	8.6	0.0	0.0	0.0	0.0	0.0	0.0	**100**
150	0.0	0.0	7.7	22.3	13.8	21.2	24.6	10.4	0.0	0.0	0.0	0.0	**100**
180	0.0	0.0	0.0	9.0	0.0	9.2	32.7	34.4	7.8	6.9	0.0	0.0	**100**
210	0.0	0.0	0.0	0.0	0.0	0.0	14.1	48.0	31.6	6.4	0.0	0.0	**100**
240	0.0	0.0	0.0	0.0	0.0	0.0	0.0	16.8	58.3	25.0	0.0	0.0	**100**
270	0.0	0.0	0.0	0.0	0.0	0.0	0.0	5.7	25.6	60.6	8.1	0.0	**100**
300	0.0	0.0	0.0	0.0	0.0	0.0	0.0	0.0	0.0	41.6	50.2	8.3	**100**
330	22.7	0.0	6.2	0.0	0.0	0.0	0.0	0.0	0.0	0.0	32.2	38.9	**100**

	65.2	**68.9**	**156.1**	**227.9**	**43.2**	**39.0**	**71.4**	**115.2**	**123.3**	**140.4**	**90.5**	**59.0**

Matrix Zij for the sites of Chasseral and Côte Sud

Prediction site index J →

Sector	0	30	60	90	120	150	180	210	240	270	300	330	
0	23.7	14.0	7.3	0.0	0.0	0.0	0.0	0.0	0.0	0.0	0.0	0.0	**45.0**
30	10.2	58.7	24.2	0.0	0.0	0.0	0.0	0.0	0.0	0.0	0.0	0.0	**93.0**
60	0.0	12.3	31.2	22.3	9.9	0.0	0.0	0.0	0.0	0.0	0.0	0.0	**75.8**
90	0.0	6.7	23.7	47.3	15.5	0.0	0.0	0.0	0.0	0.0	0.0	0.0	**93.2**
120	0.0	0.0	6.8	21.4	35.4	13.0	0.0	0.0	0.0	0.0	0.0	0.0	**76.5**
150	0.0	0.0	0.0	9.0	22.4	34.0	16.5	0.0	0.0	0.0	0.0	0.0	**81.9**
180	0.0	0.0	0.0	0.0	9.9	24.1	35.7	18.7	0.0	0.0	0.0	0.0	**88.4**
210	0.0	0.0	0.0	0.0	6.8	11.1	32.0	54.7	26.6	5.3	0.0	0.0	**136.5**
240	0.0	0.0	0.0	0.0	0.0	11.7	9.8	20.3	52.2	22.1	0.0	0.0	**116.1**
270	0.0	0.0	0.0	0.0	0.0	0.0	5.9	6.3	21.2	49.5	13.7	6.3	**102.9**
300	8.5	0.0	0.0	0.0	0.0	6.2	0.0	0.0	0.0	23.2	58.0	20.5	**116.3**
330	57.6	8.4	6.8	0.0	0.0	0.0	0.0	0.0	0.0	0.0	28.3	73.2	**174.3**

	100	**100**	**100**	**100**	**100**	**100**	**100**	**100**	**100**	**100**	**100**	**100**

H.2.2 Transposition from proportionality relationships $v_{pred} = a \cdot v_{ref}$

The sector wind speed ratios used for the transposition from Chasseral to Côte Sud can be found in Table H.1.

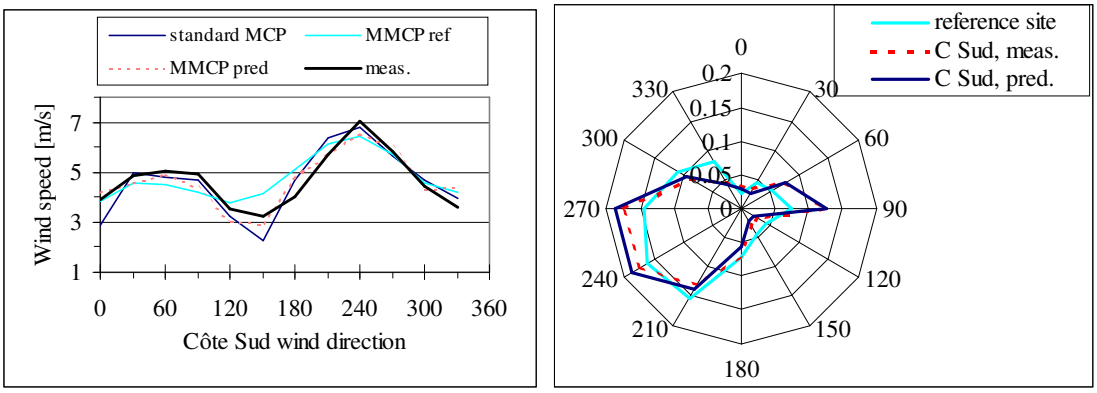

a) b)

Figure H.3. Comparison of the measurements and MCP prediction using proportionality relationships for a) the sector mean wind speed and b) the wind rose.

Table H.5. Comparison of the measured and predicted sector mean wind speed at the site of Côte Sud, using simple proportionality relationships.

Sector	Wind speed (m/s)				Relative error (%)		
	MCP-std.	MMCP-ref	MMCP-pred	Meas.	MCP-std	MMCP-ref	MMCP-pred
0	2.8	3.8	4.2	3.9	-26	-1	8
30	5.0	4.6	4.5	4.9	2	-7	-7
60	4.8	4.5	4.9	5.0	-5	-10	-3
90	4.7	4.2	4.4	4.9	-5	-15	-11
120	3.2	3.8	3.1	3.6	-9	6	-13
150	2.3	4.1	2.9	3.2	-29	28	-8
180	4.7	5.1	4.8	4.0	17	27	19
210	6.4	6.1	5.7	5.7	12	7	0
240	6.8	6.4	6.5	7.0	-3	-8	-7
270	5.6	5.7	6.0	5.8	-3	-2	3
300	4.7	4.6	4.3	4.5	4	3	-3
330	3.9	4.2	4.4	3.6	10	17	23

H.2.3 Transposition from relationships of the type $v_{pred} = m \cdot v_{ref} + c$

Table H.6. Parameters from the linear regression relating the sites of Côte Sud and Chasseral.

Sector	c_{ref}	m_{ref}	r_{ref}	c_{pred}	m_{pred}	r_{pred}
0	1.47	0.57	0.21	3.05	0.20	0.64
30	1.09	0.47	0.71	2.02	0.39	0.71
60	1.19	0.45	0.72	2.47	0.38	0.58
90	2.84	0.36	0.51	1.28	0.59	0.61
120	2.88	0.33	0.35	1.71	0.36	0.52
150	1.19	0.53	0.44	2.14	0.21	0.31
180	0.87	0.64	0.78	2.70	0.26	0.36
210	1.68	0.50	0.66	1.04	0.52	0.77
240	0.97	0.59	0.68	1.20	0.56	0.70
270	1.36	0.46	0.69	1.94	0.42	0.63
300	1.77	0.29	0.69	1.52	0.32	0.73
330	2.16	0.27	0.59	2.27	0.25	0.61

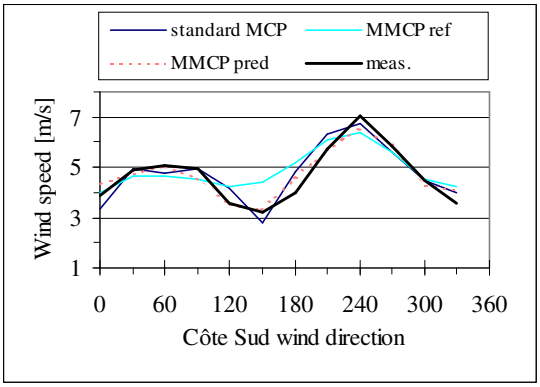

Figure H.4. Comparison of the measurements and MCP prediction using linear relationships for the sector mean wind speed.

Table H.7. Comparison of the measured and predicted sector mean wind speed at the site of Côte Sud, using linear relationships.

Sector	Wind speed (m/s)				Relative error (%)		
	MCP-std.	MMCP-ref	MMCP-pred	Meas.	MCP-std	MMCP-ref	MMCP-pred
0	3.3	4.0	4.3	3.9	-14	3	12
30	5.0	4.6	4.8	4.9	2	-5	-2
60	4.8	4.7	5.1	5.0	-6	-7	1
90	5.0	4.6	4.6	4.9	1	-8	-6
120	4.1	4.2	3.5	3.6	17	20	-2
150	2.8	4.4	3.4	3.2	-13	38	5
180	4.8	5.2	4.6	4.0	20	30	14
210	6.3	6.1	5.7	5.7	11	6	-1
240	6.8	6.4	6.6	7.0	-4	-9	-7
270	5.6	5.6	5.9	5.8	-4	-3	1
300	4.5	4.5	4.3	4.5	1	1	-4
330	4.0	4.2	4.1	3.6	12	18	15

H.3 Chasseral Côte-Est

H.3.1 Matrices

Population matrix $P = (p_{i,j})$ ***for the sites of Chasseral and Côte Est***

Prediction site index J →

Sector	0	30	60	90	120	150	180	210	240	270	300	330	
0	35	40	28	7	3	2	15	12	28	36	37	28	**271**
30	28	77	64	8	1	1	11	16	46	51	23	26	**352**
60	17	49	132	22	2	1	13	10	40	42	12	7	**347**
90	7	12	77	81	7	4	15	33	32	15	22	10	**315**
120	8	5	21	31	9	3	4	7	10	6	11	7	**122**
150	3	4	4	16	12	5	12	20	5	14	7	3	**105**
180	4	4	12	16	7	10	72	45	21	20	16	4	**231**
210	9	18	37	24	6	4	111	453	74	28	13	6	**783**
240	10	14	25	37	9	2	41	176	249	39	28	8	**638**
270	7	10	31	30	2	4	20	50	249	142	22	7	**574**
300	19	28	27	27	2	0	23	25	88	181	47	17	**484**
330	38	20	23	22	3	2	13	17	56	97	112	44	**447**

	185	**281**	**481**	**321**	**63**	**38**	**350**	**864**	**898**	**671**	**350**	**167**	**4669**

Matrix Wij (*100) for the sites of Chasseral and Côte Est

Prediction site index J →

Sector	0	30	60	90	120	150	180	210	240	270	300	330	
0	14.2	16.2	11.3	0.0	0.0	0.0	6.1	0.0	11.3	14.6	15.0	11.3	**100**
30	8.9	24.4	20.3	0.0	0.0	0.0	0.0	0.0	14.6	16.2	7.3	8.3	**100**
60	0.0	17.2	46.3	7.7	0.0	0.0	0.0	0.0	14.0	14.7	0.0	0.0	**100**
90	0.0	0.0	31.4	33.1	0.0	0.0	0.0	13.5	13.1	0.0	9.0	0.0	**100**
120	7.7	0.0	20.2	29.8	8.7	0.0	0.0	6.7	9.6	0.0	10.6	6.7	**100**
150	0.0	0.0	0.0	19.8	14.8	0.0	14.8	24.7	0.0	17.3	8.6	0.0	**100**
180	0.0	0.0	5.9	7.9	0.0	0.0	35.6	22.3	10.4	9.9	7.9	0.0	**100**
210	0.0	0.0	0.0	0.0	0.0	0.0	17.4	71.0	11.6	0.0	0.0	0.0	**100**
240	0.0	0.0	0.0	6.8	0.0	0.0	7.6	32.5	45.9	7.2	0.0	0.0	**100**
270	0.0	0.0	6.2	6.0	0.0	0.0	0.0	10.0	49.6	28.3	0.0	0.0	**100**
300	0.0	6.6	6.4	6.4	0.0	0.0	0.0	5.9	20.8	42.8	11.1	0.0	**100**
330	10.3	0.0	6.2	0.0	0.0	0.0	0.0	0.0	15.1	26.2	30.3	11.9	**100**

	41.0	**64.5**	**154.3**	**117.4**	**23.5**	**0.0**	**81.5**	**186.5**	**216.1**	**177.2**	**99.8**	**38.2**

Matrix Zij for the sites of Chasseral and Côte Est

Prediction site index J →

Sector	0	30	60	90	120	150	180	210	240	270	300	330	
0	23.8	17.2	6.7	0.0	0.0	5.6	0.0	0.0	0.0	6.1	12.7	22.4	**94.5**
30	19.0	33.2	15.2	0.0	0.0	0.0	0.0	0.0	6.0	8.7	7.9	20.8	**110.9**
60	11.6	21.1	31.4	8.0	0.0	0.0	0.0	0.0	0.0	7.1	0.0	0.0	**79.2**
90	0.0	0.0	18.3	29.6	14.0	11.1	0.0	0.0	0.0	0.0	7.6	8.0	**88.5**
120	0.0	0.0	0.0	11.3	18.0	8.3	0.0	0.0	0.0	0.0	0.0	0.0	**37.6**
150	0.0	0.0	0.0	0.0	24.0	13.9	0.0	0.0	0.0	0.0	0.0	0.0	**37.9**
180	0.0	0.0	0.0	0.0	14.0	27.8	27.0	6.2	0.0	0.0	0.0	0.0	**75.0**
210	0.0	7.8	8.8	8.8	12.0	11.1	41.6	62.6	9.7	0.0	0.0	0.0	**162.3**
240	6.8	0.0	5.9	13.5	18.0	5.6	15.4	24.3	32.7	6.6	9.6	0.0	**138.4**
270	0.0	0.0	7.4	10.9	0.0	11.1	7.5	6.9	32.7	24.1	7.6	0.0	**108.2**
300	12.9	12.1	6.4	9.9	0.0	0.0	8.6	0.0	11.5	30.8	16.2	13.6	**122.0**
330	25.9	8.6	0.0	8.0	0.0	5.6	0.0	0.0	7.3	16.5	38.5	35.2	**145.6**

	100	**100**	**100**	**100**	**100**	**100**	**100**	**100**	**100**	**100**	**100**	**100**

H.3.2 Transposition from proportionality relationships $v_{pred} = a \cdot v_{ref}$

The sector wind speed ratios used for the transposition from Chasseral to Côte Est can be found in Table H.1.

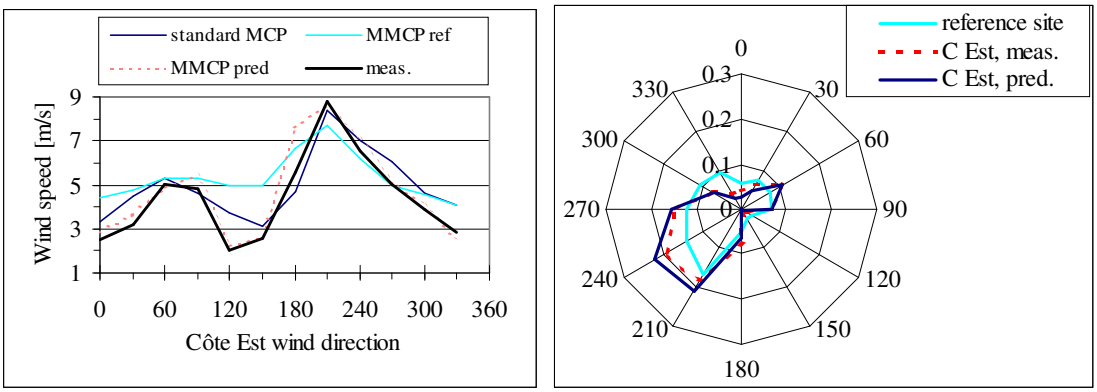

a) b)

Figure H.5. Comparison of the measurements and MCP prediction using proportionality relationships for a) the sector mean wind speed and b) the wind rose.

Table H.8. Comparison of the measured and predicted sector mean wind speed at the site of Côte Est, using simple proportionality relationships.

Sector	Wind speed (m/s)				Relative error (%)		
	MCP-std.	MMCP-ref	MMCP-pred	Meas.	MCP-std	MMCP-ref	MMCP-pred
0	3.3	4.4	2.8	2.5	34	76	13
30	4.5	4.8	3.7	3.2	41	49	15
60	5.3	5.3	4.9	5.0	6	6	-2
90	4.6	5.3	5.4	4.8	-4	11	13
120	3.7	5.0	2.2	2.0	84	147	10
150	3.1	5.0	2.7	2.6	21	92	3
180	4.7	6.7	7.6	5.6	-16	20	38
210	8.4	7.7	8.7	8.8	-4	-13	-1
240	7.0	6.2	7.1	6.5	7	-5	8
270	6.0	5.0	5.2	5.1	19	-1	2
300	4.6	4.6	4.1	3.9	20	18	6
330	4.1	4.1	2.6	2.9	41	43	-11

H.3.3 Transposition from relationships of the type $v_{pred} = m \cdot v_{ref} + c$

Table H.9. Parameters from the linear regression relating the sites of Côte Est and Chasseral.

Sector	c_{ref}	m_{ref}	r_{ref}	c_{pred}	m_{pred}	r_{pred}
0	2.80	0.20	0.21	1.92	0.08	0.31
30	3.36	0.12	0.21	2.18	0.13	0.41
60	1.13	0.41	0.62	3.02	0.20	0.44
90	3.38	0.23	0.20	4.18	0.10	0.18
120	2.67	0.49	0.18	2.22	-0.03	-0.12
150	4.37	0.01	0.00	2.02	0.04	0.15
180	1.75	0.42	0.66	2.59	0.36	0.54
210	1.52	0.49	0.61	1.52	0.56	0.71
240	0.68	0.54	0.59	1.75	0.46	0.57
270	2.13	0.34	0.52	2.01	0.30	0.59
300	1.93	0.24	0.52	2.65	0.14	0.29
330	2.59	0.14	0.30	1.65	0.13	0.35

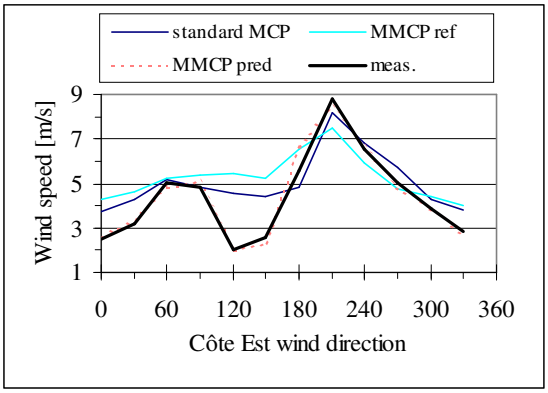

Figure H.6. Comparison of the measurements and MCP prediction using linear relationships for the sector mean wind speed.

Table H.10. Comparison of the measured and predicted sector mean wind speed at the site of Côte Est, using linear relationships**.**

Sector	Wind speed (m/s)				Relative error (%)		
	MCP-std.	MMCP-ref	MMCP-pred	Meas.	MCP-std	MMCP-ref	MMCP-pred
0	3.7	4.3	2.6	2.5	49	73	3
30	4.3	4.6	3.3	3.2	36	46	5
60	5.1	5.2	4.8	5.0	2	4	-4
90	4.8	5.3	5.1	4.8	0	11	6
120	4.5	5.4	2.0	2.0	125	169	-1
150	4.4	5.2	2.3	2.6	70	101	-11
180	4.9	6.6	6.6	5.6	-12	18	18
210	8.2	7.5	8.4	8.8	-7	-15	-4
240	6.8	5.9	6.7	6.5	4	-9	2
270	5.7	4.7	4.8	5.1	13	-6	-5
300	4.3	4.4	3.8	3.9	11	14	-1
330	3.8	4.0	2.6	2.9	32	40	-9

H.4 Chasseral Neuchâtel

H.4.1 Matrices

Population matrix $P = (p_{i,j})$ ***for the sites of Chasseral and Neuchâtel***

Prediction site index J →

Sector	0	30	60	90	120	150	180	210	240	270	300	330	
0	731	1173	1851	845	314	248	244	99	93	112	97	241	**6048**
30	279	1481	3377	1101	128	74	97	44	53	46	23	47	**6750**
60	146	1514	4978	996	138	100	62	48	60	55	22	38	**8157**
90	170	1150	4714	1485	297	148	134	71	120	134	51	53	**8527**
120	116	439	1356	716	244	242	295	117	99	115	63	45	**3847**
150	106	229	698	362	217	311	428	140	100	90	44	44	**2769**
180	129	275	743	407	266	407	649	498	591	298	141	91	**4495**
210	210	619	1813	855	501	478	704	1081	4848	2982	432	164	**14687**
240	163	566	1446	676	356	338	532	1053	4510	4517	647	153	**14957**
270	133	425	969	554	307	299	570	1169	4041	4761	1170	234	**14632**
300	293	426	840	480	368	460	647	1005	2693	3454	1788	760	**13214**
330	922	712	1196	713	465	514	570	446	907	1285	1140	1516	**10386**

	3398	**9009**	**23981**	**9190**	**3601**	**3619**	**4932**	**5771**	**18115**	**17849**	**5618**	**3386**	**108469**

Matrix Wij (*100) for the sites of Chasseral and Neuchâtel

Prediction site index J →

Sector	0	30	60	90	120	150	180	210	240	270	300	330	
0	14.9	23.9	37.7	17.2	6.4	0.0	0.0	0.0	0.0	0.0	0.0	0.0	**100**
30	0.0	24.9	56.7	18.5	0.0	0.0	0.0	0.0	0.0	0.0	0.0	0.0	**100**
60	0.0	20.2	66.5	13.3	0.0	0.0	0.0	0.0	0.0	0.0	0.0	0.0	**100**
90	0.0	15.6	64.1	20.2	0.0	0.0	0.0	0.0	0.0	0.0	0.0	0.0	**100**
120	0.0	13.3	41.2	21.7	7.4	7.4	9.0	0.0	0.0	0.0	0.0	0.0	**100**
150	0.0	9.6	29.3	15.2	9.1	13.0	17.9	5.9	0.0	0.0	0.0	0.0	**100**
80	0.0	6.7	18.0	9.8	6.4	9.8	15.7	12.0	14.3	7.2	0.0	0.0	**100**
210	0.0	0.0	15.7	7.4	0.0	0.0	0.0	9.3	41.9	25.8	0.0	0.0	**100**
240	0.0	0.0	12.5	0.0	0.0	0.0	0.0	9.1	39.1	39.2	0.0	0.0	**100**
270	0.0	0.0	8.0	0.0	0.0	0.0	0.0	9.7	33.4	39.3	9.7	0.0	**100**
300	0.0	0.0	8.0	0.0	0.0	0.0	0.0	9.5	25.6	32.8	17.0	7.2	**100**
330	10.3	7.9	13.3	8.0	0.0	0.0	6.4	0.0	10.1	14.3	12.7	16.9	**100**

	25.2	**122.1**	**370.9**	**131.3**	**29.3**	**30.2**	**49.0**	**55.6**	**164.3**	**158.6**	**39.3**	**24.1**

Matrix Zij for the sites of Chasseral and Neuchâtel

Prediction site index J →

Sector	0	30	60	90	120	150	180	210	240	270	300	330	
0	28.1	16.3	9.5	10.0	9.4	7.5	0.0	0.0	0.0	0.0	0.0	8.8	**89.5**
30	10.7	20.5	17.3	13.1	0.0	0.0	0.0	0.0	0.0	0.0	0.0	0.0	**61.6**
60	0.0	21.0	25.5	11.8	0.0	0.0	0.0	0.0	0.0	0.0	0.0	0.0	**58.3**
90	6.5	15.9	24.1	17.6	8.9	0.0	0.0	0.0	0.0	0.0	0.0	0.0	**73.1**
120	0.0	0.0	6.9	8.5	7.3	7.3	6.7	0.0	0.0	0.0	0.0	0.0	**36.8**
150	0.0	0.0	0.0	0.0	6.5	9.4	9.7	0.0	0.0	0.0	0.0	0.0	**25.7**
180	0.0	0.0	0.0	0.0	8.0	12.3	14.8	9.5	0.0	0.0	0.0	0.0	**44.6**
210	8.1	8.6	9.3	10.2	15.0	14.5	16.0	20.6	28.5	17.5	8.3	0.0	**156.6**
240	0.0	7.8	7.4	8.0	10.7	10.3	12.1	20.0	26.5	26.6	12.5	0.0	**142.0**
270	0.0	0.0	0.0	6.6	9.2	9.1	13.0	22.3	23.8	28.0	22.6	8.5	**143.0**
300	11.2	0.0	0.0	5.7	11.0	14.0	14.7	19.1	15.8	20.3	34.5	27.6	**174.1**
330	35.4	9.9	0.0	8.5	13.9	15.6	13.0	8.5	5.3	7.6	22.0	55.1	**194.7**

	100	**100**	**100**	**100**	**100**	**100**	**100**	**100**	**100**	**100**	**100**	**100**

H.4.2 Transposition from proportionality relationships $v_{pred} = a \cdot v_{ref}$

Table H.11. Mean sector wind speed ratios for the Neuchâtel site obtained from data binned according to the Chasseral (m_{ref}) and Neuchâtel (m_{pred}) wind direction. Threshold wind speed at Chasseral: 5m/s, at Neuchâtel: 0.5 m/s.

	Neuchâtel	
Sector	m_{ref}	m_{pred}
0	0.39	0.31
30	0.45	0.30
60	0.44	0.40
90	0.43	0.38
120	0.39	0.21
150	0.33	0.22
180	0.28	0.27
210	0.29	0.33
240	0.32	0.35
270	0.33	0.31
300	0.29	0.34
330	0.29	0.39

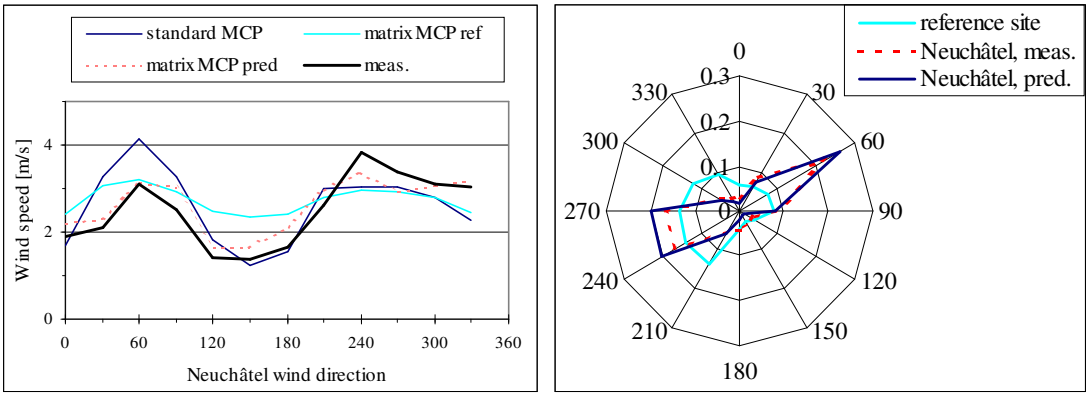

Figure H.7. Comparison of the measurements and MCP prediction using proportionality relationships for a) the sector mean wind speed and b) the wind rose.

Table H.12. Comparison of the measured and predicted sector mean wind speed at the site of Neuchâtel, using simple proportionality relationships.

Sector	Wind speed (m/s)				Relative error (%)		
	MCP-std.	MMCP-ref	MMCP-pred	Meas.	MCP-std	MMCP-ref	MMCP-pred
0	1.7	2.4	2.2	1.9	-11	28	17
30	3.3	3.1	2.3	2.1	55	44	9
60	4.1	3.2	3.1	3.1	33	3	0
90	3.3	2.9	3.0	2.5	30	16	20
120	1.8	2.5	1.6	1.4	30	77	17
150	1.2	2.3	1.7	1.4	-9	71	21
180	1.6	2.4	2.1	1.7	-6	45	26
210	3.0	2.8	3.0	2.6	15	7	13
240	3.0	3.0	3.4	3.8	-21	-23	-12
270	3.1	2.9	2.9	3.4	-9	-13	-13
300	2.8	2.8	3.1	3.1	-11	-11	-1
330	2.3	2.4	3.2	3.0	-25	-19	6

H.4.3 Transposition from relationships of the type $v_{pred} = m \cdot v_{ref} + c$

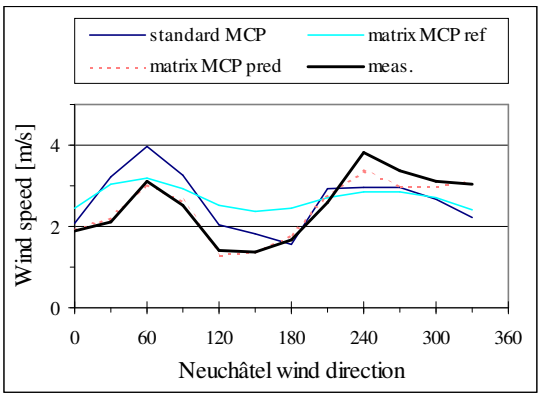

Figure H.8. Comparison of the measurements and MCP prediction using linear relationships for the sector mean wind speed.

Table H.13. Parameters from the linear regression relating the sites of Neuchâtel and Chasseral.

Sector	c_{ref}	m_{ref}	r_{ref}	c_{pred}	m_{pred}	r_{pred}
0	2.09	0.001	0.001	1.86	0.01	0.01
30	1.93	0.18	0.30	0.82	0.17	0.36
60	1.82	0.22	0.41	1.47	0.20	0.35
90	1.41	0.24	0.37	2.05	0.07	0.10
120	1.23	0.17	0.19	1.36	-0.01	-0.04
150	1.91	-0.03	-0.04	0.97	0.06	0.20
180	0.22	0.24	0.58	1.10	0.09	0.28
210	0.48	0.24	0.49	1.07	0.18	0.45
240	0.48	0.26	0.48	1.23	0.23	0.49
270	0.45	0.27	0.55	1.27	0.18	0.43
300	0.88	0.19	0.53	0.77	0.25	0.45
330	1.26	0.12	0.31	1.04	0.25	0.37

Table H.14. Comparison of the measured and predicted sector mean wind speed at the site of Neuchâtel, using linear relationships**.**

Sector	Wind speed (m/s)				Relative error (%)		
	MCP-std.	MMCP-ref	MMCP-pred	Meas.	MCP-std	MMCP-ref	MMCP-pred
0	2.1	2.5	1.9	1.9	11	31	2
30	3.2	3.0	2.2	2.1	52	44	2
60	3.9	3.2	3.0	3.1	27	2	-2
90	3.2	2.9	2.6	2.5	29	16	5
120	2.0	2.5	1.3	1.4	45	79	-9
150	1.8	2.4	1.4	1.4	31	74	1
180	1.5	2.4	1.8	1.7	-8	45	6
210	2.9	2.7	2.7	2.6	11	3	5
240	3.0	2.9	3.4	3.8	-22	-25	-12
270	3.0	2.8	3.0	3.4	-12	-16	-11
300	2.7	2.7	3.0	3.1	-14	-14	-3
330	2.2	2.4	3.1	3.0	-27	-21	2

H.5 Chasseral Chaux-de-Fonds

H.5.1 Matrices

Population matrix $P = (p_{i,j})$ ***for the sites of Chasseral and Chaux-de-Fonds***

Prediction site index J →

Sector	0	30	60	90	120	150	180	210	240	270	300	330	
0	1113	2321	703	115	6	4	27	85	432	129	96	354	**5385**
30	667	2829	2023	202	7	2	15	32	170	49	19	108	**6123**
60	571	2386	3503	510	38	6	18	27	135	36	24	114	**7368**
90	627	2001	2761	918	200	31	28	37	229	82	41	151	**7106**
120	210	408	681	600	301	93	82	80	233	147	73	75	**2983**
150	151	189	228	202	136	138	361	239	343	229	112	69	**2397**
180	100	97	101	71	43	97	556	1347	1156	550	164	77	**4359**
210	106	65	114	56	27	148	781	5245	6685	1689	254	57	**15227**
240	75	81	124	60	32	132	523	2676	9802	1364	181	39	**15089**
270	80	74	81	41	16	94	448	2211	10127	1465	248	97	**14982**
300	245	122	125	69	21	48	285	1636	6147	2843	1150	459	**13150**
330	1597	819	228	87	13	13	70	476	1690	1578	1623	1862	**10056**

	5542	**11392**	**10672**	**2931**	**840**	**806**	**3194**	**14091**	**37149**	**10161**	**3985**	**3462**	**104225**

Matrix Wij (*100) for the sites of Chasseral and Chaux-de-Fonds

Prediction site index J →

Sector	0	30	60	90	120	150	180	210	240	270	300	330	
0	22.6	47.1	14.3	0.0	0.0	0.0	0.0	0.0	8.8	0.0	0.0	7.2	**100**
30	12.1	51.3	36.7	0.0	0.0	0.0	0.0	0.0	0.0	0.0	0.0	0.0	**100**
60	8.2	34.2	50.3	7.3	0.0	0.0	0.0	0.0	0.0	0.0	0.0	0.0	**100**
90	9.9	31.7	43.8	14.6	0.0	0.0	0.0	0.0	0.0	0.0	0.0	0.0	**100**
120	8.6	16.8	28.0	24.7	12.4	0.0	0.0	0.0	9.6	0.0	0.0	0.0	**100**
150	6.8	8.5	10.3	9.1	6.1	6.2	16.3	10.8	15.5	10.3	0.0	0.0	**100**
180	0.0	0.0	0.0	0.0	0.0	0.0	15.4	37.3	32.0	15.2	0.0	0.0	**100**
210	0.0	0.0	0.0	0.0	0.0	0.0	5.4	36.4	46.4	11.7	0.0	0.0	**100**
240	0.0	0.0	0.0	0.0	0.0	0.0	0.0	19.3	70.8	9.9	0.0	0.0	**100**
270	0.0	0.0	0.0	0.0	0.0	0.0	0.0	16.0	73.4	10.6	0.0	0.0	**100**
300	0.0	0.0	0.0	0.0	0.0	0.0	0.0	13.9	52.2	24.1	9.8	0.0	**100**
330	17.4	8.9	0.0	0.0	0.0	0.0	0.0	0.0	18.4	17.2	17.7	20.3	**100**

	85.7	**198.6**	**183.2**	**55.6**	**18.5**	**6.2**	**37.1**	**133.8**	**327.1**	**99.1**	**27.5**	**27.5**

Matrix Zij for the sites of Chasseral and Chaux-de-Fonds

Prediction site index J →

Sector	0	30	60	90	120	150	180	210	240	270	300	330	
0	24.3	22.4	7.3	0.0	0.0	0.0	0.0	0.0	0.0	0.0	0.0	13.2	**67.2**
30	14.6	27.3	20.9	8.3	0.0	0.0	0.0	0.0	0.0	0.0	0.0	0.0	**71.1**
60	12.5	23.0	36.2	21.0	0.0	0.0	0.0	0.0	0.0	0.0	0.0	0.0	**92.7**
90	13.7	19.3	28.5	37.7	29.4	0.0	0.0	0.0	0.0	0.0	0.0	0.0	**128.7**
120	0.0	0.0	7.0	24.7	44.3	12.4	0.0	0.0	0.0	0.0	0.0	0.0	**88.4**
150	0.0	0.0	0.0	8.3	20.0	18.4	12.2	0.0	0.0	0.0	0.0	0.0	**58.9**
180	0.0	0.0	0.0	0.0	6.3	12.9	18.8	10.3	0.0	5.8	0.0	0.0	**54.1**
210	0.0	0.0	0.0	0.0	0.0	19.7	26.4	40.0	20.4	17.8	7.8	0.0	**132.1**
240	0.0	0.0	0.0	0.0	0.0	17.6	17.7	20.4	29.9	14.4	0.0	0.0	**100.0**
270	0.0	0.0	0.0	0.0	0.0	12.5	15.2	16.9	30.9	15.4	7.6	0.0	**98.5**
300	0.0	0.0	0.0	0.0	0.0	6.4	9.6	12.5	18.8	30.0	35.1	17.2	**129.5**
330	34.9	7.9	0.0	0.0	0.0	0.0	0.0	0.0	0.0	16.6	49.6	69.6	**178.6**
	100	**100**	**100**	**100**	**100**	**100**	**100**	**100**	**100**	**100**	**100**	**100**	

H.5.2 Transposition from proportionality relationships $v_{pred} = a \cdot v_{ref}$

Table H.15. Mean sector wind speed ratios for the Chaux-de-Fonds site obtained from data binned according to the Chasseral (m_{ref}) and Chaux-de-Fonds (m_{pred}) wind direction. Threshold wind speed at Chasseral: 5m/s, at Chaux-de-Fonds: 0.5 m/s.

	Chaux-de-Fonds	
Sector	m_{ref}	m_{pred}
0	0.49	0.32
30	0.52	0.45
60	0.40	0.44
90	0.34	0.39
120	0.30	0.38
150	0.32	0.32
180	0.38	0.34
210	0.34	0.36
240	0.36	0.34
270	0.35	0.23
300	0.27	0.25
330	0.25	0.27

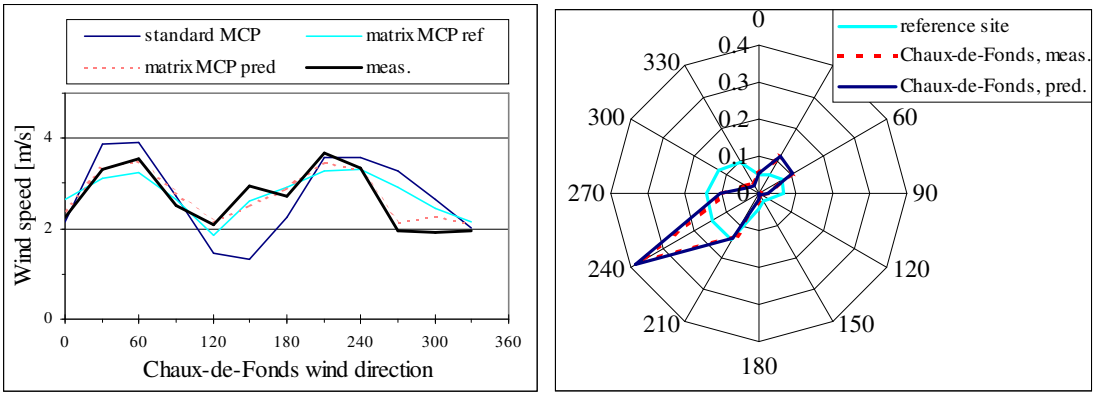

Figure H.9. Comparison of the measurements and MCP prediction using proportionality relationships for a) the sector mean wind speed and b) the wind rose.

Table H.16. Comparison of the measured and predicted sector mean wind speed at the site of Chaux-de-Fonds, using simple proportionality relationships.

Sector	Wind speed (m/s)				Relative error (%)		
	MCP-std.	MMCP-ref	MMCP-pred	Meas.	MCP-std	MMCP-ref	MMCP-pred
0	2.1	2.7	2.4	2.3	-5	18	5
30	3.9	3.1	3.3	3.3	17	-6	1
60	3.9	3.3	3.5	3.5	10	-8	0
90	2.7	2.6	2.8	2.5	8	4	12
120	1.4	1.8	2.2	2.1	-31	-11	3
150	1.3	2.6	2.5	3.0	-56	-11	-16
180	2.3	2.9	2.9	2.7	-18	7	6
210	3.6	3.3	3.5	3.7	-2	-11	-5
240	3.6	3.3	3.3	3.4	7	-1	-1
270	3.3	2.9	2.2	2.0	66	48	9
300	2.6	2.5	2.3	1.9	37	27	18
330	2.0	2.1	2.1	2.0	3	9	8

H.5.3 Transposition from relationships of the type $v_{pred} = m \cdot v_{ref} + c$

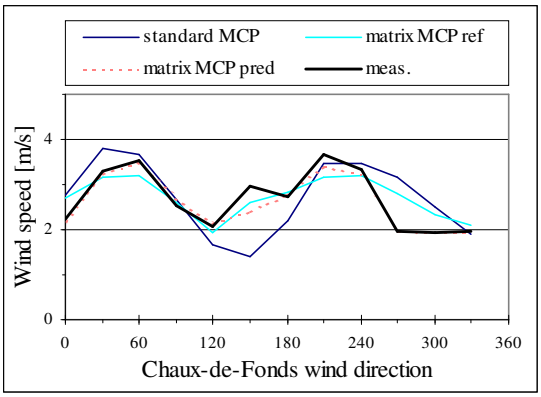

Figure H.10. Comparison of the measurements and MCP prediction using linear relationships for the sector mean wind speed.

Table H.17. Parameters from the linear regression relating the sites of Chaux-de-Fonds and Chasseral.

Sector	c_{ref}	m_{ref}	r_{ref}	c_{pred}	m_{pred}	r_{pred}
0	3.29	-0.12	-0.12	1.46	0.10	0.28
30	2.45	0.18	0.34	2.43	0.11	0.25
60	2.12	0.16	0.34	1.84	0.20	0.39
90	1.16	0.19	0.39	1.12	0.22	0.42
120	1.33	0.07	0.14	1.32	0.14	0.42
150	0.39	0.25	0.37	-0.29	0.35	0.74
180	-0.03	0.37	0.67	0.97	0.21	0.49
210	0.56	0.27	0.51	0.43	0.31	0.62
240	0.49	0.30	0.47	0.86	0.24	0.46
270	0.50	0.29	0.54	0.97	0.11	0.34
300	0.82	0.17	0.58	1.32	0.07	0.26
330	1.46	0.05	0.23	1.20	0.09	0.30

Table H.18. Comparison of the measured and predicted sector mean wind speed at the site of Chaux-de-Fonds, using linear relationships.

Sector	Wind speed (m/s)				Relative error (%)		
	MCP-std.	MMCP-ref	MMCP-pred	Meas.	MCP-std	MMCP-ref	MMCP-pred
0	2.8	2.7	2.2	2.3	23	21	-4
30	3.8	3.2	3.2	3.3	15	-4	-2
60	3.7	3.2	3.5	3.5	3	-10	-1
90	2.7	2.6	2.7	2.5	5	3	7
120	1.7	1.9	2.1	2.1	-20	-7	2
150	1.4	2.6	2.4	3.0	-53	-12	-19
180	2.2	2.8	2.8	2.7	-20	4	1
210	3.5	3.2	3.4	3.7	-6	-14	-7
240	3.5	3.2	3.2	3.4	4	-5	-4
270	3.2	2.8	2.0	2.0	61	42	-1
300	2.5	2.3	1.9	1.9	29	20	1
330	1.9	2.1	1.9	2.0	-3	7	-1

Appendix I

I Analytical formulations for the boundary layer profiles

I.1 Alexandrou's formulation

Using the boundary layer thickness h and the dissipation length l_ε as scaling variables for the boundary layer, Alexandrou (1996) proposes the following formulation for the u velocity profile over a flat plate with zero pressure gradient

eq. I.1 $$\frac{u}{u_*} = \frac{1}{\kappa}\left[\ln(\frac{\eta}{\eta + c}) - (\frac{c}{1+c} + a)\frac{\eta^2}{2} + a\eta + B - \ln(\kappa)\right]$$

where $\eta = z/h$, κ stands for the von Karman constant and a, c and B are constants of the model. In order to ensure the logarithmic behaviour of the profile close to the ground, a and c must satisfy $a = 1/c$. A relationship between B, u_*, h, a and c can be derived from the identity $u(z = h) = U_\infty$ which reads

eq. I.2 $$B = \frac{U_\infty}{u_*}\kappa - \ln(\frac{1}{1+c}) + \frac{1}{2}(\frac{c}{1+c} + a) - a + \ln\kappa$$

The advantage of Alexandrou's formulation is that it is valid for rough as well as for smooth terrain conditions.

For **rough terrain**, characterised by a roughness length z_0, the usual way of describing the velocity profile in the proximity of the ground is to use a relationship of the form

eq. I.3 $$\frac{u}{u_*} = \frac{1}{\kappa}\ln(\frac{z}{z_0})$$

Recognising that the velocity profile from Alexandrou's formulation must tend to a logarithmic profile for small values of η, one obtains the following to relate z_0 to the constants of Alexandrou's model:

eq. I.4 $$\ln(\frac{z}{z_0}) = \ln(\frac{z}{ch}) + B - \ln(\kappa)$$

Identifying the parts that do not depend on z, this becomes

eq. I.5 $$B = \ln(\frac{ch\kappa}{z_0})$$

Whereas for **smooth conditions**, Alexandrou obtains the approximation

eq. I.6 $$B \approx \ln(\frac{u_* h\kappa}{\nu})$$

The profile used to initialise the turbulent dissipation rate is

eq. I.7 $$\varepsilon = \frac{u_*^3}{h \cdot l_\varepsilon} = \frac{u_*^3}{h\kappa\eta} \cdot \exp\left\{-\left[\left(\frac{c}{1+c} + a\right) \cdot \frac{\eta^2}{2}\right]\right\}$$

A profile for the turbulent kinetic energy k was obtained from the assumption that

eq. I.8 $$\frac{\kappa z \varepsilon}{u_*^3} = \frac{\tau}{\tau_0}$$

With $\tau = \rho \cdot C_\mu \frac{k^2}{\varepsilon}\frac{\partial u}{\partial z}$ and $u_*^2 = \tau_0/\rho$, the turbulent kinetic energy k can be expressed as

eq. I.9 $$k = \left(\frac{\kappa z}{C_\mu \cdot u_*}\right)^{1/2} \cdot \varepsilon \cdot \left(\frac{\partial u}{\partial z}\right)^{-1/2}$$

where $\partial u / \partial z$ is obtained from eq. I.1:

eq. I.10 $$\frac{\partial u}{\partial z} = \frac{u_*}{h\kappa} \cdot \left[\frac{c}{\eta(\eta + c)} - \left(\frac{c}{1+c} + a\right)\eta + a\right]$$

For a boundary layer developing over flat smooth terrain, Alexandrou showed that his formulation was able to fit Klebanoff's measurements (Alexandrou, 1996) for the mean velocity profiles with c taking the value of 0.166 and B being set to 7.326. Simulating the boundary layer development over flat terrain with CFX4, we found that, for both smooth and rough ground conditions, the mean velocity profiles could be fitted by Alexandrou's formulation, with a value of the constant c which varied between 0.182 and 0.184 (see appendix A section A.2.2).

I.2 Deaves & Harris formulation

The parameterisation proposed by Deaves and Harris (1978) for the **wind speed profile** is briefly described below.

Within the boundary layer, ($0 < z < h$), the wind speed is set to be a function of z, the height above ground level, according to:

eq. I.11 $$u(z) = \frac{u_*}{\kappa}\left[\ln\left(\frac{z}{z_0}\right) + a_1 \cdot \left(\frac{z}{h}\right) + a_2 \cdot \left(\frac{z}{h}\right)^2 + a_3 \cdot \left(\frac{z}{h}\right)^3 + a_4 \cdot \left(\frac{z}{h}\right)^4\right]$$

with $a_1 = 5.75$, $a_2 = 1 - a_1/2$, $a_3 = -4/3$ and $a_4 = 0.25$, κ being the von Karman constant.

Above the boundary layer height ($z \geq h$), the wind speed is set to the value of the geostrophic wind speed G. The value of u_* is determined for a given geostrophic wind speed and roughness length z_0 by solving:

eq. I.12 $$\frac{G}{u_*}=\frac{1}{\kappa}\left[\ln(\frac{u_*}{f\cdot z_0})-A\right]$$

with $f=10^{-4}$ the Coriolis parameter and *A=-1.*

Eq. I.12 follows from eq. I.11 with the substitution $u(h)=G$ where the boundary layer height is given by:

eq. I.13 $$h=\frac{u_*}{6\cdot f}$$

From experiments in nearly homogeneous shear flows along the *x* direction, Harris et al (1977) obtain the following relationships for the diagonal elements of the stress tensor

eq. I.14 $$\frac{u'^2}{k}\cong 1 \qquad \frac{v'^2}{k}\cong 0.4 \qquad \frac{w'^2}{k}\cong 0.6$$

which allows us to derive the turbulent kinetic energy $k=\frac{1}{2}(u'^2+v'^2+w'^2)\cong u'^2=\sigma_x^2$.

Deaves and Harris proposed an 'empirical expression matching most of the known dataset' for the standard deviation of the velocity σ along the main flow direction which reads

eq. I.15 $$\sigma=2.63\cdot u_*\cdot(1-\frac{z}{h})\cdot\left[0.538+0.09\ln(\frac{z}{z_0})\right]^{(1-\frac{z}{h})^{16}}$$

and which will finally be used to initialise the profile for the turbulent kinetic energy with

eq. I.16 $$k=\sigma^2$$

The turbulent energy dissipation rate ε is obtained from

eq. I.17 $$\varepsilon=\frac{\tau}{\rho}\frac{\partial u(z)}{\partial z}$$

With the stress tensor τ obeying

eq. I.18 $$\tau=\rho\cdot u_*^2\cdot(1-\frac{z}{h})^2$$

the dissipation rate becomes:

eq. I.19 $$\varepsilon=\frac{u_*^3}{\kappa}\cdot\frac{(1-\frac{z}{h})^2}{z}\cdot\left[1+a_1\cdot\left(\frac{z}{h}\right)+2\cdot a_2\cdot\left(\frac{z}{h}\right)^2+3\cdot a_3\cdot\left(\frac{z}{h}\right)^3+4\cdot a_4\cdot\left(\frac{z}{h}\right)^4\right]$$

A comparison between the Deaves and Harris and the Alexandrou formulation for a situation defined by the parameters given in Table I.1 is given below.

Up to an altitude of about 100m, the mean velocity profiles are the same. Above this height, the Deaves & Harris formulation gives higher wind speeds. The turbulent

dissipation rates of both formulations present a very similar behaviour. The most striking difference between these two formulations concerns the turbulent kinetic energy profiles. The values of k' obtained from Deaves & Harris are generally higher than the ones obtained from Alexandrou. Moreover, the behaviour of the k' profiles are quite different. When the Deaves & Harris profiles show increasing values from the ground reaching a maximum for k' between 20 and 30 m and then decreasing again until the top of the boundary layer, the Alexandrou formulation predicts a more or less constant value of k' for the lowest 70 m of the atmosphere, followed by a slower decrease until the top of the boundary layer.

Table I.1. Constants determining the profiles presented in Figure I.1, Figure I.2 and Figure I.3**.**

	Deaves and Harris formulation	Alexandrou formulation
u_* [m/s]	0.654	0.654
z_0 [m]	0.03	-
$h = u_*/6f$ [m]	1090	1090
c [-]	-	0.183
B [-]	-	7.91

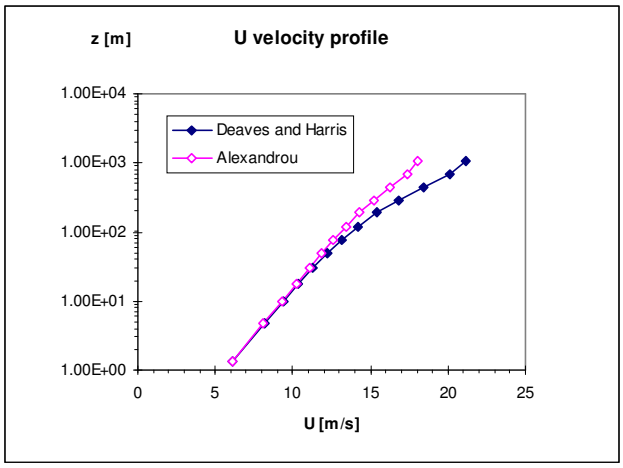

Figure I.1. Comparison of velocity profiles from the Deaves & Harris and Alexandrou formulation for same ground roughness and friction velocity. Profiles used for initial and boundary conditions.

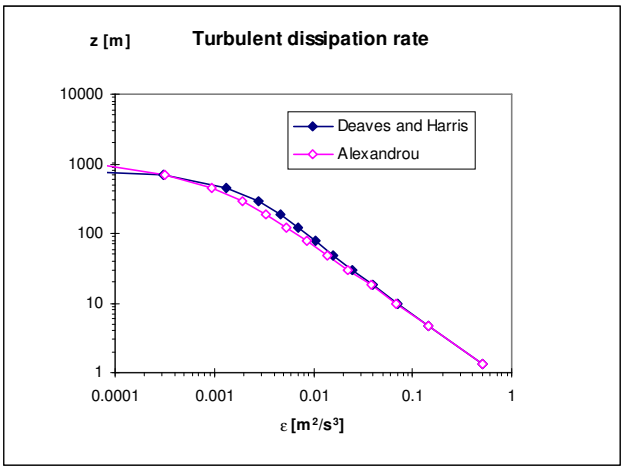

Figure I.2. Comparison of turbulent dissipation rate profiles from the Deaves & Harris and Alexandrou formulation for same ground roughness and friction velocity. Profiles used for initial and boundary conditions.

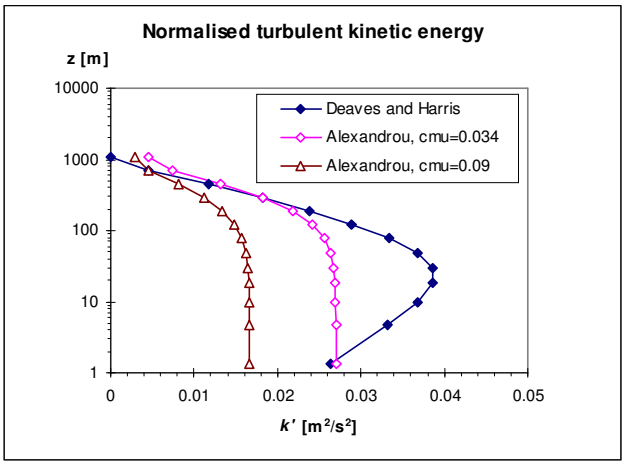

Figure I.3. Comparison of normalised turbulent kinetic energy profiles from the Deaves & Harris and Alexandrou formulation for same ground roughness and friction velocity. Profiles used for initial and boundary conditions.

Appendix J

J Calibration curves for SIAP and SCHASTA type instruments

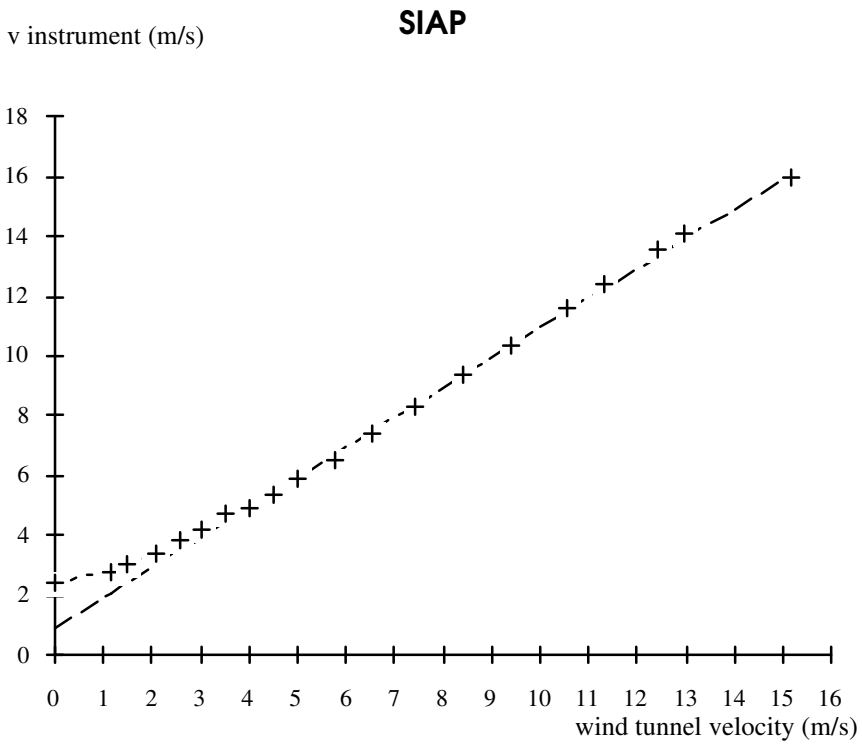

Figure J.1. Calibration curve for the SIAP anemometer.

The analytical expressions corresponding to the fits presented in Figure J.1 are the following ones:

$$v(instr) = a + b \cdot v \qquad \text{for : } v > 5 \text{ m/s}$$
$$= c + d \cdot v + e \cdot v^2 \qquad v < 5 \text{ m/s}$$

with:

$a = 0.92$
$b = 1$
$c = 2.4$
$d = 0.3$
$e = 0.08$

Note: $v(instr)$ is the velocity measured by the instrument when the wind blows with a velocity v.

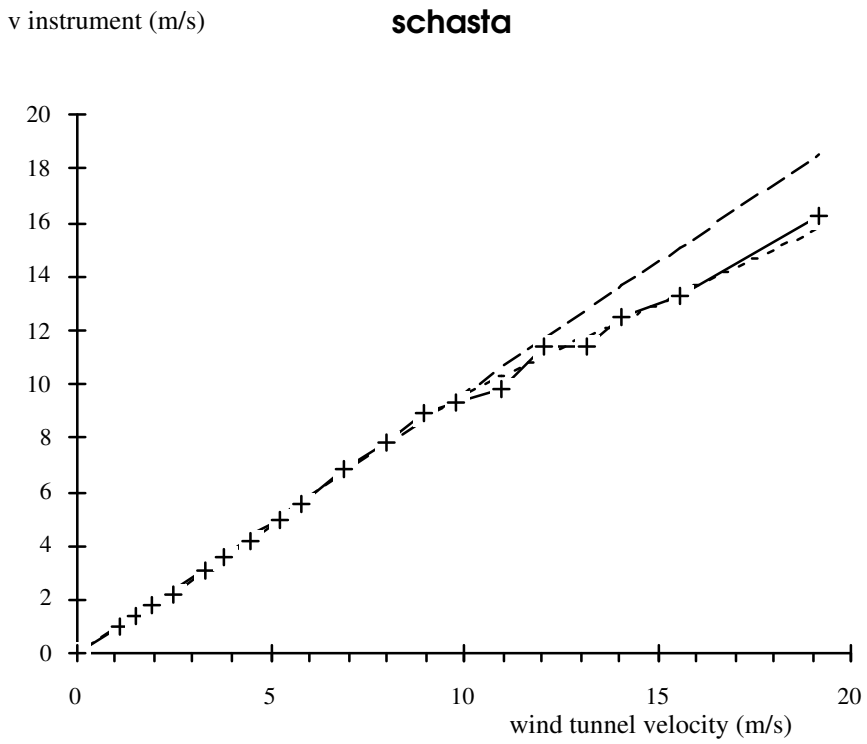

Figure J.2. Calibration curve for the SCHASTA anemometer.

The analytical expressions corresponding to the fits presented in Figure J.2 are the following ones:

$$v(instr) = a + m \cdot v \qquad \text{for:} \quad v < 10 \ \text{m/s}$$
$$= a + m \cdot v - b \cdot (v - c) \qquad v > 10 \ \text{m/s}$$

with:

$m = 0.97$
$a = 0$
$b = 0.3$
$c = 9.75$

Note: $v(instr)$ is the velocity measured by the instrument when the wind blows with a velocity v.

Appendix K

K Simple classification of the meteorological situations occurring over the Chasseral area.

From one year of wind data recorded at Chasseral and on the Ajoie Plateau, Fallot & Hertig (1991) sorted the occurring meteorological situations into two groups. The first one is characterised by situations that are essentially advective (57.4% of the cases), showing persistent winds on the Ajoie Plateau, and the second one is thermally dominated (42% of the cases), with variable (breeze) winds in Ajoie.

For all the situations, Fallot calculated, for twelve wind directions, their frequency of occurrence, the mean wind speed at Chasseral and the mean thermal stratification and ended up with the values given in Table K.1 and Table K.2. The situations showing variable wind at Chasseral were attributed to an additional bin labelled 'var'.

The vertical temperature gradients were calculated with ground temperatures measured at two stations showing an altitude difference of 400m. The temperature gradients so-obtained are strongly affected by local effects and might therefore not be representative of the free flow stratification. This explains why, especially for the thermally dominated situations Fallot obtains such a big range of variation for the vertical temperature gradients.

Table K.1. Chasseral mean wind speed and mean vertical temperature gradient for situations showing persistent winds in Ajoie. The frequency of occurrence of the situation is also given.

Chasseral wind direction [°]	Chasseral wind speed [m/s]	Frequency of occurrence [%]	Vertical temperature gradient [K/km]
30	6.94	3.3	-4.8
60	9.04	2.6	-4.4
90	9.68	4.0	-4.4
120	6.51	0.8	-5.3
150	6.17	0.1	-6.5
180	10.13	1.0	-6.5
210	13.47	11.1	-5.8
240	11.57	7.9	-6.9
270	10.45	11.5	-7.2
300	12.13	7.4	-7.3
330	9.32	6.4	-8.8
360	6.31	1.0	-6.8
Var.	6.17	0.3	-9.0
Average	10.79	57.4	-7.7

Table K.2. Same as Table K.1 for breeze situations in Ajoie.

Chasseral wind direction [°]	Chasseral wind speed [m/s]	Frequency of occurrence [%]	Vertical temperature gradient [K/km]
30	6.29	2.3	-4.1 to +1.8
60	6.34	1.2	-8.7 to –2.2
90	5.18	4.0	-8.8 to +0.9
120	4.51	2.3	-6.2 to –0.8
150	6.51	0.8	-6.3 to –1.2
180	5.43	1.2	-7.4 to +0.5
210	6.86	8.3	-2.0 to –0.1
240	7.04	2.6	-5.4 to –0.8
270	5.73	4.5	-7.4 to –0.5
300	5.77	3.1	-5.7 to –2.9
330	4.78	1.4	-5.7 to –0.4
360	4.93	1.6	-6.7 to –2.1
Var.	2.60	9.3	-5.4 to –0.1
Average	5.23	42.6	-5.4 to +0.1

Appendix L

L Boundary conditions types.

According to the terminology used in the CFX4 user guide (CFX, 1997), the various types of boundary conditions used in this work are the so called inlet, pressure, wall, symmetry and periodic boundary conditions. The kind of treatment applied to the flow variables for the various boundary condition type is briefly summarised below.

L.1 Inlet

All the flow variables (u, v, w, θ, k and ε) apart from the pressure are imposed Dirichlet boundary conditions at an inlet face.
For the pressure, a Neumann boundary condition is used.

L.2 Pressure

At pressure boundaries, Dirichlet boundary conditions are used for the pressure.
For outflow situations through a pressure boundary, Neumann boundary conditions (zero normal gradients) are set for the velocity components, for k and ε as well as for the potential temperature. In this case, the type of conditions specified is equivalent to the assumption of fully developed flow through the boundary face. It should therefore be avoided to have strong terrain slopes close to pressure boundaries.
For inflow situations, the velocity components as well as k and ε are imposed Neumann boundary conditions (zero normal gradients). The potential temperature is imposed Dirichlet conditions

L.3 Mass flow boundaries

The mass flow boundary condition is similar to the pressure boundary condition, with the difference that pressure is imposed a Neumann instead of a Dirichlet boundary condition.

L.4 Wall

At a wall boundary both the free slip/no slip boundary conditions are available for the velocity components. Unless otherwise specified, the wall boundary condition for the potential temperature assumes a zero flux through the wall.
A special treatment is applied for the k and ε variables close to the wall as described in Section 5.2.2. The behaviour of the velocity and potential temperature close to the wall is considered through wall functions.

L.5 Symmetry

At symmetry planes, all variables are mathematically symmetric across the boundary apart from the normal velocity which is antisymmetric.

L.6 Periodic boundaries

The periodic plane boundary condition is quite straightforward, with all the variables having the same values at both ends of the computational domain (periodic planes).

MONTAVON Christiane
ch. des Aubépines 39
1004 LAUSANNE
born on the 5th of January 1969
single
021/ 647 16 76 (private)
021/ 693 23 07 (prof.)

QUALIFICATION: PHYSICIST ETHZ

EDUCATION

1996	Postgraduate Study in Fluid Dynamics, IMHEF, EPF Lausanne and Ecole Centrale de Lyon.
started in 1995	PhD research aiming at the development of a methodology and numerical tool for wind power potential assessment
1993-1994	Postgraduate Study in Energy, Laboratory of Energy Systems, EPF Lausanne
1987-1992	MSc. Degree in Physics, ETH Zurich
1984-1987	Baccalauréat, Lycée cantonal, Porrentruy

WORKING EXPERIENCE

1993-1997	Research assistant at the Laboratory of Energy Systems at EPF Lausanne, working in the field of numerical simulation of atmospheric processes over complex topography. Main field of application: -boundary layer flow simulation for wind power potential assessment -probable maximum precipitation estimation over the Alps (CRUEX project)
1988-1992	Part time teaching in secondary schools

LANGUAGES

French	mother tongue
English	fluent
German	fluent (5 years in Zurich)
Spanish	basic knowledge (2 ½ months in South America)

COMPUTING SKILLS

Programming	FORTRAN (5 years)
Computer systems	UNIX, VMS
Visualisation	AVS, UNIGRAPH
Office	EXCEL, WORD, POWERPOINT

INTERESTS

sports	volleyball, badminton, skiing, cycling
other hobbies	cinema, reading, travelling

Scientific Know-how

Description	*Examples of Applications*
Numerical simulation of wind and precipitation. *Simulation of atmospheric flows using the ASTEC and FLOW3D codes. Statistical analysis of hydrometeorological data.*	• Extreme floods in the Alpine terrain: Estimation of Probable Maximum Precipitation using numerical simulation of atmospheric flows.
Site to site wind data transposition. *Numerical simulation of boundary layer flows over complex topography, Validation of model results for flows strongly coupled to the geostrophic wind and for thermally driven flows. Classification of meteorological situations.*	• Wind power potential evaluation over complex topography. • Micrositing of wind turbines on a given site. • Effect of the local topography on a wind climate.
Statistical analysis of extreme winds and associated return periods. *Meteorological data analysis, Gumbel regression, return period, gusts.*	• Determination of the exposure to extreme wind conditions for the Mentue valley bridges. • Analysis of extreme wind conditions with respect to duration using high-altitude measurement stations .
Gaussian plume dispersion.	• Buoyant plume dispersion modelling and estimation of the annual risk of ice formation on a nearby road.
Flow field visualisation using AVS.	• Animated visualisation of simulation results for a diurnal cycle simulation.
Modelling of the radiation transfer through the sun photosphere. *Infrared polarised light, Zeeman effect, spectra inversion, line shift and velocity (Doppler effect).*	• Magnetic field structure of sunspots. • Broad band circular polarisation of sunspots. • Velocity field estimation in sunspot penumbrae.

Publications of the author (1992-1998)

1. Montavon, C., 1992, 'Magnetic Field Structure of Sunspots from Infrared Data', *Diploma Thesis*, Astronomy Institute, ETH Zurich.
2. Solanki, S.K., Montavon, C.A.P., 1993, 'Uncombed Fields As The Source Of The Broad-Band Circular Polarisation Of Sunspots', in *Astron. & Astrophys.* 275,pp.283-292.
3. Solanki, S.K., Montavon, C.A.P., W. Livingston, 1994, 'Infrared Lines As Probes Of Solar Magnetic Features. VII. On The Nature Of The Evershed Effect In Sunspots', in *Astron. & Astrophys.* 283, pp.221-231.
4. Solanki, S.K., Montavon, C.A.P., W. Livingston, 'On The Nature Of The Evershed Effect', in *'Solar Magnetic Fields', M. Schüssler, W.Schmidt (Eds),* 1994, Cambridge Univ. Press.
5. Solanki, S.K., Montavon, C.A.P., 1994, 'Some Consequences Of An Uncombed And Inhomogeneous Penumbra', in *'Solar surface magnetism', R.J. Rutten, C. Schrijver (Eds),* 1994, Klüwer Acad. Publ.
6. Montavon, C., 1995, 'Wind Potential Evaluation Over Complex Terrain By Means Of A Numerical Model: Application To One Site In The Swiss Jura Mountains', *MSc thesis, Postgraduate Study in Energy*, EPF Lausanne, LASEN.
7. Montavon, C., 1995, 'Some Thoughts On A Future Sustainable Energy System' *Youth Energy Symposium* Sessions, Tokyo (World Energy Conf., October 1995).
8. Montavon, C., Alexandrou, C., Hertig, J.-A., 1995, 'Simulation of Extreme Precipitation Events in the Swiss Alps', *Symposium 'Research and Developments in the Field of Dams'* (Crans-Montana, September 1995).
9. Montavon, C., Alexandrou, C., Hertig, J.-A., 1996. 'Wind Potential Evaluation Over Complex Terrain By Means Of A Three-Dimensional Atmospheric Numerical Model', in *Proceedings Of The European Union Wind Energy Conference*, Goeteborg, 526-529. (Poster prize awarded).
10. Montavon, C., 1996, 'Validation du modèle numérique non-hydrostatique FLOW3D pour la simulation d'écoulements atmosphériques stratifiés en terrain accidenté', postgraduate course in fluid mechanics, IMHEF, EPF Lausanne.
11. Montavon, C., 1997, 'Estimation des précipitations orographiques maximales probables par modélisation numérique', in *Communication No.5*, Laboratoire des Constructions Hydrauliques, EPF Lausanne.
12. Montavon, C., 1997, 'Validation Of A Non-Hydrostatic Numerical Model To Simulate Stratified Wind Fields Over Complex Topography', in *Proceedings of the 2nd European & African Conference on Wind Engineering*, Genova, Italy, June 22-27, 1997, pp 357-364. (accepted for publication *in Jour. Of Wind Engineer. & Industr. Aerodynamics*)
13. Montavon, C., 1998, 'Askervein Hill site: a sensitivity study using the numerical model CFX4 testing the effect of the flow parameters on the resulting flow field', *Rapp. Interne no.548.104*, LASEN, EPFL, 1015 Lausanne.